Experimental study of breach mechanics in overtopped noncohesive earthen embankments

Mahmoud Al-Riffai

Thesis submitted to the
Faculty of Graduate and Postdoctoral Studies
In partial fulfillment of the requirements for the degree of

Doctorate of Philosophy in Civil Engineering (Water Resources)

Under the auspices of the Ottawa-Carleton Institute of Civil Engineering (OCICE)

Department of Civil Engineering
Faculty of Engineering
University of Ottawa

© Mahmoud Al-Riffai, Ottawa, Canada, 2014

Ioan Nistor (University of Ottawa)

DIRECTEUR (DIRECTRICE) DE LA THÈSE / THESIS SUPERVISOR

EXAMINATEURS (EXAMINATRICES) DE LA THÈSE / THESIS EXAMINERS

Ana Maria A.F. da Silva (Queen's University)

Paul J. Van Geel (Carleton University)

Colin D. Rennie (University of Ottawa)

Sai K. Vanapalli (University of Ottawa)

Thursday, July 17, 2014

DATE DE LA SOUTENANCE / DATE OF ORAL DEFENCE

Thesis Committee following defence, 17th July 2014. From left to right: Prof. Paul Van Geel, Dr. Ioan Nistor, Mahmoud Al-Riffai, Prof. Sai K. Vanapalli, Prof. Ana Maria da Silva, Prof. Colin D. Rennie (*Absent: Dr. Eric Lanteigne, Committee Chair*) (*photo courtesy of Amanj Jamal*)

Abstract

A comprehensive experimental program dealing with three-dimensional overtopping and breach development as well as two-dimensional overtopping physical tests of noncohesive earth embankments has been conducted on scale models in the Hydraulic Laboratory at the Department of Civil Engineering at the University of Ottawa. The experimental program which consisted of three phases focused on geotechnical and hydraulic aspects of the embankment breach mechanism. The first two phases focused on two test series for the three-dimensional breach overtopping tests: drainage and compaction. The test series were designed to determine the embankment breach characteristics using test parameters which have not been adequately identified or controlled in past noncohesive physical models: initial soil-water state and optimum dry unit weight. Both parameters were controlled in laboratory tests by means of compaction effort and seepage through the embankment body, respectively. The dynamic compaction technique employed in the preliminary experimental phase was refined to represent a more realistic method. A novel method was thus designed to simulate the construction of a real-size prototype embankment, where a vibratory and static load was used to apply and control, respectively, the compaction effort. The hydraulic aspects of the embankment breach mechanism were also investigated. For the first time, scale series tests have been used to assess the Froude criterion using tilted and quasi-exact geometric scales under very low inflow within the scope of three-dimensional breach overtopping. Data measurements included a time-history of water surface levels and video footage captured from three locations: upstream, downstream and above the embankment models. The analysis for the spatial breach overtopping tests involved measurement of the breach outflow hydrograph and breach channel evolution at the upstream slope, using hydrologic routing and a developed photogrammetric technique using the video footage, respectively. An expression

which estimates the breach outflow based on this apparent upstream control section was therefore derived. The relationship between the measured and estimated breach outflow was expressed in terms of breach discharge efficiency.

The third phase of the experimental program was comprised of two-dimensional overtopping tests to investigate the erodibility of a steep slope in overtopped noncohesive embankment models. A novel experimental two-dimensional configuration used to measure the pore-water-pressures within the embankment model body was developed using micro and standard tensiometer-transducer-probe assemblies, designed, assembled and tested at the Geotechnical Engineering Laboratory. A transient flownet analysis was developed using ArcGIS and the time-history of the pore-water-pressure measurements. All flow parameters were computed using the free water surface and bed profiles captured using a photogrammetric technique and the developed hydrologic routing method. Using the one-dimensional Saint-Venant equations, an analytical expression for the bed shear stress was derived to take into account the effects of unsteady flow, boundary seepage and steep slopes. Using the measured erosion rates and the sediment continuity principle, the bed mobility relationship expressed by the Shields and transport parameters was revisited to account for the effects of unsteady and supercritical flow on a downstream steep slope in the presence of boundary seepage. This novel transient flownet approach will lead to the development of new sediment mobility relationships for breach flows, instead of the classical sediment transport-capacity formulations which are based on steady, subcritical and normal flow conditions.

Résumé

Un programme expérimental intensif traitant le débordement et l'évolution de la brèche en trois dimensions, ainsi que le débordement en deux dimensions d'un ouvrage hydraulique en remblai (barrage ou digue) a été mené. Ces tests physiques ont été effectués sur des modèles réduits de remblais en matériaux non cohésifs dans le laboratoire hydraulique du Département de génie civil de l'Université d'Ottawa. Le programme expérimental comprennait trois phases axé sur les aspects géotechniques et hydrauliques et leur impact sur le mécanisme de la brèche. Les deux premières phases ont porté sur deux séries de tests pour le débordement en trois dimensions: le drainage et le compactage. La série de tests a été conçue pour déterminer les caractéristiques de la brèche digue en utilisant des paramètres de tests qui n'ont pas été identifiés ou mal contrôlés dans des modèles physiques antécédents sur des matériaux non cohésifs: le poids sec unitaire optimal et l'état hydrique initial du sol. Ces deux paramètres ont été contrôlés en laboratoire au moyen de l'effort de compression et un système de drainage du remblai, respectivement. La technique de compactage dynamique employée dans la phase expérimentale préliminaire a été faite de manière améliorée afin d'utiliser une méthode plus réaliste. Cette nouvelle méthode a été conçue pour simuler la construction d'un prototype réel de remblai, où une charge en vibration et une charge statique a été utilisées pour appliquer et contrôler, respectivement, les efforts de compactage. Les aspects hydrauliques du mécanisme d'évolution de la brèche du remblai ont également été étudiés. C'est la première fois que des tests sur un série d'échelles dans de tests de débordement en trois dimensions ont été utilisées pour évaluer le critère de Froude à l'aide d'échelles géométriques inclinés et quasi-exactes sous très faible apport. Les données mesurées incluent un historique temporel des niveaux de surface d'eau et des vidéos enregistrées à partir de trois endroits: en amont, en aval et au-dessus du remblai. L'analyse des tests tridimensionnels du débordement comprend les mesures de l'hydrogramme du débit

de sortie de la brèche et l’évolution du canal de la brèche formé du côté en amont en utilisant la méthode de «laminage hydrologique» et une technique photogramétrique avec des vidéos enregistrées, respectivement. Une expression qui estime le débit de sortie de la brèche sur la section apparente est ainsi obtenue. La relation entre les mesures et les estimations du débit de sortie de la brèche est considérée comme un paramètre d'efficacité du débit de la brèche.

La troisième phase du programme expérimental est composée de tests en deux dimensions du débordement pour étudier l'érosion de la descente raide dans les modèles de remblai non cohésifs sujet du débordement. Une nouvelle configuration expérimentale en deux dimensions utilisée pour mesurer la pression interstitielles à l'intérieur du remblai du modèle a été développée en utilisant des tensiomètres électroniques très petite taille et d’autres de taille conventionnelle, conçus, assemblés et testés au laboratoire géotechnique. Une analyse de réseau d’écoulement transitoire a été développée en utilisant ArcGIS et les mesures de l’évolution temporelle de la pression interstitielle. Tous les paramètres du débit ont été calculés en utilisant la surface libre de l’eau et les profils du fond à l'aide d'une technique de photogrammétrie et la méthode de laminage hydrologique développé. En utilisant les équations unidimensionnelles de Saint-Venant, une expression analytique de la contrainte de cisaillement du fond a été introduite pour prendre en compte les effets de l'écoulement instable, les infiltrations aux limites et les descentes raides du remblai. En utilisant les mesures d'érosion et le principe de la continuité des sédiments, la relation de la mobilité du fond exprimée par la formule Shields et le paramètre de transport a été revue pour tenir compte des effets de l'écoulement instable et supercritique sur une descente raide en présence d'une infiltration aux limites. Cette nouvelle approche conduit à l'établissement de nouvelles relations de transport des sédiments pour les débits de la brèche, à la place des formules classiques de transport des sédiments qui sont basés sur des conditions de débit stationnaire constant, conditions d'écoulement sous-critiques et normales.

Acknowledgements

I would like to express my sincere and profound gratitude to my thesis supervisor, Dr. Ioan Nistor, for supporting and guiding me throughout this journey that I have embarked over the past few years. Indeed he has gone beyond his duty as a thesis supervisor as he has also assumed the role of both a mentor and a friend during my academic career. His patience and invaluable moral support as well as his belief in my capabilities of both a researcher and teacher, has earned me great professional achievements. He has never failed to endorse me in such prospects and I shall never forget this support.

I am also grateful to Professor Sai Vanapalli for his continuous encouragement and endorsement throughout my academic career, as well as bestowing me his knowledge in the field of classical and unsaturated soil mechanics. I would also like to thank Professor Colin Rennie, Dr. Won Taek Oh and Dr. Jules-Angel Infante-Sedano for their advice and discussion on some of the experimental aspects of this this research. Many thanks are directed to Professor Paul Van Geel, from Carleton University, a member of my PhD advisory committee for his valuable comments on the progress and contribution of this thesis. Certainly, the above mentioned, as well as many other professors at the Faculty of Engineering as a whole, have been an inspiration to both my research and teaching experience at the University of Ottawa.

I would also like to express my sincere appreciation to the following technical staff at the University of Ottawa for providing me with expert advice and extraordinary assistance in the acquisition as well as development of the equipment and tools necessary to conduct this research, and from whom I have learnt a vast and instrumental knowledge:

- Mark Lapointe, Technical Officer of the Hydraulics Laboratory;

- Jean-Claude Celestin, current Technical Officer and Kulan Ambalavanar, former Technical Officer of the Geotechnical Engineering Laboratory;
- Muslim Majid, Technical Officer of the Structural Engineering Laboratory;
- Leo Denner, Stanley Weedmark, John Perrins, Michael Burns and James Macdermid at the Mechanical and Civil Engineering Machine Shop;
- Dominic Blouin and Xavier Erdmer at the Multimedia Distribution Service

It is without doubt that my physical resilience has been challenged far beyond the human limit during this research program. Movement of the vast quantities of (dry and wet) sand used in the numerous physical tests conducted in the Hydraulics Laboratory was possibly the most laborious experience I have ever encountered. I am therefore, and particularly, thankful to my colleagues (Marta López, Jeffrey Ma and Amanj Jamal) and several undergraduate students who volunteered along with both University of Ottawa (Philippe St-Germain and Mathieu Toupin) and overseas interns (Sihame Mimid, Pierre Moreels, Claire Doerrer, Yann Boscher and Jeremy Bortolotti: University of Limoges, France, Bastien Flechoux: l'Ecole d'ingenieur du Cesi, France, Romain Pagniez: ICAM, France and Telse Bartens: Technical University of Braunschweig, Germany), and who have shared this burden with me. Exposure to the construction environment has undeniably allowed me to appreciate the importance and level of expertise required for any physical work.

I would like to acknowledge the invitation offered by Professor Richard Bathurst and Dr. Greg Siemens from the Department of Civil Engineering at the Royal Military College, Canada, to discuss the design of the tensiometer-transducer devices used in their research. I would also like to express my appreciation to Mehdi Arezoomand who has provided me a version of his computer code which has helped me register the images that I have captured and Dr. Mohamed Abdallah who has helped me create and configure the VI Tasks using LabVIEW. I am also very pleased and thankful that my brother, Mohammed Al-Riffai, and my dear friends, Omar Elhamy and M'hammed Kilito, have helped me with some of the photography and lighting installations.

I would like to express my gratitude to the University of Ottawa and Ministry of Training, Colleges and Universities of Ontario for financial support through the Admissions Scholarship and Ontario Graduate Scholarship, respectively. Funding of the experimental program was made possible through the CRTI Grant “Vulnerability of Infrastructure to Extreme Loading”.

Last but not least, I would like to give my thanks to all my family, particularly my mother and father, Susan and Hussein, for their unconditional support, encouragement, patience, and their daily prayers. Thank you for always being there for me. This is in recognition to your love and affection and for being my first teachers. I dedicate all my efforts to you. God bless you.

Remerciements

Je tiens à exprimer ma reconnaissance la plus sincère et la plus profonde à mon directeur de thèse, Dr. Ioan Nistor, pour m'avoir guidé et soutenu durant toutes les années de ma thèse. En effet, il est allé au-delà de son devoir en tant que directeur de thèse, et a également été, tout au long de mes études de doctorat, à la fois un encadrant et un ami. Sa patience et son grand appui moral, ainsi que sa confiance en mes capacités à la fois de chercheur et de professeur, m'ont permis de m'épanouir et d'accomplir de grandes réalisations professionnelles. Il n'a jamais cessé de m'aider dès qu'une opportunité se présente et je n'oublierai jamais ce soutien.

Je suis également reconnaissant envers le Professeur Sai Vanapalli pour ses encouragements, son appui tout au long de ma thèse et le partage de ses connaissances dans le domaine de la mécanique des sols en général et en particulier dans le domaine de la mécanique des sols non saturés. Je tiens également à remercier le Professeur Colin Rennie, Dr. Won Taek Oh, et Dr. Jules-Ange Infante-Sedano pour toutes les discussions techniques que nous avons tenues ainsi que pour leurs nombreux conseils reliés à certains aspects expérimentaux de mon sujet de recherche. Mes sincères remerciements sont également dirigés vers le Professeur Paul Van Geel de l'Université Carleton, membre du comité de direction de ma thèse, pour ses précieux commentaires sur le progrès et les contributions scientifiques de ma thèse. Les personnes mentionnées ci-dessus, ainsi que de nombreux autres professeurs de la Faculté de génie, ont été pour moi une source d'inspiration, à la fois dans mes recherches et dans mon enseignement à l'Université d'Ottawa.

Je tiens aussi à exprimer ma profonde reconnaissance envers le personnel technique de l'Université d'Ottawa dont les noms sont cités ci-dessous. Ces personnes m'ont offert leur expertise et une assistance extraordinaire dans

l'acquisition ainsi que dans le développement de l'équipement et des outils nécessaires pour mener à bien mes travaux de recherche. Leur collaboration m'a permis d'acquérir une vaste connaissance sur l'instrumentation:

- Mark Lapointe, responsable technique du Laboratoire d'hydraulique;
- Jean-Claude Célestin, responsable technique et Kulan Ambalavanar, ancien responsable technique du Laboratoire de génie géotechnique;
- Muslim Majid, responsable technique du Laboratoire de génie civil;
- Leo Denner, Stanley Weedmark, John Perrins, Michael Burns et James Macdermid de l'Atelier d'usinage de génie mécanique et civil;
- Dominic Blouin et Xavier Erdmer du Service de distribution multimédia.

Ma résistance physique a sans doute été testée au-delà de la limite humaine au cours de ces recherches. Déplacer des quantités importantes de sable (sec et humide) nécessaires aux nombreux essais expérimentaux effectués dans le laboratoire d'hydraulique, fut pour moi une expérience pénible à laquelle je n'avais jamais été confrontée. Pour avoir partagé ce fardeau avec moi, je suis particulièrement reconnaissant envers mes collègues (Marta López, Jeffrey Ma et Amanj Jamal), ainsi qu'envers plusieurs étudiants du premier cycle de l'Université d'Ottawa (Philippe St-Germain et Mathieu Toupin) et stagiaires étrangers (Sihame Mimid, Pierre Moreels, Claire Doerrer, Yann Boscher et Jeremy Bortolotti: Université de Limoges, France, Bastien Flechoux: l'École d' ingénieur du Cesi, France, Romain Pagniez: ICAM, France et Telse Bartens: Université Technique de Braunschweig, Allemagne). La construction en laboratoire m'a certainement permis de mieux comprendre les efforts, et le niveau d'expertise requis pour effectuer de la recherche expérimentale.

Je tiens à souligner l'invitation offerte par le professeur Richard Bathurst et Dr. Greg Siemens du Département de génie civil au Collège militaire royal du Canada, pour discuter de la conception des dispositifs tensiomètre-transducteurs (tensiomètre électronique) utilisés dans leurs recherches. Je tiens également à exprimer ma gratitude envers Mehdi Arezoomand, qui m'a fourni une version de son code

informatique qui a été très utile pour enregistrer les images prises durant les tests. Je remercie aussi Dr. Mohamed Abdallah, qui m'a aidé à créer et configurer les tâches de script de VI en utilisant LabVIEW.

Je tiens à exprimer ma gratitude envers l'Université d'Ottawa, le Ministère de la formation et des collèges et l'Université de l'Ontario pour le soutien financier par le biais respectivement de la Bourse d'excellence à l'admission et de la Bourse d'études supérieures de l'Ontario. Le financement du programme expérimental a été rendu possible grâce à la subvention de l'IRTC "Vulnérabilité des infrastructures aux charges extrêmes". Je suis aussi extrêmement reconnaissant envers mon frère, Mohammed Al-Riffai, et mes chers amis, Omar Elhamy et M'hammed Kilito, qui m'ont aidé avec la préparation de lumières et autres installations photographiques.

Le dernier point, mais non le moindre, je voudrais offrir mes remerciements à toute ma famille, en particulier ma mère et mon père, Susan et Hussein, pour leur soutien inconditionnel, leurs encouragements, leur patience et leurs prières quotidiennes. Merci d'avoir toujours été là pour moi. Ceci est en reconnaissance de votre amour et affection, vous étiez mes premiers instructeurs. Je vous dédie tous mes efforts. Que Dieu vous bénisse.

شكر و تقدير

أود أن أعبر عن خالص شكرى و امتناني للمشرف الأكاديمي على الرسالة الدكتور إيوان نيستور لدعمه و توجيهه خلال مشواري الأكاديمي الذى بدأته خلال السنوات القليلة الماضية. لقد ذهب أبعد من الدور المطلوب منه كمشرف على الرسالة، فقد جمع ما بين تعليمى و صداقتى خلال مسيرتى الأكاديمية. وأشهد له بالصبر ودعمه المعنوى لى و ثقته فى قدراتى كباحث و معلم مما ساعد على اكتسابي الخبرات المهنيه. كما إنه لم يتوانى عن دفعى لتحقيق تلك الإنجازات و سأتذكر دائماً ما قدمه لى من دعم.

كما أعرب أيضاً عن امتناني للأستاذ ساي فانابالي لتشجيعه المتواصل و تأييده خلال مسيرتى الأكاديمية بما قدمه لي من معلومات فى مجال ميكانيكا التربة وبالتحديـــــد ميكانيكا التربة الغير المشبعة. وأود أن أوجه جزيل الشكر إلى الدكتور كولن ريني، و الدكتور وان تايك اوه و الدكتور خوليـــو أنخـل إنفانتي ســـيدانو لنصائحهم ومناقشتهم لبعض الجوانب التجريبية فى هذا البحث.

كما أود ان أتوجه بشكري للأستاذ بول فان جيل بجامعة كارلتون عضو اللجنة الاستشارية لمناقشة الرسالة لمساهمته بملاحظاته القيمة أثناء عملي في هذه الرسالة. بالإضافة الى ماتم ذكرهم، أود أن أشير الى كثير من أساتذة كلية الهندسة بجامعة أوتاوا الذين كانوا مصدر إلهام لى و الذين استفدت منهم كثيراً فى اكتساب خبراتي فى مجال البحث و التدريس.

مع شكري وتقديري للعاملين بمختبرات كلية الهندسة-جامعة أوتوا لما قدموه من المشورة و المساعدة المتميزة فى الحصول و تطوير المعدات و الادوات اللازمة لإجراء هذا البحث و قد اكتسبت منهم معلومات كثيرة عن الأجهزة و استخداماتها.

- مارك لابوانت، المسؤول التقني بمختبر الهيدروليكا؛
- جان-كلود سلستين، المسؤول التقني الحالي، و كولان أمبالافانار، المسؤول التقني السابق بمختبر الهندسة الجيوتقنية؛
- مسلم مجيد، المسؤول التقني بمختبر الهندسة الإنشائية؛
- ليو دينير، ستانلي ويدمارك، جون بيرينز، مايكل بيرنز و جيمس ماكديرميد بورشة أقسام كلية هندسة الميكانيكا و المدني؛
- دومينيك بلواين و زافيير إردمر بقسم خدمة توزيع الوسائط المتعددة.

و بالتأكيد و خلال هذا البحث استطعت أن أتغلب على بعض التحديات التي واجهة مرونتي الجسدية والتي كانت أقوى من أي احتمال بشري، خاصة أثناء نقل و خلط الكميات الكبيرة من الرمال الجافة والرطبة التي استخدمت في المعمل

الهيدروليكا و التي اعتبرتها تجربة شاقة في ذلك الوقت. و لذا أود شكر زملائي (مارتا لوبيز، جيفري ما و امانج جمال) و الطلبة المتدربين (فيليب سانت-جيرمين و ماثيو توبين) و العديد من المتطوعين من جامعة أوتاوا و متدربين أخرين من خارج كندا (سيهام ميميد، بيير موريلز، كلير دورير، يان بوشيه و جيريمي برطولوتي: جامعة ليموج بفرنسا، باستيان فليشو: كلية الهندسة CESI بفرنسا، رومين بانييه: ICAM بفرنسا و تلسا بارتنز: جامعة براونشفيج للتكنولوجيا بألمانيا)، الذين شاركوني في تحمل هذا المجهود. كما أن تعرضي لبيئة البناء جعلني أقدر أهمية و مستوى الخبرة التي يتطلبها أي عمل بدني.

مع تقديري أيضاً للدعوة التي قدمت من الأستاذ ريتشارد باثرست و الدكتور جريج سيمنز من قسم الهندسة المدني بالكلية العسكرية الملكية-كندا-لمناقشة تصميم أجهزة قياس ضغط المياه المسام المستخدمة في أبحاثهم. و أشكر المهندس مهدي أريزوماند الذي وفر لي برنامجه بالحاســـوب الذي استخدمته لتعديل العديد من الصور التي قمت بالتقاطها. أشكر أيضاً الدكتور محمد عبدالله الذي ساعدني في تكوين VI Tasks في برنامج LabView.

خالص امتناني لجامعة أوتاوا و وزارة التدريب و معاهد و جامعات أونتاريو لدعمهم المدي من خلال منح القبول و المنح الدراسية، على التوالي. تم تمويل الجزء التجريبي لهذا البحث من خلال منحة CRTI بإسم "ضعف البنية التحتية بسبب التحميل المفرط". و من دواعي سروري و امتناني أن أخي العـــزيز محمد الرفاعي و اصدقائي الأعزاء عمر إلهامي و محمد كيليطو قاموا بمساعدتي في تصميم وتجهيز بعض معدات التصوير و الإضاءة.

أخيراً وليس أخراً، أشكر جميع أفراد عائلتي خاصة أمي و أبي، سوزان و حسين، لتشجيعهم و صبرهم و دعائهم الدائم. أشكركم لوجودكم معي. هذا مع التقدير لحبكـــم و مـــودتكم و لكـــونكم الأولين من علمتونـــي. أهدي اليكم هذه الرسالة. بارك الله فيكم.

Agradecimientos

Me gustaría expresar mi más sincero y profundo agradecimiento a mi director de tesis doctoral, Dr. Ioan Nistor, por su apoyo y orientación a lo largo de este viaje en el que me he embarcado estos últimos años. De hecho, él ha ido más allá de su deber como director de tesis ya que también ha asumido el papel de ambos; mentor y amigo durante mi carrera académica. Su paciencia e incalculable apoyo moral, así como su confianza en mi capacidad como investigador y maestro, me ha ganado grandes logros profesionales. Él nunca ha dejado de respaldarme en tales desafíos y nunca olvidaré este sustento.

También estoy agradecido al profesor Sai Vanapalli por su continuo apoyo durante toda mi carrera académica, así como por compartir su conocimiento en el campo de la Mecánica de Suelos Clásica e especialmente la Mecánica de Suelos Insaturados. También me gustaría agradecer al Profesor Colin Rennie, Dr. Won de Taek Oh y Dr. Jules-Ángel Infante-Sedano por su asesoramiento y discusión sobre algunos de los aspectos experimentales de esta investigación. Mis agradecimientos se extienden al profesor Paul Van Geel, de la Universidad de Carleton y miembro de mi tribunal, por sus valiosos comentarios sobre el progreso y su contribución a esta tesis doctoral. Ciertamente, los anteriormente mencionados, así como muchos otros profesores de la Facultad de Ingeniería en su conjunto, han sido una inspiración tanto para mi investigación, como para mi experiencia docente en la Universidad de Ottawa.

También me gustaría expresar mi más sincero agradecimiento al siguiente personal técnico de la Universidad de Ottawa por haberme proporcionado su asesoramiento experto y su asistencia extraordinaria en la adquisición y el desarrollo de los equipos y gracias a los cuales he adquirido un vasto conocimiento instrumental:

- Mark Lapointe, Oficial Técnico del Laboratorio de Ingeniería Hidráulica;

- Jean-Claude Celestin, Actual Oficial Técnico, y Kulan Ambalavanar, ex Oficial Técnico del Laboratorio de Ingeniería Geotécnica;
- Muslim Majid, Oficial Técnico del Laboratorio de Ingeniería Estructural;
- Leo Denner, Stanley Weedmark, John Perrins, Michael Burns y James Macdermid, personal del Taller de Ingeniería Mecánica y Civil;
- Dominic Blouin y Xavier Erdmer del Servicio de Distribución Multimedia

Sin lugar a dudas, mi capacidad de resistencia física ha sido cuestionada mucho más allá del límite humano durante este programa de investigación. El movimiento de grandes cantidades de arena (seca y húmeda) utilizada en las numerosas pruebas físicas llevadas a cabo en el Laboratorio de Hidráulica es posiblemente la experiencia más laboriosa a la que jamás me he enfrentado. Por lo tanto, estoy especialmente agradecido a mis colegas (Marta López, Jeffrey Ma y Amanj Jamal) y a varios voluntarios, tanto estudiantes universitarios de la Universidad de Ottawa (Philippe St-Germain y Mathieu Toupin) como estudiantes internacionales (Sihame Mimid, Pierre Moreels, Claire Doerrer, Yann Boscher y Jeremy Bortolotti: Universidad de Limoges, Francia, Bastien Flechoux: l' Ecole d'Ingenieur du Cesi, Francia, Romain Pagniez: ICAM, Francia y Telse Bartens: Universidad Técnica de Braunschweig, Alemania), que han compartido esta carga conmigo. La exposición al ambiente de la construcción ha permitido sin duda mi apreciación a la importancia y al nivel de conocimientos técnicos necesarios para efectuar cualquier tipo de trabajo físico.

Me gustaría agradecer la invitación ofrecida por el profesor Richard Bathurst y el Dr. Greg Siemens del Departamento de Ingeniería Civil del Colegio Real Militar, Canadá, para discutir el diseño de los tensiómetros transductores utilizados en sus investigaciones. También me gustaría expresar mi agradecimiento a Mehdi Arezoomand que me ha proporcionado una versión de su código que me ha ayudado a registrar las imágenes que he capturado y el Dr. Mohamed Abdallah, que ha ayudado a crear y configurar el VI Task utilizando LabVIEW. También estoy muy contento y agradecido que mi querido hermano, Mohammed Al-Riffai, y mis

queridos amigos, Omar Elhamy y M'hammed Kilito, me han ayudado con algunas de las instalaciones de la fotografía y la iluminación.

Me gustaría expresar mi gratitud a la Universidad de Ottawa y al Ministerio de Capacitación, Formación Profesional y Universidades de Ontario por el apoyo financiero recibido a través de la Beca de Admisión y de la Beca de Posgrado, respectivamente. La financiación del programa experimental fue posible gracias a la Subvención proporcionada por CRTI "Vulnerabilidad de la Infraestructura para Carga Extrema".

Por último, pero no menos importante, me gustaría dar las gracias a toda mi familia, especialmente a mi madre y a mi padre, Susan y Hussein, por su apoyo incondicional, empuje, paciencia y por sus oraciones diarias. Gracias por estar siempre ahí. En reconocimiento por todo esto, además de vuestro amor, afección y por ser mis primeros maestros, yo siempre os dedicaré todos mis esfuerzos. Que Dios os bendiga.

Table of Contents

Acknowledgements ..... **v**

Remerciements ..... **viii**

شكر و تقدير ..... **xi**

Agradecimientos ..... **xiii**

List of Figures ..... **xix**

List of Tables ..... **xxvi**

List of Symbols ..... **xxvii**

Chapter 1 Introduction **1**

1.1 Problem Definition 1
1.2 Research Needs 3
1.3 Scope 6
1.4 Research Objectives 7
1.5 Contributions and Novelty of Research Program 8
1.6 Organization of Manuscript 10

Chapter 2 History and Background of Embankment Failures **13**

2.1 Dam Failures during Ancient Civilizations 13
2.2 Dam and Dike Breaching Disasters in the Modern World 17
2.3 Failure Mechanisms of Embankments 21
2.3.1 Types of Embankments 21
2.3.2 Size of Dams and Safety Hazard 23
2.3.3 Causes of Embankment Failures 25
2.3.4 Embankment Breach in Warfare 28

Chapter 3 Literature Review **30**

3.1 Embankment Breach Modeling 30
3.2 Mathematical Modeling 32
3.2.1 Empirical Models 32
3.2.2 Parametric and Dimensionless Models 36
3.2.3 Physically-based Numerical Models 40
3.3 Experimental Modeling: Laboratory and Field Tests 52
3.3.1 European Legislation and Initiatives 53
3.3.2 Influence of Compaction 56
3.3.3 Breach Channel Control Section 59
3.3.4 Breach Channel Mapping Techniques 59
3.3.5 Seepage and Pore-Water-Pressure Measurement 61
3.3.6 Similitude and Scaling Criteria 68
3.4 Discussion 71

Chapter 4 Theory of Embankment Breach Hydromechanics 76

4.1 Dambreak and Embankment Breach Flow Hydrodynamics 76
4.1.1 General 3-Dimensional Hydrodynamic Equations 76
4.1.2 Shallow Water Equations (SWE) 81
4.1.3 Wall Laws 86
4.1.4 Curvature Effects 90
4.1.5 Flow Overtopping 92
4.2 Breach Erosion Mechanics 98
4.2.1 Transport Characteristic Parameters 98
4.2.2 Sediment Transport Mechanisms 104
4.2.3 Incipient Sediment Motion 107
4.2.4 Sediment Transport-Capacity Formulations 111
4.2.5 Non-equilibrium Sediment Transport, Erodibility and Detachment-Limit Capacity Formulations 117
4.2.6 Non-Newtonian Flow 123
4.3 Reservoir Routing 127
4.4 Geomechanics 128
4.5 Engineering Properties of Unsaturated Soils 131
4.5.1 Soil-Water Characteristic Curve 134
4.5.2 Flow Behaviour 147
4.5.3 Shear Strength 155
4.6 Seepage-Induced Slope Instabilities and Erosion 158
4.6.1 Seepage across Porous Boundaries 158
4.6.2 Slope Stability Analyses using Mohr-Coulomb Failure Criterion 159
4.6.3 Slope Stability Analyses using Static Liquefaction Criterion 164
4.6.4 Seepage-induced Erosion Mechanisms 167
4.6.5 Hindered Erosion 173
4.7 Similitude and Scaling Criteria 175

Chapter 5 Preliminary Work: Numerical and Experimental Investigations 179

5.1 Embankment Breach Numerical Modeling 179
5.1.1 Modeling Parameter Characteristics 179
5.1.2 Sensitivity Analysis Results 186
5.2 Embankment Breach Experimental Modeling – Standard Tests (Phase I) 193
5.2.1 Small Flume Tests 194
5.2.2 Large Flume Tests 210
5.3 Discussion 218
5.4 Conclusions and Recommendations 220
5.4.1 Embankment Breach Numerical Modeling 220
5.4.2 3-D Breach Overtopping Tests 221

Chapter 6 3-D Breach Overtopping Tests – Development of New and Improved Construction and Testing Techniques (Phase II) 223

6.1 Improved Construction Technique and New Geotechnical Investigations 224
6.2 Scale Series Tests 224
6.2.1 Compaction Tests (Series “D”) 226

6.2.2 Drainage Tests (Series “E”) 226
6.2.3 Tilted Geometric Scale Tests (Series “F”)..... 226
6.2.4 Quasi-Exact Geometric Scale Tests (Series “G”) 227
6.3 Experimental Setup 228
6.4 Breach Channel Entrance Mapping..... 231
6.5 Estimation of Breach Channel Outflow..... 237
6.6 Results and Analysis 239
6.6.1 Qualitative Remarks on Three Observed Breaching Phases 239
6.6.2 Scaling Laws..... 242
6.6.3 Breach Outflow Hydrographs..... 244
6.6.4 Breach Channel Control Section Morphology..... 253
6.7 Discussion 270
6.8 Conclusions and Recommendations 273
6.8.1 Conclusions 273
6.8.2 Recommendations for Future Work..... 277

Chapter 7 2-D Overtopping Tests (Phase III)..... 278

7.1 Development of a Novel Experimental 2-D Overtopping Configuration.. 279
7.1.1 Overtopping Head..... 282
7.1.2 Instrumentation 282
7.1.3 Construction Process and Experimental Setup 287
7.2 Data Acquisition Procedure..... 290
7.3 Data Extraction, Analysis and Results..... 291
7.3.1 Breach Outflow Hydrographs..... 291
7.3.2 Piezometric and PWP Measurements 292
7.3.3 Water Surface and Bed Profile Measurements..... 298
7.3.4 Transient Flownet Analysis..... 298
7.3.5 Hydrodynamics in the Boundary Seepage Zone 300
7.4 Discussion 306
7.5 Conclusions and Recommendations 310
7.5.1 Conclusions 310
7.5.2 Recommendations for Future Work..... 313

Chapter 8 Summary..... 315

References 318

Appendix A Physically-Based Embankment Breach Mathematical Models. 338

Appendix B Embankment Breach Experimental Programs 356

Appendix C Geotechnical Engineering Investigations..... 447

Appendix D Embankment Construction Techniques, Equipment Design and Instrument Installation Instructions and Calibration..... 475

Appendix E Computer Codes 522

Appendix F 2-D Overtopping Tests: Data and Results 548

List of Figures

Figure 3.1: Hypothetical inflow, breach outflow and routed hydrographs 30
Figure 3.2: Breach growth models (after Froehlich, 2008) 37
Figure 3.3: Modeling processes and input parameters in embankment breach models (examples of computational parameters are related to discretization of the spatial and temporal domain and numerical schemes) 41
Figure 3.4: (a) Arc failure analysis for overtopping flow, and (b) forces considered in method of slices (Tingsanchali and Chinnarasri, 2001) 46
Figure 3.5: Calibration of pore-water-pressure coefficient, C_U (Tingsanchali and Chinnarasri, 2001) 47
Figure 3.6: Control volume and variables schematic in Faëh (2007) 49
Figure 3.7: Experimental results from IMPACT Project laboratory Test No. 10 (PT is pressure transducer, WSL is water surface level, U/S is upstream and D/S is downstream) (using data from Morris *et al.* 2007 and IMPACT, 2004a) 62
Figure 3.8: Top view of embankment showing sliding failures on downstream slope during overtopping (Morris, 2002b) 63
Figure 3.9: Side view of final breach channel showing sliding failures on downstream slope (left) Morris, 2002b (right) Morris, 2002c 64
Figure 3.10: Seepage on downstream slope of dike model (left) before overtopping (right) during overtopping, geotextile installation (Geisenhainer and Kortenhaus, 2006) 64
Figure 3.11: Downstream slope of dike model showing geotextile installation (left) after construction (right) during overtopping (Geisenhainer and Kortenhaus, 2006) 65
Figure 3.12: UMS T-5 tensiometer probes cited in Pickert *et al.* (2004, 2011) (UMS, 2012) 66
Figure 3.13: Pore-water-pressure measurements for medium sand (Pickert *et al.* 2011) 66
Figure 3.14: Proposed instrumentation used for a dike test with breach initiation at landward side (Geisenhainer and Oumeraci, 2008) 68
Figure 4.1: Infinitesimal fluid element showing (top) mass fluxes (bottom) surficial stresses (τ is shear or tangential stress and σ is normal stress) 77
Figure 4.2: Flow on a sloping channel showing vertical flow depth, η_z, section (or perpendicular) flow depth, η_n, and pressure-head equivalent flow depth, η_h (after French, 1985) 84
Figure 4.3: Boundary layer development and regions (after French, 1985; Crowe *et al.* 2009) 87
Figure 4.4: Pressure gradient due to curvilinear flow (left) concave bed (right) convex bed (after French, 1985 and Chaudhry, 2008) 91
Figure 4.5: Flow geometry due to slope and curvature effects (after Hager and Hutter, 1984) 92

Figure 4.6: Hydraulic flow regimes and erosion zones during overtopping (Powledge *et al.* 1989) 93
Figure 4.7: Slope retreat on upstream face 94
Figure 4.8: Overtopping flow showing recirculation zone, water surface level, bed profile and energy grade line 95
Figure 4.9: Schematic showing trapezoidal breach channel cross-section (lower water surface line represents water surface level in breach channel, depicted by elevation, η_{bc}) 97
Figure 4.10: Longitudinal profile showing seidment balance in three layers for a 1-D model (Armanini and Di Slvio, 1988) 105
Figure 4.11: Relationship between rolling, saltation and suspension and dimensionless shear stress (Hu and Hui, 1996; Θ is referred in their study as flow intensity which is the dimensionless shear stress) 106
Figure 4.12: Tractive force coefficient against grain Reynolds number (Shields, 1936) 108
Figure 4.13: Initiation of motion from the Shields diagram in Vanoni (1975) (after Prasuhn, 1992) 109
Figure 4.14: Modified Shields curve by Govers (1987) (source: Yang, 1996) 110
Figure 4.15: Relationship between erosion rate and shear stress for compacted silty sands (Fujisawa *et al.* 2008) 120
Figure 4.16: Dimensionless erosion rates by Winterwerp *et al.* (1992) and van Rijn (1984a) 122
Figure 4.17: Effect of sediment concentration on erosion rate (Winterwerp *et al.* 1992).... 123
Figure 4.18: Sediment concentration and breach outflow during a breach event (Broich, 2003) 124
Figure 4.19: Shear stress relations for different types of fluids 125
Figure 4.20: Rheograms of hyperconcentrated flows (Julién and Lan, 1991) 126
Figure 4.21: Trapezoidal breach channel cross-section showing vertical erosion progression and successive side-slope failures 129
Figure 4.22: Longitudinal section showing region with potential collapse during overtopping failure in composite embankments 130
Figure 4.23: Longitudinal section showing region with potential collapse during piping failure 131
Figure 4.24: Process of desaturation and air filling voids in a saturated soil (adapted after Oh and Vanapalli, 2011) 132
Figure 4.25: Stress-state variables in saturated and unsaturated soil mechanics (Fredlund, 1996) 133
Figure 4.26: Soil-water characteristic curves for sand and clayey silt (Fredlund, 1996) 134
Figure 4.27: Hypothetical desorption soil-water characteristic curve for a sand and clay .. 136
Figure 4.28: Variation of dry density with compaction water content for two compaction efforts (Ng and Pang, 2000) 137

Figure 4.29: Comparison between the measured and predicted SWCC based on a GSD model and the mathematical model by Fredlund and Xing (1994) for a fine sand (Yang *et al.* 2004) 138
Figure 4.30: Capillary rise in soil specimen (Yang *et al.* 2004) 139
Figure 4.31: Influence of desorption/adsorption cycles on the SWCC of a volcanic soil (Ng and Pang, 2000) 141
Figure 4.32: Desorption and adsorption SWCC and drying and wetting scanning curves (Pham *et al.* 2005) 142
Figure 4.33: Process for predicting adsorption bounding SWCC from a known bounding desorption SWCC (Pham *et al.* 2003)..... 143
Figure 4.34: Comparison between the predicted adsorption and measured initial and boundary SWCCs for Beaver Creek sand (Pham *et al.* 2003)..... 144
Figure 4.35: Initial and bounding SWCCs (Pham *et al.* 2005)..... 146
Figure 4.36: Hysteretic SWCCs for a fine sand (Yang *et al.* 2004) 147
Figure 4.37: Cubic soil element showing mass fluxes (v_{dx}, $v_{dy}$and v_{dz} are discharge velocities in the x, y and z direction, respectively) 149
Figure 4.38: Flownet for homogeneous embankment body on impervious foundation under steady-state seepage conditions (after Cedergren, 1989)..... 151
Figure 4.39: Hypothetical relationship between SWCCs (shown at the top) and hydraulic conductivity functions (shown at the bottom) for two soil types 152
Figure 4.40: Extended Mohr-Coulomb failure envelope for soils under unsaturated conditions (Ng and Menzies, 2007 after Fredlund and Rahardjo, 1993)..... 155
Figure 4.41: Hypothetical relationship between SWCCs (shown at the top) and shear strength (shown at the bottom) for two soil types 157
Figure 4.42: Types of slope instabilities (Craig, 2004) 160
Figure 4.43: Mass failure analysis (W: weight of soil above failure surface; d_W: moment arm; L_a: length of failure surface; θ: arc angle)..... 161
Figure 4.44: Slope stability analysis showing method of slices (ΔL_i: incremental length of base slice)..... 162
Figure 4.45: Stability analysis of saturated infinite slope using (left) boundary pore pressure method (right) seepage force method (after Soong and Koerner, 1996) 164
Figure 4.46: Flownet on a sloping bed showing flow (seepage) and equipotential lines (n: coordinate perpendicular to bed plane) 165
Figure 4.47: Stability criteria for single particle and continuum approaches (van Rhee and Bezuijen, 1992) 167
Figure 4.48: Seepage and hydrodynamic forces acting on a sediment particle (FG' submerged gravitational force) 169
Figure 4.49: Computed and measured erosion velocity (van Rhee, 2010) 175
Figure 5.1: Various inflow conditions simulated 182
Figure 5.2: Reservoir-storage characteristics for different upstream valleys..... 183
Figure 5.3: Reservoir-surface area characteristics for different upstream valleys..... 183

Figure 5.4: Breach outflow hydrographs for various soil porosities (left) HR-BREACH (right) NWS-BREACH 187
Figure 5.5: Breach channel width evolution for various soil porosities (left) HR-BREACH (right) NWS-BREACH 188
Figure 5.6: Breach channel outflow and morphology for HR and NWS models for soil porosity, $\lambda = 0.27$ 188
Figure 5.7: Breach depth evolution for various soil porosities (left) HR-BREACH (right) NWS-BREACH 190
Figure 5.8: Breach outflow and final dimensions sensitivity for soil porosity 191
Figure 5.9: Breach temporal characteristics sensitivity for soil porosity 192
Figure 5.10: Embankment model without drainage element in compaction tests (Series "A") 194
Figure 5.11: Embankment model with horizontal drainage element in drainage tests (Series "B") 195
Figure 5.12: Experimental setup for compaction and drainage tests (Series "A": η = 0.23m, x_1 = 8.84m, x_2= 0.3m, x_3= 1.46m, x_4= 1.60m; Series "B": η = 0.28m, x_1= 6.75m, x_2 = 2.0m, x_3 = 1.75m, x_4 = 1.70m) 196
Figure 5.13: Locations of piezometer taps (numbered Pz_1 to Pz_6) and piezometers (numbered h_1 to h_6) in drainage tests (Series "B") 197
Figure 5.14: Sapping/piping erosion near downstream toe 199
Figure 5.15: Wave gauge data offset (wave gauge 3 in test no. 4) 201
Figure 5.16: Filtering data from wave gauge 4 in Test No. 9 202
Figure 5.17: Comparison between breach outflow hydrograph computed using four different filtering configurations (Test No. 4; 5 blows; 5cm drop height) and measured using wave gauge in outlet tank (*i.e.* through triangular weir) 202
Figure 5.18: Comparison between computed and measured breach outflow hydrograph and head above V-notch tank (Test No. 4) 204
Figure 5.19: Outflow hydrograph computed for small flume (top) compaction series (bottom) drainage series (dashed lines indicate breach channel reached side-walls) . 205
Figure 5.20: Measured and computed (SEEP/W) steady-state piezometric head along embankment model foundation for two compactions (5 blows and 20 blows) at η = 280, 185 and 50mm (top) without drain (bottom) with drain 208
Figure 5.21: Numerical simulation of steady-state PWP distribution [kPa] and phreatic surface in embankment model constructed with 20 blows (η = 28cm) (top) without drain (bottom) with drain 209
Figure 5.22: Experimental setup in large flume (Series "C") 211
Figure 5.23: Pilot test in large flume simulating breaching due to blast-induced crater (Test No. 1) 213
Figure 5.24: Hydrographs and upstream WSLs for Phase I large flume tests (Series "C") 215
Figure 5.25: Upstream view of breach channel side-slope failures in large flume tests (left) Test No. 3, no undertoe-drain (right) Test No. 6, undertoe-drain 216
Figure 5.26: Lagged hydrographs and WSLs for Tests No. 3 and 6 217

Figure 6.1: Tilted geometric scales (Series “F”) 227
Figure 6.2: Quasi-exact geometric scales (Series “G”) 228
Figure 6.3: Experimental setup in large flume tests for Phase II (*d*istance, x, between WG2 and WG3 ranged between 2m and 14.4m) 229
Figure 6.4: Longitudinal profile of embankment model for large flume tests in Phase II 230
Figure 6.5: Upstream boundary used in large flume 231
Figure 6.6: Planform view showing breach channel entrance forming on upstream slope of Test No. 4 (t = 37s) 232
Figure 6.7: Mapping and projecting breach channel top boundary onto one plane 233
Figure 6.8: (left) Georeferencing reference image captured before impoundment (right) applying georeferencing to an image captured after 280 seconds into breach progression 234
Figure 6.9: Transformation showing (left) reference image (right) image after 280 seconds into breach progression 235
Figure 6.10: Idealised overtopping in breach channel of embankment model showing (top) longitudinal section (bottom) planform view (red dot shows inflection point and WSL at breach channel centreline) 236
Figure 6.11: Detailed and rotated planform view of submerged arched crest showing entrance, top and constriction widths of breach channel 237
Figure 6.12: Breach outflow hydrographs for Phase II of experimental program (C1, high compaction, C2 intermediate compaction; C3: low compaction; D: drainage series; T: tilted geometric scale series; QE: quasi-exact geometric scale series; S1: scale 1; S2: scale $1/2$; S3: scale $1/3$; Dr is relative density, D_r) 245
Figure 6.13: Breach outflow hydrographs for Phase II of experimental program lagged to the onset of breaching time 246
Figure 6.14: Comparison between breach outflow hydrograph in the caseof drained and undrained embankment models 247
Figure 6.15: Lagged breach outflow hydrographs for repeated tests (top) benchmark embankment model, Tests No. 2 and 3 (middle) quasi-exact scale series $1/2$, Tests No. 8 and 9 (bottom) quasi-exact scale series, $1/3$ Tests No. 10 and 11 249
Figure 6.16: Experimental breach outflow hydrograph characteristic ratios for tilted and quasi-exact scale series compared with Froude criterion (top) peak flow (middle) time-to-peak (bottom) base-time 251
Figure 6.17: Comparison of the lagged and Froude-scaled breach outflow hydrograph between tilted scale series tests 252
Figure 6.18: Comparison of the lagged and Froude-scaled breach outflow hydrograph between quasi-exact scale series tests 252
Figure 6.19: Two examples of asymmetry showing georeferenced upstream and planform view images from ArcGIS superimposed by arcs representing the breach channel entrance at various times (top) Test No. 3, $t = 120s$) (bottom) Test No. 4, $t = 110s$) 254
Figure 6.20: Morphology of the breach channel control section represented by entrance (top) width (bottom) chord height showing maximum values 255

Figure 6.21: Morphology of the breach channel control section represented by the arc entrance (top) radius (bottom) arc length 256

Figure 6.22: Evolution of ratio between measured and estimated breach outflow with respect to time 257

Figure 6.23: Evolution of two discharge efficiency related dimensionless parameters (top) breach channel entrance crest length-to-width ratio (bottom) arc angle 259

Figure 6.24: Morphology of the breach channel control section with respect to a normalised time represented by the dimensionless arc entrance (top) width (bottom) chord height 262

Figure 6.25: Morphology of the breach channel control section with respect to a normalised time represented by the dimensionless arc entrance (top) radius (bottom) length 263

Figure 6.26: Evolution of ratio between measured and estimated breach outflow with respect to a time normalised by (top) time-to-peak (bottom) base-time 264

Figure 6.27: Evolution of two discharge efficiency related dimensionless parameters with respect to a time normalised by time-to-peak (top) breach channel entrance crest length-to-width ratio (bottom) arc angle 265

Figure 6.28: Head above inflection point at centreline of breach channel entrance (top) dimensional plot (bottom) dimensionless plot (head is normalised by crest elevation and time is normalised by time-to-peak) 269

Figure 7.1: Experimental setup for Phase III showing gate design “D” and LED light fixture (PWP transducer assemblies shown as red dots) 279

Figure 7.2: Longitudinal section of embankment model in overtopping tests showing undertoe-drain and gate design “D” 280

Figure 7.3: Antidune formation during overtopping (left) $\Delta\eta_0$ = 2cm (Test No. 2) (right) $\Delta\eta_0$ = 5cm (Test No. 5) 282

Figure 7.4: M-TTPA and S-TTPA 283

Figure 7.5: Locations of TTPAs (control TTPAs "P" and "Q" on left-side wall; locations “F” and “K” remained unused) and piezometers installed on flume side-walls and bottom, respectively 284

Figure 7.6: TTPAs installed through flume side-walls prior to impoundment and overtopping (left) right-side (right) left-side 287

Figure 7.7: View from upstream showing (left) installation of gravel medium (middle) installation of filter medium (right) completed undertoe drain 288

Figure 7.8: Setup in small hydraulic flume showing: TTPAs (blue dot corresponds to control check measurement), wave-gauges, light emitting diode (LED) fixture, release gate, piezometric head measurements (piezometers and connection to piezometer panel), three water surface levels using in steady-state tests and water surface level prior to overtopping (not shown is the head tank at the upstream section of the small flume) 289

Figure 7.9: Outflow hydrographs computed for overtopping tests (Phase III), lagged to time of vertical gate release 291

Figure 7.10: PWP time-history due to falling reservoir head (top) undrained embankment model (Test No. 10) (bottom) drained embankment model (Test No. 8) 295

Figure 7.11: PWP time-history due to overtopping for embankment models with (top) undertoe-drain (Test No. 8) (bottom) no drain (Test No. 10) 297

Figure 7.12: PWP interpolation and transient flownet analysis (Test No. 6, t = 6 seconds)299

Figure 7.13: Flownet on an overtopped steep slope showing upward seepage (Ψ_{i-1}, Ψ_i and Ψ_{i+1} are seepage angles for three adjacent flow lines) 300

Figure 7.14: Forces acting on accelerating fluid influenced by seepage (F_{H1} and F_{H2}: LHS and RHS hydrostatic pressure forces, respectively) 301

Figure 7.15: Shear stress distribution for three time-steps showing initial outline of embankment model (Test No. 6) 304

Figure 7.16: Erosion (Test No. 6) as indicated in supercritical hydrostatic region and recirculation zones by (left) an erosion rate (right) a mobility relationship 304

Figure 7.17: Initial embankment outline in test No. 6 showing (left) Froude numbers (right) overtopping velocity 305

Figure 7.18: Dimensionless transport rate and Shields parameter relationship for three time-steps (Test No. 6) 306

List of Tables

Table 2.1: Major dam failures, their causes, breach characteristics and loss of lives (sources: Lou, 1981; Singh and Quiroga, 1988; Singh and Scarlatos 1988; Wohl, 2000; Gee, 2008; Rico *et al.* 2008; Xu and L.M. Zhang, 2009; Tsakiris *et al.* 2010) 19

Table 2.2: Size classification (USACE, 1979) 24

Table 2.3: Hazard potential classification System (FEMA, 2004) 24

Table 2.4: Statistics of dam failure modes 28

Table 3.1: Empirical relationships for estimating embankment breach parameters 35

Table 3.2: Sensitivity analysis of peak outflow for various input parameters using HR-BREACH (Morris *et al.* 2004) 52

Table 4.1: Matrix showing variants of SVE (after Miller, 1984 and Julién, 2002) 85

Table 5.1: Embankment geometry and geotechnical parameters: benchmark values and input ranges 180

Table 5.2: Hydraulic and computational parameters: benchmark values and input ranges 185

Table 5.3: Percentage variation in embankment breach characteristics for geometric and geotechnical input parameters 193

Table 5.4: Test matrix for small flume tests (compaction and drainage) 198

Table 5.5: Summary of results for compaction and drainage series 206

Table 5.6: Test matrix for large flume tests (Series “C”) 212

Table 5.7: Summary of large flume tests of Phase I (series “C”) 215

Table 6.1: Test matrix in large flume tests for Phase II 225

Table 6.2: Results summary from breach outflow hydrograph analysis for Phase II tests . 246

Table 6.3: Summary of breach channel control section results for Phase II 261

Table 6.4: Best-fit expression and peak values for breach channel discharge efficiency .. 267

Table 6.5: Best-fit expressions describing morphology of dimensionless breach channel entrance parameters with respect to normalised time 268

Table 7.1: Test matrix for Phase III (Series “H”) 281

Table 7.2: TTPA configurations used in overtopping tests 285

Table 7.3: Overtopping tests and corresponding TTPA configuration 286

Table 7.4: Flow and erosion parameters extracted by 1-D hydrodynamic code 302

List of Symbols

Lower-case Roman Letters

a_b Reference height in van Rijn (1984c), [m]
a_s Parameter for modifying critical shear stress due to steep slopes in Fread (1991), [–]
a_u Uncertainty coefficient in Mohamed *et al.* (1999), [–]
a_ψ Curve fitting parameter for soil-water characteristics curve, [FF]
b Width, [m]
b_c Empirical constant in Meyer-Peter-Müller (1948) formulation for cohesive soil, [FF]
b_V Bottom width of trapezoidal channel bottom, [m]
b_ψ Curve fitting parameter for bounding SWCC in Feng and Fredlund (1999), [FF]
$b_{\psi,d}$ Curve fitting parameter for desorption bounding SWCC in Pham *et al.* (2005), [FF]
$b_{\psi,w}$ Curve fitting parameter for adsorption bounding SWCC in Pham *et al.* (2005), [FF]
c Soil cohesion, [kPa]
c' Drained or effective soil cohesion, [kPa]
c_b Offset factor in Von Thun and Gillette (1990) breach width equation, [m]
c_c Empirical constant in Meyer-Peter-Müller (1948) formulation for cohesive soil, [FF]
c_u Undrained soil cohesion, [kPa]
d^* Dimensionless grain size, [–]
d_0 Characteristic grain size, [mm or m]
d_1 Diameter of solitary particle in Dey and Zanke (2004), [m]
d_2 Diameter of densely-packed particles in Dey and Zanke (2004), [m]
d_{50} Median embankment material particle size, [mm]
d_h Pressure-head in curvilinear flow, [m]
d_M Mean grain size, [mm]
d_s Representative particle size in suspension, [m]
d_w Characteristic pore diameter in Pickert *et al.* (2011), [mm or m]
d_W Moment arm to center of slice or soil above failure surface, [m]
d_z Pressure-head in curvilinear flow, [m]
d_ψ Curve fitting parameter for bounding SWCC in Feng and Fredlund (1999), [FF]
$d_{\psi,d}$ Curve fitting parameter for desorption bounding SWCC in Pham *et al.* (2005), [FF]
$d_{\psi,w}$ Curve fitting parameter for adsorption bounding SWCC in Pham *et al.* (2005), [FF]
dQ Discharge through arc segment, [m^3/s]
ds Length of arc segment, [m]
dt Differential time-step, [m]
$d\theta$ Arc segment rotation, [radians]
e Void ratio, [–]
$\mathbf{e}$ Natural number, [–]
e_{max} Maximum void ratio, [–]
e_{min} Minimum void ratio, [–]
f Darcy-Weisbach resistance coefficient, [–]
f' Darcy-Weisbach resistance coefficient due to grain roughness, [–]
g Acceleration due to gravity, [m/s^2]

g_{bs} Gravimetric bedload transport rate (mass per unit width and time), [kg/ms]
g_{ss} Gravimetric suspended load transport rate (mass per unit width and time), [kg/ms]
h Piezometric head, [m]
h_b Elevation of embankment breach channel bottom at the inflection point in Coleman *et al.* 2002, [m]
h_B Breach channel height, [m]
h_c Capillary height in Pickert *et al.* 2011, [m]
h_{cr} Embankment crest height, [m]
h_d Drop in reservoir level during breach, [m]
h_D Dam height, [m]
h_r Reservoir depth, [m]
h_s Height of soil specimen, [m]
h_W Depth of water above breach invert at time of failure, [m]
i Counter or interval, [INT]
i_c Critical hydraulic gradient, [–]
i_e Exit hydraulic gradient, [–]
i_ψ Hydraulic gradient, [–]
j Counter, [INT]
j_{max} Maximum counter, [INT]
k_d Erodibility coefficient, [cm^3/Ns]
k_l Hydraulic conductivity of the sheared layer in van Rhee (2010), [m/s]
k_r Bed form correction factor in Meyer-Peter-Müller (1948), [–]
k_s Equivalent sand grain roughness, [m]
k_{sat} Hydraulic conductivity of a saturated soil, [m/s]
$k_{sat,c}$ Saturated hydraulic conductivity calculated at zero pressure in Green and Corey (1971), [m/s]
$k_w(\psi)$ Hydraulic conductivity function of soil, [m/s]
m_a Rate of change of volumetric water content with respect to net normal stress, [m^2/N]
m_v Coefficient of volume change, [m^2/N]
m_w Rate of change of volumetric water content with respect to matric suction, [m^2/N]
m_ψ Curve fitting parameter for soil-water characteristics curve, [FF]
n Distance or coordinate along axis normal to bed, [m]
n_{E} Empirical erosion exponent, [FF]
n_M Manning's roughness coefficient, [s/m$^{1/3}$]
n_q Shear stress exponent, [FF]
n_Q Empirical exponent, [FF]
n_s Empirical exponent, [FF]
n_Θ Empirical exponent, [FF]
n_τ Plasticity exponent, [FF]
n_ψ Curve fitting parameter for soil-water characteristics curve, [FF]
p Pressure, [N/m^2]
$\bar{p}$ Time-averaged pressure, [N/m^2]
p_{gc} Parameter that accounts for interaction of various pore classes in Green and Corey (1971), [–]
q Specific flow discharge, [m^2/s or l/s/m]
q^* Dimensionless transport rate, [–]
q_{bs} Volumetric bedload transport rate (discharge) per unit width, [m^2/s]
q_{bs}^* Dimensionless bedload transport rate, [–]

q_L Lateral inflow per unit area, [m/s]
q_{ss} Volumetric suspended load transport rate (discharge) per unit width, [m^2/s]
q_{ss}^* Dimensionless suspended load transport rate, [–]
q_{ts} Total volumetric sediment transport rate (discharge) per unit width, [m^2/s]
q_T^* Taylor's function, [–]
r Radius of curvature, [m]
r_a^* Dimensionless breach channel entrance radius of curvature, [–]
s Distance along axis tangential to bed, [m]
t Time, [s, hr]
t^* Time normalised by time-to-peak, [–]
t_a Time at which the chord height of the breach channel entrance is maximum, [s]
t_B Embankment breach outflow hydrograph base-time, [hr]
t_f Embankment breach formation time, [hr]
t_F Embankment breach failure time, [hr]
t_f^* Dimensionless embankment breach formation time, [–]
t_L Embankment breach outflow hydrograph lag-time, [s or hr]
t_P Embankment breach outflow hydrograph time-to-peak, [s], [hr]
t_P^* Dimensionless embankment breach outflow hydrograph time-to-peak, [–]
t_R Rise-time, [hr]
u Instantaneous velocity in x-direction, [m/s]
u' Turbulent velocity fluctuation in x-direction, [m/s]
u^+ Relative velocity, [–]
u^* Shear (or grain) velocity, [m/s]
$u^{*\prime}$ Shear (or grain) velocity in van Rijn (1984b, c), [m/s]
$\bar{u}$ Time-averaged velocity in x-direction, [m/s]
$\hat{u}$ Instantaneous dimensionless velocity in x-direction, [–]
u_a Pore-air-pressure, [N/m^2]
u_b Particle velocity in van Rijn (1984b), [m/s]
u_c^* Critical shear (or grain) velocity, [m/s]
u_c Froude-critical streamwise velocity, [m/s]
$\bar{u}_c$ Depth-averaged velocity for incipient motion in Yang (1973), [m/s]
u_m Approach velocity acting on particle, [m/s]
u_w Pore-water-pressure, [N/m^2]
v Instantaneous velocity in y-direction, [m/s]
$\bar{v}$ Time-averaged velocity in y-direction, [m/s]
$\hat{v}$ Instantaneous dimensionless velocity in y-direction, [–]
v_d Discharge velocity in porous media, [m/s]
v_s Seepage velocity in porous media, [m/s]
w Instantaneous velocity in z-direction, [m/s]
w' Turbulent velocity fluctuation in z-direction, [m/s]
$\bar{w}$ Time-averaged velocity in z-direction, [m/s]
$\hat{w}$ Instantaneous dimensionless velocity in z-direction, [–]
w_0 Fall (or settling) velocity for a single particle in van Rhee (2010), [m/s]
w_{cr} Crest width, [m]
w_s Particle fall (or settling) velocity, [m/s]
$w_{s,c}$ Modified particle fall (or settling) velocity according due to sediment concentration, [m/s]
x Streamwise distance, or coordinate along longitudinal axis, [m]

$\hat{x}$ Dimensionless longitudinal or streamwise distance, [–]
x_a Chord height of breach channel entrance, [m]
$x_{a,max}$ Maximum chord height of breach channel entrance, [m]
x_a^* Dimensionless chord height of breach channel entrance, [–]
x_η Inclined distance between upstream apex of embankment crest and upstream water surface elevation, [m]
x_s Arc segment coordinate in longitudinal direction, [m]
y Cross-stream distance, or coordinate along lateral axis, [m]
$\hat{y}$ Dimensionless lateral or cross-stream distance, [–]
y^+ Relative distance from wall boundary, [–]
y_0 Initial breach channel flow depth, [m]
y_n Normal flow depth, [m]
y_s Arc segment coordinate in transverse or lateral direction, [m]
y_ψ Dummy variable of integration representing soil-suction in Fredlund *et al.* (1994), [kPa]
z Elevation, or coordinate along vertical axis, [m]
$\hat{z}$ Dimensionless vertical distance or elevation, [–]
z_b Bed elevation, [m]
z_c Elevation of embankment breach channel bottom at the inflection point, [m]
z_{cr} Embankment crest elevation, [m]
z_{pb} Pilot channel invert elevation, [m]
z_{BB} Elevation of breach channel bottom, [m]
z_{DS} Embankment downstream slope factor, [–]
z_{SS} Breach channel side-slope factor, [–]
z_{US} Embankment upstream slope factor, [–]

Upper-case Roman Letters

A Area or cross-sectional area, [m^2]
A_b Cross-sectional area of breach in Coleman *et al.* 2002, [m^2]
A_S Reservoir surface area, [m^2]
$\bar{B}$ Average breach width, [m]
$\bar{B}^*$ Dimensionless average breach width in Froehlich (2008), [–]
B_0 Instantaneous breach channel width, [m]
B_{BW} Breach channel bottom width, [m]
B_{CW} Breach channel constriction width, [m]
B_{EW} Breach channel entrance width, [m]
$B_{EW,a}$ Breach channel entrance width corresponding to maximum chord height, [m]
B_{EW}^* Dimensionless breach channel entrance width, [–]
B_r Breach channel width-to-depth ratio, [–]
B_{TW} Breach channel top width, [m]
B_W Breach width, [m]
C Chézy roughness coefficient, [$m^{1/2}/s$]
C_0 Maximum bed concentration in van Rijn (1984b, c), [m^3/m^3]
C_1^* Dimensional discharge coefficient in Singh *et al.* (1988) equation, [$m^{1/2}/s$]
C_2^* Dimensional discharge coefficient in Singh *et al.* (1988) equation, [$m^{1/2}/s$]
C_a Reference concentration in van Rijn (1984c), [m^3/m^3]
C_b Near-bed or bedload concentration in van Rijn (1984b, c), [m^3/m^3]
C_C Coefficient of curvature, [–]

C_d Coefficient of discharge, [FF]
C_D Coefficient of drag, [–]
C_E Empirical erosion coefficient, [FF]
C_{est} Total load sediment concentration in Yang (1979) expressed in parts per million, [kg/kg]
C_f Coefficient of skin friction, [–]
C_I Constant of integration, [FF]
C_L Coefficient of lift, [–]
C_m Gravimetric concentration, [kg/kg]
C_q Transport coefficient, [FF]
C_s Depth-averaged transport-capacity suspended load concentration, [m^3/m^3]
C_{s*} Depth-averaged actual suspended load concentration, [m^3/m^3]
C_S Coefficient of submergence, [FF]
C_u Coefficient of pore-water-pressure in Tingsanchali and Chinnarasri (2001), [–]
C_U Coefficient of uniformity, [–]
C_V Volumetric concentration, [m^3/m^3]
C_w Coefficient of discharge based on weir shape, [FF]
C_W Breach widening coefficient in Hanson *et al.* (2005), [FF]
C_X Headcut migration material dependent coefficient in Hanson *et al.* (2005), [FF]
C_Θ Empirical coefficient, [FF]
C_τ Flow consistency index, [FF]
C_Ψ Ratio of seepage force on interfacial grains to that of grains below, [–]
Ca Cauchy number, [–]
$C(\psi)$ Correction factor in Fredlund and Xing (1994)
$\dot{D_m}$ Gravimetric deposition rate, [kg/m^2s]
D_r Relative density, [%]
D_{SL} Distance between bounding SWCCs measured from inflection points in Pham *et al.* (2005), [Log-cycle]
E Energy, [Nm]
E_M Modulus of Elasticity, [N/m^2]
$\dot{E}$ Volumetric erosion rate, [mm/s, m/s, m/h]
$\dot{\bar{E}}$ Average volumetric erosion rate, [m/min], [mm/s], [m/s]
$\dot{E_m}$ Gravimetric erosion (mass pick-up) rate, [kg/m^2s]
$\dot{E}_n$ Orthogonal volumetric erosion rate, [m/s]
$\dot{E}_{net}$ Net erosion velocity of the bed, [m/s]
E_V Amount of erosion required in bank face to induce failure in Hahn *et al.* (2002), [m^3]
Eu Euler number, [–]
$F_\parallel$ Force acting parallel to bed plane, [N]
$F_\perp$ Force acting perpendicular to bed plane, [N]
F_B Buoyancy force, [N]
F_{BC} Cohesive force acting at bottom of wedge, [N]
F_{BS} Shear force acting at bottom of wedge, [N]
F_L Drag force, [N]
F_{fr} Frictional force, [N]
F_G Gravity force, [N]
F'_G Submerged gravitational force, [N]
F_{gr} Mobility number in Ackers and White (1973), [–]
F_H Hydrostatic force, [N]

F_{H1} Left hand-side hydrostatic force, [N]
F_{H2} Right hand-side hydrostatic force, [N]
F_L Lift force, [N]
F_N Normal force, [N]
F_s Correction factor for suspended load rate in van Rijn (1984c), [–]
F_S Shear force, [N]
F_{SC} Cohesive force acting at saturated-unsaturated interface, [N]
F_{SS} Shear force acting at saturated-unsaturated interface, [N]
F_τ Boundary shear stress, [N]
F_ψ Seepage force, [N]
FOS Factor of safety, [–]
FOS_F Force equilibrium factor of safety, [–]
FOS_M Moment equilibrium factor of safety, [–]
Fr Froude number, [–]
G Modeling input parameter, [UV]
G_s Specific gravity of sediment, [–]
H_0 Overall height in headcut in Hanson *et al.* (2005), [m]
K_0 Failure mode factor in Froehlich (1995a), [–]
K_1 Adjustment factor to account for subhydrostatic pressure in recirculation zone in Annandale (1995), [–]
L Length, [m]
L_0 Characteristic length, [m]
L^* Dimensionless characteristic length, [–]
L_a Failure surface or arc length at the breach channel entrance, [m]
L_a^* Dimensionless breach channel entrance arc length, [–]
L_b Non-equilibrium adaptation length for bedload, [m]
L_{cr} Crest length, [m]
L_{DS} Length of downstream slope in Mohamed *et al.* (1999), [m]
L_e Horizontal width of crest in Coleman *et al.* 2002, [m]
L_{rr} Length scale or geometric scale ratio between prototype and model, [–]
L_s Non-equilibrium adaptation length for suspended load, [m]
L_t Non-equilibrium adaptation length for total load, [m]
M_0 Bending moment acting on overhanging material in Mohamed *et al.* (2002), [Nm]
M_d Moment of driving forces, [Nm]
M_r Moment of resisting forces, [Nm]
N Normal reaction force, [N]
N_s Total number of pore classes in Green and Corey (1971), [–]
P_w Wetted perimeter, [m]
PI Plasticity index, [%]
Q Discharge, [m^3/s]
Q_e Estimated breach outflow, [m^3/s]
Q_B Breach channel outflow, [l/s, m^3/s, cfs]
Q_{cr} Crest overflow, [m^3/s]
Q_I Inflow, [m^3/s]
Q_m Measured breach outflow, [m^3/s]
Q_O Outflow, [m^3/s]
Q_P Peak discharge, [m^3/s or cfs]
Q_P^* Dimensionless peak discharge, [–]
Q_s Sediment transport rate in Fread (1991), [cfs]

$\overline{Q_s}$ Average sediment transport rate in Mohamed *et al.* (1999), [m^3/s]
Q_{sp} Spillway overflow, [m^3/s]
R^* Rouse number, [–]
R^2 Square of the multiple correlation coefficient, [–]
R_c Relative compaction, [%]
R_h Hydraulic radius, [m]
R_{SL} Ratio of slope on the straight-line segments of the bounding SWCCs in Pham *et al.* (2005), [–]
R_W Reservoir characteristic, [UV]
Re Reynolds number, [–]
Re^* Grain Reynolds number, [–]
Re_p Particle Reynolds number, [–]
Re_s Reynolds number specific to flow in porous media, [–]
S_b Bed slope, [–]
S_f Friction slope, [–]
S_{fs} Friction slope in the s-direction, [–]
St Strouhal number, [–]
T Transport stage parameter, [–]
T_m Modified transport stage parameter due to slope effects and hindered erosion in van Rhee (2010), [–]
U Depth-averaged velocity in x-direction, [m/s]
U_0 Characteristic velocity, [m/s]
U_∞ Free-stream velocity, [m/s]
U_g Average flow velocity over recirculation zone in Annandale (1995), [m/s]
U_s Depth-averaged flow velocity along a streamline, [m/s]
V_0 Reservoir volume at time of breach initiation, [m^3]
V_F Reservoir volume at time of failure, [m^3]
V_F^* Dimensionless reservoir volume at time of failure in Froehlich (2008), [–]
V_{OUT} Volume of water discharged through breach, [m^3]
V_{OUT}^* Dimensionless volume of water discharged through breach, [–]
V Depth-averaged velocity in y-direction, [m/s]
V_R Reservoir storage volume, [m^3]
V_w Volume above breach invert at time of failure, [m^3]
W Weight, [N]
W_{sat} Saturated weight, [N]
X_T Average distance of movement between failure in Hahn *et al.* (2002) [m]
X Longitudinal geometric or length scale, [m]
Y Lateral geometric or length scale, [m]
Z Vertical geometric or length scale, [m]
Z_s Suspension parameter in van Rijn (1984c), [–]
Z_s' Modified suspension parameter in van Rijn (1984c), [–]

Lower-case Greek Letters

α Angle between the base slice and horizontal, [radians]
α_{DS} Downstream slope angle, [radians]
α_{jet} Angle of impinging jet with respect to horizontal, [radians]
α_Q Empirical constant, [FF]

α_{SS} Breach channel side-slope angle, [radians]
α_{US} Upstream slope angle, [radians]
α_{ψ} Curve fitting parameter for soil-water characteristics curve, [FF]
α_{Ψ} Coefficient for modifying shear stress due to seepage effects on boundary layer, [–]
β Coefficient related to diffusion in van Rijn (1984c), [–]
β_0 Downstream face slope angle in Visser (1998), [radians]
β_1 Maximum breach channel slope angle on downstream face in Visser (1998), [radians]
β_M Momentum correction factor in Cheng and Chiew (1998), [–]
β_{Ψ} Coefficient for modifying shear stress due to seepage effects on uppermost grains, [–]
γ Unit weight of soil, [kN/m^3]
γ_d Dry unit weight of soil [kN/m^3]
γ_f Specific weight of fluid, [kN/m^3]
γ_i Unit weight of soil for slice i in Tingsanchali and Chinnarasri (2001), [kN/m^3]
γ_s Specific weight of sediment particles, [kN/m^3]
γ_{sat} Unit weight of saturated soil, [kN/m^3]
δ Boundary layer thickness, [m]
δ_b Saltation height in van Rijn (1984c), [m]
δ_L Laminar boundary layer thickness, [m]
δ_T Turbulent boundary layer thickness, [m]
δ_v Laminar (or viscous) sublayer thickness, [m]
ε_s Eddy diffusivity of sediment, [m^2/s]
ζ Dimensionless erodibility parameter in Walder and O'Connor (1997), [–]
η Water surface elevation, [m]
$\bar{\eta}$ Flow depth to still water level, [m]
η_{bc} Water surface elevation in breach channel, [m]
η_{br} Water surface elevation at onset of breaching, [m]
η_c Froude-critical flow depth, [m]
η_h Flow depth corresponding to equivalent pressure-head, [m]
η_{max} Maximum water surface elevation, [m]
η_n Section flow depth (water surface elevation measured normal to bed), [m]
η_{OT} Water surface elevation at onset of overtopping, [m]
η_r Water surface elevation in upstream reservoir, [m]
η_z Vertical flow depth (water surface elevation along vertical axis), [m]
θ Arc angle, [radians, degrees]
θ_n Normalised volumetric water content, [–]
θ_r Residual volumetric water content, [m^3/m^3]
θ_s Volumetric water content at saturation, [m^3/m^3]
θ_w Volumetric water content, [m^3/m^3]
$\theta_{w,i}$ Volumetric water content corresponding to the ith pore class in Green and Corey (1971), [m^3/m^3]
κ Von Kármán coefficient, [FF]
κ_{ψ} Fitting parameter in Vanapalli *et al.* (1996), [–]
λ Porosity for soil, [–]
λ_0 Porosity for underlying layer of soil in van Rhee (2010), [–]
λ_l Porosity for top layer of soil in van Rhee (2010), [–]
λ_{max} Maximum porosity of soil, [–]

λ_ψ Pore-size distribution index, [–]
μ Dynamic viscosity, [Ns/m^2]
μ_p Plastic viscosity, [Ns/m^2]
ν Kinematic viscosity, [m^2/s]
ν' Turbulent velocity fluctuation in y-direction, [m/s]
ξ Breach channel discharge efficiency, [–]
ξ_P Breach channel peak discharge efficiency, [–]
π_ψ Osmotic suction, [kPa], [kN/m^2]
ρ Fluid density, [kg/m^3]
ρ_m Fluid-sediment mixture density, [kg/m^3]
ρ_s Sediment density, [kg/m^3]
σ Normal stress, [N/m^2]
σ_a Actual bending moment in Mohamed *et al.* (2002), [Nm]
σ_f Tensile strength, [kPa]
σ_n Total normal stress on a failure plane, [kN/m^2], [kPa]
σ_s Geometric standard deviation of bed material, [–]
σ_t Surface tension, [N/m]
τ Shear (or tangential) stress, [N/m^2]
τ^* Dimensionless bed shear stress, [–]
τ_m Applied shear stress, [kN/m^2]
τ_{yd} Shear stress at yield, [N/m^2]
τ_b Bed shear stress, [N/m^2]
τ_c Critical bed shear stress, [N/m^2]
$\tau_{c,\Psi}$ Critical shear stress due to boundary seepage, [N/m^2]
τ_c^* Dimensionless critical bed shear stress (Shields parameter), [–]
$\tau_{c,s}^*$ Shields parameter due to sloping bed, [–]
$\tau_{c,s,d}^*$ Shields parameter due to sloping bed and hindered erosion in van Rhee (2010), [–]
τ_u Unconfined compressive strength, [kPa]
τ_Ψ^* Dimensionless shear stress due to boundary seepage, [–]
ϕ Angle of internal friction, [radians, degrees]
φ Correction factor to suspension parameter in van Rijn (1984c), [–]
ϕ' Drained or effective angle of internal friction, [radians]
ϕ_b Bed slope angle, [radians]
ϕ_r Angle of repose, [radians]
ϕ_{wn} Water surface slope angle coinciding with orthogonal flow depth trajectory, [radians]
ϕ_{wz} Water surface slope angle coinciding with vertical flow depth, [radians]
ψ Matric suction, [kPa], [kN/m^2]
ψ_b Bubbling pressure or air-entry value, [kPa], [kN/m^2]
ψ_T Total suction, [kPa], [kN/m^2]
ω Gravimetric moisture content, [%]
$\bar{\omega}$ Average gravimetric water content, [%]
ω_r Gravimetric water content at relatively high suction in Feng and Fredlund (1999), [%]
ω_u Gravimetric water content at zero suction in Feng and Fredlund (1999), [%]
ω_f Frequency of oscillation, [Hz]

Upper-case Greek Letters

Γ Embankment breach characteristic, [UV]
Γ_{unc} Uncertainty in embankment breach characteristics, [UV]
Δ_b Bedform height in van Rijn (1984c), [m]
ΔA Incremental area, [m^2]
ΔE Energy dissipation, [Nm]
ΔG Range of modeling input parameter, [UV]
Δh Difference in piezometric head between two adjacent flow lines, [m]
Δh_i Vertical distance from free surface of overtopping flow to the bottom of the arc failure at slice i in Tingsanchali and Chinnarasri (2001), [m]
Δh_w Head above weir invert, [m]
ΔL Incremental length, [m]
Δm_b Mass of eroded bed, [kg]
Δs Incremental distance along flow path or tangential direction, [m]
Δt Incremental time-step, [m]
Δx Incremental distance in x-direction, [m]
Δy Incremental distance in y-direction, [m]
Δz Incremental distance in z-direction, [m]
Δz_b Incremental change in bed elevation, [m]
$\Delta \eta$ Incremental water surface elevation, [m]
$\Delta \eta_0$ Initial overtopping head, [m]
$\Delta \forall_b$ Volume of eroded bed, [m^3]
Θ Dimensionless shear stress in Hu and Hui (1996), [–]
Θ_{TC} Sediment transport capacity, [m^3/s]
Λ Scale series parameter, [–]
Φ_e Dimensionless erosion rate in Winterwerp *et al.* (1992), [–]
Φ_p Pick-up function in van Rijn (1984a), [–]
Ψ Exit seepage angle with respect to normal plane, [radians]
Ψ_e Dimensionless erosion function in Winterwerp *et al.* (1992), [–]
Ψ_q Boundary flux source term in Richards' equation, [s^{-1}]
Ω_c Critical shear stress parameter in Fread (1991), [ft]

Symbols

$\mathbb{S}$ Degree of saturation of soil, [–]
$\mathbb{S}_e$ Effective degree of saturation of soil, [–]
$\mathbb{S}_r$ Residual degree of saturation of soil, [–]
$\mathbb{S}_u$ Maximum degree of saturation, [–]
$\mathbb{v}$ Velocity, [m/s]
$\forall$ Volume, [m^3]
$\forall_{max}$ Maximum volume, [m^3]

NOTE:

FF refers to "force-fit" units, derived from empirical relationships which vary depending on the application
INT refers to an integer (1, 2, 3…etc.)
UV refers to "variable" units, which vary depending on the application

Subscripts

i	Discretization counter or interval [INT]
ff	Represents the conditions at the failure envelope on a failure plane
mm	Represents a model parameter
pp	Represents a prototype parameter
rr	Represents a parameter scale ratio between model and prototype
x	Represents x-direction
y	Represents y-direction
z	Represents z-direction

Operators

$\mathcal{F}$	Function

Abbreviations

1-D	One-dimensional
2-D	Two-dimensional
3-D	Three-dimensional
AEV	Air-Entry Value
ARS	Agricultural Research Service (U.S. Department of Agriculture)
ASCE	American Society of Civil Engineers
ASDSO	Association of State Dam Safety Officials
ASTM	American Society for Testing and Materials
CADAM	Concerted Action on Dambreak Modelling
CFL	Courant-Friedrichs-Lewy
EC	European Commission
EGL	Energy Grade Line
EMI	Electro-Magnetic Interference
FEMA	Federal Emergency Management Agency
FOS	Factor of Safety
GLE	General Limit Equilibrium
GSD	Grain-Size Distribution
GVF	Gradually-Varied Flow
HERU	Hydraulic Research Unit (U.S. Department of Agriculture)
ICOLD	International Commission of Large Dams
JET	Jet Erosion Test
IMPACT	Investigation of Extreme Flood Processes and Uncertainty
LED	Light Emitting Diode
LES	Large Eddy Simulation
LHS	Left-Hand-Side
MLU	Mirror Lock-up
MPM	Meyer-Peter-Müller
M-TTPA	Micro-Tensiometer-Transducer-Probe Assembly
NRCS	Natural Resources Conservation Service
NSE	Navier-Stokes Equations
NSTL	National Soil Testing Laboratory
NID	National Inventory of Dams
NOAA	National Oceanic and Atmospheric Administration (U.S. Department of Commerce)

NPDP	National Performance of Dams Program
NWS	National Weather Service
OWC	Optimum Water Content
PAP	Pore-Air-Pressure
PPM	Parts Per Million
PWP	Pore-water-pressure
RANS	Reynolds-Averaged Navier-Stokes
RHS	Right-Hand-Side
RSV	Residual Suction Value
RVF	Rapidly-Varied Flow
SCS	Soil Conservation Service
S-TTPA	Standard-Tensiometer-Transducer-Probe Assembly
SVE	Saint-Venant Equations
SWCC	Soil-Water Characteristic Curve
SWE	Shallow Water Equations
TTPA	Tensiometer-Transducer-Probe Assembly
TUD	Delft University of Technology
USACE	U.S. Army Corps of Engineers
USBR	U.S. Bureau of Reclamation
USCS	Unified Soil Classification System
USDA	U.S. Department of Agriculture
VIS	Virtual Instrument Subroutines
VOF	Volume of Fluid
WG	Wave Gauge
WSL	Water Surface Level

Chapter 1
Introduction

1.1 Problem Definition

Hydraulic structures such as dams and dikes have served mankind as flood control, water supply and irrigation systems for over five millennia. Over the past two centuries, earth embankments have also been commissioned for the hydropower generating industry. Their reliability was initially sought to extend for a long period of time, exceeding hundreds of years. However, recent changes in global climatic patterns and the lack of maintenance for earth dams and dikes have increased the potential of breach failures by overtopping and piping and the consequence of life threatening floods. Over the past fifty years, the modeling of earth embankment failures due to overtopping and piping, and routing of the consequential outflow breach hydrographs has been developed, mainly using mathematical techniques.

The outflow breach hydrograph can be essentially characterised by a time-to-peak and a peak flow. Such characteristics, as well as breach growth rate, can be predicted using empirical relationships, parametric models, dimensionless models and physically-based numerical models (Wahl, 1998; Wishart, 2007). Very few experimental models simulating a breach at prototype scale have been developed (e.g. Visser, 1990; Shuibo *et al.* 1993; Hahn *et al.* 2000; Vaskinn, 2004; J. Zhang *et al.* 2009). Empirical and dimensionless models may provide quick estimates for determining the embankment breach characteristics, yet they do not provide a full representation of the time history of the outflow hydrograph required for flood routing (Morris, 2005). Physically-based mathematical models estimate the breach outflow hydrograph using both numerical and analytical solutions. However, the physical processes governing an embankment breach failure must be known *a priori* for the

development of such methods. Once an estimate of the breach outflow hydrograph can be determined, it can therefore be routed downstream using flood routing algorithms, whereby a computation can be made to determine the extent of the flood and the time it takes for it to affect areas with high populations.

Flood routing methods, techniques and algorithms are reliable in generating inundation maps by disaster mitigation teams. Undoubtedly, we are presently experiencing a period when computing power has advanced to a degree where dynamic flood inundation maps can be generated over complex topography of valleys and urban centres within minutes. This is due to the super computers which are equipped with fast flood routing algorithms and multiprocessing systems. Flood inundation maps combining multiple failure scenarios (*e.g.* piping failure initiating at different elevations and locations, or overtopping failures under different reservoir levels) are no longer necessary. The swiftness in disaster mitigation is now contingent upon issuance of warnings and response times for evacuation teams. A warning time of 15 minutes will likely cause human casualties 2,500 times greater than a 90-minute warning time (Graham, 1999). However, what use is a capable downstream flood routing model without an accurate prediction of the hydrograph at the flood source? For the past sixty years, the embankment breach problem has challenged researchers and emergency management agencies due to the complex nature of the breach phenomenon. Several efforts at developing numerical models have since been employed to simulate breach failures and predict the breach outflow hydrograph.

The complexity of the breach phenomenon lies in the nonlinearity of the breach process itself. The breach mechanism is governed by the following processes: hydrodynamics, soil erosion, reservoir routing, sudden collapse mechanisms and other geotechnical processes. Numerical modeling of breach channel initiation and propagation due to overtopping flow requires coupling of these nonlinear physical processes governing a breach at the boundary conditions. The task becomes even more challenging in composite embankments, due to a high variability in the

erosional properties and failure mechanisms between cohesive and noncohesive soil. Other challenges are attributed to complexities in breach flow hydraulics, specifically to secondary currents and transcritical flow present within the breach channel. Hence, at present, it is not mathematically or computationally feasible for a physically-based numerical model to incorporate all of the physical processes governing an overtopping breach failure. Instead, such models tend to consider the most dominant mechanisms and simplify or neglect the rest of them. This often leads to substantial uncertainties in predicting the breach outflow hydrograph.

1.2 Research Needs

Following an exhaustive literature review of the experimental studies conducted on overtopped noncohesive embankment models, the author concluded that there is a significant lack of understanding of how some of the important geotechnical properties and soil behaviours influence the breach mechanism. As a result, these geotechnical aspects have also been overlooked in the development of many mathematical breach models. This problem stems from the fact that hydraulic engineers, who have worked on both past and present embankment breach models, are often unfamiliar or unappreciative of these geotechnical aspects and their influence on the breach mechanism. Nonetheless, limitations of the current earthfill embankment breaching models have become clear not only to the author, but to much of the dam engineering community (Morris *et al.* 2009a, b). Examples of those geotechnical aspects which have often been oversimplified or neglected include: soil moisture conditions and compaction effort during construction, initial soil-water state prior to overtopping, and the boundary seepage mechanism due to overtopping flow. There is a need for addressing these aspects in physical experiments since they influence the two most dominant mechanisms governing an embankment breach: soil erosion and side-slope failures.

Several studies have documented the procedures by which cohesive embankments have been constructed in laboratory and field environments (*e.g.* Hahn *et al.* 2000;

Hanson *et al.* 2003; IMPACT, 2004a; Vaskinn *et al.* 2004; Hanson *et al.* 2005; Hunt *et al.* 2005; Hassan and Morris, 2008). The construction techniques referred to in these studies are often scaled-adaptations of construction methods pertaining to real-size embankment prototypes. These studies have also described how construction parameters, such as water content and compaction, influence the erosion and consequent breach of cohesive embankments. To date, there are no studies which have adopted a realistic construction method scaled for a laboratory or hydraulic flume models using noncohesive embankment materials. Furthermore, experimental studies which have simulated the overtopping mechanism in noncohesive embankment models have used arbitrary approaches in simulating the compaction of embankment materials and the initial soil-water state at overtopping. It is therefore necessary to develop construction and testing techniques which offer an adequate standard of control for those soil parameters. These particular measures were deemed necessary before addressing any other aspect of breach overtopping.

While some previous experiments have investigated the influence of compaction on the breaching mechanism in noncohesive embankments (Simmler and Samet, 1982; Steetzel and Visser, 1992), only two compaction tests have been performed to date. This may be due to difficulties in compacting noncohesive soils. Furthermore, the studies which have been conducted did not describe the spatio-temporal evolution of the breach channel due to the effects of densification.

The influence of boundary seepage on erosion has been investigated by several studies on mild or horizontal bed slopes under subcritical flow conditions (Baldock and Holmes, 1998; Nielsen, 1998; Cheng and Chiew, 1999b; Simon and Collison, 2001; Francalanci *et al.* 2008). There have been no studies to date which have investigated this mechanism due to overtopping flow, where the bed slope is steep and the flow is supercritical. The three-dimensional (3-D) breach overtopping experiments by Pickert *et al.* (2004, 2011) featured measurements of pore-water-pressures (PWP) within the embankment body under a constant reservoir head

using only four to six probes. Measurement of the PWP time-history using an instrumentation technique featuring a denser distribution throughout the embankment body can provide a better understanding of the behaviour of the boundary seepage mechanism. This requirement has yet to be achieved in both 3-D breach overtopping as well as two-dimensional (2-D) overtopping tests. Furthermore, no study to date has attempted to measure the PWP throughout the embankment body under a falling reservoir head.

The extensive literature review was also useful in identifying the critical knowledge gaps related to hydraulic aspects of embankment breach overtopping. A lack of information on the similarity of outflow characteristics (*i.e.* peak flow and time-to-peak) between model and prototype scales, and the corresponding scale effects (Morris *et al.* 2009a, b), has shifted the focus and demand on the development of mathematical models for predicting such characteristics. Over the past three decades, there have been a number of experimental programs which have addressed scaling in earth embankments (Tinney and Hsu, 1961; Chee, 1978; Pugh, 1985; Shuibo *et al.* 1993; IMPACT, 2004a; Stretch and Parkinson, 2006; Schmocker and Hager, 2009). Some of these investigations have been specifically designed for fuse plug embankments (*e.g.* Tinney and Hsu, 1961; Chee, 1978; Pugh, 1985; Shuibo *et al.* 1993). Others investigations have been more qualitative where only one model and one prototype have been used (*e.g.* IMPACT, 2004a), or, have expressed dimensionless parameters in terms of breach channel width, height and volume as well as reservoir volume (*e.g.* Stretch and Parkinson, 2006). The experimental program in Schmocker and Hager (2009) was comprised of a comprehensive investigation of scale effects, one of which involved three geometric scale ratios (1, 0.5 and 0.25). Their investigation, however, incorporated scale series using planar (*i.e.* 2-D) overtopping tests with high inflow-to-outflow ratios. In fact, most of the investigations have employed high inflow-to-outflow ratios in their model and prototype experiments where the Froude criterion, traditionally employed in rigid bed hydraulic modeling, has also been applied to scale the flow parameters. There is yet a need for validating existing (or proposing new) scaling relationships of

breach outflow characteristics using 3-D breach overtopping tests with a prevalent falling head characteristic.

Breach outflow is often simplified using weir-type equations, which assume regime control at the constriction of the breach channel. Several experimental observations, however, have raised attention towards the control section forming at the upstream slope during 3-D breach overtopping tests (Coleman *et al.* 2002; IMPACT, 2004a; Stretch and Parkinson, 2006; Morris *et al.* 2007). This control section, described as a curved or crescent-shaped weir, was larger than the constriction width. The investigation by Coleman *et al.* (2002) described the breach discharge and the channel dimensions based on this curved-shaped weir as a function of reservoir head in dimensionless terms. However, their tests were performed under a constant head. A similar investigation needs to be conducted using a falling head for this apparent control section in the case of finite reservoirs.

In order to observe and effectively grasp the fundamental processes governing the overtopping failure mechanism, the physical tests need to be carried out using homogeneous embankment models. A complete scrutiny of the breaching mechanism using simple configurations, such as homogeneous embankments models, is deemed necessary before attempting similar tests on more complex geometries such as composite embankments, or even modeling within the computational realm.

1.3 Scope

The primary goal of this study was to bridge the knowledge gap between the hydraulic and geotechnical processes governing an embankment breach failure. In some aspects, this study has also considered geotechnical and hydraulic parameters and processes which are not necessarily dependent or interactive with each other. *The scope of this study, however, was limited to the experimental investigations in which noncohesive homogeneous embankment models are overtopped*. Reference to numerical models in breach overtopping of noncohesive

embankments is often made in this study since this has reflected on the current perspective of the research community, and has therefore been useful in defining the requirements and solutions for this problem.

1.4 Research Objectives

This research study was initiated by conducting a preliminary numerical and experimental investigation program (described in Chapter 5) which then helped set the groundwork for an extensive experimental investigation using consistent testing procedures. The objectives of this study can be categorized into two types: (1) development of novel model construction and testing procedures, and, (2) the investigation of physical model parameters. The overall objectives of this research study can be summarised below in point form:

1. Develop a new construction technique for laboratory earthfill embankments using noncohesive soil.
2. Investigate the influence of material compaction and initial soil-water state on the embankment breach mechanism.
3. Conduct scale series experiments for various geometric embankment model scales.
4. Determine the progression of the upstream control section forming on the upstream slope in an embankment breach.
5. Develop a novel experimental 2-D configuration used to measure the PWP time-history through an embankment due to overtopping flow.

The specific objectives of this study are summarised below in point form:

1. Develop a new construction technique emulating a prototype embankment construction in which the compaction of a noncohesive embankment material can be varied and where the optimum density is based on *in situ* conditions.
2. Develop a testing procedure for 3-D breach overtopping tests with very low inflows, and address test repeatability.

3. Develop a testing procedure where the initial soil-water state can be varied in breach overtopping tests.
4. Investigate the influence of both compaction and initial soil-water state (*i.e.* two test series) on the breach outflow hydrograph using 3-D breach overtopping tests.
5. Investigate the influence of tilted and quasi-exact geometric scale series (*i.e.* two additional test series) on the breach outflow hydrograph using 3-D breach overtopping tests in which the Froude criterion and the associated scale effects can be evaluated.
6. Apply a non-intrusive photogrammetric technique for extracting the dimensions of the curved-shaped weir at the entrance of the breach channel
7. Derive an expression for the breach outflow using the dimensions of the breach channel entrance assuming Froude-critical conditions, and compare it with the measured values.
8. Develop a minimum intrusion instrumentation technique in which the PWP through an embankment body can be measured for 2-D overtopping tests.
9. Investigate the influence of seepage on erosion mechanics using 2-D overtopping tests under drained and undrained conditions including initially dry conditions.

1.5 Contributions and Novelty of Research Program

The optimum density and moisture conditions for prototype embankments are usually based on compaction levels attained using laboratory equipment (*i.e.* Standard Proctor mold). Controlling and matching compaction in prototype embankments based on laboratory conditions, however, is quite difficult (Hanson and Hunt, 2007). Due to differences in confinement between the field and laboratory, optimum conditions must be defined using an *in situ* compaction curve. The novel construction technique which has been developed is based on the *in situ* compaction curve. Compaction of the noncohesive embankment material was applied and controlled using vibratory and static loads.

The 3-D breach overtopping tests were conducted under a falling hydraulic head (*i.e.* finite reservoir), and were initiated using very low inflows. It was important to isolate the effect of the inflow in order to ensure that the breaching mechanism and scaling laws were entirely represented and assessed, respectively, based on the falling head characteristic. As a result, this testing standard has contributed to a less biased assessment of the spatio-temporal scale effects, especially during the breach initiation and development stages. While several studies have addressed the effect of downstream slope on breach overtopping, this is the first study where the entire geometry of the hydraulic model, including the upstream impoundment, has been scaled in embankment breach 3-D overtopping experiments.

A novel experimental technique comprised of sixteen micro tensiometer-transducer devices, designed and fabricated by the author in the Geotechnical Laboratory at the University of Ottawa, has been developed to investigate the influence of the seepage mechanism on overtopping erosion. These inexpensive devices were capable of measuring the PWP through the body of an embankment slope with minimum-intrusion in the soil and water mediums. Their fast response time allowed them to be used in overtopping experiments where erosion on the downstream slope accelerated the drainage of pore-waters. A novel transient flownet analysis technique used to estimate the exit hydraulic gradient and boundary discharge velocity based on the interpolated PWP through the downstream slope of the embankment was proposed in this study. The one-dimensional (1-D) Saint-Venant equations were derived to account for the effects of boundary seepage and steep slopes. Based on the 1-D hydrodynamic equation, the bed shear stress was then computed using the extracted free water surface and bed profiles. Erodibility of the soil for the plane overtopping tests was investigated for three different initial degrees of saturation.

This type of analysis could be used in the future to derive expressions featuring a seepage-induced grain mobility based on the measured erosion rates and the modified bed shear stress. Such expressions can replace the classical transport-

capacity sediment formulations which have been developed for steady, uniform and rectilinear flow with impervious bed conditions. The geotechnical parameters and processes investigated in this study (*e.g.* initial soil-water state, dry unit weight and the boundary seepage mechanism) would be important to include in future numerical models which, unlike their performance at present, should be able to capture the physical nature of breach growth. The compaction test series conducted on overtopped noncohesive embankment models will also provide some insight on adopting compaction control as a technique for scaling other mobile bed hydraulic models. Also, having standardised guidelines related to embankment model construction and testing techniques, particularly in laboratory environments, can be instrumental to the research community. Establishing such guidelines can dramatically expand the current experimental database and facilitate the exchange of information between the researchers as well as allow new embankment breach parameters to be incorporated.

1.6 Organization of Manuscript

Chapter 1 identifies the embankment breach problem, the scope and objectives of this research as well as the important contributions to the research community. Chapter 2 debuts with an account of historical documents and legends of dams and dam failures in the ancient world. A classification of the types of dams, their size and safety hazards and causes of failures in the modern world is also presented in this chapter. Chapter 3 provides a detailed literature review of embankment breach modeling, wherein mathematical and experimental models pertinent to the scope of this research are discussed. Chapter 4 includes the theory relevant to embankment breach hydromechanics. It entails all the aspects and fundamental equations governing the following breach processes: hydrodynamics, breach erosion mechanics, reservoir routing, sudden enlargement mechanisms, classical versus unsaturated soil mechanics, role of seepage on slope instability and erosion, and finally, dimensional analysis and similitude. Its goal is to serve as a fundamental and

comprehensive theory of embankment breach processes, particularly for future graduate students.

Chapter 5 presents the preliminary work conducted in this research program. The results of a study on the sensitivity analysis on two embankment breach numerical models, NWS-BREACH and HR-BREACH, has been described. In this chapter, Phase I of the experimental program, which is comprised of 3-D breach overtopping experiments, is also described in detail. Phase I of the experimental program was conducted in a small and large hydraulic flume as a preliminary program to investigate the potential experimental parameters which were adopted in Phase II and Phase III. All embankment models tested in the first experimental phase were constructed using a dynamic compaction technique.

Chapter 6 presents the 3-D breach overtopping experiments conducted as part of Phase II of the experimental program following a refined construction technique. The parameters which were investigated in this experimental phase were compaction effort, initial soil-water state, and two geometric scale series, tilted and quasi-exact.

Chapter 7 presents Phase III of the experimental program. It was conducted to investigate the seepage mechanism due to 2-D overtopping flow wherein the transient response of the PWP was recorded in the eroding slope. A novel experimental 2-D configuration comprised of PWP measurement devices as well as a model to determine the contribution of boundary seepage on the bed shear stress is proposed in this chapter. Chapter 8 concludes with a summary of this research and is followed by a list of references cited in this manuscript.

Appendix A includes a brief description of two numerical models, NWS-BREACH and HR-BREACH, which were used in the embankment breach modeling sensitivity analysis. A brief description of the five-stage BRES model is also included in this appendix. Appendix B presents a state-of-the-art review and summary of the methodology, results and conclusions, for a large number of overtopping and piping experiments conducted over the past twenty-five years, as part of field and

laboratory investigations. Similar to Chapter 3, the intent of this appendix is to guide future graduate students on potential parameters which can be investigated. A matrix comprising the key information for the tests conducted in laboratory flume is also provided in this appendix. In Appendix C, details and results of geotechnical tests performed using laboratory equipment and *in situ* for all three experimental phases are provided. In Appendix D, details on the construction techniques, design, as well as installation and calibration instructions of equipment are provided. Details on the construction techniques of the embankment models tested in the three experimental phases are also described. Included in Appendix E are all the computer codes which have been developed during the three phases of this experimental program. Included in Appendix F, are the data and results for the 2-D overtopping tests.

Chapter 2
History and Background of Embankment Failures

2.1 Dam Failures during Ancient Civilizations

Since the dawn of civilization, hydraulic engineering systems have been developed to serve two of the most important human essentials: agriculture and water supply. The construction of dams and irrigation systems allowed many ancient civilizations in Africa, Asia and Europe to thrive off agriculture, whereas simple water distribution networks comprised of canals, tunnels and aqueducts led to the early settlements in the vicinity of rivers and streams. It is no doubt that historical records of water retention structures, such as earth embankments and masonry dams, dating back as far as 4,000 BC, were part of irrigation and flood defence systems. The *Jawa* reservoir was the result of a 5m-high masonry gravity and earth dam design, constructed roughly during the 4^{th} millennium BC in the Black Desert of present day Jordan (Dam, 2012; Fahlbusch, 2009). Its primary use was to retain water from a stream runoff to cultivate land downstream. *Sadd el Kafara* (Dam of the Pagans) was a 14m-high rockfill dam with a silty-sand/gravel core and a limestone slope protection on both upstream and downstream faces. It is known to be the world's oldest large dam, and was constructed in *Wadi el Garawi* in 2,650 BC near the ancient Egyptian capital, *Memphis*, 30km south of current day Cairo, Egypt, possibly as a flood defence structure for downstream installations or simply for water storage (Mays, 2010). However, even the world's oldest large dam could not measure up to the fury of floods. The Bronze Age dam was overtopped after a heavy rainfall event. It is believed that it was probably destroyed during its construction phase (Fahlbusch, 2009).

The first Dynasty of Ancient Egypt (3,100 – 2,890 BC) was the first to witness basin irrigation. Floodwaters were conveyed into a succession of basins using canals dug from the Nile River using a system of transverse and longitudinal dikes and berms and masonry regulators for controlling the flow. This drainage system was also particularly useful during high floods, where diversion of the Nile flood waters was conveyed to *Birket Qarun* (Lake Moeris) northwest of the *Fayum* depression. This depression was thus used to protect Lower Egypt (*i.e.* Nile Delta) from floods and soon after became a cultivation basin (Garbrecht, 1996). During this era, the water levels in Lake Moeris were high enough such that it was possible to return the flood waters back to the Nile. In 2,300 BC, an earth dam was constructed to divert the flood waters into the depression, while a second dam was constructed to convey the stored water back into the Nile River (Little, 1959). To implement such a control system, the ancient Egyptians had to breach the dams in succession (*i.e.* before and after the annual flood), and immediately begin reconstruction of the dams to prepare for the floods in the following year.

During the Graeco-Roman period (*i.e.* after 332 BC*)*, water levels in the lake dropped significantly (Mays, 2010) after a 5km long and 4m-high dike upstream of the channel leading to the depression was constructed as part of a land reclamation project. Although it was not possible to resort to the earlier control system for water storage, the lowered lake meant more arable land and a more prosperous cultivation. The study by Garbrecht (1996) mentions an archaeological survey which described a 8km long, earth dam approximately 2m high (with a 7.5m maximum height) with masonry water retaining walls, that was constructed south east of the depression during the Ptolemaic period (323 – 30 BC). This dam was meant to serve basin irrigation and flood storage. There are three to four locations which the dam is believed to have been breached. The results of the survey also state that the dam was breached (and rebuilt) at least four times, the first breach to have probably occurred during the Byzantine era (30 BC – 641 AD).

Archeological records date early irrigation systems in Southern Arabia in the ancient *Mā'rib* watershed (present day Yemen) began between 4,000 BC and 2,000 BC (Brunner and Haefner, 1986; Brunner, 2000; Francaviglia, 2000). The Sabaeans (people of Sheba) relied greatly on flood irrigation, and so have built the Great Mā'rib Dam, an earth embankment boasting two sluice structures, two stilling basins and a spillway. During the 6th century AD, it was overtopped and breached by floods, probably due to reservoir volume decrease due to siltation. It met its last demise in the 7th century AD by *Sayl al Arim* (transl. 'barrier flood') and with it the fall of the South Arabian Kingdom and dispersion of its people across the Arabian Peninsula (*Qur'an 27:33*; Brunner and Haefner, 1986; Brunner, 2000).

The most ancient dam constructed in Anatolia, in the present day Turkey, is the Karakuyu Dam, which dates back to the Hittite period (2,000 – 700 BC). It was an 8m high embankment with a main crest length of 200m, built to support agriculture by means of irrigation canals. It is believed to have failed due to seepage along the bottom outlet of the embankment (Öziş 1996).

Perhaps the most remarkable dam ever constructed and to have endured the test of time, is the Marduk Dam. It was constructed on the Tigris River near Samarra, 125km north of Baghdad, Iraq, and dates back to roughly 2,000 BC. Despite its extraordinary longevity, little is known about the Marduk Dam, except that it had survived the Assyrian, Chaldean, Persian, Greek, Roman and Sassanid empires before being breached and left in ruin in 1256 AD (El-Yussif, 1983; Wurbs, 1992).

Ancient legends often speak about China's two largest rivers, *Chang Jiang* (Yangtze River) and *Huang He* (Yellow River), the cradle of the Chinese civilization. The two rivers which drain 40% of China's watersheds have brought both prosperity and sorrow for the early Chinese inhabitants. It is for these reasons that the ancient Chinese revolutionised the art and science of flood management. The first record of a flood from the Yellow River dates back to 2,297 BC (Hoyt and Langbein, 1955), while in 2,280 BC, Chinese engineers, under the rule of Emperor Yau, began the construction of dams and dikes in lower reaches of the river to direct its course to

the sea (Li, 2005; Bhattacharyya, 2011). Historical records indicate that the Yellow River has changed its course 26 times, and overtopped its dikes 1,590 times, and has resulted in the killing of millions of inhabitants (Li, 2005).

Early inhabitants of ancient Ceylon (present day Sri Lanka) were renowned for their achievements in irrigation works. The cultivation of rice fields in that era was perfected by means of constructing reservoirs in succession, where each tank or reservoir was at a different elevation in order to control overflow from one reservoir to the other using sluice gates. Such advanced irrigation techniques was made possible by constructing embankments, dating back to 370 BC (Schnitter, 1994, as cited in Bhattacharyya, 2011). The paralysis (and consequent destruction) of irrigation communities in ancient Ceylon due to malaria and warfare consequently caused the earth embankments to be breached (Pereira, 1973, as cited in Bhattacharyya, 2011).

The *Junagadh* rock inscription by King Rudradaman (dated 150 AD) near the coast of the state of Gujarat, India, records the repair of the *Urjayat* dam, constructed in 300 BC during the reign of Maurya Raja Chandragupta. It burst in 129 AD after a storm caused bushes and stones to block the outlet works, causing the water to rise and eventually overtop and destroy the dam (Singh, 2008). The dam was reconstructed to three times its original size, using mud and brick stone, in 137 AD, under orders by King Rudradaman. It was once more overtopped in 449 AD by heavy rainfall after the sluices failed to drain the flood waters entering the lake. The resulting embankment breach, 20 cubits in length and 20 cubits in width and 75 cubits deep (~ 10m x 10m x 40m), depleted lake *Sudarśana* (literally ‘beautiful to look at’) and converted it into a sandy desert, or lake *Durdarśana* (literally ‘extremely ugly to look at’) (Jamsedjee, 1891; Singh, 2008). In 456 AD, the dam was restored by Viceroy Chakrapâlita within two months. It is unknown for how long this dam lasted, and what caused it to break again.

The ancient Roman era led to many marvels in hydraulic engineering infrastructure. The Roman engineers and concrete masons perfected construction techniques and

consequently built aqueducts, baths, fountains and sewers, fit for a great empire. The Alcantarilla Dam, built in the Tajo basin on the Guajaraz River near Toledo, Spain, is the oldest dam constructed in ancient Rome (Arenillas and Castillo, 2003). The semi-arid Iberian Peninsula and North African coast were the first regions where Romans built their early hydraulic works. The construction of the Alcantarilla Dam was in the form of a 557m long and 17m high earth dam of sandy clay soil, with an upstream retaining wall and a sloping downstream face. It was constructed to supply water to the captured city of Toledo, roughly around the 2nd century BC. Archeological surveys of its ruins revealed that the upstream retaining wall was very thin for its height, only 4m at its base. Masonry ruins were found upstream of the dam's location, over a central distance of 200m. This suggests that the retaining wall was pushed upstream, where the breach may have resulted due to the saturated soil's push against the upstream wall, during the emptying of the reservoir (Arenillas and Castillo, 2003; Bretas *et al.,* 2012). Some of the masonry ruins were located downstream, which may suggest that a large flood followed the collapse of the retaining wall.

The reign of Emperor Nero (54-68 AD) witnessed the first dam construction for the sole purpose of recreation. Three masonry dams in Subiaco near Rome were constructed to create recreational lakes near Emperor Nero's villa. In 1305 AD, one of these three dams, a 40m high masonry dam, collapsed after two monks removed stones from its foundation in an attempt to drain the impoundment after their land had been flooded (Smith, 1970).

2.2 Dam and Dike Breaching Disasters in the Modern World

The Industrial Revolution marked an important milestone in the evolution of powered machinery and great improvement in the standard of living of inhabitants in Western Europe, North America and Japan. The discovery of great technologies in various domains of science towards the end of the 19th century led to greater investments and marked growth in the economies of several countries. The world's newly found

production wheel triggered a large growth in human population, particularly after improved sanitary conditions and better health practices. The increasing demands of a growing population generated an increase in the utilization and management of water resources. By the mid-18th century, embankments were not limited to irrigation and flood control; they were constructed to power mills and guarantee drinking water supplies to nearby villages and communities. Towards the end of the 19th century, the concept of embankments was revolutionized, and began to serve the electrical power generation sector. Modern inventions such as the Francis Turbine in 1848, by James B. Francis, and the Pelton Turbine in the 1870s, by Lester Allan Pelton, led the way to scientists and engineers to develop hydroelectric power plants (Grahl-Madsen, 2009). During the early 1900s, advances in classical soil mechanics led by the founding father, Karl Terzaghi; improved the construction of embankment dams, particularly for hydroelectric plants. Later, embankments were used for flow diversion, inland navigation, fire prevention and even recreation.

Several studies investigated and chronicled the catastrophes caused by the failure of earth dams, including their causes, their breach characteristics and impact on humans over the past 200 years (1802 to 1980). A summary of the most catastrophic 21 dam failures is provided in Table 2.1 (Lou, 1981; Singh and Quiroga, 1988; Singh and Scarlatos 1988; Wohl, 2000; Gee, 2008; Rico *et al.* 2008; Xu and Zhang, 2009; Tsakiris *et al.* 2010).

Table 2.1: Major dam failures, their causes, breach characteristics and loss of lives (sources: Lou, 1981; Singh and Quiroga, 1988; Singh and Scarlatos 1988; Wohl, 2000; Gee, 2008; Rico *et al.* 2008; Xu and L.M. Zhang, 2009; Tsakiris *et al.* 2010)

Dam/Country	Type	Year built/failed	Cause of failure	Height [m]	Storage [x 10^6 m^3]	Peak flow [m^3/s]	Failure time [hr]	Human losses
Puentes, Spain	Gravity	1791/1802	Piping	50	-	-	-	600
Bradfield, England	Earthfill	1858/1864	Structural	29	3.2	1,150	<0.5	238
El Habra, Algeria	Gravity	1872/1881	Structural	-	-	-	-	209
South Fork, USA	Earthfill	1838/1889	Overtopping	23	18.9	8,500	3.5	2,200
Saint Francis, USA	Gravity	1926/1928	Abutment	62.5	46.9	14,100	-	450
Vega de Tera, Spain	Buttress	1957/1959	Structural	-	-	-	-	144
Malpasset, France	Arch	1954/1959	Abutment	66.5	51	-	-	421
Orós, Brazil	Earthfill	1960/1960	Overtopping	35.4	650	9,630	8.5	50
Babi Yar, USSR	Earthfill	N/A/1961	Overtopping	-	-	-	-	145
Hyokiri, S. Korea	-	N/A/1961	Overtopping	-	-	-	-	250
Quebrada La Chapa, Columbia	Earthfill	N/A/1963	-	-	-	-	-	250
Vaiont, Italy	Arch	1959/1963	Overtopping	267	240	-	-	3,000
Baldwin Hills, USA	Earthfill	1951/1963	Piping	49	1.1	1,100	1.3	3
Vratsa, Bulgaria	Tailings	N/A/1961	Overtopping	-	0.45	-	-	600
Zgorigrad, Bulgaria	Tailings	N/A/1966	-	12	1.52	-	-	96
Nanak Sagar, India	Earthfill	1962/1967	Piping	16	210	-	-	100
Sempor, Indonesia	Rockfill	1967/1967	Overtopping	-	-	-	-	200
Buffalo Creek, USA	Tailings	1972/1972	Overtopping	14	0.61	1,420	0.5	118
Banqiao, China	Earthfill	1953/1975	Overtopping	24.5	492	78,100	5.5	85,600
Teton, USA	Earthfill	1975/1976	Piping	93	356	66,000	4	11
Machhu II, India	Earthfill	1972/1979	Overtopping	60	110	-	-	2,000

Perhaps the worst disaster in the history of dams during this past century is the Banqiao Dam failure in China. In 1953, the Chinese government constructed the Banqiao Dam, an earthfill embankment with a clay core, as a flood defence structure on the Ru River in Henan province. The dam underwent a modification in 1956 due to settlement after its first impoundment, and was therefore reinforced using a compacted backfill along its length (Xu and Zhang, 2009). The Nina Typhoon, a 2,000-year return period storm, struck the Henan province on 4 August, 1975, lasting five days and resulting in 544 mm precipitation per day over the entire Huai River watershed. Initially designed to withstand 306 mm of precipitation per day (corresponding to an 1,000-year return period storm), the maximum reservoir capacity was exceeded by 24%, overtopping the embankment and eroding it very quickly due to its poorly compacted soil and due to the 238.5 million m^3 of water (40% of the existing volume) that additionally drained into the reservoir during its overtopping (Liu *et al.* 2009; Xu and Zhang, 2009). The propagating flood wave affected 12 million inhabitants bringing disease, famine and food poisoning and incurring 1.6 billion US dollars in damages. Sources regarding the death toll vary significantly, ranging between 85,600 (official count) to 230,000 (Topping, 1998; Liu *et al.* 2009).

Between 1874 and 1995, failures in earthen dams have led to 2,927 casualties in the United States alone (FEMA; 2005; Graham, 2009). The failure of the Teton Dam in Idaho, U.S.A. on June 5th, 1976, was one of the most disastrous in the history of U.S. earthfill dam failures. Seepage on the downstream slope, caused by a defect in the right abutment, appeared after its first impoundment by spring runoff. Within a few hours, the piping leak progressed and developed into an overtopping failure. The 93m high dam eventually collapsed, releasing downstream 308 million m^3 of water from the reservoir (Smalley, 1992). The downstream flood claimed 11 lives and incurred close to one billion dollars of property damages and claims. The environmental impact due to this failure is seldom mentioned in literature. Large quantities of chemicals such as DDT, organophosphate pesticides, urethanes and chlorinated compounds were released into the Snake River (Young et al. 2004). On

November 6th of the following year, the U.S. witnessed another catastrophic failure near Toccoa, Georgia, when 39 lives were lost and 3 million US dollars in damages where incurred after the Kelly Barnes Dam collapsed. The U.S. Federal Investigative Board did not issue a conclusive cause for the failure, however, it points to a combination of events where a piping failure initiated, and consequently led to the saturation and erosion of the downstream face of the dam and the subsequent slope failure. The eventual collapse of the 13 m high structure released 777,000 m^3 of water downstream of the dam (USBR, 2002).

2.3 Failure Mechanisms of Embankments

2.3.1 Types of Embankments

To understand the failure mechanism of an embankment, it is necessary first to distinguish between the two types embankments: earthfill and non-earthfill. Earthfill dams and embankments are structures which are usually trapezoidal in cross-section, that retain water, and are comprised of compacted, yet sufficiently pervious materials such as clay, silt, sand and gravel. Contrary to earthfill embankments, masonry and concrete dams do not allow water seepage through the impounding structure since they are constructed using watertight or impervious materials such as poured concrete or masonry (bricks and stones sealed with mortar). Physical processes governing the failure of earthfill embankment differ significantly from those occurring in non-earthfill embankments since erosion is excluded in the latter. This thesis focuses on the failure mechanism, and the consequential “breach” of earthfill embankments, characterised by a gradual process, as opposed to the failure of concrete or masonry dams, which is characterised by a sudden “dambreak” and the release of a shock-like wave.

There are two main types of earthfill embankments according to the studies by Costa (1985) and Clague and Evans (2000): natural and man-made. Natural dams are formed when large earth movements or landslides impound large volumes of water. Peak flows are generally very large with magnitudes often exceeding 10,000

m^3/s and the time-to-peak flow is short (minutes to hours). Moraine dams are formed in glacial regions, when debris collapsing into valleys obstructs retreating glaciers. The soil composition of naturally occuring moraine dam soils is heterogeneous, with a wide variety of particle sizes, ranging from silt sediments to large boulders. They are generally much larger than manmade earth dams (few tens of metres high) and are steep with width-to-height ratios between 0.1 – 0.2. Jökulhlaups (or glacier bursts in Icelandic) are enormous floods released by water bodies draining from glacier-dammed lakes with peak flows generally lower than moraine dams. Volcanic dams are formed after volcanic activity, when molten lava solidifies blockading valleys where rivers and streams normally flow. They can also develop when floods from heavy rainfall are drained within volcanic craters. In March 28, 1982, molten lava from El Chichon Volcano dammed the Rio Magdalena Valley, (Mexico) impounding a large lake. Two months later, the lake was drained releasing flood waters down the valley. Water temperature from the flood wave recorded 10 km downstream was as high as 82°C. Landslide dams are formed after large land movements such as landslides from nearby valleys and hill slopes. Such mass movements can be triggered by mass wasting or debris flow following seismic activity or high degrees of water saturation in the soil after storm events. Landslide dams are by far the largest dams, reaching heights of several hundred metres high (Korup, 2002).

Classifications of manmade earth embankments comprise structures such as river dikes, coastal dikes, earthfill dams and rockfill dams. In the case of earthfill embankments, PWP through the structure can be dissipated by using fine-grained soils. A homogeneous embankment is comprised of one soil material, usually clay or silty-sand, to ensure adequate dissipation of PWP, except for slope protections which are usually constructed using rip-rap, rock armour and/or concrete. Reducing the water seepage potential can also be achieved by using non-homogeneous embankments. In a non-homogeneous embankment (*i.e.* composite or zoned), the core is comprised of a fine-grained soil such as clay, silty-clay, silt or silty-sand, while the shell is comprised of a coarser grained soil such as sand or fine gravel.

Controlling seepage through homogeneous earthfill embankments can also be made possible by installing drainage elements made of much coarser soils (*e.g.* gravel) within the embankment body, typically using a horizontal orientation at the downstream toe or on the upstream face. Drainage elements can also be installed vertically in the core of the embankment in the form of drainage walls. In the case of drainage elements, it is important to use appropriate gradation between the different soil layers to prevent migration of fines and reduce exit gradients. This is carried out using a filter medium comprised of soils with an intermediate grain size.

The study by Costa (1985) presents statistics obtained from the ICOLD (1973) study of dams built by type. The statistics state that about 58% of dams built in Western Europe between 1900 and 1969 were earthfill embankments, with a 1.2% failure rate, the second highest number of such structures after buttress dams (2.6% failure rate). The study also presents that the highest percentage of failures is attributed to earthfill dams, at 74%. L.M. Zhang *et al.* (2009) studied more than 1,600 dam failures cases throughout the world (excluding China) and compiled a database from extensive literature sources. Their study stated that 66% of dam failures were those of earthfill embankments, while 83% of the cases occurred in the U.S. and about 62% were attributed to embankments lower than 15m in height. The ICOLD (1973) study, presented in Yen (1993), stated that the probability of failure (per year per dam) for dams with a height lower than 15m, between 15 and 29m, between 30 and 49 m and over 50m is 0.23%, 0.12%, 0.11% and 0.04%, respectively. Graham (1999) studied 21 dam failures in the USA between 1960 and 1998, for which 86% of the 318 deaths recorded were caused by dams less than 15m high.

2.3.2 Size of Dams and Safety Hazard

The U.S. Army Corps of Engineers (USACE, 1979) defines categories for classifying the size of dams based on the water impoundment volume and dam height. The criteria are based on three categories; small, intermediate and large, as summarised in Table 2.2.

Table 2.2: Size classification (USACE, 1979)

Category	Reservoir storage volume, V_R [m^3]	Dam height, h_D [m]
Small	61.7 x 10^3 < V_R < 1.23 x 10^6	7.6 < h_D < 12.2 m
Intermediate	1.23 x 10^6 < V_R < 61.7 x 10^6	12.2 < h_D < 30.5 m
Large	61.7 x 10^6 < V_R	30.5 m < h_D

The potential hazard of a dam is another important classification which considers factors such as the potential loss of human life and/or property in the event of a dam failure. The report by FEMA (2004) categorises the potential hazard as low, significant and high, as shown in Table 2.3 below. It is important to note, however, that small reservoir sizes are considered in fact as high risks for an embankment breach. In January 1998, the 7.6 m high Archus Creek Dam was overtopped due to a 5 year return period storm, where only 11cm of precipitation fell over a few hours. However, the extremely large ratio of the watershed to reservoir surface area of 226:1 along with the restricted spillway capacity due to clogging of the fish retaining screens by debris, caused the dam to be overtopped (Newhouse *et al.* 2010).

Table 2.3: Hazard potential classification System (FEMA, 2004)

Category	Loss of human life	Economic loss
Low	None expected	Low; limited to owner
Significant	None expected	Yes
high	Probable. One or more expected	Yes, although not necessary for this classification

A system of hazard potential enables a hazard assessment on downstream communities in the event of a dam failure. Project design/construction and dam failure analysis is carried out mainly by engineering consulting firms and occasionally by research organizations (*i.e.* universities and research institutes). Emergency preparedness on the other hand, requires the involvement of the following stakeholders: flood mapping and hazard mitigation teams, insurance and asset management companies, as well as national security and civil defence authorities and organizations.

Breach analyses on existing and new dams must therefore be conducted in order to help hazard assessment and mitigation teams plan for such events, and thwart any risk on human life. Aging of existing embankment infrastructure, including dams and flood protection dikes, is compelling evidence that such hazard assessments need to be performed. According to the Hazard Potential Classification System for Dams by the Federal Emergency Management Agency (FEMA, 2004), over 15,000 out of the 85,000 dams in 2009 registered in the National Inventory of Dams (NID), which are a large subset of all U.S. dams, have a high-hazard potential, about 4,000 of which are considered deficient or unsafe (ASCE, 2009). For the past decade, the Infrastructure Report Card issued by the American Society of Civil Engineers, has consistently given a "D" grade to dams at the national level (ASCE, 2009).

The average U.S. dam has a design life of 50 years. In 2000, about 25% of dams had already reached their age limit, and by the year 2020, 85% of these dams will have exceeded their design life (Lane 2007). The aging infrastructure is also a concern in Europe, where 65% of the 55 large dams in Finland require rescue efforts (FEMA, 2005). The National Performance of Dams Program (NPDP) at Stanford University (McCann, 2009) maintains 4,491 historical records of dam incidents in the U.S., of which 3,233 are considered non-neutral incidents (i.e. records which do not relate to construction, modification, maintenance, design, replacement or ownership changes and only constitute catastrophes such as earthquakes, failures or breaches, inflow floods and sabotage). 42% of the non-neutral incidents were reported for failed dams leading to both partial and complete failures.

2.3.3 Causes of Embankment Failures

Foster *et al.* (2000) investigated the failure modes of the world's embankment population built prior to 1986, and excluding ones constructed in pre-1930 Japan and China. Their study stated that the average failure frequency is 1.2% (136 failed embankments out of a world population of 11,192), similarly presented in the 1973 study conducted by the International Commission of Large Dams (ICOLD). The work by Wahl (1998) investigates 108 embankment failures between 1864 and 1996,

90% of which were in the USA. The study by Costa (1985) discusses several investigations conducted by other researchers on the causes of dam failures, both on a national (*i.e.* US) and international scale. One of the described studies is by ICOLD, who conducted surveys of global failures of 135 dams which were more than 15m in height, for earthfill and concrete dams (72% and 28%, respectively). There are four main causes of failure of earth embankment; overtopping, piping erosion, seismic loading and slope instabilities.

2.3.3.1 Overtopping Failures

Overtopping failure in earth embankments can be triggered when the upstream water level exceeds that of the crest of the dam, or that of the dike due to wave overtopping. The occurrence of overtopping is usually attributed to many reasons, such as: inadequate design height in spillways or embankment crest, losses in storage capacity due to lack of maintenance, seiches or surges induced by seismic activity, large displacements of water volumes in the reservoir due to rock/soil slides and mass wasting of channel banks and ice avalanches (Clague and Evans, 2000), wind set-up, waves, and malfunctions in spillways, gates or pipe outlets (Foster *et al.* 2000). Current tensions in the global political climate have led government agencies to investigate overtopping failures from man-induced causes such as acts of war, sabotage and terrorist attacks. Research studies that have addressed blast-induced dam failures are yet at the pioneering stage (Nistor and Rennie, 2005; Orendorff *et al*. 2009).

2.3.3.2 Piping Failures

Piping in embankments is initiated when high hydraulic exit gradients near the downstream face and below the phreatic surface cause exfiltration of the surficial soil. At this point, outward seepage through the saturated subsurface soil occurs, wherein a tubular cavity between the exit surface and the head source occurs. The continuous void reaching the downstream side of the embankment may appear as “a soft wet area to a flowing spring” (Ohio Department of Natural Resources, 1994).

The insufficient design or absence in a gradation filter between two soils of different particle sizes is extremely prone to piping. The migration of fines into larger pore sizes, coupled by seepage of water through the voids, may dislodge enough material to disrupt the homogeneity of the soil and lead to piping. Once piping is initiated, exfiltration will continue to enlarge the tubular cavity, possibly to a degree where the soil above the cavity collapses under its own weight, in which the mode of failure becomes overtopping. Although the mechanism of piping is not fully understood, post-failure geotechnical investigations often identify defects in the foundation or abutment regions as the root cause. Piping may also occur when the shell material of upstream and downstream slopes is weakened due to burrowing activity, root growth from vegetation, cracks and fissures (Onda and Itakura, 1997).

2.3.3.3 Seismic-Induced Slope Instability

Seismic loading (earthquakes), although not very common, can be rather catastrophic to earth embankments as to masonry dams. Sudden and large increases in PWP may cause the soil to lose its strength and stiffness, and eventually liquefy, behaving as a fluid. The eventual slide or collapse of the soil material can take place in either slope of the embankment and can lower the crest significantly (*e.g.* San Fernando Dam, in L.A., California in 1971; ASDSO, 2012). Another uncommon mode of failure in earth embankments is slope instability. Rapid drawdowns in the reservoir result in residual PWP in the embankment's upstream slope, reducing the effective stress of the soil and causing it to shear at a failure plane due to its own weight. The resulting downward slide of the upstream slope will undermine the integrity of the embankment due to the high hydrostatic forces present in the reservoir, eventually leading to an overtopping failure. A similar slide could also occur in the downstream slope, after large underslope zones become saturated, a common occurrence in high intensity and prolonged rainfall events. It is for this reason that downstream slopes are lined with vegetation to increase the shear strength of the soil and resist high degrees of saturation. Alternatively, the

downstream slope can be impermeabilized using concrete or riprap to prevent the soil from reaching a saturated state.

Table 2.4 shows a summary of statistics attributed by the mode of failures discussed above.

Table 2.4: Statistics of dam failure modes

Population	Time Period	Overtopping	Piping	Sliding	Earthquake	Unknown
97[1]	1900-1969	35%	59%	unknown	unknown	6%
108[2]	1864 - 1996	38%	52%	1%	unknown	8%
136[3]	Pre-1900 to 1986	45%	43%	5%	1.5%	5.5%
129[4]	Pre-1800 to 1996	44%	27%	6.5%	4.5%	18%

[1]ICOLD, 1973 (total number of dams surveyed is 135); [2]Wahl, 1998 (88% of population are U.S. embankments); [3]Foster et al., 2000 (excluding dams constructed in pre-1930 Japan and China); [4]L.M. Zhang et al. 2009 (excludes data from China. Only 129 cases were considered from the total of 1,065 failures studied)

The study by Graham (2009) presented casualties related to dam failures between 1874 and 1995 and indicated that 2,927 life casualties in the U.S. were due to earthfill or rockfill dam failures (92% and 8% respectively). Overtopping alone was responsible for 89% of these deaths, whereas 6%, 5% and 0.2% were attributed to slope slides, piping failures, and defects in the foundation, respectively.

2.3.4 Embankment Breach in Warfare

Historical records have shown that breaching of embankments was also deliberate or politically motivated. The Arthashastra, a book of written narratives on warfare and political and economic strategies, belonging to the Prime Minister of the Mauryan Empire (in current day India) between 321 – 297 BC, was one of those which revealed such accounts. It mentioned that a leader should drown enemy lands by breaching dams and dikes, thus paralyzing infantry movements through the flooded terrain (Bhattacharyya, 2011). In 1642, dikes at *Kaifeng* along the Yellow River were breached by a collapsing Ming Empire in China to prevent a Manchu led rebellion (Loeser, 1973). In 1938, Chiang Kaishek, a military leader in the Chinese

army, repeated history by making several dike-breaching attempts in the Henan Province to ward off the Japanese armies from the south. It took three attempts by the General to breach the dikes, one of which involved digging cavities and using explosives to blast them. The final attempt, led to a breach failure, widened to several hundred feet across with the help of Chinese soldiers burrowing the soil with shovels. Several reports of casualties were issued for three affected provinces; ranging between 300,000 to 900,000 dead and 3 million to 12 million displaced (Lary, 2001).

In May 1943, allied forces bombed the Eder and Möhne concrete gravity dams in Germany killing 1,294 inhabitants, 493 of which were foreigners (mainly Ukrainian women) working on farmlands downstream (Chant, 2008). On 6 October, 1973, Operation *Badr* was launched by the Egyptian Armed Forces to reclaim the Sinai Peninsula. The major success of the infantry's crossing east of the Suez Canal was accredited to the method by which the Israeli-constructed Bar-Lev line, a 25 m-high steep sand embankment and fortification, was breached in multiple locations. The breaches were carved using water hoses supplied from high-pressure pumps mounted on marine vessels. After 8 hours from the launch, a total of 65 breaches were carved out and 90,000 m^3 of earth was removed.

Chapter 3

Literature Review

3.1 Embankment Breach Modeling

In order to effectively carry out downstream flood routing due to an overtopped embankment, it is necessary to accurately model and predict the initiation and evolution of an embankment breach. Over the past 50 years, researchers have developed several methods for modeling overtopped embankment breaching. The main objective of those models, detailed in the following section, is to predict the variation of the discharge, Q, with respect to time, t, which is conveyed through the evolving breach channel and which propagates downstream. This temporal variation of the discharge is referred to as the breach outflow hydrograph (see Figure 3.1). A secondary objective of these models is to describe the breach evolution or time-dependent breach channel geometries (Wishart, 2007).

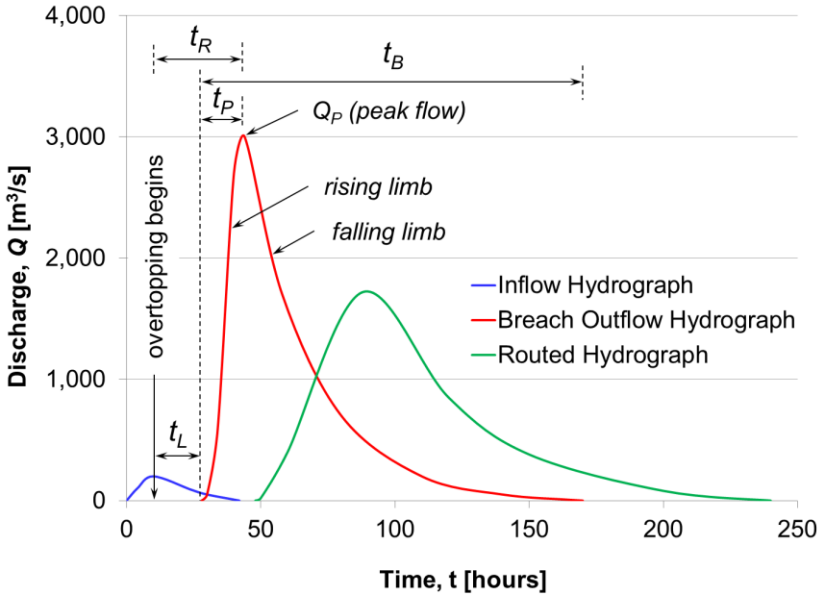

Figure 3.1: Hypothetical inflow, breach outflow and routed hydrographs

Based on previous experimental research (discussed in more detail in Section 3.3 as well as Appendix B), the failure of an embankment due to overtopping or piping can be described as having three stages: breach initiation, formation and propagation. In the case of overtopping, the first phase pertains to flow over the embankment crest, and usually occurs at a location where the crest elevation is lowest due to choice of design or due to construction issues or settlements. At the initial stages of the embankment breach, the outflow is negligible and its damage is only limited to saturating the downstream slope whereby a breach channel in the downstream vertex of the embankment's crest is initiated. The increasing hydraulic head in the reservoir coupled with the saturated conditions on the downstream slope augments the erosion in the breach channel. In piping failures, high exit gradients near the soil boundary lead to the initiation of a conduit through the shoulder slopes of the embankment. As the flow in this conduit intensifies, bulk material is transported and deposited downstream. In the breach formation stage leading to overtopping failures, transport of material from the breach channel downstream of the embankment's crest eventually leads to carving a shallow breach channel on the entire downstream slope. In piping failures, the conduit increases in diameter, as more material is eroded and transported through the conduit. Breach outflow at this stage increases for both failure mechanisms, but is still noticeably low. During the breach propagation stage in overtopping failures, the increasing breach outflow amplifies the erosion and deposition further, where a fully formed breach channel begins to propagate and extends vertically and laterally. Side-slope failures in the breach channel appear in this stage, adding to the enlargement of the breach channel in the lateral direction. In piping failures, the conduit eventually collapses due to the weight of the soil above, whereby the failure mode shifts to an overtopping failure, caused by the large cavity in the embankment. During this stage, the breach outflow reaches a peak value (*i.e.* following the rising limb of the hydrograph as shown in Figure 3.1), whereas the breach channel experiences further downward and lateral degradation as well as an increased frequency of side-slope failures. Beyond that stage, the breach channel bottom reaches the valley

floor. As the volume in the reservoir is depleted (*i.e.* following the receding limb of the hydrograph as shown in Figure 3.1), little changes in the breach process occur further. A detailed five-stage breach erosion process has been proposed by Visser (1998) for noncohesive embankments and by Zhu (2006) for cohesive embankments. Hahn *et al.* (2000), Hanson *et al.* (2003a, b) also describe a four-stage breach process for cohesive embankments.

Breach models are of two types: mathematical and experimental. Mathematical models are categorised as follows: empirical, parametric, and physically-based (Wahl, 1998; Wishart, 2007). Empirical models estimate the embankment breach characteristics (*i.e.* peak outflow and time-to-peak) using empirical relationships, derived from case study data, and expressed in terms of reservoir size, dam geometry and empirical coefficients. Parametric models are solved analytically or numerically, while physically-based models are solved numerically. Experimental models are mobile-bed embankment models constructed in laboratory or field conditions. They are used to scale up the embankment model breach characteristics to determine prototype characteristics, or simply used to observe the breach phenomena and mechanisms with the support of multimedia and other data acquisition instruments.

3.2 Mathematical Modeling

3.2.1 Empirical Models

One method for evaluating the magnitude of floods due to embankment breaching and identifying the extent of its damage uses empirical relationships. These relationships usually estimate the peak outflow in the form of a power law as shown below (Wishart, 2007):

$$Q_P = \alpha_Q {R_W}^{n_Q} \tag{3.1}$$

where, $\alpha_Q$is an empirical constant, R_W is a reservoir characteristic and n_Q is the exponent of the power law. Examples of reservoir characteristics are: volume of

water released, average reservoir depth, drop in reservoir level during breach and the reservoir's potential energy with reference to a downstream reach.

Empirical relationships are based on databases that contain statistical data of embankment breach failures. Data such as peak flow is seldom measured during an embankment breach due to the lack of readiness and to the high risk imposed by the flood waters. Instead, peak flow is estimated from the flood's stage and the bathymetry of its conveyance from post-flood field surveys and hydraulic approximations. Given the highly erosive peak flows and the enormous volumes of sediment released (and redeposited) during the course of an embankment breach, as well as the continuously changing flood bathymetry and stage, survey measurements are mere estimates. Therefore, they do not necessarily represent the flood at peak-flow conditions, especially during this very short duration of a usually prolonged flood. Another problem which may lead to inaccuracies is that peak flows are usually estimated at locations downstream of the breach, where attenuation and translation (*i.e.* lag) effects are not properly accounted for and corrected (Walder and O'Connor, 1997).

The accuracy of the empirical relationship greatly depends on the number of failures documented in the database. On the other hand, this accuracy also suffers from the very assumption of similarity between embankment breach failures. The reality is that the breach peak flow cannot be solely determined from reservoir characteristics or the drop in the reservoir water level, since there is a multitude of factors and causes pertaining to the breach processes and physics, such as dam geotechnical properties and geometry as well as other hydraulic conditions. The study by Manville (2001) stated that estimates of breach peak flows can vary by one order of magnitude. For this reason, empirical relationships serve as a quick approach for estimating the peak flow from embankment breaches where a more thorough verification is performed using other methods.

Parameters that are related to the temporal and geometric evolution of the breach are known as secondary breach parameters, and can also be estimated using

empirical relationships. Time-related parameters are; time-to-peak, t_P, breach lag-time, t_L, (often referred to as breach initiation time in embankment breach literature), failure time, t_F, or breach base-time, t_B (see Figure 3.1). The breach initiation or lag-time refers to the duration of time between the onset of flow overtopping the embankment crest and the moment when there is a measurable flow through the breach channel. The parameter t_F in embankment breach literature usually refers to the time for the breach channel to fully develop; more specifically the time it takes for the breach channel invert to reach the upstream face (Wahl, 1998). The rise time, t_R, is also a parameter which defines the time between the onset of overtopping and peak flow conditions. Other secondary breach parameters that can be estimated are breach width, B_W, and breach channel side-slope factor, z_{SS}. Table 3.1 summarises empirical relationships which estimate embankment breach parameters as proposed by several embankment breach studies by Wahl (1998), Wahl (2004), Wishart (2007) and Pierce *et al.* (2010).

Empirical relationships are derived by regression analysis from several case studies (see Table 3.1). There are two types of regression analyses; single-regression, which uses only one reservoir or embankment variable or multiple regression which uses more than one variable (Pierce *et al.* 2010). Most empirical relations use linear best-fit curves, whereas only a few use curvilinear regression techniques. The studies by Walder and O'Connor (1997) and Xu and Zhang (2009) state that multiple-regression techniques using variables such as reservoir volumes (*e.g.* V_0, V_{OUT} and V_W) as well as embankment/breach channel heights, h_{cr} or h_B, respectively, provide a more accurate estimate to the breach parameters over single-regression techniques. The model by Xu and Zhang (2009) estimates five embankment breach parameters, h_B, Q_P, t_F, B_W and $\bar{B}$ using independent variables such as embankment dam height, reservoir shape, embankment dam configuration (*e.g.* homogeneous, composite and concrete-faced dams and embankments with core-walls) and erodibility. Their model, which is derived from a multivariate regression analysis of 182 earthfill and rockfill dams, stated that erodibility is the most important factor influencing the embankment breach parameters. Two other

studies include erodibility in their empirical relationships; Von Thun and Gillette (1990) and Walder and O'Connor (1997).

Table 3.1: Empirical relationships for estimating embankment breach parameters

Reference	Case Studies	Proposed Relationship(s)
Kirkpatrick (1977)	38	$Q_P = 1.268(h_W + 0.3)^{2.5}$
SCS (1981) for dams > 31.4m	38	$Q_P = 16.6(h_W)^{1.85}$
Hagen (1982)	31	$Q_P = 1.205(V_F h_W)^{0.48}$
USBR (1988)	40-80	$Q_P = 19.1\left(h_W^{1.85}\right)$ $t_F = 0.011\bar{B}$ $\bar{B} = 3h_W$
Singh and Snorrason (1984)	38	$Q_P = 13.4(h_{cr}^{1.89})$ $Q_P = 1.776(V_0^{0.47})$ $2h_D < \bar{B} < 5h_{cr}$
MacDonald and Langridge-Monopolis (1984)	37-60	$Q_P = 1.154(V_W h_W)^{0.412}$ $t_F = 0.00475(V_W h_W)^{0.28}$
Costa (1985)	31	$Q_P = 1.122\left(V_0^{0.57}\right)$ $Q_P = 0.981(V_0 h_{cr})^{0.42}$
Evans (1986)	39	$Q_P = 0.72\left(V_W^{0.53}\right)$
Von Thun and Gillette (1990)	57	$t_F = 0.015h_W$ (highly erodible) $t_F = 0.02h_W + 0.25$ (erosion resistant) $t_F = \bar{B}/(4h_W)$ (highly erodible) $t_F = \bar{B}/(4h_W + 61)$ (erosion resistant) $\bar{B} = 2.5h_W + c_b$
Froehlich (1995a)	77	$t_F = 0.00254(V_W)^{0.53}(h_B)^{-0.9}$ $\bar{B} = 0.1803K_0(V_W)^{0.32}(h_B)^{0.19}$
Froehlich (1995b)	22	$Q_P = 0.607\left(V_W^{0.295} h_W^{1.24}\right)$
Walder and O'Connor (1997)	35	$Q_P = 1.51\left(g^{0.5} h_d^{2.5}\right)^{0.6}\left(\frac{\dot{E}V_{OUT}}{h_d}\right)^{0.94}$; $\zeta < 0.6$ $Q_P = 1.94\left(g^{0.5} h_d^{2.5}\right)\left(\frac{h_{cr}}{h_d}\right)^{0.75}$; $\zeta \gg 1$ $t_P \approx 1.24\left[\frac{V_{OUT}}{\dot{E}^2(gh_d)^{1/2}}\right]^{1/3}$; $\zeta \ll 1$ $t_P = \frac{h_d}{\dot{E}}$; $\zeta \gg 1$

h_W is depth of water above breach invert at time of failure; V_F is reservoir volume at time of failure; $\bar{B}$ is the average breach width; h_{cr} is embankment crest height; V_0 is the reservoir volume at time of breach initiation; V_W is volume of water above breach invert at time of failure; c_b is an offset factor in Von Thun and Gillette (1990) breach width equation and varies as a function of reservoir volume; h_B is breach channel height; g is the gravitational acceleration; K_0 is 1.4 for overtopping and 1.0 for piping in Froehlich (1995a); h_d is the drop in reservoir level during breach; $\dot{E}$ is erosion rate [m/h]; $\bar{\dot{E}}$ is the average erosion rate; V_{OUT} is volume of water discharged through breach; ζ is a dimensionless breach parameter in Walder and O'Connor (1997).

3.2.2 Parametric and Dimensionless Models

Parametric models use the same relationships as empirical models to estimate embankment breach parameters such as breach width, failure time, time-to-peak, and breach channel side-slope factor, z_{SS}. Often, some of those parameters are input by the user, based on one's experience. In this case, the user will be required to select the final breach dimensions (width, depth and side-slope factor) and failure times from similar case studies. Using the embankment breach parameters, the parametric models simulate the breach channel evolution as a linear growth rate, whereas breach outflow is solved using weir flow hydraulics (Wahl, 1998) (see Subsection 4.1.5 for more details).

Field observations often describe the final breach channel geometry after an embankment dam failure as trapezoidal, triangular or parabolic. The vast majority of those records, however, are embankment breach channels of a trapezoidal cross-section (Wahl, 1998). The study by Froehlich (2008) describes three types of breach growth models proposed in embankment dam breaching literature as shown in Figure 3.2. In Model "*A*" (*e.g.* Macchione, 2008), the embankment breach channel cross-section is initially triangular and proceeds to evolve until it reaches the valley floor, where the cross-section continues to evolve as a trapezoid. In Model "*B*", the embankment breach channel evolves as a trapezoid throughout the breach failure. In Model "*C*", the bottom breach width, B_{BW}, is constant. It is important to note that in reality, breach channel erosion occurs below the water surface and not above as shown in Figure 3.2 (*e.g.* Mohamed *et al.* 2002). This process, however, leads to undercutting in the breach channel and consequently side-slope failures. Nevertheless, lateral erosion (*i.e.* Model "B") would occur most in locations downstream of the breach channel constriction, due to high convective accelerations. Such processes are often accounted for in physically-based numerical models, and which are described in Subsection 3.2.3. Parametric and dimensionless models, on the other hand, simplify the breach process by assuming

uniform erosion and regular breach shapes such as trapezoids, triangles, rectangles and parabolas.

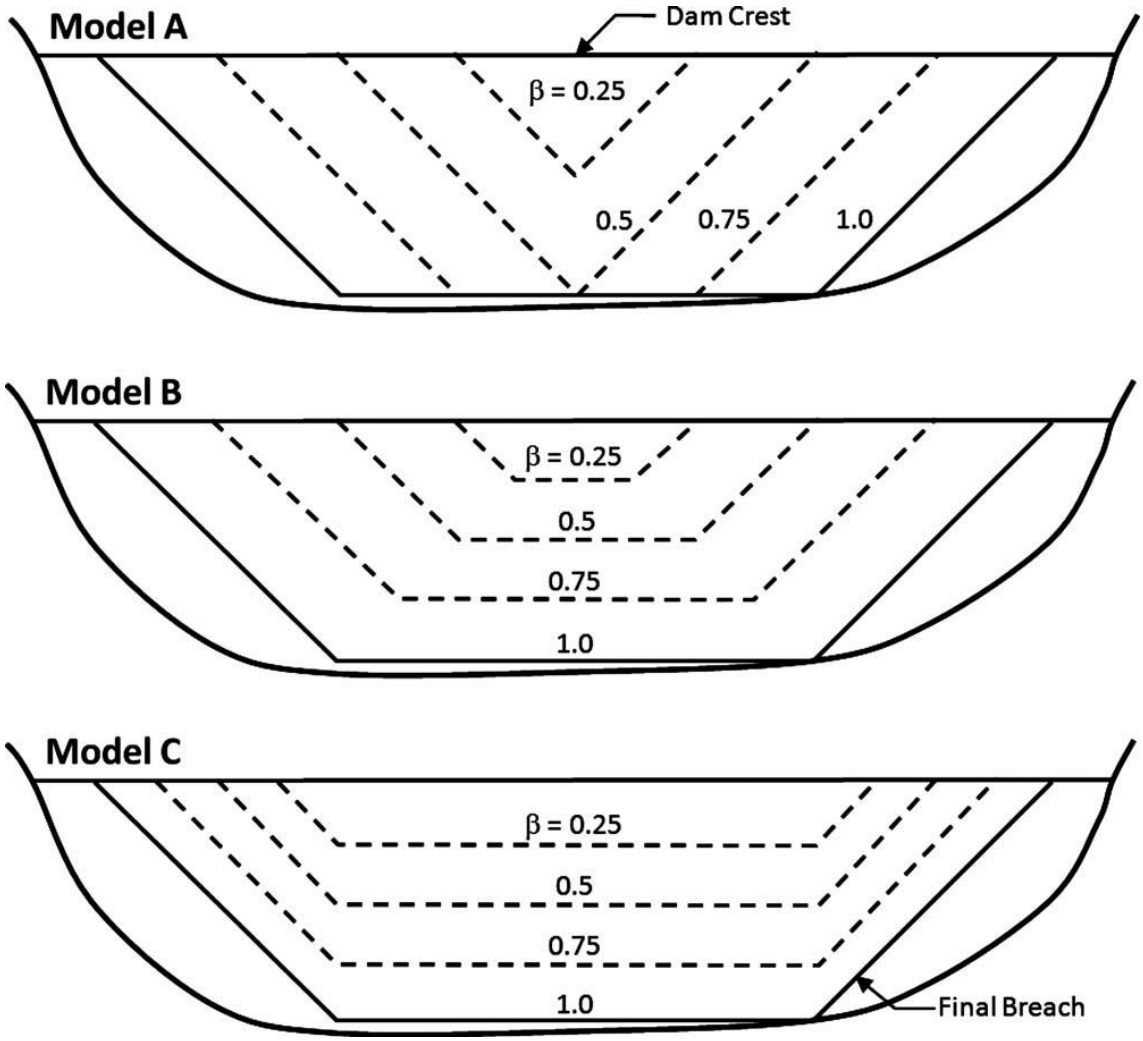

Figure 3.2: Breach growth models (after Froehlich, 2008)

Dimensionless models, similar to empirical and parametric models, use empirical relationships to describe embankment breach characteristics. Their main assumption is that there is similitude in breach formation and mechanics between all embankments. First, the embankment breach characteristics and independent breach variables are expressed in dimensionless form, based on a dimensional analysis method (*e.g.* Buckingham Π Theorem). The next step involves the derivation of an expression between the embankment breach characteristics and

independent breach variables in dimensionless form, using regression analysis. Finally, the dimensional breach characteristics can be determined from the dimensionless expression. Due to the subjectivity in selecting the repeating variables, the dimensionless form of the embankment breach parameters usually varies in literature (Webby, 1996; Chinnarasri *et al.* 2004).

The study by Walder and O'Connor (1997) define the dimensionless embankment breach characteristics such as peak flow, Q_P^*, time-to-peak, t_P^* drained volume, V_{OUT}^*, as follows:

$$Q_P^* = \frac{Q_P}{g^{1/2} h_d^{5/2}} \tag{3.2}$$

$$V_{OUT}^* = \frac{V_{OUT}}{h_d^3} \tag{3.3}$$

$$t_P^* = \frac{t_P \dot{\bar{E}}}{h_d} \tag{3.4}$$

Walder and O'Connor (1997) took into account the relative breach erodibility or the erosive potential of the reservoir by means of a dimensionless erodibility parameter. Their regression analysis was thus divided into two expressions, each defining the relationship between the dimensionless embankment breach characteristics and independent breach variables, which are dependent on the value of this erodibility parameter (*e.g.* when $\zeta \gg 1$, breach formation is rapid).

$$\zeta = \left(\frac{\dot{\bar{E}}}{\sqrt{g h_d}}\right)\left(\frac{V_{OUT}}{h_d^3}\right) \tag{3.5}$$

The study by Webby (1996) applies different repeating variables, g and V_0, and proposed a dimensionless ratio for peak outflow, Q_P^*, using the following expression:

$$Q_P^* = \frac{Q_P}{\sqrt{g V_0^{5/3}}} \tag{3.6}$$

The embankment breach characteristic, Q_P^*, was estimated using regression analysis as shown in the equation below.

$$\frac{Q_P}{\sqrt{gV_0^{5/3}}} = 0.0443\left(\frac{h_r}{V_0^{1/3}}\right)^{1.40} \quad (3.7)$$

where, h_r is reservoir depth.

The regression analysis by Chinnarasri *et al.* (2004) used the same dimensionless peak flow ratio as proposed by Webby (1996). Their study also took into account other parameters such as the median embankment material particle size, d_{50}, and the embankment downstream slope factor, z_{DS}, in their dimensionless regression analysis as shown in the expression below.

$$\frac{Q_P}{\sqrt{gV_W^{5/3}}} = 0.002\ln\left[\frac{h_W^2 d_{50} z_{DS}}{V_W}\right] + 0.032 \quad (3.8)$$

The study by Froehlich (2008) defined the dimensionless reservoir volume at failure time, V_F^*, and the secondary embankment breach parameters, average breach width and breach formation time in dimensionless form, $\overline{B^*}$ and t_f^*, respectively, as follows:

$$V_F^* = \frac{V_F}{h_B^3} \quad (3.9)$$

$$\overline{B^*} = \frac{\bar{B}}{h_B} \quad (3.10)$$

$$t_f^* = t_f\sqrt{g/h_b} \quad (3.11)$$

The study then estimated the secondary embankment breach parameters using regression analysis as:

$$\bar{B}^* = 0.27K_0{V_F^*}^{0.32} \quad (3.12)$$

$$t_f^* = 63.2{V_F^*}^{0.50} \quad (3.13)$$

From Equations (3.10) and (3.12), and Equations (3.11) and (3.13), the average breach width and failure time was expressed as follows:

$$\bar{B} = 0.27K_0{V_F}^{0.32}h_B^{0.04} \quad (3.14)$$

$$t_f = 63.2\sqrt{V_F/gh_B^2} \quad (3.15)$$

3.2.3 Physically-based Numerical Models

Physically-based numerical embankment breach models predict the breach outflow hydrograph by simulating the many processes which govern an embankment breach failure, such as: hydrodynamics, soil erosion, reservoir routing, sudden collapse mechanisms and other geotechnical processes. The tedious task by which these physical processes are described in the form of detailed physical-mathematical relationships and coupled as a physical model has challenged researchers for the past 50 years. Solving the highly nonlinear and 3-D processes using a computational algorithm further complicates the numerical models. However, the complexity of the breach mechanism has often compelled researchers to neglect or oversimplify some of those physical processes. Having a thorough understanding of the breach mechanism and the several approaches and limitations of each physically-based numerical model is therefore an essential matter for any numerical modeller. Based on these approaches and limitations, the modeller needs to determine the appropriate physically-based model for the analysis of the embankment breach project.

For the past 50 years, over 40 physically-based numerical models have been developed to predict the outflow hydrograph from an embankment breach failure (see Table A-1 of Appendix A for a list of the numerical models). What is common between those numerical models is that they acknowledge, to some extent, the interplay between the physical processes governing a breach failure. Their design is based on a description of the breaching processes within a physical domain, consisting of the embankment, initial and upstream and downstream boundary conditions, such as inflow characteristics, initial breach geometry, embankment material and size, reservoir impoundment and often downstream valley geometry. How the breaching process is reflected in terms of physical-mathematical relationships (and assumptions) and how it is treated within the computational algorithm is unique to each model. Figure 3.3 illustrates the four main breaching processes (or modules in a numerical model) and the interconnection between the

various input breaching parameters (*i.e.* initial and boundary conditions) in most physically-based numerical embankment breach models. It is important to note that some of the theoretical processes are still vague or unknown, and the obligation is on the experimental investigators to reveal them.

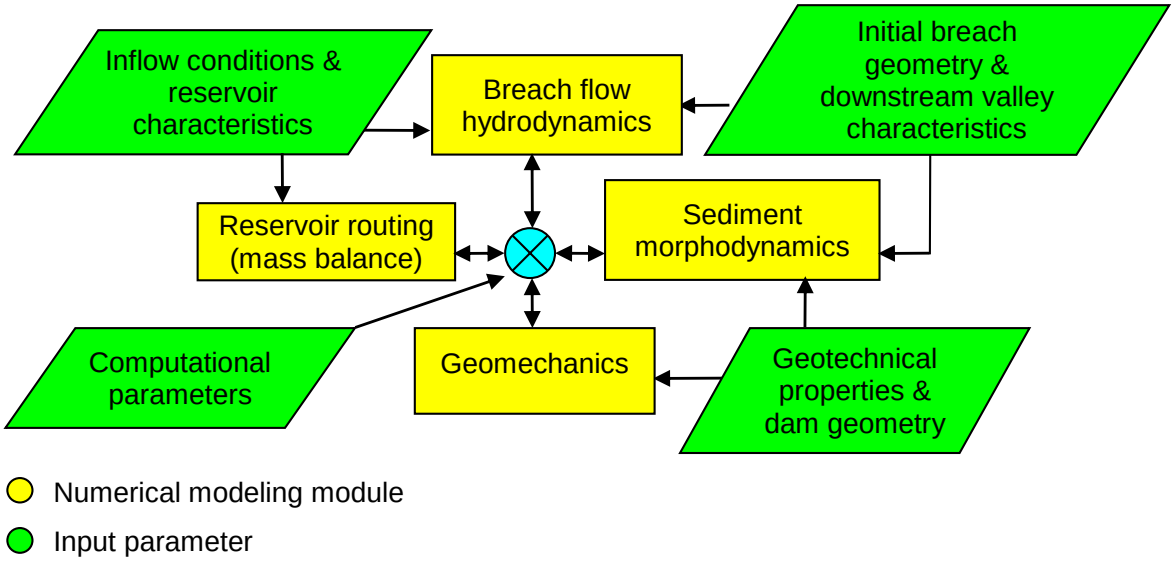

Figure 3.3: Modeling processes and input parameters in embankment breach models (examples of computational parameters are related to discretization of the spatial and temporal domain and numerical schemes)

The Task Committee on Dam/Levee Breaching study (EWRI TC, 2011), of which the author of this thesis is a member, classifies physically-based numerical models into two types: simplified and detailed. According to this classification, simplified models are usually 1-D and assume or approximate the breach shape (*i.e.* triangular, rectangular or trapezoidal). Detailed models, on the other hand, are spatially-discretized as 1-D or multi-dimensional (*i.e.* depth-averaged (*i.e.* 2-D) or 3-D) and include rigorous hydrodynamic and sediment transport algorithms. In the latter, breach morphology is captured by coupling the differential equations describing hydrodynamics, often including turbulent flow characteristics, sediment deposition, armouring and sorting. Morris *et al.* (2009b) stated that this subdivision is also based on the degree of empiricism embedded within the models, and the lack of theoretical

processes which dominate the embankment breaching mechanism. For instance, in simplified models, critical flow conditions are assumed to occur on the embankment crest, where the breach outflow is estimated using weir equations (Morris *et al.* 2009b). Different classifications on the type of physically-based models exist (*e.g.* Wahl, 1998; D'Eliso, 2007; Kahawita, 2007). Nevertheless, while all models hold assumptions and approximations, a crystal clear distinction between simplified and non-simplified physically-based mathematical model (as described herein) would be almost impossible to establish. A complete list of physically-based mathematical models can be found in Table A-1 in Appendix A.

3.2.3.1 Simplified Models

As reported by Fread (1984a), the first physically-based model was developed by Cristofano (1965). The model simulated sediment morphodynamics in the embankment breach section by proposing an empirical relationship between the forces of the flowing water to the shear strength of the soil particles in the breach section. In his model, Cristofano assumed the breach geometry to develop as a trapezoidal cross-section with a constant breach bottom width, whereas the side-slopes of the breach section and the longitudinal slope of the breach channel could be determined by the angle of repose, ϕ_r, and angle of internal friction, ϕ, of the embankment material, respectively. Breach outflow was computed using broad-crested weir equations in the breach section. Later, Brown and Rogers (1977) developed a computer model (BRDAM) based on Harris and Wagner's (1967) analytical model which assumed a breach channel with a parabolic cross-section to commence immediately upon overtopping and progressed until the breach reached the embankment foundation. The rate of erosion was estimated using the Schoklitsch (1934) bedload equation (Wahl, 1998; Morris *et al.* 2009a). Breach outflow due to overtopping and piping was estimated using broad-crested weir and orifice flow equations, respectively. Ponce and Tsivoglou (1981) derived their own model which estimated the breach outflow by coupling the 1-D unsteady Saint-Venant equations, sediment continuity (Exner) equation and Meyer-Peter-Müller

(MPM) (1948) bedload transport equation. Their model was the first to couple hydrodynamics and sediment transport in breach mechanics, but it suffered from numerical instabilities due to its computationally expensive algorithm (Wahl, 1998). The DAMBRK model, developed by Fread (1977), simulates breach propagation by applying linearized time-dependent erosion to the breach channel entrance, and computes the outflow hydrograph from broad-crested weir flow equations and includes a reservoir continuity module. It was the first model to simultaneously route the outflow hydrograph in the downstream valley to compute the attenuated flood wave. In 1984, the National Weather Service released NWS-DAMBRK, an expanded version of the DAMBRK model (Fread, 1984b). In 1988, it was replaced by NWS-FLDWAV model which was equipped with advanced flood routing capabilities to account for mud/debris (non-Newtonian) flow, bridge/embankment flow constrictions, tributary inflows, river sinuosity and tidal effects (Fread and Lewis, 1998).

The first and one of the very few current commercially available embankment breach models is NWS-BREACH, developed by Fread (1984a) at the U.S. National Weather Service, Office of Hydrology. Using physical and mathematical relationships to describe the breaching process, this 1-D model assumes an initial breach channel with a rectangular cross-section which evolves into a trapezoid, where a FORTRAN algorithm simultaneously assesses side-slope stability and sediment erosion. It is considered to be one of the most versatile embankment breach models for its ability to predict the outflow hydrograph for overtopping and piping failures in homogeneous, composite and grass-lined embankments. The model also takes into account side-slope instabilities, downstream submergence effects and breach enlargement by sudden collapses upstream of the breach channel due to hydrostatic forces in the reservoir. The model on the other hand relies on a great deal of empiricism, and many of its assumptions are simplistic. One of the main assumptions is the constant breach shape and slope of the breach channel. It simplifies the flow within the breach channel by assuming quasi-steady normal flow depth by iterations using Manning’s equation. In this model, the

Manning coefficient, n_M, is derived from Strickler's formula which is based on embankment grain size. Another unrealistic assumption is the induced erosion above the water surface. This assumption may only be valid for large dams where normal flow depth can be achieved at further downstream distances from the dam crest, where positive and negative wave effects are more gradual for large reservoirs. Importantly, the NWS-BREACH is the first model to use a sediment equation which has been modified for steep slopes (Smart, 1984); however, it is limited to a gradation of 20°.

The first version of the HR-BREACH model was developed by Mohamed *et al.* (2002) at HR Wallingford after three years of research and development on embankment breach modeling (experimental and numerical). It was developed following several tests on the NWS-BREACH model which deemed it to oversimplify certain breaching processes (Morris *et al.* 2009b). It incorporates a different methodology for assessing side-slope stability as well as a non-uniform shear stress distribution within the breach channel according to that proposed by Lane (1953) for trapezoidal channels. The model uses a 2-D approach for simulating breach morphology. Breach hydraulics is described using a 1-D quasi-steady flow model for a discretized embankment profile (Morris *et al.* 2009b). In the critical section, breach flow conveyance is governed by a weir flow equation, while upstream and downstream of this reach nonuniform flow is assumed. It routes the eroded sediment by using the 1-D sediment continuity equation and hence does not assume a breach channel with constant slope. A detailed sensitivity analysis performed by the author of this thesis on the NWS-BREACH and HR-BREACH models is presented in Section 5.1.

A rather common model used to predict the outflow hydrograph from breached sea-dikes is BRES (Visser, 1998). It describes breach evolution using a five-stage process. A brief description of this model can be found in Section A.3 of Appendix A.

3.2.3.2 Non-simplified Models

Broich (1998a) categorized embankment breaching numerical models into the following categories based on their spatial discretization:

- 1-D: spatial discretization in longitudinal (*i.e.* x) dimension
- 2-D: spatial discretization in longitudinal and transverse (*i.e.* x and y) dimensions

The study by Tingsanchali and Chinnarasri (2001) presented a 1-D morphodynamic numerical model which couples the Shallow Water Equations (SWE) with breach erosion using five sediment transport formulations together with the sediment continuity equation. The numerical model was calibrated using a series of laboratory experiments performed on large-scale homogeneous noncohesive embankment models for fixed bed and mobile bed conditions. An algorithm was included to determine slope failures on the downstream face of the embankment using a safety factor, which is defined as the ratio between resisting forces and driving forces acting on the failure plane. The method of assessing slope stability was the method of slices as shown in Figure 3.4. Their method takes into account the PWP in the dam body acting on the upstream and downstream face of the slice. The PWP acting on the upstream and downstream sides are computed using the following equation:

$$u_w = C_U \sum \gamma_i \Delta h_i \tag{3.16}$$

where C_U is a PWP coefficient, γ_i is the unit weight of the soil at slice i, and Δh_i is the vertical distance from the free water surface of the overtopping flow to the bottom of the arc failure at slice i.

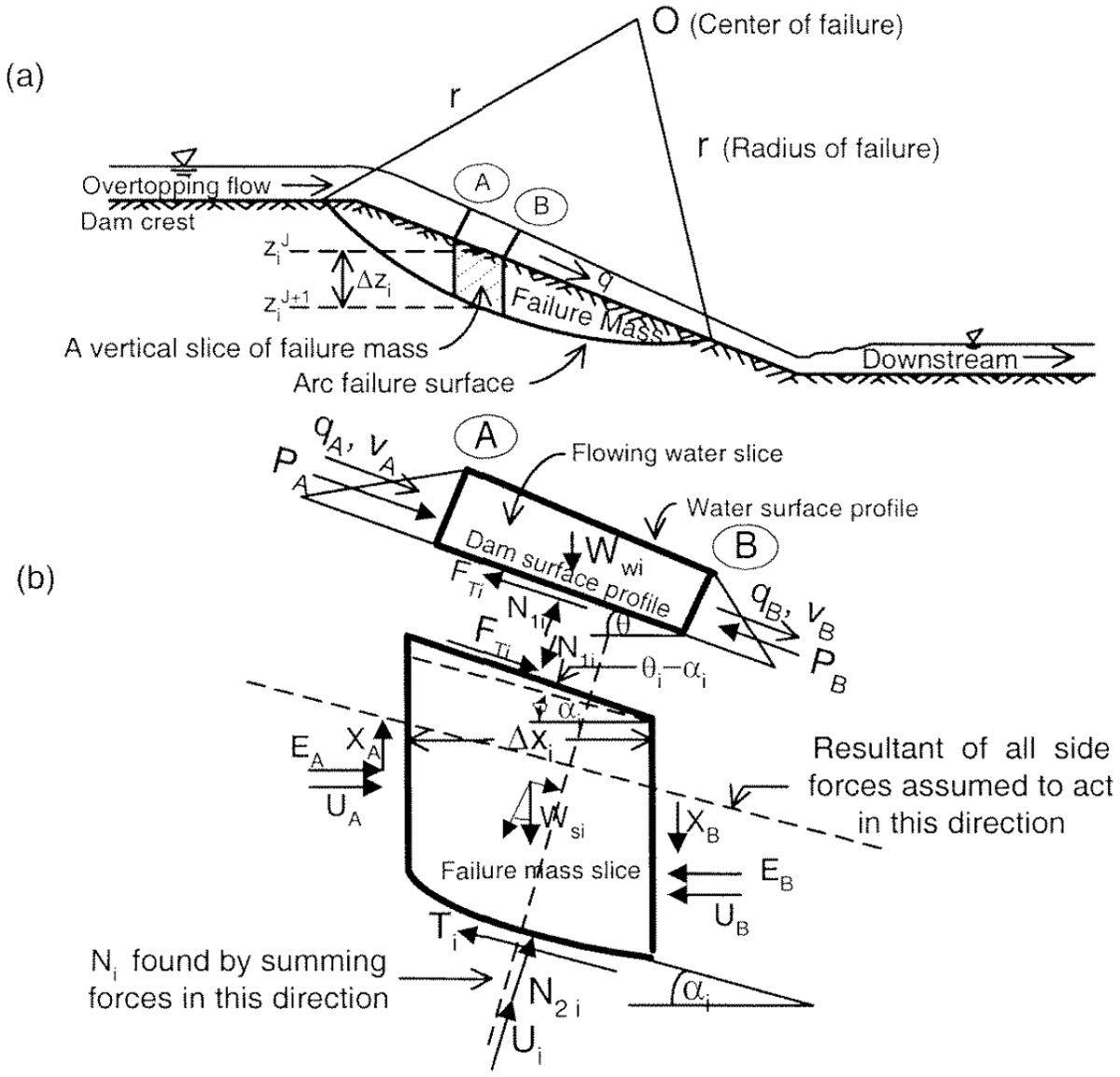

Figure 3.4: (a) Arc failure analysis for overtopping flow, and (b) forces considered in method of slices (Tingsanchali and Chinnarasri, 2001)

The slope stability computation was calibrated using a data set where the downstream slope was varied from 1:2 to 1:5, thus simulating steep and mild slopes, respectively. During this calibration, it was found that it is necessary to incorporate the mass sliding algorithm, where the coefficient C_U was adjusted to 0.8 (see Figure 3.5). The study also gave some account on a sensitivity analysis performed on the calibrated coefficients, parameters and numerical weighing factors. It was found that the coefficient C_U was amongst the most influential. The Manning roughness,

median grain size, d_M, and adjustments to the critical shear stress for bed slopes, were amongst other parameters calibrated. The study stated that erosion is reasonably simulated using the Smart (1984) sediment transport equation.

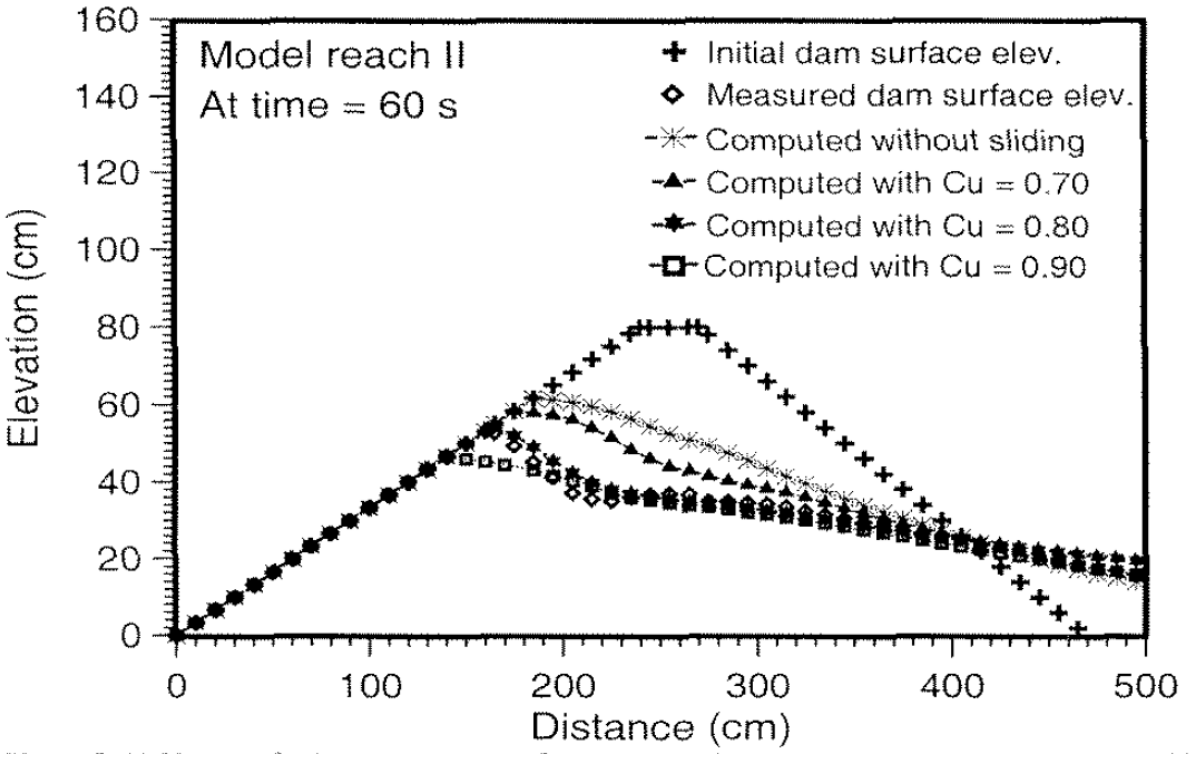

Figure 3.5: Calibration of pore-water-pressure coefficient, C_U (Tingsanchali and Chinnarasri, 2001)

The model by Wang and Bowles (2006a, b, c) is an example of a quasi-3-D noncohesive embankment breach physically-based mathematical model. In their model, breach hydrodynamics is governed by the 2-D SWE while erosion is governed by an empirical erosion rate proposed by Chen and Anderson (1987) and then validated against the flow's transport-capacity as defined by Smart (1984). A 3-D slope stability analysis model is also incorporated into their algorithm. Similar to NWS-BREACH, three erosion stages are defined for their model:

- The first stage is defined as the period from the onset of overtopping until when erosion reaches the upstream apex of the embankment crest

- The second stage ends when the breach channel reaches the embankment foundation
- During the third stage, the remainder of the embankment dam is eroded

The material from the successive slope instabilities and erosion is transported by the flow based on transport-capacity at the end of the computational time-step. The model was validated against embankment breach data from laboratory experiments, field tests, as well as a historical full-scale case showing promising results. Later, their model incorporated a feature to compute breaches at multiple locations, and under wave and wind action (Wang and Bowles, 2006c). The authors advocate modeling of erosion rates of sediments based on their measured erodibility from physical tests (Wang and Bowles, 2006b).

Faëh (2007) developed the numerical model, 2dMb, for breach erosion in river embankments. This morphodynamic model is governed by 2-D depth-averaged SWE and sediment transport using a bedload and suspended load formulation. In his model, the control volume used to solve the SWE is divided into three layers: a flow field layer, a surface sediment (active) layer and a subsurface (inactive) layer (see Figure 3.6). The model, however, considers momentum transfer in the active layer only (*i.e.* water). With respect to the active layer, three flow variables, flow depth, longitudinal and lateral specific discharge, as well as the concentration for each sediment fraction are solved. The 2-D SWE in 2dMb solves the shear stress acting on the bed using resistance laws while the turbulent shear stresses are solved using the eddy viscosity (see Subsection 4.1.2).

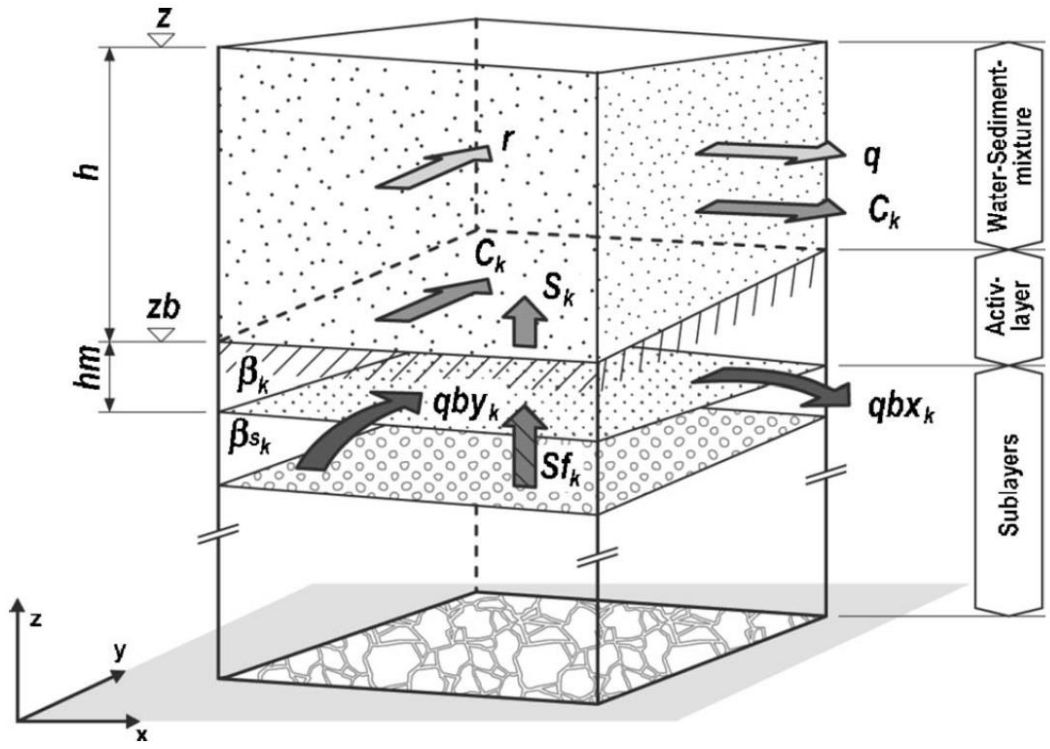

Figure 3.6: Control volume and variables schematic in Faëh (2007)

The sediment concentration for each grain class is computed using the convection-diffusion equation which includes a source term solved using deposition-entrainment empirical parameters. Since suspension is based on the theoretical transport capacity of the flow, it is excluded from the bedload portion using an empirically-defined allocation parameter. Instead it is based on the ratio of shear to fall velocities. The bed load transport was then computed based on the allocated portion defined using a modified version of the MPM for each grain class, where a hiding parameter, which is a function of the Shields parameter, was imposed. The thickness of the active layer was solved using an empirical relationship, where armouring was accounted in the case of bed degradation. Lateral erosion in the breach channel was computed using a bedload transport on transverse slope equation. Side-slope failure was solved using a predefined critical failure angle.

The calibration process for the model consisted of a sensitivity analysis of the parameters required for calibration while the experimental data of Bechteler and

Kulisch (1998) (see Subsection B.1.2 in Appendix B) was used. It was found that a +45% to -35% peak breach outflow variation was attributed to the value selected for the critical failure angle. The effect of reducing the size of the pilot channel on the embankment crest from 10cm to 6cm resulted in a 25% decrease in peak outflow. With respect to the model's sensitivity on the type of transport formulation, a 20% deviation in peak flow was observed. The model was also used to simulate the flood due to a dike breach along the Elbe River which occurred in 2002. Due to the fact that the main channel was simulated with a fixed bed, the model did not capture the deposition of the eroded sediment downstream the breach. Sediment deposition would normally lead to backwater effects at the location of the breach, and which would consequently lead to an increase in the peak breach outflow. Faëh (2007) stated that while incorporating sediment transport processes in the main channel can improve the predictive ability of the 2dMb model, further improvements could even be made if geotechnical processes such as slope instabilities and seepage were better understood.

3.2.3.3 Performance of Current Numerical Models

During the CADAM meeting in Munich in 1998, blind tests were run to compare the performance of several numerical models for two test cases: two runs as presented by Bechteler and Kulisch (1998) and the Yahekou Phase I fuse-plug embankment field test performed in China (described in more detail in Subsection B.2.2 in Appendix B). Conclusions from the test case modeling indicate that numerical simulations are still "far from perfect". Peak flow estimates were within the 50% of the measured values, while time estimates were even less accurate. Broich (1998a) stated that numerical models which combine shallow water equations with sediment transport formulae performed reasonably better. However, the output of the numerical models seemed very sensitive to the choice of model-related parameters, and future modification and calibration is absolutely required to improve accuracy. The conclusions of the meeting also raised the issue of the need to conduct future

large-scale experiments in order to facilitate the calibration of the numerical models with well instrumented data obtained from carefully controlled experimental tests.

Under the EC-funded IMPACT project, both ‘blind’ and ‘aware’ numerical simulations were conducted using several embankment breach models, and compared to results from laboratory and field tests (see Subsections B.1.4 and B.2.4 in Appendix B). The Final Technical Report, released in 2005 (Morris, 2005), stated that the accuracy for predicting peak breach outflow was within ±30%. However, when the numerical models were used to predict the outflow from a real case study (Tous Dam failure) the error range shifted to +50 and -20%. The report also described the prediction of other embankment breach characteristics such as breach channel dimensions and time duration of the breaching process as unreliable and far worse than the peak flow predictions, while the shape of the hydrograph was poorly predicted. ***It was found that physical models which considered geotechnical failure processes in their computations, had an improved performance, with an overall accuracy reaching ±20%, compared to the overall ±50% average, considering prediction of the global embankment breach characteristics (i.e. timing, dimensions and peak flow) (Morris et al. 2004).***

The performance of the numerical model can also be described by the output’s dependency on the input parameters and how the model simplifies certain physical processes. The study by Morris *et al.* (2004) described a sensitivity analysis conducted on the third Norwegian *Mo i Rana* Field Test (see Subsection B.2.4 in Appendix B) which included 44 model runs using HR-BREACH on several input parameters and a base run, representing the best engineering judgement of the authors. The study revealed that the selection of the input parameters could result in a large variability of the peak flow, from the base simulation, as shown in Table 3.2. The authors stated that while the accuracy of the prediction from the base simulation was within 10% of the observed peak value, it is expected that the uncertainty in predicting peak flow will add uncertainty in predicting inundation levels downstream. The authors also cautioned against the averaging of the soil properties for numerical

models simulating breach failure in composite embankments, since this can only be justified for homogeneous embankments. Numerical simulations on the Tous Dam failure, a composite dam which was overtopped and subsequently failed in 1982, yielded a peak outflow variation of 300% when erosion was simulated using a geometrically-identical homogeneous structure.

Table 3.2: Sensitivity analysis of peak outflow for various input parameters using HR-BREACH (Morris *et al.* 2004)

Input Parameter	Input Parameter Range		Output Parameter Variation Analysis									
			Min.	Max.	Mean	Base	% Var. from Mean			% Var. from Base		
							Min.	Max.	Range	Min.	Max.	Range
Sediment transport eq.	N/A	N/A	50	236	118	131	-57	100.4	157.7	-62	80.4	142.1
Sediment flow factor	0.5	3.0	61	190	132	131	-54	44.6	98.2	-53	45.3	98.7
ϕ[°]	25	45	67	166	122	131	-45	35.9	80.6	-49	26.4	75.0
B_W/h_B	0.5	2.5	49	116	93	131	-47	24.8	71.5	-62	-12	73.9
C_D	1.5	1.9	115	193	160	131	-28	20.6	48.7	-12	47.4	59.5
γ_d [kN/m^3]	19	23	67	127	104	131	-35	21.7	57.1	-49	-3.2	51.8
n_M [s/m$^{1/3}$]	0.020	0.045	115	146	132	131	-13	10.1	22.7	-12	11.1	23.0
d_{50} [mm]	3	6	124	151	138	131	-10	9.8	19.5	-5	15.3	20.5
c [kN/m^2]	0	10	120	132	126	131	-5	4.4	9.1	-8	0.5	8.8

3.3 Experimental Modeling: Laboratory and Field Tests

Since the late 1950s, there have been numerous laboratory experiments on the failure of earth embankments due to piping and overtopping. A number of large and small scale experimental configurations ranging from homogeneous, composite and grass-lined embankments to embankments constructed from cohesive and non-cohesive sediments have been performed in laboratory as well as *in situ* environments (see Table B-1 in Appendix B). A detailed literature review on the laboratory and field tests with respect to the experimental method, construction techniques as well as results is included in Section B.1 and Section B.2 of Appendix

B. A summary presenting the findings of the experimental research and its relevance to the proposed study is discussed in this Section.

3.3.1 European Legislation and Initiatives

Following the Malpasset Dam failure in 1959, French legislation was presented in 1968 for dambreak risk analysis, and soon after many countries in Europe followed suit after weighing the risks of failure against the high population density downstream of many of the dams (Morris *et al.* 1998). However, it was not until December 1994 that an official initiative occurred, following the passing of a French law which stipulated that all owners of large dams must update their emergency maps within five years (Petitjean, 1998). In September 1995, the IAHR Working Group on Dambreak Modelling was initiated, and three years later, the European Commission (EC) began funding the Concerted Action on Dambreak Modelling (CADAM) programme (~ €250K) for a period of two years (February 1998 – February 2000). The CADAM programme, coordinated by HR-Wallingford, had participants from over 10 countries, including: UK, France, Belgium, Germany, Norway, Poland, Italy, Portugal, Spain, Switzerland and Sweden. The programme was rolled out in four meetings/workshops: Wallingford, UK (March 1998), Munich, Germany (October 1998), Milan, Italy (May 1999) and Zaragoza, Spain (November 1999). The main goals of this programme were to promote cooperative research and exchange of information between universities, research organizations and industry, in the field of dambreak experimental and numerical modeling. One of the topics raised during these meetings, was the uncertainty of the breach formation and subsequent development processes as well as of the outflow hydrograph (Morris, 1998). Topics of the meetings included several physical experiments and numerical models related to the dambreak problem, embankment breach lab and field test cases (Bechteler and Kulisch, 1998; Loukola and Huokona, 1998), parametric dam breach models (Macchione and Rino, 1999), a morphological embankment breach numerical model (Peviani, 1999), and a new methodology to assess breaching in non-cohesive embankments based on experiments (Mohamed *et al.* 1999).

Findings, conclusions and recommendations from the four meetings/workshops can be summarised as follows:

- Breach formation is better estimated using physically-based models
- Breach growth is not always trapezoidal
- Constant breach shape and erosion is not realistic (hence, the importance of modeling successive side-slope failures using physical-mathematical relationships)
- Need for better quality field and laboratory data and less reliance on human observations
- Scale effects in laboratory scales need to considered and addressed
- Need for large scale testing
- Better parameter identification for physical and numerical breach models
- Modeling unsteady sediment transport and erosion
- Exchange of information between a wider range of researchers working on these issues

The termination of the CADAM programme in November 1999 was followed by the commencement of another EC funded project (Morris *et al.* 2004). The Investigation of Extreme Flood Processes and Uncertainty (IMPACT) project was a three-year project (December 2001 - November 2004), funded under the EC 5th framework programme (~ €2.6M). The project assessed the risks of floods due to natural extreme events or the failure of embankments/dikes and other flood defence structures such as concrete dams. The IMPACT project, coordinated by HR-Wallingford, had participants from the following countries: Germany, Belgium, France, Italy, Spain, Portugal, Sweden, Norway, Finland, Hungary, Czech Republic, Austria, Poland, Canada, U.S.A and UK. Four project meetings/workshops took place: Wallingford, UK (16-17 May, 2002), *Mo i Rana*, Norway (12-13 September, 2002), Louvain-la-Neuve, Belgium (5-7 November, 2003) and Zaragoza, Spain (3-5 November, 2004). Following the conclusions and recommendations of the CADAM

programme, the IMPACT project was designed to engage in 4 main areas, or work packages (WPs):

- WP2: Breach formation
- WP3: Flood propagation
- WP4: Sediment movement
- WP5: Uncertainty analysis
- WP6: Geophysics data collection

For this thesis, the most relevant aspect of the above WPs is breach formation. The IMPACT project for this WP conducted and investigated a series of experimental (field and laboratory) tests in order to provide case study data, and to develop and validate embankment breach numerical models. The researchers also focused on factors that may affect breach location, such as embankment material and field parameters (*i.e.* WP6) as well as uncertainties corresponding to breach numerical modeling (*i.e.* WP5) (Morris *et al.* 2004). The experimental investigation was comprised of 5 field tests (4-6 m high embankments) and twenty two laboratory tests (1:10 models) and is presented in more detail in Subsection B.1.4 and Subsection B.2.4 of Appendix B. Due to the uniqueness of each set of tests, it was difficult to establish dimensionless relationships between the embankment breach evolution and characteristics. However, the data (*e.g.* soil properties, video footage, inflows and outflows) and knowledge collected from the extensive field and laboratory tests with respect to embankment breach physical processes allowed the researchers to develop and validate next generation numerical models.

At the end of 2004, FLOODsite was initiated as the next generation project under the framework programme of the European Commission. It was funded until 2009 (~ €14M) an expansion of the objectives and scope of both the IMPACT and CADAM programmes. The project addresses the area of flood risk analysis and management through an extensive program of research and development work. Its integrated approach encompasses the physical, environmental and socio-economic aspects of flood hazards from the river banks to the estuaries and coasts. The project is broken

down into a total of seven themes, each of which contains subthemes, where the subtheme structure comprises of an objective, an approach and several tasks. For instance, “Modeling Breach Initiation and Growth” is Task 6 of the “Hazard (Risk Pathways)” subtheme, under Theme 1, “Risk Analysis: Scientific Knowledge and Understanding”. The vast scope of the project was supported by 37 research organizations, institutes and universities from countries around Europe and the rest of the world. With respect to breaching failures, the project identified 3 main areas where a knowledge gap had existed: wave-action induced breach, effects of soil state, and breach flow processes (Morris *et al.* 2009a, b). The shortcomings on soil state and breach flow processes mentioned in the FLOODsite reports include: poor accuracy of breach flow and dimension predictions, understanding the soil-water-structure interactions, influence of soil state on erodibility (including measurement techniques), understanding scale-effects and improvements in the prediction of pipe formation. Experimental work on the piping failure mechanism remains very limited.

3.3.2 Influence of Compaction

Geotechnical engineers qualitatively describe the compaction in the field as relative density or relative compaction. Both terms, however, are not the same. The relative density, D_r, is expressed as follows:

$$D_r = \frac{e_{max} - e}{e_{max} - e_{min}} \times 100\% \tag{3.17}$$

where, e is the void ratio of the soil, e_{max} is the void ratio of the soil in its loosest state, and e_{min} is the void ratio of the soil in its densest state

The relative compaction (also referred to as degree of compaction), R_c, is expressed as follows:

$$R_c = \frac{1 + e_{min}}{1 + e} \times 100\% \tag{3.18}$$

While the influence of compaction on embankment breaching has been investigated for cohesive soils, some experiments did in fact investigate the influence of

compaction in noncohesive soils on embankment breaching. In the experimental study on the stability of rockfill dams by Martins (1981), the compaction of the rockfill material was measured. However, it was found that the compaction was nearly identical in two of the test series used, and therefore the influence of compaction on the failure process could not be detected. The study by Simmler and Samet (1982) on plane overtopping of homogeneous as well as composite earth embankments investigated the influence of compaction on the breaching process. Results of their study on noncohesive homogeneous embankments were reported in terms of the evolution of the eroded volume and discharge volume for two relative densities (D_r = 0.11 and 0.57), extracted from side-view breach channel profiles and water surface levels, respectively. Their evaluation revealed that compaction had no significant influence on overtopping erosion. Nevertheless, it is difficult to isolate the erosion of the noncohesive earthfill in that case due to the presence of a central impervious element. Laboratory experiments on sea dikes by Steetzel and Visser (1992) demonstrated that increasing the porosity of a coarse dune sand (d_{50} = 0.218mm) from 0.38 to 0.45, increased the transport rate by only 5%. In their study, there is no mention of the construction technique and compaction method used with the coarse sand. Overtopping laboratory tests by Dodge (1988) on clayey sand (USCS Type SC-CL; ASTM, 2010), with d_{50} = 0.1mm and 49% fines, revealed that increasing the compaction effort from 95% to 102% of Standard Proctor values reduced erosion by 50%. The influence of compaction effort and compaction water content on breach overtopping was also demonstrated in the IMPACT Project laboratory experiments. The report by IMPACT (2004a) stated that by halving the compaction or by compacting the soil at a water content 6% drier than optimum will increase peak flow by approximately 70%. The influence of compaction on breach outflow due to overtopping flow was investigated for only cohesive embankments during the IMPACT Project.

Large-scale overtopping tests by Hunt *et al.* (2005) revealed that an increase in the compaction water content of a silty-sand (*i.e.* Soil No. 2) by 1.5% (*i.e.* Tests No. 1 and 2) increased the breach widening rate by 3.3 times. The experimental

investigation by Hanson *et al.* (2005) used the same silty-sand in three of the seven tests (*i.e.* Tests No. 2, 5 and 7), which were also conducted at the Agricultural Research Service-Hydraulic Research Unit (ARS-HERU) field laboratory. However, the soil composition and properties stated in the investigation by Hanson *et al.* (2005) suggests that the silty-sand is cohesive in nature (6% clay, with a soil cohesion, c, value of 10.3kPa; Hahn *et al.* 2000).

The influence of compaction water content and compaction effort was also studied on compacted samples using laboratory equipment such as the jet erosion test (JET) apparatus and horizontal flumes. Erodibility tests were performed on the ARS-HERU large-scale samples, (Hanson and Hunt, 2007). The flume tests by Gaucher *et al.* (2010) showed that noncohesive samples (comprised of sand and gravel mixtures) compacted at Standard Proctor optimum values were more resistant than samples compacted at lower compaction efforts (85 – 92% Proctor optimum). Their study also revealed that bed load transport rates were reduced by 50% in some cases. Erodibility tests by Wan and Fell (2004) revealed a correlation between high compaction efforts and wet of optimum compaction water contents to higher erosion resistance for most of the soil samples tested. Laboratory tests on silty sand specimens (with 10% clay content) state that erodibility linearly decreased with dry unit weight (Fujisawa *et al.* 2008). Laboratory tests using the JET apparatus by Hanson and Hunt (2007) on Soil No. 2 (silty-sand) and Soil No. 3 (lean clay) used in the large-scale ARS-HERU overtopping tests also showed that compaction increased erosion resistance. Their study also revealed that the erodibility is more sensitive towards achieving optimum conditions if compacted on the dry side of optimum. An in-depth investigation on the influence of compaction on noncohesive soils, however, remains yet to be addressed in order to fully understand the breaching processes and consequently breach channel evolution due to overtopping flow (Gaucher *et al.* 2010).

3.3.3 Breach Channel Control Section

Observations made by Morris *et al.* (2007) and IMPACT (2004a) during the *Mo i Rana* Norwegian field tests and by Coleman *et al.* (2002) and Stretch and Parkinson (2006) during their laboratory tests drew attention to the formation of a curved or crescent-shaped weir created by erosion on the upstream face of the embankments, whereas the length of this control section is significantly larger than the breach width. The flow phases between upstream and downstream reaches changes from curved weir control in the upstream reach, to converged weir control to open channel flow (Morris *et al.* 2009b). The characteristic length employed in weir equations for determining the flow through an embankment breach, must therefore incorporate the curved upstream dimensions of the breach channel entrance rather than the smallest horizontal distance between the side walls of the breach channel. It is also impossible to relate these two lengths during breach formation, if only final dimensions of the breach channel are reported. This can be carried out if dimensions of the curved control section are recorded during overtopping as performed by Coleman *et al.* (2002).

3.3.4 Breach Channel Mapping Techniques

In previous overtopping tests, breach channel evolution has been determined by measurement of the breach channel cross-section using two methods: direct (*i.e.* intrusive) and indirect (*i.e.* nonintrusive).

Direct methods usually interfere with the breach flow and erosion and indirect methods typically involves a photogrammetric technique. The direct methods are usually conducted using instruments such as thin staff gauges mounted above the breach channel (Chinnarasri *et al.* 2004) or an overhead rolling carriage fixed with point gauges (AlQaser, 1991; Hahn *et al.* 2000; Hanson *et al.* 2003). Another direct method previously used was the overtopping half-breach channel method, where the breach flow was stopped followed by measurements of the breach channel dimensions and later followed by a reconstruction of the setup in successions (*e.g.*

Coleman *et al.* 2002). Geisenhainer and Kortenhaus (2006) implemented a similar method to Coleman *et al.* (2002) in their dike overtopping tests; however, a full-breach instead of a half-breach channel was simulated. Half-width models were also utilized in the studies by Pickert *et al.* (2004, 2011), Wishart (2007), Feliciano-Cestero (2010) and Schmocker (2011). Based on measured discharge, a comparison between half-width and full-width models by Feliciano-Cestero (2010) revealed good agreement between the two techniques. The experimental study by Feliciano-Cestero (2010) investigated a method that employed coloured foam tracers, embedded in the four layers of the constructed dike model. The appearance of the tracers on the flow's surface marked the moment of their detachment. Movement, deformation and vibration sensors have been used to monitor breach channel morphology in large-scale embankment dam and dike breach field tests (Visser, 2000; Vaskinn *et al.* 2004; J. Zhang *et al.* 2009). Unfortunately, the use of tracers in embankment breach tests is limited to the colour and suspension characteristics of the embankment material. Coloured pieces of cork were also used as tracers in the trial tests by Orendorff (2009). The attempts were unsuccessful due to poor visibility of the sediment-laden tailwater.

For 2-D overtopping tests, photogrammetric methods were the most common (Tingsanchali and Chinnarasri, 2001; Chinnarasri *et al.* 2003; Schmocker and Hager, 2009), wherein the breach evolution was determined by mapping coordinates of the embankment profile using side-view images. Photogrammetric techniques employed to determine the breach evolution of 3-D breach overtopping tests in both laboratory and field conditions incorporated the measurement of the top width from top-view images (Visser, 1990, 2000; Shuibo *et al.* 1993; Hahn *et al.* 2000; Hanson *et al.* 2003; Chinnarasri *et al.* 2004; IMPACT, 2004; Vaskinn *et al.* 2004; Geisenhainer and Kortenhaus, 2006; Wishart, 2007; J. Zhang *et al.* 2009). Extraction of breach channel coordinates, however, was not always carried out using gridlines in these studies. Although nonintrusive photogrammetric techniques used in 3-D breach overtopping tests, such as fringe projection (Pickert *et al.* 2004, 2011), grid projection (Schmocker, 2011) and sweeping laser light sheet system

(Spinewine *et al.* 2004), are more complex to setup, they are far more advantageous than relying on gridlines since they are capable of determining the 3-D topographic map of the breach channel temporal evolution.

3.3.5 Seepage and Pore-Water-Pressure Measurement

The IMPACT Technical Report (IMPACT, 2004a) stated that similar to the field tests, PWP were also measured using pressure sensors for both test series. The study by Morris *et al.* (2007) stated that five pressure sensors were used to measure PWP in the second series tests (i.e. cohesive embankments) whereas the presentation by Morris (2002a) stated that pressure beneath the embankment was amongst the data logged during the first series tests (i.e. noncohesive embankment models). AutoCAD drawings provided in the appendix in Morris *et al.* (2007) show only four at the embankment centreline (P1-P4) without an indication of the precise locations or coordinates of the installed sensors. Indeed, data files found in the appendix for the second series included the time-history of five pressure transducers in millibars, while data files for the calibration of instruments showed that the pressure transducers were calibrated in metres of water [m-H_20] versus voltage [V] for increasing and decreasing positive heads. Nevertheless, the experimental results for Test No. 10 (*i.e.* second series), which included the time history of upstream and downstream water surface levels, pressure transducers and inflow hydrographs (obtained from the digital appendix provided by Morris *et al.* 2007) as well as the outflow hydrograph (obtained from the technical report IMPACT, 2004a), was plotted on a single graph, shown in Figure 3.7.

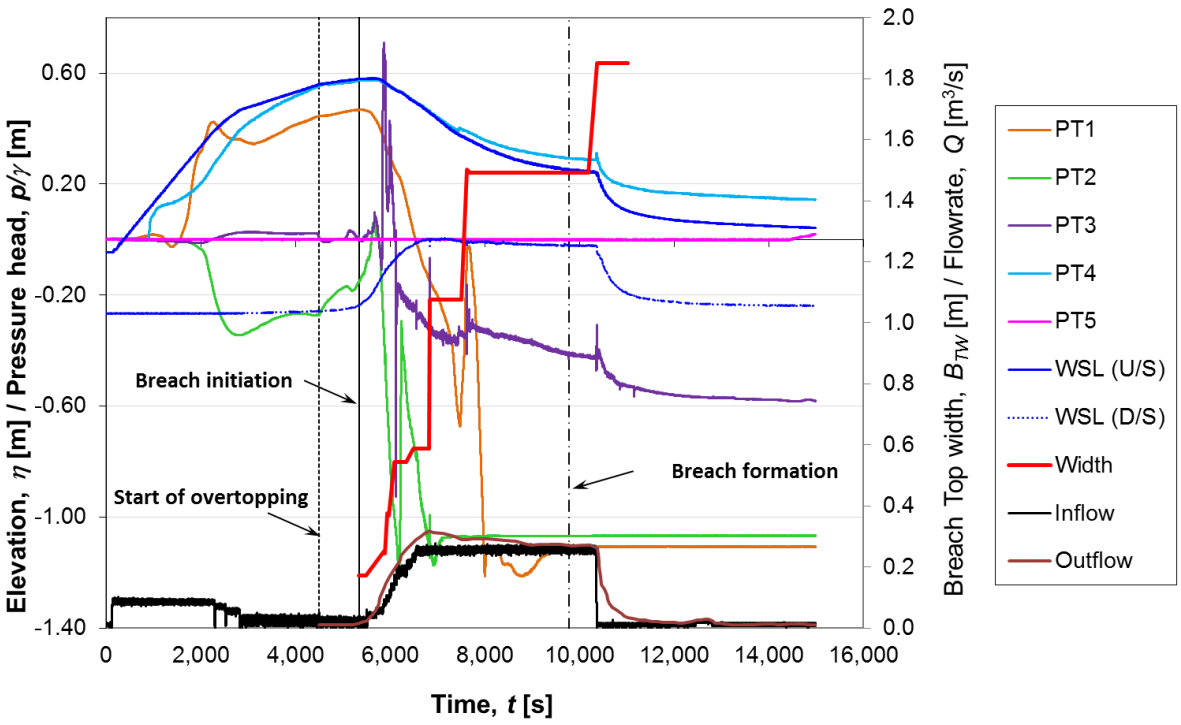

Figure 3.7: Experimental results from IMPACT Project laboratory Test No. 10 (PT is pressure transducer, WSL is water surface level, U/S is upstream and D/S is downstream) (using data from Morris *et al.* 2007 and IMPACT, 2004a)

Figure 3.7 shows the recorded values of PWP began at zero m-H_20 (or millibars, if the units of measure were indeed so), and then recorded either an increase (PT1 and PT4), a decrease (*i.e.* PT2) or remained at zero (PT3 and PT5) until overtopping was initiated. Since calibration was carried out for positive heads, it was likely that the sensors only operated within the positive PWP range. However, it can be seen from Figure 3.7 that the PWP dropped below zero during the breach initiation and formation stages, especially PT2 which was negative even before overtopping was initiated. This indicates that the pressure sensors were capable in fact of recording negative pressures. However, since the PWP recorded zero readings at the beginning of the test, it is possible that contact between the soil and the transducer was not properly established until seepage through the embankment models caused a rearrangement of the soil particles around the sensors. It is difficult, however, to make conclusive correlations between PWP and breach evolution without the following conditions:

- Precise locations of the pressure transducers
- Appropriate units of measurement (millibars vs. metres of water)
- Range of operation of the pressure transducers

It is clear from Figure 3.7, that the inflow used at the beginning of the test for the second series tests for filling the reservoir was the same as the one used for the first series (approximately 0.08m^3/s). The inflow was then dropped to a smaller value (approximately 0.03m^3/s) before it was increased again to approximately 0.25m^3/s, possibly to establish steady-state seepage through the embankment models. However, by observing the response of the pressure sensors, steady-state seepage was not established for two sensors (PT1 and PT4). With respect to the first series of tests, Test No. 9 was conducted to establish the effects of seepage on breach outflow. This particular embankment model was overtopped after steady-state seepage was established. Peak breach outflow for this test was 0.82 m^3/s, as opposed to 0.91m^3/s for the same embankment models with drier conditions. Problems were encountered in maintaining steady-state seepage prior to overtopping. Images from repeated tests (Tests No. 2 and 3 using uniform grading) as seen in Figure 3.8 and Figure 3.9, show seepage and sliding failures endured on the downstream slope, due to the absence of a drainage element.

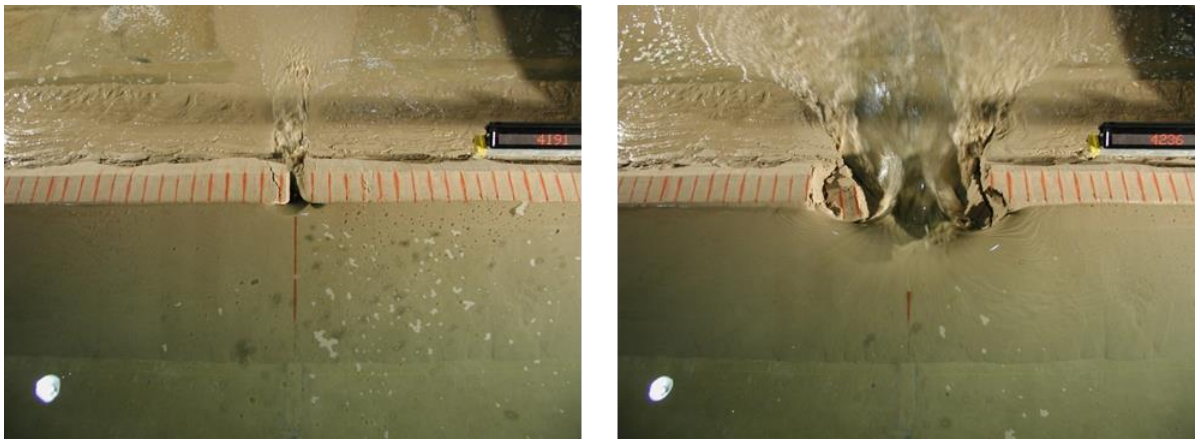

Figure 3.8: Top view of embankment showing sliding failures on downstream slope during overtopping (Morris, 2002b)

Figure 3.9: Side view of final breach channel showing sliding failures on downstream slope (left) Morris, 2002b (right) Morris, 2002c

In fact, the presentation by Morris (2002a) does state that steady-state seepage was an issue for the first series tests. The study by Geisenhainer and Kortenhaus (2006) on dike breach overtopping tests with and without waves encountered similar problems (see Figure 3.10); however, they decreased the time between filling the reservoir and overtopping to improve slope stability. During their wave overtopping tests, they installed a geotextile on the downstream slope as a more effective preventative measure (see Figure 3.11).

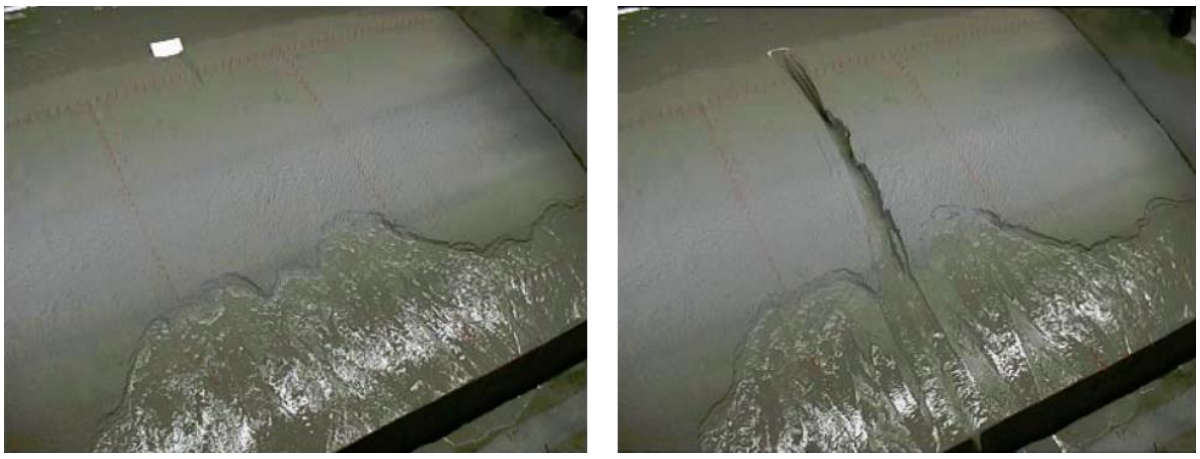

Figure 3.10: Seepage on downstream slope of dike model (left) before overtopping (right) during overtopping, geotextile installation (Geisenhainer and Kortenhaus, 2006)

Figure 3.11: Downstream slope of dike model showing geotextile installation (left) after construction (right) during overtopping (Geisenhainer and Kortenhaus, 2006)

The authors report that they encountered difficulties in maintaining a constant water content throughout the dike body during construction, which took approximately 1.5 days to complete. Their construction method was comprised of using a backfill of dry sand in 10cm lifts, followed by water irrigation and manual compaction using a wooden plank and then followed by irrigation of the entire dike body. In their report, they state that long construction durations resulted in a decrease in water content. They suggest that construction time must be reduced in order to avoid such problems. The authors also state that while seepage failure is relevant to river dikes, it is less relevant to coastal dikes. The study by Wishart (2007) investigated the influence of seepage on the breaching mechanism in both homogeneous and heterogeneous rock-avalanche dam models. The migration of the phreatic front was monitored during impoundment and during overtopping. Saturation of the dam materials before impoundment yielded in peak flows 36% higher for homogeneous models and 10% higher in heterogeneous models (*i.e.* carapace dams).

In order for a comprehensive investigation on the influence of geotechnical processes and mechanisms on embankment breach overtopping to be carried out, a seepage analysis must be performed. This can be carried out by measurement of PWP. The study by Pickert *et al.* (2004, 2011) on overtopping of noncohesive embankments incorporated six pressure transducers imbedded into the

embankment body at a location coinciding with the initial phreatic surface (see Figure 3.12, Figure 3.13 and Figure B-19 in Appendix B).

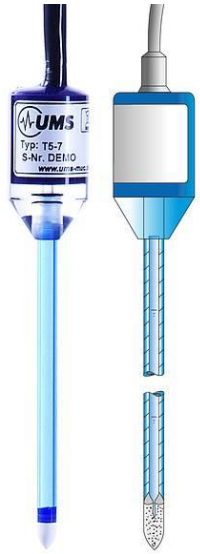

Figure 3.12: UMS T-5 tensiometer probes cited in Pickert *et al.* (2004, 2011) (UMS, 2012)

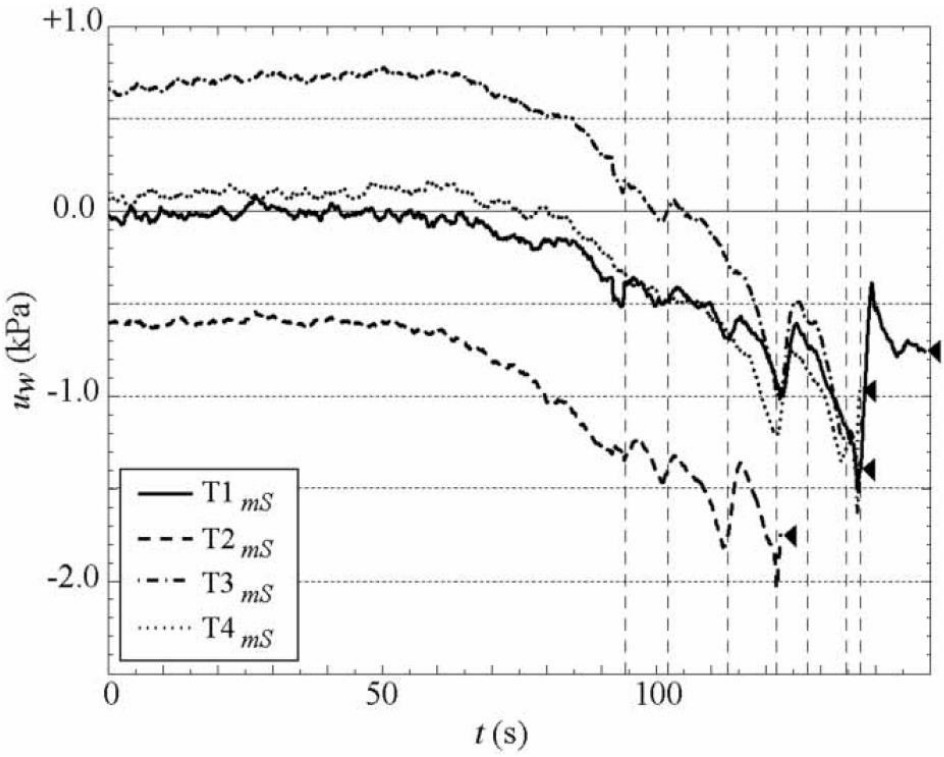

Figure 3.13: Pore-water-pressure measurements for medium sand (Pickert *et al.* 2011)

Their embankment model also controls seepage by using an undertoe drain (*e.g.* Coleman *et al.* 2002, Pickert *et al.* 2004). Other studies control seepage by using an upstream cohesive clay lining (Chinnarasri *et al.* 2003, 2004) and an upstream undertoe drainage element (Schmocker and Hager, 2009). However, the planar dike overtopping tests by Schmocker and Hager (2009) avoided seepage-induced failures (*i.e.* slope slides) in their simulations by limiting the grain size (d_{50} < 5.5mm).

Measurements of the PWP in Pickert *et al.* 2011 were used to assess side-slope stability and identify the method of failure (*i.e.* shear and tension). Their study concluded that side-slope failures were influenced by apparent cohesion or the matric suction, and in particular, the air entry value of the noncohesive embankment material. The authors proposed that the phenomenon of apparent cohesion can be approximated by tension failure. During the IMPACT Project field test investigations PWP measurements were carried out (Vaskinn *et al.* 2004; Morris *et al.* 2007). The report by Geisenhainer and Kortenhaus (2006) on small-scale overtopping of sea dikes with and without waves, describes potential instrumentation that would be used in the large-scale tests which were carried out in 2008 in the Large-Wave Flume (GWK) in Hanover, Germany (Geisenhainer and Oumeraci, 2008). Included in the proposed list of instrumentation were tensiometers and pore-pressure probes for the measurement of PWP and water tension measurement within the clay cover and sand core of their large-scale embankment model (see Figure 3.14). However, no data on PWP or associated instrumentation was presented or discussed in their reports which describe the large-scale tests (Geisenhainer and Oumeraci, 2008). The report by Geisenhainer and Kortenhaus (2006) does, however, mention that scaling seepage flow between model and prototype during the IMPACT Project was based on the Froude number.

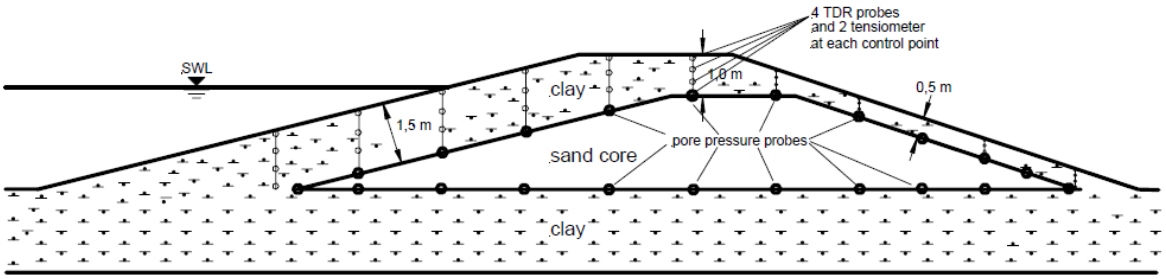

Figure 3.14: Proposed instrumentation used for a dike test with breach initiation at landward side (Geisenhainer and Oumeraci, 2008)

3.3.6 Similitude and Scaling Criteria

In physical modeling of hydraulic structures, the notion of similitude implies a physical similarity between a prototype and its (smaller) scale hydraulic model. By assuming similarity, information from the hydraulic model can be used to predict the behaviour in the prototype case. Hughes (1993) described four different methods for achieving similitude. One method of establishing similitude is by calibration, in which the hydraulic model is calibrated in order to reproduce past conditions in the prototype using trial and error. Another method of achieving similitude is by using differential equations. In this case, the differential equation governing the physical process is nondimensionalized and the resulting dimensionless parameters are then used as the similitude criteria. The most common method for establishing similitude, and which is described in more detail in Section 4.7, is by dimensional analysis. In this method, the behaviour between the prototype and model is correlated by defining a set of dimensionless products or groups (*e.g.* Froude, Fr, or Reynolds, Re, numbers). The fourth method of similitude is by scale series. In this method, several models at different geometric scales are constructed and the similitude criteria are then extrapolated from the physical tests.

In this study, the scale ratio (with subscript rr) is the ratio between the model to prototype parameter (with subscripts mm and pp, respectively), where the geometric scale ratio, L_{rr}, can be defined for the three Cartesian dimensions, namely the longitudinal, lateral and vertical geometric scale ratios, X_{rr}, Y_{rr}, and Z_{rr},

respectively. Julién (2002) describes three types of hydraulic model geometric similitude: exact (*i.e.* $X_{rr} = Y_{rr} = Z_{rr} = L_{rr}$), distorted (*i.e.* $Z_{rr} \neq Y_{rr}$) and tilted (*i.e.* $Z_{rr} \neq X_{rr}$). A detailed description of the theory on similitude and dimensional analysis with reference to the geometric scale ratios can be found in Section 4.7.

In the 1980s, hydraulic modeling of fuse plug embankments was studied in the laboratory by scaling the sediment gradation (Pugh, 1985). The study by Schmocker and Hager (2009) on dike overtopping investigated scale effects performed on exact scale series of non-cohesive dikes using 3 scaling ratios, $L_{rr} = 1$, 0.5, and 0.25. The overtopping experiments by Schmocker and Hager (2009) spanned the entire width of the flume, where only the 2-D characteristics of breach mechanics were represented (*i.e.* widening phase in the breach channel was not simulated). Their experiments are also described in more detail in Subsection B.1.8 in Appendix B.

Embankment breach literature often refers to a geometric scale ratio between the laboratory model and the prototype (*e.g.* 1:10 or 1:100) and they address the Froude criterion as the scaling law for the embankment breach outflow characteristics (*e.g.* Tingsanchali *et al.* 2001; Franca and Almeida, 2002, 2004; Coleman *et al.* 2002; Pickert *et al.* 2004; Geisenhainer and Kortenhaus, 2006; Davies *et al.* 2007; Dupont *et al.* 2007; Wishart, 2007). While the IMPACT Project laboratory tests were based on 1:10 scales of field tests, a comprehensive scale effect analysis between model and prototype was not confirmed. The report by IMPACT (2004a) mentions that only a qualitative comparison has been conducted with respect to some aspects of cohesive and noncohesive breach morphodynamics (*e.g.* headcut formation and migration and erosion). For instance, the effects of certain processes such as seepage were not taken into account. The authors stated that while such geotechnical processes and conditions are important and must not be neglected, such a detailed analysis was not possible due to the limited timeframe of the IMPACT Project.

It is also difficult to assess the scale effects within an experimental realm when inflow and breach outflow are comparable in magnitude for both laboratory and field

tests (see Figure 3.7). It is likely that a high inflow-to-breach outflow ratio would by default validate the Froude criterion, due to dominance of the flow conditions over the mobile-bed aspect of the hydraulic model. Although the impoundment volume between the laboratory and field tests of the IMPACT Project may have been scaled, the reservoir characteristics corresponding to vertical side-walls in a laboratory flume did not match the nonlinear characteristic pertaining to the *Mo i Rana* reservoir.

The study by Schmocker and Hager (2009) investigated scale effects in overtopping of noncohesive river dikes using three scale ratios (L_{rr} = 1, 0.5, 0.25). Scale effects were examined on the premises of morphological evolution and breach outflow with respect to the bed profile. Their study used falling head conditions with peak outflow to inflow ratios ranging between 1 and 1.5 while reservoir volume was comparatively small (Schmocker and Hager, 2012). This suggests that breach outflow may have been dominated by the constant inflow conditions as opposed to a falling head corresponding to a large reservoir volume. It is, however, understandable that the purpose of their investigation was to model the breaching of noncohesive river dikes, where inflow conditions are usually large and remain uniform for a relatively short period of time. Apart from applying a 2-D analysis (*i.e.* plane dike-breach overtopping) and high inflow-to-outflow ratio in their scale effects study, the authors prevented seepage-induced failures (*i.e.* due to sliding) in their experiments by limiting the grain size, even though a drainage element was incorporated into their model. It was found, however, that the Froude criterion was not satisfied along the dike's profile during the early stages of the breach at the dike's crest. Deviations in the Froude number profile (see Subsection B.1.8 in Appendix B) during the remaining duration of the experiment were also reported in downstream locations due to deviations in deposition patterns attributed to viscous effects in smaller scales.

The laboratory tests by Stretch and Parkinson (2006) on temporary open/closed estuaries investigated breach overtopping on 24 berm configurations under falling heads. Although dimensionless relationships were established between breach

width and outflow volume (*i.e.* referred as the $1/3$ rule in their literature, see Subsection B.1.7 in Appendix B), validation of the Froude criterion was neither presented nor discussed with respect to the breach outflow characteristics and breach channel morphology.

Scaling hydraulic laboratory models to prototype configurations with respect to fixed bed free water surface applications is often based on the (default) Froude similitude criterion. However, flow parameters in highly unsteady conditions, such as in the case of an embankment breach failure are impossible to satisfy using one scaling criterion due to the presence of tensiometric, frictional, elastic and viscous effects. It is therefore imperative to first evaluate the validity of the Froude similitude criterion in embankment breach failures due to overtopping by conducting a scale effect analysis using evolutional approaches for the entire breach outflow hydrograph rather than on the peak outflow or time-to-peak alone. An evolutional approach can also be applied to conduct a scale effects analysis in the case of the breach channel geometry, where the morphology of the relevant or characteristic dimensions is considered instead of final dimensions.

3.4 Discussion

An important finding emerging from the CADAM Programme and IMPACT Project workshops was that existing embankment breach numerical models are highly sensitive to model-related parameters. This weakness could only be overcome by a more in-depth representation of the physical processes governing an embankment breach failure with the help of physical experiments. However, parameters, which are known to significantly influence the physical breaching processes, can be either hydraulic or geotechnical in nature. While deficiencies exist in addressing both of these two types of parameters in an experimental setting, it was necessary to address parameters for whose influence a significant knowledge gaps exists.

- *It is therefore of absolute importance to investigate these parameters using the most basic embankment configurations (i.e. homogeneous geometries).*

Laboratory and field experiments simulating breach failures using cohesive embankment materials have often adopted (and adequately documented) construction techniques used in prototype-size embankment prototypes. However, in embankment models comprised of noncohesive materials, the construction technique was rarely addressed. In current physical experiments, the representation of some of the embankment material parameters, such as: soil moisture conditions and compaction effort during the construction phase and the initial soil-water state prior to the overtopping event, has been arbitrary with respect to noncohesive soils.

- *In order to consider any other geotechnical or hydraulic-related parameters in an experimental test program, it is therefore of primary importance to develop a controlled construction technique used in a laboratory flume using a prototype-scale method.*
- *The optimum conditions for this newly developed construction technique are based on an in situ assessment rather than on laboratory-based ones (e.g. using a Proctor mold).*

In addition to geotechnical parameters such as the compaction effort and the moisture content during construction and initial soil-water state prior to overtopping, the boundary seepage mechanism also needs to be addressed experimentally. It is anticipated that this seepage mechanism would influence the spatio-temporal evolution of the breach channel through two dominant breach mechanisms: soil erosion and side-slope failures. Pickert *et al.* (2011) has already investigated the side-slope failure aspect of an embankment breach using an instrumentation technique comprised of four to six tensiometers.

- *Investigation of the erosion mechanism is therefore carried out using a 2-D analysis, meanwhile the instrumentation technique comprised more than just a few devices*.
- *Careful consideration needs to be also provided regarding the interference between these devices and the soil and water mediums where minimum intrusion device are used*.

- *The resulting experimental setup investigated in this study, does not only capture the PWP behaviour due to overtopping erosion, but will also lead to an understanding of the seepage mechanisms on steep slopes under supercritical and unsteady flow conditions (see Subsection 4.6.4 for previous investigation performed on mild slopes with subcritical and gradually-varying or normal flow conditions)*.
- *Although this experimental setup can be useful using both constant and falling reservoir head conditions, in the study the breach overtopping problem is simulated using a falling-head characteristic.*

The boundary seepage mechanism, described by geotechnical principles, is also important in mobile bed mechanics. Observations of the water surface profiles in embankment breach overtopping tests have indicated that the flow accelerates on the downstream slope (Powledge *et al.* 1989, Visser,1998, Chinnarasri *et al.* 2003, Schmocker and Hager, 2009), with the exception perhaps of long channel reaches (Visser, 1998) such as in the case of landslide dams (Fread, 1984a). But this extensive literature review showed that it is the approach on how erosion is applied in breach modeling, particularly in noncohesive embankments, which must be reassessed (Coleman *et al.* 2004; Morris, 2005). The classical sediment transport formulations, which are based on the hydromechanics of transport-capacity, steady and uniform riverine systems with mild bed slopes, may not apply to embankment breach flows.

- *In the present study, a newly derived bed shear stress expression to account for boundary seepage (using a transient flownet analysis) and steep slopes is utilized to reassess the existing sediment transport expressions for breach flow overtopping steep slopes*.

The lack of understanding of the scale effects in modeling the breach overtopping problem using experimental methods has led emergency planners, who are in need for an accurate prediction of the breach outflow hydrograph, to resort to numerical models instead. There have been detailed experimental investigations which have

thoroughly addressed prototype-model scaling with respect to fuse plug embankments (Tinney and Hsu, 1961; Chee, 1978; Pugh, 1985; Shuibo *et al.* 1993). However, such hydraulic structures are designed to fail in a controlled and predictable manner and therefore an interest in such investigations is quite logical. Applying simple scaling laws governing the failure of complex structures to homogeneous embankment dams or dikes is not feasible.

- *Therefore, the author of this thesis found it necessary to develop or evaluate existing scaling laws which can be applied to the more basic embankment configurations. Such scaling laws would first have to be investigated using small geometric scales if they are to be adapted to the larger prototype embankments*.
- *These scaling laws are also assessed with respect to two aspects of similarity: (1) breach outflow characteristics and (2) breach channel morphology. For instance, neither the study of Stretch and Parkinson (2006), nor the IMPACT Project laboratory and field tests (IMPACT, 2004a) confirmed whether the parameters related to flow and breach channel evolution were in agreement with the Froude criterion.*
- *Similar to the study of Schmocker and Hager (2009), three scale ratios are investigated in this study. However, the current experimental setup is unique in the sense that it simulated the 3-D breach overtopping mechanism, in addition to maintaining a prevalent falling head characteristic.*
- *A minimal inflow feature of this experimental setup serves as a fair evaluation of the robustness of the Froude number with respect to 3-D breach overtopping in physical models.*
- *Both tilted and quasi-exact geometric scale series test are addressed as part of this hydraulic aspect of the 3-D breach overtopping.*

In this experimental program, in addition to the investigation of the resulting breach outflow characteristics (*i.e.* breach outflow hydrograph), breach channel morphology is investigated in terms of the apparent control section forming on the upstream

slope (Coleman *et al*. 2002; IMPACT, 2004a; Stretch and Parkinson, 2006; Morris *et al*. 2007). This is particularly important since the commonly-used weir-flow expressions assume that the control section is at the breach channel constriction. Similar to the study of Coleman *et al*. (2002), the measurements of the breach channel entrance at the upstream slope are also determined.

- *In the present study, this is achieved by using a photogrammetric (i.e. non-intrusive measurement) technique.*
- *Also, a breach discharge efficiency expression is derived based on upstream control and its time-dependence is correlated to the observed breach mechanisms for both the hydraulic and geotechnical parameters investigated in this research work.*

Chapter 4
Theory of Embankment Breach Hydromechanics

As part of any modeling work, it is important to consider the several mechanisms which characterize an embankment breach. Numerical models tend to oversimplify or neglect certain physical processes which may in fact dominate the breaching mechanism. In terms of breach channel hydrodynamics, it is usually the unsteadiness and nonuniformity of the flow which is oversimplified. With respect to breach geomechanics, the soil properties and geotechnical processes such as seepage are often ignored or oversimplified. In the case of erosion mechanics, most physically-based numerical models employ sediment transport equations which have been developed for steady flow and for transport-equilibrium conditions. Neglecting the high degree of coupling between all these processes can also cause the physically-based numerical model to misrepresent the entire breaching process. This chapter covers the fundamental premises derived from hypotheses, as well as explanations with respect to some of the processes which occur in an embankment breach failure.

4.1 Dambreak and Embankment Breach Flow Hydrodynamics

4.1.1 General 3-Dimensional Hydrodynamic Equations

The fundamental equations governing hydrodynamic flow can be derived by applying the momentum and mass conservation principles (*i.e.* Newton's second law and continuity equation, respectively) to an infinitesimal fluid particle volume in motion, as shown in Figure 4.1.

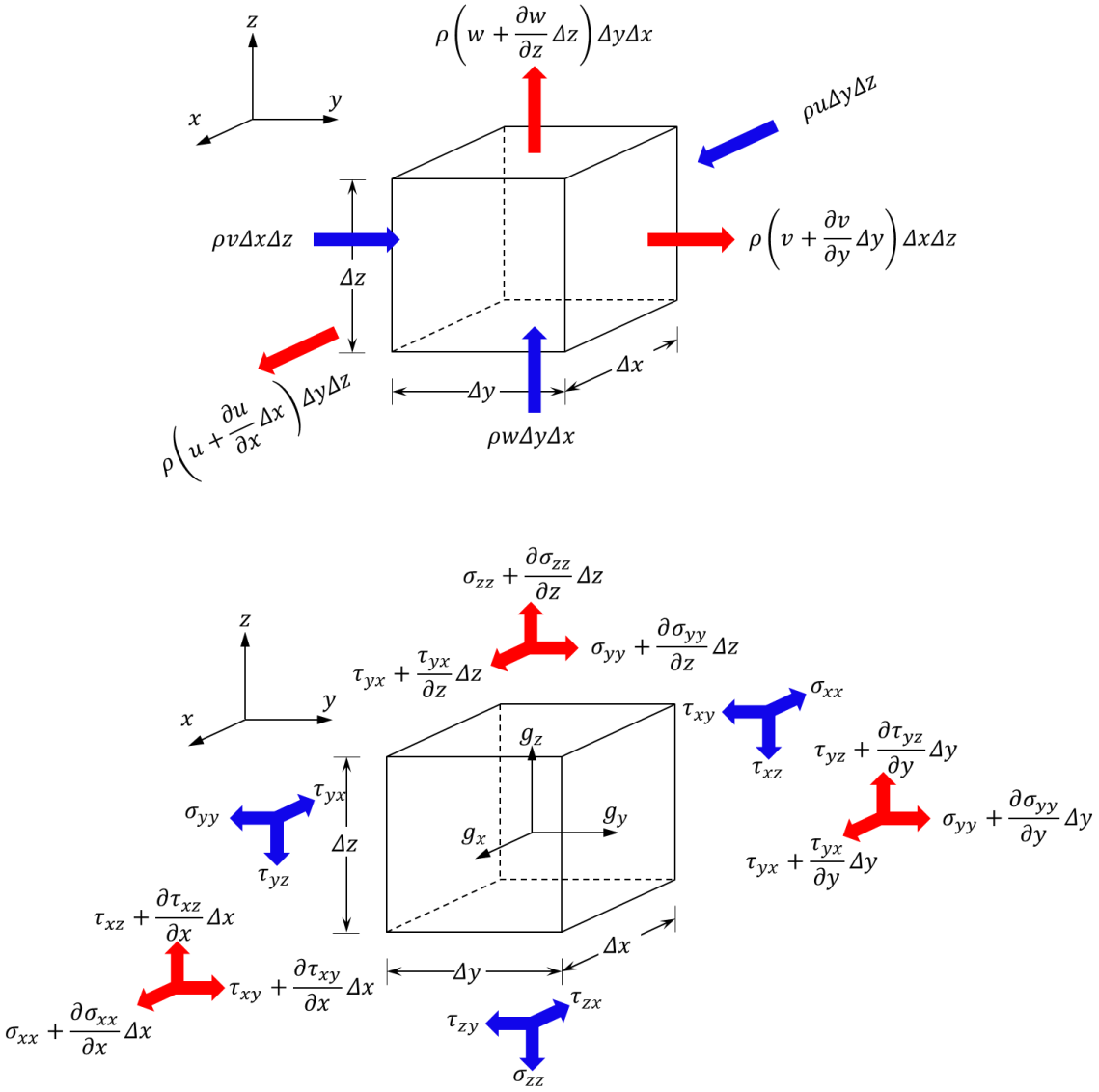

Figure 4.1: Infinitesimal fluid element showing (top) mass fluxes (bottom) surficial stresses (τ is shear or tangential stress and σ is normal stress)

The resulting 3-D partial differential equations derived from the momentum conservation principle using an Eulerian frame of reference are known as the Navier-Stokes equations (NSE), after Claude-Louis Navier (1785-1836) and George Gabriel Stokes (1819-1903) (Crowe *et al.* 2009). Below are the continuity and Navier-Stokes partial differential equations for an incompressible Newtonian fluid in the rectilinear coordinate system (Welty *et al.* 2001):

$$\frac{\partial u}{\partial x}+\frac{\partial v}{\partial y}+\frac{\partial w}{\partial z}=0 \tag{4.1}$$

$$\rho\left(\frac{\partial u}{\partial t}+u\frac{\partial u}{\partial x}+v\frac{\partial u}{\partial y}+w\frac{\partial u}{\partial z}\right)=-\frac{\partial p}{\partial x}+\mu\left(\frac{\partial^2 u}{\partial x^2}+\frac{\partial^2 u}{\partial y^2}+\frac{\partial^2 u}{\partial z^2}\right)+\rho g_x \tag{4.2}$$

$$\rho\left(\frac{\partial v}{\partial t}+u\frac{\partial v}{\partial x}+v\frac{\partial v}{\partial y}+w\frac{\partial v}{\partial z}\right)=-\frac{\partial p}{\partial y}+\mu\left(\frac{\partial^2 v}{\partial x^2}+\frac{\partial^2 v}{\partial y^2}+\frac{\partial^2 v}{\partial z^2}\right)+\rho g_y \tag{4.3}$$

$$\rho\left(\frac{\partial w}{\partial t}+u\frac{\partial w}{\partial x}+v\frac{\partial w}{\partial y}+w\frac{\partial w}{\partial z}\right)=-\frac{\partial p}{\partial z}+\mu\left(\frac{\partial^2 w}{\partial x^2}+\frac{\partial^2 w}{\partial y^2}+\frac{\partial^2 w}{\partial z^2}\right)+\rho g_z \tag{4.4}$$

where, u, v and w, are instantaneous fluid velocities in the x, y and z directions, respectively, p is pressure, g_x and g_y and g_z are the components of the gravitational acceleration in the x, y and z directions, respectively, and μ and ρ are the dynamic viscosity and density of the fluid, respectively.

The first term on the left-hand-side (LHS) of the momentum equations (Equations (4.2) to (4.4)) represents the local accelerations, while the remaining terms represent the convective accelerations in each direction. The first term on the right-hand-side (RHS) of the momentum equations represents the pressure gradient in the respective direction while the higher order second term represents the viscous shear forces (see Figure 4.1). The third term in the RHS of the momentum equation in the z-direction (Equation (4.4)) represents the force of gravity resolved in each direction. While analytical solutions for Equations (4.2) to (4.4) do not exist, they can be solved using numerical techniques. Numerical algorithms such as the Direct Numerical Simulation (DNS) are common methods for solving the flow domain in laminar conditions. They are on the other hand, computationally expensive, since solutions for all length and time scales are required (Pope, 2000).

Prior to the development of an algorithm and process of discretization of the physical domain, it may be in the interest of the modeler to scale the NSE. This process examines the rationale behind each term in those fundamental equations and therefore possibly reduces a complex equation into a simpler form (French, 1985). The procedure is carried out by expressing each of the dependent and independent variables as follows:

$$\hat{x}=\frac{x}{L_0};\ \hat{y}=\frac{y}{L_0};\ \hat{z}=\frac{z}{L_0};\ \hat{t}=\frac{tU_0}{L_0}$$

$$\hat{u} = \frac{u}{U_0};\ \hat{v} = \frac{v}{U_0};\ \hat{w} = \frac{w}{U_0};\hat{p} = \frac{p}{\rho U_0^2} \tag{4.5}$$

where, L_0 and U_0 are a characteristic length and velocity in the flow domain. By substituting Equation (4.5) in Equations (4.2) to (4.4), the NSE can be expressed as follows:

$$\frac{U_0^2}{L_0}\frac{\partial \hat{u}}{\partial \hat{t}} + \frac{U_0^2}{L_0}\hat{u}\frac{\partial \hat{u}}{\partial \hat{x}} + \frac{U_0^2}{L_0}\hat{v}\frac{\partial \hat{u}}{\partial \hat{y}} + \frac{U_0^2}{L_0}\hat{w}\frac{\partial \hat{u}}{\partial \hat{z}} = -\frac{U_0^2}{L_0}\frac{\partial \hat{p}}{\partial \hat{x}} + \frac{\mu U_0}{\rho L_0^2}\left(\frac{\partial^2 \hat{u}}{\partial \hat{x}^2} + \frac{\partial^2 \hat{u}}{\partial \hat{y}^2} + \frac{\partial^2 \hat{u}}{\partial \hat{z}^2}\right) + \mathrm{g}_x \tag{4.6}$$

$$\frac{U_0^2}{L_0}\frac{\partial \hat{v}}{\partial \hat{t}} + \frac{U_0^2}{L_0}\hat{u}\frac{\partial \hat{v}}{\partial \hat{x}} + \frac{U_0^2}{L_0}\hat{v}\frac{\partial \hat{v}}{\partial \hat{y}} + \frac{U_0^2}{L_0}\hat{w}\frac{\partial \hat{v}}{\partial \hat{z}} = -\frac{U_0^2}{L_0}\frac{\partial \hat{p}}{\partial \hat{y}} + \frac{\mu U_0}{\rho L_0^2}\left(\frac{\partial^2 \hat{v}}{\partial \hat{x}^2} + \frac{\partial^2 \hat{v}}{\partial \hat{y}^2} + \frac{\partial^2 \hat{v}}{\partial \hat{z}^2}\right) + \mathrm{g}_y \tag{4.7}$$

$$\frac{U_0^2}{L_0}\frac{\partial \hat{w}}{\partial \hat{t}} + \frac{U_0^2}{L_0}\hat{u}\frac{\partial \hat{w}}{\partial \hat{x}} + \frac{U_0^2}{L_0}\hat{v}\frac{\partial \hat{w}}{\partial \hat{y}} + \frac{U_0^2}{L_0}\hat{w}\frac{\partial \hat{w}}{\partial \hat{z}} = -\frac{U_0^2}{L_0}\frac{\partial \hat{p}}{\partial \hat{z}} + \frac{\mu U_0}{\rho L_0^2}\left(\frac{\partial^2 \hat{w}}{\partial \hat{x}^2} + \frac{\partial^2 \hat{w}}{\partial \hat{y}^2} + \frac{\partial^2 \hat{w}}{\partial \hat{z}^2}\right) + \mathrm{g}_z \tag{4.8}$$

Equations (4.6) to (4.8) can be expressed in dimensionless form by dividing both sides by U_0^2/L_0, which then yields:

$$\frac{\partial \hat{u}}{\partial \hat{t}} + \hat{u}\frac{\partial \hat{u}}{\partial \hat{x}} + \hat{v}\frac{\partial \hat{u}}{\partial \hat{y}} + \hat{w}\frac{\partial \hat{u}}{\partial \hat{z}} = -\frac{\partial \hat{p}}{\partial \hat{x}} + \frac{\mu}{\rho U_0 L_0}\left(\frac{\partial^2 \hat{u}}{\partial \hat{x}^2} + \frac{\partial^2 \hat{u}}{\partial \hat{y}^2} + \frac{\partial^2 \hat{u}}{\partial \hat{z}^2}\right) + \frac{g_x L}{U_0^2} \tag{4.9}$$

$$\frac{\partial \hat{v}}{\partial \hat{t}} + \hat{u}\frac{\partial \hat{v}}{\partial \hat{x}} + \hat{v}\frac{\partial \hat{v}}{\partial \hat{y}} + \hat{w}\frac{\partial \hat{v}}{\partial \hat{z}} = -\frac{\partial \hat{p}}{\partial \hat{y}} + \frac{\mu}{\rho U_0 L_0}\left(\frac{\partial^2 \hat{v}}{\partial \hat{x}^2} + \frac{\partial^2 \hat{v}}{\partial \hat{y}^2} + \frac{\partial^2 \hat{v}}{\partial \hat{z}^2}\right) + \frac{g_y L}{U_0^2} \tag{4.10}$$

$$\frac{\partial \hat{w}}{\partial \hat{t}} + \hat{u}\frac{\partial \hat{w}}{\partial \hat{x}} + \hat{v}\frac{\partial \hat{w}}{\partial \hat{y}} + \hat{w}\frac{\partial \hat{w}}{\partial \hat{z}} = -\frac{\partial \hat{p}}{\partial \hat{z}} + \frac{\mu}{\rho U_0 L_0}\left(\frac{\partial^2 \hat{w}}{\partial \hat{x}^2} + \frac{\partial^2 \hat{w}}{\partial \hat{y}^2} + \frac{\partial^2 \hat{w}}{\partial \hat{z}^2}\right) + \frac{g_z L}{U_0^2} \tag{4.11}$$

Two dimensionless groups appear in Equations (4.9) to (4.11), $\mu/\rho U_0 L_0$ and $\mathrm{g}L_0/U_0^2$, which correspond to the inverse of the Reynolds number and the squared inverse of the Froude number respectively (see Section 4.7 for additional details). Therefore, in a flow domain with a very high Reynolds number, the second order terms on the RHS may be neglected.

The phenomenon of turbulence exists in almost all open channel flows which renders the DNS option almost impossible from a computational standpoint. Under turbulent conditions, the fluid and flow properties vary with time such that macroscopic flow structures are caused by fluctuations in the flow velocities. These fluctuations induce additional viscous forces between the fluid particles. By substituting the instantaneous velocities with time-averaged and fluctuating components and averaging each term, the NSE for an incompressible Newtonian fluid under turbulent conditions can therefore be expressed as follows (Hughes, 1993):

$$\frac{\partial \bar{u}}{\partial t}+\bar{u}\frac{\partial \bar{u}}{\partial x}+\bar{v}\frac{\partial \bar{u}}{\partial y}+\bar{w}\frac{\partial \bar{u}}{\partial z}=-\frac{1}{\rho}\frac{\partial \bar{p}}{\partial x}+\nu\left(\frac{\partial^2 \bar{u}}{\partial x^2}+\frac{\partial^2 \bar{u}}{\partial y^2}+\frac{\partial^2 \bar{u}}{\partial z^2}\right)-\left(\frac{\partial \overline{u'^2}}{\partial x}+\frac{\partial \overline{u'v'}}{\partial y}+\frac{\partial \overline{u'w'}}{\partial z}\right)+\mathrm{g}_x \tag{4.12}$$

$$\frac{\partial \bar{v}}{\partial t}+\bar{u}\frac{\partial \bar{v}}{\partial x}+\bar{v}\frac{\partial \bar{v}}{\partial y}+\bar{w}\frac{\partial \bar{v}}{\partial z}=-\frac{1}{\rho}\frac{\partial \bar{p}}{\partial y}+\nu\left(\frac{\partial^2 \bar{v}}{\partial x^2}+\frac{\partial^2 \bar{v}}{\partial y^2}+\frac{\partial^2 \bar{v}}{\partial z^2}\right)-\left(\frac{\partial \overline{u'v'}}{\partial x}+\frac{\partial \overline{v'^2}}{\partial y}+\frac{\partial \overline{v'w'}}{\partial z}\right)+\mathrm{g}_y \tag{4.13}$$

$$\frac{\partial \bar{w}}{\partial t}+\bar{u}\frac{\partial \bar{w}}{\partial x}+\bar{v}\frac{\partial \bar{w}}{\partial y}+\bar{w}\frac{\partial \bar{w}}{\partial z}=-\frac{1}{\rho}\frac{\partial \bar{p}}{\partial z}+\nu\left(\frac{\partial^2 \bar{w}}{\partial x^2}+\frac{\partial^2 \bar{w}}{\partial y^2}+\frac{\partial^2 \bar{w}}{\partial z^2}\right)-\left(\frac{\partial \overline{u'w'}}{\partial x}+\frac{\partial \overline{v'w'}}{\partial y}+\frac{\partial \overline{w'^2}}{\partial z}\right)+\mathrm{g}_z \tag{4.14}$$

where, u', v' and w' are the turbulent fluctuating components of the velocity in the x, y and z directions, respectively, $\bar{u}$, $\bar{v}$ and $\bar{w}$ are the time-averaged velocities in the x, y and z directions, respectively, $\bar{p}$ is the time-averaged pressure, and ν is the kinematic viscosity of the fluid. The turbulent contributions to the shear stress due to mixing and consequent momentum exchange between the fluid particles are referred to as the Reynolds stresses, whereby Equations (4.12) to (4.14) are referred to as the Reynolds Averaged Navier-Stokes (RANS) equations. However, the RANS equations introduce six unknowns since three of the nine terms are repeated; therefore additional relationships need to be established. A setup of this process is known as closure modeling. The most popular closure model is the Boussinesq assumption, which lumps all the turbulent fluctuation terms with the viscous forces terms using an eddy viscosity, ν_t as shown in the formulations below (French, 1985):

$$\frac{\partial \bar{u}}{\partial t}+\bar{u}\frac{\partial \bar{u}}{\partial x}+\bar{v}\frac{\partial \bar{u}}{\partial y}+\bar{w}\frac{\partial \bar{u}}{\partial z}=-\frac{1}{\rho}\frac{\partial \bar{p}}{\partial x}+(\nu+\nu_t)\left(\frac{\partial^2 \bar{u}}{\partial x^2}+\frac{\partial^2 \bar{u}}{\partial y^2}+\frac{\partial^2 \bar{u}}{\partial z^2}\right)+g_x \tag{4.15}$$

$$\frac{\partial \bar{v}}{\partial t}+\bar{u}\frac{\partial \bar{v}}{\partial x}+\bar{v}\frac{\partial \bar{v}}{\partial y}+\bar{w}\frac{\partial \bar{v}}{\partial z}=-\frac{1}{\rho}\frac{\partial \bar{p}}{\partial y}+(\nu+\nu_t)\left(\frac{\partial^2 \bar{v}}{\partial x^2}+\frac{\partial^2 \bar{v}}{\partial y^2}+\frac{\partial^2 \bar{v}}{\partial z^2}\right)+g_y \tag{4.16}$$

$$\frac{\partial \bar{w}}{\partial t}+\bar{u}\frac{\partial \bar{w}}{\partial x}+\bar{v}\frac{\partial \bar{w}}{\partial y}+\bar{w}\frac{\partial \bar{w}}{\partial z}=-\frac{1}{\rho}\frac{\partial \bar{p}}{\partial z}+(\nu+\nu_t)\left(\frac{\partial^2 \bar{w}}{\partial x^2}+\frac{\partial^2 \bar{w}}{\partial y^2}+\frac{\partial^2 \bar{w}}{\partial z^2}\right)+g_z \tag{4.17}$$

This logic behind the eddy viscosity is derived from Newton's viscosity law shown below:

$$\tau_{zx}=\mu\frac{du}{dz} \tag{4.18}$$

where, τ_{zx} is the shear stress, τ, acting on the x–y plane and in the x-direction, and du/dz is the streamwise velocity gradient along the vertical direction.

The value of this added viscosity can therefore be adjusted by calibration of the numerical model using experimental data. Other closure models have been developed, however, they are not discussed since this is beyond the intended scope of this research.

Turbulence models are computationally intensive even for relatively simple open channel flow scenarios. However, recent studies have shown that 3-D turbulence modeling (*e.g.* using $\kappa-\varepsilon$, large eddy simulation (LES) and volume of fluid (VOF) closure approaches) are capable of simulating the free surface and velocities in dambreak flows successfully (Yue *et al.* 2003; Biscarini *et al.* 2010; Larocque *et al.* 2013), with a precision higher than the shallow water equations (SWE) approach (Biscarini *et al.* 2010; Larocque *et al.* 2013). However, the accuracy of numerical models always comes at the cost of computational efficiency with simulation times in 3-D turbulence models one order of magnitude higher (Biscarini *et al.* 2010).

It is unclear when 3-D or even 2-D depth-averaged turbulence models will be coupled with mobile bed models and become capable of accurately and efficiently simulating the highly erosive embankment breach flows. Nevertheless, 2-D depth-averaged and 3-D hydrodynamic equations have been widely used in highly-nonlinear morphodynamic applications over the past 40 years.

4.1.2 Shallow Water Equations (SWE)

The SWE are a system of partial differential equations derived using the momentum and mass conservation principle using the control volume approach for open channel flow. The SWE are essentially an approximation of the NSE where “shallow” surface flow is principally assumed, hence the name. The study by Audusse *et al.* (2011) classifies the types of SWE-type derivations into hydrostatic and non-hydrostatic. The most common system of equations used in open channel hydraulics that assumes hydrostatic conditions is the de Saint-Venant equation (SVE), which neglects curvature effects of the water surface. The Boussinesq equations are SWE which do take into account curvature effects as well as vertical velocities, and

therefore are classified as non-hydrostatic. Boussinesq equations are derived using the Euler equations, therefore inviscid and irrotational flow is predominantly assumed (Sainte-Marie and Bristeau, 2008). Since SWE are a depth-averaged adaptation of the NSE, boundary conditions at the bed and free surface need to be defined. Nevertheless, derivations of both hydrostatic and non-hydrostatic SVE have been presented where velocities have been solved between the free and bed surfaces using a multi-layered approach (Audusse *et al.* 2011).

Similar to the NSE, the SVE are nonlinear due to the convective acceleration terms, and therefore cannot be solved analytically. However, they are easier to solve using numerical techniques. SVE solve the flow domain in one or two Euclidian space in terms of flow depth and the horizontal velocities, and are most common in flood routing applications (Mujumdar, 2001). They are commonly used in solving the dambreak problem. Below are the 2-D depth-averaged SVE for a wide prismatic open channel in conservative form (George, 2011):

$$\frac{\partial \eta}{\partial t} + \frac{\partial}{\partial x}(\eta U) + \frac{\partial}{\partial y}(\eta V) = 0 \tag{4.19}$$

$$\frac{\partial}{\partial t}(\eta U) + \frac{\partial}{\partial x}\left(\eta U^2 + \frac{1}{2} g\eta^2 \cos\phi_{bx}\right) + \frac{\partial}{\partial y}(\eta UV) = \mathrm{g}\eta\left(\sin\phi_{bx} - S_{fx}\right) \tag{4.20}$$

$$\frac{\partial}{\partial t}(\eta V) + \frac{\partial}{\partial x}(\eta UV) + \frac{\partial}{\partial y}\left(\eta V^2 + \frac{1}{2} g\eta^2 \cos\phi_{by}\right) = \mathrm{g}\eta\left(\sin\phi_{by} - S_{fy}\right) \tag{4.21}$$

where, η is the water surface level, U and V are the depth-averaged streamwise and lateral velocity components, respectively, $\phi_{bx}$and ϕ_{by} are the bed slope angles with respect to the x and y directions, respectively, S_{fx} and S_{fy} are the friction slopes in the x and y directions, respectively, and can be expressed as follows:

$$S_{fx} = \frac{n_M^2 U\sqrt{U^2+V^2}}{\eta^{4/3}} \tag{4.22}$$

$$S_{fy} = \frac{n_M^2 V\sqrt{U^2+V^2}}{\eta^{4/3}} \tag{4.23}$$

where, the Manning coefficient for roughness, n_M, and can be expressed using the following Manning-Strickler relationship (Julién and Simons, 1985) based on the median sediment particle size with units in [mm]:

$$n_M = 0.0132 d_{50}^{1/6} \tag{4.24}$$

The primary assumption in the resulting derivation shown in Equations (4.19) to (4.21) is that velocities in the horizontal direction are much larger than in the vertical direction (*i.e.* $w = dw/dt \approx 0$). The assumption of negligible vertical velocities and accelerations in the flow domain leads to the hydrostatic assumption. The pressure force term in Equation (4.20) and (4.21) was derived based on the vertical flow depth instead of a "pressure-head equivalent" flow depth (French, 1985), implying a mild slope assumption. **Note:** Figure 4.2 illustrates the following terminology of flow depth in river hydraulics: vertical flow depth, section (or perpendicular) flow depth and pressure-head equivalent flow depth, which is the vertical projection of the section flow depth (see Subsection 4.1.4 for the corresponding hydrostatic flow depth in curvilinear flow). A factor of $\cos^2 \phi_{bx}$ between the section flow depth and the pressure-head equivalent flow depth will need to be considered for $\phi_{bx} > 10°$ (French, 1985). However, for mild slopes ($\phi_{bx} < 10°$), $\cos \phi_{bx} = \cos \phi_{by} \approx 1$, $\sin \phi_{bx} \approx \tan \phi_{bx} = dz/dx = S_{bx}$, and $\sin \phi_{by} \approx \tan \phi_{by} = dz/dy = S_{by}$, where S_{bx} and S_{by} are the local bed slopes in the *x*- and *y*- directions, respectively.

For the mild slope assumption, the 2-D momentum equations for a wide prismatic open channel become:

$$\frac{\partial}{\partial t}(\eta U) + \frac{\partial}{\partial x}\left(\eta U^2 + \frac{1}{2} g \eta^2\right) + \frac{\partial}{\partial y}(\eta U V) = g\eta\left(S_{bx} - S_{fx}\right) \tag{4.25}$$

$$\frac{\partial}{\partial t}(\eta V) + \frac{\partial}{\partial x}(\eta U V) + \frac{\partial}{\partial y}\left(\eta V^2 + \frac{1}{2} g \eta^2\right) = g\eta\left(S_{bx} - S_{fy}\right) \tag{4.26}$$

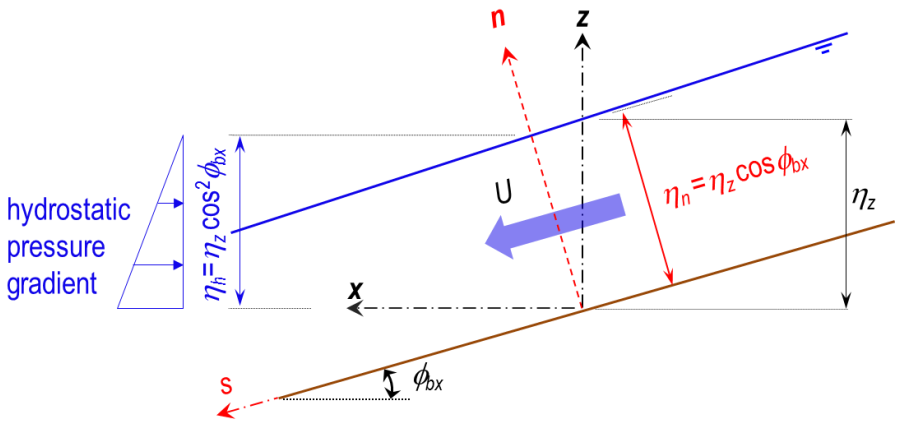

Figure 4.2: Flow on a sloping channel showing vertical flow depth, η_z, section (or perpendicular) flow depth, η_n, and pressure-head equivalent flow depth, η_h (after French, 1985)

Due to the adopted control volume approach in their derivation, the SVE expresses the viscous forces between the fluid particles on the sides of the control volume (*i.e.* due to turbulence) and the bottom boundary shear force into one lumped value, usually described by an empirical resistance laws corresponding to the Manning or Chézy roughness or friction coefficient (Hager and Hager 1985; Litrico and Fromion, 2009). This may be counterintuitive, especially if the purpose of the model is to simulate a rapidly-varying and/or unsteady flow domain. For a wide prismatic open channel, with a lateral inflow per unit area, q_L, the 1-D SVE can be expressed in conservative form as follows (Daluz Vieira, 1983):

$$\frac{\partial \eta}{\partial t} + \frac{\partial}{\partial x}(\eta U) = q_L \tag{4.27}$$

$$\frac{\partial}{\partial t}(\eta U) + \frac{\partial}{\partial x}\left(\eta U^2 + \frac{1}{2} g \eta^2\right) = g\eta\left(S_{bx} - S_{fx}\right) - q_L U \tag{4.28}$$

where, S_b is bed slope, and the friction slope, S_f, can be expressed using the Manning or Chézy equations as follows (Daluz Vieira, 1983; Litrico and Fromion, 2009):

$$S_f = \frac{n_M^2 U^2}{\eta^{4/3}} \tag{4.29}$$

$$S_f = \frac{U^2}{C^2 \eta} \tag{4.30}$$

where, C is Chézy roughness coefficient.

Equation 4.28 is also known as the dynamic wave equation or full SVE. Miller (1984) and Julién (2002) describe four model variants of the dynamic wave equation as shown in Table 4.1. The steady-dynamic wave variant of the SVE assumes that the unsteady term is very small, which corresponds to the backwater equations for gradually-varied flow (GVD) (Julién, 2002). This quasi-steady approximation does, however, breakdown in critical and supercritical flows (Parker, 2013). Julién (2002) also stated that in subcritical flow the convective acceleration term is negligible, which reduces the steady-dynamic wave equation to the diffusion equation. For negligible changes in the pressure force gradient, the diffusion wave equation reduced to the kinematic wave equation. It is important to note that for supercritical flow conditions, computations using the kinematic approximation should start upstream and follow downstream following the direction of wave propagation (Olsen, 2012). While terms from the momentum equation are eliminated to achieve the different variants of the SVE, all terms of the continuity equation, including the unsteady term, are used.

Table 4.1: Matrix showing variants of SVE (after Miller, 1984 and Julién, 2002)

Model	Momentum terms (Equation (4.28))				
	Unsteady	Convective	Pressure gradient	Gravity	Friction slope
	$\frac{\partial}{\partial t}(\eta U)$	$\frac{\partial}{\partial x}(\eta U^2)$	$\frac{\partial}{\partial x}\left(\frac{1}{2}g\eta^2\right)$	$g\eta S_b$	$g\eta S_f$
Dynamic wave (SVE)	●	●	●	●	●
Steady-dynamic wave		●	●	●	●
Diffusion wave			●	●	●
Kinematic wave				●	●
Gravity	●	●	●		

The hydrostatic SVE are not ideal to model flow domains with sharp discontinuous boundaries such as undular bores or weir flows (Litrico and Fromion, 2009). This is also true for embankment overtopping flows where slopes are steep and curvature effects are significant. An adaptation of the SVE to consider steep slopes in 1-D is

described in Subsection 7.3.5. As previously mentioned, the Boussinesq equation accounts for curvilinear effects using a third order mixed derivative term which corrects to some extent the pressure to reflect non-hydrostatic conditions. The study by Basco (1989) presents the basic 1-D Boussinesq equations in 1-D for flow in a wide prismatic open channel as follows:

$$\frac{\partial \eta}{\partial t} + \frac{\partial (\eta U)}{\partial x} = 0 \tag{4.31}$$

$$\frac{\partial U}{\partial t} + U\frac{\partial U}{\partial x} + g\frac{\partial \eta}{\partial x} = -\bar{\eta}\frac{\partial^3 \eta}{\partial x \partial t^2} \tag{4.32}$$

where, $\bar{\eta}$ is flow depth measured from the channel's bed to the still water level. Mohapatra and Chaudhry (2004) express the 1-D Boussinesq momentum equation including the gravitational and viscous terms in conservative form as follows:

$$\frac{\partial (U\eta)}{\partial t} + \frac{\partial (U^2\eta)}{\partial x} + \frac{\partial \left(g\eta^2/_2\right)}{\partial x} - \frac{\eta^3}{3}\frac{\partial^3 U}{\partial x^2 \partial \mathrm{t}} - \frac{\eta^3}{3}U\frac{\partial^3 U}{\partial x^3} + \frac{\partial}{\partial \mathrm{x}}\left[\frac{\eta^3}{3}\left(\frac{\partial \mathrm{U}}{\partial \mathrm{x}}\right)^2\right] = g\eta\left(S_b - S_f\right) \tag{4.33}$$

Subsection 4.1.4 describes methods for determining the pressure head in curvilinear flow.

4.1.3 Wall Laws

The shear stress is represented by viscous and Reynolds stress, shown in Equations (4.12) to (4.14) in the form of second order terms. Shear stress is also the principal flow parameter which quantifies sediment motion (see Section 4.2 for more details). Although the 3-D NSE can be readily integrated into a numerical model to capture the free (viscous) shear flows far from boundaries, special adaptations need to be made to determine the flow conditions near those boundaries. A no-slip boundary condition implies that Reynolds stresses are zero and consequently the shear stress is dominated by viscous effects (Pope, 2000). Unless a large number of grid cells are defined at wall-bounded regions, wall laws are required to solve the high local velocity gradients (Olsen, 2012). Wall laws are empirical formulations which were initially developed to capture the near-bed and midrange velocity profile in wall-bounded turbulent flows. These laws are often described as log-laws since

they state that the velocity is log-linear with depth. The time-averaged streamwise velocity, $\bar{u}$, can therefore be expressed in the following form (Welty *et al.* 2001):

$$\bar{u} = \frac{\sqrt{\tau_b/\rho}}{\kappa} \ln z + C_I \tag{4.34}$$

where, κ the von Kármán coefficient can be assumed to be 0.41 and C_I is the constant of integration. Equation (4.34) has been derived based on Prantdl's mixing length hypothesis from a 2-D perspective, however, it is known to fit the velocity profile very well (Welty *et al.* 2001). The constant of integration in Equation (4.34) represents the velocity directly above the roughness element present in the fluid's boundary. The final form of the log-law will therefore depend on the type of boundary surface.

In order to classify a boundary surface as hydraulically smooth or rough, it is first necessary to briefly describe the boundary layer concept as found in the work of French (1985), Welty *et al.* (2001) and Crowe *et al.* (2009), and illustrated in Figure 4.3.

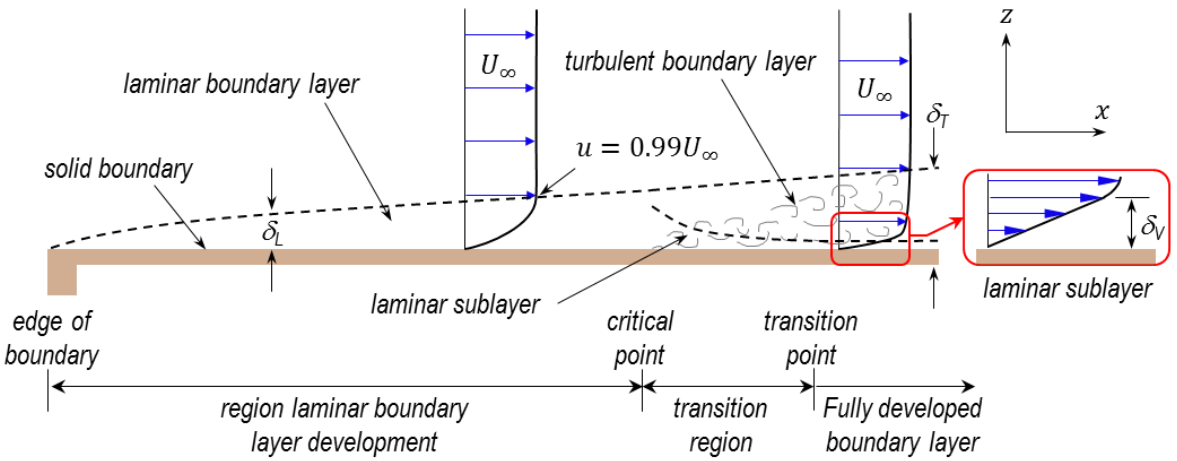

Figure 4.3: Boundary layer development and regions (after French, 1985; Crowe *et al.* 2009)

As the flow approaches the edge of a boundary, the velocity of particles adjacent to the surface is reduced due to the no-slip condition (*i.e.* $u = 0$) at the boundary. The velocity gradient is therefore very steep and consequently, the boundary shear

stress, τ_b, will be very high. Meanwhile, a boundary layer begins to develop such that its thickness, δ, represents the distance away from the surface where the velocity is 99% of the free-stream velocity, U_∞. As the flow progresses downstream, the velocities of other particles above the particles adjacent to the surface will also be reduced due to viscous forces. The velocity gradient adjacent to the wall is reduced as the flow progresses further downstream and consequently τ_b will decrease. The flow within the growing boundary layer (shown in Figure 4.3 with a thickness equal to δ_L) behaves as laminar flow, while outside of the laminar boundary layer (*i.e.* at the free-stream) the flow can be assumed to be inviscid (*i.e.* free-shear flow). At a certain distance downstream (shown in Figure 4.3 as the critical point), the boundary layer becomes unstable and fluctuations between laminar and turbulent flow take place. At this stage, a laminar (or viscous) sublayer with a thickness, δ_V, begins to develop. At the transition point, flow within the boundary layer is becomes fully turbulent. French (1985) stated that in open channel flow, the turbulent boundary layer thickness, δ_T, can even extend to the free surface. Crowe *et al.* (2009) stated that severe mixing within the turbulent boundary layer may increase the effective viscosity up to threefold. This condition causes the velocity gradient to steepen once more, giving rise to an increase in the shear stress acting on the boundary. The laminar sublayer within the turbulent layer is dominated by viscous forces, and is characterized by a steep and linear velocity gradient. The experimental investigation by Winterwerp *et al.* (1992) indicated that high sediment concentrations near the bed caused the viscous sublayer to increase significantly giving rise to higher bed shear stresses.

French (1985) stated that for hydraulically smooth boundaries, the roughness elements remain within the laminar sublayer envelope. The opposite is true for hydraulically rough boundaries, where the roughness elements extend beyond the laminar sublayer and affecting the free shear region. In hydraulically rough boundaries, the flow's resistance is governed by turbulent fluctuations (Shields, 1936). Schlichting (1968) defines criteria based on a pseudo-Reynolds number to

distinguish between hydraulically smooth, transition and hydraulically rough boundaries as follows:

$$0 \leq \frac{k_s u_*}{\nu} \leq 5 \tag{4.35}$$

$$5 \leq \frac{k_s u_*}{\nu} \leq 70 \tag{4.36}$$

$$70 \leq \frac{k_s u_*}{\nu} \tag{4.37}$$

where, k_s is equivalent sand or grain roughness size (also referred to as Nikuradse roughness size) and u_* is shear or friction velocity (often referred to as the grain velocity in hydraulic engineering terms) and is determined as follows:

$$u_* = \sqrt{\tau_b/\rho} \tag{4.38}$$

There is much debate about how to represent the value of k_s. French (1985) stated that k_s is not only a function of the height of the roughness elements, but it is dependent on their orientation, clustering, geometry and spacing. The sand grain roughness is usually expressed as a fraction of a certain sediment measurement size. The sediment size ranges between 35% and 90% of the sediment by weight is finer, while the fraction ranges anywhere between 1 and 6.6. As a result, an estimate of k_s is often difficult to obtain. The study by Yen (2002) summarised the expressions by twenty-one investigations. For one of the types of sands used in this study (sand Type III, see Figure C-9 in Appendix C), the computation of k_s ranged between 0.23mm and 2.64mm and the average value was 0.97mm (approximately four times the value of d_{50}). Furthermore, van Rijn (1993) points out that k_s is also a function of dimensionless shear stress, τ^*, (see Subsection 4.2.1) when $\tau^* \geq 1$:

$$k_s = 3\tau^* d_{90} \tag{4.39}$$

where, d_{90} is grain size at which 90% by weight of the sediment is finer.

For smooth boundaries, the constant of integration be expressed as follows (Crowe *et al.* 2009):

$$C_I = 5.56 - \frac{1}{\kappa}\ln\frac{zu_*}{\nu} \tag{4.40}$$

Keulegan (1938) expressed the log-law for hydraulically rough boundaries using the following expression:

$$\bar{u} = \frac{u_*}{\kappa} \ln \frac{30z}{k_s} \tag{4.41}$$

The depth-averaged log-law can be expressed as:

$$\bar{U} = \frac{u_*}{\kappa} \ln \frac{11R_h}{k_s} \tag{4.42}$$

where, R_h is the hydraulic radius, expressed as:

$$R_h = \frac{A}{P_w} \tag{4.43}$$

where, A is the cross-sectional area and $P_w$is the wetted perimeter.

Welty *et al.* (2001) described the velocity distribution using a universal log-law for wall-bounded turbulent flows. The velocity distribution is characterized by three distinguished regions which are defined by a pseudo-Reynolds number, but one which is somehow different than that of Schlichting (1968) (see Equations (4.35) to (4.37)):

Laminar sublayer, $5 > y^+ > 0$	$u^+ = y^+$	(4.44)
Buffer layer, $30 \geq y^+ \geq 5$	$u^+ = -3.05 + \ln y^+$	(4.45)
Turbulent core, $y^+ \geq 30$	$u^+ = 5.5 + \ 2.5 \ln y^+$	(4.46)

where, $y^+$is the relative distance from the boundary and is described as $u_* z/v$ and u^+ is the relative velocity and is described as $\bar{u}/u_*$.

4.1.4 Curvature Effects

In most river hydraulics applications where normal or gradually varied flow can be assumed, curvature effects are minimal and flow streamlines are parallel and a hydrostatic pressure assumption can therefore be made. Besides vertical velocities and accelerations and steep slopes (see Subsection 4.1.2), rapidly-varied flow (RVF) conditions, characterized by significant curvature effects, will also invalidate the hydrostatic assumption. Examples of RVF are flows over weirs, falls, spillway

chutes, embankment dams and downstream sluice gates. French (1985) and Chaudhry (2008) modify the pressure head due to the centrifugal force in curvilinear flow as follows:

$$d_h = d_z\left(1 \pm \frac{1}{g}\frac{U_s^2}{r}\right) \tag{4.47}$$

where, d_h is the total pressure-head, d_z is the pressure-head for hydrostatic conditions, r is the radius of curvature, and U_s is the depth-averaged velocity along the streamlines. A positive sign applies when the streamlines are concave and a negative sign applies when the streamlines are convex. The first term in the RHS of Equation (4.47) represents the pressure-head due to hydrostatic conditions, while the second term represents the pressure-head due to the centrifugal force, d_c. Figure 4.4 shows the effect of curvilinear flow measured by a piezometer and the modified pressure gradient for both concave and convex streamlines.

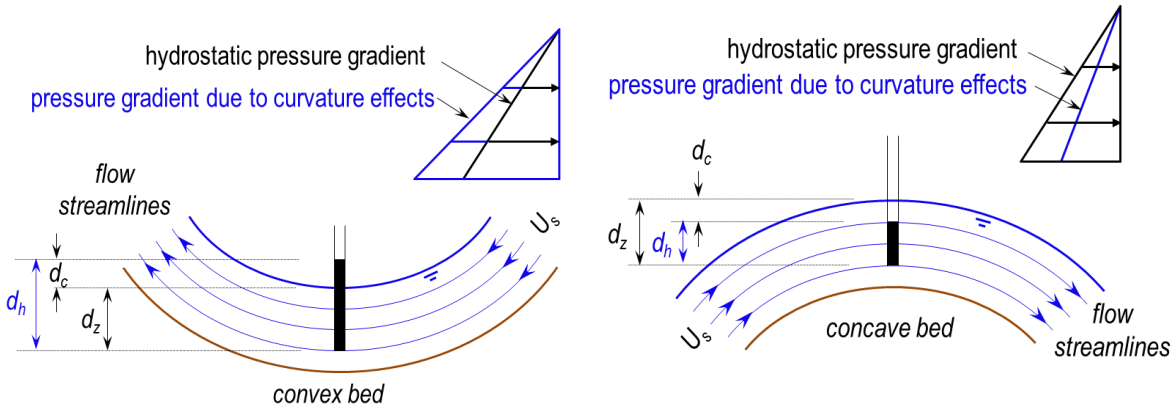

Figure 4.4: Pressure gradient due to curvilinear flow (left) convex bed (right) concave bed (after French, 1985 and Chaudhry, 2008)

The study by Hager and Hutter (1984) derived expressions for the inviscid Euler equations in a Laplacian flow-field influenced by both slope and curvature effects. They expressed the perpendicular flow depth as the length of an orthogonal trajectory to the bottom boundary shown as follows:

$$\eta_n = \eta_z \frac{(\phi_{bx} - \phi_{wn})}{\cos\phi_{bx}(\tan\phi_{bx} - \tan\phi_{wn})} \tag{4.48}$$

where, ϕ_{wn} is the angle at which the orthogonal trajectory intersects the free surface with respect to the horizontal direction. Similarly, the pressure-head equivalent was expressed by Hager and Hutter (1984) as:

$$\eta_h = \eta_n \frac{\tan\phi_{bx} - \tan\phi_{wn}}{\phi_{bx} - \phi_{wn}} \tag{4.49}$$

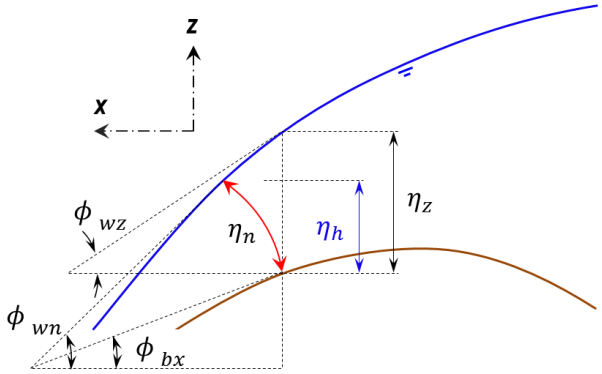

Figure 4.5: Flow geometry due to slope and curvature effects (after Hager and Hutter, 1984)

The expressions derived in Hager and Hutter (1984) are based on the assumption that the water surface slope intersects the orthogonal trajectory at the same angle with the vertical flow depth, η_z. A similar expression can be derived for two independent water surface slope angles, ϕ_{wn}, and the angle at which the vertical flow depth intersections the free surface, ϕ_{wz} (see). Assuming that ϕ_{wn}, ϕ_{wz} and η_z can be readily measured, the following expression for the flow depth based on the equivalent pressure-head is therefore proposed for more pronounced curvatures:

$$\eta_h = \eta_z \frac{1}{1+\tan\left(\frac{\phi_{wn}+\phi_{wz}}{2}\right)} \frac{(\sin\phi_{wn} - \sin\phi_{bx})}{(\cos\phi_{bx} - \cos\phi_{wn})} \tag{4.50}$$

4.1.5 Flow Overtopping

Powledge *et al.* (1989) classifies the flow above an embankment dam into three regimes as shown in Figure 4.6.

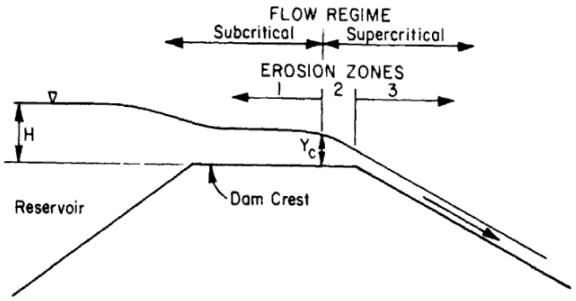

Figure 4.6: Hydraulic flow regimes and erosion zones during overtopping (Powledge *et al.* 1989)

Zone 1: The flow depth is subcritical ($Fr < 1$) or transcritical ($Fr = 1$) and pertains to a low energy level (the datum being the crest elevation). The low hydraulic forces attributed to the subcritical flow induce small tractive forces on the bed material and erosion will take place in highly erodible materials for this locality.

Zone 2: In this region the water profile experiences a drawdown effect where the flow depth is below critical ($Fr > 1$) and pertains to a low energy level since the there is no change in elevation. The high hydraulic forces have little impact on bed material erosion due to the limited distance over which they are exposed to.

Zone 3: In this region, flow is supercritical ($Fr > 1$) and pertains to a high energy level. The large hydraulic forces generated will induce significant erosion to the bed material. Erosion can also be induced if a hydraulic jump occurs along the downstream slope leading to momentous scour in the locality. However, erosion can be initiated anywhere regardless of whether the hydraulic jump occurs or not. It is first initiated by a small overfall in the downstream slope through the development of a scour hole. The propagation of the dug channel in the downstream face of the embankment then erodes downward and upstream where the channel length is increased such that there is a continuous flow from the reservoir to the downstream slope (see Figure 4.7).

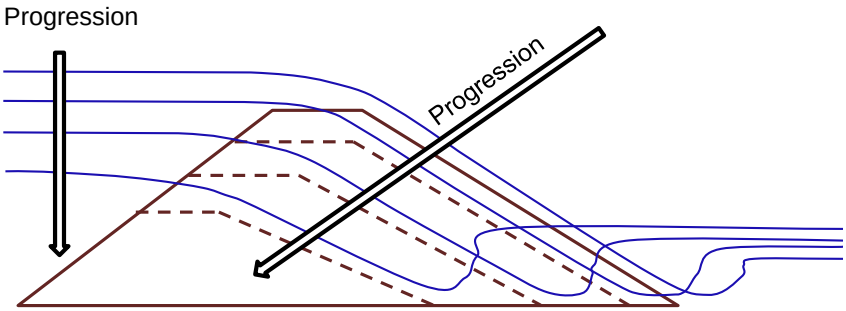

Figure 4.7: Slope retreat on upstream face

Often in downstream valleys that have high sinuosity or are narrow or densely vegetated, downstream control may govern the breach outflow. The high tailwater due to the channel's roughness may submerge the flow through upstream reaches of the embankment breach channel, altering the flow regime from supercritical to subcritical. In this condition, backwater effects must be considered and the breach outflow is corrected for flow submergence.

4.1.5.1 2-D Breach Hydrodynamics

Vertical erosion on an embankment's downstream slope begins as far upstream as the abrupt increase in bed slope (*i.e.*, immediately downstream the crest). In this vicinity, negative pressures develop due to flow separating from the boundary, and therefore a subhydrostatic pressure distribution occurs due to recirculating flow (Powledge *et al.* 1989; Annandale, 1995; Kirsten *et al.* 2000). Further downstream this transition zone; the flow regime is supercritical. As the flow accelerates, the turbulent energy production and dissipation is increased. Figure 4.8 illustrates the WSL, bed profile and energy grade line (EGL) in a 2-D hypothetical scenario where flow is overtopping the steep slope of an embankment. Annandale (1995) stated that the rate of energy dissipation increases immediately downstream of the crest due to energy dissipation over the recirculation zone as well as within the recirculation zone itself. The energy dissipation, ΔE, within the recirculation zone, as proposed by Annandale (1995), can be expressed as:

$$\Delta E = \frac{[1-\cos(\alpha_{jet}-\phi_{bx})]}{[1+\cos(\alpha_{jet}-\phi_{bx})]} \frac{K_1 U_g^2}{2g} \tag{4.51}$$

where, α_{jet} is the impingement angle with respect to the horizontal, U_g is the average flow velocity over the recirculation zone and K_1 is an adjustment factor to account for subhydrostatic pressure in the recirculation zone and is approximately equal to one (Annandale, 1995).

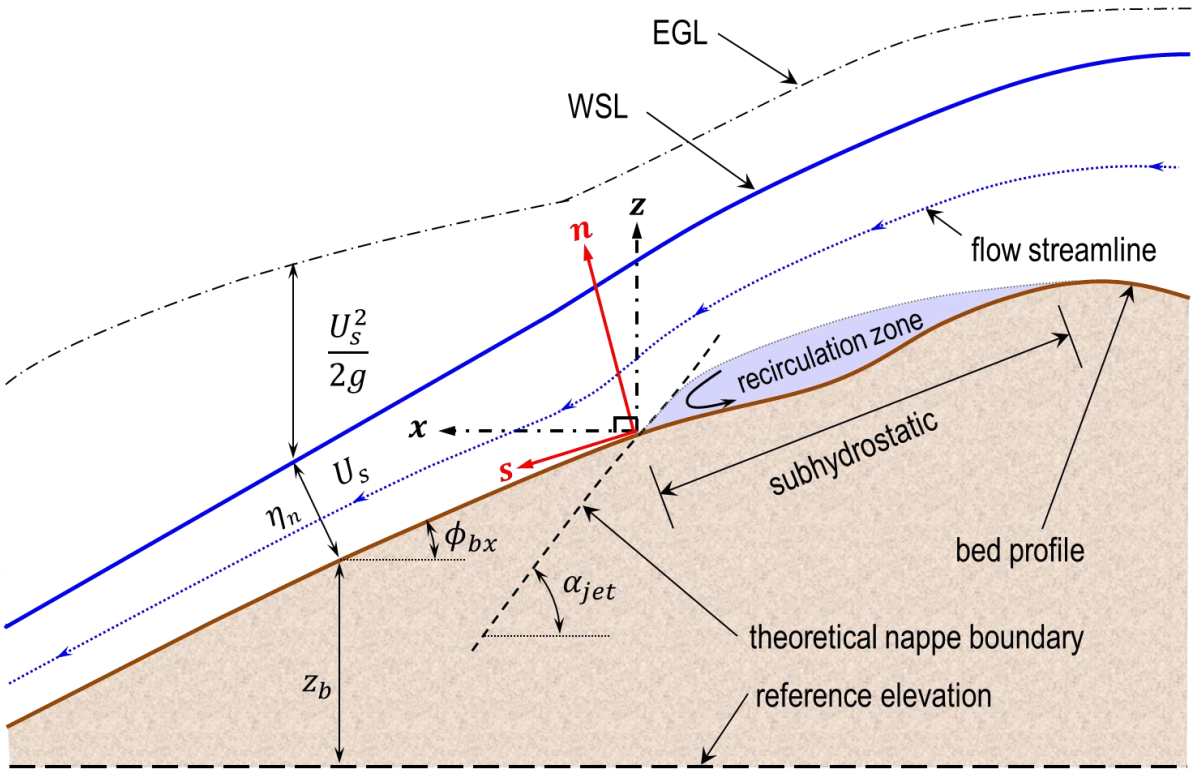

Figure 4.8: Overtopping flow showing recirculation zone, water surface level, bed profile and energy grade line

The depth-averaged flow velocity with respect to a local coordinate system (s, n), can be calculated as $U_s = q/\eta_n$. In the supercritical region, downstream the recirculation zone, the pressure distribution can be assumed to be hydrostatic where the total energy follows:

$$E = z_b + \eta_n \cos\phi_{bx} + \frac{U_s^2}{2g} \tag{4.52}$$

In the case of uniform flow, the bed shear stress has been traditionally expressed in terms of the friction slope (*i.e.* the slope of the EGL, $S_f = dE/dx$), or bed slope, S_b, as:

$$\tau_b = \gamma_f R_h S_f \quad (4.53)$$

$$\tau_b = \gamma_f R_h S_b \quad (4.54)$$

where, γ_f is specific weight of the fluid.

The hydraulic radius of the bed region adapted for side-wall effects in shallow flows where the flow depth is less than half of the flume width ($\eta_n < b/2$) is expressed as (Vanoni and Brooks, 1957):

$$R_h = \frac{\eta_n(b-\eta_n)}{b} \quad (4.55)$$

4.1.5.2 Broad-Crested Weir Flow

When the flow through the breach channel and over the embankment crest cannot be solved using the 3-D NSE or even 2-D SWE, an approximation is sometimes made using weir flow equations. Simplified and parametric models assume a flat reservoir water surface level during an embankment breach where the total breach outflow conveyed from the reservoir can be determined using broad-crested weir flow expressions combined with known reservoir-volume or reservoir-surface area relationships. The flows overtopping the flat embankment crest and through the breach channel of a trapezoidal cross-section, Q_{cr} and Q_B, respectively, can be estimated using the following expressions (Singh *et al.* 1988):

$$Q_{cr} = C_1^*(L_{cr} - B_{TW})(\eta_r - z_{cr})^{3/2} \quad (4.56)$$

$$Q_B = [C_1^* B_{BW} + C_2^*(\eta_r - z_{BB})\tan(\pi/2 - \alpha_{SS})](\eta_r - z_{BB})^{3/2} \quad (4.57)$$

where, C_1^* and C_2^* are dimensional discharge coefficients, 1.7 and 1.35 [$m^{1/2}/s$], respectively, L_{cr} is crest length, B_{TW} is breach channel top width, η_r is the water surface level in the upstream reservoir, z_{cr} is the embankment crest elevation, z_{BB} is elevation of the breach channel bottom, and α_{SS} is breach channel side-slope angle with the horizontal ($\alpha_{SS} = \tan^{-1} z_{SS}$) (see Figure 4.9).

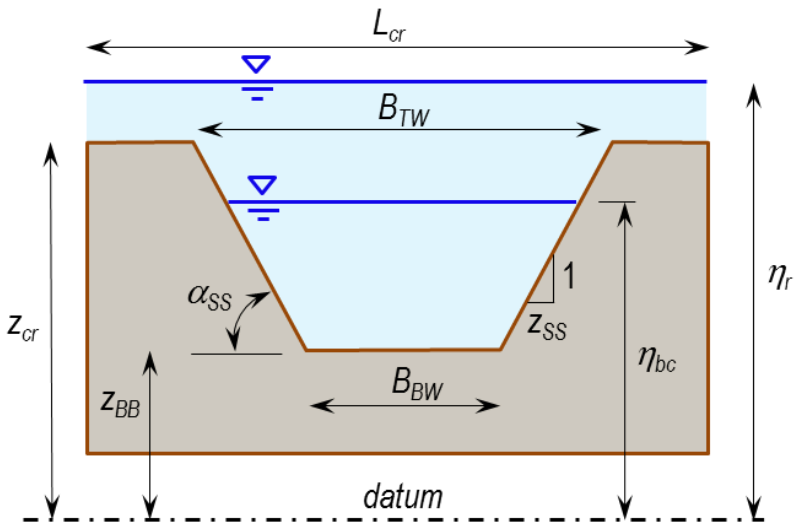

Figure 4.9: Schematic showing trapezoidal breach channel cross-section (lower water surface line represents water surface level in breach channel, depicted by elevation, η_{bc})

Equation (4.57) can also be applied in the case of a triangular cross-section where B_{BW} is nil, or for a rectangular cross-section where the side slope angle, α_{SS}, is $\pi/2$. Experimental studies have also reported breach channels with parabolic cross-sections (Mohamed et al. 1999; Coleman *et al.* 2002). Parabolic breach growths have been solved in the analytic models of Harris and Wagner (1967) and Brown and Rogers (1977). Generally, the breach channel outflow can be expressed using a generic breach width, B_W, and coefficient of discharge based on the weir shape, C_W, as:

$$Q_B = C_W B_W (\eta_r - z_{BB})^{3/2} \tag{4.58}$$

The coefficient C_W ranges between 1.6 and 2.15, with a typical value of 1.9 for level-crested structures (Powledge *et al.* 1989). In the case of tailwater submergence, the breach outflow must be modified using a submergence factor C_S/C_W), where C_S is coefficient of submergence, usually rated by percentage of submergence (Powledge *et al.* 1989). The report by Morris *et al.* (2009b) stated that the coefficient of discharge for shape described by Equation (4.58) could vary between 1.5 for a sharp edged broad-crested weir to 2.2 for a round-shaped or ogee weir, which may

give rise to a 30% variation for the estimated breach discharge. It is therefore important that parametric and simplified physically-based mathematical models update this parameter during the breaching process to reflect the breach morphological characteristic. A quasi-steady uniform flow assumption is normally assumed when weir formulas are used to predict the overtopping flow. **Note:** The term “quasi-steady” implies that the normal flow depth in the breach channel is determined at each computational time-step. Based on this assumption, the normal flow depth (for 1-D flow) can be estimated using the following Manning or Chézy equations:

$$U = \frac{1}{n_M} R_h^{2/3} \sqrt{S_f} \tag{4.59}$$

$$U = C\sqrt{R_h S_f} \tag{4.60}$$

4.2 Breach Erosion Mechanics

4.2.1 Transport Characteristic Parameters

This subsection defines the parameters that are commonly found in literature and that are used in characterising the behaviour of sediment in flow. The source of the parameters is shown in parenthesis.

Particle specific gravity (general)

It is the ratio of the density of the sediment, ρ_s, to the density of the fluid, ρ:

$$G_s = \frac{\rho_s}{\rho} \tag{4.61}$$

Dimensionless particle diameter or grain size (Ackers and White, 1973)

$$d^* = d_{50} \left[\frac{(G_s - 1)g}{\nu^2}\right]^{1/3} \tag{4.62}$$

Shear stress (general)

When there are no means of computing the friction slope, the bed shear stress can be computed using a friction coefficient such as the Darcy-Weisbach resistance coefficient, f (*e.g.* Wang and Bowles, 2006a), coefficient of skin friction, C_f, coefficient of Manning roughness, n_M or coefficient of Chézy roughness, C. The corresponding bed shear stress-friction coefficients are given as follows:

$$\tau_b = \frac{f}{8}\rho u^2 = \frac{C_f}{2}\rho u^2 = \frac{g}{C^2}\rho u^2 = \frac{g n_M^2}{R_h^{1/3}}\rho u^2 \tag{4.63}$$

The existence of bedforms contributes to an additional shear stress due to form roughness. In the case where bedforms are present, the shear stress contribution due to grain shear stress must be separated from the total boundary shear stress. The process by which the total boundary shear stress is sorted into components is known as shear stress partitioning (Buffington and Montgomery, 1997):

$$\tau_b = \tau' + \tau'' + \tau''' + \tau'''' + \cdots + \tau^n \tag{4.64}$$

where, τ', τ'', τ''', τ'''' is shear stress due to grain roughness, form roughness, side wall effects, large woody debris, … etc.

The bed shear stress can also be represented in dimensionless form:

$$\tau^* = \frac{\tau_b}{\gamma_f (G_S - 1) d_{50}} \tag{4.65}$$

Similarly, the shear stress for incipient motion, τ_c, can be expressed in dimensionless form:

$$\tau_c^* = \frac{\tau_c}{\gamma_f (G_S - 1) d_{50}} \tag{4.66}$$

Dimensionless transport rates (general)

The dimensionless forms of volumetric transport rates (volume per unit width per unit time) for the bedload and suspended load are given as:

$$q_{bs}^{*} = \frac{q_{bs}}{\sqrt{d_{50}^{3}(G_s-1)g}} \tag{4.67}$$

$$q_{ss}^{*} = \frac{q_{ss}}{\sqrt{d_{50}^{3}(G_s-1)g}} \tag{4.68}$$

where, q_{bs} and q_{ss} are volumetric bedload and suspended load transport rates, respectively. Similarly, the dimensionless form of the total load is given as:

$$q^{*} = \frac{q_{ts}}{\sqrt{d_{50}^{3}(G_s-1)g}} \tag{4.69}$$

Often the transport rates are reported in gravimetric form where g_{bs} and g_{ss} are the bedload and suspended load transport rates (mass per unit time and width). Conversion from gravimetric to volumetric transport rates can be carried out as follows:

$$q_{bs} = \frac{g_{bs}}{\rho_s} \text{ and } q_{ss} = \frac{g_{ss}}{\rho_s} \tag{4.70}$$

where, ρ_s is the density of the sediment.

When transport rates are reported as a “submerged” mass, the mass above water can be obtained by multiplying the submerged mass by $G_s/(G_s - 1)$.

Transport stage parameter (van Rijn, 1984a, b, c)

$$T = \frac{\tau_b' - \tau_c^{*}}{\tau_c^{*}} = \frac{u^{*\prime 2} - u_c^{*2}}{u_c^{*2}} \tag{4.71}$$

where, τ_b' is bed shear stress due to grain roughness and $u^{*\prime}$ is shear (or grain) velocity determined as follows:

$$u^{*\prime} = \frac{\sqrt{g}}{18\log\left(\frac{12R_h}{3d_{90}}\right)} \tag{4.72}$$

and, u_c^{*} is the (critical) shear velocity according to the Shields diagram (see Subsection 4.2.3).

Sediment concentration (general)

The sediment concentration is expressed in either a volumetric (*i.e.* m^3/m^3) or gravimetric form (*i.e.* kg/m^3 or mg/L). A conversion between gravimetric concentration, C_m, and volumetric concentration, C_V, is:

$$C_V = \frac{C_m}{G_s(1-C_M)+C_M} \tag{4.73}$$

Van Rijn (1984b,c) defined three sets of concentrations required for an estimation of the suspended transport load:

reference concentration $$C_a = 0.015 \frac{d_{50}}{a_b} \frac{T^{1.5}}{d^{*3}} \tag{4.74}$$

where, a_b is a reference height pertaining to the roughness scale (*i.e.* above bedload layer):

with bedforms $$a_b = \min\left(\frac{\Delta_b}{2}, 0.01\eta\right) \tag{4.75}$$

without bedforms $$a_b = \text{minimum}(k_s, 0.01\eta) \tag{4.76}$$

where, Δ_b is bedform height.

maximum bed concentration $$C_0 = 0.65 \tag{4.77}$$

near-bed sediment concentration $$C_b = \frac{q_{bs}}{u_b \delta_b} \tag{4.78}$$

where, u_b and δ_b are particle velocity and saltation height (or bedload layer thickness), respectively, and can be expressed as follows:

$$u_b = u^* \left[9 + 2.6 \log d^* - 8\left(\frac{\tau_c^*}{\tau_b^*}\right)^{0.5}\right] \tag{4.79}$$

$$\delta_b = 0.3 d_{50} d^{*0.7} T^{0.5} \tag{4.80}$$

The near-bed sediment concentration can also be expressed as:

$$C_b = 0.18 C_0 \frac{T}{d^*} \tag{4.81}$$

The depth-averaged suspended sediment concentration can also be expressed in terms of the transport rate as follows:

$$C_s = \frac{q_{ss}}{q} \tag{4.82}$$

Particle Reynolds number (general)

This dimensionless number is analogous to the Reynolds number, but on the grain or sediment scale. It usually takes the following form:

$$Re^* = \frac{u^* d_0}{\nu} \tag{4.83}$$

where, d_0 is a characteristic grain size, taken as the median particle diameter in most literature. However, since this dimensionless number describes the flow regime near the bed, it would be suitable to employ the equivalent grain roughness for a consistent characterization between hydraulically smooth, transition and hydraulically rough boundaries (Schlichting, 1968) as defined in Equations (4.35) to (4.37).

The Particle Reynolds number may also be expressed with respect to the velocity of descent for a single particle, w_0, as shown below (van Rhee, 2010):

$$Re_p = \frac{w_0 d_{50}}{\nu} \tag{4.84}$$

Particle fall (or settling) velocity (van Rijn, 1984c)

The fall velocity is the velocity at which a sediment particle falls through a clear and quiescent fluid. The forces opposing a particle's weight are buoyancy and resistance. At the initiation of the particle's descent, it accelerates, until the gravitational force is balanced by the resistance and buoyancy forces and the particle reaches a terminal velocity. This velocity is termed the particle fall (or settling) velocity. Van Rijn (1984c) expresses the fall velocity for various grain sizes:

$d_s < 100\mu m$ $$w_s = \frac{1}{18}\frac{(G_s-1)g d_s^2}{\nu} \tag{4.85}$$

$100\mu m < d_s < 1{,}000\mu m$ $$w_s = 10\frac{\nu}{d_s}\left\{\left[1 + \frac{0.01(G_s-1)g d_s^3}{\nu^2}\right]^{0.5} - 1\right\} \tag{4.86}$$

$d_s < 100\mu m$ $$w_s = 1.1[(G_s - 1)g d_s]^{0.5} \tag{4.87}$$

where, d_s is the representative particle size in suspension and can be determined as follows:

$$d_s = d_{50}[1 + 0.011(\sigma_s - 1)(T - 25)] \tag{4.88}$$

where, σ_s is geometric standard deviation of bed material and can be determined as follows:

$$\sigma_s = 0.5(d_{84}/d_{50} + d_{16}/d_{50}) \tag{4.89}$$

where, d_{16} and d_{84} are grain sizes at which 16% and 84%, by weight of the sediment is finer, respectively.

For a particle to remain in suspension, the vertical turbulent velocity component must exceed the fall velocity. The fall velocity is also affected by the sediment concentration, a process referred to as hindered settling by Winterwerp *et al.* (1992) and van Rhee (2010). Therefore, the settling velocity was modified according to the following expression by Richardson and Zaki (1954):

$$w_{s,c} = w_s(1 - C_b)^{n_s} \tag{4.90}$$

where, n_s is an empirical exponent defined as follows (Rowe, 1987):

$$n_s = \frac{4.7 + 0.41 Re_p^{0.75}}{1 + 0.715 Re_p^{0.75}} \tag{4.91}$$

Similar to incipient motion, there have been several studies which developed a criterion for suspension (Bagnold, 1966; van Rijn, 1984c; Cheng and Chiew, 1999a).

Suspension Parameter (van Rijn, 1984c)

The suspension parameter defined in van Rijn (1984c) represents the dominance of upward turbulent fluid forces on the gravity forces exerted on a particle in suspension.

$$Z_s = \frac{w_s}{\beta \kappa u^*} \tag{4.92}$$

where, β is the ratio of sediment to fluid mixing coefficient and can be determined as follows:

$$\beta = 1 + 2\left(\frac{w_s}{u^*}\right)^2 \tag{4.93}$$

The suspension parameter is modified using a term, φ, which account for the effects of volume occupied by the particles, reduction of particle fall velocity and damping of turbulence due to suspension is also defined as follows:

$$\varphi = 2.5\left(\frac{w_s}{u^*}\right)^{0.8}\left(\frac{C_a}{C_0}\right)^{0.4} \tag{4.94}$$

The modified suspension parameter can therefore be defined as follows:

$$Z_s' = Z_s + \varphi \tag{4.95}$$

4.2.2 Sediment Transport Mechanisms

Sediment particles are transported with the water column following three distinct transport modes or mechanisms: bedload, suspended load and washload. Washload is the process by which extremely fine alluvial material is transported. Although this material is transported in suspension, it is independent of the bedload and suspended bed material load transport mechanisms (Armanini and Di Silvio, 1988). Naturally, suspended load measurements will include washload. The bed material on the other hand is transported near the bed and in suspension, hence the term bedload and suspended load transport, respectively.

Several studies have been conducted over the past decades to clearly define bedload and suspended load. Armanini (1995) and Armanini and Di Silvio (1988) defined the flow in a riverine system comprising of three layers: an upper (or water stream) layer, bottom layer and a mixing or surface layer (see Figure 4.10). In the upper layer, the bed material and washload are transported in suspension by turbulent structures. While the washload is uniformly distributed in the water column, the sediment concentration for the suspended load is asymptotic along the vertical with a maximum concentration at the bottom boundary of the upper layer. In the

bottom layer (below the upper layer), the bed material is transported in the streamwise direction by sliding, rolling and saltation. In this layer, the sediment concentration is highest. The mixing layer is below the bottom layer where the bed material is immobile. In this layer, particles move up or down into or from the bottom layer, depending whether there is degradation (erosion) or aggradation (deposition) of the bed. According to Armanini (1995), the mixing layer thickness is ~ $3d_{90}$. In equilibrium conditions, there is neither erosion nor deposition (Armanini and Di Silvio, 1988). Additional conservation equations for bedload, suspended load and the bed material therefore need to be solved in non-equilibrium conditions, where erosion and deposition rates are not equal.

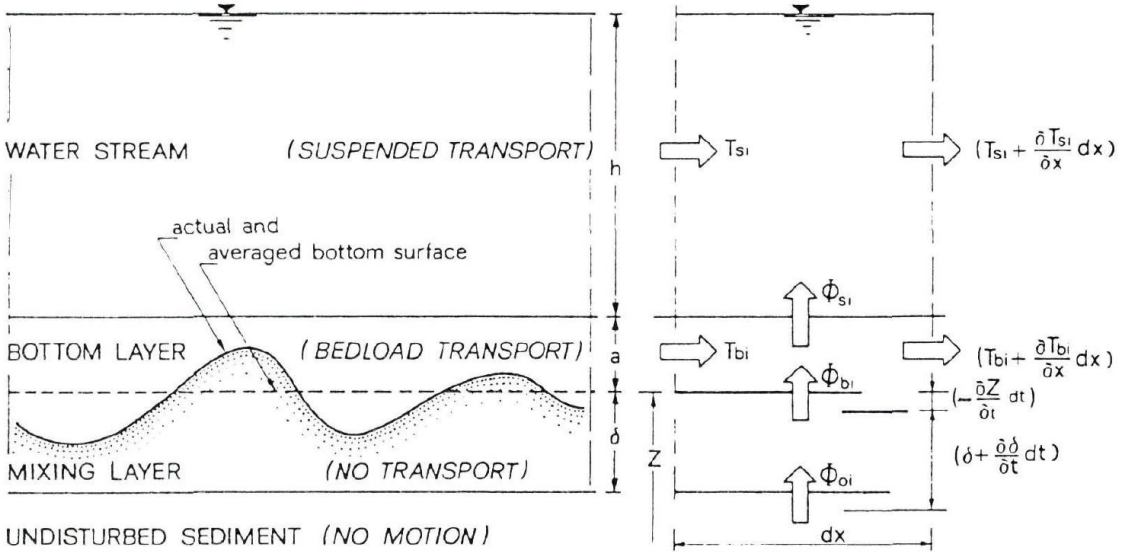

Figure 4.10: Longitudinal profile showing sediment balance in three layers for a 1-D model (Armanini and Di Slvio, 1988)

The study by Hu and Hui (1996) defined bedload as a complex mechanism which is responsible for transporting bed material near a river bed in large quantities. They stated that rolling and saltation are the dominant form of bedload movement depending on the flow intensity. From Figure 4.11, it can be noted that the dominant mechanism for bedload transport is saltation for the majority of flow conditions, which explains why most investigations (including that of van Rijn, 1984b,c) observed bedload transport mainly from a saltation point of view. Gao and

Abrahams (2004) stated that momentum is transferred from the fluid to the bed particles due to mobilization. This momentum transfer is increased as bed particles collide with neighbouring particles which consequently increases flow resistance (Song *et al.* 1998). Gao and Abrahams (2004) referenced a threshold value for dimensionless shear stress, $0.5 < \tau^* < 1$, where sheet flow dominates the bedload transport mechanism. This is in line with the theory by Bagnold (1966) on carpet layer transport. As defined by Abrahams (2003), sheet flow occurs when there is no suspension. The very collisions which reduce the momentum in the flow yield a dispersive stress normal to the bed which acts as a provision to bedload conveyance. Abraham's study showed that for sheet flow the bedload transport efficiency, as defined by Bagnold (1966), is much higher than initially believed. It is important to note that the data set shown in the investigation by Gao and Abrahams (2004) indicated that flow conditions were supercritical where relative submergence,d_M/η, was between 0.05 and 1.

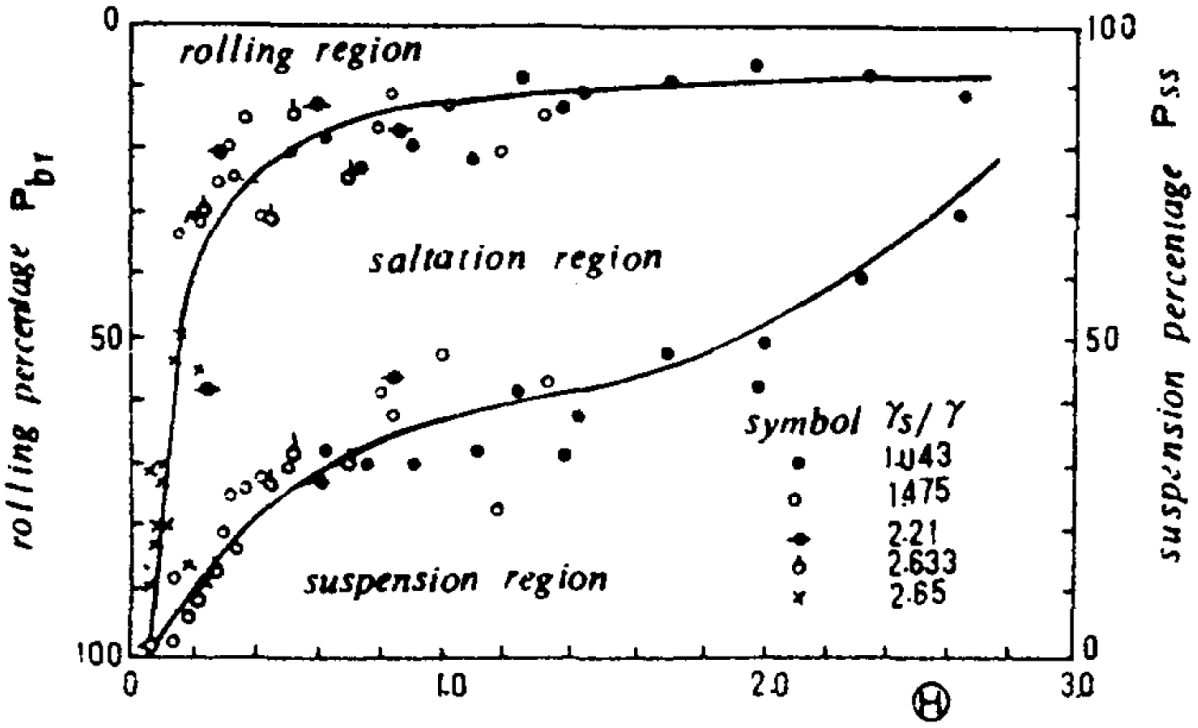

Figure 4.11: Relationship between rolling, saltation and suspension and dimensionless shear stress (Hu and Hui, 1996; Θ is referred in their study as flow intensity which is the dimensionless shear stress)

4.2.3 Incipient Sediment Motion

The criterion for incipient motion is an unsettled topic. It generally refers to a critical condition where sediment is mobilized from a bed. Its subjectivity lies in the quantitative approach in which it is determined. Over the past century, several methods have been developed in order to estimate this critical condition. The analytical constituent of the methods often employed a moment or force balance on an interfacial sediment grain (see Subsection 4.6) in relation to dimensionless groups or the angle of repose. Closure of the method is then followed by physical tests. The most significant and widely used method, despite its controversies, was defined by Shields (1936). Shields' definition of the critical condition was based on the following dynamic similitude law:

$$\frac{\tau_c}{(\gamma_s-\gamma_f)d_{\mathrm{M}}} = \mathcal{F}\left(\frac{u_c^* d_{\mathrm{M}}}{\nu}\right) \tag{4.96}$$

where, τ_c is critical or "tractive" shear stress.

The dimensionless term on the LHS is the dimensionless critical shear stress, and is also referred to as Shields parameter or tractive force coefficient (Shields, 1936). The RHS term is the particle Reynolds number. Based on the mentioned dynamic similarity, the Shields parameter can be obtained from the Shields curve (see Figure 4.12). In hydraulically rough flows, the Shields parameter was found to be 0.06. It is important to note that the dimensionless analysis that Shields adopted considered the resistance force as the cause behind a sediment particle's dislodgement and neglected its weight component along the slope as well as the lift force acting on the particles. Shields' experiments were conducted on relatively mild bed slopes (<1:200) and sediments of uniform grain size. Deviations in the experimental results were noticed when the relative submergence, d_M/η, was larger than 0.04. Shields cautioned that values of relative roughness should not exceed 0.025.

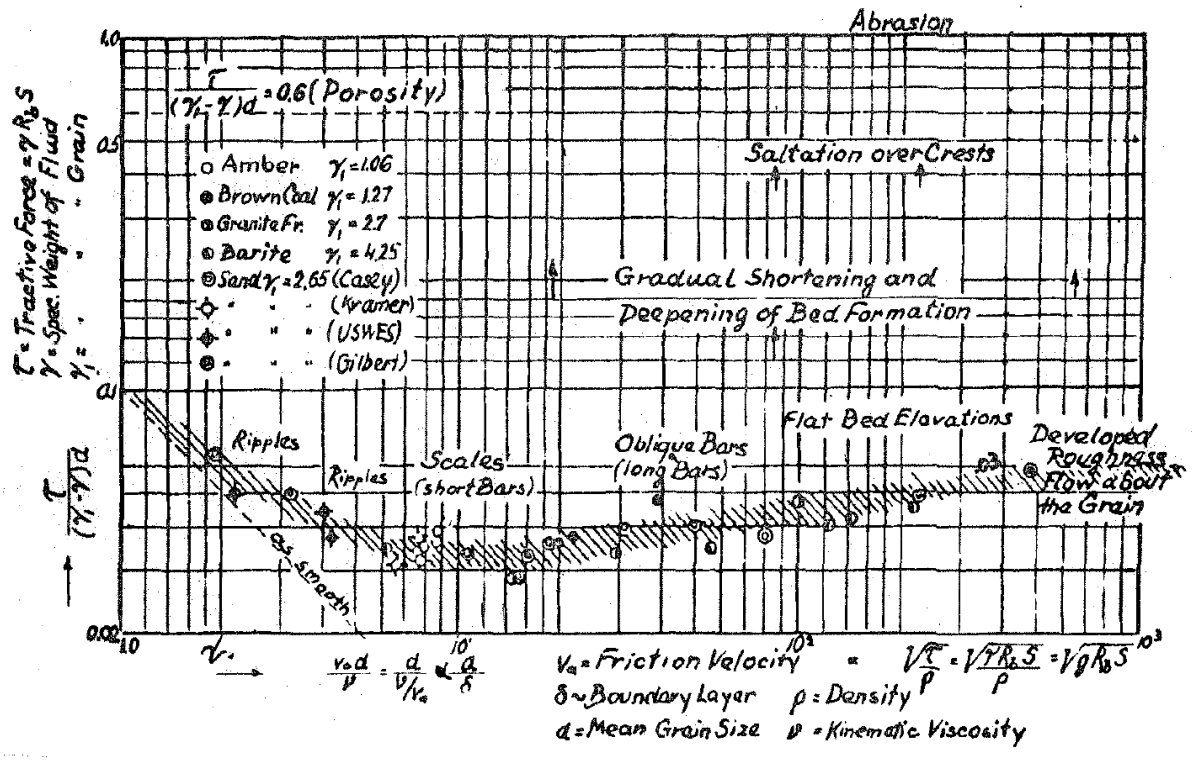

Figure 4.12: Tractive force coefficient against grain Reynolds number (Shields, 1936)

Yang (1973) also points out that Shields' analysis of incipient motion was based on the laminar sublayer theory, where the laminar sublayer should not influence the velocity distribution for $Re^* > 70$. According to the Shields diagram, however, the dimensionless shear stress continues to increase when $Re^* > 70$. Yang (1973) also stated that it is not appropriate to explicitly describe the state of incipient motion when the shear stress and shear velocity are defined as dependent and independent variables, respectively, since they are interchangeable by Equation (4.38). In this case, the value of critical shear stress can be extrapolated from the Shields diagram by iteration. Van Rijn (2007) points out that the Shields curve may not be very accurate for fine sand. Van Rijn stated that a better definition by Miller *et al.* (1977) can be expressed as a function of the dimensionless grain size as follows:

$$d^* < 4 \qquad \tau_c^* = 0.115 d^{*-0.5} \qquad (4.97)$$

$$4 \leq d^* < 10 \qquad \tau_c^* = 0.14 d^{*-0.64} \qquad (4.98)$$

Several researchers have developed their own analyses on incipient motion or modified the analysis of Shields to express the critical condition explicitly using experimental data. For instance, Yang (1973) defined the critical condition in terms of a dimensionless critical velocity, $\bar{u}_c/w_s$, and Re^*:

$$0 < \frac{u^* d_{50}}{\nu} < 70 \qquad \frac{\bar{u}_c}{w_s} = \frac{2.5}{\log\left(\frac{u^* d_{50}}{\nu}\right) - 0.06} + 0.66 \tag{4.99}$$

$$70 < \frac{u^* d_{50}}{\nu} \qquad \frac{\bar{u}_c}{w_s} = 2.05 \tag{4.100}$$

where, $\bar{u}_c$ is the depth-averaged velocity for incipient motion.

The method by Hunter Rouse defines the critical condition explicitly using the Rouse number, R^*, (Guo, 2002) shown in Figure 4.13:

$$R^* = \frac{d_{50}\sqrt{0.1(G_S - 1)g d_{50}}}{\nu} \tag{4.101}$$

The Shields diagram has been redrafted by Govers (1987) following modifications by various investigators (see Figure 4.14).

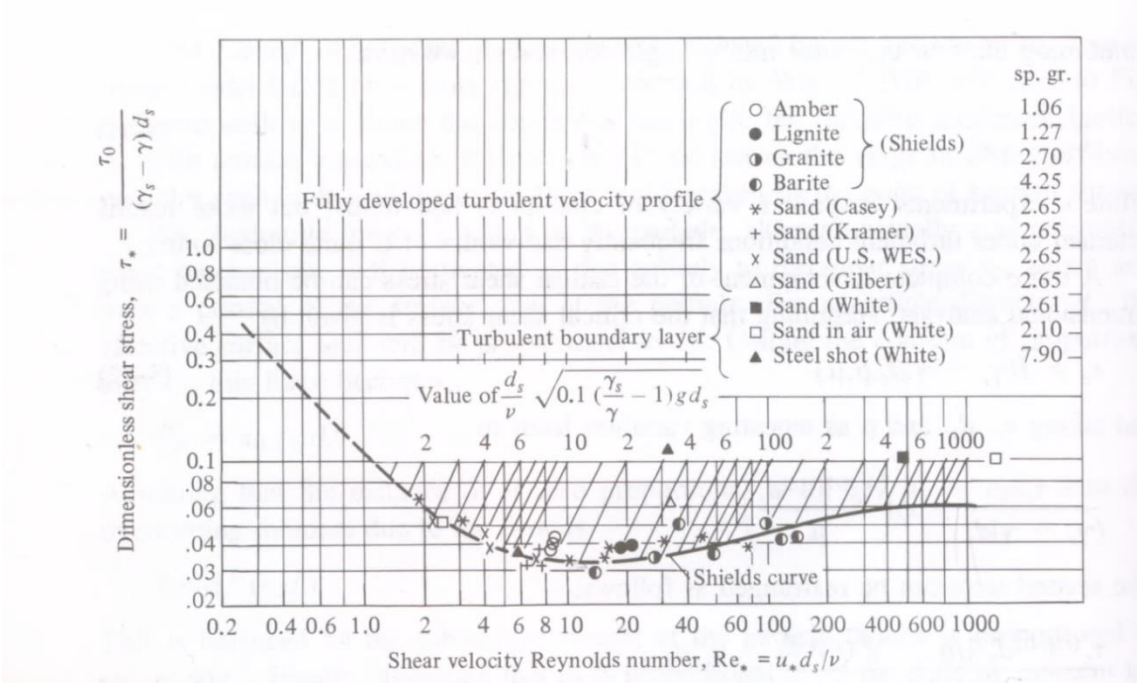

Figure 4.13: Initiation of motion from the Shields diagram in Vanoni (1975) (after Prasuhn, 1992)

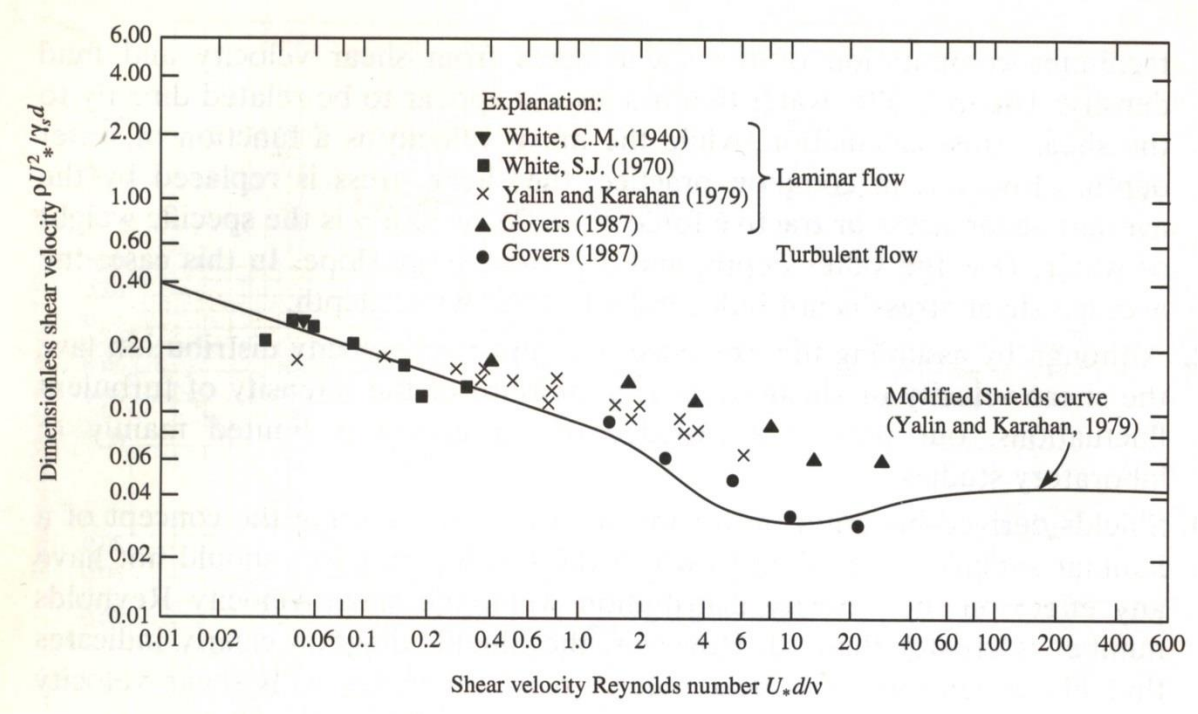

Figure 4.14: Modified Shields curve by Govers (1987) (source: Yang, 1996)

Methods for defining the threshold condition were also based on observations from physical tests, where the critical shear stress can be directly measured. However, such methods are prone to an individual interpretation of threshold mobility and are therefore considered subjective (Buffington and Montgomery, 1997). Other methods incorporate the measurement of bedload transport at various flow conditions, whereas the incipient condition was extrapolated at a zero transport rate. This method, however, would overestimate the critical shear stress in the case of bedforms (Chiew and Parker, 1994). Buffington and Montgomery (1997) state that the incipient condition is probabilistic due to the effects of turbulence and the interfacial sediment geometry and is therefore controlled by mechanisms such as packing and sorting.

For a sloping bed, the dimensionless critical shear stress can be modified using the following relationship (Macchione and Sirangelo, 1988; Winterwerp et al. 1992; Chiew and Parker, 1994; Chen *et al.* 2010):

$$\tau_{c,s}^{*} = \tau_{c}^{*} \cos\phi_b \left(1 - \frac{\tan\phi_b}{\tan\phi_r}\right) \tag{4.102}$$

where, ϕ_b is bed slope angle, while Fernandez Luque and van Beek (1976), Bisschop *et al.* (2010) and van Rhee (2010) report the following relationship:

$$\tau_{c,s}^{*} = \tau_{c}^{*} \frac{\sin(\phi_r - \phi_b)}{\sin\phi_r} \tag{4.103}$$

Ulrich (1987) considered that the hydrostatic pressure gradient on a steep slope is not vertical; in fact it will be normal to the bed. Ulrich (1987) derived a similar expression to Equation (4.102) by means of a moment balance on a particle impending motion, where the buoyancy force is perpendicular to the bed:

$$\tau_{c,s}^{*} = \tau_{c}^{*} \cos\phi_b \left(1 - \frac{G_s}{1-G_s} \frac{\tan\phi_b}{\tan\phi_r}\right) \tag{4.104}$$

4.2.4 Sediment Transport-Capacity Formulations

Numerous classical formulations have been developed for estimating the bedload transport rate in riverine systems. They are expressed in either volumetric or gravimetric form and stem from distinctive theories on sediment transport mechanics and dimensional analysis. These formulations are calibrated using empirical data collected from laboratory as well as field experiments. Therefore there is an inherent degree of empiricism involved. The experiments are performed under steady and normal flow conditions and the methods by which the corresponding data is fitted are termed transport-capacity models. The models therefore imply that sediment transport rates are governed by the maximum transport-capacity under steady, normal flow and equilibrium conditions (Yang and Simões, 1999; Wang and Bowles, 2006a). Some of the transport-capacity bedload, suspended load and total load formulations, commonly cited in embankment breach literature are referred to in this subsection. Most of the formulations can be expressed using a single expression, whereas others are comprised of a series of equations.

4.2.4.1 Bedload Transport-Capacity Formulations

The approaches which employ bedload transport-capacity in literature are based on a dominant variable, Γ, in the form of a power-law relationship:

$$\Theta_{TC} = C_{\Theta}(\Gamma - \Gamma_c)^{n_{\Theta}} \tag{4.105}$$

where, Θ_{TC} is transport-capacity rate, C_{Θ} is an empirical coefficient, n_{Θ} is an empirical exponent, and Γ_c is the dominant variable for incipient motion conditions.

This dominant variable may either describe a flow parameter or flow geometry (*e.g.* shear stress, τ, velocity, $\mathbb{v}$, bed slope, S_b, stream power, $\tau\mathbb{v}$, unit stream power, $\mathbb{v}S_f$, and specific flow discharge, q) (Prosser and Rustomji, 2000; Yang, 2006; Tayfur and Singh, 2012).

Most transport-capacity formulations use the excess shear stress approach and were first introduced by Du Boys in 1879. The sediment transport rate formulations have the following form:

$$q_{bs} = C_q(\tau_b - \tau_c)^{n_q} \tag{4.106}$$

where, C_q is transport coefficient and n_q, the shear stress exponent is typically found to be 1.5 in most riverine sediment transport models.

The study by Ponce and Tsivoglou (1981) stated that in the case of an embankment breach, the selection of a sediment transport formulation should be suitable for the high Froude number and steep slopes associated with breach flows. Indeed, many of the bedload transport formulations developed for flat beds can be used for steep slopes with adjustments to empirical parameters (Rickenmann, 1997). For instance, the field study by Istanbulluoglu *et al.* (2003) on gully incision in steep mountain slopes stated that the shear stress exponent may be twice that of classical sediment transport formulations developed for riverine flow. Ponce and Tsivoglou (1981) also noted that the characteristic steep bottom slope in breach channels will result in a bed shear stress several orders of magnitude higher than the critical shear stress

(*i.e.* $\tau_b \gg \tau_c$). Consequently, the sediment transport rate will also be much higher than in riverine channels. This conclusion was generally stated in the work by Wilson (1966,1987) on flows dominated by high shear stresses. In such scenarios, the sediment transport rate can be expressed as:

$$q_{bs} = C_q {\tau_b}^{n_q} \tag{4.107}$$

Meyer-Peter-Müller (1948)

The MPM equation was initially derived to serve gravel-bed river computations, however, it is used in a broad range of fluvial hydraulics. It has been shown that it underestimates sediment transport rates for slopes steeper than 3%.

$$q_{bs}^* = 8[\tau^* k_r^{1.5} - \tau_c^*]^{1.5} \tag{4.108}$$

where, k_r is a correction factor which considers bedforms and is computed as:

$$k_r = \sqrt{\frac{f'}{8}} \frac{U}{\sqrt{g R_h S_f}} \tag{4.109}$$

where, f' is the Darcy-Weisbach resistance coefficient due to grain roughness and can be obtained from the Moody diagram where $Re = 4UR_h/\nu$ and relative roughness as $k_s/4R_h$. While τ_c^* has been generalized in their formulation with 0.047, this value is no longer identified nowadays with incipient motion.

Schoklitsch (1962)

$$q_{bs} = \frac{2.5}{G_s} S_b^{1.5} (q - q_c) \tag{4.110}$$

where the critical discharge is expressed as:

$$q_c = 0.26(G_s - 1)^{5/3} \frac{d_{40}^{3/2}}{S_b^{7/6}} \tag{4.111}$$

where, d_{40} is grain size at which 40% by weight of the sediment is finer.

Bagnold (1966)

Bagnold (1966) departed from the conventional force-based dominant variable to a variable based on the rate of energy expenditure (*i.e.* stream power per unit area) in deriving both a bedload and suspended load formulation. Bagnold's hypothesis on bedload transport is that a surface layer (or carpet) flows near the bed where its weight is supported by a dispersive stress normal to the bed caused by particle collisions.

$$q_{bs} = \tau_b U \frac{e_b}{\tan\phi - \tan\phi_b} \tag{4.112}$$

where, e_b is the flow's efficiency for transporting bedload and was estimated as 0.13.

Smart (1984)

The Smart (1984) is the modified version of the MPM equation for steep slopes. It has been calibrated using the same data used in MPM in addition to data for 3%, 7%, 10%, 15% and 20% slopes. This formulation is not recommended for slopes which fall beyond this range, nor for grain-size distributions (GSD) where $d_{90}/d_{30} > 8.5$.

$$q_{bs}^* = 4\left[\left(\frac{d_{90}}{d_{30}}\right)^{0.2} S_b^{0.6} C\sqrt{\tau^*}(\tau^* - \tau_c^*)\right] \tag{4.113}$$

where, d_{90} and d_{30} are grain sizes at which 90% and 30%, by weight of the sediment is finer, respectively.

van Rijn (1984b)

Van Rijn (1984b) expressed bedload transport rate as the product of saltation height, particle velocity and bedload concentration (see Equations (4.78) to (4.81)). Van Rijn (1984b) developed and validated the following formulation using 130 flume experiments, using grain-sizes where $0.2mm < d_{50} < 2mm$.

$$q_{bs}^{*} = 0.053 \frac{T^{2.1}}{d^{*0.3}} \quad (4.114)$$

Bathurst *et al.* (1987)

The formulation by Bathurst *et al.* (1987) is a modification of the Schoklitsch (1962) formulation for the steep slopes of mountain rivers. It has been calibrated using flume data with bed slopes in the range of 0.25 to 10% and d_{50} in the range of 11.5mm to 44.3mm. The same bedload formulation by Schoklitsch (1962) was used, however, a critical discharge expression was derived by the authors as follows:

$$q_c = 0.21 S_b^{-1.12} d_{16}^{3/2} \sqrt{g} \quad (4.115)$$

Rickenmann (1991)

This formulation was developed using data from 252 experiments with bed slopes ranging between 0.1% and 20%. Similar to the one by Smart (1984), this formulation accounts for nonuniform sediments.

$$q_{bs}^{*} = \frac{3.1}{\sqrt{G_s - 1}} \left(\frac{d_{90}}{d_{30}}\right)^{0.2} \sqrt{\tau^{*}} (\tau^{*} - \tau_c^{*}) Fr^{1.1} \quad (4.116)$$

4.2.4.2 Suspended Load Transport-Capacity Formulations

Bagnold (1966)

Bagnold (1966) applied the same concept of rate of energy expenditure (*i.e.* stream power per unit area) in suspended load transport. Bagnold's hypothesis on suspended load transport, however, is that the bed material will remain in suspension due to the power generated by the upward turbulent shear stresses.

$$q_{ss} = \tau_b U \frac{e_s}{(w_s/U) - \tan \phi_b} \quad (4.117)$$

where, e_s is the flow's efficiency for transporting suspended sediment load and was estimated as 0.01.

Van Rijn (1984c)

$$q_s = F_s U \eta C_a \tag{4.118}$$

where, F_s is a correction factor and can be expressed as:

$$F_s = \frac{\left(\frac{a_b}{\eta}\right)^{Z_s'} - \left(\frac{a_b}{\eta}\right)^{1.2}}{\left(1 - \frac{a_b}{\eta}\right)^{Z_s'}} \tag{4.119}$$

4.2.4.3 Total Sediment Load Transport Capacity Formulations

Ackers and White (1973)

Ackers and White (1973) expressed the sediment transport rate as a function of stream power using dimensionless groups related to the particle diameter mobility and transport rate. For coarse sediments an approach using grain shear and represented by depth-averaged velocity was used. For fine sediments, an approach involving shear velocity was used. Their formulation was derived using 1,000 flume experiments. The total sediment load in dimensional form is expressed as follows:

$$q_{ts} = 0.025 \frac{q d_{35}}{\eta} \left(\frac{F_{gr}}{0.17} - 1\right)^{1.5} \tag{4.120}$$

where, F_{gr} is a sediment mobility number and can be determined using the following expression:

$$F_{gr} = \frac{1}{\sqrt{g d_{35}(G_s - 1)}} \left[\frac{U}{\sqrt{32}\log\left(\frac{10\eta}{d_{35}}\right)}\right] \tag{4.121}$$

where, d_{35} is grain size at which 35% by weight of the sediment is finer.

Their expression applies to sand with particle diameters ranging between 0.04mm and 2.5mm. The authors question the formulation's performance in high flow intensities where $Fr > 0.8$.

Yang (1979)

Yang (1979) applied the approach of unit stream power, which is the rate of potential energy expenditure per unit weight of water, to derive the following total sediment load concentration (expressed in parts per million (PPM) by weight):

$$\begin{aligned}\mathrm{Log}\, C_{est} = 5.165 - 0.153 \log\left(\frac{w_s d_{50}}{\nu}\right) - 0.297 \log\left(\frac{u^*}{w_s}\right) + \\ \left[1.780 - 0.360 \log\left(\frac{w_s d_{50}}{\nu}\right) - 0.480 \log\left(\frac{u^*}{w_s}\right)\right] \log\left(\frac{US_f}{w_s}\right)\end{aligned} \quad (4.122)$$

4.2.5 Non-equilibrium Sediment Transport, Erodibility and Detachment-Limit Capacity Formulations

In reality, the exchange between the bed material and the flow is not instantaneous due to spatial or time-delays. Yang and Ahn (2011) describes two scenarios where this can be very important: a sudden gain in carrying capacity as clear water enters a highly erodible bed, and a sudden loss in the carrying capacity of a fully-laden flow. In an embankment breach, the former scenario can be characterised by upstream reaches, giving rise to erosion, while the latter can be characterised by downstream reaches, giving rise to deposition. As previously mentioned, non-equilibrium sediment transport require additional conservation equations to account for the bedload and suspended load as well as the flux between the active layer, bedload layer and water column. Such formulations can be expressed in 1-D or 2-D, and some variants also exist for discrete grain-size classes or for bed material sorting and armouring (see Armanini and Di Silvio, 1988; Armanini, 1995; Yang and Simões, 1999; Wu *et al.* 2000; Wu, 2004; Faëh, 2007; Bor, 2008; and Tayfur and Singh, 2012 for additional details). The following are a convection-diffusion formulation for suspended sediment load and mass-balance for formulation for bedload transport (Wu, 2004) corresponding to uniform grain-sizes:

$$\frac{\partial(\eta C_{s*})}{\partial t} + \frac{\partial(\eta U C_{s*})}{\partial x} + \frac{\partial(\eta V C_{s*})}{\partial y} = \frac{\partial}{\partial x}\left(\varepsilon_s \eta \frac{\partial C_{s*}}{\partial x}\right) + \frac{\partial}{\partial y}\left(\varepsilon_s \eta \frac{\partial C_{s*}}{\partial y}\right) + \frac{\eta U}{L_s}(C_s - C_{s*}) \quad (4.123)$$

$$\frac{\partial(\delta_b C_{b*})}{\partial t} + \frac{\partial(q_{bs*}\cos\phi_{bx})}{\partial x} + \frac{\partial(q_{bs*}\cos\phi_{by})}{\partial y} + \frac{1}{L_t}(q_{bs*} - q_{bs}) = 0 \quad (4.124)$$

$$(1-\lambda)\frac{\partial z_b}{\partial t} = \frac{\eta U}{L_s}(C_{s*} - C_s) + \frac{1}{L_t}(q_{bs*} - q_{bs}) \quad (4.125)$$

where, λ is bed porosity, C_{s*} and C_{b*} are actual depth-averaged sediment concentrations for suspended load and bedload, respectively, ε_s is diffusivity coefficient of sediment (assumed to be isotropic), and q_{bs*} is actual bedload sediment transport rate. Actual concentrations and erosion and deposition rates are solved using empirical expressions. L_s and L_t are non-equilibrium adaptation lengths for the suspended and total load, respectively, and can be determined as follows:

$$L_t = \text{maximum}(L_b, L_s) \tag{4.126}$$

where, L_b is non-equilibrium length for bedload. Equation (4.125) is a form of the following 1-D sediment continuity (Exner) equation:

$$(1-\lambda)\frac{\partial z_b}{\partial t} + \frac{\partial \mathrm{q}_{ts}}{\partial \mathrm{x}} = 0 \tag{4.127}$$

Wu *et al.* (2000) state that there is a large degree of uncertainty in estimating the non-equilibrium lengths. According to the study by Kooi and Beaumont (1994), the non-equilibrium lengths represent an erosion-deposition length scale where the sediment particles adapt to the flow conditions under equilibrium conditions. Wu *et al.* (2000) and Wu (2004) refers to the adaptation lengths in their model as length scales of sediment motion, bedforms and channel geometry, and are often prescribed by bedform geometry in the case of bedload transport. In the case of suspended load transport, the non-equilibrium length is proportional to w_s/u^* (Armanini and Di Silvio, 1988). As the non-equilibrium lengths decrease, the residual transport-capacity is reduced and the sediment transport mechanism approaches equilibrium conditions (Kooi and Beaumont, 1994; Yang and Ahn, 2011).

The term erodibility is often used to describe the detachment process in cohesive sediments where particle sizes are less than 75μm. The erodibility formulations in cohesive sediment are different than the classical sediment transport relationships for noncohesive sediments since they reflect the actual rate of erosion and deposition rather than the flow's transport capacity (Yang and Simões, 1999). When sediments have a low erodibility, the term detachment-limit capacity is used. The erodibility for a cohesive soil can be expressed in either gravimetric or volumetric

form as the mass or volume of the eroded bed, Δm_b and $\Delta \forall_b$, respectively, per unit area, ΔA, and time, Δt. Often both forms of erodibility can be described in terms of the excess shear stress as shown (Wan and Fell, 2004; Plew *et al.* 2007; Fujisawa *et al.* 2008; Chang and Zhang, 2010):

$$\dot{E_m} = \frac{\Delta m_b}{\Delta A \Delta t} = C_{\mathrm{E}}(\tau - \tau_c)^{n_{\mathrm{E}}} \tag{4.128}$$

$$\dot{E} = \frac{\Delta \forall_b}{\Delta A \Delta t} = \frac{\Delta z_b}{\Delta \mathrm{t}} = C_{\mathrm{E}}(\tau - \tau_c)^{n_{\mathrm{E}}} \tag{4.129}$$

where, $\dot{E_m}$ is referred to as mass pick-up rate and is in units [kg/m^{2}s], C_{E} is an empirical erosion coefficient, n_{E} is an empirical erosion exponent, $\dot{E}$ is referred to as erosion velocity of the bed and is in units [m/s], and Δz_b is an incremental change in the bed elevation, z_b. Usually $n_{\mathrm{E}} = 1$ such that the erosion rate is linear with the excess shear stress. The gravimetric erosion (*i.e.* mass pick-up) rate can therefore be converted into volumetric erosion rate as:

$$\dot{E} = \frac{\dot{E_m}}{\rho_s(1-\lambda)} \tag{4.130}$$

where, ρ_s is sediment density.

Cohesive soils tend to have higher critical shear stresses due to their cohesive strength. When they are eroded, they either break off as particles or in clusters. As a result, the soil in in cohesive embankments erodes slower, where a series of headcuts are formed on the downstream slope. Nevertheless, cohesive embankments are also prone to failure by slope slides due to higher residual PWP during a reservoir drawdown.

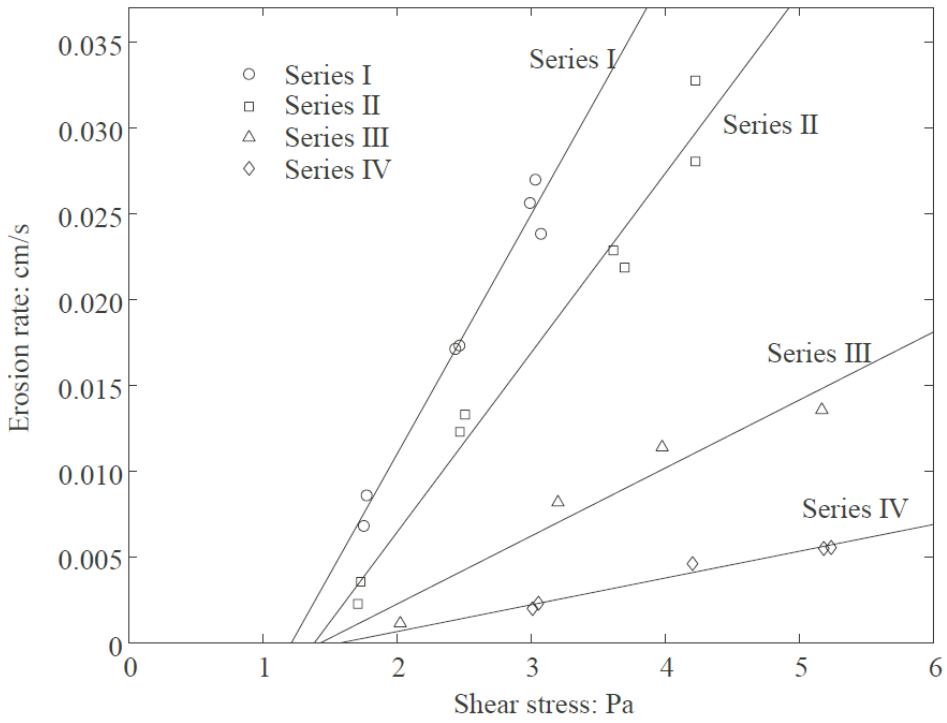

Figure 4.15: Relationship between erosion rate and shear stress for compacted silty sands (Fujisawa *et al.* 2008)

In non-equilibrium conditions, it may be desirable to express the sediment transport rate for noncohesive sediment using empirical expressions similar to those of soils of a cohesive nature. The model by Wang and Bowles (2006a, b, c) used the following expression for volumetric erosion rate by Chen and Anderson (1987) for noncohesive soils with $d_{50} < 8mm$:

$$\dot{E} = 0.0513(\tau_b - \tau_c)^{1.3} \tag{4.131}$$

where, $\dot{E}$, τ_b and τ_c are in units [m/s], [kPa] and [kPa], respectively.

The physical tests described in Winterwerp *et al.* (1992) on steep slopes ($0.3\% < S_b < 40\%$) of fine sand ($0.12mm < d_{50} < 0.225mm$) under supercritical flow conditions, yielded a dimensionless erosion function (equivalent to the dimensionless transport rate) as follows:

$$\Psi_e = 0.012\left(\sqrt{\tau^*} - 1.3\right)d^{*0.3} \tag{4.132}$$

In order to account for the reduced stability of the sediment particles on steep slopes, the dimensionless erosion function was modified using the factor $(1 - \tan\phi_b/\tan\phi_r)$ and an expression for the dimensionless erosion rate was defined as:

$$\Phi_e = 0.012\frac{(\sqrt{\tau^*}-1.3)d^{*0.3}}{1-\frac{tan\,\phi_b}{tan\,\phi_r}} \tag{4.133}$$

The factor $\rho_s\sqrt{gd_{50}(G_s-1)}$ was then used to define a dimensional gravimetric erosion rate as:

$$\dot{E_m} = 0.012\frac{\rho_s\sqrt{gd_{50}(G_s-1)}(\sqrt{\tau^*}-1.3)d^{*0.3}}{1-\frac{\tan\phi_b}{\tan\phi_r}} \tag{4.134}$$

The experimental investigation by Van Rijn (1984a) led to the development of a "pick-up" function for equilibrium sediment transport where flow velocities ranged from 0.5 – 1.0m/s:

$$\Phi_p = 0.00033T^{1.5}d^{*0.3} \tag{4.135}$$

Winterwerp *et al.* (1992) plotted their data along with the data by van Rijn (1984a), represented by the dimensionless erosion function, Ψ_e, and pick-up function, Φ_p, respectively, against a shear stress parameter, $\tau^* d^{*0.3}$. It can be noted from Figure 4.16 that the data trend using the method by Winterwerp *et al.* (1992) lies lower than the classical pick-up function defined by van Rijn (1984a).

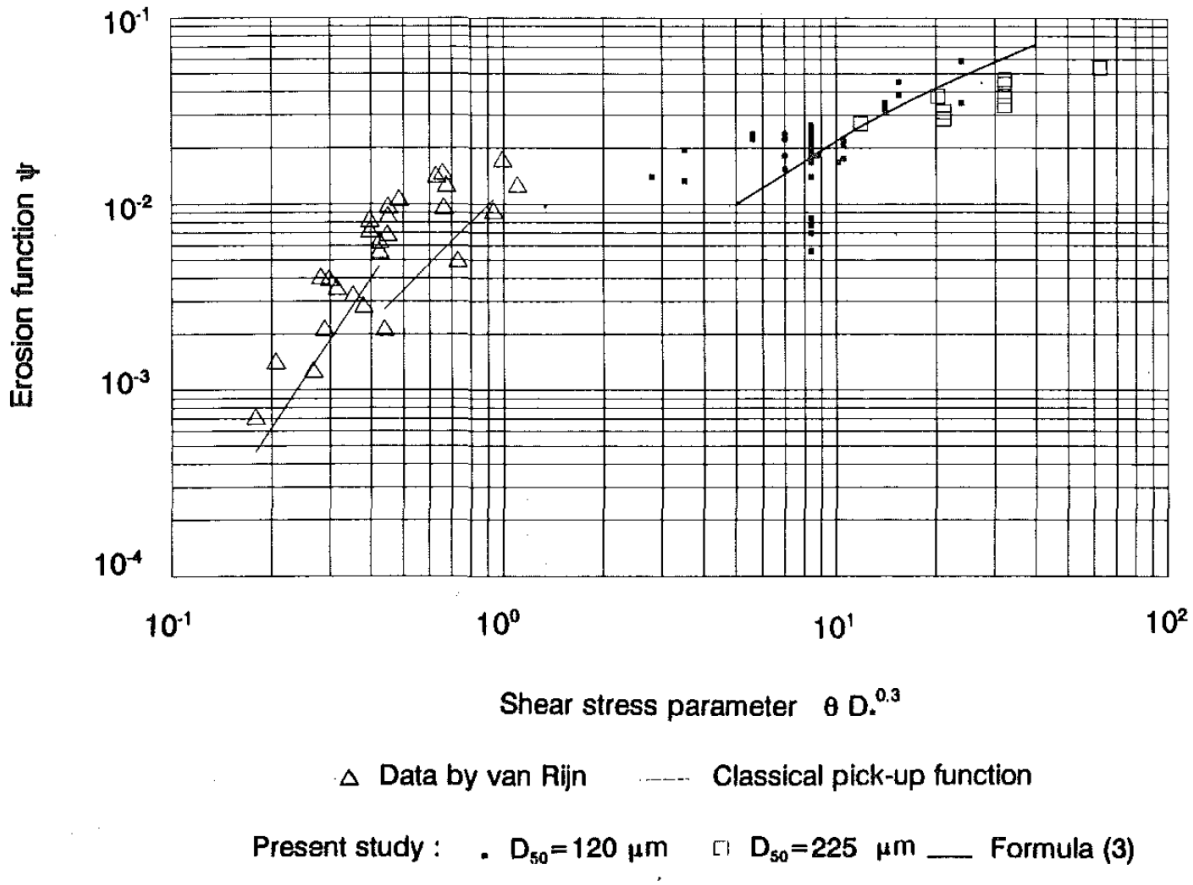

Figure 4.16: Dimensionless erosion rates by Winterwerp *et al.* (1992) and van Rijn (1984a)

They also expressed the deposition rate in gravimetric form (mass of sediment deposited per unit area and time) as follows:

$$\dot{D_m} = \rho_s w_0 C_b (1 - C_b)^4 \tag{4.136}$$

Their study indicated that for high concentrations, both erosion and deposition were hindered due to damping effects from the near-bed concentration and suspension, respectively (see Figure 4.17). The net erosion velocity of the bed was expressed with respect to the net erosion mass flux as:

$$\dot{E}_{net} = \frac{\dot{E_m} - \dot{D_m}}{\rho_s(1-\lambda)} = 0.012 \frac{\sqrt{g d_{50}(G_s-1)}(\sqrt{\tau^*}-1.3) d^{*0.3} - w_0 C_b (1-C_b)^4}{(1-\lambda)\left(1-\frac{\tan\phi_b}{\tan\phi_r}\right)} \tag{4.137}$$

Using the van Rijn (1984a) pick-up function for erosion and the Winterwerp *et al.* (1992) function for sedimentation, the net erosion velocity would be expressed as:

$$\dot{E}_{net} = \frac{\dot{E_m} - \dot{D_m}}{\rho_s(1-\lambda)} = \frac{\sqrt{gd_{50}(G_s-1)}0.00033T^{1.5}d^{*0.3} - w_0C_b(1-C_b)^4}{(1-\lambda)\left(1-\frac{\tan\phi_b}{\tan\phi_r}\right)} \quad (4.138)$$

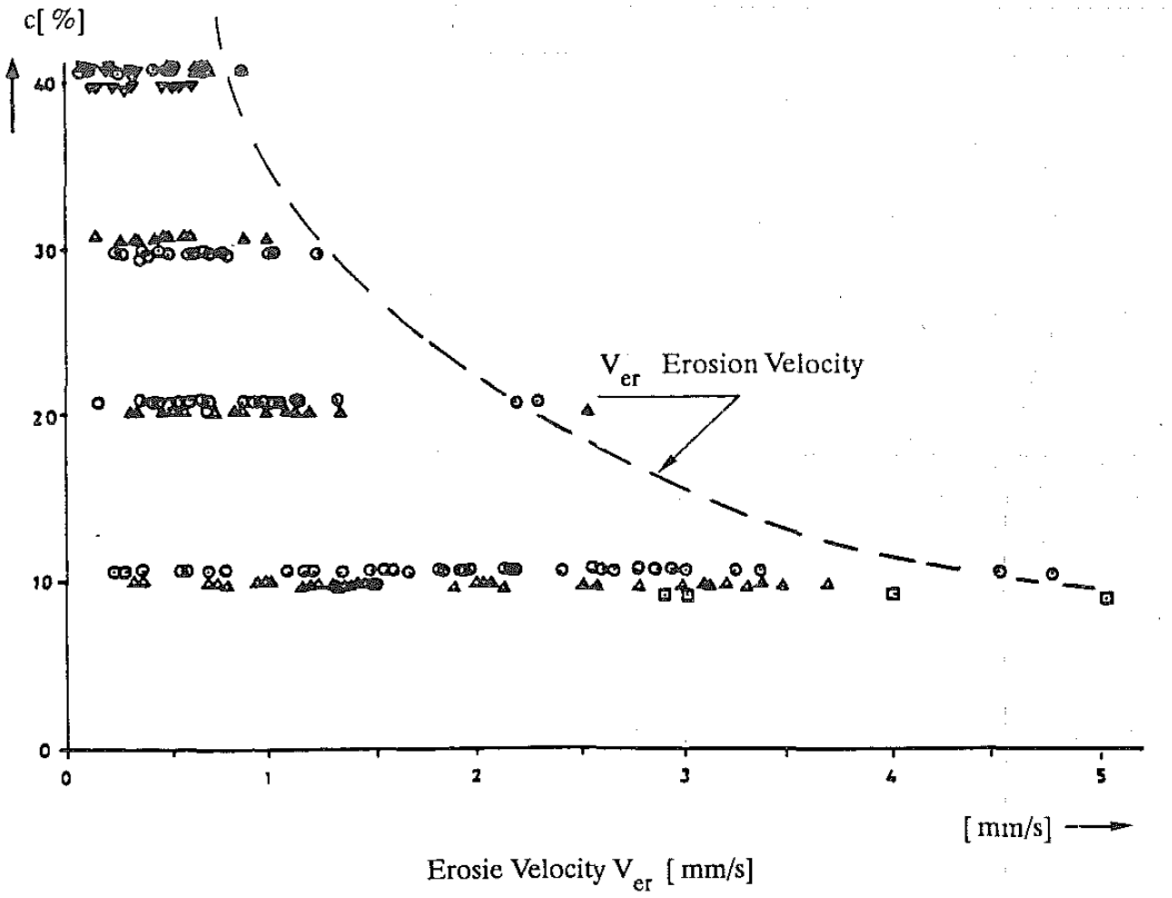

Figure 4.17: Effect of sediment concentration on erosion rate (Winterwerp *et al.* 1992)

4.2.6 Non-Newtonian Flow

Most numerical models employ bedload formulations and tend to neglect the sediment suspended load. Following the embankment breach experiments by Kulisch (1994), the sediment concentration extrapolated by Broich (2003) were as high as 14% (see Figure 4.18). Such peak concentrations will cause a significant

increase (37%) in flow density and viscosity. Although this condition applies to the initial stages of the breach, the estimated discharge could bear significant errors.

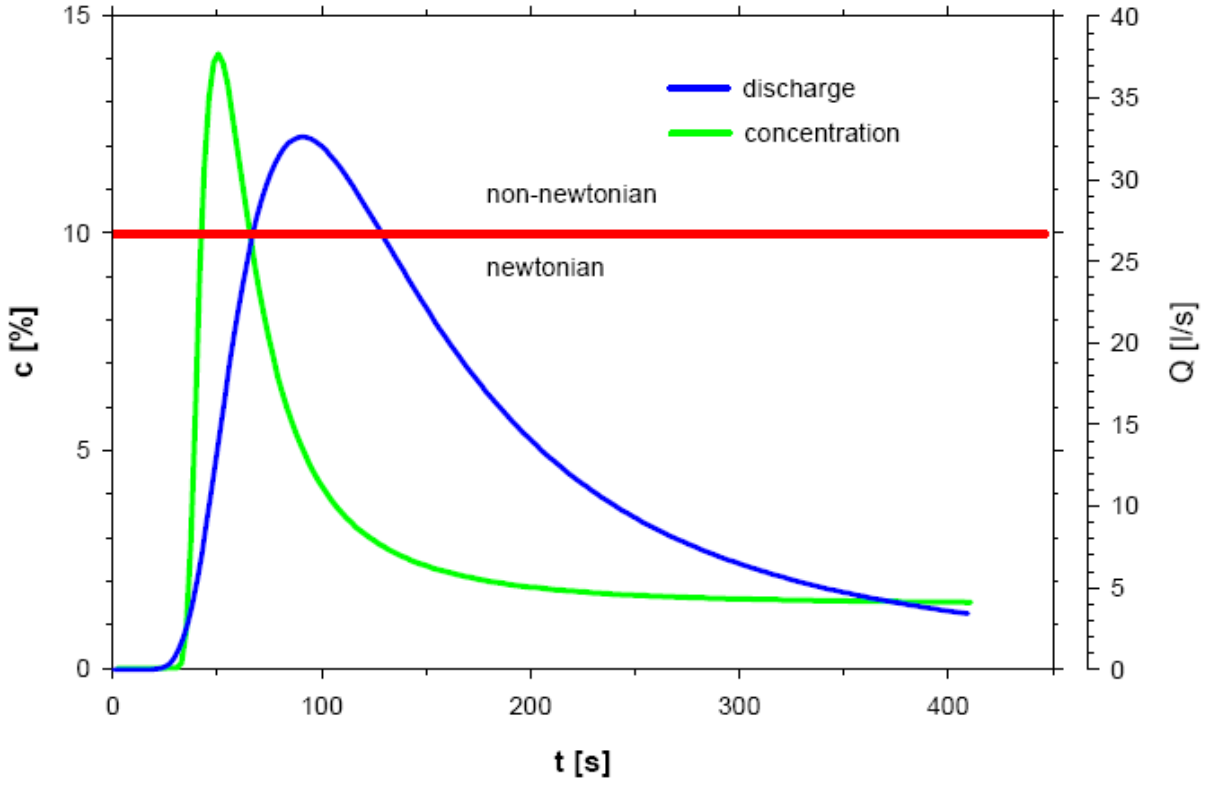

Figure 4.18: Sediment concentration and breach outflow during a breach event (Broich, 2003)

The density of the fluid can therefore be modified to reflect high sediment concentration by means of the fluid-sediment mixture density as follows:

$$\rho_m = C_{s*}\rho_s + (1 - C_{s*})\rho \tag{4.139}$$

In non-Newtonian fluids, the viscosity is not constant. The shear stress strain rate (or shear rate according to some literature), du/dz, is the velocity gradient with respect to the vertical direction (see Equation (4.18)). There are different types of fluids which fall under the non-Newtonian category (see Figure 4.19):

- Bingham fluids are known to exhibit a linear relationship between shear stress and shear strain after a certain yield stress, τ_{yd}, is applied. The fluid is

known to be viscoplastic and it behaves like a solid when the shear stress is less than a yield value. Beyond the yield value, the fluid exhibits motion.

- Shear thickening (or dilatant) fluids exhibit an increase in viscosity with an increase in shear rate. Examples of such fluids are flows with high sediment concentrations such as in sheet flows (Bagnold, 1966).
- Shear thinning (or pseudoplastic) fluids exhibit a decrease in viscosity when shear rate increases.
- Thixotropic fluids have a viscosity which decreases with time under a constant shear stress. The viscosity then recovers when the stress is removed. Antithixotropic (or rheopectic) fluids behave opposite to thixotropic fluids.

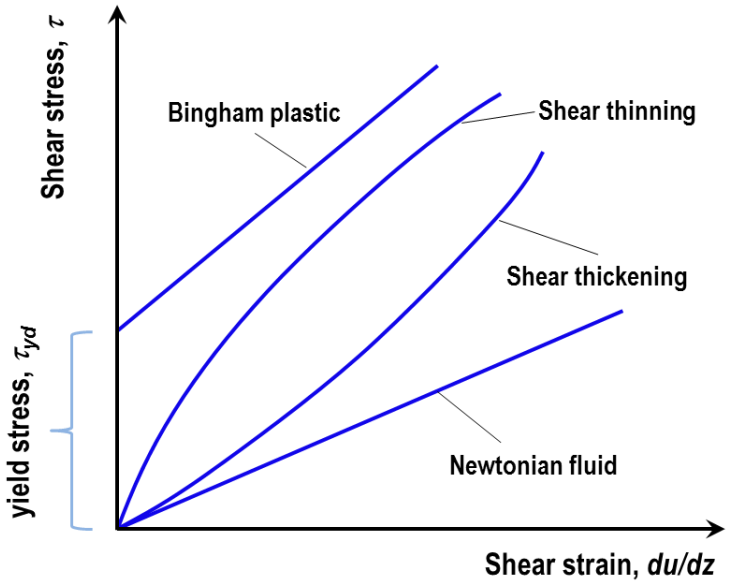

Figure 4.19: Shear stress relations for different types of fluids

Several models have been developed to describe the rheology of non-Newtonian fluids (see Figure 4.20). Power laws are used to describe the behaviour of shear-thickening and shear-thinning fluids as:

$$\tau = C_\tau \left(\frac{du}{dz}\right)^{n_\tau} \tag{4.140}$$

where, C_τ is flow consistency index and n_τ is plasticity exponent.

Bingham fluids are modeled using the following expression:

$$\tau = \tau_{yd} + \mu_p \frac{du}{dz} \tag{4.141}$$

where, μ_p is plastic viscosity.

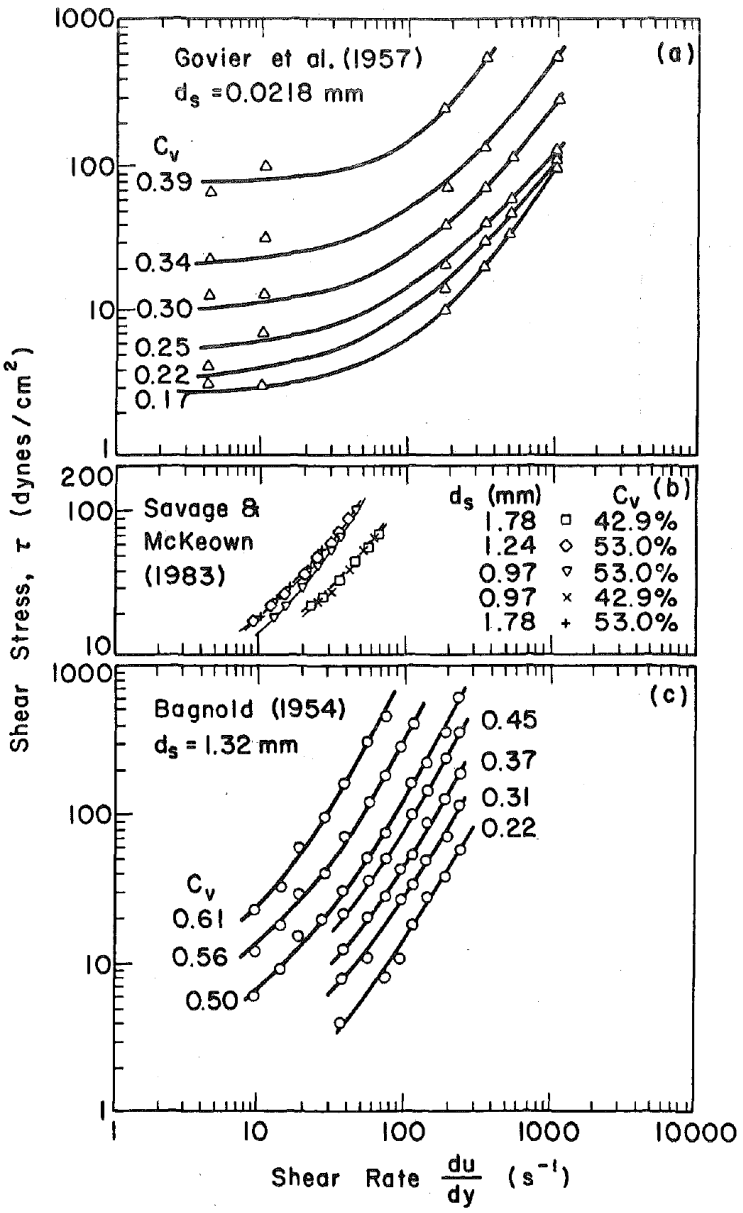

Figure 4.20: Rheograms of hyperconcentrated flows (Julién and Lan, 1991)

4.3 Reservoir Routing

Boundary conditions governing an embankment breach are as important upstream as they are downstream. Upstream of the breach channel is the reservoir, which is very likely bound by an incoming flood hydrograph, $Q_I(t)$, in upstream reaches. At the same time, the total outflow, Q_O, which is comprised of breach channel outflow, Q_B, crest overflow, Q_{cr}, and flow in the spillway, Q_{sp}, causes depletion in the reservoir level. In reaches downstream of the breach channel, rising tailwater surface levels in the river valley may influence the breach outflow due to submerged flow conditions. A standard hydrologic storage routing equation based on the mass conservation balance between the incoming flood, reservoir and downstream valley can be applied in differential form as:

$$\sum Q_I - \sum Q_O = \frac{d\forall}{dt} \tag{4.142}$$

where $d\forall$ is the change in reservoir volume, $\forall$, over a differential time-step, dt

Equation (4.142) can be further expanded by averaging the summation of inflows and outflows during an incremental time-step, Δt, and expressing the change of reservoir volume in terms of the reservoir surface area, A_S, and incremental reservoir elevation, $\Delta\eta$:

$$\frac{(\sum_t Q_I + \sum_{t+\Delta t} Q_I)}{2} - \frac{(\sum_t Q_O + \sum_{t+\Delta t} Q_O)}{2} = \frac{[A_S)_t + A_S)_{t+\Delta t}]\Delta\eta}{2\Delta t} \tag{4.143}$$

By separating the known variables from the unknown variables, the equation above can be rewritten as follows:

$$\left(Q_I - Q_B - Q_{sp} - Q_{cr}\right)_t + \left(Q_I - Q_B - Q_{sp} - Q_{cr}\right)_{t+\Delta t} = (A_S|_t + A_S|_{t+\Delta t})\frac{\Delta\eta}{\Delta t} \tag{4.144}$$

From Equation (4.144), the water surface level at $t + \Delta t$ can be expressed as:

$$\eta_{t+\Delta t} = \eta_t + \frac{(A_S|_t + A_S|_{t+\Delta t})\left[\left(Q_I - Q_B - Q_{sp} - Q_{cr}\right)_t + \left(Q_I - Q_B - Q_{sp} - Q_{cr}\right)_{t+\Delta t}\right]}{\Delta t} \tag{4.145}$$

Reservoir characteristics are usually known from topographic maps prior to reservoir impoundment and/or from recent surveys. The surface area-stage relationship describes the reservoir surface area as a function of the water surface elevation as:

$$A_S = \mathcal{F}(\eta) \tag{4.146}$$

The variables, η and A_S, at $t + \Delta t$ can be determined by solving Equations (4.145) and (4.146) numerically using iterative methods. Finally, the breach channel outflow, Q_B, can be solved using weir flow equations or any other hydrodynamic equation, as explained in Subsection 4.1.5.2.

The derivation of the upstream boundary condition for the breach channel shown in Equations (4.142) to (4.146) assumes a gradual breach where velocities in the reservoir are small and inertial effects are localized (Fread, 1984b; Singh *et al.* 1988). This assumption is valid when reservoir sizes are large, where the breach outflow does not produce negative waves within the reservoir or where the incoming flood is not large enough to cause positive waves through the reservoir (Fread, 1984b). For thin and long or branched reservoirs, the dynamic effects from upstream waves may control the discharge through the embankment breach, requiring dynamic routing techniques to compute the breach outflow.

4.4 Geomechanics

Geomechanics are large scale mechanisms which yield sudden enlargements during an embankment breach. They are important processes as they are part of the interplay between breach flow hydrodynamics, erosion and reservoir routing and eventually govern the shape of the breach outflow hydrograph. During the breach formation and propagation stages of overtopping, steepening and undercutting in the steep breach channel sides induces side-slope failures. These instabilities in the breach channel side-slopes have been observed in many physical models (see Figure 4.21).

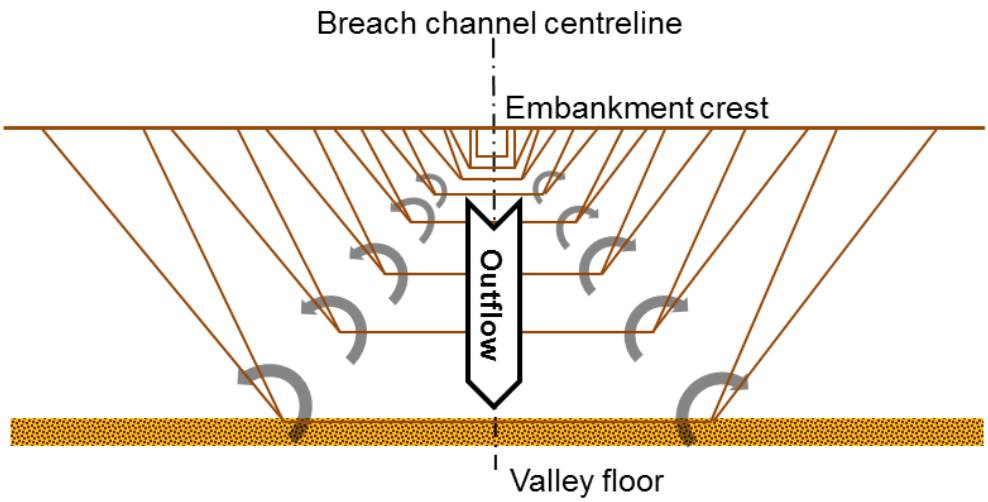

Figure 4.21: Trapezoidal breach channel cross-section showing vertical erosion progression and successive side-slope failures

Observations from physical models often describe the failure of the side-slopes as mass sliding, slumping, overturning and collapsing. The shear failure (*i.e.* sliding and slumping) mechanism is a result of the imbalance between the stabilizing forces (*i.e.* hydrostatic, cohesive and shear strength forces) within the breach channel and the destabilizing forces (*i.e.* excess pore-water pressures and gravity forces) within the side-slopes themselves. This is also known as a Coulomb-sliding or shear failure. Another failure mode which is not to be confused with the Coulomb shear failure, and which also give rise to side-slope instabilities, is static liquefaction. In this failure mode, the soil deforms and flows like a fluid. Slope instabilities along the longitudinal direction can also occur according to those two failure modes. These two failure modes are briefly described in Section 4.6. The bending failure (*i.e.* collapsing and overturning) mechanism is a result of the tensile stress exceeding the tensile strength within the soil matrix. This usually occurs when the side-slope angle is adverse, which gives rise to an overhang and consequently bends and breaks off. The shear failure mode for side-slopes was first introduced in the NWS-BREACH model by Fread (1984a) using a Coulomb-failure approach. The bending failure mode for side-slopes was first introduced in the study by Mohamed *et al.* (1999) and adopted in the HR-BREACH numerical model (Mohamed *et al.* 2002).

Side-slope failures are governed by the combined effect of breach channel steepening due to vertical erosion, drawdown effects in the reservoir and undercutting in the breach channel sides. The geotechnical properties of the soil such as hydraulic conductivity, cohesion and shear strength (or angle of internal friction) play a key role in the widening processes of the breach channel. Soil properties such as hydraulic conductivity and shear strength vary significantly with the degree of saturation, therefore a saturated-unsaturated stability analysis must be addressed. The theory of unsaturated soil mechanics is briefly described in Section 4.5.

A stability analysis can also be conducted in the case of composite embankments, when hydrostatic forces in the reservoir exceed the stabilizing forces in a saturated wedge below the breach channel entrance and the unsaturated clay core of the embankment (Fread, 1984a, 1991). In Figure 4.22, the destabilizing force is the hydrostatic force, F_H, and the stabilizing forces are the shear and cohesive forces acting at the bottom of the wedge, F_{BS} and F_{BC}, respectively, and the shear and cohesive forces acting at the interface of the saturated-wedge and unsaturated-core, F_{SS} and F_{SC}, respectively.

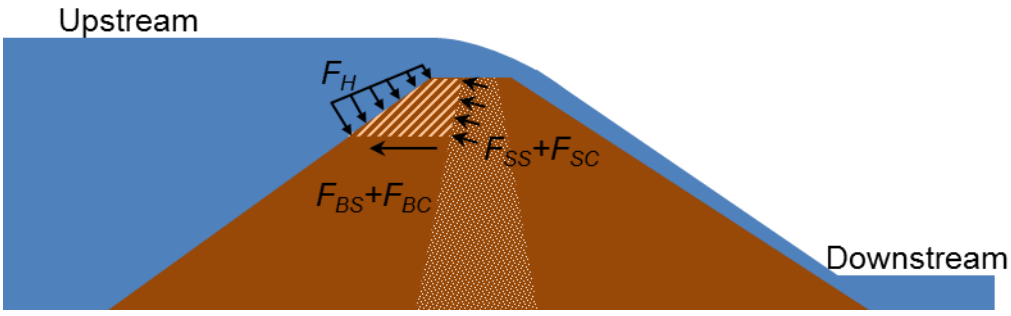

Figure 4.22: Longitudinal section showing region with potential collapse during overtopping failure in composite embankments

During the breach formation stage in piping failures, instability due to hydrostatic forces acting on the enlarged conduit and the weight of the roof above, may cause a large wedge to collapse (see Figure 4.23). In the event of such instability, the

conveyance of the collapsed embankment material will be governed by the transport-capacity of the breach outflow. After the collapse has occurred, the breach mechanism will then resume as an overtopping failure.

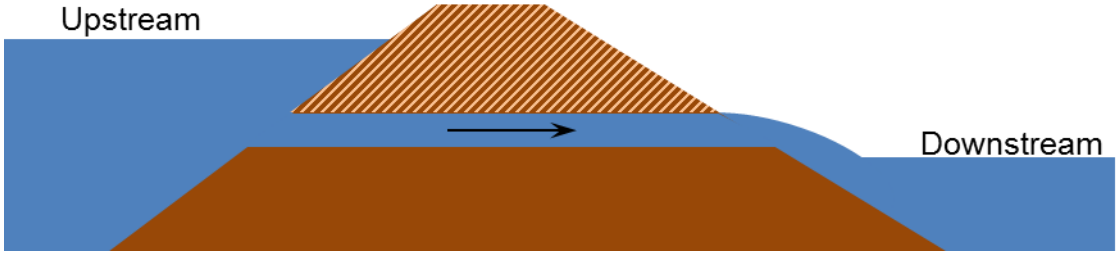

Figure 4.23: Longitudinal section showing region with potential collapse during piping failure

4.5 Engineering Properties of Unsaturated Soils

Hydraulic conductivity, shear strength and volume change are the key engineering properties of a soil and are very important in embankment engineering applications. In classical soil mechanics, soils are in a saturated state where the pore-air-pressure (PAP), u_a, is zero, and PWP, u_w, is positive and increases linearly with the depth below the phreatic surface (under steady conditions). The downstream slope of noncohesive earthfill embankments is usually in an unsaturated state due to the presence of seepage control structures such as drainage systems or cohesive cores which depress the phreatic surface. Drainage systems are comprised of two or three materials and installed in accordance with an inverse-type gradation to prevent the migration of fines (USBR, 1987). The orientation of such drainage systems can be horizontal, vertical or oblique. Central cohesive cores are also used to control seepage and consequently reduce the PWP through the embankment. They are usually comprised of clays or clay-silt mixtures, depending on local availability. Embankments with central cores are often referred to as composite embankments.

During an embankment breach, the resulting drawdown in the upstream impoundment induces a further depression in the phreatic surface which is located below the downstream slope. This gives rise to a further decrease in the degree of

saturation, $\mathbb{S}$, of the soil. As the phreatic surface lowers, water is drained from the soil and air enters into the largest inter-granular pores, transiting from a saturated state to one in which a three-phase system (solid, water, and air) is present (see Figure 4.24). In fact, the air-water interface (also referred to as the "contractile skin"), which is considered a fourth phase, has a significant effect on the properties as well as the physical behaviour of partially-saturated soils (Fredlund and Morgenstern, 1977).

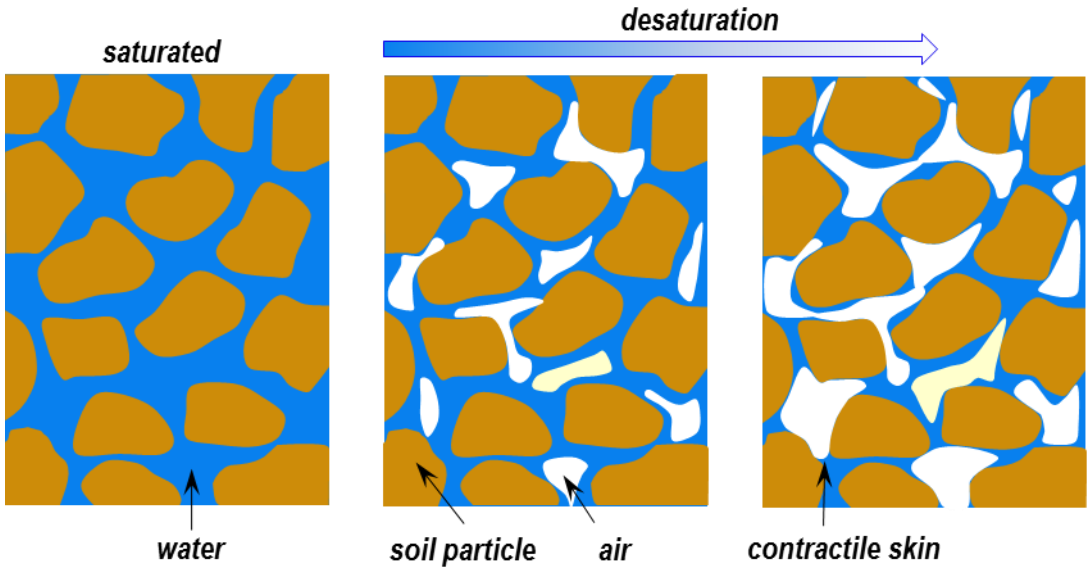

Figure 4.24: Process of desaturation and air filling voids in a saturated soil (adapted after Oh and Vanapalli, 2011)

In classical soil mechanics, only one stress-state variable is used to describe the mechanical behaviour such as shear strength and volume change for a soil. This stress-state variable is known as the effective stress. It represents the component of the inter-granular normal forces in the vertical direction per unit cross-sectional area of the soil mass and can be defined as:

$$\sigma_n' = \sigma_n - u_w \tag{4.147}$$

where, σ_n is the total normal stress on a failure plane.

In unsaturated soil mechanics, two independent stress-state variables are necessary to formulate the constitutive equations that describe the engineering properties and behaviour for a soil (see Figure 4.25). These stress-state variables are matric (*i.e.* capillary) suction and the net normal stress, and can be defined as:

$$\text{matric suction} = \psi = (u_a - u_w) \tag{4.148}$$

$$\text{net normal stress} = (\sigma_n - u_a) \tag{4.149}$$

where, ψ is expressed in terms of pressure [kPa] or [kN/m^2] and the PAP ($u_a \neq 0$) is the air reference pressure, and which is not to be confused with atmospheric pressure. However, at saturation, $u_a = u_w$.

The total suction is comprised of the matric component and an osmotic component of suction as follows:

$$\psi_T = (u_a - u_w) + \pi_\psi \tag{4.150}$$

where, π_ψ is the osmotic component of the total suction.

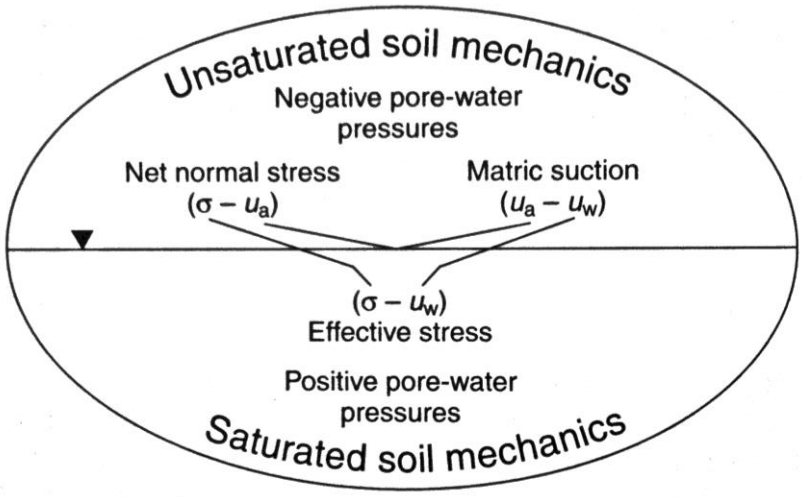

Figure 4.25: Stress-state variables in saturated and unsaturated soil mechanics (Fredlund, 1996)

The mechanism which gives rise to matric suction is the capillary forces present in the inter-granular curved menisci. As more air enters into the voids, the radius of the meniscus decreases while the capillary forces increase. The osmotic (or solute)

suction is the suction in the soil due to the presence of dissolved salts in the pore-water and is therefore less relevant in unsaturated soils that are granular and salt-free (Ng and Menzies, 2007). The unsaturated state of the soil renders the flow path more tortuous reducing its hydraulic conductivity and enhances the shear strength due to apparent cohesion. Another key engineering property which is influenced by the unsaturated state is the compression and swelling characteristics, however, it is beyond the scope of this research since the effects are negligible in noncohesive soils.

4.5.1 Soil-Water Characteristic Curve

The soil-water characteristics curve (SWCC) describes the relationship between water content and suction and is also known as the capillary-moisture retention curve. At zero or very low suctions, the volumetric water content, θ_w, is at or near its saturated value, (*i.e.* $\theta_w = \theta_s$). As matric suction is increased (or PWP decreased), the volumetric water content is reduced drastically as shown in Figure 4.26, until it encounters very little change with any further increase in matric suction. At this point, residual conditions are reached, where the volumetric water content is referred to as the residual volumetric water content, θ_r.

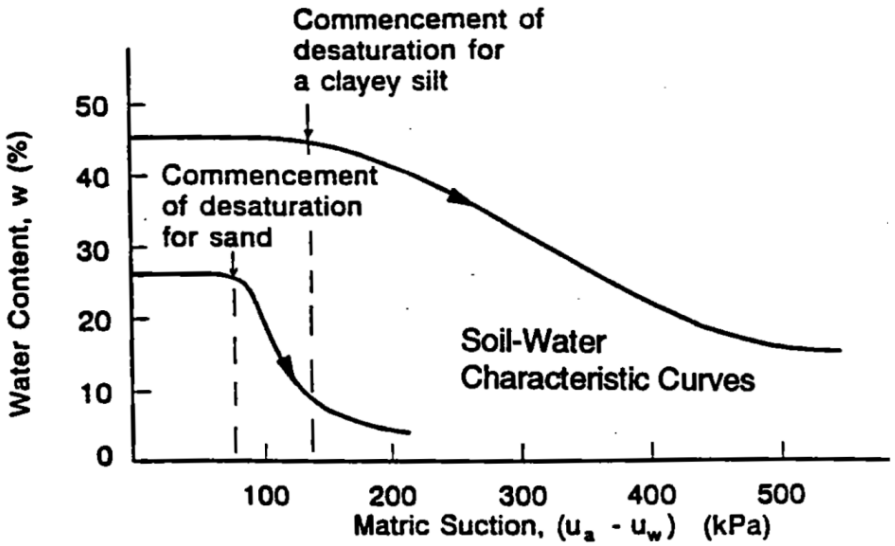

Figure 4.26: Soil-water characteristic curves for sand and clayey silt (Fredlund, 1996)

It is often advantageous to represent the SWCC using a dimensionless form of water content, such as the degree of saturation, $\mathbb{S}$, which can be expressed as:

$$\mathbb{S} = \frac{\omega G_s}{e} = \frac{\theta_w(1+e)}{e} = \frac{\theta_w}{\lambda} \tag{4.151}$$

where, ω is gravimetric water content, expressed as a percentage [%] and e is void ratio. The resulting curve is useful since a comparison between more than one type of soil can be observed for a matric suction ranging from 0kPa to 10^6kPa, which represent saturation and dry conditions, respectively.

The process of desaturation for any soil can be described using its drying (or desorption) SWCC using the following three important characteristics: air-entry value (AEV) or bubbling pressure (ψ_b), which is the value for matric suction at which air begins to enter the largest voids, the desorption rate or slope of the inflection point with respect to matric suction, and the residual suction value (RSV), ψ_r, which represents the matric suction beyond which no further significant decrease in degree of saturation occurs. A graphical construction procedure which estimates the residual suction value based on a computational construction technique is described in Vanapalli *et al.* (1998). A comparison between the SWCCs for coarse and fine-grained soils is shown in Figure 4.27. Noncohesive soils have larger interstitial spaces where air enters with less effort than cohesive soils, and the process of water draining from within the pores follows suit.

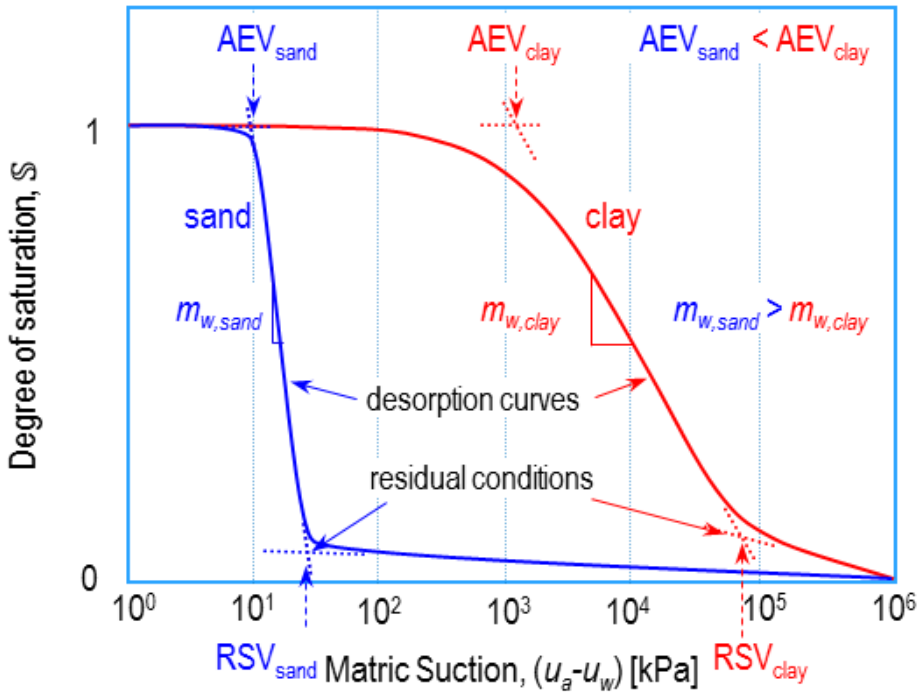

Figure 4.27: Hypothetical desorption soil-water characteristic curve for a sand and clay

The soil structure or arrangement of soil particles is another factor which influences the SWCC parameters. For instance, angular and loosely-packed sands will exhibit lower AEVs and higher desorption rates than densely-packed sands. For fine-grained soils, the compaction water content and compaction effort also influence the SWCC parameters (see Figure 4.28). Fine-grained soils compacted at dry-of-optimum conditions (*i.e.* flocculated soil structures) using high compaction efforts will exhibit higher AEVs than at low compaction efforts. At wet-of-optimum conditions (*i.e.* dispersed soil structures), the fine-grained soils will exhibit even higher AEVs in dry-of-optimum conditions. The water content and dry density are therefore considered two independent soil parameters that influence the soil properties under a saturated as well as unsaturated state.

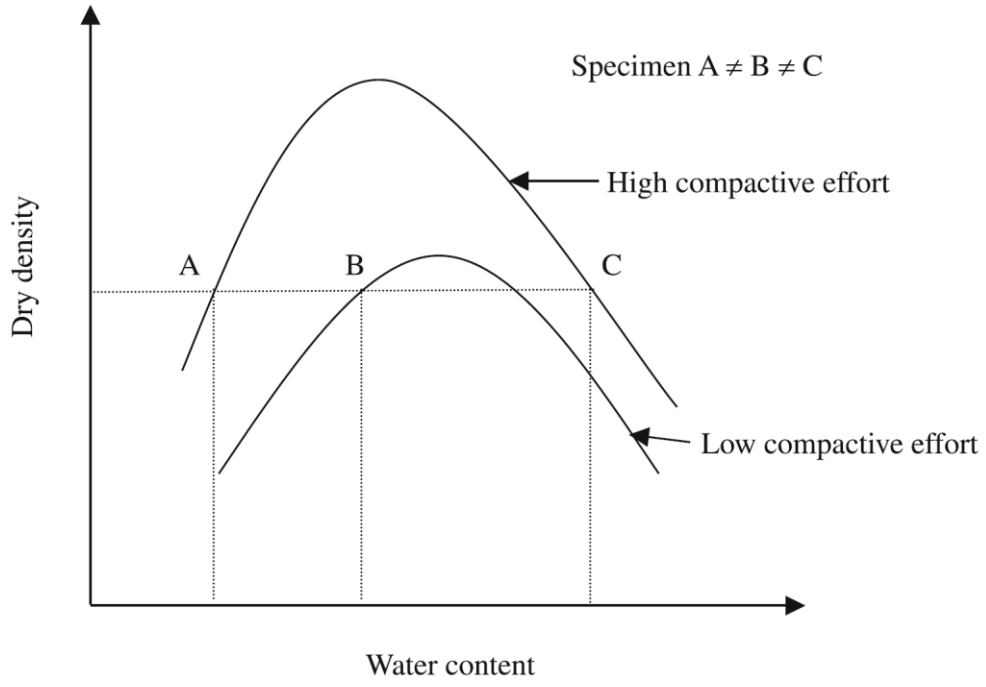

Figure 4.28: Variation of dry density with compaction water content for two compaction efforts (Ng and Pang, 2000)

Several techniques have been developed for measurement of the SWCC of a soil. Ng and Menzies (2007) describe two types of procedures for measuring soil suction: direct and indirect. A direct procedure is one which measures matric suction by direct contact whereas indirect procedures deduce the matric suction from another property that can easily be measured (*e.g.* relative humidity, conductivity, or resistivity). Difficulties arise when the soil suction approaches 1 atm (*i.e.* -1 atm gauge), since water in the measuring system begins to cavitate. A method to counter such problems is by elevating the PAP in the measuring system above atmospheric pressure. This method is referred to as the axis translation technique (Hilf, 1956). One common method for measuring the SWCC, and which uses the axis translation technique, is the Tempe cell pressure apparatus (ASTM, 2000a). The limiting suction in this method is the AEV of the porous plate through which the water from the soil is drained during desorption. High air-entry ceramic materials are often used with AEVs usually exceeding 1,500kPa (Ng and Menzies, 2007). Such materials are very small in pore-size and prevent the migration of the fine material

from the soil specimen. However, in the case of coarse-grained soils, neither the AEV nor the pore-size of the ceramic material is of concern, at least for a large range of soil suction. In fact, the slope of the straight line segment of the SWCC resembles that of the GSD (Yang *et al.* 2004) (see Figure 4.29).

The measured air pressure in the Tempe cell will therefore correspond to the matric suction ($\psi = u_a - u_w$, where $u_w = 0$ at the top of the porous plate). However, there is a negative hydrostatic pressure distribution due to the capillary rise within the soil specimen (see Figure 4.30), where $u_w = -0.5\rho g h_s$. The matric suction can be corrected based on the average PWP in the soil specimen as follows (Yang *et al.* 2004):

$$\psi = u_a + 0.5\rho g h_s \tag{4.152}$$

where, h_s is height of the soil specimen. The corrected matric suction in a soil specimen with height of 28mm due to a capillary rise will therefore correspond to 0.14kPa. This may be of importance in noncohesive soils such as coarse-sand and gravels which exhibit low AEVs.

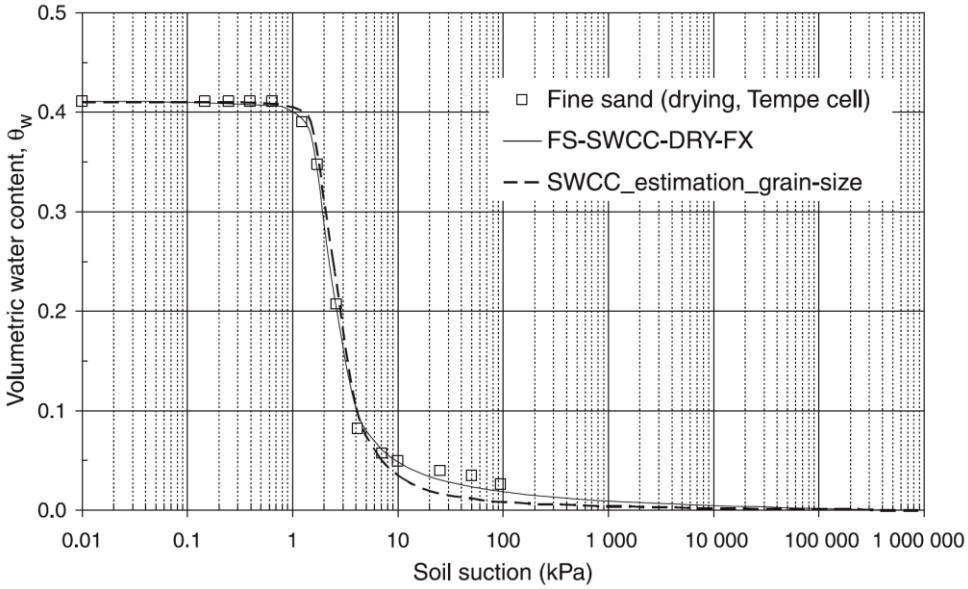

Figure 4.29: Comparison between the measured and predicted SWCC based on a GSD model and the mathematical model by Fredlund and Xing (1994) for a fine sand (Yang *et al.* 2004)

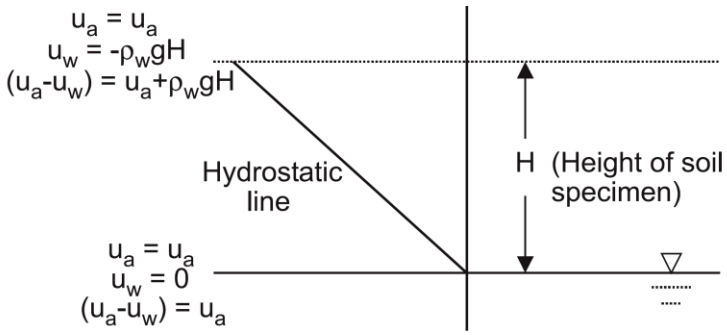

Figure 4.30: Capillary rise in soil specimen (Yang *et al.* 2004)

The SWCC can also be predicted using semi-empirical functions derived directly from pore or GSD data (*e.g.* Arya and Paris, 1981; Fredlund *et al.* 2000) or by curve-fitting using mathematical models (*e.g.* Brooks and Corey, 1964; Mualem, 1976; van Genuchten, 1980; Fredlund and Xing, 1994). Brooks and Corey (1964) expressed the SWCC in the form of a normalised water content using the following power-law expression:

$$\theta_n = \frac{\theta_w - \theta_r}{\theta_s - \theta_r} = \left(\frac{\psi_b}{\psi}\right)^{\lambda_\psi} \text{ for } \psi > \psi_b \tag{4.153}$$

where, λ_φ is pore-size distribution index and corresponds to the negative slope (linear-logarithmic) of the straight lines segment of the SWCC when the normalised water content is defined as its ordinate. The normalized water content can also be expressed in terms of the dimensionless degree of saturation as (Mualem, 1978; Barbour, 1998):

$$\mathbb{S}_e = \frac{\theta_w - \theta_r}{\theta_s - \theta_r} = \frac{\mathbb{S} - \mathbb{S}_r}{1 - \mathbb{S}_r} \tag{4.154}$$

where, $\mathbb{S}_e$ is referred to as the effective degree of saturation, and $\mathbb{S}_r$ is residual degree of saturation.

Van Genuchten (1980) used the following expression for estimating the SWCC:

$$\theta_n = \left[\frac{1}{1+(\alpha_\psi \psi)^{n_\psi}}\right]^{m_\psi} \tag{4.155}$$

where, α_ψ, n_ψ and m_ψ are curve-fitting parameters which are primarily a function of the AEV, slope of straight line segment in SWCC and the residual water content, respectively. The method by Mualem (1976) is similar to van Genuchten (1980), except that only two curve-fitting parameters are used, where $m_\psi = 1 - \left(1/n_\psi\right)$.

Fredlund and Xing (1994) assumed that the theoretical shape of the SWCC is a function of the pore-size distribution. They introduced a fourth parameter into their model, a correction factor, $C(\psi)$, which forces the SWCC into the dry-state at very low suctions as:

$$\theta_w = C(\psi)\frac{\theta_s}{\left\{\ln\left[\mathbf{e}+\left(\frac{\psi}{a_\psi}\right)^{n_\psi}\right]\right\}^{m_\psi}} \tag{4.156}$$

where, **e** is the natural number, a_ψ is a curve-fitting parameter (primarily a function of AEV), and the correction factor can be expressed as:

$$C(\psi) = 1 - \frac{\ln\left(1+\frac{\psi}{\psi_r}\right)}{\ln\left(1+\frac{1000000}{\psi_r}\right)} \tag{4.157}$$

The Fredlund and Xing (1994) and van Genuchten (1980) models are the most widely used. They are more suitable for fitting experimental data since they are based on three curve-fitting parameters as opposed to only one or two by earlier models (*e.g.* Burdine, 1953; Brooks and Corey, 1964; Mualem, 1976). The curve-fitting parameters are therefore expected to be different for each mathematical model.

It is important to note that the process of adsorption (*i.e.* wetting) in an unsaturated soil will not necessarily be represented by the same SWCC for desorption. This irreversible phenomenon between desorption and adsorption, referred to as hysteresis (Haines, 1930; Richards, 1931; Mualem, 1974; van Genuchten, 1980), is attributed to two main causes: the occluded air bubbles within the large pores which oppose water entry as well as the lower contact angle (or larger radius of curvature) of the advancing meniscus during the wetting process. Other causes are: non-

homogeneous pore-size distributions, capillary condensation and swelling/shrinking (for fine-grained soils). Similar to the process of desorption, the adsorption SWCC is measured by decreasing the matric suction of a nearly dry soil, and measuring its corresponding water content until an effective saturation state is established.

The study by Ng and Pang (2000) described the influence of desorption and adsorption history on the SWCC. Figure 4.31 and Figure 4.32 illustrate that for a saturated soil specimen, the hysteresis loop is different than when the same specimen underwent cyclic desorption and adsorption. After the first desorption-adsorption cycle, the degree of saturation does not fully recover due to the occluded air in the pore spaces. Following the first desorption/adsorption cycle, the hysteresis becomes consistent, where desorption/adsorption SWCCs are referred to as the (hysteretic) bounding SWCCs. The scanning curves are intermediate curves which represent the capillary-moisture relationship as the partially-saturated soil is dried or wetted Figure 4.32. While the desorption SWCC is easier to measure (Pham *et al.* 2003), there are methods available in literature for predicting the adsorption SWCC for unsaturated soils (*e.g.* Mualem, 1974; Pham *et al.* 2003, 2005) or scanning curves (*e.g.* Parlange, 1976).

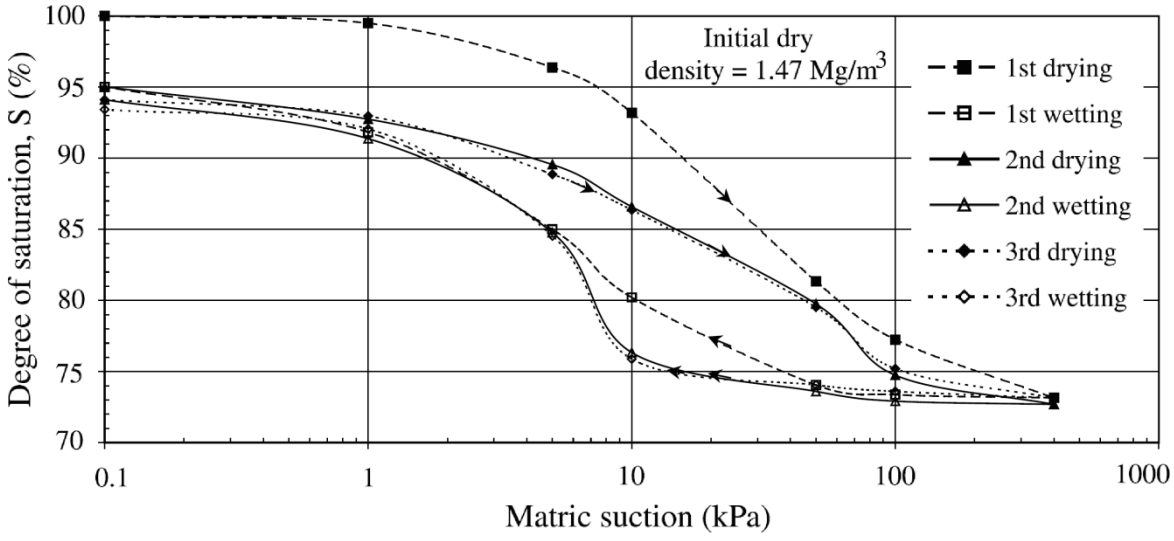

Figure 4.31: Influence of desorption/adsorption cycles on the SWCC of a volcanic soil (Ng and Pang, 2000)

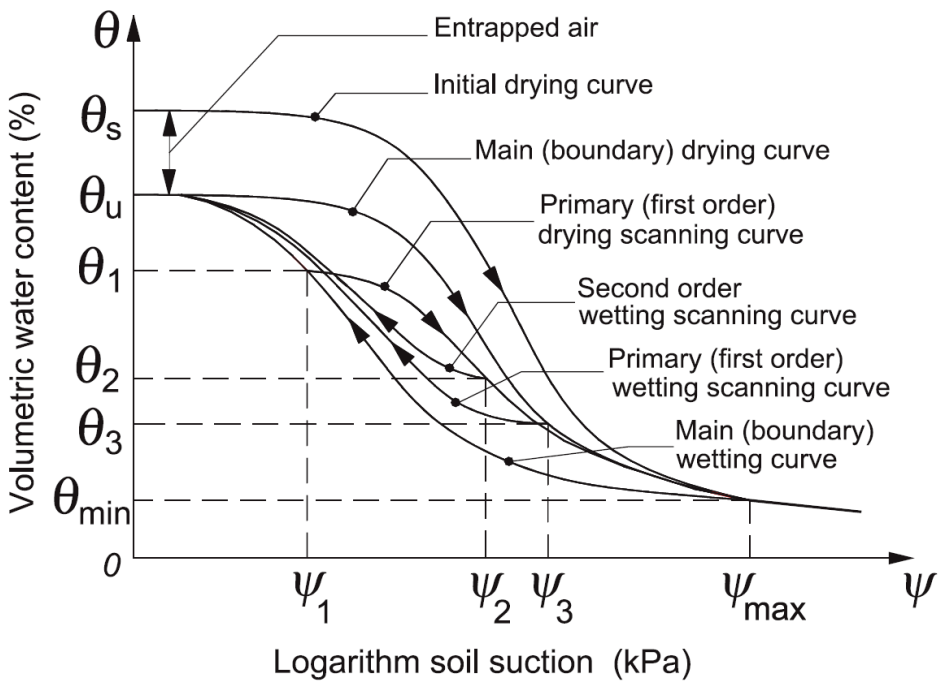

Figure 4.32: Desorption and adsorption SWCC and drying and wetting scanning curves (Pham *et al.* 2005)

Pham *et al.* (2005) classified the hysteresis models into two types: physically-based and empirical. The empirical method by Pham *et al.* (2003) for low swelling soils is based on the Feng and Fredlund (1999) curve-fitting function which represents the bounding SWCCs as follows:

$$\omega(\psi) = \frac{\omega_u b_\psi + \omega_r \psi^{d_\psi}}{b_\psi + \psi^{d_\psi}} \tag{4.158}$$

where, $\omega(\psi)$ is the gravimetric water content as a function of matric suction, ω_r and ω_u are gravimetric water contents at relatively high and zero suction, respectively, and b_ψ and d_ψ are both curve-fitting parameters, respectively.

The expression by Feng and Fredlund (1999) is capable of predicting one bounding SWCC from another using two additional points; however, the location of those two points was not mentioned. The study by Pham *et al.* (2003) proposed that the first point (shown as “F” in Figure 4.33) should be close to the AEV of the existing

bounding curve. The second point (shown as “D” in Figure 4.33) was proposed as having a suction value twice the distance between the first suction value and a vertical line passing through the inflection point of the bounding curve which is to be determined. Based on a statistical analysis of 34 datasets, they proposed that the location of this vertical line can be obtained using the slope of the straight line segment of the known bounding SWCC. As shown in Figure 4.33 and Figure 4.34, the water content at residual conditions and zero suction is considered the same for both bounding SWCCs. While their study described the procedure for predicting a bounding adsorption SWCC, as shown in Figure 4.33 and Figure 4.34, their scaling method can also be applied to predict a bounding desorption SWCC from a known adsorption SWCC.

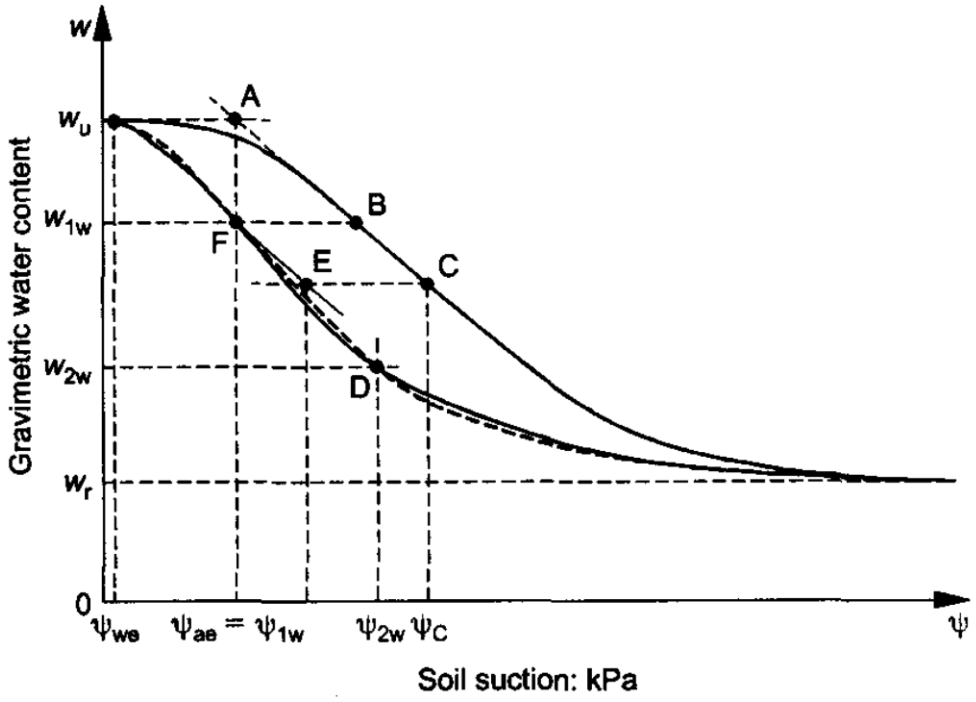

Figure 4.33: Process for predicting adsorption bounding SWCC from a known bounding desorption SWCC (Pham *et al.* 2003)

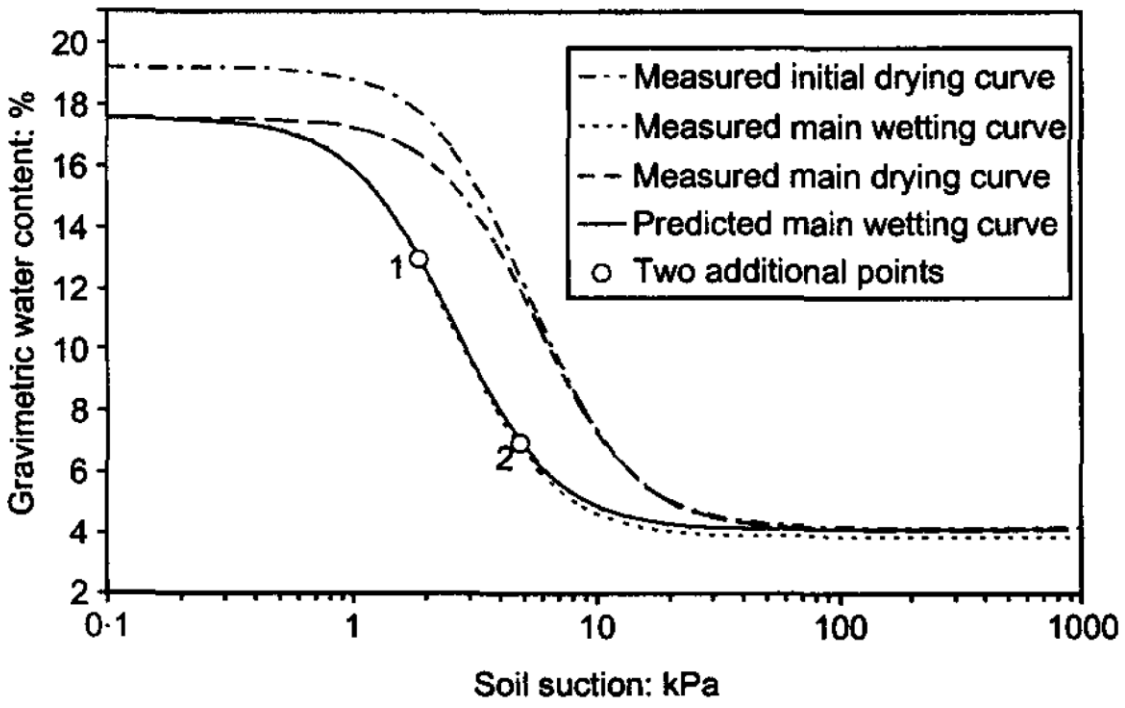

Figure 4.34: Comparison between the predicted adsorption and measured initial and boundary SWCCs for Beaver Creek sand (Pham *et al.* 2003)

The method was further simplified by the same authors in 2005. Pham *et al.* (2005) employed the Feng and Fredlund (1999) curve-fitting expression to investigate the relationships between the initial and the two bounding SWCCs using a database of 34 SWCC data. They found that the Feng and Fredlund (1999) expression described the two bounding SWCC as having inflection points lying halfway between the maximum and residual saturation (see Figure 4.35). The maximum saturation, $\mathbb{S}_u$, in the case of the bounding SWCCs is lower than that for the initial SWCC by 5 to 15% (based on their statistical analysis). In their study, they defined the following parameters for the bounding SWCCs:

- Ratio of slopes on the straight-line segments, R_{SL}, defined as:

$$R_{SL} = \frac{d_{\psi,d}}{d_{\psi,w}} \tag{4.159}$$

- Equal degrees of saturation at residual and maximum values, $\mathbb{S}_r$ and $\mathbb{S}_u$, respectively.
- Distance between the two inflection points on a logarithmic soil suction abscissa, D_{SL}, as:

$$D_{SL} = \log b_{\psi,d}^{\,1/d_{\psi,d}} - \log b_{\psi,w}^{\,1/d_{\psi,w}} \tag{4.160}$$

where, the additional subscripts d and w imply desorption and adsorption bounding SWCCs, respectively.

Their method requires only one point on the bounding SWCC for its complete prediction. The entire hysteretic loop including the initial desorption SWCC can be determined with knowledge of one SWCC. They combined the Fredlund and Xing (1994) correction factor with Equation (4.158) and expressed the SWCC with the degree of saturation function as:

$$\mathbb{S}(\psi) = \left[1 - \frac{\ln\left(1+\frac{\psi}{\psi_r}\right)}{\ln\left(1+\frac{1000000}{\psi_r}\right)}\right] \frac{\mathbb{S}_u b_\psi + \mathbb{S}_r \psi^{d_\psi}}{b_\psi + \psi^{d_\psi}} \tag{4.161}$$

Following their statistical analysis, they suggested that the corresponding values for R_{SL} and D_{SL} would be, 1 and 0.2 log-cycles, respectively, for sands. This implies that the slopes of the two bounding SWCCs will be parallel on a linear-logarithmic scale. The study by Yang *et al.* (2004) also found that the magnitude of hysteresis for fine sand with $d_{50} = 0.3mm$ was 0.2 (see Figure 4.36).

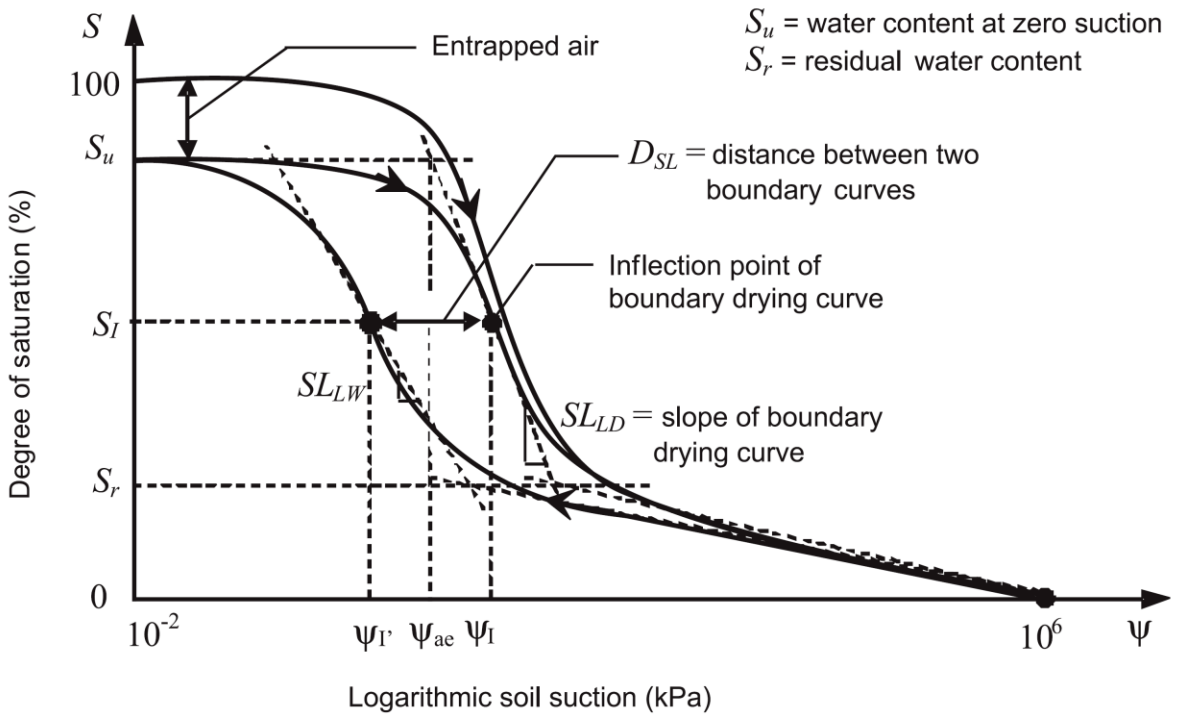

Figure 4.35: Initial and bounding SWCCs (Pham *et al.* 2005)

Pham *et al.* (2005) described the procedure for predicting the two bounding curves with knowledge of the initial desorption SWCC. The same curve-fitting parameters used for the initial desorption SWCC would be used for the desorption bounding curve. The two desorption curves could then be plotted using Equation (4.161) where $\mathbb{S}_u = 1$ in the case of the initial desorption SWCC. Based on the suggested values of R_{SL} and D_{SL}, $d_{\psi,w}$ and $b_{\psi,w}$ can be obtained from Equations (4.159) and (4.160), respectively. Using Equation (4.161) the adsorption bounding SWCC can therefore be predicted.

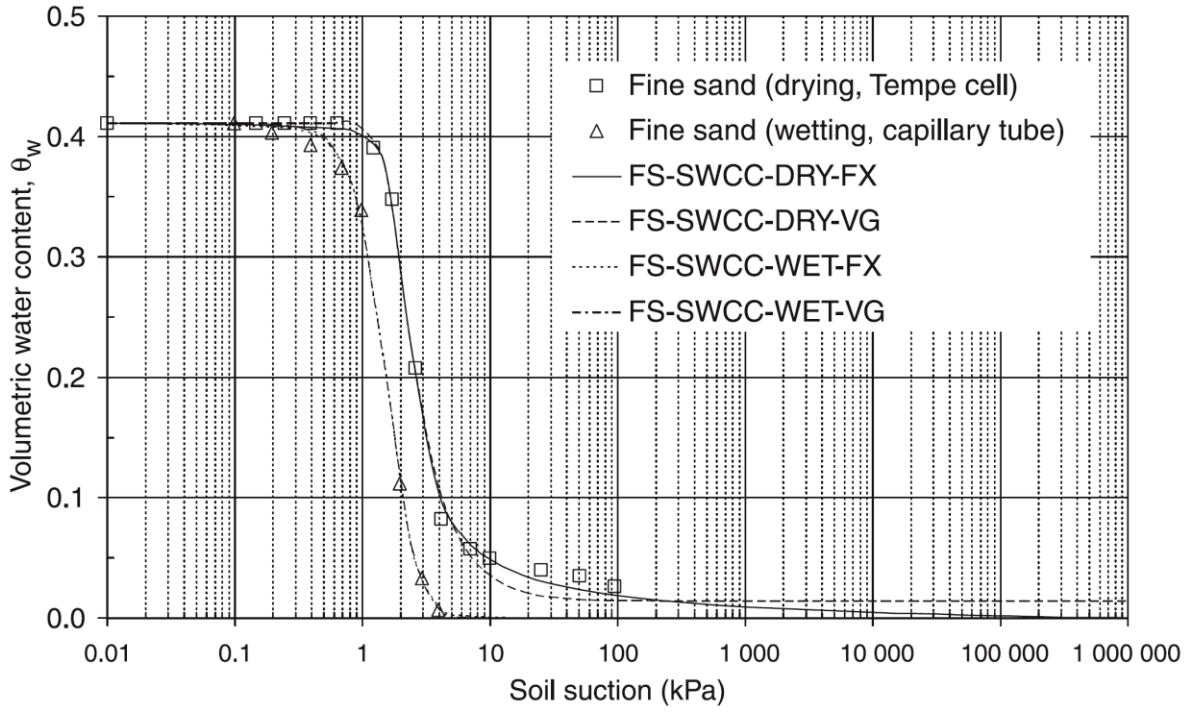

Figure 4.36: Hysteretic SWCCs for a fine sand (Yang *et al.* 2004)

4.5.2 Flow Behaviour

The hydraulic gradient is the fundamental driving potential for flow in porous media. It is described as the space rate of energy dissipation per unit weight of fluid and is expressed as (Harr, 1991):

$$i_\psi = -\frac{\Delta h}{\Delta s} \tag{4.162}$$

where, Δh is the difference in piezometric head between two adjacent equipotential lines and Δs is an incremental distance along the flow path. Note that the direction of the exit gradient will follow a decreasing piezometric head potential.

The flow velocity based on the gross cross-sectional area in the soil is referred to as the discharge velocity, and can be defined using Darcy's law as:

$$v_d = -\frac{\Delta h}{\Delta s} k_{sat} = k_{sat} i_\psi \tag{4.163}$$

where, k_{sat} is the saturated hydraulic conductivity of the soil and can either be measured or estimated using the following empirical formulations:

Chapuis (2004) $$k_{sat} = 10^{1.291e-0.6435}(d_{10})^{10^{0.5504-0.2937e}} \quad (4.164)$$

Den Adel (1987) $$k_{sat} = \frac{g}{160\nu} d_{15}^2 \frac{\lambda^3}{(1-\lambda)^2} \quad (4.165)$$

where, k_{sat} in den Adel (1987) is in units [m/s], and in Chapuis (2004) is in units [cm/s], e is void ratio, d_{10} is grain size in units [mm] at which 10% by weight of the sediment is finer and d_{15} is grain sizes in units [m] at which 15% by weight of the sediment is finer.

Although Darcy's law is expressed in differential form, it was derived using a continuum approach and therefore does not describe the flow behaviour on inter-granular scale (Harr, 1991). It is viewed as the equivalent of the Navier-Stokes equations in viscous laminar ground flow. The criterion for laminar flow in soil is often defined using the following criterion (Harr, 1991):

$$Re_s = \frac{v_d d_{50}}{\nu} \leq 1 \quad (4.166)$$

Where, Re_s is Reynolds number specific to flow in porous media.

The seepage velocity, v_s, which is the actual flow velocity through the void spaces is larger than v_d and can be expressed as:

$$v_s = \frac{k_{sat} i_\Psi}{\lambda} \quad (4.167)$$

In unsaturated soils, Darcy's law is also valid, but only for low hydraulic gradients (Richards, 1931) such that:

$$v_d = -\frac{\Delta h}{\Delta s} k_w(\psi) = k_w(\psi) i_\Psi \quad (4.168)$$

$$v_s = \frac{k_w(\psi) i_\Psi}{\lambda} \quad (4.169)$$

where, $k_w(\psi)$ is the hydraulic conductivity function.

Similar to hydrodynamic flow, the mass conservation principle can be applied to porous media (see Figure 4.37). Assuming low hydraulic gradients and that Darcy's law (see Equation (4.163)) also holds in the unsaturated zone, the 3-D unsteady partial differential equation governing flow through porous media can therefore be expressed as:

$$\frac{\partial}{\partial x}\left[k_{wx}(\psi)\frac{\partial h}{\partial x}\right]+\frac{\partial}{\partial y}\left[k_{wy}(\psi)\frac{\partial h}{\partial y}\right]+\frac{\partial}{\partial z}\left[k_{wz}(\psi)\frac{\partial h}{\partial z}\right]+\Psi_q=\frac{\partial \theta_w}{\partial t} \qquad (4.170)$$

or

$$\left(\frac{\partial k_{wx}(\psi)}{\partial x}\frac{\partial h}{\partial x}+\frac{\partial k_{wy}(\psi)}{\partial y}\frac{\partial h}{\partial y}+\frac{\partial k_{wz}(\psi)}{\partial z}\frac{\partial h}{\partial z}\right)+ k_{wx}(\psi)\frac{\partial^2 h}{\partial x^2}+k_{wy}(\psi)\frac{\partial^2 h}{\partial y^2}+k_{wz}(\psi)\frac{\partial^2 h}{\partial z^2}+\Psi_q=\frac{\partial \theta_w}{\partial t} \qquad (4.171)$$

where, $k_{wx}(\psi)$, $k_{wy}(\psi)$, and $k_{wz}(\psi)$ are hydraulic conductivity functions in the x, y and z-directions, respectively, and h is piezometric head (*i.e.* $h=u_w/\gamma_f+z$) and Ψ_q is a source term representing the volume of water per unit time entering across the soil boundary (*i.e.* boundary flux) per unit volume of soil. It is assumed that PAP is zero if no external loads are applied (Ng and Menzies, 2007).

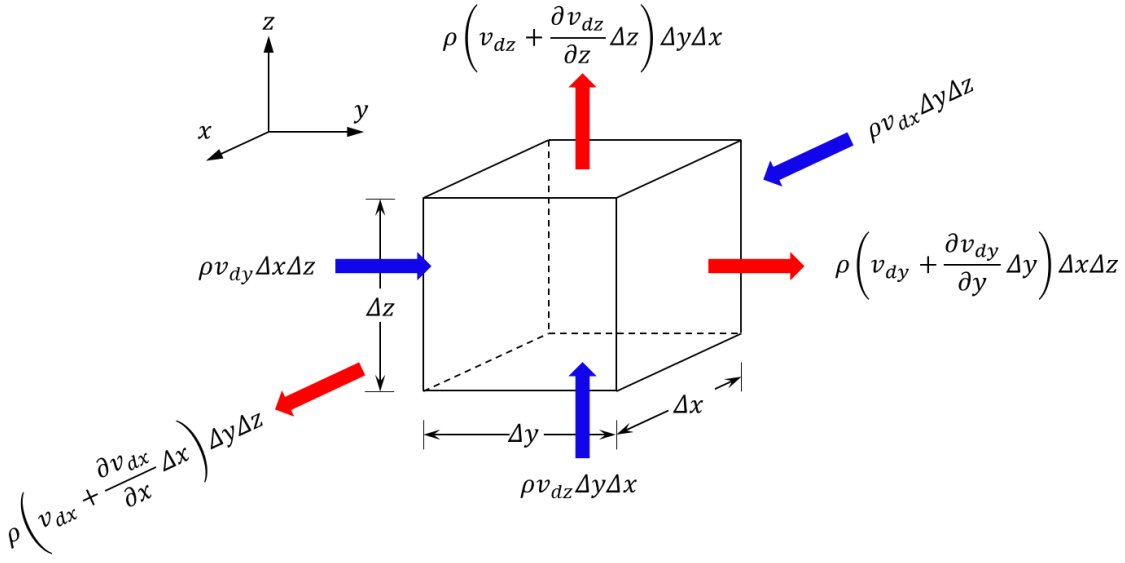

Figure 4.37: Cubic soil element showing mass fluxes (v_{dx}, v_{dy} and v_{dz} are discharge velocities in the x, y and z direction, respectively)

The unsteady term, $\partial\theta_w/\partial$t, in Equation (4.170) represents the rate of storage change and can be due to both matric suction and the net normal stress as follows (Ng and Shi, 1998):

$$\frac{\partial\theta_w}{\partial \mathrm{t}} = \frac{\partial\theta_w}{\partial(\sigma_n - u_a)}\frac{\partial(\sigma_n - u_a)}{\partial \mathrm{t}} + \frac{\partial\theta_w}{\partial(u_a - u_w)}\frac{\partial(u_a - u_w)}{\partial \mathrm{t}} = m_a\frac{\partial(\sigma_n - u_a)}{\partial \mathrm{t}} + m_w\frac{\partial(u_a - u_w)}{\partial t} \tag{4.172}$$

where, m_a and m_w are coefficients and can be considered constant over one time-step. Ng and Shi (1998) state that under saturated conditions, m_a is equivalent to the coefficient of volume change, m_v. Under transient conditions, it is assumed that both σ_n and u_a remain constant, and therefore the rate of storage change can be expressed only in terms of matric suction as follows:

$$\frac{\partial\theta_w}{\partial \mathrm{t}} = m_w\frac{\partial(u_a - u_w)}{\partial t} \tag{4.173}$$

where, m_w is the slope of the SWCC when the volumetric water content is defined as the ordinate.

Both Equation (4.170) and Equation (4.172) comprise Richards' Equation (Richards, 1931), which is commonly cited in literature as the fundamental equation that governs flow in saturated/unsaturated media (Wang and Anderson, 1982; Cedergren, 1989; Fredlund *et al.* 1994; Ng and Shi, 1998; Fredlund, 2000; Simon and Collison, 2001; Fredlund, 2006; Ng and Menzies, 2007; Fox *et al.* 2010; Flores-Berrones and Lopez-Acosta, 2011; Botros *et al.* 2012).

Under saturated conditions ($\theta_w = \theta_s$ or $\mathbb{S} = 1$), the hydraulic conductivity is constant and is defined as k_{sat}. Under isotropic soil conditions, $k_{wx}(\psi) = k_{wy}(\psi) = k_{wz}(\psi) = k_w(\psi)$, and under homogeneous soil conditions, $\partial k_{wx}(\psi)/\partial x = \partial k_{wy}(\psi)/\partial y = \partial k_{wz}(\psi)/\partial z = 0$.

Assuming, isotropic, homogeneous and steady-state seepage conditions, Richards' Equation therefore reduces to:

$$\frac{\partial^2 h}{\partial x^2} + \frac{\partial^2 h}{\partial y^2} + \frac{\partial^2 h}{\partial z^2} = 0 \qquad (4.174)$$

Equation (4.174) is a Laplacian equation which is represented by two families of curves, flowlines and equipotential lines, which intersect at right angles (Cedergen, 1989). These two families of curves are referred to as a “flownet”. Figure 4.38 illustrates a flownet for a homogeneous embankment body under steady-state seepage conditions. The Poisson equation by Richards (1931) differs from Equation (4.174), since a transient flownet analysis is required to solve the flow through the porous media (Cedergren, 1989).

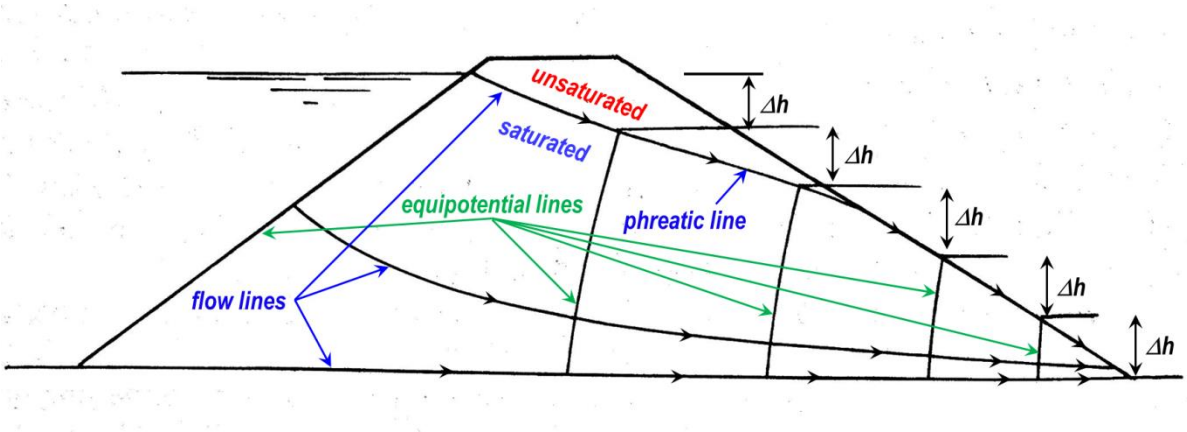

Figure 4.38: Flownet for homogeneous embankment body on impervious foundation under steady-state seepage conditions (after Cedergren, 1989)

The hydraulic conductivity is largely a function of the stress-state within the soil as well as the pore size. At zero soil-suction, the hydraulic conductivity is at its saturated value and remains constant at relatively low suction values. As air begins to enter into the largest pores, discontinuities appear in the water phase and the hydraulic conductivity significantly decreases. It continues to decrease linearly (on a logarithmic abscissa) until the residual conditions have been reached, after which it reaches a pseudo-constant value (Fredlund, 2000,2006). At high suction values, the hydraulic conductivity of noncohesive soils can even become lower than for cohesive soils (Fredlund, 2000; Ng and Menzies, 2007) (see Figure 4.39). In the

case of cohesive soils swelling and shrinking due to the matric suction will likely complicate the matter.

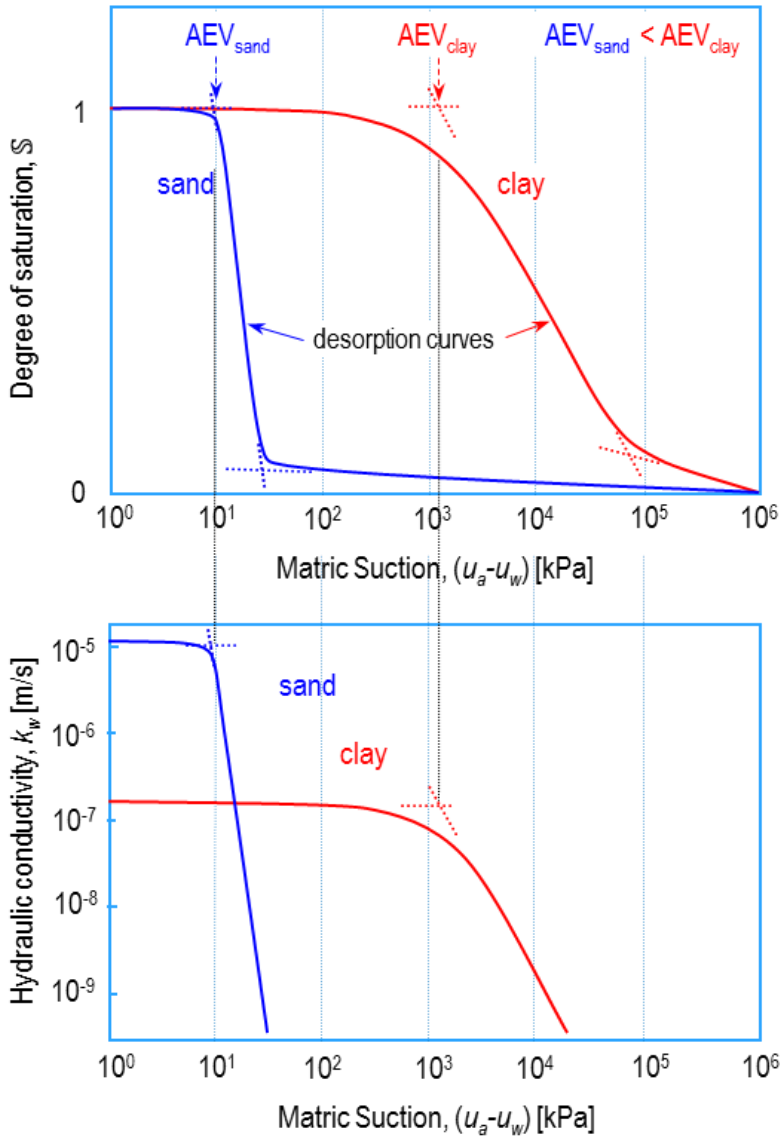

Figure 4.39: Hypothetical relationship between SWCCs (shown at the top) and hydraulic conductivity functions (shown at the bottom) for two soil types

When experimental methods for determining the hydraulic conductivity of a soil under unsaturated conditions are not available, indirect methods must be employed. Similar to the SWCC, the theoretical shape of the hydraulic conductivity function, a relationship between hydraulic conductivity and matric suction, can also be

predicted. Fredlund *et al.* (1994) described two approaches for predicting the hydraulic conductivity function: empirically and statistically-based. Empirically-based approaches require that the number of measured data points exceed the number of curve-fitting parameters that are to be employed. Statistically-based approaches relate pore-size distribution to the hydraulic conductivity function and require the knowledge of the saturated hydraulic conductivity and the SWCC (Fredlund, 2006). Van Genuchten (1980) referred to the latter approach, as Burdine-based equations (*e.g.* Burdine, 1953; Brooks and Corey, 1964). The hydraulic conductivity function is usually defined in terms of the SWCC parameters.

Brooks and Corey (1964) expressed the permeability function using the following expression:

$$k_w(\psi) = k_{sat} \text{ for } \psi < \psi_b$$

and

$$k_w(\psi) = k_{sat}\mathbb{S}_e^{\frac{2+3\lambda_\psi}{\lambda_\psi}} = k_{sat}\left(\frac{\psi_b}{\psi}\right)^{2+3\lambda_\psi} \text{ for } \psi > \psi_b \quad (4.175)$$

Green and Corey (1971) derived the hydraulic conductivity based on Poiseuille's formulation and using pore-size distribution data in the following form:

$$k_w(\theta_{w,i}) = \frac{k_{sat}}{k_{sat,c}}\frac{\sigma^2\rho g}{2\mu}\frac{\lambda^{p_{gc}}}{N_s^2}\sum_{j=i}^{j_{max}}\left[(2j+1-2i)\psi_j^{-2}\right] \quad (4.176)$$
$$i = 1,2,\dots,j_{max}$$

where, $\theta_{w,i}$ is volumetric water content corresponding to the ith pore class computed between θ_s and $\theta_w = 0$, p_{gc} is a parameter that accounts for interaction of various pore classes ($1.0 < p_{gc} < 2.0$), σ_t is surface tension, N_s is total number of pore classes between θ_s and $\theta_w = 0$, i is the interval which increases with decreasing water content, j is a counter from 1 to j_{max}, which is the pore class corresponding to the lowest water content, $k_{sat}/k_{sat,c}$ is a matching factor (measured saturated hydraulic conductivity ÷ calculated hydraulic conductivity, where $k_{sat,c}$ is the calculated hydraulic conductivity at zero pressure and can be expressed as:

$$k_{sat,c} = \sum_{j=1}^{j_{max}}\left[(2j+1-2i)\psi_j^{-2}\right] \quad (4.177)$$

Van Genuchten (1980) proposed the following expression for predicting the hydraulic conductivity as:

$$k_w(\psi) = \frac{\left\{1-(\alpha_\psi \psi)^{n_\psi - 1}\left[1+(\alpha_\psi \psi)^{n_\psi}\right]^{-m_\psi}\right\}^2}{\left[1+(\alpha_\psi \psi)^{n_\psi}\right]^{m_\psi/2}} \tag{4.178}$$

Fredlund *et al.* (1994) integrated the Fredlund and Xing (1994) curve-fitting equation with a model which predicts the hydraulic conductivity using pore-size distributions. Their integral-form expression for the hydraulic conductivity function is:

$$k_w(\psi) = k_{sat} \int_{\ln(\psi)}^{\ln(1000000)} \frac{\theta_w(\mathbf{e}^{y_\psi}) - \theta_w(\psi)}{\mathbf{e}^{y_\psi}} \theta_w'(\mathbf{e}^{y_\psi}) dy_\psi \div \int_{\ln(\psi_r)}^{\ln(1000000)} \frac{\theta_w(\mathbf{e}^{y_\psi}) - \theta_s}{\mathbf{e}^{y_\psi}} \theta_w'(\mathbf{e}^{y_\psi}) dy_\psi \tag{4.179}$$

where, y_ψ is a dummy variable of integration representing soil-suction, and θ_w' is the derivative of the SWCC when the ordinate is volumetric water content.

While there is lack of data on the hydraulic conductivity function beyond residual conditions, all the expressions seem to provide reasonable predictions from saturation conditions and well beyond the air entry value (Fredlund, 2000, 2006). It is expected, however, that if there is hysteresis in the capillary-moisture relationship, there will also be hysteresis in the hydraulic conductivity function (Ng and Menzies, 2007). However, this hysteresis will not transpire if hydraulic conductivity is assessed from a water content dependency point of view. Van Genuchten (1980) stated that regardless of whether the soil undergoes desaturation or saturation, the mathematical models which predict the hydraulic conductivity (as a function of matric suction) could still be applied.

4.5.3 Shear Strength

In saturated soils, positive PWP reduces the total stress carried by the grain particles according to the effective stress balance in Equation (4.147). The failure shear stress on the failure plane for soils under saturated soil conditions can be expressed using the following Mohr-Coulomb failure criterion:

$$\tau_{ff} = c' + (\sigma_n - u_w)_{ff} \tan \phi' \tag{4.180}$$

where, c' and ϕ' are the soil cohesion and angle of internal friction, respectively, determined using an effective stress analysis approach, and $(\sigma_n - u_w)_{ff}$ is the effective stress such that the subscript ff represents the conditions at the failure envelope on a failure plane.

The contractile skin present due to the occluded air bubbles creates attraction forces which stabilize the soil matrix. This phenomenon can be illustrated by extending the Mohr-Coulomb shear-failure criteria by means of the two stress-state variable, net normal stress and matric suction as shown in Figure 4.40.

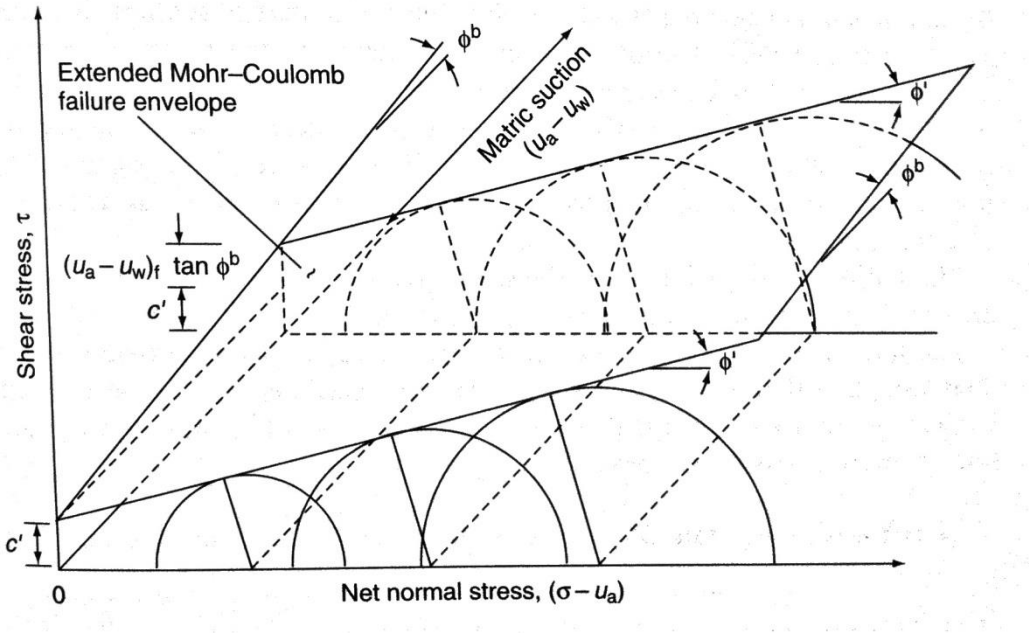

Figure 4.40: Extended Mohr-Coulomb failure envelope for soils under unsaturated conditions (Ng and Menzies, 2007 after Fredlund and Rahardjo, 1993)

Fredlund *et al.* (1978) proposed the shear strength failure envelope as a function of the stress-state as follows:

$$\tau_{ff} = c' + (\sigma_n - u_a)_{ff} \tan \phi' + (u_a - u_w)_{ff} \tan \phi^b \qquad (4.181)$$

where, ϕ^b is an angle which represents the rate of increase in shear strength due to matric suction.

The last (and nonlinear) term in Equation (4.181) is also referred to as apparent cohesion or soil cohesion due to matric suction. For all soil types, the matric suction at saturated or near saturated soil conditions is present at all contact points of the soil matrix, where $\phi' = \phi^b$. As the matric suction increases the shear strength increases linearly. However, as the AEV is approached the number of occluded air bubbles increases and consequently reduces the contractile skin interphase and the shear strength contribution due to suction. Coarse-grained soils can even exhibit a reduction in shear strength during desorption (see Figure 4.41).

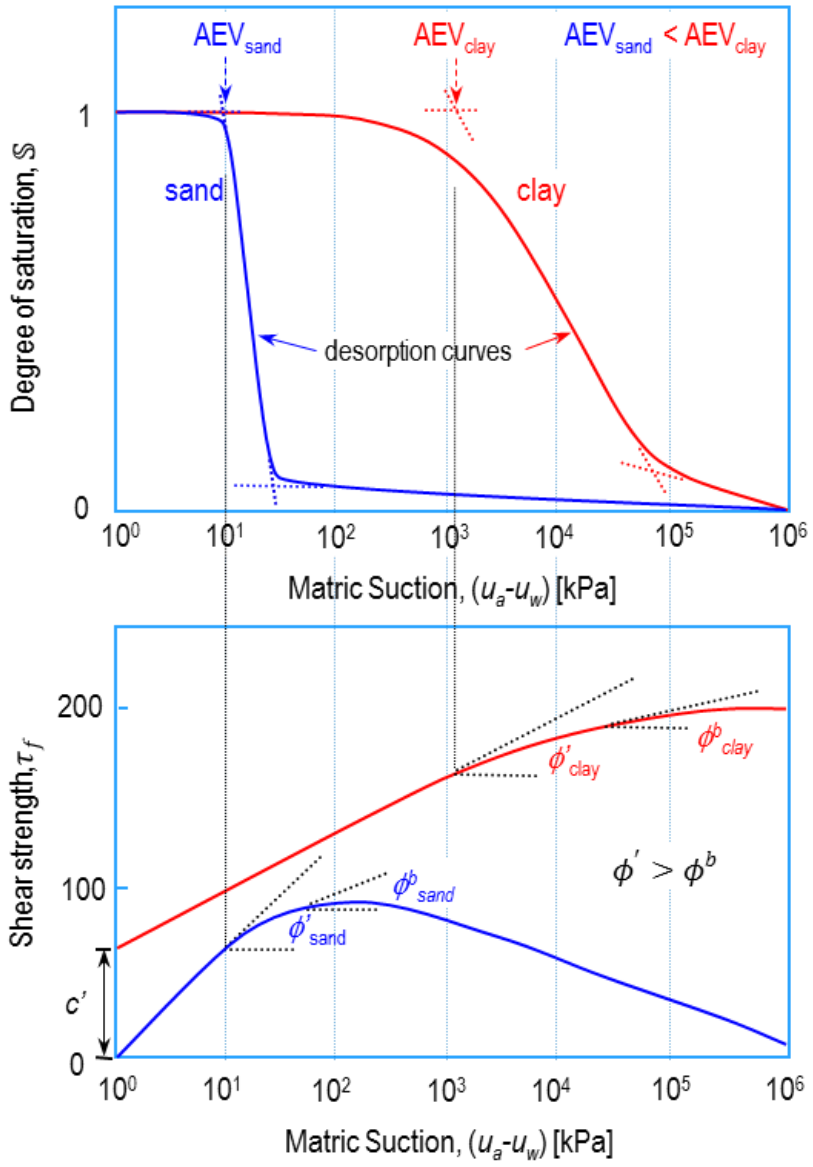

Figure 4.41: Hypothetical relationship between SWCCs (shown at the top) and shear strength (shown at the bottom) for two soil types

It is often difficult and time consuming to determine the unsaturated shear strength of a soil using experimental methods (Öberg and Sällfors, 1997). Several empirical relationships have therefore been developed for predicting the unsaturated shear strength of a soil using the SWCC. Lamborn (1986) extended the theory of micromechanics of irreversible thermodynamics to the energy-volume relationship in

saturated-unsaturated porous media (Vanapalli and Fredlund, 1999). The shear strength, τ_m, was expressed in Lamborn's model as:

$$\tau_{ff} = c' + (\sigma_n - u_a)\, tan\, \phi' + (u_a - u_w)\theta_w\, tan\, \phi' \qquad (4.182)$$

Vanapalli *et al.* (1996) developed two approaches that describe the non-linear behaviour of the shear strength due to matric suction:

Procedure I $$\tau_{ff} = c' + (\sigma_n - u_a) \tan \phi' + (u_a - u_w)\mathbb{S}^{\kappa_\psi} \tan \phi' \qquad (4.183)$$

Procedure II $$\tau_{ff} = c' + (\sigma_n - u_a) \tan \phi' + (u_a - u_w)\mathbb{S}_e \tan \phi' \qquad (4.184)$$

where, κ_ψ is a fitting parameter.

Öberg and Sällfors (1997) proposed the following expression for the shear strength of unsaturated silts and sands:

$$\tau_{ff} = c' + (\sigma_n - u_a)\, tan\, \phi' + (u_a - u_w)\mathbb{S}\, tan\, \phi' \qquad (4.185)$$

4.6 Seepage-Induced Slope Instabilities and Erosion

4.6.1 Seepage across Porous Boundaries

The influence of seepage on slope instability and particle mobility may be investigated using force/moment balances on a soil continuum or a single particle, respectively. Several approaches have been developed to define slope stability and particle mobility using incipient motion criteria, however, the resulting formulations are numerous due to the various hydraulic and geotechnical aspects involved. A strictly hydraulic approach may consider the influence of seepage as well as the hydrodynamic forces acting on the interfacial grains on a steep slope. A strictly geotechnical approach, on the other hand, may evaluate the instability due to seepage by means of a Mohr-Coulomb equilibrium or bed fluidization (*i.e.* static liquefaction). The slope instability mechanism is planar (*i.e.* 2-D), therefore all the analyses described are evaluated based on unit widths.

4.6.2 Slope Stability Analyses using Mohr-Coulomb Failure Criterion

Slope stability analyses are methods by which the shear stress developed along an expected failure surface is compared with the shear strength of a soil (Das, 2002). The surface which is most prone to failure is the surface which yields the lowest factor of safety (FOS), a ratio which describes the condition of limiting equilibrium. The FOS can be defined as the ratio of shear stress at failure to the applied shear strength:

$$FOS_F = \frac{\tau_{ff}}{\tau_m} \tag{4.186}$$

While the FOS in Equation (4.186) is represented by horizontal equilibrium of forces, the FOS can also be defined as the ratio of the resisting and driving moments, M_r and M_d, respectively:

$$FOS_M = \frac{M_r}{M_d} \tag{4.187}$$

The general limit equilibrium (GLE) method employs both equilibrium approaches (Krahn, 2004), however, it does not formulate all the physical laws governing slope instability since strains and displacements are not taken into account (Krahn, 2004).

Slope instabilities are categorised into rotational, translational or compound slips (see Figure 4.42). Craig (2004) stated that rotational slips are curved, and often take the form of a circular arc. Circular slips occur in homogeneous and isotropic soil conditions, whereas non-circular and curved slips are attributed to non-homogeneous soil conditions. Translational and compound slips occur when the failure surface is driven by the presence of an underlying soil region with different shear strength.

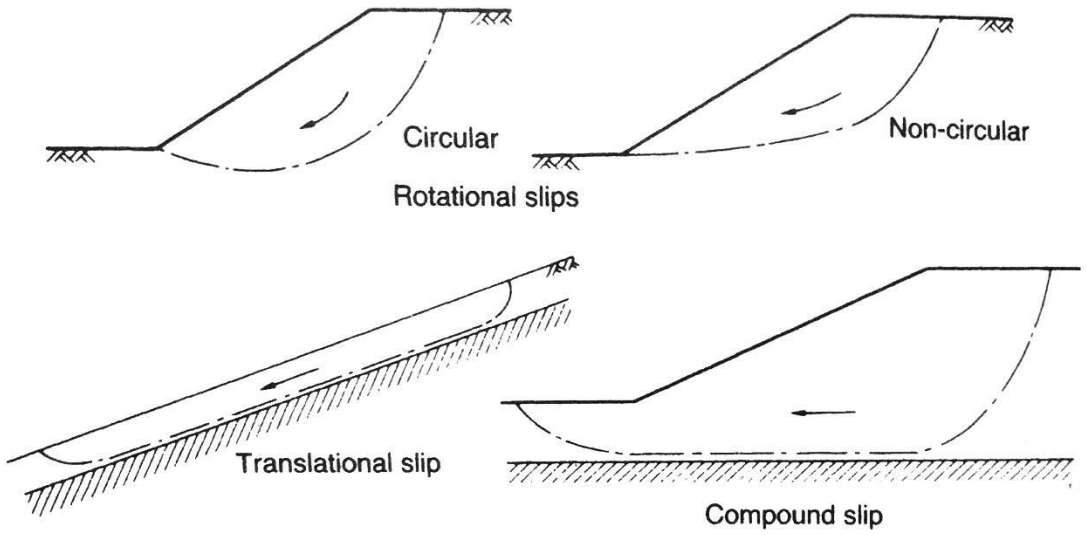

Figure 4.42: Types of slope instabilities (Craig, 2004)

Das (2002) distinguished between two stability analyses: mass procedure and method of slices. Both methods assume that the potential failure surface is a concave circular arc with a radius of curvature, r, and a centre, O, using a series of trials. The critical failure surface will then be based on the trial which yields the lowest FOS. The mass procedure shown in Figure 4.43, considers the soil above the potential failure surface as one unit, thus assuming homogeneous soil conditions. It is often used in undrained shear strength scenarios such that the shear strength is only comprised of the undrained cohesion, c_u (*i.e.* $\tan\phi = 0$) and which does not vary with depth. The maximum applied shear stress using the force equilibrium method can be expressed as:

$$\tau_m = \frac{\tau_{ff}}{FOS_F} = \frac{c_u}{FOS_F} \tag{4.188}$$

For equilibrium, the moments about O can be equated:

$$\tau_m L_a r = W d_W \tag{4.189}$$

where, L_a is arc length, W is the weight of soil above the failure surface, and d_W is the moment arm. The FOS can therefore be expressed as:

$$FOS_F = \frac{c_u L_a r}{W d_W} \tag{4.190}$$

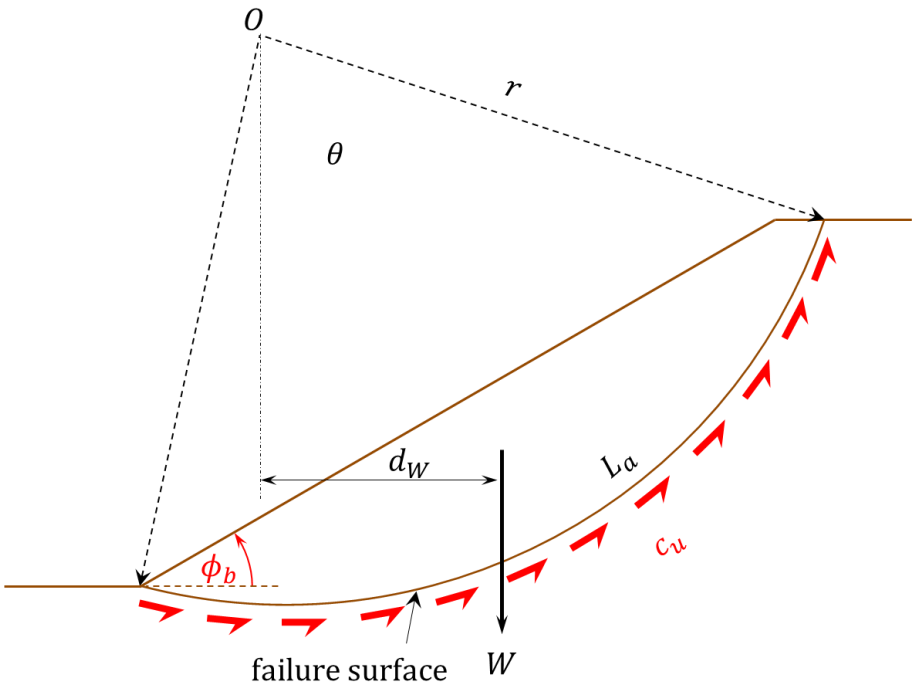

Figure 4.43: Mass failure analysis (W: weight of soil above failure surface; d_W: moment arm; L_a: length of failure surface; θ: arc angle)

The method of slices, shown in Figure 4.44, is more versatile since it discretizes the soil above the potential failure surface into vertical planes and therefore considers soil heterogeneity and variations in PWP (Das, 2002). The FOS using a force and moment equilibrium for a saturated-unsaturated soil undergoing a circular slip can therefore be expressed as (Fredlund, 1987):

$$FOS_F = \frac{\sum_{i=1}^{i=i_{max}} \left\{ c_i' b_i \cos\alpha_i + \left[N_i - u_{w,i} b_i \frac{\tan\phi^b}{\tan\phi'} - u_{a,i} b_i \left(1 - \frac{\tan\phi^b}{\tan\phi'} \right) \right] \tan\phi' \cos\alpha_i \right\}}{\sum_{i=1}^{i=i_{max}} N_i \sin\alpha_i} \tag{4.191}$$

$$FOS_M = \frac{\sum_{i=1}^{i=i_{max}} \left\{ c_i' b_i r + \left[N_i - u_{w,i} b_i \frac{\tan\phi^b}{\tan\phi'} - u_{a,i} b_i \left(1 - \frac{\tan\phi^b}{\tan\phi'} \right) \right] r \tan\phi' \right\}}{\sum_{i=1}^{i=i_{max}} W_i x_i} \tag{4.192}$$

where, subscript i implies a vertical slice, i_{max} is the maximum number of slices, N_i is the normal reaction force acting at the base slice, α_i is the angle of the base slice with respect to the horizontal, x_i is the distance between the centre of the base slice

to the centre of rotation, $\phi^b = \phi'$ for saturated soils and u_w may be positive or negative depending on the location of the phreatic surface (see Figure 4.44).

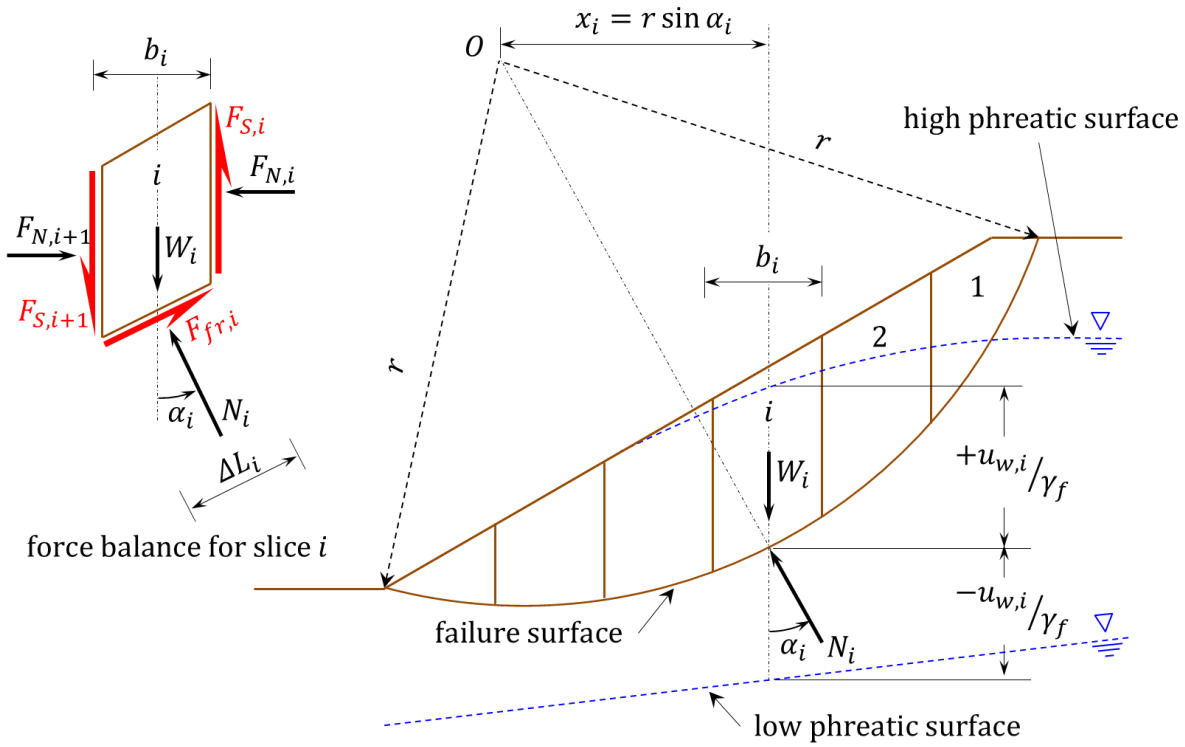

Figure 4.44: Slope stability analysis showing method of slices (ΔL_i: incremental length of base slice)

The summation of the normal forces acting on the sides of the vertical slice, $F_{N,i}$ and $F_{N,i+1}$, can be expressed as:

$$F_{N,i} - F_{N,i+1} = \left[W_i - \left(F_{S,i} - F_{S,i+1}\right)\right] \tan \alpha_i - \frac{F_{fr,i}}{\cos \alpha_i} \tag{4.193}$$

where, F_S is the vertical interslice shear force and F_{fr} is the frictional force acting at the base slice and can be defined as:

$$F_{fr,i} = \frac{\mathrm{b}_i\left[c_i' + (\sigma_n - u_a)_i \tan \phi' + (u_a - u_w)_i \tan \phi^b\right]}{FOS_F} \tag{4.194}$$

A second relationship relating the normal and vertical shear forces acting on the sides of the slice in the form of a mathematical function can be found in Fredlund

(1987) and Krahn (2004). As a matter of fact, there are several methods by which the method of slices can be solved. The Morgenstern method of slices has been developed to determine the FOS for a potentially unstable slope due to a rapid drawdown condition. Additional details on this method as well as other methods for slope stability analyses can be found in Das (2002), Craig (2004) and Krahn (2004).

Krahn (2004) stated that for noncohesive soils, the slope instability will tend towards the infinite slope scenario. This implies a translational slope movement where the radius of curvature will tend to infinity. The FOS in the case of translational slope movement and where $u_w = 0$ can be defined as (Das, 2002; Craig, 2004; Krahn, 2004):

$$FOS_F = \frac{\tan \phi'}{\tan \phi_b} \tag{4.195}$$

The stability of a slope comprised of a saturated noncohesive soil with parallel seepage can be evaluated using the seepage force or boundary pore method (see Figure 4.45). Soong and Koerner (1996) demonstrated that both methods will yield the same result. The FOS can therefore be expressed as (Soong and Koerner, 1996; Das, 2002; Craig, 2004):

$$FOS_F = \frac{\gamma_f (G_s - 1)}{\gamma_{sat}} \frac{\tan \phi'}{\tan \phi_b} \tag{4.196}$$

where, γ_{sat} is the saturated unit weight of the soil defined as:

$$\gamma_{sat} = \frac{\gamma_f (G_s + e)}{1 + e} \tag{4.197}$$

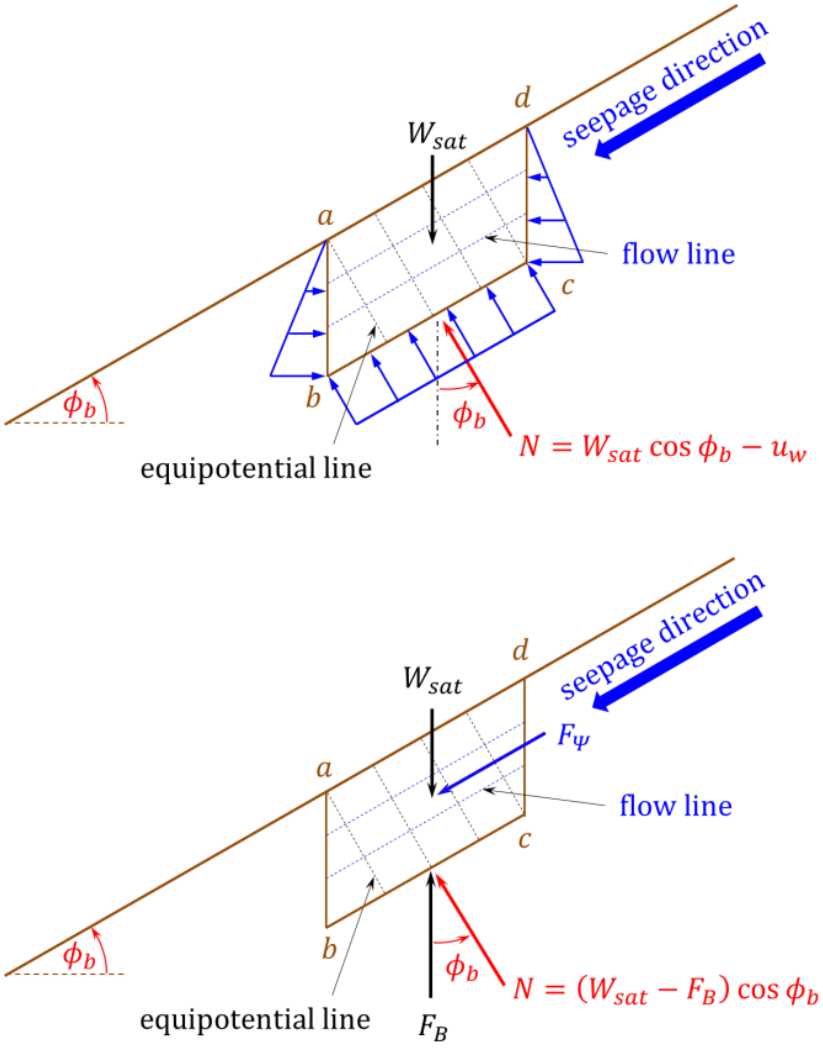

Figure 4.45: Stability analysis of saturated infinite slope using (top) boundary pore pressure method (bottom) seepage force method (after Soong and Koerner, 1996)

The forces shown in Figure 4.45 can be expressed as:

Saturated weight	$W_{sat} = \gamma_{sat} \forall_{abcd}$	(4.198)
Buoyancy force	$F_B = \gamma_f \forall_{abcd}$	(4.199)
Seepage force	$F_\psi = i_\psi \gamma_f \forall_{abcd}$	(4.200)

4.6.3 Slope Stability Analyses using Static Liquefaction Criterion

Static liquefaction will occur when the seepage forces give rise to a zero effective stress in the vertical direction. This occurs when the hydraulic gradient reaches its

critical value, i_c. For a soil-air or soil-water boundary, the incipient bed fluidization criterion can be defined by means of an exit hydraulic gradient, i_e, such that $i_e \leq i_c$ and where i_e is positive into the bed (*i.e.* downward seepage). For a horizontal bed, the critical value for the hydraulic gradient can be expressed as:

$$i_c = -(1-\lambda)(G_s - 1) \tag{4.201}$$

For a steep slope with steady-state seepage and atmospheric pressure conditions at the boundary as shown in Figure 4.46, the exit hydraulic gradient along the seepage line can be expressed as (Howard and McLane, 1988; Ghiassian and Ghareh, 2008):

$$i_e = -\frac{\Delta h}{L} = -\frac{\sin\phi_b}{\cos\left(\frac{\pi}{2}-\Psi\right)} = -\frac{\sin\phi_b}{\sin\Psi} \tag{4.202}$$

where, Ψ is the seepage exit angle.

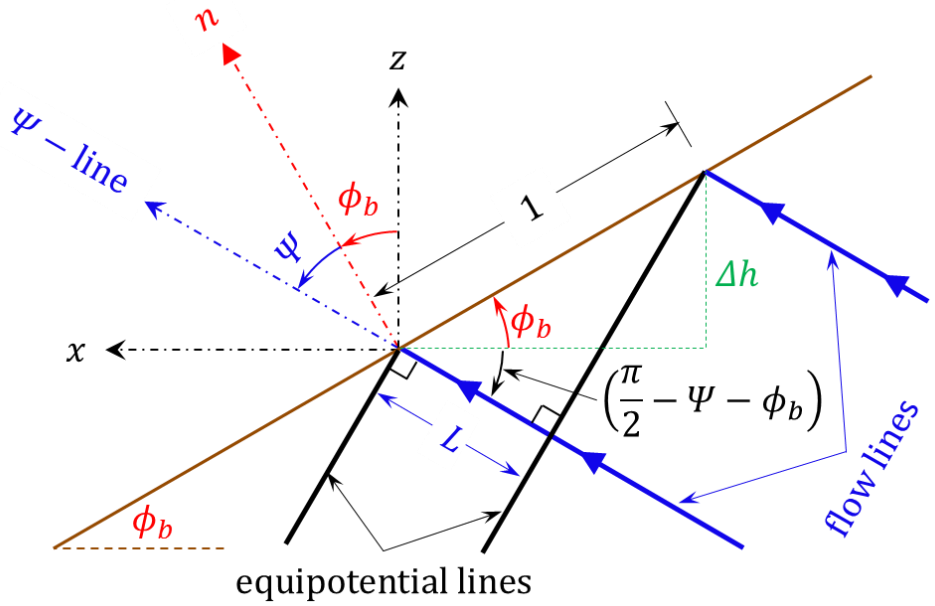

Figure 4.46: Flownet on a sloping bed showing flow (seepage) and equipotential lines (n: coordinate perpendicular to bed plane)

Van Rhee and Bezuijen (1992) distinguished between two methods that describe the incipient bed fluidization criterion for a sandy slope: a single particle approach,

which considers the forces acting on a single grain (*e.g.* Martin and Aral, 1971; van Rhee and Bezuijen, 1992; Chu-Agor *et al.* 2009), and a continuum approach, which considers the forces acting on a surficial soil element (Madsen, 1974; van Rhee and Bezuijen, 1992; Iverson and Major, 1986; Wörman, 1993; Soong and Koerner, 1996; Ghiassian and Ghareh, 2008; Chu-Agor *et al.* 2009). These two approaches have also been described by Chu-Agor *et al.* (2009) as single particle mobilization and mass failure, respectively.

Van Rhee and Bezuijen (1992) found that the single particle approach was in better agreement with their experiments in the case of infiltration (*i.e.* downward seepage), while the continuum approach gave a better experimental agreement for exfiltration (*i.e.* upward seepage) (see Figure 4.47). They derived the hydraulic gradient for a critically stable slope based on a seepage force normal to the bed using moment and force equilibrium balances, respectively, shown in the following expressions:

Single particle approach $$i_c = -\frac{4}{3}(G_s - 1)\frac{\sin(\phi_r - \phi_b)}{\sin\phi_r} \quad (4.203)$$

Continuum approach $$i_c = -(1 - \lambda)(G_s - 1)\frac{\sin(\phi_r - \phi_b)}{\sin\phi_r} \quad (4.204)$$

where, i_c is positive into the slope (*i.e.* downward seepage). Note the same slope factor used for the incipient motion in Equation (4.103).

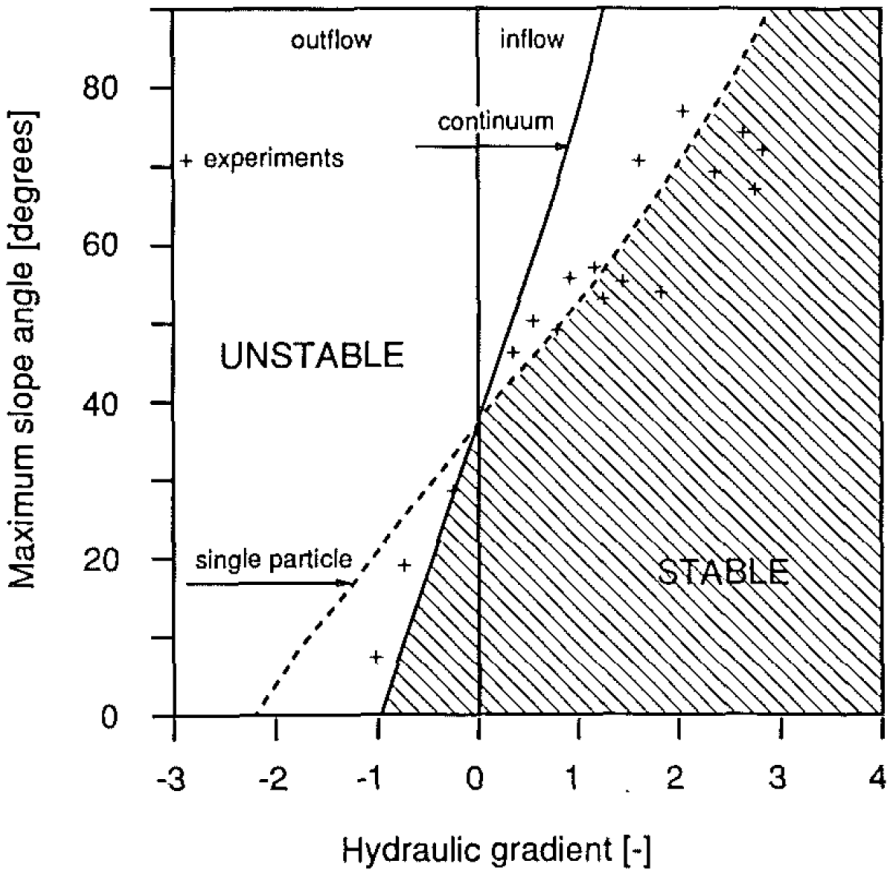

Figure 4.47: Stability criteria for single particle and continuum approaches (van Rhee and Bezuijen, 1992)

Ghiassian and Ghareh (2008) derived an expression for the critical seepage angle for Coulomb-sliding and static liquefaction using the infinite slope theory as:

Coulomb-sliding $$\Psi_c \leq \tan^{-1}\left(\frac{\tan\phi_b \tan\phi'}{\tan\phi' - 2\tan\phi_b}\right) \quad (4.205)$$

Static liquefaction $$\Psi_c \leq \tan^{-1}\left(\frac{\tan\phi_b}{2\tan^2\phi_b + 1}\right) \quad (4.206)$$

4.6.4 Seepage-induced Erosion Mechanisms

As stated in Subsection 4.2.3, incipient motion for a submerged particle is largely a function of the drag force. At near incipient bed-fluidisation conditions, the seepage force across the porous boundary becomes very important. An upward seepage force will therefore decrease particle stability. Several studies have extended the

single particle approach to include the hydrodynamic forces such as drag and lift (*e.g.* Martin, 1970; Howard and McLane, 1988; Wörman, 1993; Baldock and Holmes, 1998; Cheng and Chiew, 1999b; Simon and Collison, 2001; Dey and Zanke, 2004; Francalanci *et al.* 2008). Few studies, however, have considered the lift force in their force/moment balance analysis to determine the incipient motion criterion in noncohesive (Cheng and Chiew, 1999b) and cohesive (Simon and Collison, 2001) beds. The analysis of both studies, however, was limited to mild or horizontal slopes. As shown in Figure 4.48, the forces acting on a uniform sediment particle of spherical shape can be expressed as:

Drag $$F_D = C_D \frac{\pi d_0^2}{8} \rho u_m^2 \quad (4.207)$$

Lift $$F_L = C_L \frac{\pi d_0^2}{8} \rho u_m^2 \quad (4.208)$$

Gravity $$F_G = \frac{\pi d_0^3}{6} \gamma_f G_s \quad (4.209)$$

Buoyancy $$F_B = \frac{\pi d_0^3}{6} \gamma_f \quad (4.210)$$

and the submerged gravitational force is defined as:

$$F_G' = \frac{\pi d_0^3}{6} \gamma_f (G_s - 1) \quad (4.211)$$

where, C_D and C_L are the coefficients of drag and lift for a spherical object, u_m is the approach velocity acting on the particle and which varies with Re^*, and the characteristic grain size, d_0, is uniform for all sediment particles.

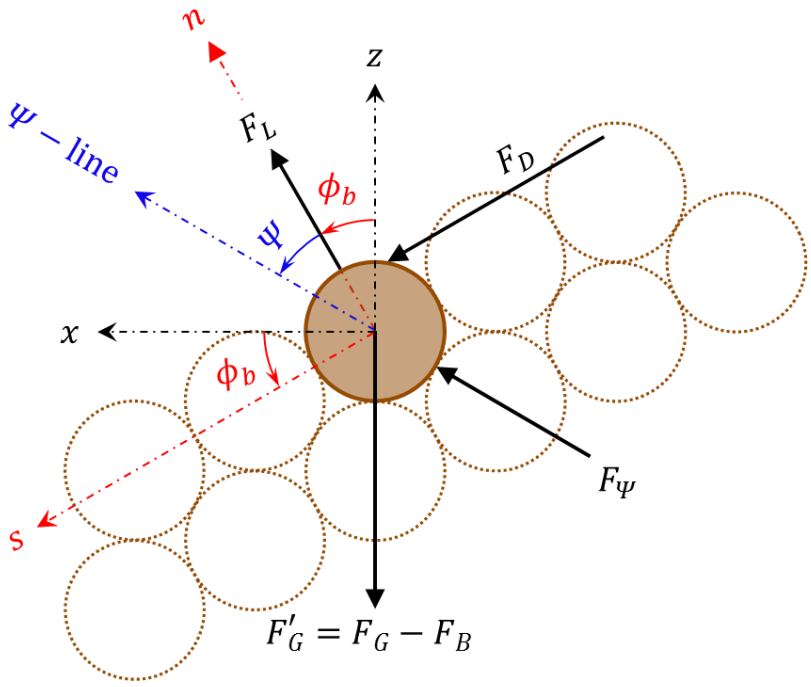

Figure 4.48: Seepage and hydrodynamic forces acting on a sediment particle (F'_G submerged gravitational force)

The seepage force bears various representations in literature. Van Rhee and Bezuijen (1992) considered that the seepage force is a result of the exit hydraulic gradient acting on the lower half of the interfacial grain, such that:

$$F_\Psi = \frac{\pi d_0^2}{8} i_e \gamma_f \tag{4.212}$$

Cheng and Chiew (1999b) evaluated the number of spherical particles with diameter, d_1, per unit volume of solids to be $6(1-\lambda)/\pi d_0^3$ and therefore expressed the seepage force as:

$$F_\Psi = \frac{\pi d_0^2}{6(1-\lambda)} i_e \gamma_f \tag{4.213}$$

Simon and Collison (2001) assumed that the seepage force acts over the entire volume of the particle, such that:

$$F_\Psi = \frac{\pi d_0^2}{6} i_e \gamma_f \tag{4.214}$$

Dey and Zanke (2004) considered the seepage force on the most stable 3-D configuration of solitary spherical particle with diameter, d_1, over three densely-packed particles having a diameter, d_2. They expressed the seepage force as:

$$F_\Psi = \frac{\rho}{6}\frac{v_d^2}{\lambda^2}\pi\left(\frac{d_1 d_2}{d_1+d_2}\right)^2 \tag{4.215}$$

Martin (1970) expressed the condition of instability in terms of the coefficient of static friction:

$$\tan\phi_r = \frac{\sum F_\parallel}{\sum F_\perp} \tag{4.216}$$

where, $\sum F_\parallel$ and $\sum F_\perp$ is the summation of forces acting parallel and perpendicular to the bed plane, respectively. The Shields function in Equation (4.96) was then modified to account for boundary seepage as:

$$\frac{\tau_{c,\Psi}}{[\gamma_s-\gamma_f-C_\Psi(1-\lambda)\gamma_f i_e]d_M\, tan\,\phi_r} = \mathcal{F}\left(\frac{u_c^* d_M}{\nu}\right) \tag{4.217}$$

where, C_Ψ is the ratio of seepage force on interfacial grains to that of grains well within the bed (*i.e.* $F_\Psi = i_e C_\Psi \gamma_f \forall$).

Baldock and Holmes (1998) and Cheng and Chiew (1999b) expressed the modified dimensionless shear stress due to the presence of seepage across a porous boundary as:

$$\frac{\tau_\Psi^*}{\tau^*} = \frac{1}{\left(1-\frac{i_e}{i_c}\right)} \tag{4.218}$$

However, the boundary seepage mechanism is not as straightforward as it seems, since it also influences the boundary layer (Martin, 1970; Cheng and Chiew, 1998; Nielsen *et al.* 2001; Chen and Chiew, 2004). For upward seepage (exfiltration out of the bed), the boundary layer becomes thicker and therefore the shear stress is reduced. For downward seepage (infiltration into the bed), the boundary layer becomes thinner giving rise larger velocity gradients and a larger shear stress.

Furthermore, Martin (1970) and Martin and Aral (1971) state that the exit hydraulic gradient for the grains in the uppermost layer will be approximately one half of that in deeper layers ($C_\Psi = 0.35 - 0.40$). Nielsen (1998) addressed this mechanism as well as the effect of seepage on the boundary layer for the modified dimensionless shear stress as follows:

$$\tau_\Psi^* = \frac{\tau_b\left(1-\alpha_\Psi\frac{v_d}{u^*}\right)}{\rho g d_{50}\left(G_s-1-\beta_\Psi\frac{v_d}{k}\right)} \tag{4.219}$$

where, α_Ψ and β_Ψ are dimensionless coefficient which alter the shear stress due to seepage effects on the boundary layer and vertical drag force, respectively. The experimental study by Nielsen *et al.* (2001) found that the coefficients have the values 16 and 0.4, respectively.

Francalanci *et al.* (2008) used a similar expression to Nielsen (1998) without the dimensionless coefficients:

$$\tau_\Psi^* = \frac{\tau_b}{\rho g d_{50}(G_s-N_h)} \tag{4.220}$$

where, N_h is a dimensionless number which represents the deviation from the hydrostatic pressure distribution, and is expressed as:

$$N_h = -\frac{1}{\rho g}\frac{dp}{dz} = 1 + \frac{v_d}{k} \tag{4.221}$$

Cheng and Chiew (1998) and Francalanci *et al.* (2008) derived expressions for the porous-boundary shear stress in the presence of seepage. Their flume tests were comprised of a mobile bed fitted with a perforated surface underneath. Measurements of the water surface levels and flow velocities enabled them to evaluate the boundary shear stress resulting from upward and downward seepage. The bed shear stress for gradually-varied flow on mild slopes and steady flow conditions was expressed by Cheng and Chiew (1998) and Francalanci *et al*. (2008), respectively, as:

$$\tau_b = -\rho g \eta \frac{d\eta}{dx}\left(1 - \frac{\beta_M U^2}{g\eta}\right) - 2\beta_M \rho U v_d \tag{4.222}$$

$$\tau_b = \rho g \eta S_b - \rho g \eta \frac{d\eta}{dx}\left(1 - \frac{U^2}{g\eta}\right) - 2\rho U v_d \quad (4.223)$$

where, β_M is a momentum correction factor in Cheng and Chiew (1998).

Francalanci *et al.* (2008) estimated the sediment flux from the eroded bed using the 1-D sediment continuity equation. They interpolated a bedload transport formulation from the bed measurements, which resembled the MPM transport-capacity equation. Their interpolated bedload transport formulation was:

$$q_{bs}^* = 4.4158(\tau_\Psi^* - \tau_c^*)^{1.5} \quad (4.224)$$

Baldock and Nielsen (2010) stated that the expressions by Nielsen (1998) and Francalanci *et al.* (2008) do not give rise to zero effective stress for bed-incipient fluidization conditions, which was later acknowledged (Francalanci *et al.* 2010). They also stated that the particle fall velocity is two orders of magnitude larger than the maximum discharge velocity, therefore once a particle is mobilized and departs the bed matrix, it will not be influenced by the seepage forces. Baldock and Holmes (1998) note the same for saltating particles. As a result, Baldock and Nielsen (2010) challenged the notion of modifying the dimensionless bed shear stress and for its utilization in estimating the bedload transport rate. However, the authors concurred that the case would be different for sheet flow, where the sediment-fluid layer would have a direct interaction with the porous boundary (Baldock and Holmes, 1998; Baldock and Nielsen, 2010). Francalanci *et al.* (2010) challenge the statement by Baldock and Nielsen (2010) on whether seepage does in fact influence the physics of a departing bed particle. They insisted that bedload transport is a function of both entrainment and particle trajectory, and while the latter component has no direct interaction with seepage across a porous boundary, the former does. In closure, however, Francalanci *et al.* (2010) acknowledged that the influence of seepage on the dimensionless shear stress in comparison to the incipient motion criterion would be somewhat weaker. A comprehensive and state-of-the-art review of experimental investigations performed on seepage across mobile and porous boundaries over the past 40 years is presented in the study by Lu *et al.* (2008).

4.6.5 Hindered Erosion

The studies by van Rhee (2010) and Bisschop *et al.* 2010 described a seepage mechanism in noncohesive sediments which takes place at very high flow velocities. The studies stated that at velocities > 30 m/s, the top layer of the bed is sheared resulting in grain configurations with a higher porosity. This increased porosity or dilatant behaviour causes the water to flow into the sheared zone, therefore inducing a positive hydraulic gradient between the flow and the soil boundary. The downward seepage force therefore hinders particle entrainment and consequent erosion. This seepage mechanism described in this subsection is not reflected in the classical sediment transport formulations; however, the bed dilatancy due to dispersive stresses has been discussed by Bagnold (1966). Van Rhee (2010) expresses the relative porosity due to dilation as:

$$\Delta\lambda = \frac{\lambda_l - \lambda_0}{1-\lambda_l} \tag{4.225}$$

where, λ_l and λ_0 are porosity of the sheared and underlying layers, respectively.

Van Rhee (2010) assumed that the porosity of the sheared layer may be considered as the maximum porosity, λ_{max}. The hydraulic gradient for the top layer due to hindered erosion was then expressed as (van Rhee, 2010):

$$i_l = -\frac{\dot{E}}{k_l}\frac{\lambda_l - \lambda_0}{1-\lambda_l} = -\frac{\dot{E}}{k_l}\frac{\lambda_{max} - \lambda_0}{1-\lambda_{max}} \tag{4.226}$$

where, k_l is the corresponding hydraulic conductivity of the sheared layer and $\dot{E}/k_l$ is referred to as the relative erosion rate.

Van Rhee (2010) noted that this derivation is based on an instantaneous increase in porosity due to dilation, while in fact this increase in porosity is gradual. Van Rhee (2010) used a force balance to express the incipient motion criterion due to the effects of slopes and hindered erosion as follows:

$$\frac{\tau^*_{c,s,d}}{\tau^*_c} = \left[\frac{\sin(\phi-\phi_b)}{\sin\phi} + \frac{\dot{E}}{k_l}\left(\frac{\lambda_l-\lambda_0}{1-\lambda_l}\right)\frac{1}{(1-\lambda_0)(G_s-1)}\right] \tag{4.227}$$

Van Rhee (2010) used the pick-up function of van Rijn (1984a) and defined the net erosion velocity of the bed while taking into account the near-bed concentrations:

$$\dot{E}_{net} = \frac{\dot{E_m} - \dot{D_m}}{\rho_s(1-\lambda-C_b)} = \frac{\sqrt{gd_{50}(G_s-1)}0.00033T_m^{1.5}d^{*0.3} - w_0C_b}{(1-\lambda-C_b)} \quad (4.228)$$

Apart from the effect of near-bed concentration, Equation (4.228) by van Rhee (2010) differs from that of van Rijn (1984a) (see Equation (4.138)) due to a modification in the transport parameter to reflect the hindered erosion. It can be noted from Equation (4.228) that the effect of slope and hindered settling was neglected. Erosion tests conducted in a flume with fine sand ($0.08mm < d_{50} < 0.12mm$) and flow velocities of approximately 1m/s were used to validate the hindered erosion hypothesis. The sedimentation mechanism was neglected due to the low near-bed concentrated and the following expression was then derived:

$$\frac{\dot{E}_{net}(1-\lambda-C_b)}{\sqrt{gd_{50}(G_s-1)}} - 0.00033T_m^{1.5}d^{*0.3} = 0 \quad (4.229)$$

where, T_m is the modified transport stage parameter due to slope effects and the hindered erosion mechanism.

The measured and computed net erosion velocity was plotted following the methods by van Rijn (1984a) and van Rhee (2010). It can be noted from Figure 4.49 that the formulation by van Rijn (1984a) overestimates the erosion rate for hindered erosion, while the formulation by van Rhee (2010) fits the data well.

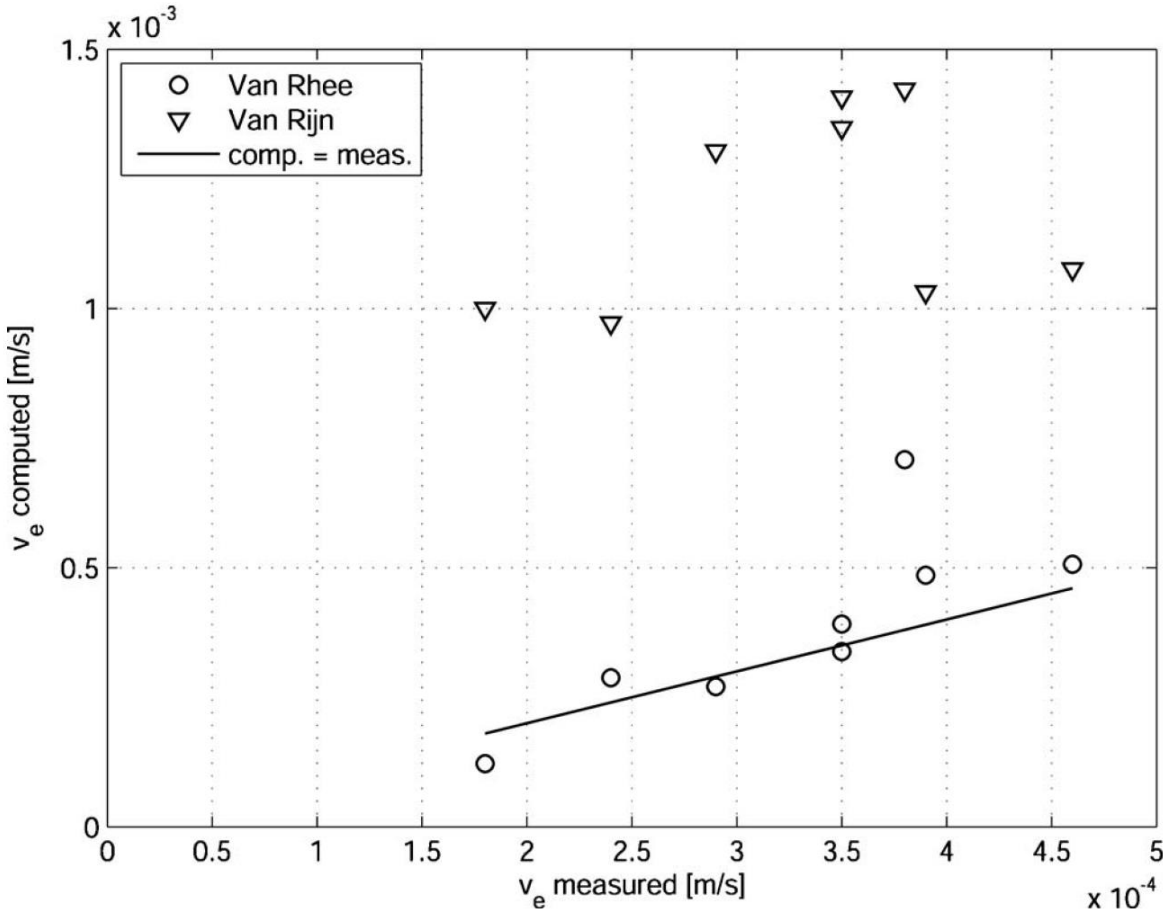

Figure 4.49: Computed and measured erosion velocity (van Rhee, 2010)

4.7 Similitude and Scaling Criteria

The similarities between a hydraulic model and its prototype are categorised as geometric, kinematic and/or dynamic. The criteria of similitude between the model and prototype are based on the physical relationships between the hydraulic parameters and are addressed in dimensionless form. The conditions of similarity involves the choice of using one or more of these scaling criteria for the design of the hydraulic model (Hughes, 1993). The scaling criterion can be determined by assuming similitude between the model and prototype in terms of the two inherent and major (hydraulic) forces (*i.e.* dynamic similarity). For instance, the inertial forces are always significant in any flow problem (Hughes, 1993), therefore the scaling

criterion could be expressed by addressing the second major force interacting within the hydraulic domain. The effects of some of those major forces are described as viscid, gravitational, surface tension, elastic, pressure and temporal. Below is a list of the most commonly used forces in hydraulic or flow problems from Hughes (1993):

- Inertial, $Mass \times (Convective)\ Acceleration = (\varrho\forall)\left(U_0 \frac{\partial U_0}{\partial L}\right) = (\varrho L^3)(U_0^2/L) = \varrho L^2 U_0^2$
- Viscid, $Viscosity \times (velocity/length) \times Area = \mu(U_0/L)A = \mu(U_0/L)L^2 = \mu L U_0$
- Gravitational, $Mass \times (Gravitational)\ Acceleration = (\varrho\forall)(g) = \varrho L^3 g$
- Surface tension, $Surface\ Tension \times Length = \sigma_t L$
- Elastic, $Modulus\ of\ Elasticity \times Area = EA = EL^2$
- Pressure, $Pressure \times Area = pA = pL^2$
- Temporal, $Mass \times (Temporal)\ Acceleration = (\varrho\forall)\left(\frac{\partial U_0}{\partial t}\right) = (\varrho L^3)(U_0/t) = \varrho L^3 U_0/t$

where, ∀ is the volume, L is length and E is the Modulus of Elasticity.

When viscous forces are dominant, the scaling criterion is known as the Reynolds number and is expressed as follows:

$$Re = \frac{inertial\ force}{viscous\ force} = \frac{\varrho L^2 U_0^2}{\mu L U_0} = \frac{\varrho L U_0}{\mu} \tag{4.230}$$

When gravity forces are dominant, the scaling criterion is known as the Froude number and is expressed as follows:

$$Fr = \sqrt{\frac{inertial\ force}{gravity\ force}} = \sqrt{\frac{\varrho L^2 U_0^2}{\varrho L^3 g}} = \sqrt{\frac{U_0^2}{Lg}} = \frac{U_0}{\sqrt{Lg}} \tag{4.231}$$

When elastic or compressive forces are significant, the scaling criterion is known as the Cauchy number, Ca, and is expressed as follows:

$$Ca = \frac{inertial\ force}{elastic\ force} = \frac{\varrho L^2 u^2}{EL^2} = \frac{\varrho \mathrm{U}_0^2}{E} \tag{4.232}$$

When pressure forces are of concern, the scaling criterion is known as the Euler number, Eu, and is expressed as follows:

$$Eu = \frac{pressure\ force}{inertial\ force} = \frac{pL^2}{\varrho L^2 \mathrm{U}_0^2} = \frac{p}{\varrho \mathrm{U}_0^2} \tag{4.233}$$

When the hydraulic application involves large oscillations or unsteadiness, the scaling criterion is known as the Strouhal number, *St*, and is expressed as follows:

$$St = \frac{temporal\ inertial\ force}{convective\ inertial\ force} = \frac{\varrho L^3 U_0}{\varrho L^2 U_0^2 t} = \frac{L}{ut} = \frac{\omega_f L}{U_0} \tag{4.234}$$

where, ω_f is the frequency of oscillation.

Usually the hydraulic application can be described by two or more physical relationships and consequently more than one scaling criterion. However, since it is mathematically impractical to satisfy two or more of these scaling laws, the modeller must choose the criterion which describes the dominant hydraulic identity governing the physical model. The modeller may also be forced to include additional scaling criteria to satisfy a turbulent flow regime or spatial constraint present in a hydraulic facility and therefore must also resort to scaling laws governing surface resistance or distorted/tilted geometries. Not conforming to such challenges, however, will introduce scale effects and consequently distort the scaled results (Chanson, 1999).

Most free surface flow models are gravity-dominant, whereby a bias towards Froude modeling over the viscous-prevailing Reynolds criterion can be assumed. In mobile-bed models, three additional scaling criteria must be considered: grain Reynolds, Re^*, Shields parameter, τ^*(Julién, 2002), and dimensionless grain size, d^* (see Equations (4.62)).

The two following additional scaling criteria, dimensionless characteristic length (Hugh, 1993) and Taylor's function (Pugh, 1985), are often recommended, and can be expressed as:

$$L^* = \frac{L_0}{d_0} \tag{4.235}$$

$$q_T^* = \frac{q_{ts}}{u^* d_0} \tag{4.236}$$

where, d_0 is characteristic grain size (usually d_{50}) and q_{ts} is the total volumetric sediment transport rate (*i.e.* discharge) per unit width.

While satisfying the customary scaling criteria in fixed-bed and mobile-bed hydraulic models may be impractical, the highly unsteady flow regime in the 3-D breach overtopping mechanism complicates the matter even further. In such complex scenarios when the conventional methods of similitude are unfeasible, similitude criteria can be achieved by scale series (Hughes, 1993). Hughes (1993) also emphasizes the importance of conducting a scale effects analysis between the model and prototype when scale series are used.

Chapter 5
Preliminary Work: Numerical and Experimental Investigations

5.1 Embankment Breach Numerical Modeling

The objective of this study was to gauge the sensitivity of input parameters with respect to the temporal and final embankment breach characteristics for two physically-based numerical models: NWS-BREACH and HR-BREACH. A (2000) version of the NWS-BREACH numerical model (Fread, 1991) was acquired from the National Weather Service (NWS) of the National Oceanic and Atmospheric Administration (NOAA). A (2006) version of the HR-BREACH numerical model (Mohamed 2002), limited to simulating overtopping failures in homogeneous embankments, was provided to the author of this thesis at the University of Ottawa by HR-Wallingford (United Kingdom). Using these two numerical models (described in detail in Section A.1 and A.2 of Appendix A), a total of nineteen input parameters with geotechnical, hydraulic, hydrometeorological and computational attributes were therefore evaluated. The breach characteristics investigated in this sensitivity analysis are: breach outflow, breach channel height, breach width, rise time (lag-time + time-to-peak), base time, and breach channel height-to-width ratio (h_B/B_W). The sensitivity analysis concerning the geotechnical input parameters are described in Al-Riffai *et al.* (2007).

5.1.1 Modeling Parameter Characteristics

First, a model or stencil embankment was designed such that a realistic range for the input parameters could be defined. Second, the range of input parameters was defined based on typical upper and lower values in real embankment prototypes.

While sources of uncertainty are of two types: natural variability and knowledge uncertainty (IMPACT, 2004b), this study assumed the range is due to the latter. The modeling parameters used in this study were identical for both numerical models.

5.1.1.1 Dam Geometry

The study included a hypothetical earthfill embankment, bordering a cohesive/noncohesive embankment material. An embankment with a crest height of 25m, based on an intermediate size classification (12m < h_{cr} < 30m) according to USBR (1987), was chosen after surveying 3,275 U.S. earth embankments from McCann (2009). Typical reservoir volumes for such a height ranged between 2 Mm^3 and 950 Mm^3 with an average value of approximately 200 Mm^3. A reservoir volume of 8 Mm^3 was chosen for the investigation. The values for the crest width, w_{cr}, as well as upstream and downstream slope factors, z_{US} and z_{DS}, respectively, are shown in Table 5.1. More detail on the selection of the benchmark modeling parameters as well as their ranges can be found in the comparative study by Al-Riffai (2006). A total of 19 simulations were run for each model for the three dam geometry input parameters. Each input parameter was varied separately.

Table 5.1: Embankment geometry and geotechnical parameters: benchmark values and input ranges

	Modeling parameter	Benchmark value	Input values
w_{cr} [1,2]	Crest width [m]	10.5	0, 5, 10, 15, 20
z_{US} [1,3,4]	Upstream slope factor [1V:H]	3.5	2, 2.5, 3, 3.5, 4, 4.5, 5
z_{DS} [1,3,4]	Downstream slope factor [1V:H]	3	2, 2.5, 3, 3.5, 4, 4.5, 5
d_{50} [2,5]	Median particle size [mm]	0.075	0.075, 0.15, 0.3, 0.45, 0.6, 0.8, 1, 2
d_{90}/d_{30} [3,5]	Soil gradation	10	1, 2, 5, 10
ϕ [1]	Angle of internal friction [degrees]	31	25, 31, 35, 38, 40, 45
λ [2]	Soil porosity	0.32	0.27, 0.32, 0.37, 0.42, 0.47
c [2]	Soil cohesion [kPa]	20	1, 5, 10, 15, 20, 30, 40
PI [2,5]	Plasticity Index† [%]	15	0.1, 5, 10, 15, 16, 20, 30, 40, 50
γ_d [6]	Dry unit weight [kN/m^3]	18	10, 14, 18, 22, 25
σ_f	Tensile strength‡ [kPa]	0	0, 5, 10, 15, 20, 25

[1]USBR (1987); [2]Singh and Varshney (1995); [3]Goldin and Rasskazov (1992); [4]Kutzner (1997); [5]Thomas (1976); [6]Vanapalli *et al.* (1998) and Vanapalli (1994); †Simulated only for cohesive soils; ‡ HR-BREACH simulations only

5.1.1.2 Material Properties

In order to model the breach of an actual dam, it was necessary to select a soil type commonly used in earth fill dams. Although neither model utilized the coefficient of permeability as an input parameter, it remained a key factor in deciding the soil type. It is suggested to use a fine-grained soil with a coefficient of permeability lower than 10^{-7}m/s (Singh and Varshney, 1995; Kutzner, 1997). Another factor was the plasticity index, PI, which can significantly influence the erosion. A cohesive soil where $PI < 15$ is conventionally recommended (Thomas 1976; Singh and Varshney, 1995). Well-graded soils with relatively higher dry densities are also favourable for homogeneous embankments since they reduce the risks of erosion and piping (Thomas 1976; Singh and Varshney 1995). The properties of the clayey-sand (*i.e.* USCS Type – SC; ASTM, 2010) selected as the embankment material, are summarised in Table 5.1. The HR-BREACH model uses an input parameter additional to the NWS-BREACH model, which is the soil tensile strength, σ_f. Due to this reason, that parameter was set to zero for the stencil embankment. A total of 50 simulations were run for each model using 8 geotechnical parameters.

5.1.1.3 Other Modeling Parameters

In addition to the dam geometry and geotechnical parameters, simulations were carried out for input parameters with hydrometeorologic, hydraulic and computational attributes.

The hydrometeorologic parameters addressed various inflow conditions and reservoir-storage characteristics. Four unique rainfall hydrographs resulting from different watersheds were used in the simulation. The watershed feature was simulated by varying the symmetry of the rainfall runoff hydrographs. Watershed characteristics such as runoff coefficient and drainage area were not varied such that the inflow hydrograph would give rise to the same total catchment volume. The inflow hydrographs were designed based on a total catchment volume producing a 0.5m rise in the reservoir level. The inflow hydrographs were simulated as follows:

constant inflow, peak inflow at ½ the base time, peak inflow of ¼ base time and peak time of ¾ base-time as shown in Figure 5.1.

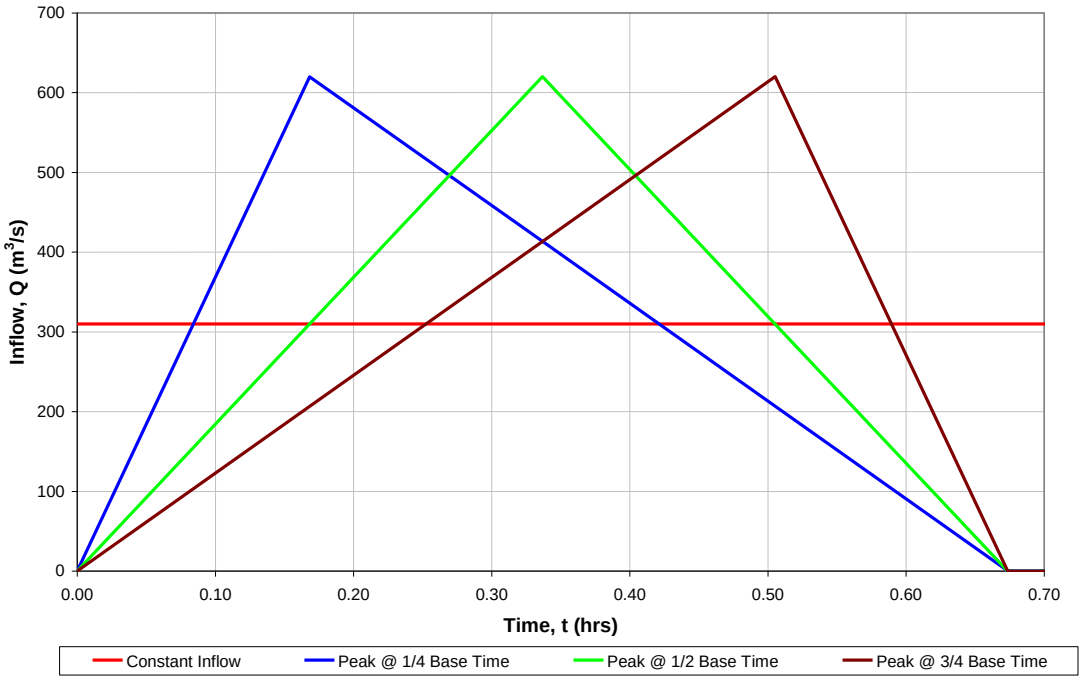

Figure 5.1: Various inflow conditions simulated

The reservoir-storage characteristic was simulated by varying the steepness of the upstream valley. Seven different reservoir-storage characteristics were therefore designed. Five of the reservoir-storage characteristics demonstrated a variable slope in the topography where two were comprised of a constant upstream valley cross-section with trapezoidal and rectangular shapes (see Figure 5.2 and Figure 5.3). The length of all the upstream reservoirs was 3km. A total of 11 simulations were run for each model for the two hydrometeorologic parameters described.

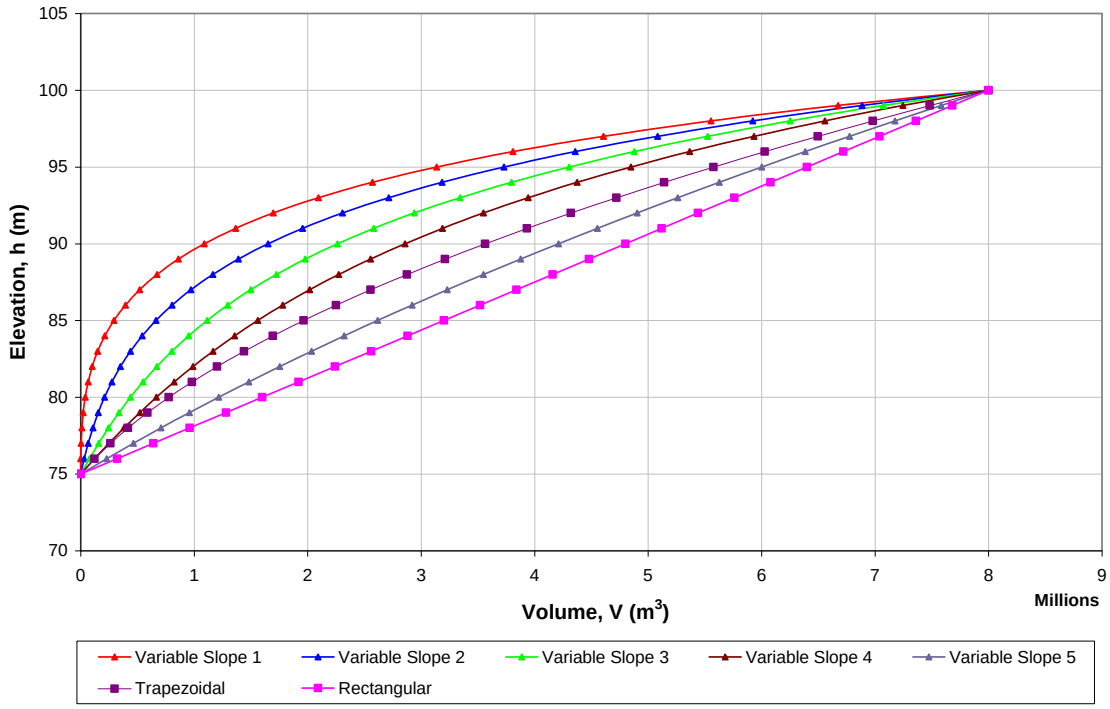

Figure 5.2: Reservoir-storage characteristics for different upstream valleys

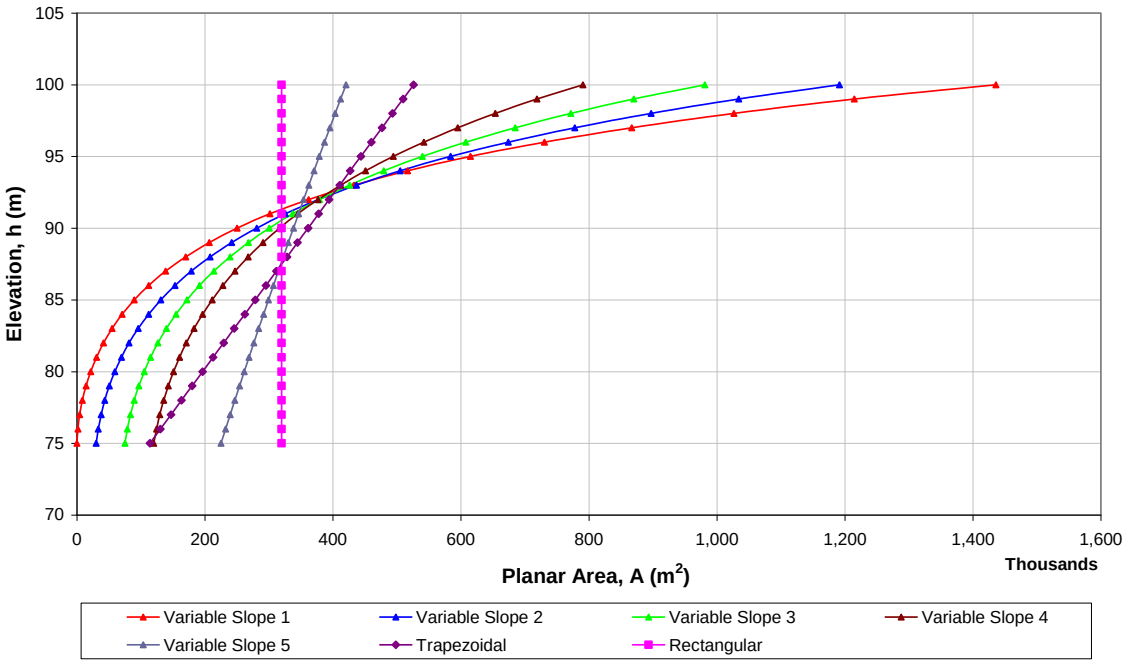

Figure 5.3: Reservoir-surface area characteristics for different upstream valleys

Hydraulic parameters considered were as follows: initial breach channel width (B_0), downstream conditions and sediment transport formulation. Preliminary simulations showed that using a minimum initial breach depth of 0.2 m was suitable for the breach in the stencil embankment. Larger values of 0.4, 0.6, 0.8, 1 and 2 m were used in the sensitivity analysis. The initial breach depth was input at the same value such that the ratio between the initial breach width-to-depth ratio, B_r, was 1.

The HR Wallingford model is capable of defining the downstream boundary using two methods: downstream rating curve, or, immediate downstream valley cross-section, valley roughness and bed slope. Even though both methods are inter-related by means of hydraulic efficiency (normal flow depth), the latter was chosen due to the input limitations in the NWS model, as well as the need for a more independent parametric study of downstream boundary conditions. The significance of incorporating those parameters was to understand the effect of tailwater conditions on the breach outflow.

For the sake of simplicity, a downstream valley cross-section with a trapezoidal shape was defined with a side-slope angle, bottom width, b_V, Manning roughness coefficient and bed slope equal to 45°, 500m, 0.05 and 0.001, respectively.

The NWS model is capable of simulating erosion using the MPM formulation for cohesive and non-cohesive sediments. The MPM formulation for cohesive soil is activated if the plasticity index, and empirical constants b_c and c_c are defined. Since the HR model is capable of using eight different sediment transport formulations, a cohesive soil MPM formulation for the stencil embankment was employed. The hydraulic input parameters are summarized in Table 5.2. For the five hydraulic parameters described, 21 simulations were run for HR-BREACH and 15 simulations were run for NWS-BREACH.

Table 5.2: Hydraulic and computational parameters: benchmark values and input ranges

	Modeling Parameter	Benchmark Value	Input Value
B_0	Initial breach width [m]	0.2	0.2, 0.4, 0.6, 0.8, 1.0, 2.0
n_M	Manning roughness	0.050	0.025, 0.030, 0.035, 0.040, 0.050
S_b	Downstream valley slope	0.001	0.0001, 0.001, 0.01
b_V	Downstream valley bottom width [m]	500	100, 200, 300, 400, 500
–	Sediment transport formulation†	MPM	8 different formulations
Δt	Time-step for HR-BREACH [s]	2.5	2.5, 5, 10, 20, 40
Δt	Time-step for NWS-BREACH [s]	3.6	3.6, 5, 10, 20, 40
Δx	Space-step for HR-BREACH‡ [m]	5	5, 10, 20

†Benchmark embankment used MPM (*i.e.* MPM, 1948) formulation for cohesive soil, while six additional formulations were included in HR-BREACH simulations only; ‡time-step was also varied for different space-step values

Preliminary tests using the HR-BREACH model indicated that a minimum time-step of 2.5s for the stencil embankment was required to initiate a breach failure. The minimum and maximum time-steps defined in the NWS-BREACH model is 0.001 hours (3.6s) and 12 hours (720s), respectively. Therefore, a minimum time-step of 3.6s and 2.5s was used for the stencil embankment for NWS-BREACH and HR-BREACH simulations, respectively.

Since the NWS-BREACH model assumes a constant breach-channel longitudinal and side-slopes, no input for a space-step is included in its computations. The HR-BREACH model, on the other hand, requires such an input since it employs the sediment continuity equation over the entire length of the breach channel. A space-step equal to 5m was found to satisfy the Courant-Friedrichs-Lewy (CFL) condition as well as the minimum two space-step suggestion on the embankment crest. The range of values used for this study was between 5m and 20m, using different time-step ranges. For the two computational parameters described, 15 simulations were run for HR-BREACH and 5 simulations were run for NWS-BREACH (see Table 5.2).

5.1.2 Sensitivity Analysis Results

A total of 100 simulations for the NWS model and 116 simulations for the HR model were run on a CPU with a processing speed of 2.6GHz and 1GB RAM. The HR model solved the breach outflow using spatial discretization, and therefore required a much longer simulation time (a few minutes) in comparison to the NWS model which processed the simulations in less than a few seconds. The graphical user interface of HR-BREACH also augmented the processing requirements of the simulations. Overall, the HR model was relatively stable. In all simulations, the NWS model truncated the output data before the specified simulation time due to a limiting condition on the number of iterations within its code. The following subsections give a summary of the general observations regarding the output of the breach outflow hydrograph, the temporal breach width, breach depth and ratio of breach width to depth as well as the sensitivity of the input parameters for both models.

5.1.2.1 Breach Outflow hydrograph

The breach outflow curve computed by HR-BREACH was unique in terms of its irregularity and multiple peaks; unlike the outflow hydrographs by NWS-BREACH which were more uniform and bell-shaped (see Figure 5.4). The rise-time in the HR computation was more random and step-shaped than the permanent sudden increase exhibited by the NWS-BREACH model (see Figure 5.4). This is due to the successive side-slope failures resulting from the new methodology adopted in the model. Generally, the lag-time of the outflow hydrograph in HR-BREACH was larger than that of NWS-BREACH. Both peak outflows were of the same magnitude, however, the HR-BREACH simulations yielded larger peaks and hence a smaller base-time. Even though the output in NWS-BREACH was truncated, the base-time was estimated by extrapolating the terminus of the hydrograph.

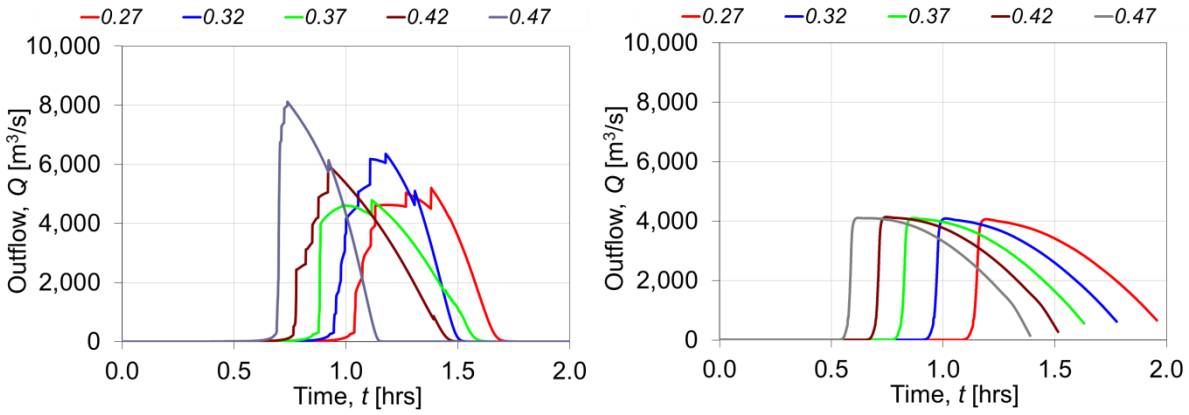

Figure 5.4: Breach outflow hydrographs for various soil porosities (left) HR-BREACH (right) NWS-BREACH

5.1.2.2 Temporal Breach Dimension Variation

5.1.2.2.1 Breach Widening

The plots in Figure 5.5 and Figure 5.6 revealed how lateral erosion and side-slope failures are incorporated in both models. The NWS simulations displayed 3 breach widening phases. The first phase of widening was a gradual increase in the breach top and bottom width to about 10m, where $t \cong t_L$. This can be explained by the dominant lateral erosion mechanism employed by the model during breach initiation. The second phase illustrated a nearly vertical increase in top width to about 40m (where $t \cong t_P$). During this vertical increase, the breach channel bottom width remained constant, indicating that the second widening phase only takes place at the top of the breach channel as a result of the successive side-slope failure mechanism. The third phase demonstrated a 10m gradual increase in the breach channel's top and bottom widths to a maximum value of 45m and 15m, respectively. The gradual increase in the breach channel's top and bottom widths in the third phase indicated the dominant lateral erosion mechanism during the depletion of the reservoir. For all simulations, the breach channel side-slope angle (reported with respect to the vertical) was always 29.5°. This value was achieved within two time-steps, which clearly signifies the sudden response of the NWS-BREACH model. The

version of the HR-BREACH model obtained did not report the side-slope angle. However, its slower response indicated that it was more gradual.

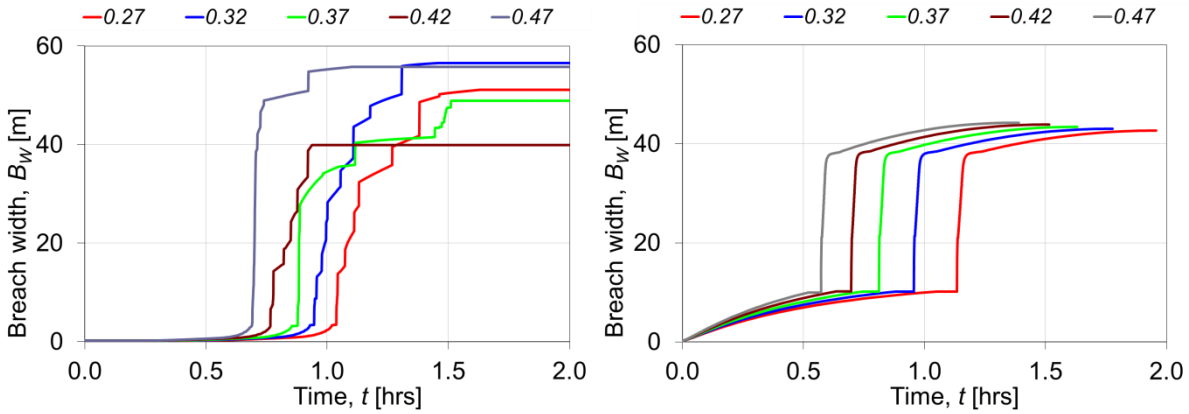

Figure 5.5: Breach channel width evolution for various soil porosities (left) HR-BREACH (right) NWS-BREACH

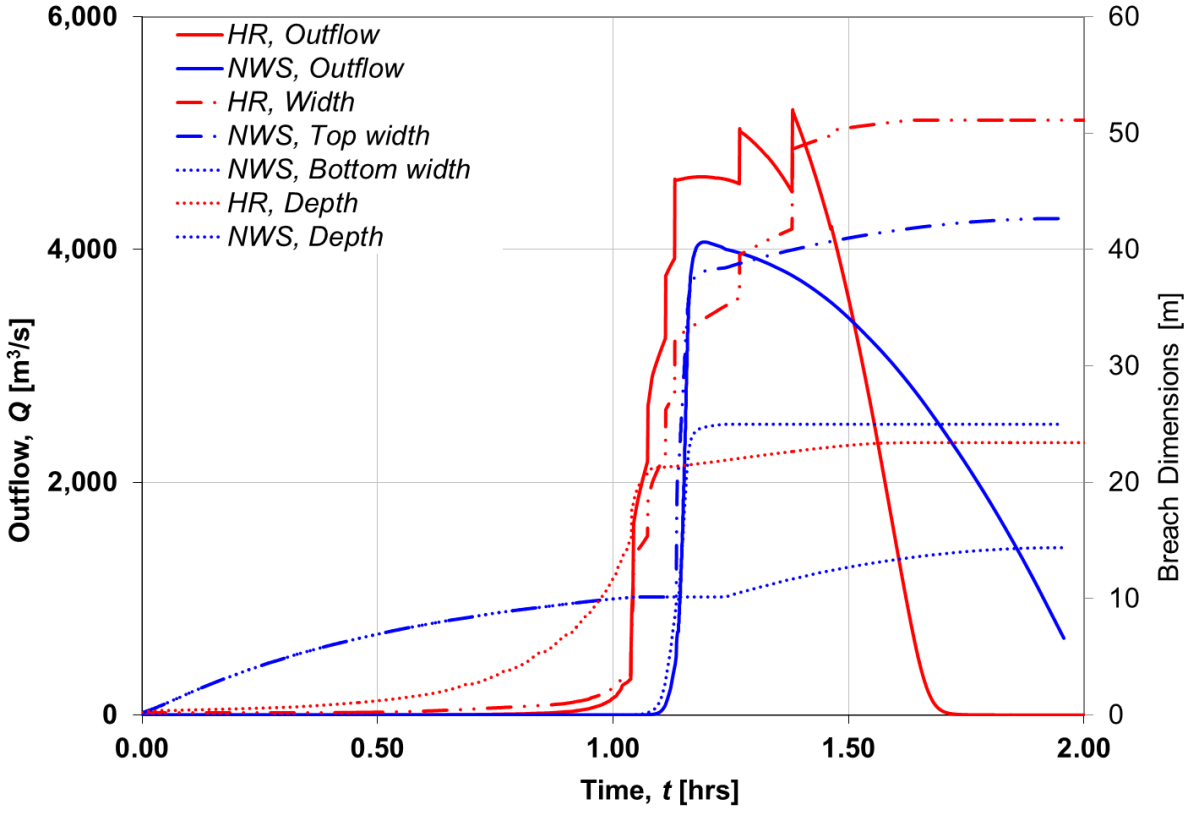

Figure 5.6: Breach channel outflow and morphology for HR and NWS models for soil porosity, $\lambda = 0.27$

For the HR model, only two phases of breach widening were observed. The first phase was more gradual than NWS-BREACH due to longer lag-times. Another noticeable aspect of the initial breach widening phase in the HR model was the rate of increase of the breach width. While HR-BREACH displayed an increase in that rate with time, NWS-BREACH displayed a decrease in that rate with respect to time. The HR-BREACH model displayed a transitional effect between the first and second phase whereas NWS-BREACH displayed this transition in a more abrupt manner. The second phase of breach widening by the HR-BREACH model was slightly more gradual and step-shaped indicating the side-slope channel failures. The second phase, unlike NWS-BREACH, extended beyond the peak time, and ended approximately at the midpoint of the receding limb of the hydrograph. The range of values at the terminus of the second phase was between 35 and 70m. It was found that the variation in the input parameters' values caused a larger variation in final breach channel width. This was opposite to NWS-BREACH, which displayed an almost identical final breach width with respect to input parameter variation. An important aspect of HR-BREACH is that breach widening was not limited to the rise time as shown in NWS-BREACH; rather it showed a greater degree of sensitivity to breach outflow beyond the peak value.

5.1.2.2.2 Breach Depth

The two embankment characteristics which appear in the weir-flow equation are breach channel width and depth. While breach outflow is proportional to the breach width, the relationship between outflow and breach depth is based on an exponent equal to 1.5. Therefore, any change in breach outflow is predominantly reflected by the variation in breach depth.

From Figure 5.6 and Figure 5.7, the final depth for both models is almost the same (≅25m) which indicated that erosion of the breach channel reached the valley floor where peak values for both models were comparable. For NWS-BREACH, the breach depth variation can be described by a single stage; a sudden increase from the initial value (at lag-time) to the maximum value (25m) before the peak time. This

indicated that the model's solution is more towards an instantaneous failure. The duration of the entire depth variation did not exceed the rise-time, and was usually much less (by 0.1hrs) for all simulations. It is clear that there was no sensitivity for this parameter for NWS-BREACH, except that the increase was offset by the difference in lag-time corresponding to the variation of the input parameter.

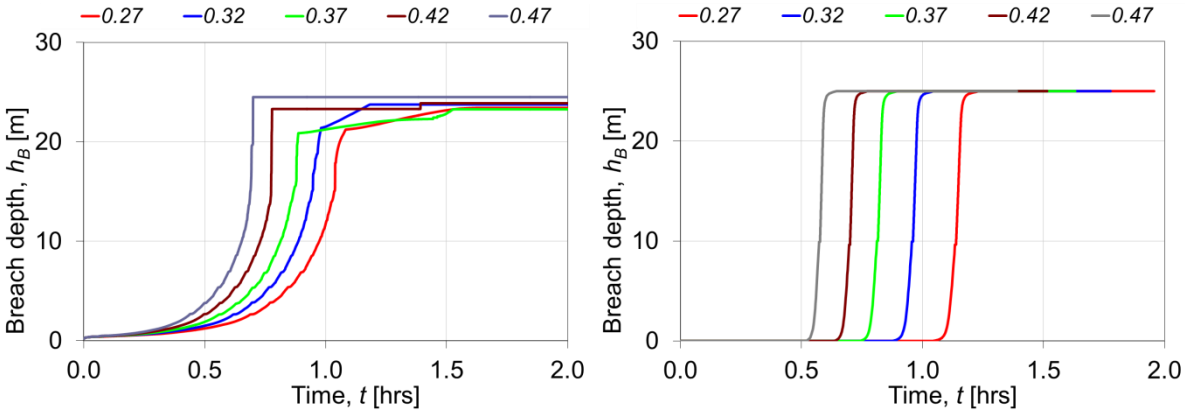

Figure 5.7: Breach depth evolution for various soil porosities (left) HR-BREACH (right) NWS-BREACH

The breach depth variation for HR-BREACH can be described by three stages. The first stage is a more gradual (and exponential) increase in breach channel depth than NWS-BREACH. Generally the end of this stage occurred once significant outflow was conveyed through the breach channel. The second stage can be described by a sudden increase in breach channel depth and ended once the hydrograph reached its first peak (or first side-slope instability). The third stage was comprised of a gradual increase (≅ 5m) until the terminus of the hydrograph, during which there may have been a series of side-slope instabilities occurring. This was noticeable on the outflow hydrograph and breach channel width evolution plots (see Figure 5.4 and Figure 5.5). The second stage of vertical erosion coincided with the second stage of lateral widening in both models, where the response in both stages was sudden. This indicated that there was a sudden increase in the breach channel dimensions during rise time where breach formation was dominated by both lateral and vertical erosion. However, the third stage of breach widening in HR-BREACH

may have influenced the peak flow, unlike NWS-BREACH where peak outflow was mainly influenced by the coinciding stages of vertical erosion and lateral widening due to successive side-slope failures.

5.1.2.3 Input Parameter Sensitivity

Figure 5.8 and Figure 5.9 show a sensitivity plot for both models with respect to the soil porosity input parameter. While plots similar to the ones shown (*i.e.* Figure 5.4 to Figure 5.9) were generated for each input parameter, a summary of the sensitivity is presented in this subsection. Generally, the model with the higher degree of sensitivity towards the input parameters was HR-BREACH. It was found that the most sensitive hydrometeorologic input parameter was reservoir bathymetry, where variations in peak flow, lag-time and rise time was 53%, 44% and 93%, respectively, for the HR model. For the NWS model those variations were 10%, 51% and 51%, respectively. It was found that all downstream hydraulic boundary conditions had a negligible effect on lag-time.

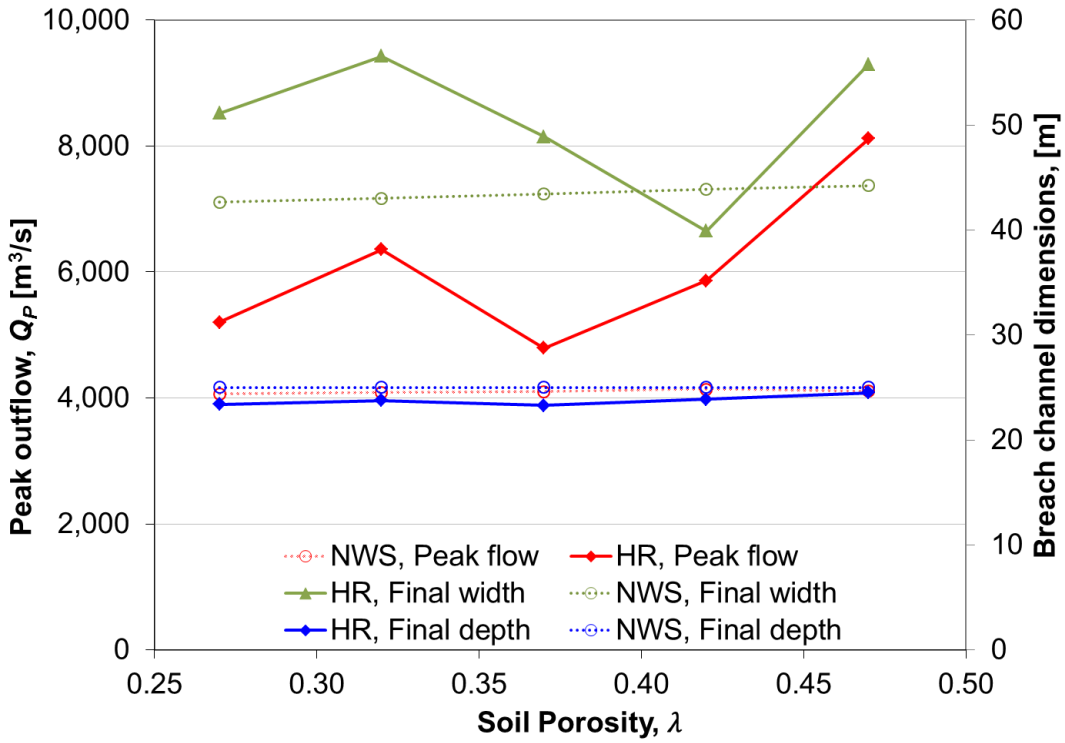

Figure 5.8: Breach outflow and final dimensions sensitivity for soil porosity

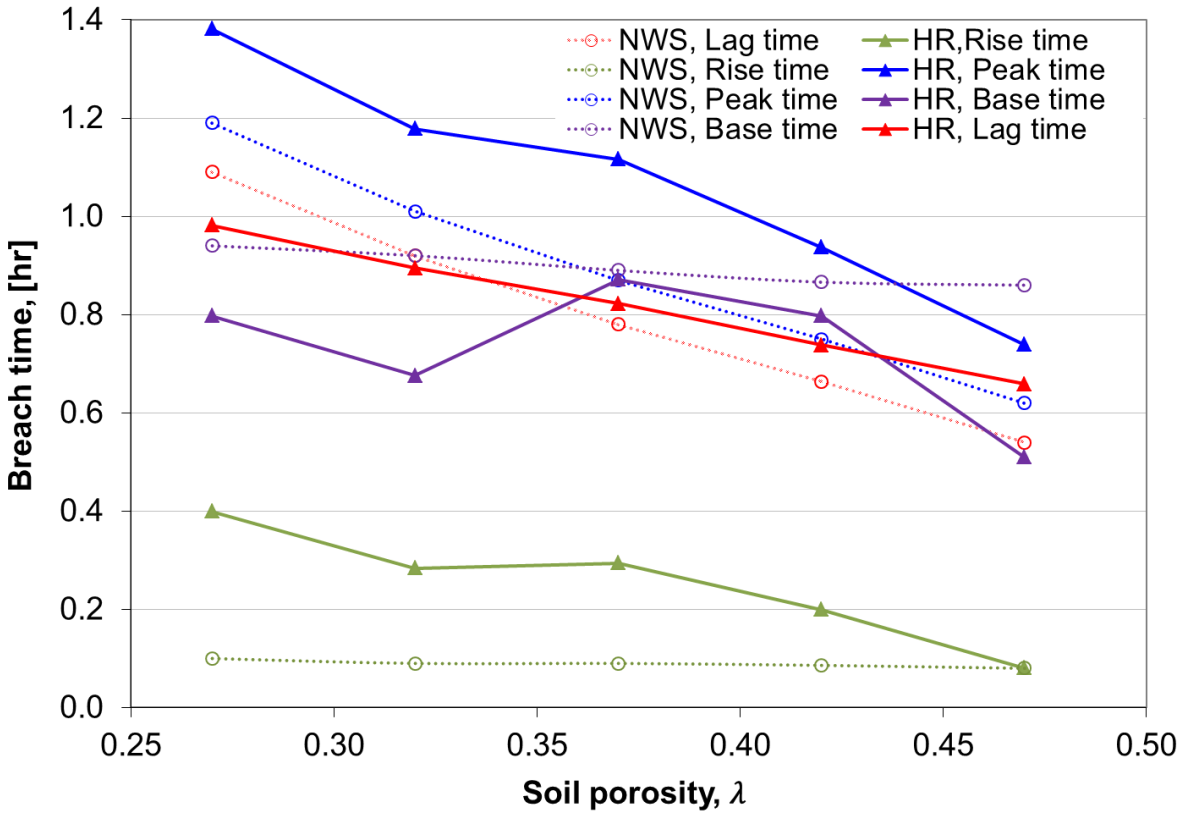

Figure 5.9: Breach temporal characteristics sensitivity for soil porosity

A summary of the sensitivity analysis for the remaining input parameters can be found in Table 5.3. Variations were computed with respect to the highest values. It is evident from Table 5.3 that the most sensitive embankment breach characteristic is the rise-time, with an average variation of 78% and 33% for HR-BREACH and NWS-BREACH, respectively. The least sensitive embankment breach characteristic was lag-time, with an average variation of 32% and 24% for HR-BREACH and NWS-BREACH, respectively. The most sensitive input parameter was the crest width, with an average variation of 76% and 43% for HR-BREACH and NWS-BREACH, respectively. The angle of internal friction was the least sensitive input parameter, with an average variation of 34% and 16% for HR-BREACH and NWS-BREACH, respectively.

Table 5.3: Percentage variation in embankment breach characteristics for geometric and geotechnical input parameters

Parameter	Variation [%]									
	HR-BREACH					NWS-BREACH				
	Q_P	t_L	t_R	t_P	h_B/B_W	Q_P	t_L	t_R	t_P	h_B/B_W
w_{cr}	58	82	96	76	66	12	100	43	58	3
z_{US}	75	31	94	42	80	7	0	8	3	6
z_{DS}	55	73	71	67	47	43	49	79	57	31
d_{50}	47	2	82	41	50	0	0	0	0	0
d_{90}/d_{90}	40	48	41	27	42	11	44	7	18	9
ϕ	41	1	72	19	38	12	0	31	14	24
λ	41	34	84	46	30	7	35	4	22	6
n_M	69	58	49	46	77	26	0	73	31	31
c	63	22	82	27	66	33	39	65	21	41
PI	13	3	93	19	12	0	0	0	0	0
γ_d	43	4	92	19	30	22	0	48	19	29
σ_f	45	22	74	30	28	-	-	-	-	-

5.2 Embankment Breach Experimental Modeling – Standard Tests (Phase I)

The embankment breach experimental program was conducted in the Hydraulic Laboratory at the University of Ottawa and began in May 2008, using two flumes with different geometric and flow characteristics. The parameters investigated in this phase were compaction and degree of saturation. The test description and results of Phase I were published in Al-Riffai and Nistor (2010a), Al-Riffai and Orendorff (2009), Al-Riffai *et al.* (2009) and Al-Riffai and Nistor (2010b). Other spatial embankment breach tests were also conducted in collaboration with a Master's thesis project which investigated various initial breach geometries, such the effects of blasts, as well as composite and homogeneous clay embankments. The methodology and results for these tests is described in Orendorff (2009), Orendorff *et al.* (2009) and Orendorff *et al.* (2013). A series of geotechnical tests were conducted on embankment material samples at the Geotechnical Engineering Laboratory of the University of Ottawa prior to construction and testing. The geotechnical tests are described in detail in Section C.1 in Appendix C, while the

experimental method for the small and large flume tests is described in Subsections 5.2.1 and 5.2.2, respectively.

5.2.1 Small Flume Tests

The embankment breach experimental program at the Hydraulic Laboratory at the University of Ottawa began with spatial breach overtopping tests conducted in an elevated flume 0.38m wide, 12.2m long and 0.61m high with glass side-walls. The flume bottom was smooth and impervious, with a null slope. Two test series were conducted in the small flume: compaction (Series “A”) and drainage (Series “B”) tests, using embankment models 250mm and 300mm high, respectively (see Figure 5.10 and Figure 5.11). The upstream and downstream shoulder slopes were always 1V:2.5H and 1V:3H, respectively. The crest width was 80mm and 100mm for Series “A” and Series “B”, respectively. Embankment models in both test series were constructed at four different compaction efforts, while the drainage tests were constructed with and without drainage elements at two compaction efforts.

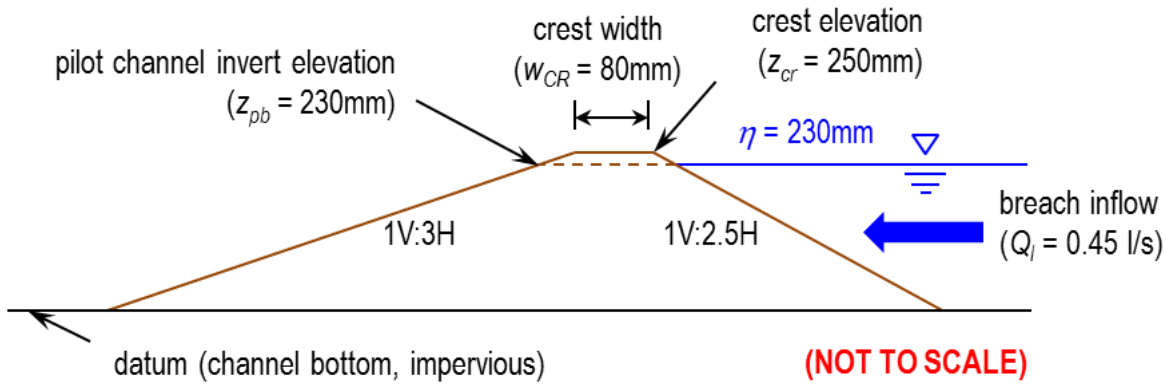

Figure 5.10: Embankment model without drainage element in compaction tests (Series “A”)

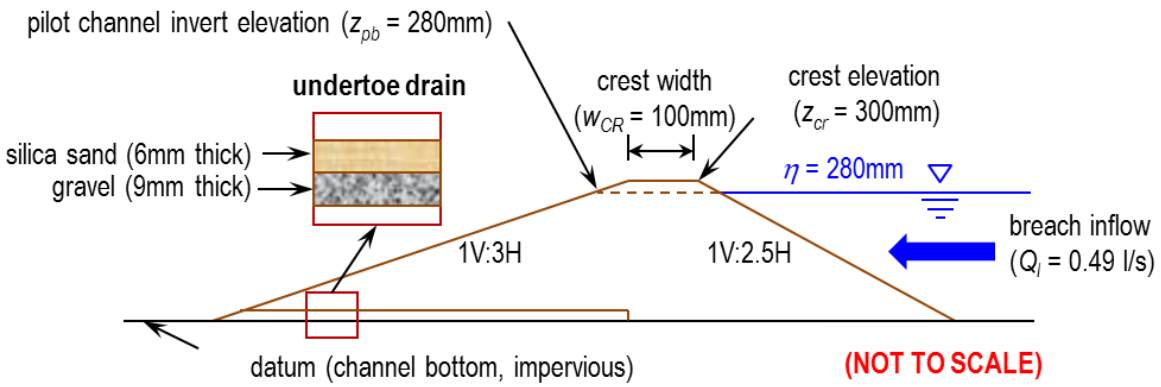

Figure 5.11: Embankment model with horizontal drainage element in drainage tests (Series "B")

The overtopped embankment models for the compaction and drainage series conducted in the small flume were constructed using sand Type I. The standard geotechnical tests conducted for the embankment materials are described in detail in Section C.1 of Appendix C. The compaction of the embankment models used in the small flume tests was applied using dynamic compaction, similar to the methods described by Simmler and Samet (1982), Shuibo *et al.* (1993), Spinewine *et al.* (2004), Geisenhainer and Kortenhaus (2006) and Morris *et al.* (2007). The compaction technique for the small flume test series is described in detail in Subsection D.1.1.1 of Appendix D.

5.2.1.1 Experimental Setup

The experimental setup is shown in Figure 5.12. A total of four WG-50 capacitance wave gauges (WG) were used to measure the time-history of water surface elevations during the tests using a sampling rate of 30 Hz. Three of the wave gauges were installed in the upstream reservoir, while one wave gauge was installed in the outlet tank beneath the flume outlet. A 90° V-notch weir at the side of the outlet tank was used to discharge the breach outflow into the laboratory's underground reservoir. Prior to their installation in the small flume, the wave gauges were calibrated using three known WSLs (see Subsection D.2.1 in Appendix D for more detail). The calibration process was conducted prior to each test. Video footage was captured using high definition video cameras mounted on fixtures at

three locations: upstream, downstream and above the crest as shown in Figure 5.12. A fourth video camera and lighting setup was used to capture the side-view footage of tailwater depths as well as planar overtopping flow conducted in some pilot tests (see Subsection D.3.1 in Appendix D).

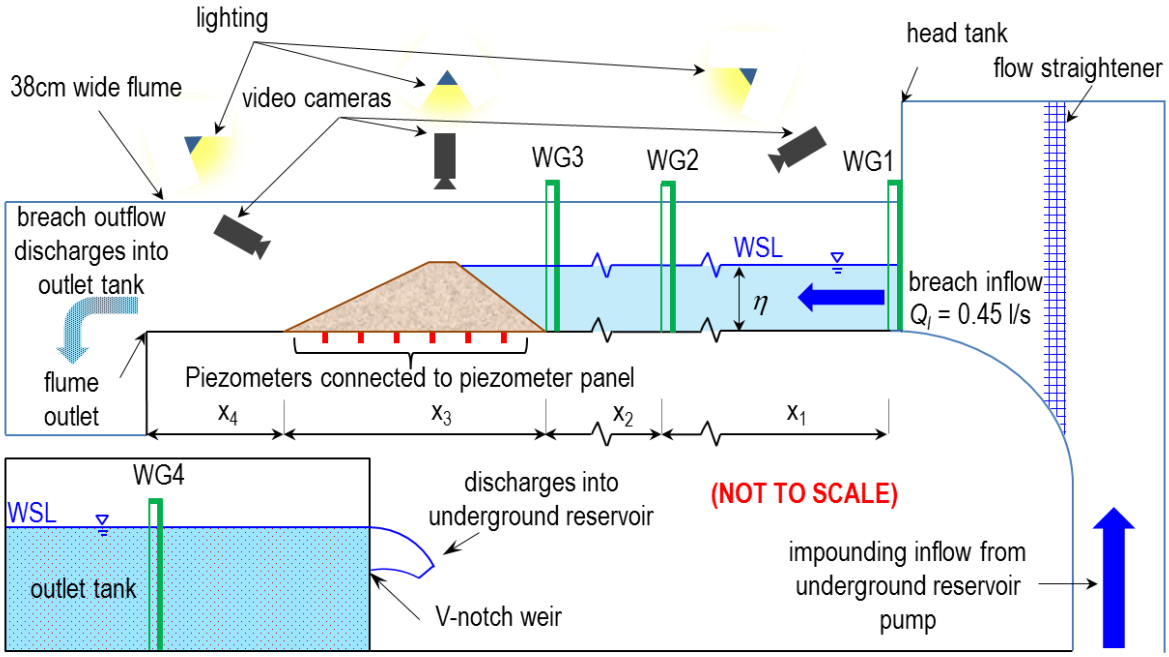

Figure 5.12: Experimental setup for compaction and drainage tests (Series "A": η = 0.23m, x_1 = 8.84m, x_2 = 0.3m, x_3= 1.46m, x_4= 1.60m; Series "B": η = 0.28m, x_1 = 6.75m, x_2 = 2.0m, x_3 = 1.75m, x_4 = 1.70m)

For the drainage series, six piezometers connected to existing taps located at the bottom of the flume were used to measure piezometric head at the embankment foundation (see Figure 5.13). The piezometers taps were covered with a screen with an aperture size of 200μm to prevent sediment from clogging the piezometer lines.

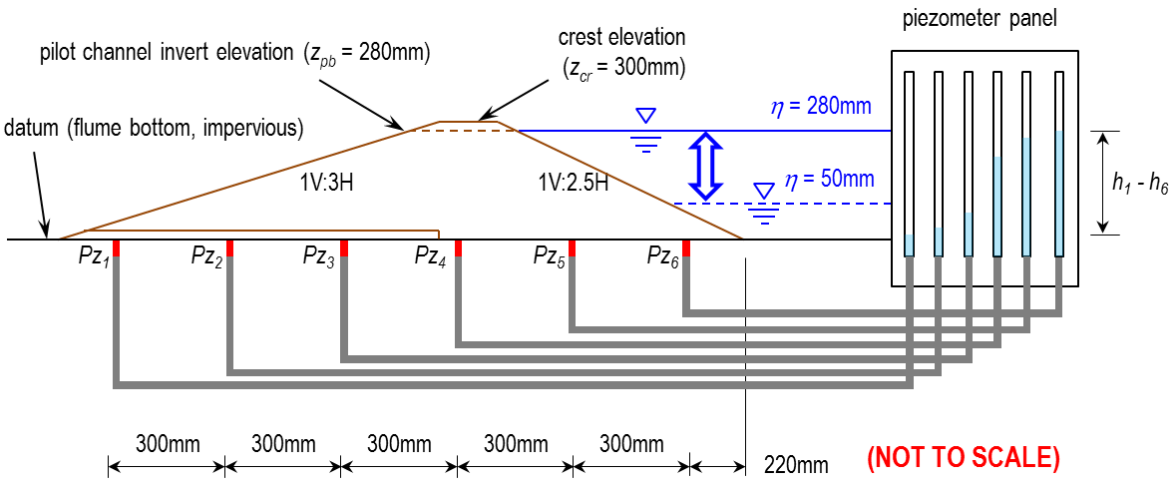

Figure 5.13: Locations of piezometer taps (numbered Pz_1 to Pz_6) and piezometers (numbered h_1 to h_6) in drainage tests (Series "B")

The upstream reservoir was again impounded slowly (3 to 4mm/min) to prevent occlusion of air bubbles in would be saturated zones of the embankment model. Once steady-state seepage was observed, the piezometric heads were recorded at water surface levels (WSL) ranging between 5cm and 28cm in 3 to 5cm increments. Measurement of the WSL under steady-state conditions was confirmed using a point gauge, while measurement of the piezometric head was carried out using a graduated scale adjacent to the piezometer panel.

Two pilot tests were conducted to determine a suitable compaction effort as well as the method of impoundment required for an overtopping failure. Impoundment of the reservoir was carried out by means of a water hose connected to a municipal water supply ($Q_I = 0.45\ l/s$). The inflow was ceased once the overtopping reached the downstream toe of the embankment model. For the drainage tests, the inflow remained constant during the entire experiment. As shown in Table 5.4, a total of 16 tests were carried out in the small flume, including two pilot tests as well as two spatial breach overtopping tests conducted using natural and remoulded clay.

Table 5.4: Test matrix for small flume tests (compaction and drainage)

Test No.	Test series†	Date‡	Crest dimensions		Compaction		Notes
			Height, h_{cr} [cm]	Width, w_{cr} [cm]	No. of blows	Drop height [cm]	
1	A (Pilot test)	14 May	25	8	Arbitrary (low compaction)		-
2	A (Pilot test)	30 May	25	8	Arbitrary (medium compaction)		-
3	A	31 July	25	8	5	5	Successfully breached. However, unused due to unconfirmed density.
4	A	19 Aug.	25	8	5	5	Successfully breached. Irregular inflow.
5	A	20 Aug.	25	8	10	5	Failed test. Overtopping occurred near flume side-walls.
6	A	21 Aug.	25	8	1	5	Failed test. Downstream slope failed during impoundment.
7	A	25 Aug.	25	8	5	10	Successfully breached. Incomplete wave gauge data.
8	A	27 Aug.	25	8	10	10	Successfully breached.
9	A	28 Aug.	25	8	20	10	Successfully breached.
10*	Clay (natural)	4 Sep.	25	8	5	10	Partially breached. Qualitative test.
11*	Clay (remoulded)	19 Sep.	25	8	5	10	Partially breached. Qualitative test.
12	B (no drain)	04 Mar.	30	10	20	10	Piezometric head successfully measured.
13	B (drain)	08 Mar.	30	10	20	10	Piezometric head successfully measured. Embankment model accidentally breached.
14	B (drain)	10 Mar.	30	10	20	10	Piezometric head measurements/breach tests successful.
15	B (no drain)	12 Mar.	30	10	5	10	Piezometric head successfully measured.
16	B (drain)	22 Mar.	30	10	5	10	Piezometric head measurements/breach tests successful.

†Drainage tests were conducted with and without drains. For embankment models without undertoe drains only piezometric measurements were recorded whereas for embankments models with undertoe-drains, both piezometric measurements and breaching tests were carried out; ‡Test No. 1 to 11 in year 2008; Test No. 12 to 16 in year 2009; *Upstream and downstream slopes were 1V:2H for the homogeneous clay embankment models.

For the compaction series, the compaction was varied using four compaction efforts. Out of the 9 tests performed, only 4 tests were deemed useable (Tests No. 4, 7, 8 and 9). The drainage tests were designed after observing sapping/piping erosion near the downstream toe due to the excess PWP in the downstream slope (see Figure 5.14) and as observed by other researchers (Howard and McLane, 1988; Dunne, 1990; Wörman, 1993). In fact, after reservoir impoundment it was necessary to conduct the breaching tests as soon as possible to avoid a downstream slope slide. Therefore, an under toe-drain was incorporated in tests using two compaction efforts, 5 blows and 20 blows, from a drop height of 100mm.

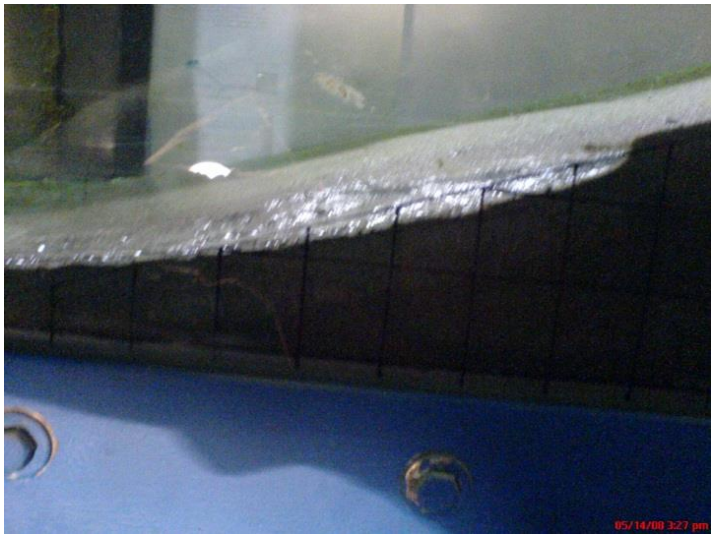

Figure 5.14: Sapping/piping erosion near downstream toe

Sand Type I was purchased in bulk from a local quarry. The GSD tests performed on soil specimens that were sampled from the same pit over a period of time, revealed some variations, mainly in soil gradation. After the embankment model in Test No. 13 was accidentally breached, and to avoid depletion of the available sand, the embankment models without under-toe drains were not breached (*i.e.* Test No. 12 and 15). The purpose of those two tests only served for measurement of the piezometric head at the embankment model's foundation. The salvaged embankment material was then reused for spatial breach overtopping tests using

under toe-drains (Test No. 14 and 16). The piezometric heads at the embankment model's foundation were also recorded for the drained embankments models.

5.2.1.2 Data Analysis

Data from the three wave gauges installed in the upstream reservoir were input into a developed FORTRAN code (see Section E.1 of Appendix E) to compute the breach outflow hydrograph using the standard hydrologic routing method described by Equation (4.142). Data from the wave gauge installed in the outlet tank was used to compute the breach outflow hydrograph using the discharge equation for triangular (90°) weirs (Prasuhn, 1992):

$$Q_O = C_w \Delta h_w^{2.5} \tag{5.1}$$

where, C_w is a coefficient of discharge based on weir shape (C_w is 1.38 for triangular 90° weirs) and Δh_w is the head above the V-notch weir invert.

In some tests, wave gauge data displayed peculiar behaviour. The water surface elevations were seen to spike sporadically for a given time interval, followed by despiking from the offset value. After the completion of this phase, and following a correspondence with the wave gauge supplier, it was found that this problem was caused by electro-magnetic interference (EMI) between the wave gauge components. The suggested 2m minimum separation distance between each adjacent wave gauge was respected in later phases of the experimental program. The wave gauge data for the experiments in the compaction series, however, had to be manually offset to remove spikes in data as shown in Figure 5.15.

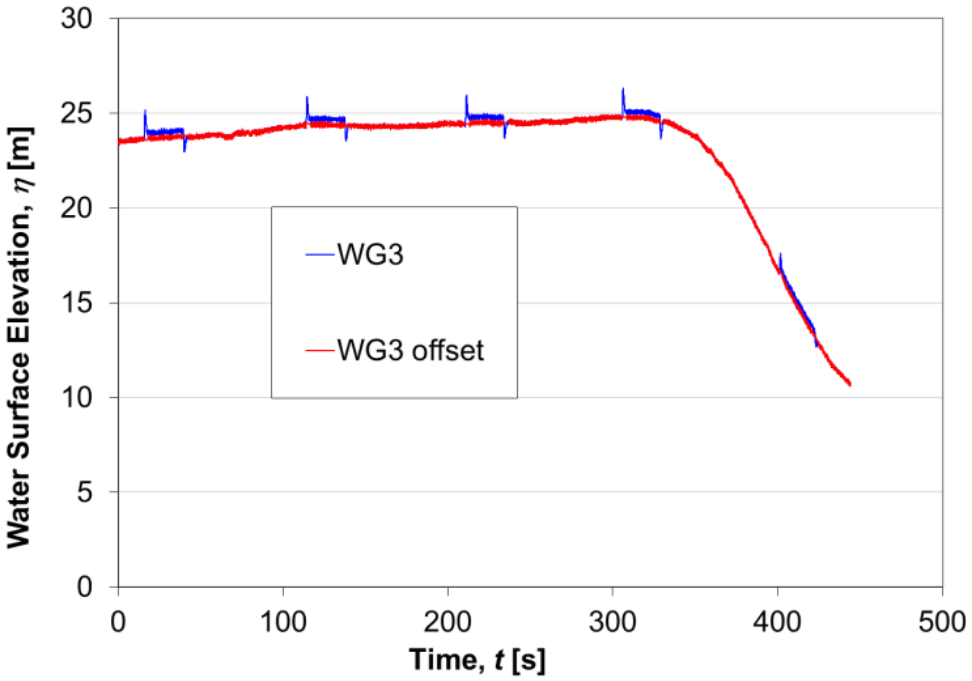

Figure 5.15: Wave gauge data offset (wave gauge 3 in test no. 4)

The breach outflow hydrograph determined using the hydrologic routing technique yielded large spikes due to noise in the wave gauge data. It was therefore necessary to process the wave gauge data using a Butterworth filter algorithm using MATLAB (Rennie, 2009), to remove such noise (see Section E.2 of Appendix E). The filtering process was conducted by defining two parameters for each wave gauge: order of the low-pass Butterworth filter and the normalised cut-off frequency. Figure 5.16 shows wave gauge data before and after the filtering process. Figure 5.17 shows the difference in the computed breach outflow hydrograph using four different simulations, each representing a unique Butterworth filter.

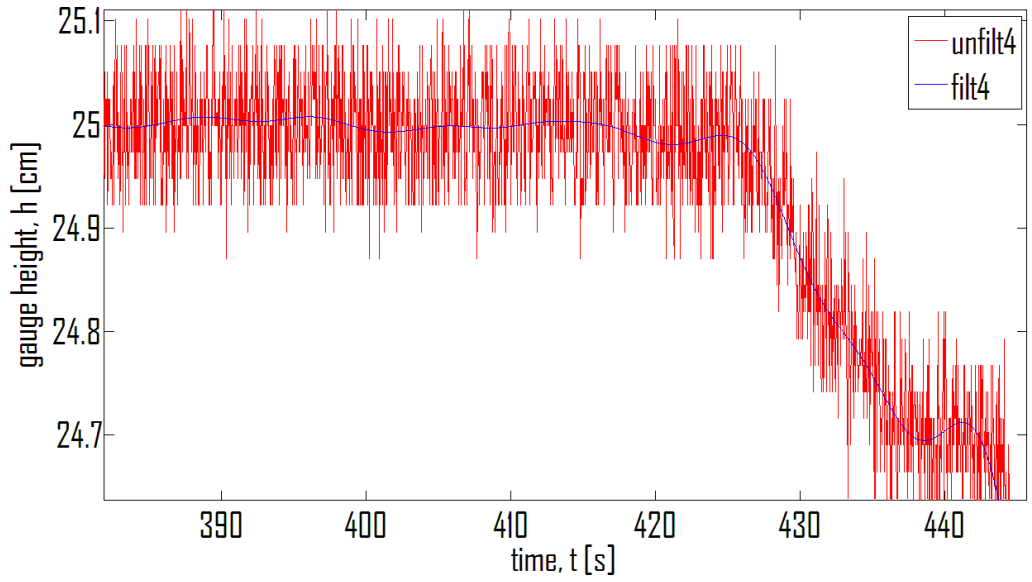

Figure 5.16: Filtering data from wave gauge 4 in Test No. 9

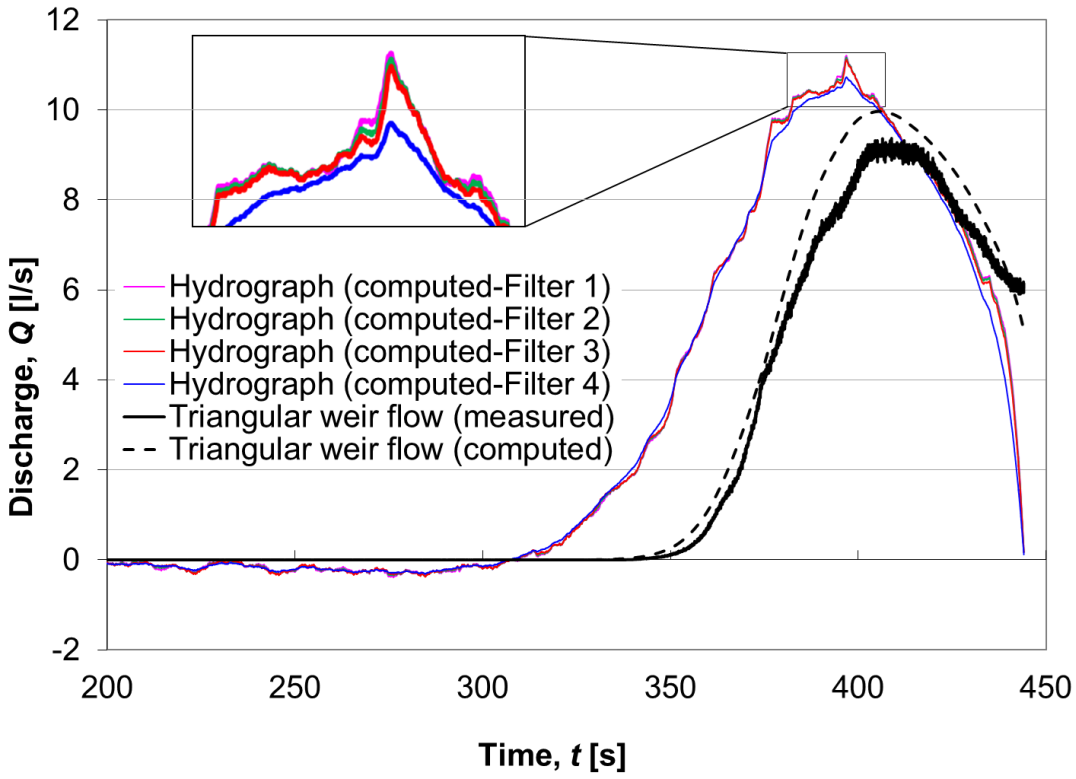

Figure 5.17: Comparison between breach outflow hydrograph computed using four different filtering configurations (Test No. 4; 5 blows; 5cm drop height) and measured using wave gauge in outlet tank (*i.e.* through triangular weir)

From Figure 5.17 it can also be shown that the hydrograph computed from the wave gauge installed in the outlet tank using Equation (5.1) in comparison to the hydrograph computed using the hydrologic routing method (*i.e.* Equation (4.142) in conjunction with the wave gauges installed in the upstream reservoir), is lagged and attenuated. As a check, the computed hydrograph ("Hydrograph (computed-Filter 4) as shown Figure 5.17) was routed into the outlet tank while the head above the V-notch was calculated also using a hydrologic routing method (see code in Section E.3 of Appendix E) and the WSL above the V-notch tank was computed. A comparison between the measured and computed flow over the V-notch is also shown in Figure 5.17. The measured flow over the V-notch tank still did exhibit a lag and attenuation in comparison to the computed hydrograph. This difference can be explained due to the storage of breach outflow occurring downstream of the embankment model during breach development. Figure 5.18 also shows the same comparison between the measured and computed outflows in addition to the WSLs in the V-notch tank. The hydrograph routing method based on Equation (4.142) was therefore preferred over the measured triangular weir flow. This method was employed in the analysis for the remainder of the experiments.

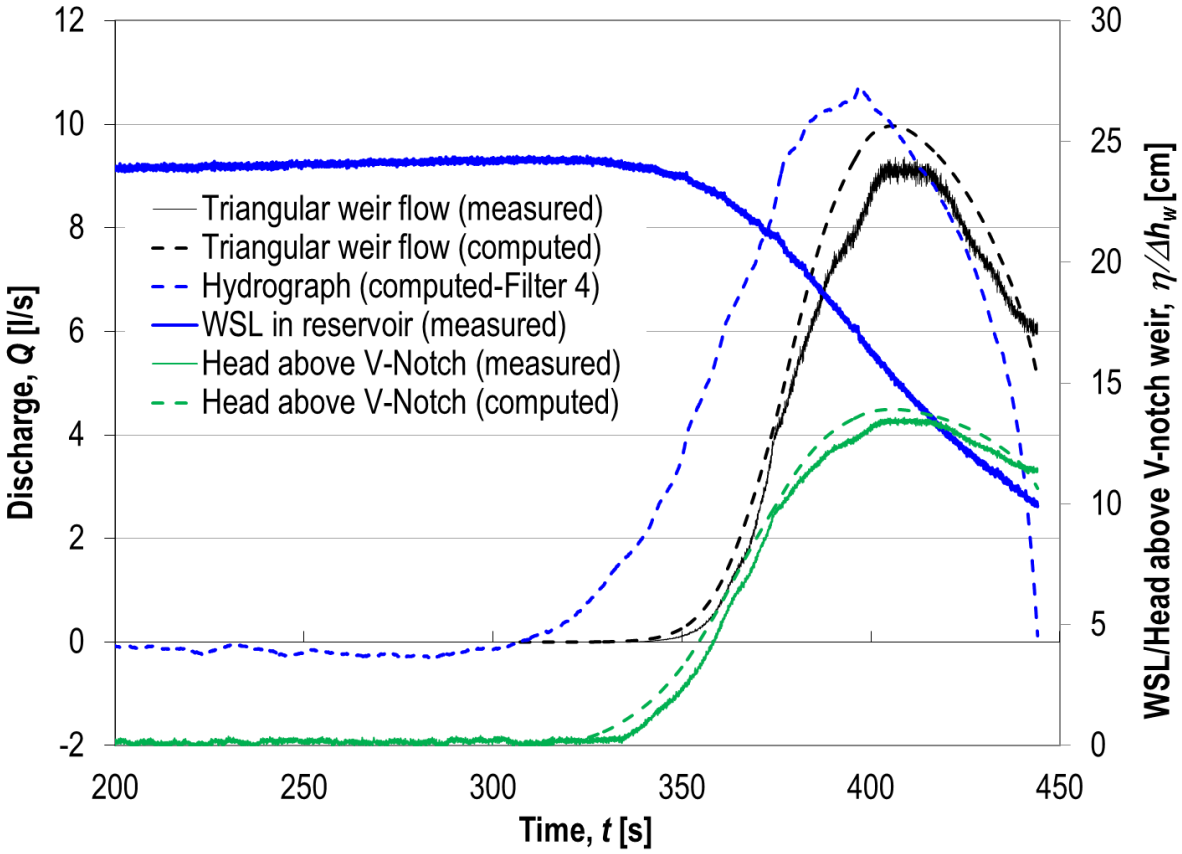

Figure 5.18: Comparison between computed and measured breach outflow hydrograph and head above V-notch tank (Test No. 4)

5.2.1.3 Results

The initial purpose of the small flume tests was to investigate the influence of compaction on embankment breach characteristics such as lag-time, time-to-peak, peak flow, and the base-time. However, the 38cm wide flume was too narrow for the embankment height, where the widening of the breach channel reached the side-walls too soon. Therefore, the only hydrograph characteristic viable for extraction was the lag-time as shown in Figure 5.19.

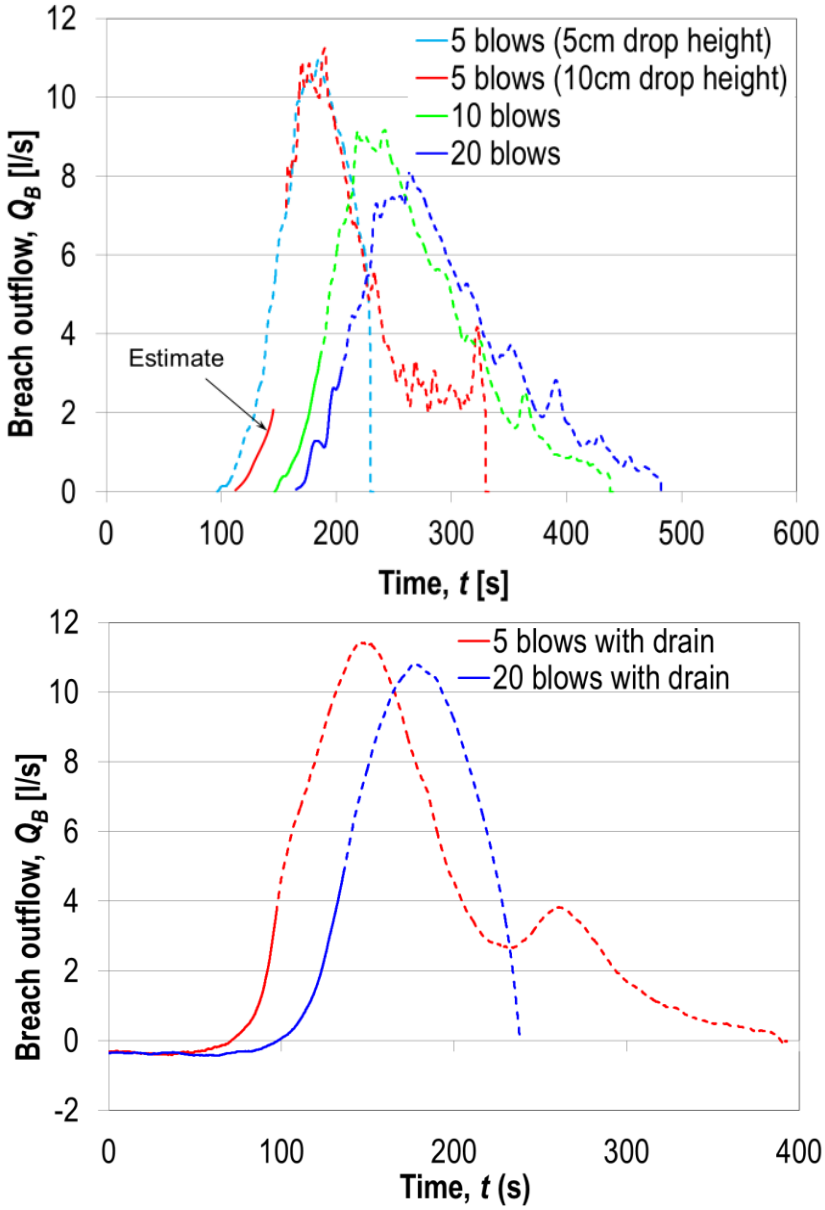

Figure 5.19: Outflow hydrograph computed for small flume (top) compaction series (bottom) drainage series (dashed lines indicate breach channel reached side-walls)

The lag-time herein is defined as the time between the onset of water traversing the downstream apex of the embankment crest slope through the V-notched pilot channel, and the onset of measureable breach outflow. Due to incomplete wave gauge data for the 5 blow compaction with a 10cm drop height (*i.e.* Test No. 7), the lag-time was estimated based on downstream WSLs captured from side-view cameras. The hydrograph segment representing the onset of measurable outflow

was also extrapolated based on the tailwater depth. From Figure 5.19, it can be shown that compaction increases the lag-time for both the compaction and drainage tests. Table 5.5 shows a summary of the significant data and results for the spatial overtopping breach tests in both test series. For test series "A" (*i.e.* compaction), the construction water content was not controlled which resulted in water contents larger than optimum (*i.e.* >11%; see Subsections C.1.5 and C.1.6 of Appendix C) and with large variations between the lifts (7-13%).

Table 5.5: Summary of results for compaction and drainage series

Test series	Test No.	γ_d [kN/m^3]	$\bar{\omega}^{\dagger}$ [%]	Drainage	z_{cr} [cm]	w_{cr} [cm]	η_{max} [cm]	$\forall_{max}$ [m^3]	t_L [s]
A	6	14.68	14.0 (N/A)	None	25	8	24.9	1.40	96
A‡	9	15.02	12.3 (7.0)	None	25	8	N/A	N/A	110
A	10	15.32	14.9 (8.9)	None	25	8	25.6	1.45	146
A	11	15.68	20.5 (13.2)	None	25	8	25.2	1.43	165
B	15	15.02	10.6 (2.8)	None	30	10	-	-	-
B	16	15.02	11.0 (4.9)	Undertoe	30	10	29.0	1.62	71
B	12	15.68	10.6 (2.8)	None	30	10	-	-	-
B	14	15.68	10.4 (2.9)	Undertoe	30	10	29.3	1.63	98

†construction water content reported as an average between all lifts constructed (variation in water content between parentheses); ‡wave gauge data incomplete, t_L estimated based on tailwater depth; η_{max}: maximum water surface elevation; $\forall_{max}$: maximum reservoir volume in the reservoir

Given the difference in embankment model heights and inflow patterns between the compaction and drainage tests, the embankment breach characteristics could not be compared. However, steady-state piezometric heads measured at the embankment model's foundation for the four drainage tests were analysed and compared to a numerical simulation. First, a steady-state seepage simulation was modeled by defining a homogeneous soil domain without a drainage element. The material properties (hydraulic conductivity at saturated conditions, k_{sat}; soil water characteristic curve; volumetric water content at saturated conditions) and upstream boundary conditions were input using three WSLs (η = 280, 185 and 50mm) in SEEP/W (GEO-SLOPE, 2004).

The numerical simulation was calibrated by adjusting the anisotropy ratio for hydraulic conductivity to achieve a best fit against the measured piezometric head. Using an anisotropy ratio, $k_{wy}(\psi)/k_{wx}(\psi) = 0.6$, a steady-state seepage simulation was then conducted for the embankment models with the undertoe-drain for the three WSLs. Soil parameters such as GSD and saturation water content for the filter and drain medium were required for input into SEEP/W in order to predict the SWCC and hydraulic conductivity function. The methods by Arya and Paris (1981) and Green and Corey (1971) available in SEEP/W (GEO-SLOPE 2004) were used to derive the SWCC and permeability function, respectively (see Figure C-15 and Figure C-20 in Appendix C). Figure 5.20 shows the measured and computed piezometric head along the embankment foundation using two compaction efforts (5 blows and 20 blows) at for three WSLs under steady-state conditions. The numerical simulations were quite reasonable.

It can be noted from Figure 5.20, that the measured piezometric head nearest to the downstream toe was higher than the embankment's profile. This was due to some slight deformation in the downstream slope as sliding prevailed. Figure 5.20 also shows that the presence of a toe-drain greatly influences the piezometric measurements, where the piezometric head for a higher compaction effort was lower under drained conditions, particularly near the drain. This phenomenon emphasizes the importance of compaction on PWP buildup near a drain. Higher compactions reduce the pore-sizes in a soil, giving rise to a lower hydraulic conductivity and therefore a lower phreatic surface. This effect is more noticeable in downstream regions of the embankment model since the drain acts as a high flow sink. The effect is diminished in upstream regions (*i.e.* near the reservoir).

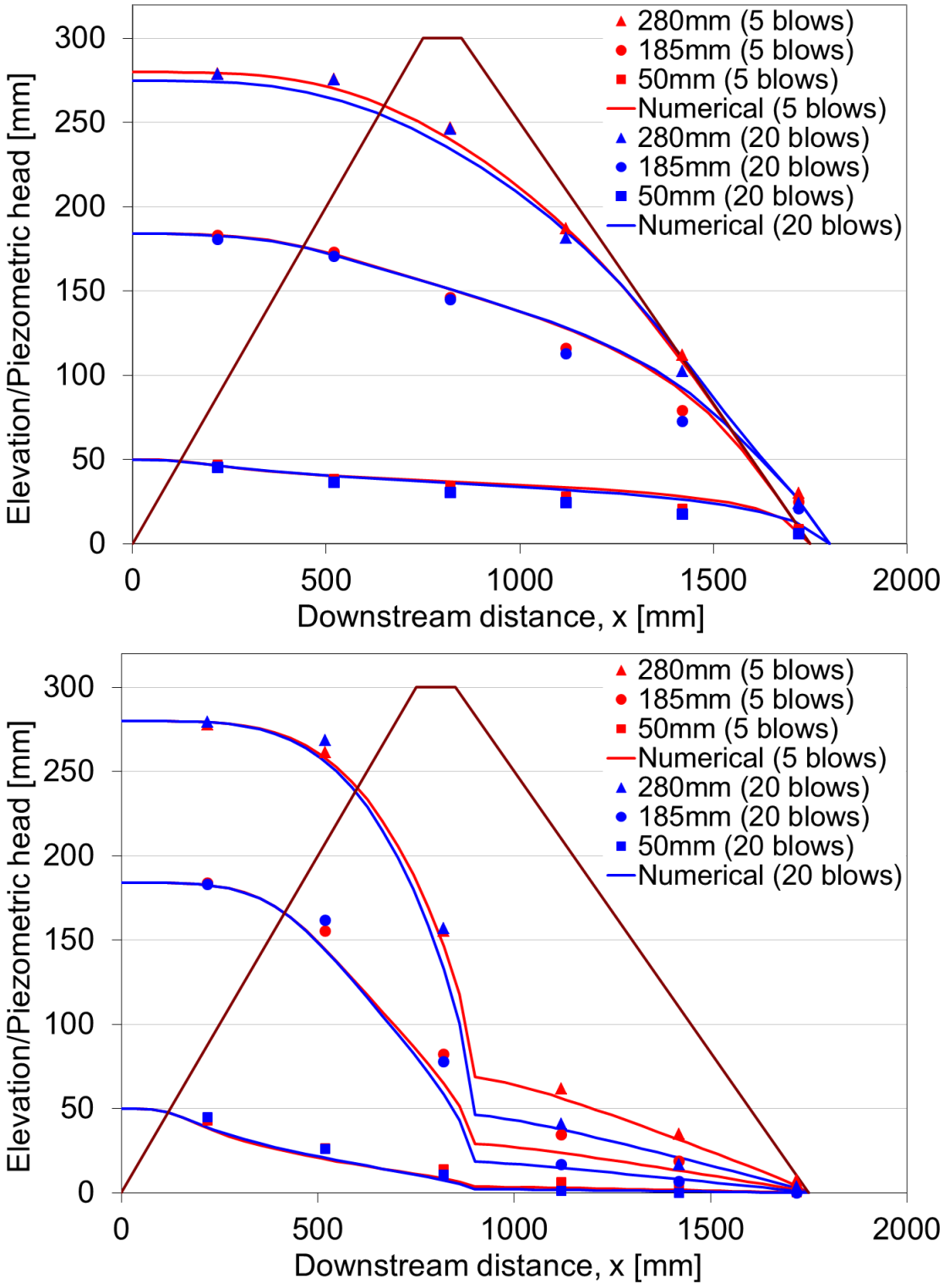

Figure 5.20: Measured and computed (SEEP/W) steady-state piezometric head along embankment model foundation for two compactions (5 blows and 20 blows) at η = 280, 185 and 50mm (top) without drain (bottom) with drain

The simulated PWP distribution in both drained and undrained embankment models by SEEP/W, shown in Figure 5.21, illustrates how the presence of a drain reduces the PWP in the downstream slope as well as the potential for slope instabilities.

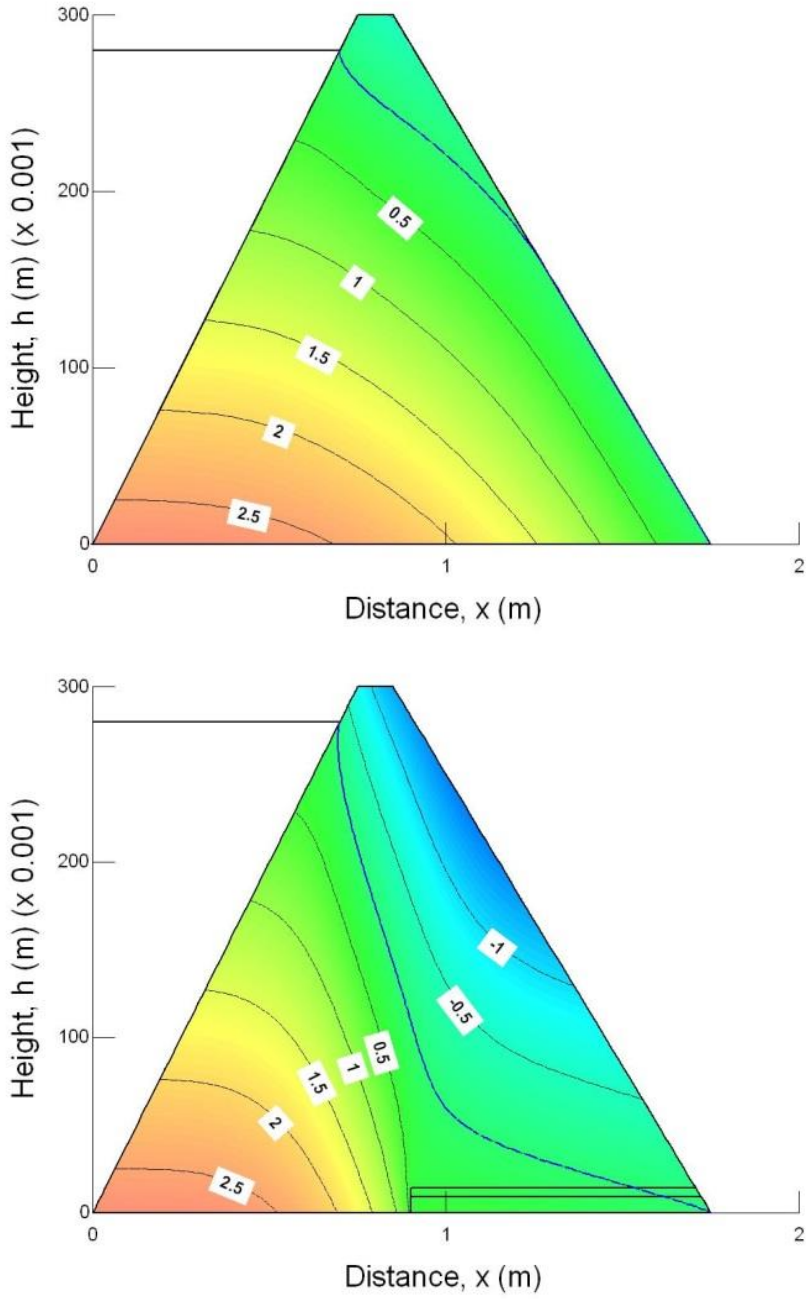

Figure 5.21: Numerical simulation of steady-state PWP distribution [kPa] and phreatic surface in embankment model constructed with 20 blows (η = 28cm) (top) without drain (bottom) with drain

5.2.2 Large Flume Tests

As part of Phase I of the experimental program, 3-D breach overtopping tests were also conducted in a larger hydraulic flume, 1.5m wide, 29.2m long and 0.77m high. The flume bottom was smooth and impervious, with a null slope. Located at the downstream end of the flume, is a drop-off outlet which leads to a reservoir below the laboratory floor. The large flume tests of Phase I of the experimental program (Series “C”) were comprised of drainage and initial breach geometry tests as part of a collaborative effort with a Master’s thesis project (Orendorff, 2009). The overtopped embankment models for Series “C” conducted in the large flume were constructed using a new batch of sand (*i.e.* sand Type II). Although the gradation for sand Type II was slightly different than sand Type I (see Section C.1 in Appendix C for detailed results of standard geotechnical tests), both sands were considered to be very similar. The compaction of the embankment models constructed in the large flume tests was the same as the embankment models overtopped in the small flume (*i.e.* using dynamic compaction). The construction technique for the large flume test series is described in detail in Subsection D.1.1.2 in Appendix D.

5.2.2.1 Experimental Setup

The experimental setup for the large flume tests is shown in Figure 5.22. A total of four WG-50 capacitance wave gauges were used to measure the time-history of WSLs in the upstream reservoir during the tests. The same sampling rate (30Hz) was used for the wave gauges. Similar to the small flume tests, the wave gauges were calibrated prior to each overtopping test (see Subsection D.2.1 in Appendix D for calibration process). Video footage was captured using high definition video cameras mounted on fixtures at three locations: upstream, downstream and above the crest as shown in Figure 5.22 (see Subsection D.3.2 in Appendix D for more details). A fourth high definition video camera captured roaming footage of the experiment. Impoundment of the upstream reservoir was carried out using the pump in the Hydraulic laboratory reservoir. The impoundment rate was deliberately slow (3-4mm/min) to prevent occlusion of air bubbles in saturated zones of the

embankment model. The impoundment was ceased once the WSL in the upstream reservoir reached 28cm, after which it was confirmed by means of a point gauge. Overtopping was initiated by introducing inflow (Q_I = 0.45 l/s) into the upstream reservoir using a water hose throughout the entire duration of the test.

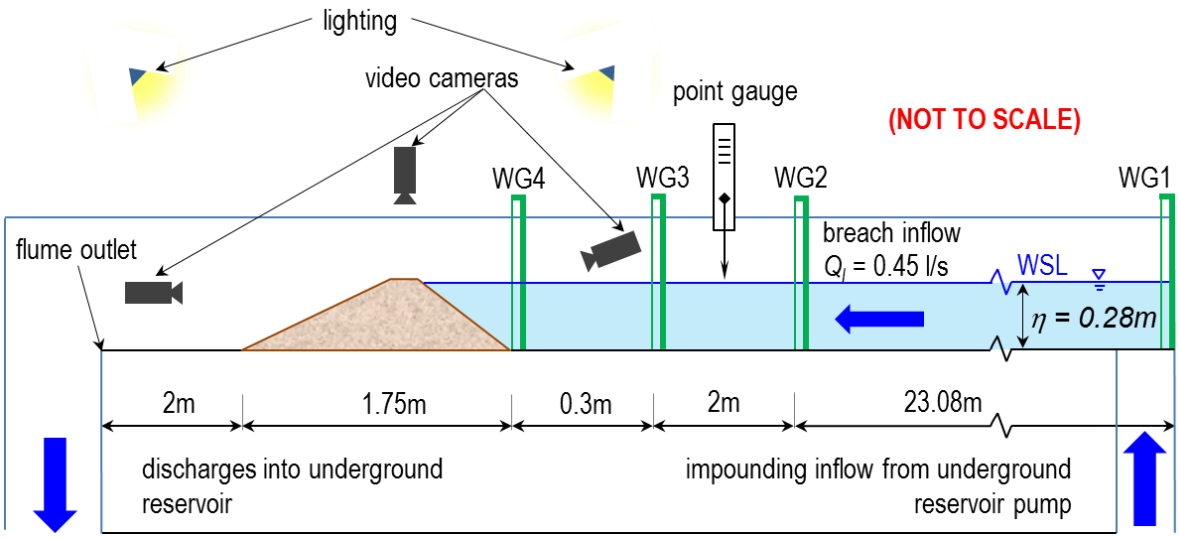

Figure 5.22: Experimental setup in large flume (Series “C”)

As shown in Table 5.6, a total of 7 tests were carried out in the large flume, including two pilot tests, one of which had failed. The upstream and downstream shoulder slopes of the embankment models were 1V:2.5H and 1V:3H, respectively, identical to the embankment models used in the drainage tests (see Figure 5.11 for embankment dimensions). An undertoe drain was installed in all embankment models with the exception of: two pilot tests, a composite test, and one test used to investigate the absence of drainage conditions. The construction technique for the large flume embankment models constructed for Series “C” can be found in Subsection D.1.1.2 of Appendix D.

Table 5.6: Test matrix for large flume tests (Series "C")

Test No.	Test characteristic	Date†	Crest dimensions		Compaction‡		Notes
			Elevation, z_{cr} [cm]	Width, w_{cr} [cm]	No. of blows	Drop height [cm]	
1	Pilot test (no drain)	9 Jul.	60	20	Arbitrary (medium compaction)		Blast crater as initial breach geometry. Successfully breached.
2	Pilot test (no drain)	23 Sep.	25	8	5	10	Tapered crest as initial breach geometry. Failed test.
3	V-notch (no drain)	30 Sep.	30	10	5	10	Successfully breached.
4	Blast crater (drain)	15 Dec.	30	10	5	10	Successfully breached.
5	Tapered crest (drain)	22 Dec.	30	10	5	10	Successfully breached.
6	V-notch (drain)	13 Jan.	30	10	5	10	Successfully breached.
7	Blast crater (composite)	20 Feb.	30	10	5	10	Successfully breached.

†Test No. 1 to 5 in year 2008; test No. 6 and 7 in year 2009; ‡all embankment models had a dry unit weight of 15.02kN/m^3

The main purpose of the pilot tests was to determine an appropriate embankment height such that the breach channel did not reach the side walls during the full duration of the breaching process of the 1.5m wide flume. The first pilot test was comprised of a 60cm high embankment, compacted arbitrarily using the hand tamper (see Figure 5.23). An initial breach geometry with the shape of a blast crater was excavated from the embankment crest at the centreline of the flume. The excavation was then backfilled into the crater and confined within a geotextile. The upstream water surface level was monitored using the point gauge. Immediately after the water surface elevation reached the embankment crest height, the excavated backfill was removed and the breaching process observed. All the large flume embankment models were constructed with a dry unit weight equal to 15.02 kN/m^3. This *in situ* unit weight corresponds to 5 blows dropped from a 10cm height (see Subsection D.1.1.2 of Appendix D).

Figure 5.23: Pilot test in large flume simulating breaching due to blast-induced crater (Test No. 1)

Similar to the earlier small flume tests, the breaching process was too rapid and the lateral erosion mechanism in the breach channel reached the side-walls of the flume before a total drawdown in the reservoir was achieved. The second pilot test performed was comprised of a 25cm high embankment model without an undertoe-drain. The crest of the embankment model was flat with a slight taper towards the crest's centreline to initiate breach away from the flume's side-walls. Nevertheless, breaching occurred far from the centreline due to the insufficient crest height. It was also noticed during the second pilot test that the downstream gate in the flume was accidently raised by 3cm. The test was considered a failure due to the subsequent lateral erosion reaching the flume side-walls too soon as well as the influence of the tailwater on the breaching process. For the two pilot tests, tracers in the form of coloured cork fragments were embedded between each lift in an effort to trace the breach channel morphology (Orendorff, 2009), similar to Feliciano-Cestero (2010). This technique was discarded from future tests since the cork tracers could not be located from the video footage due to the severe opaqueness of the breach outflow. Flow tracers comprised of Styrofoam spheres were scattered in the reservoir upstream to compute surface velocities within the vicinity of the breach channel.

Based on the breaching process observed in the two large flume pilot tests, a 30cm embankment model height was seen as the most feasible. The composite (i.e. clay

core) embankment model unlike the homogeneous embankment models, was much more resistant to erosion, and consequently prolonged the breach time. Therefore, out of the seven tests performed, only four tests were deemed useable for analysis (Test No. 3 to 6 in Table 5.6). The two tests which were of particular interest to this study were Tests No. 3 and 6, and which their results are presented and discussed in the following subsection. Some of the results of the initial breach geometry tests are also shown in the following subsection. However, the detailed methodology, results and conclusions regarding those tests can be found in Orendorff (2009), Orendorff *et al.* (2009) and Orendorff *et al.* (2013).

5.2.2.2 Results

The same data analysis used for the small flume was applied to the large flume tests. The 2m separation distance was respected and no spikes in wave gauge data were observed. Hydrographs from wave gauge data were computed using the hydrologic routing method (see Section E.4 of Appendix E) and plotted alongside upstream WSL as shown in Figure 5.24. The lateral progression of the breach channel did not reach the flume side-walls, which indicated that the embankment model height was suitable, and the test was a success. The hydrograph time shown in Figure 5.24 is referenced with respect to the onset of overtopping. A summary of the embankment breaching characteristics for the large flume tests in Phase I of the experimental program is shown in Table 5.7. Only the tests which were initiated using a V-notch carved on the centreline of the embankment model's crest (*i.e.* Test No. 3 and 6) are discussed in detail in this study.

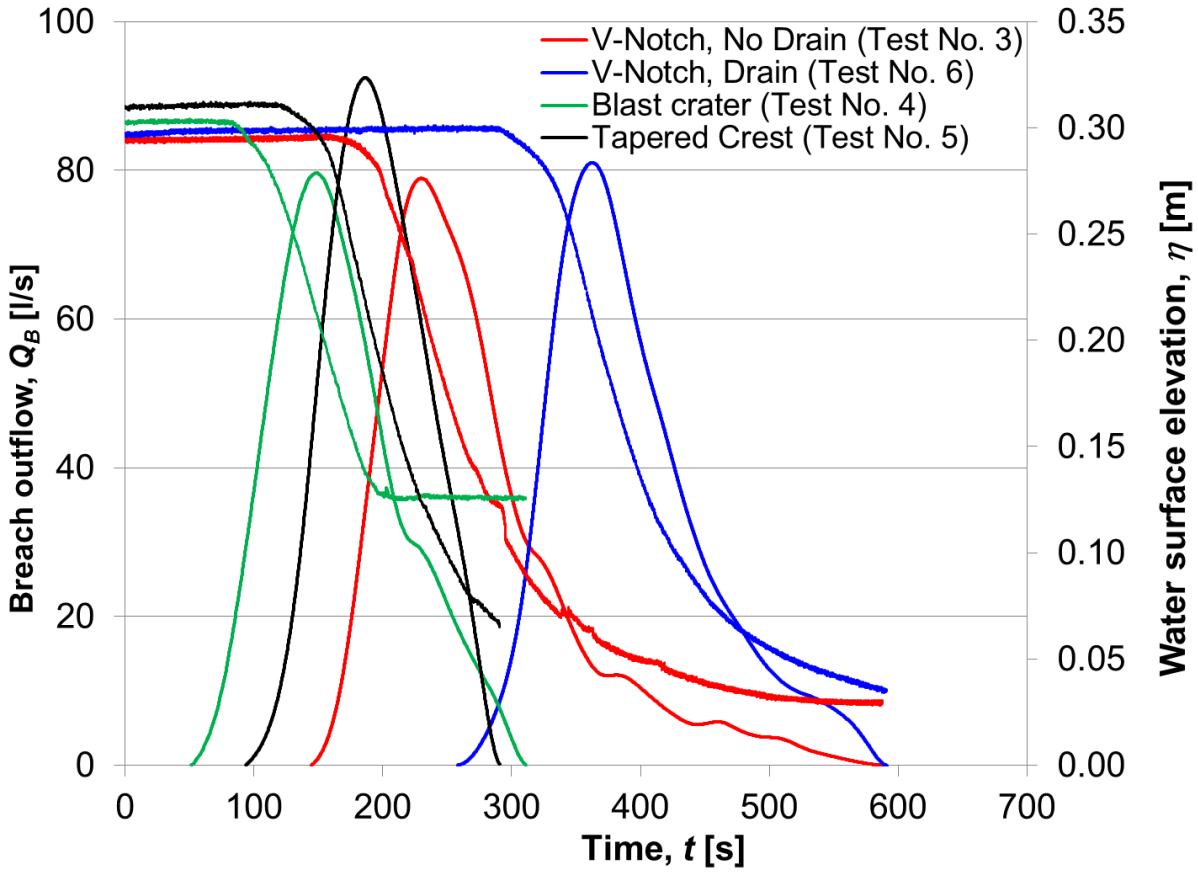

Figure 5.24: Hydrographs and upstream WSLs for Phase I large flume tests (Series "C")

Table 5.7: Summary of large flume tests of Phase I (series "C")

Test characteristic	Test No.	$\bar{\omega}^{\dagger}$ [%]	η_{OT} [cm]	η_{max} [cm]	$\forall_{max}$ [m^3]	Q_P [l/s]	t_L [s]	t_P [s]	t_B [s]
V-notch (no drain)	3	12.8 (8.8)	29.4	29.7	11.45	78.92	145	85	442
Blast crater (drain) ‡	4	13.4 (7.1)	30.3	30.4	11.78	79.7	51	97	260
Tapered crest (drain)	5	11.8 (4.8)	31.0	31.2	12.05	92.4	93	93	197
V-notch (drain)	6	14.1 (2.4)	29.7	30.1	11.54	81.0	258	104	332

†construction water content reported as an average between all lifts constructed (variation in water content between parentheses); ‡wave gauge data incomplete, hydrograph estimated using three out of four wave gauges; η_{OT}: water surface elevation at onset of overtopping

Not considering lag-time, the embankment breach outflow characteristics (*i.e.* t_P, t_B and Q_P) for all Series "C" tests were similar, with the exception of the embankment model with the tapered crest. The volume accumulated upstream the embankment

model with the tapered crest was larger due to the absence of a conveyance channel on the embankment model's crest which facilitated the initiation of the breach channel. The undertoe-drain present in the embankment model with the V-notch initial breach geometry delayed the breach initiation by a factor of 1.8. It was also noticed that the undercutting mechanism in the breach channel entrance was much larger in the absence of a drainage layer wherein the type of slope instability was in the form of slides rather than collapses (see Figure 5.25). The undercutting mechanism gave rise to adverse side-slopes in the breach channel and consequently led to the formation of large soil overhangs. This has also been observed by other researchers (Mohamed *et al.* 1999; Coleman *et al.* 2002; Hunt *et al.* 2005; Geisenhainer and Kortenhaus, 2006; Stretch and Parkinson, 2006; Pickert *et al.* 2011). Video footage also showed that the lag-time was prolonged due to the time elapsed in saturating the downstream slope prior to the inception of significant erosion.

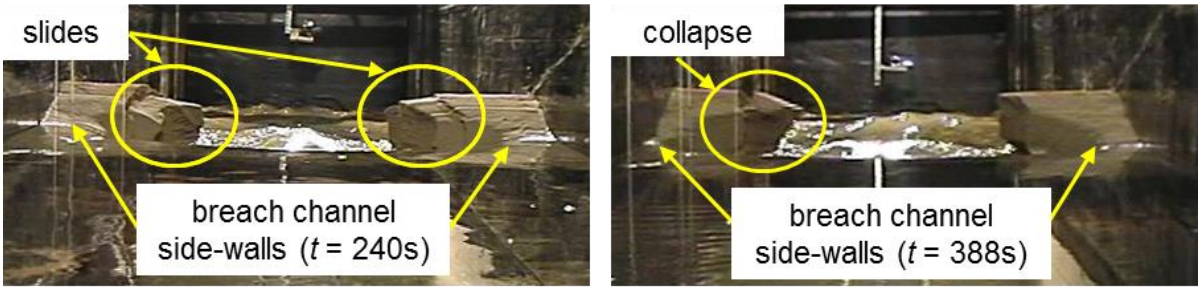

Figure 5.25: Upstream view of breach channel side-slope failures in large flume tests (left) Test No. 3, no undertoe-drain (right) Test No. 6, undertoe-drain

Figure 5.26 shows the lagged hydrographs and water surface levels in the reservoir to reflect the onset of breaching (*i.e.* measurement of considerable flow) as the reference time for Tests No. 3 and 6.

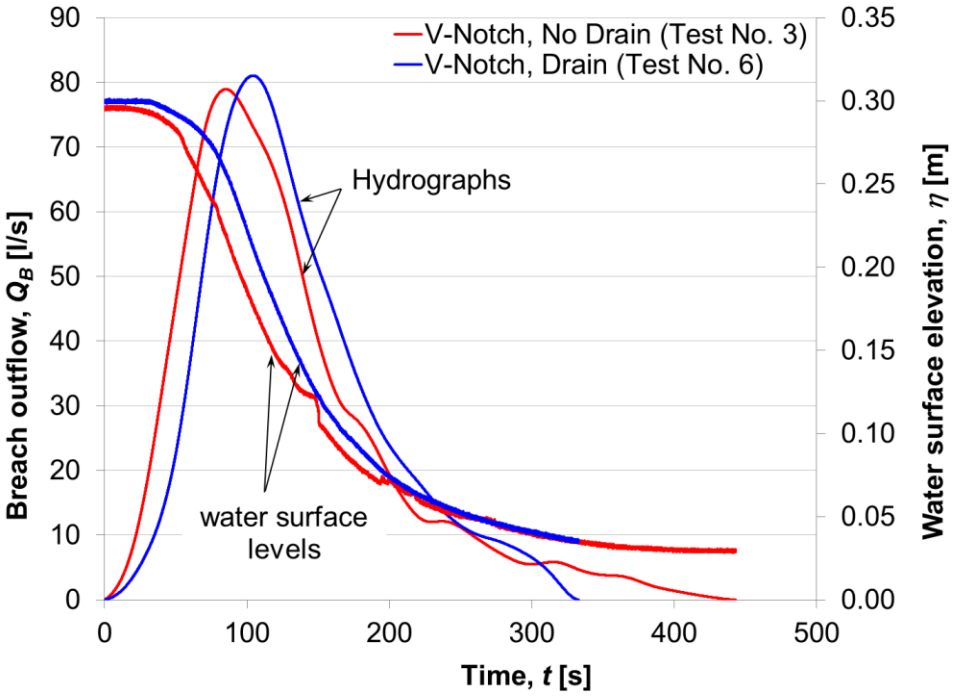

Figure 5.26: Lagged hydrographs and WSLs for Tests No. 3 and 6

Video footage on the evolution of the breach channel revealed that slope failures were less frequent and more discrete in the case when the embankment model included a drainage element. However, it was noticed that the slope failures predominantly occurred above the water surface line (see Figure 5.25) and on the downstream shoulder slope. This is contrary to other experiments which showed side-slope failures occurring below the water surface line (see Figure 3.8). The slope failures therefore did not notably influence the submerged breach channel width due to the hydrostatic forces which stabilised the breach channel side-slopes. Since breach outflow is governed by both the vertical and lateral breach channel dimensions (*i.e.* weir flow), it can therefore be argued that the dominant breach mechanism in these tests was vertical erosion and not slope failures. This can also be confirmed by comparing the peak flow and time-to-peak for the hydrographs between Tests No. 3 and 6, which were in fact very similar (see Figure 5.26). On the other hand, slope failures generally reduced the breach outflow due to submerged flow conditions (*i.e.* backwater effects) caused by the flow obstruction by the slumped material in the breach channel.

5.3 Discussion

This preliminary work was valuable in terms of correlating the numerical and experimental aspects of the embankment breach problem with the knowledge gap stated in literature. The numerous simulations carried out in the sensitivity analysis, explained how simplifications and new methodologies of certain embankment breach processes (*e.g.* side-slope instabilities) are reflected in the outflow hydrograph. In the case of the NWS-BREACH model, the outflow hydrograph was uniform in shape and characterised by a very consistent and short time-to-peak. The breach depth development was almost instantaneous. The HR-BREACH model's new methodology for adjusting the top width of the breach channel by bending or shear failure, gave rise to outflow hydrographs with multiple peaks and irregular breach times.

The sensitivity analysis using the two mentioned physically-based numerical models provided a useful insight on the uncertainty for input parameter selection for the two numerical models. However, the outcome of the analysis cannot be applied as a general rule for all embankment designs. This is due to the fact that the performed analysis was based on a selected range of values which were unique to the stencil embankment. For a different embankment, the analysis would have yielded different results. Therefore, it is suggested to conduct such an analysis for any proposed embankment design.

In order to determine the global uncertainty in an embankment breaching characteristic due to more than one input parameter, a sensitivity analysis may be carried out by combining the uncertainties using the following expression (IMPACT, 2004b):

$$\Gamma_{unc} = \sqrt{\left[\left(\frac{\partial \Gamma}{\partial G_i}\right)\Delta G_i\right]^2 + \left[\left(\frac{\partial \Gamma}{\partial G_{i+1}}\right)\Delta G_{i+1}\right]^2 + \cdots + \left[\left(\frac{\partial \Gamma}{\partial G_{i_{max}}}\right)\Delta G_{i_{max}}\right]^2} \qquad (5.2)$$

where Γ is the embankment breach characteristic of interest, and G_i, G_{i+1} and $G_{i_{max}}$, are the input parameters on which Γ depends, $\partial\Gamma/\partial G_i$, $\partial\Gamma/\partial G_{i+1}$ and $\partial\Gamma/\partial G_{i_{max}}$ are the sensitivities of characteristic Γ on input parameters G_i, $G_{I+1}$and $G_{i_{max}}$, respectively, and ΔG_i, ΔG_{i+1} and $\Delta G_{i_{max}}$, are the range of the input parameters, respectively. The HR-BREACH numerical model employs the Monte Carlo analysis which is an alternative method for determining the global uncertainty. It is described in more detail in Subsection A.2.6 of Appendix A.

The results of the 3-D breach overtopping tests conducted in the small flume revealed that the compaction effort influenced the erosion and the side-slope failure mechanism in both drainage configurations. The lag and higher peak of the hydrograph in Figure 5.19 implied that compaction does in fact influence the breaching mechanism. But in order to describe the influence of compaction for the entire breach process, a wider flume is required. It is for this reason that the compaction test series were conducted in a wider hydraulic flume as part of Phase II of the experimental program. Based on the results of the small flume tests, it was necessary to observe the minimum separation distance (2m) between wave gauges as well as establish a method for controlling the construction water content.

The 3-D breach overtopping tests conducted in the large flume revealed that using an initially unsaturated soil-water state can significantly prolong the lag-time due to the infiltration of water in the downstream slope. In the breach development stage, the side-slope failure mechanism also varied significantly in terms of mode and frequency between the two drainage configurations. This implied that breach overtopping experiments must scale, or at least reflect to some degree, the soil-water state and the densification of the embankment material. The duplicability of an overtopping experiment for an embankment model with a material which has been arbitrarily compacted, or unregulated in terms of initial soil-water state, simply cannot be guaranteed. A novel construction technique mimicking a prototype construction was therefore designed and implemented in the following experimental

phase. A number of guidelines have been defined in order to achieve better control over many of the embankment parameters in the improved construction technique.

Due to the high nonlinearity and degree of coupling existing between the breach processes, scaling of the soil-water state or densification may prove to be an extreme challenge. The method of scale series (Hughes, 1993) for determining the scaling criteria (and the corresponding scale effects) in an overtopped homogeneous embankment model was therefore employed in the following experimental phase. It was also necessary to investigate the overtopping mechanism with respect to the morphology of the curved breach channel entrance (*i.e.* control section) forming on the upstream slope, rather than the constriction width of the breach channel. Phase II of the experimental program therefore presents a more in-depth investigation on breach channel morphology and the scaling of geotechnical and hydraulic parameters. This experimental phase was carried out on embankment models constructed in a 1.5m-wide hydraulic flume, and using a controlled construction technique comprised of both vibratory and static loads for achieving optimum moisture conditions.

5.4 Conclusions and Recommendations

5.4.1 Embankment Breach Numerical Modeling

First, a detailed sensitivity analysis was performed using two embankment breach numerical models, NWS-BREACH and HR-BREACH for a total of nineteen (19) input modeling parameters including geometric, geotechnical, hydrometeorologic, hydraulic and computational attributes. A total of 100 simulations using the NWS-BREACH model and 116 simulations using the HR-BREACH model were performed on embankment models and the breach outflow, temporal breach width, depth and ratio of breach width-to-depth were determined. Several findings from this work emerged:

- Modeling of lateral growth in the breach channel as discrete side-slope failures due to bending and shear by the HR-BREACH model resulted in breach outflow hydrographs with multiple peaks and irregular breach times.
- The breach outflow hydrograph for the NWS-BREACH model was more uniform than that generated by the HR-BREACH model and had no outflow fluctuations. The breach side-slope angle with respect to the vertical was always reported to be 29.5° for all NWS-BEACH simulations.
- The NWS-BREACH model was the least sensitive of the two with respect to the input parameters used, where the time-to-peak embankment breach characteristic was almost identical in each simulation.
- Although the sensitivity analysis is a useful method to assess model uncertainty, it has its limitations since the input parameters are often case-dependent. An alternative method for assessing model uncertainty could involve conducting a Monte Carlo simulation analysis.

5.4.2 3-D Breach Overtopping Tests

Subsequently, an experimental program (Phase I) was initiated to investigate parameters that govern the hydraulic modeling as well as the breaching process of noncohesive embankment models due to overtopping flow using laboratory scales. The chosen parameters addressed geotechnical parameters such as compaction effort during construction and initial soil-water state prior to overtopping. In this preliminary experimental phase, the influence of these geotechnical parameters on the breaching process was investigated using two test series: a compaction test series, comprised of embankment models constructed using different compaction efforts, and a drainage test series, comprised of embankment models constructed with and without horizontal undertoe drains. Construction of the embankment models was carried out by compacting the embankment material (fine sand) using a dynamic technique. The instrumentation used in this experimental phase included wave gauges, piezometers, and video cameras. The 3-D breaching overtopping tests were conducted in small and large flumes, 0.38m and 1.5m wide, respectively,

in the Hydraulics Laboratory. The breach outflow hydrographs were computed from the recorded water surface elevations using a hydrologic routing method.

- Based on the measured and numerically simulated piezometric head, it is of particular importance to address compaction near the undertoe drain of a noncohesive embankment.
- The embankment breach characteristics for the small flume tests could not be fully analysed since the breach channel reached the flume side-walls too soon (*i.e.* prior to peak conditions).
- A noticeable correlation existed between both the initial soil-water state and compaction effort and the breach outflow hydrograph's lag-time, t_L. Lag-time increased for seepage-controlled and denser embankment models.
- For the drainage series conducted in the large flume, the presence of a horizontal undertoe drain resulted in a lower frequency of side-slope failures, where the mode of failure was collapses rather than slides as observed for the undrained embankment model. For both drainage configurations, however, the rest of the hydrograph characteristics; time-to-peak, t_P, base-time, t_B, and peak flow, Q_P, were almost identical.
- Based on the noticeable difference in the lag-time as well as the observed side-slope failure mechanism between the two drainage configurations, it is strongly advised that initial soil-water state should not be treated arbitrarily, particularly when other test parameters are varied within a test series. A similar precaution should be made with respect to the compaction effort used to densify embankment materials in physical models. *Arbitrary treatment of those two geotechnical parameters will not ensure repeatability of the experiments.* It is suggested that compaction in laboratory models should be scaled based on the erodibility of the embankment material.
- Due to the rapid lateral evolution of the breach channel, it would be useful to conduct the compaction test series in a wide hydraulic flume (addressed in Phase II of this experimental program).

Chapter 6

3-D Breach Overtopping Tests – Development of New and Improved Construction and Testing Techniques (Phase II)

The second phase of the embankment breach experimental program at the University of Ottawa began in May 2009 and was conducted in a wide flume of the Hydraulics Laboratory. The second experimental phase comprised the following:

- Development of a novel compaction method simulating a prototype construction using vibratory and static loads applied at optimum *in situ* moisture conditions
- Scale series tests that investigated the degree of compaction as a geotechnical scaling parameter quantified by the relative density
- Scale series tests which investigated geometric scales as hydraulic scaling parameters quantified by tilted and quasi-exact geometric scale ratios
- Drainage series test using embankment models constructed with the new compaction method
- Hydrograph analysis and breach channel entrance mapping for the test series
- Evaluation of the Froude number as a scaling criterion for both tilted and quasi-exact geometric scales series and the resulting scale effects
- Investigation of test repeatability

Part of the test description and results of Phase II were published in Al-Riffai *et al.* (2011) and Al-Riffai and Nistor (2011). A journal publication for this experimental phase is in preparation at the date of submission of this thesis (Al-Riffai and Nistor, 2014a).

6.1 Improved Construction Technique and New Geotechnical Investigations

A new construction method mimicking a typical prototype construction was developed for the granular embankment material using a vibratory load whereby the compaction effort was controlled by means of a static load. The compaction of the embankment material was based on *in situ* optimum conditions as opposed to the optimum conditions identified under conventional laboratory conditions (*i.e.* Standard Proctor tests). Several attempts were made in order to produce soil lifts, 5cm high, in a consistent and uniform manner. The compaction technique comprised a vibratory compactor to which a static load (4kPa) was applied to further densify the embankment material. Details on the finalized novel compaction technique, including the initial attempts made, are described in Subsection D.1.2 of Appendix D. Since the tests utilized a new batch of fine sand (sand Type III), the same geotechnical tests described in Phase I of the experimental program were repeated for the new sand. The adopted new compaction technique was more efficient at densifying the fine sand and resulted in higher dry unit weights. Additional standard geotechnical tests such as maximum and minimum density tests and SWCC, which were not included in Phase I, were also performed for the new embankment material (see Subsections C.2.1 and C.2.2, respectively, of Appendix C for details). Tests pertaining to the *in situ* density corresponding to the newly developed construction method were also carried out. The methodology and results of the *in situ* density determination tests are described in detail in Subsection C.2.3 of Appendix C. All the tests conducted on sand Type III samples were carried out in the Geotechnical Engineering Laboratory of the University of Ottawa, prior to construction and testing, whereas the *in situ* density tests were conducted in the large flume of the Hydraulics Laboratory.

6.2 Scale Series Tests

The 3-D breach overtopping tests in Phase II of the experimental program were investigated in the same large flume used in Phase I. The Phase II large flume test

series were subdivided as follows: compaction, drainage, tilted and quasi-exact, described herein as test Series “D”, “E”, “F” and “G”, respectively. In addition to the experimental parameters which were varied in the test series, the aspect of repeatability was also investigated. A test matrix for the spatial breach overtopping tests conducted in Phase II of the experimental program is shown in Table 6.1. All embankment models were successfully breached. Test No. 2 in Table 6.1 was comprised of an embankment model constructed at the largest-scale and compacted at an intermediate degree of compaction (as described in this subsection). This embankment model was considered the benchmark (or prototype), for which all the remaining tests where compared against. It was repeated amongst other tests in order to gauge the aspect of repeatability in 3-D embankment breach overtopping.

Table 6.1: Test matrix in large flume tests for Phase II

Test No.	Test series	Date	Scale ratios†				Crest height, h_{cr} [m]	Notes
			X_{rr}	Z_{rr}	e	D_r[%]		
1	D (high compaction)	3 Sep. 2010	1	1	0.516	80	0.30	-
2‡	D (intermediate compaction)	21 Sep. 2010	1	1	0.606	52	0.30	-
3‡	D (intermediate compaction)	22 Jun. 2011	1	1	0.606	52	0.30	Test No. 2 repeated
4	D (low compaction)	22 Oct. 2010	1	1	0.740	7	0.30	-
5	E (no drain)	27 Sep. 2010	1	1	0.606	52	0.30	-
6	F (tilted scale $1/2$)	29 Oct. 2010	$1/2$	1	0.606	52	0.30	-
7	F (tilted scale $1/3$)	4 Nov. 2010	$1/3$	1	0.606	52	0.30	-
8	G (quasi-exact scale $1/2$)	26 May 2011	$1/2$	$1/2$	0.606	52	0.15	-
9	G (quasi-exact scale $1/2$)	20 Jun. 2011	$1/2$	$1/2$	0.606	52	0.15	Test No. 8 repeated
10	G (quasi-exact scale $1/3$)	11 May 2011	$1/3$	$1/3$	0.606	52	0.10	-
11	G (quasi-exact scale $1/3$)	9 Jun. 2011	$1/3$	$1/3$	0.606	52	0.10	Test No. 10 repeated

†geometric scale ratios are based on 30cm high embankment model, with a 10cm crest width and 1V:2.5H and 1V:3H upstream and downstream slopes, respectively; ‡benchmark tests

6.2.1 Compaction Tests (Series “D”)

The objective of the compaction series in Phase II of the experimental program was to investigate the influence of compaction effort on the breaching mechanism in noncohesive earth embankment models. The compaction series was carried out using high, intermediate and low compaction efforts with dry unit weights equal to 17.80 kN/m^3, 16.80 kN/m^3 and 15.50 kN/m^3, respectively, with relative densities equal to 80%, 52% and 7%, respectively (see Subsection C.2.3 of Appendix C for details on how the compaction efforts was achieved). The 3-D breach overtopping test for the embankment model constructed using an intermediate compaction was repeated.

6.2.2 Drainage Tests (Series “E”)

Since the construction technique and embankment material in Phase II of the experimental program were both different, it was necessary to repeat the drainage tests conducted in the large flume. The purpose of the drainage series was to compare the breaching mechanism between two embankment models with and without a horizontal drainage element. The embankment models were constructed with an intermediate compaction effort (*i.e.* γ_d = 16.8kN/m^3; $D_r = 52\%$).

6.2.3 Tilted Geometric Scale Tests (Series “F”)

The purpose of the tilted scale series tests was to investigate the applicability of the Froude scaling criterion for 3-D breach overtopping tests using a variable longitudinal geometric scale ratio, X_{rr}. It is expected that an increase in the embankment model’s downstream slope will proportionately increase the shear stress acting on the bed, as defined by Equation (4.54). The tilted embankment models were constructed with an intermediate compaction effort (*i.e.* γ_d = 16.8kN/m^3; $D_r = 52\%$). The breaching process in two embankment models with longitudinal scale ratios, $X_{rr} = 1/2$ and $X_{rr} = 1/3$, was compared with the full scale embankment model constructed for the compaction series (*i.e.* $X_{rr} = 1$), as shown in

Figure 6.1. The lateral and vertical scale, Y_{rr} and Z_{rr}, respectively, was the same for each embankment model (*i.e.* $Y_{rr} = Z_{rr} = 1$). The tilted geometric scale series tests were not repeated.

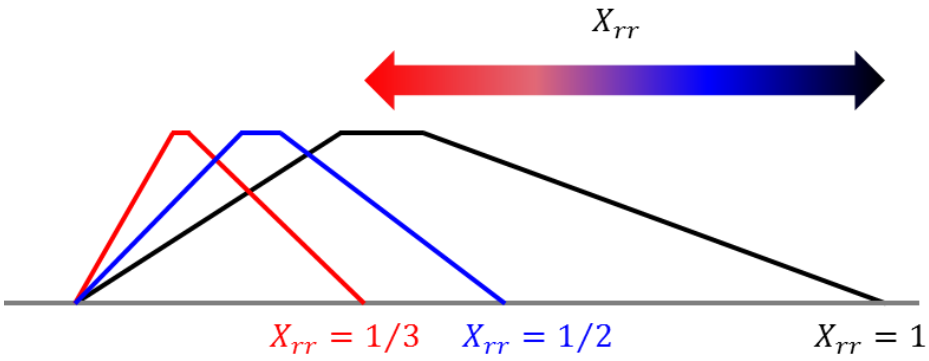

Figure 6.1: Tilted geometric scales (Series "F")

The advantages of using models with a tilted geometric scale are that the Reynolds number similarity is improved (since Re_{mm} is greater) where a more accurate depth measurement can be obtained (Chanson, 1999). A disadvantage of using tilted models is that the lateral and vertical time-scales represented by the breach channel morphology become irrelevant due to model distortion (Julién, 2002). It was not possible to reduce the longitudinal geometric scale any further since the shoulder slopes would be too steep and possibly make them vulnerable to failure, particularly the upstream slope during reservoir drawdown.

6.2.4 Quasi-Exact Geometric Scale Tests (Series "G")

The purpose of the quasi-exact geometric scale series tests was to investigate the applicability of the Froude scaling criterion for 3-D breach overtopping tests using variable geometric scale ratios in both the longitudinal and vertical directions, X_{rr} and Z_{rr}, respectively. The quasi-exact scale series differs from exact scale series in terms of the lateral scale, Y_{rr}, which was uniform for all embankment models (*i.e.* $Y_{rr} = 1$). The embankment models were constructed using an intermediate compaction effort (*i.e.* γ_d = 16.8kN/m^3; $D_r = 52\%$). The breaching process in the two

embankment models with both longitudinal and vertical scale ratios, X_{rr} and Z_{rr}, equal to $1/2$ and $1/3$, respectively, were compared with the full scale embankment model constructed for the compaction series (*i.e.* $X_{rr} = Z_{rr} = 1$), as shown in Figure 6.2. Each of the quasi-exact geometric scale series tests was repeated once.

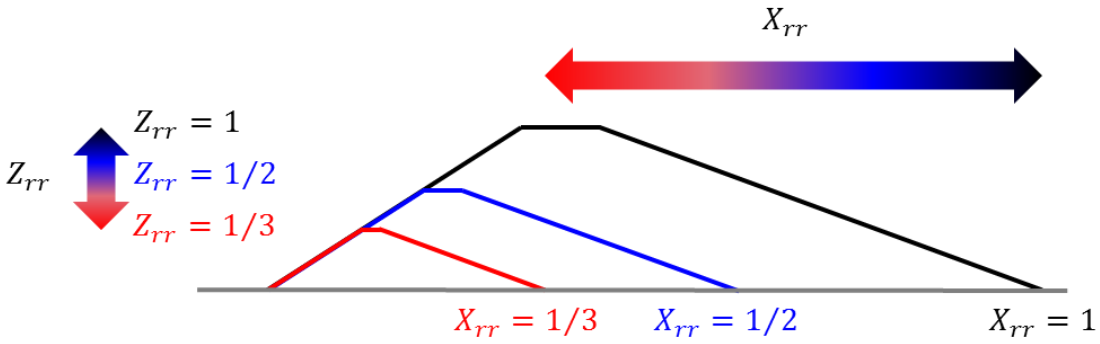

Figure 6.2: Quasi-exact geometric scales (Series “G”)

6.3 Experimental Setup

An illustration of the experimental setup is shown in Figure 6.3. The instrumentation was comprised of three WG-50 capacitance wave gauges, used to measure the time-history of water surface elevations in the flume during the tests. The same sampling rate (30Hz) was used for the wave gauges (see Subsection D.2.1 in Appendix D for the calibration process). The minimum suggested separation distance (2m) was respected in this experimental setup. The same video equipment and impoundment process in the large flume tests of Phase I was also adopted (see Subsection D.3.2 of Appendix D for more details). The lighting was discarded in this experimental setup, since it created a glare on the water surface and affected the visibility of the curved control section forming on the upstream slope.

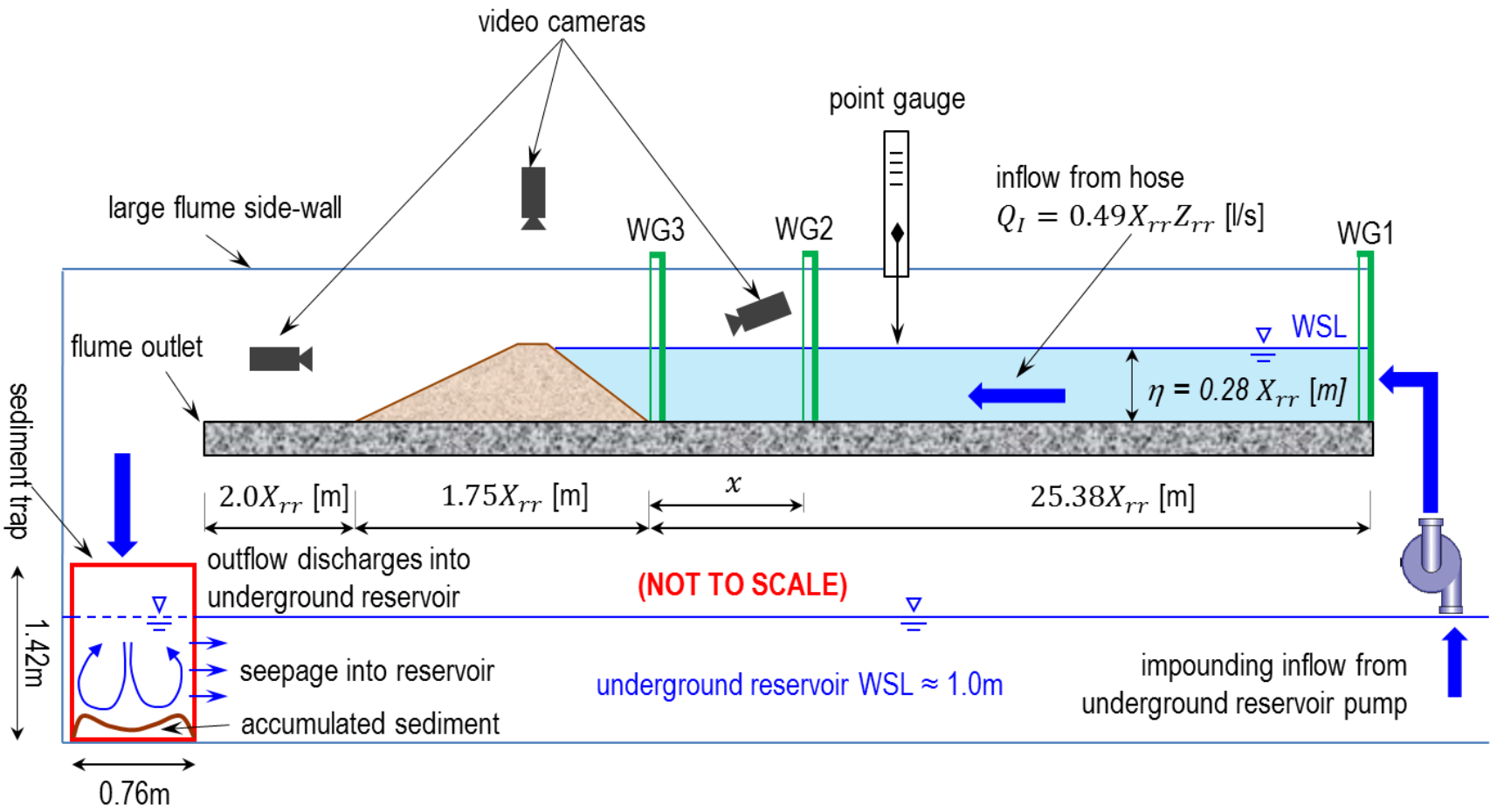

Figure 6.3: Experimental setup in large flume tests for Phase II (*d*istance, x, between WG2 and WG3 ranged between 2m and 14.4m)

The geometry of the embankment model and V-notch, which was carved on the crest's centreline, as well as inflow for all the scale series tests were scaled in accordance with the prescribed longitudinal and vertical geometric scale ratios shown in Figure 6.4. The 3-D breach overtopping tests were initiated by introducing inflow ($Q_I = 0.49X_{rr}Z_{rr}$ l/s) using a water hose and remained constant throughout the entire duration of the experiment.

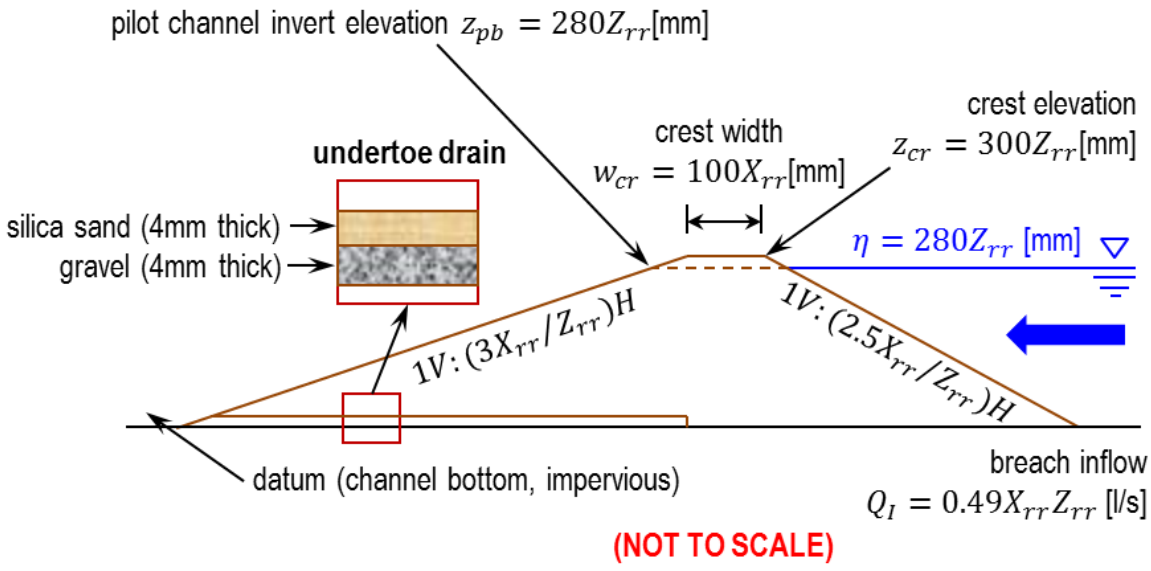

Figure 6.4: Longitudinal profile of embankment model for large flume tests in Phase II

The upstream boundary of the impoundment reservoir in the tilted and quasi-exact geometric scale series tests was regulated by means of an L-shaped fixture comprised of two plywood planks as shown in Figure 6.5. The influence of tailwater conditions on the breaching process was considered in the longitudinal scale for where $X_{rr} = 1/2$ and $X_{rr} = 1/3$, by moving the embankment model downstream in accordance with the prescribed longitudinal geometric scale ratios. A sediment trap comprised of a cage and non-woven high flow geotextile, designed and constructed in the Hydraulics Laboratory, was lowered into the Hydraulics Laboratory reservoir, downstream the large flume outlet, to collect the transported sediment and prevent the fine sand from contaminating the water storage facility underneath (see Figure 6.3). Prior to each test, the sediment trap was lowered into the underground

reservoir downstream the large flume outlet using a hoist attached to a gantry frame. The accumulated embankment material was then removed after each test. The design and construction of the gantry frame and sediment trap is described in Sections D.4 and D.5, respectively, of Appendix D.

Figure 6.5: Upstream boundary used in large flume

6.4 Breach Channel Entrance Mapping

The purpose of the spatial breach overtopping experiments was to determine the breach outflow hydrograph and understand the mechanisms leading to the evolution of the breach channel forming on the upstream slope for the four tests series. The outflow hydrograph was computed using the same hydrologic routing method used in Phase I of the experimental program (see E.5 of Appendix E). The evolution of the control section forming on the upstream shoulder slope was determined by applying a photogrammetric technique similar to Orendorff *et al.* (2009).

The photogrammetric technique developed in Orendorff *et al.* (2009) was comprised of measuring dimensions obtained from images extracted from upstream, planform and downstream, video footage. The images were georeferenced by mapping the coordinates defined by the gridlines installed onto the shoulder slopes of the embankment model. The images were then corrected for lens distortion by transforming them to the correct coordinate of the model where the breach channel

dimensions could be extracted. The elevation of the breach channel bottom could not be extracted from the upstream video footage for the following two reasons: high turbidity in the water-sediment mixture and the undetermined depth-of-field in the video camera perspective. The breach channel depth was therefore considered an unknown.

The arched breach channel crest or entrance forming on the upstream slope, and described by other researchers as the “curved control section”, and shown in Figure 6.6, was visible through the water. In this study, the focus was then aimed at extracting the dimensions of the upstream section of the breach channel forming below the WSL. It was possible to apply this photogrammetric technique to map the full dimensions of the control section for the breach channel using only 2-D images. The top peripheral boundary of the breach channel forming on the shoulder slopes and embankment crest, previously marked by the gridlines, was mapped and projected onto one single plane (see Figure 6.7).

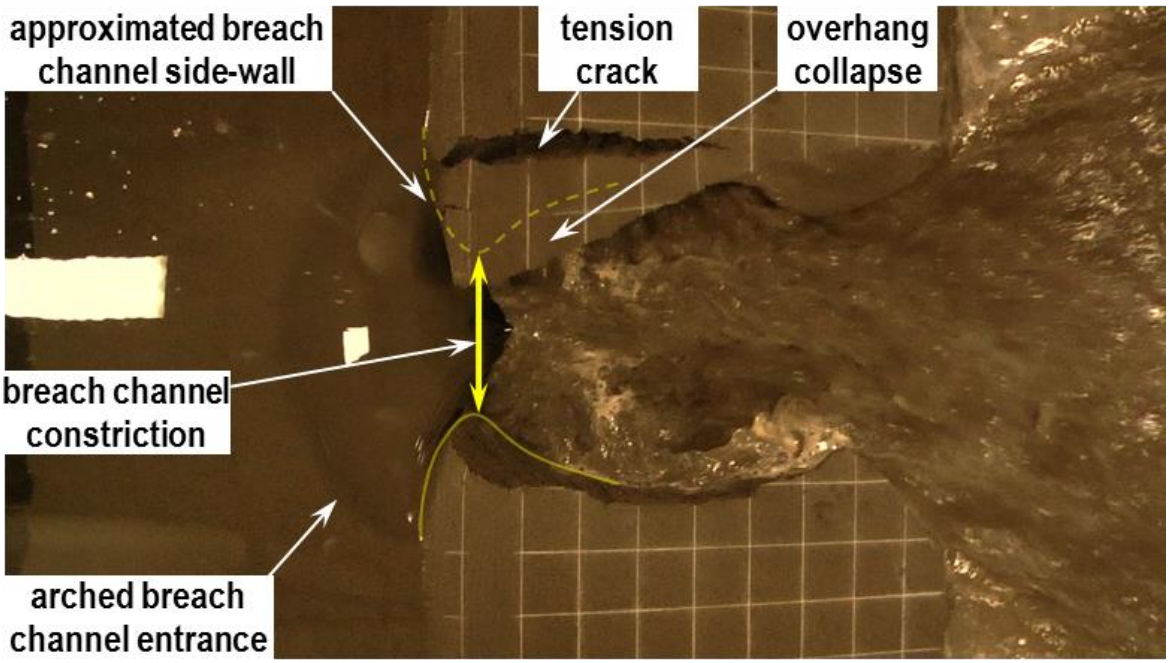

Figure 6.6: Planform view showing breach channel entrance forming on upstream slope of Test No. 4 (t = 37s)

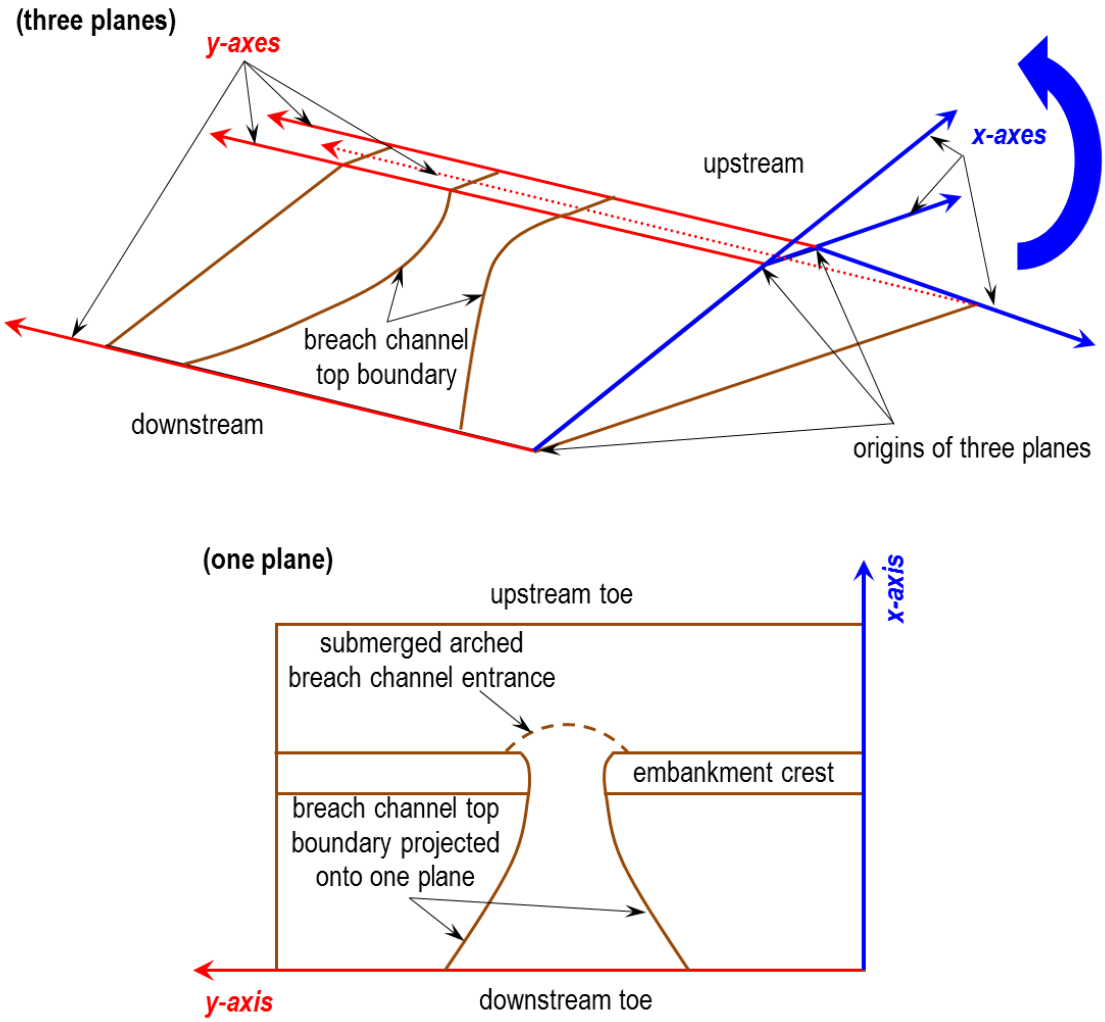

Figure 6.7: Mapping and projecting breach channel top boundary onto one plane

Similar to the top boundary of the breach channel, the external contours of the arched ogee-like crest were also mapped and projected using the described photogrammetric technique and shown in Figure 6.8 and Figure 6.9:

- Images were extracted from the upstream, downstream and planform view video footage before impoundment and during the breach progression at 10s time intervals and later imported into ArcGIS.

- The x and y coordinates of the gridlines on the shoulder slopes and embankment crest of the reference images (*i.e.* prior to impoundment) were georeferenced using the georeferencing tool in ArcGIS. For the planform view, it was necessary to use the reference coordinate system from an image captured before water impoundment since the gridlines on the upstream slope were washed away after impoundment.
- The georeferenced coordinates were transformed using a spline transformation and a georeferencing table was generated for the reference images such that the three planes lying on the dam surface could be mapped onto one plane.
- The spline transformation was then applied to the breach progression images using the georeferencing table generated for the reference images captured before water impoundment.
- The breach channel external contours including the arched breach channel crest were digitised from the transformed images for the entire breach progression.

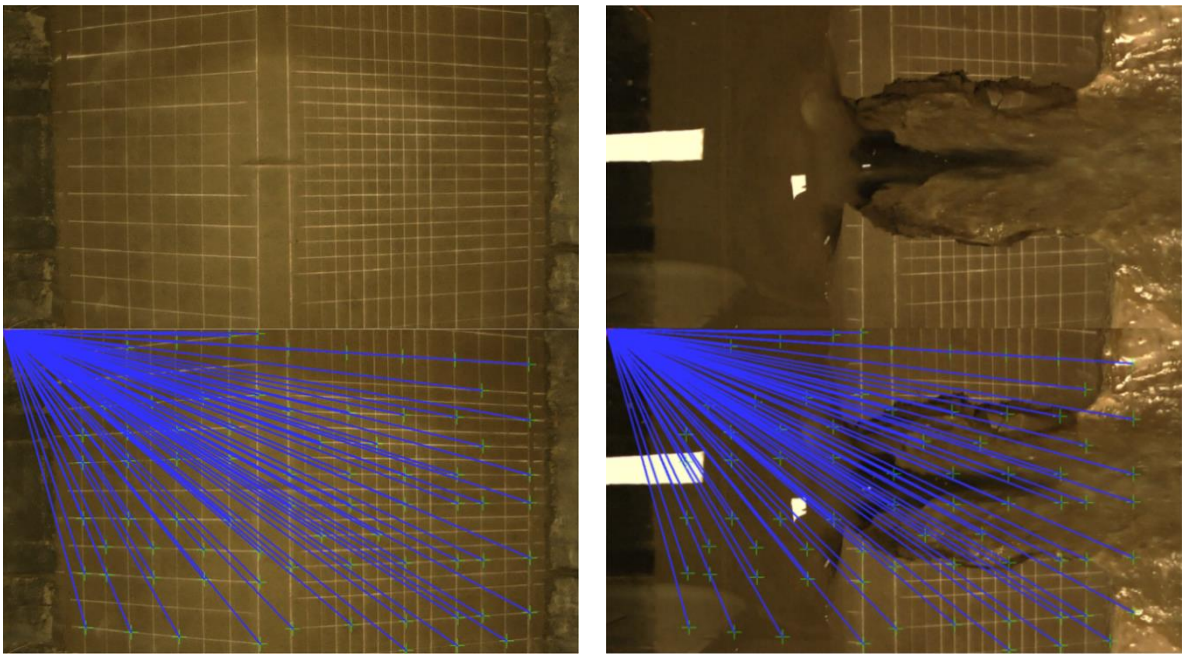

Figure 6.8: (left) Georeferencing reference image captured before impoundment (right) applying georeferencing to an image captured after 280 seconds into breach progression

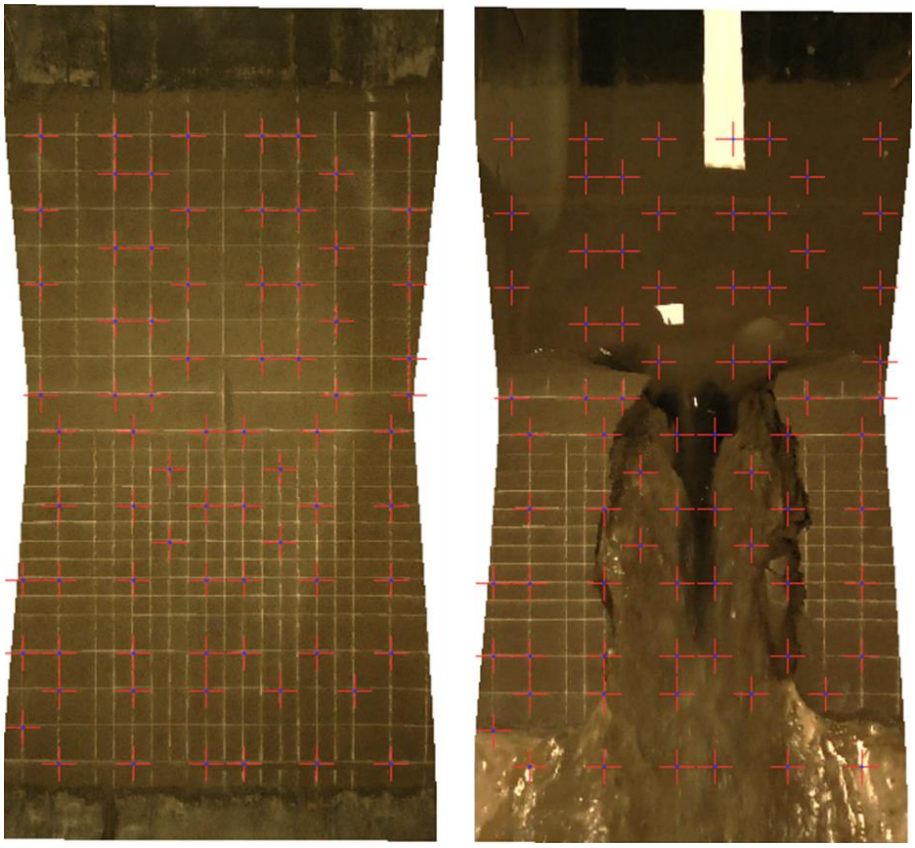

Figure 6.9: Transformation showing (left) reference image (right) image after 280 seconds into breach progression

Figure 6.10 illustrates the flow over the downstream slope of an overtopped and subsequently breached embankment, idealized by an upstream control point at the inflection point (*i.e.* crest) of the breach channel with an elevation, z_c. Also shown in Figure 6.10, is the upstream and downstream slope angles, α_{US} and α_{DS}, respectively, the Froude-critical flow depth, η_c, and the water surface elevation at a point further upstream, η_r. The lateral dimensions of the breach channel, top width (*i.e.* coinciding with the peripheral contours of the embankment shoulder slopes and crest) and entrance width (*i.e.* chord length), B_{TW} and B_{EW}, respectively, were extracted from the upstream, planform and downstream views. The breach constriction width, B_{CW}, measured from the undercut sides could not be detected due to its concealment below the overhang. The shape of the arched crest forming on the upstream face of the embankment model, approximated as an arc with length

, L_a, in Figure 6.10 was extracted from images transformed from the upstream and planform views, where r is the radius of curvature, x_η is the inclined distance from the upstream apex of the embankment crest to the intersection between the arc and water surface level (*i.e.* at the side of breach channel entrance), and x_a is the chord height of the arc (see Figure 6.11 for a detailed view).

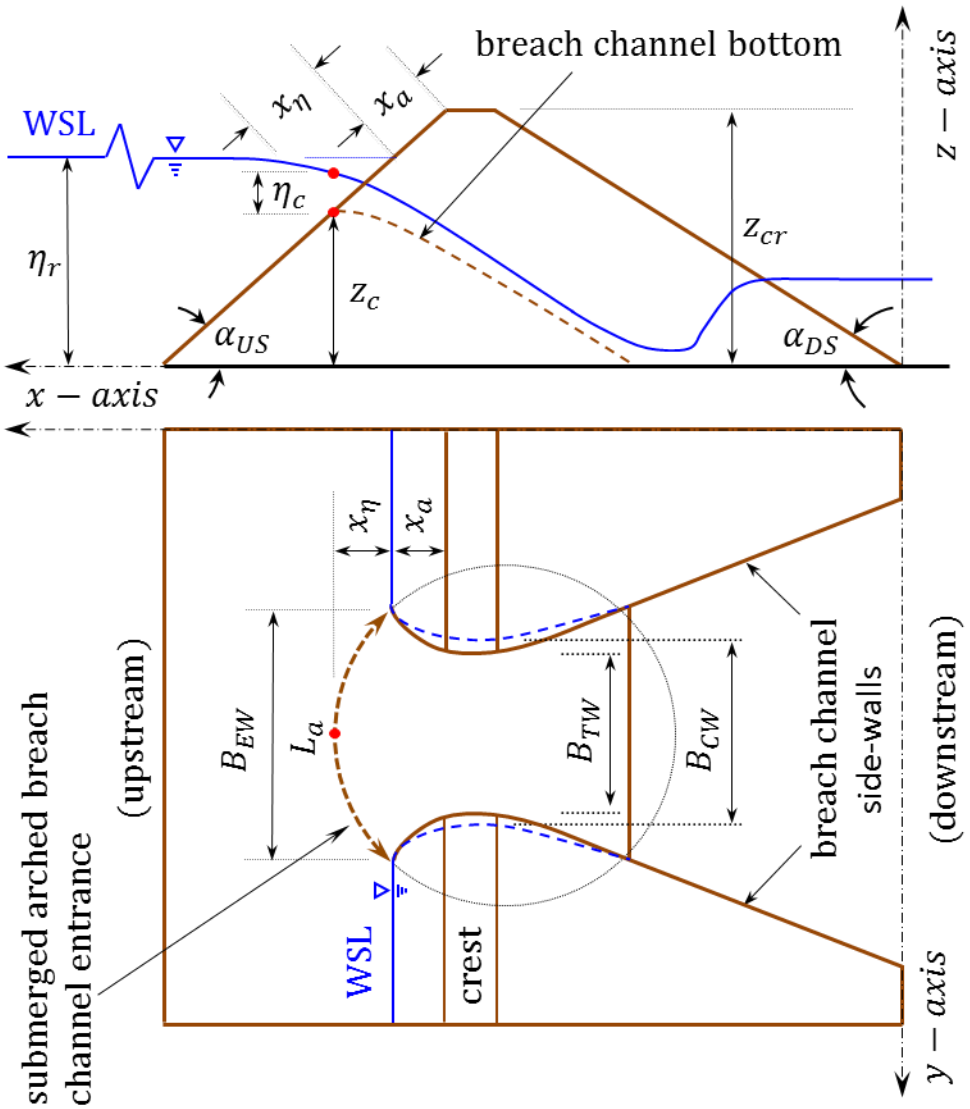

Figure 6.10: Idealised overtopping in breach channel of embankment model showing (top) longitudinal section (bottom) planform view (red dot shows inflection point and WSL at breach channel centreline)

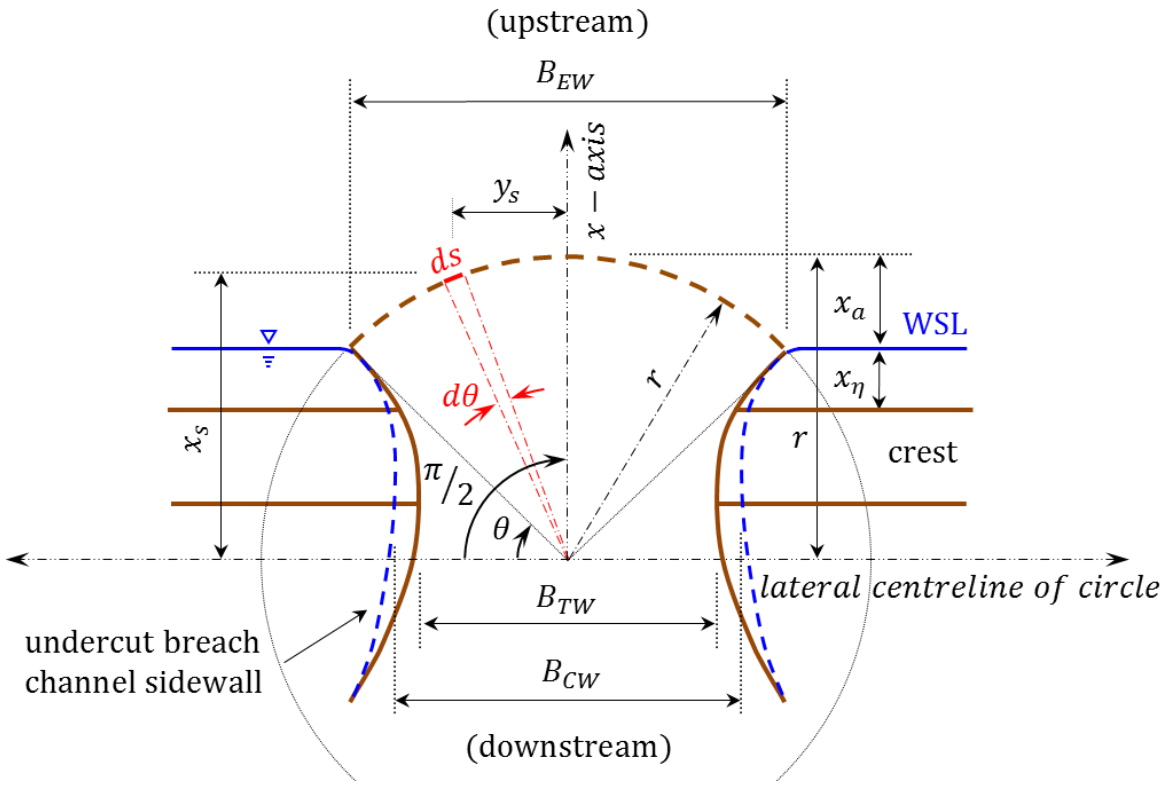

Figure 6.11: Detailed and rotated planform view of submerged arched crest showing entrance, top and constriction widths of breach channel

6.5 Estimation of Breach Channel Outflow

The arc forming on the upstream slope can also be described as the locus of inflection points on the breach channel entrance, where each arc segment, ds, is rotated by an angle $d\theta$ and has coordinates (x_s, y_s). The length of the arc segment, ds, can be expressed as:

$$ds = rd\theta \tag{6.1}$$

Neglecting the headloss between a point upstream and the arched breach channel entrance, the Froude-critical flow depth at the inflection point can be derived from the energy equation as follows:

$$\eta_c = \frac{2}{3}(\eta_r - z_c) \tag{6.2}$$

The elevation of the inflection point can be expressed as follows:

$$z_c = z_{cr} - \left(x_\eta + x_a - r + x_s\right) \sin \alpha_{US} \tag{6.3}$$

where, the *x*-coordinate of the arc segment can be expressed in terms of the arc angle, θ, as:

$$x_s = r\sin\theta \tag{6.4}$$

By applying the Froude-critical criterion (*i.e.* $Fr = 1$) and substituting L by the critical flow depth, η_c, in Equation (4.231), the streamwise Froude-critical velocity, u_c, can be expressed as:

$$u_c = \sqrt{g\eta_c} \tag{6.5}$$

The discharge, dQ, through the arc segment in Equation (6.1) can therefore be expressed as follows:

$$dQ = u_c \eta_c ds \Rightarrow \sqrt{g}\eta_c^{3/2} r d\theta \tag{6.6}$$

Substituting Equations (6.2) to (6.4) into Equation (6.6) yields:

$$dQ = r\sqrt{g}\left(2/3\right)^{3/2}\left[\eta_r - z_{cr} + \left(x_\eta + r\sin\theta - r + x_a\right)\sin\alpha_{US}\right]^{3/2} d\theta \tag{6.7}$$

Assuming symmetry in the breach channel about the *x*-axis shown in Figure 6.10 and Figure 6.11 and integrating dQ between angles θ and $\pi/2$, the discharge over the arched breach entrance can be estimated as follows:

$$Q_e = 2r\sqrt{g}\left(2/3\right)^{3/2} \int_{\theta=\sin^{-1}\left[(r-x_a)/r\right]}^{\pi/2} \left\{\eta_r - z_{cr} + \left[x_\eta + x_a + r(\sin\theta - 1)\right]\sin\alpha_{US}\right\}^{3/2} d\theta \tag{6.8}$$

The dimensions x_a, B_{EW} (and therefore r and θ), and L_a were extracted at 5 to 10 second time intervals using the photogrammetric technique described, while the dimension x_η was computed using the wave gauge data. Finally the breach outflow expressed by Equation (6.8) was estimated by numerical integration using 60 arc segment divisions.

The discharge efficiency can be described as the ratio between the measured and estimated breach outflow:

$$\xi = \frac{Q_m}{Q_e} \tag{6.9}$$

where, the measured value of the breach outflow, Q_m, is equal to the computed value using the hydrologic method described in Subsection 5.2.1.2 (i.e. $Q_m = Q_B$).

The head above the inflection point, Δh_w, was also determined from the visible arc as:

$$\Delta h_w = \eta_r - z_c \tag{6.10}$$

6.6 Results and Analysis

6.6.1 Qualitative Remarks on Three Observed Breaching Phases

6.6.1.1 Breach Initiation

Similar to the large flume tests in Phase I, the breach initiation phase was first dominated by infiltration of water into the embankment body. A leak was then observed exfiltrating directly below the embankment model's crest, which resulted in the formation of a narrow stream on the downstream slope. This led to the erosion of the saturated embankment material in the downstream vicinity of the embankment crest, where it was deposited at the downstream toe. The narrow stream was shallow with a sediment-laden low velocity. The flow hydrodynamics in this breach initiation phase was therefore dominated by viscous and surface tension forces. As the flow velocity in the narrow stream increased, more material was eroded downstream of the crest.

As previously mentioned, the impoundment rate was deliberately set low (approximately 0.75mm/min) during the entire duration of the experiment in order to isolate the influence of inflow from the other breach mechanisms. As the WSL in the impoundment rose, water was seen to enter the invert of the V-notched pilot

channel. The chalk from the gridlines present on the embankment model's shoulder slopes and crest degraded the visibility of the WSL in the V-notch. At this point, it was difficult to use the same criterion established in Phase I of the experimental program that defined the onset of overtopping (see Subsection 5.2.1.3). Instead, the overtopping criterion was modified to reflect the time when the leak flowing below the embankment crest could be observed. The time span during which this exfiltration mechanism evolved rendered the observance of the incipient overtopping criterion somewhat subjective. Nevertheless, the observance of this criterion was attempted as strictly as possible for all Phase II tests.

6.6.1.2 Breach Channel Formation and Propagation

Following the breach initiation phase was breach channel formation and propagation. During this phase, two erosion mechanisms were observed at the eroded V-notched pilot channel entrance:

- Convective accelerations due to the constricting flow which led to high shear forces at the sides of the breach channel entrance and consequently gave rise to lateral erosion. This mechanism was 2-D and acted along the free water surface plane in the cross-stream directions.
- Higher flow velocities immediately downstream of the embankment model's crest led to downward erosion which caused the sediment to deposit at the downstream toe of the embankment model. In this study, this mechanism is referred to as downcutting. This mechanism was also 2-D and acted along a plane perpendicular to the bottom boundary of the breach channel.

The lateral erosion at the sides and downcutting at the centre of the breach channel resulted in an undercut breach channel entrance as observed by previous researchers (*e.g.* Mohamed *et al.* 1999; Coleman *et al.* 2002; Geisenhainer and Kortenhaus, 2006; J. Zhang *et al.* 2009; Pickert *et al.* 2011). Although no considerable outflow was yet measured, this initial undercutting mechanism played a large role in the formation and evolution of the breach channel. While downcutting

was initiated in the immediate and downstream vicinity of the embankment model crest, it quickly propagated downstream and was highest at the downstream toe due to the accelerating breach flow.

6.6.1.3 Breach Channel Development

Since this study investigated the evolution of the breach channel entrance at the upstream slope of embankment models, the breach development phase is considered in this regard. The formation of the breach channel entrance on the upstream slope preceded any measurable breach outflow following the hydrologic routing method. However, a measurable breach outflow in itself was a criterion for applying the concept of discharge efficiency to the upstream breach channel entrance. The onset of breaching was then defined as the time at which the hydrograph indicated a measurable outflow. This particular definition also avoided the more subjective criterion which would have been based on the incipient formation of the upstream breach channel. It is important to note, however, that following the measurable breach outflow criterion, the breach channel had already reached the flume bottom at the downstream toe of the embankment model.

At a considerable breach outflow (> 2-3 l/s), side-slope failures in the breach channel were observed near the downstream toe. This was then followed by a succession of failures which started halfway through the downstream slope and propagated towards the downstream end of the embankment model's crest. It was during this first succession of side-slope failures that the two planar mechanisms described in the breach formation stage as lateral erosion and downcutting had now merged into a single 3-D mechanism. The helical flow pattern originating at the breach channel entrance sides propagated below the breach channel constriction towards the downstream toe and resulted in adverse side-slope angles. As the gap between the side-walls grew and as the overhangs on the sides collapsed, this mechanism became more severe and eventually dominated the undercutting mechanism in the entire breach channel. This severe helical flow pattern acted as a large destabilisation component of the breach channel side-slopes (J. Zhang *et al.*

2009; Morris *et al.* 2009b; Paul Samuels, personal communication, October 7, 2010). Downcutting, however, was still prevalent at the breach channel centre.

The side-slope failure mode of the undrained embankment model in Phase II differed from the earlier test conducted in Phase I of the experimental program. The failure mode of the side-slopes in the undrained embankment model tended more towards collapses rather than slides. This was attributed to the new compaction technique which was more efficient at densifying the noncohesive embankment material. The side-slope failures were, however, more frequent than the benchmark embankment model which led to smaller undercuts.

The side-wall angles following the side-slope failures for all embankment models were vertical. The side-slope collapses in embankment models constructed with lower compaction efforts were more frequent resulting in a smaller overhang size. In the case of the lowest compaction effort (*i.e.* $D_r = 7\%$), the side-slope failures were the most frequent and most continuous. This gave rise to higher tailwater levels in the breach channel as the collapsed soil obstructed the breach channel flow. In the case of the embankment model with the highest compaction (*i.e.* $D_r = 80\%$), downcutting dominated the evolution of the breach channel, and as a result the size of the overhangs were larger. As the longitudinal geometric scale was reduced in the titled scale series, the side-slope collapses were more frequent and abrupt due to the smaller width of the embankment as well as the higher inclination of the failure plane with respect to the horizontal. The hydrodynamic forces of the helical flow at the base of the embankment were also contributing to the failure of the narrower overhangs. In the smaller quasi-exact geometric scales, flow submergence due to material collapses and deposition was observed.

6.6.2 Scaling Laws

It is important to note that during the breach initiation phase, similitude laws cannot be formulated without taking into consideration the dominant surface tension effects (*i.e.* Weber criterion). Coleman *et al.* (2002) cautioned against the effects of not

scaling surface tension effects correctly in models with shallow flow. Although lag-times are reported in this study for all tests, the scaling criteria used for this particular embankment breach outflow characteristic were not addressed.

After the breach initiation and the consequent breach channel formation phase, it is usually assumed that the substantial water storage or gravity source upstream the embankment is in favour of applying the Froude criterion for scaling of the embankment breach outflow characteristics. Following the breach initiation phase, the flow can be described as fully turbulent. This is substantiated by the undercutting of the breach channel entrance, the helical flow pattern in the breach channel as well as the considerable erosion on the downstream slope. Although a fully turbulent flow regime implies that viscous forces are negligible, this needed to be verified and quantified using experimental data.

By imposing dynamic similarity between the prototype and model parameters, the Froude criterion for tilted and quasi-exact geometric model scales can be applied as follows:

$$Fr_{rr} = \frac{Fr_{mm}}{Fr_{pp}} = \frac{\left(u/\sqrt{Lg}\right)_{mm}}{\left(u/\sqrt{Lg}\right)_{pp}} = 1 \tag{6.11}$$

The flow depth represents the characteristic length in the case of Froude modeling where $L_{rr} = Z_{rr}$. Also, since $\sqrt{g_{mm}/g_{pp}} = 1$, the streamwise velocity scale ratio, u_{rr}, can be expressed as follows:

$$u_{rr} = \sqrt{Z_{rr}} \tag{6.12}$$

The discharge scale ratio through a vertical plane can be expressed as:

$$Q_{rr} = u_{rr} Y_{rr} Z_{rr} \tag{6.13}$$

Since $Y_{rr} = 1$, Equations (6.12) and (6.13) can be then combined as follows:

$$Q_{rr} = Z_{rr}\sqrt{Z_{rr}} = Z_{rr}^{3/2} \tag{6.14}$$

Similarly, the time scale ratio can be derived in terms of the longitudinal length scale ratio, X_{rr}, and the streamwise velocity scale ratio, u_{rr}, as follows:

$$t_{rr} = {}^{X_{rr}}/_{u_{rr}} \tag{6.15}$$

Equations (6.12) and (6.14) can then be combined to yield the following expression:

$$t_{rr} = {}^{X_{rr}}\Big/_{\sqrt{Z_{rr}}} \tag{6.16}$$

6.6.3 Breach Outflow Hydrographs

The hydrographs obtained for the Phase II large-flume embankment models were much more attenuated than those obtained in Phase I. The decrease in peak flow (approximately 10 l/s lower than in Phase I), was due to the new and more efficient compaction technique. The dry unit weights for the benchmark embankment models in Phase I and II were 15.02kN/m^3 and 16.8kN/m^3, respectively. Figure 6.12 shows the measured breach outflow hydrographs for the four test series while Figure 6.13 shows the hydrographs lagged from the onset of breaching (*i.e.* measurement of noticeable discharge). A summary of all the hydrograph characteristics, including the lag-time, are shown in Table 6.2.

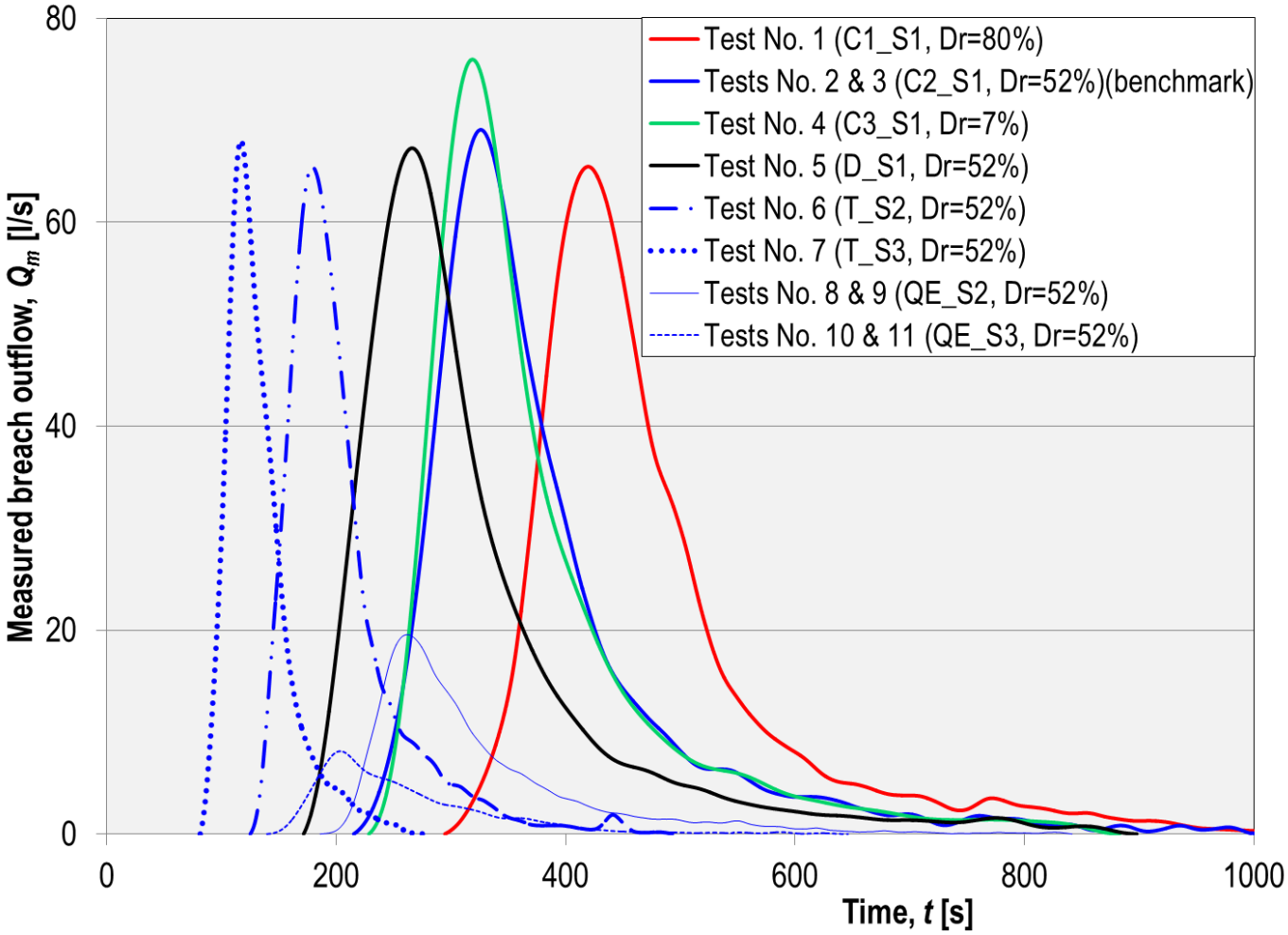

Figure 6.12: Breach outflow hydrographs for Phase II of experimental program (C1, high compaction, C2 intermediate compaction; C3: low compaction; D: drainage series; T: tilted geometric scale series; QE: quasi-exact geometric scale series; S1: scale 1; S2: scale $1/2$; S3: scale $1/3$; Dr is relative density, D_r)

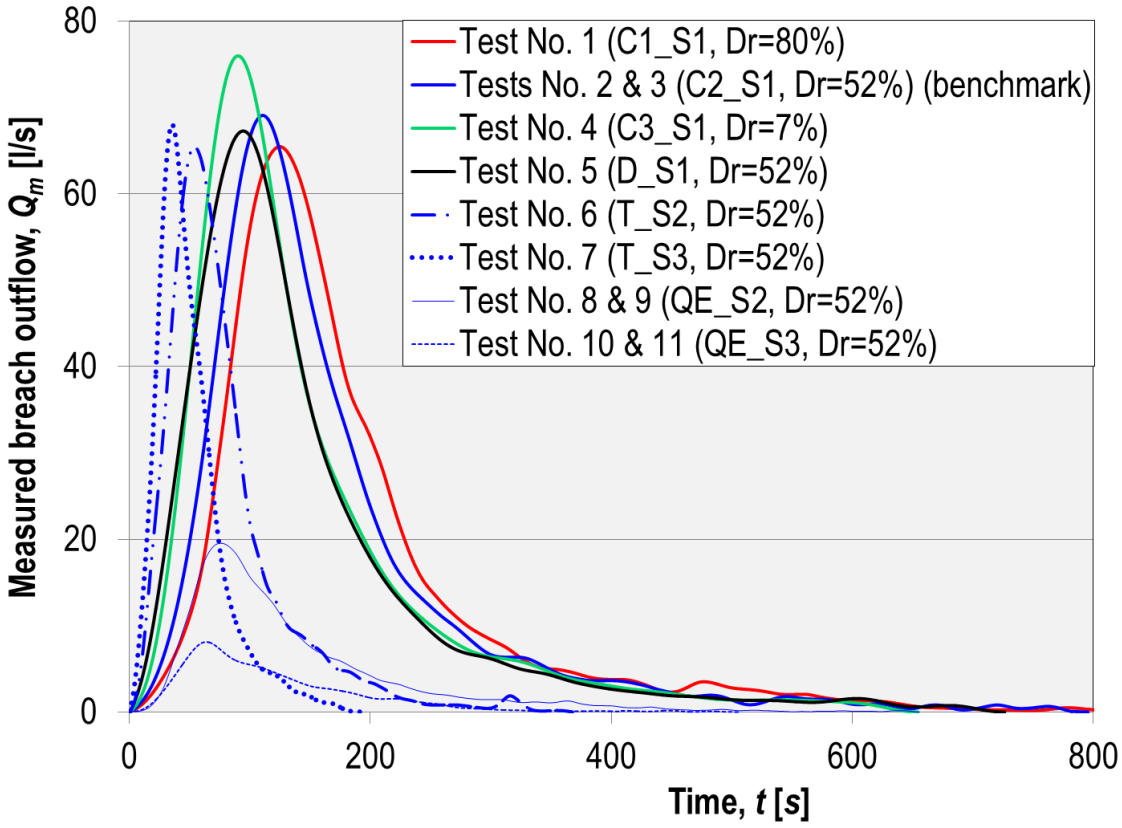

Figure 6.13: Breach outflow hydrographs for Phase II of experimental program lagged to the onset of breaching time

Table 6.2: Results summary from breach outflow hydrograph analysis for Phase II tests

Test No.	Test series	Scale ratios†			Volumes [m^3]		η_{OT} [cm]	η_{br} [cm]	Hydrograph characteristics			
		X_{rr}	Z_{rr}	D_r [%]	$\forall_{max}$	Depletion [%]			Q_P [l/s]	t_P [s]	t_B [s]	t_L [s]
1	D	1	1	80	11.03	89	28.72	28.97	65.5	125	1007	295
2‡	D	1	1	52	10.86	89	28.38	28.65	68.0	109	795	218
3‡	D	1	1	52	10.85	90	28.19	28.47	70.4	113	782	213
4	D	1	1	7	11.00	90	28.66	28.89	76.0	90	655	229
5	E	1	1	52	10.84	88	28.22	28.48	67.3	95	726	172
6	F	1/2	1	52	5.34	92	27.88	28.04	65.5	54	367	125
7	F	1/3	1	52	3.59	93	28.20	28.30	68.0	36	196	81
8	G	1/2	1/2	52	2.75	86	14.44	14.54	20.5	79	656	186
9	G	1/2	1/2	52	2.74	82	14.28	14.40	18.7	75	567	186
10	G	1/3	1/3	52	1.23	76	9.74	9.77	8.4	64	506	133
11	G	1/3	1/3	52	1.22	75	9.54	9.57	7.9	63	406	146

†geometric scale ratios are based on 30cm high embankment model, with a 10cm crest width and 1V:2.5H and 1V:3H upstream and downstream slopes, respectively; ‡benchmark tests; η_{br} is water suface elevation at the onset of breaching

As shown in Table 6.2, the percentage depletion of reservoir volumes was less for smaller scales due to the effect of ponding in the reservoir after side-slope collapses and the consequent soil deposition in the breach channel. The resulting outflow hydrographs indicated a 16% attenuation in peak flow and a 28% increase in time-to-peak between the lowest and highest compaction effort.

Figure 6.14 shows the breach outflow hydrographs for the drained and undrained embankment model at the onset of overtopping. Both models were compacted with the same compaction effort and were constructed using the same geometric scale ($i.e. D_r = L_{rr} = 1$).

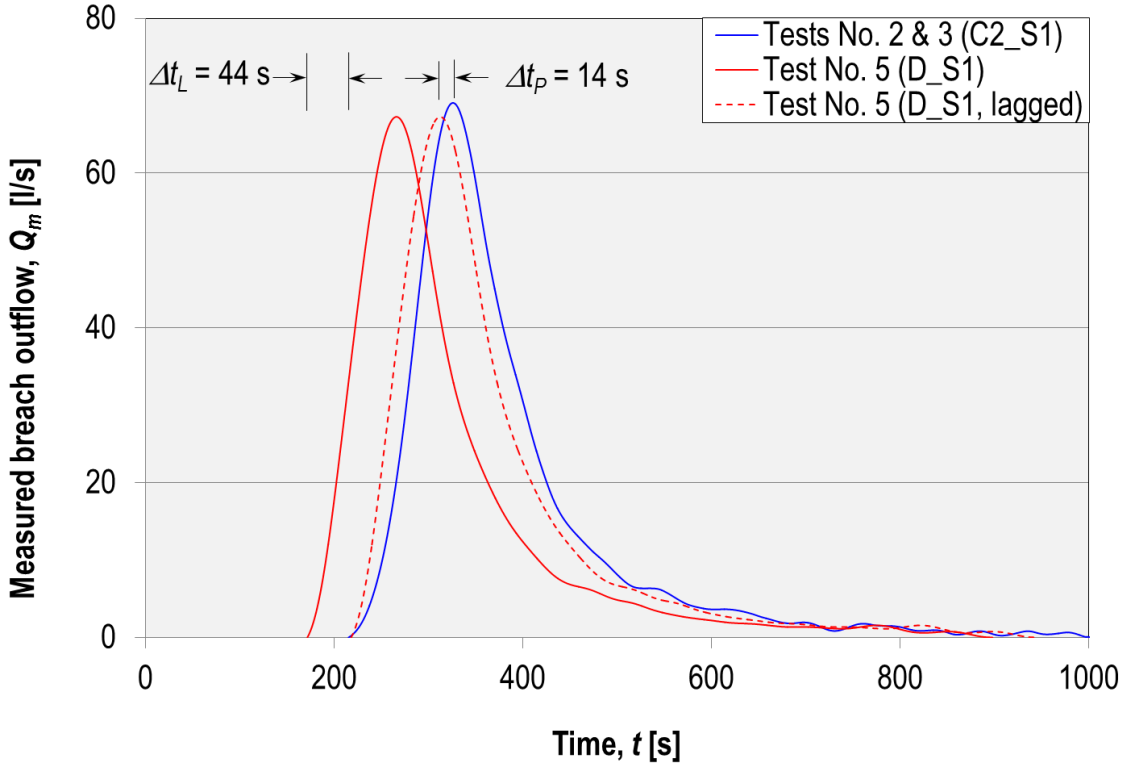

Figure 6.14: Comparison between breach outflow hydrograph in the caseof drained and undrained embankment models

Similar to tests conducted in Phase I of the experimental program, there was a lag between the two outflow hydrographs due to the drainage conditions (see Figure 5.24 and Figure 5.26). Although the new construction technique resulted in a more

compacted embankment material, the drainage element which was used was comprised of a slightly thinner gravel layer (see Figure 5.11 and Figure 6.4 for a comparison). It is expected that this thinner gravel layer would render the embankment models more susceptible to erosion due to their higher phreatic surface, particularly at the breach initiation, formation and propagation phases. In addition to the drainage layer, the criterion for overtopping was also modified. The resulting lag-time for the embankment model used in Phase II was 42s lower (216s versus 258s). However, the lag-time for the undrained embankment model in Phase II was 27s higher than in Phase I (172s versus 145s). The difference in lag-time between the two drainage configurations due to the new construction method was 44s as opposed to 113s using the dynamic compaction technique. For the distorted geometric scale series, the peak flow was almost identical. The time scales of the hydrographs, however, were reduced for the smaller scale ratios. In the case of the quasi-exact geometric scale series, both the peak flow and time scales were reduced for the smaller scale ratios.

Figure 6.15 shows the hydrographs for the repeated tests. Peak flow and time-to-peak variations were generally low, with the exception of the quasi-exact geometric scale $1/2$, peak flow variation was slightly higher (9%). The variations in base-time, however, increased with smaller scale ratios. The base-time characteristic is sensitive to errors due to the criterion by which it is computed and the downstream hydraulic conditions, particularly for smaller scale ratios. This is discussed in more detail in Section 6.7. Despite these variations, the fundamental shape and time scales of the breach outflow hydrographs measured for the repeated tests was well preserved. It can therefore be concluded that the tests were conducted within a reasonable level of control. Since the hydrographs for the repeated tests were very similar, the corresponding hydrograph analysis for the repeated test series is represented by an arithmetic average (*e.g.* Tests No. 2 and 3, Tests No. 8 and 9 and Tests No. 10 and 11 in Figure 6.12 and Figure 6.13).

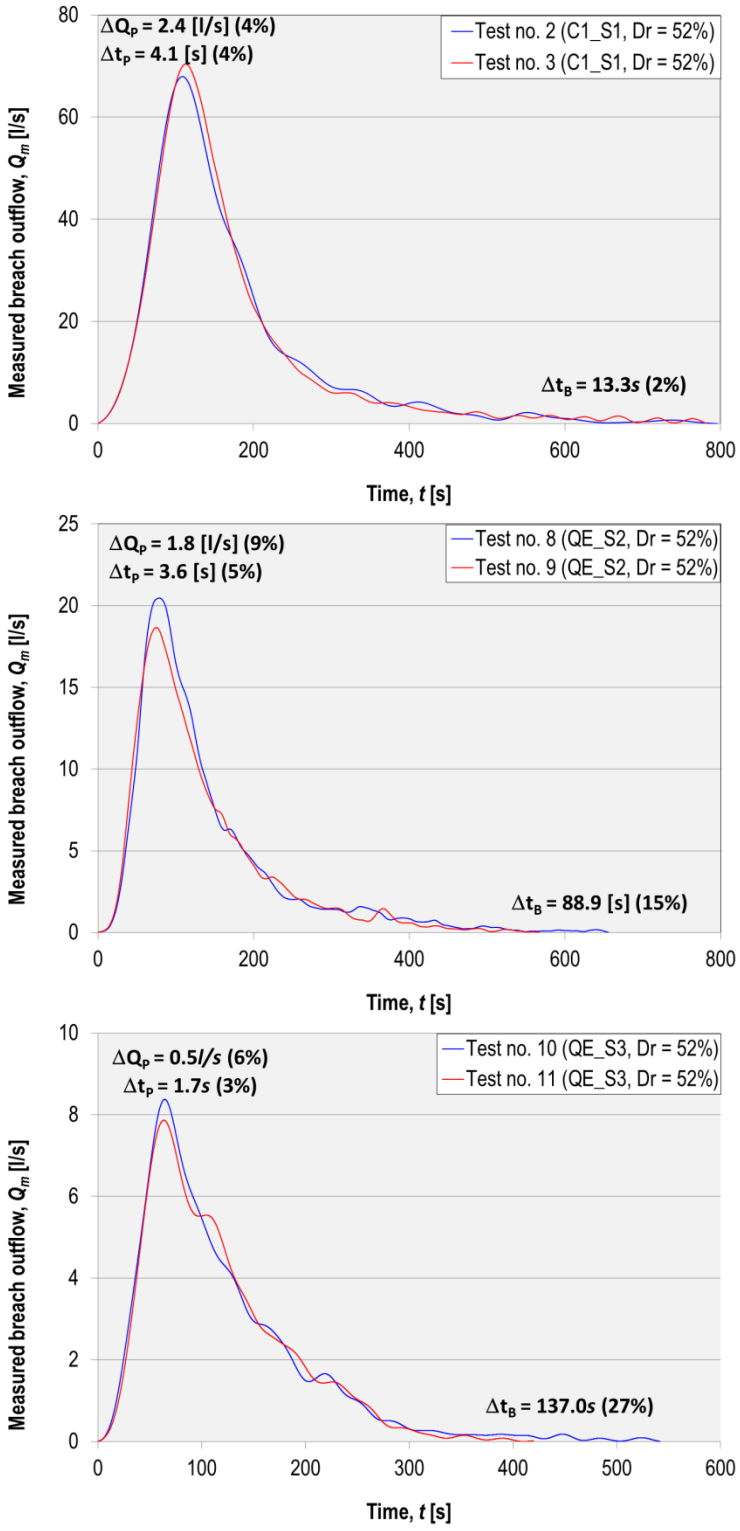

Figure 6.15: Lagged breach outflow hydrographs for repeated tests (top) benchmark embankment model, Tests No. 2 and 3 (middle) quasi-exact scale series $1/2$, Tests No. 8 and 9 (bottom) quasi-exact scale series, $1/3$ Tests No. 10 and 11

The embankment breach outflow characteristic scale ratios, $Q_P)_{rr}$, $t_P)_{rr}$ and $t_B)_{rr}$,, were determined for the tilted and quasi-exact scale series tests using “scale 1” test as the benchmark or reference (*i.e.* the average of Tests No. 2 and 3). In this study, a scale series parameter, Λ, was defined as the scale series ratio such that $\Lambda = D_r$, $\Lambda = X_{rr} =$ and $\Lambda = X_{rr} = Z_{rr}$ for the compaction, tilted and quasi-exact scale series tests, respectively. The experimental embankment breach outflow characteristic scale ratios were compared to the Froude criterion using Equations (6.14) and (6.16) as shown in Figure 6.16. The ordinate and abscissa of the hydrographs for two smaller tilted and quasi-exact geometric scales were Froude-scaled also using Equations (6.14) and (6.16), respectively, with reference to the benchmark (*i.e.* largest scale) test. This was carried out in order to gauge the scale effects for the entire breach duration, as shown in Figure 6.17 and Figure 6.18.

It can be shown from Figure 6.16 that the Froude criterion can be applied to scale the two most important breach outflow hydrograph characteristics, Q_P and t_P, for the tilted geometric scale series. The base-time characteristic, as mentioned previously, is sensitive to how the criterion for hydrograph termination is defined. This is discussed in more detail in Section 6.7. However, as shown in Figure 6.17, the Froude criterion remarkably scaled the outflow for the entire breach duration for the tilted geometric scale series, even near the terminus of the hydrograph. In the case of the quasi-exact geometric scale series presented in Figure 6.16, the Froude criterion scaled the time-to-peak characteristic well. However, scaling of the peak flow and base-time was deficient. This is also evident in Figure 6.18, where the Froude-scaled peak flows for scale $1/2$ and $1/3$ corresponded to 80% and 61%, respectively, of the benchmark test. The poor similarity in flow characteristics between the Froude-scaled hydrographs, particularly in scale $1/3$, is emphasised by the different slope of the receding limb as well as the Froude-scaled outflow volumes. The smaller quasi-exact geometric scales clearly exhibited scale effects due to relatively higher tailwater conditions. The backwater effects were as a result of similitude not being satisfied with respect to resistance, entrainment and deposition (*i.e.* coarser drainage particles and therefore a larger settling velocity).

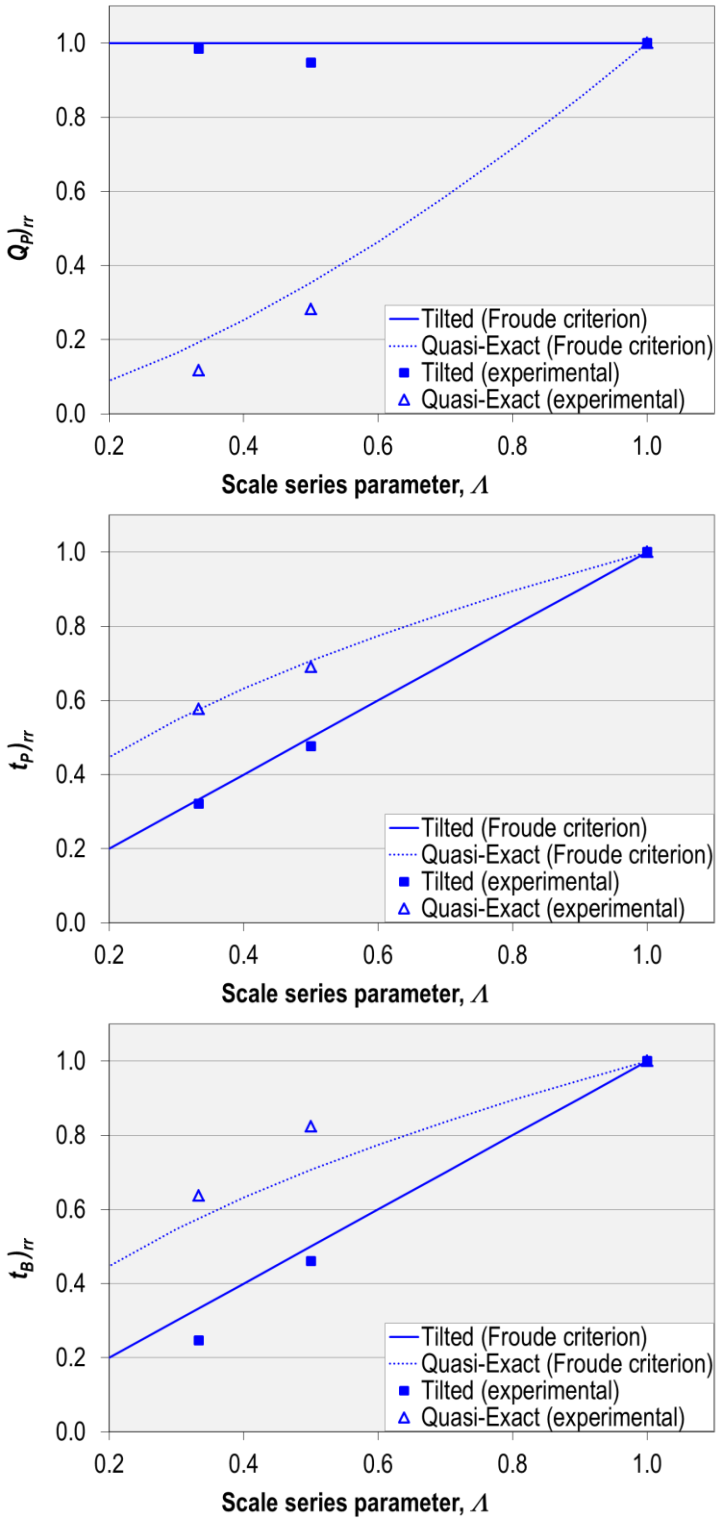

Figure 6.16: Experimental breach outflow hydrograph characteristic ratios for tilted and quasi-exact scale series compared with Froude criterion (top) peak flow (middle) time-to-peak (bottom) base-time

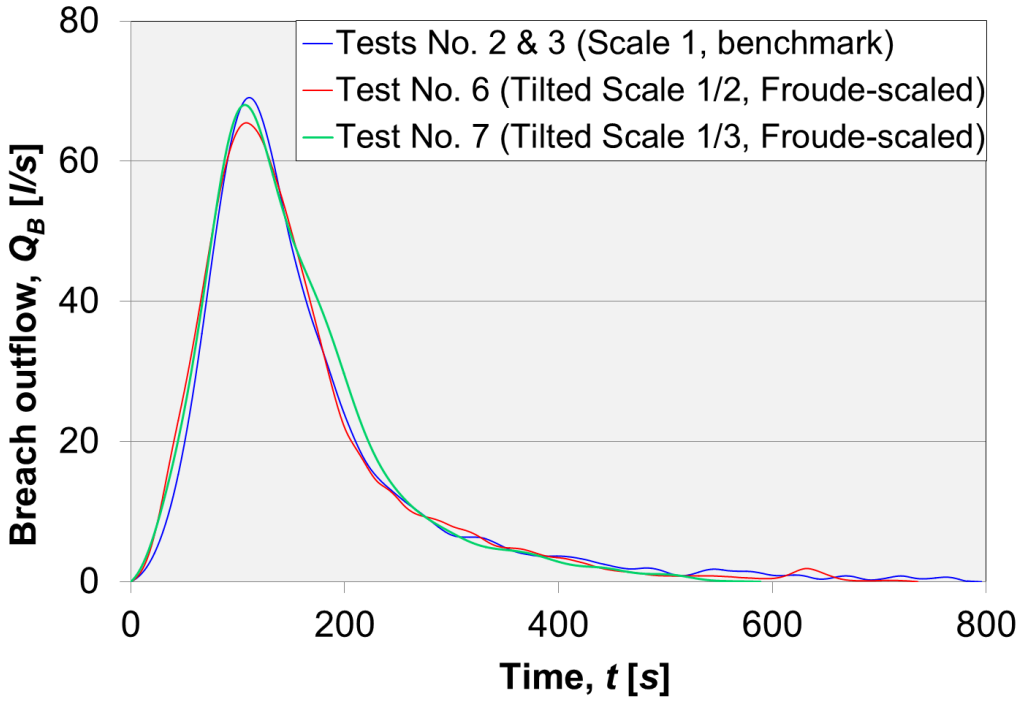

Figure 6.17: Comparison of the lagged and Froude-scaled breach outflow hydrograph between tilted scale series tests

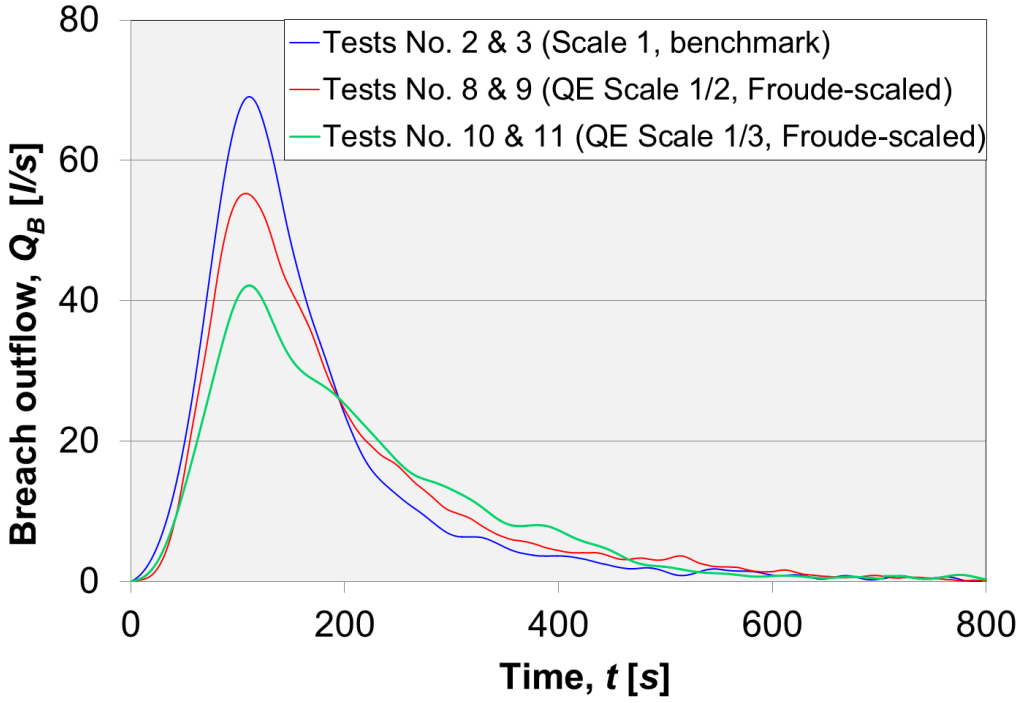

Figure 6.18: Comparison of the lagged and Froude-scaled breach outflow hydrograph between quasi-exact scale series tests

6.6.4 Breach Channel Control Section Morphology

Extraction of the breach channel entrance was only visible until the time-to-peak after which the inflection point reached the upstream toe of the embankment model. The analysis described in this section is therefore applicable to the rising limb of the breach outflow hydrograph. For the duplicated tests, the mapping was performed for Tests No. 3, 8 and 10.

Sources of errors in mapping the breach channel dimensions, and the corresponding estimation of the breach channel outflow, are due to the following reasons: optical refraction; particularly at greater depths where the upstream shoulder slopes are high (*e.g.* tilted scale series Test No. 7), asymmetry in the breach channel entrance and the ambiguity as well as broadness of the demarcations pertaining to the upstream control section. The crest of the upstream control section was distinguished by discolorations in the image. The maximum demarcation width in the upstream control section was 4mm during early overtopping stages to 3cm in the later stages. This gave rise to a maximum error of 3% in the breach channel entrance width where the corresponding error for the discharge efficiency was ±4%.

Since both the mapping technique and Equation (6.8) assume symmetry, deviations or rotations in the breach channel centreline may influence the results. Initial conditions, such as heterogeneity in the embankment material and/or geometry may contribute to this asymmetry. However, for Phase II tests, asymmetry was minor and usually occurred in later stages of overtopping. It was governed by the deviation or rotation of the breach channel centreline due to flow being obstructed on one side of the breach channel after a side-slope failure. For all the tests conducted, the maximum deviation and rotation in the breach channel centreline was 4cm in the transverse direction and 1.5° about the vertical axis, respectively. This was reflected near peak flow conditions and contributed to an error of 4% in the breach entrance width and ±5% in the discharge efficiency, respectively. Figure 6.19 illustrates two

scenarios showing a noticeable and a milder case of asymmetry. The effect of refraction was not quantified in this study.

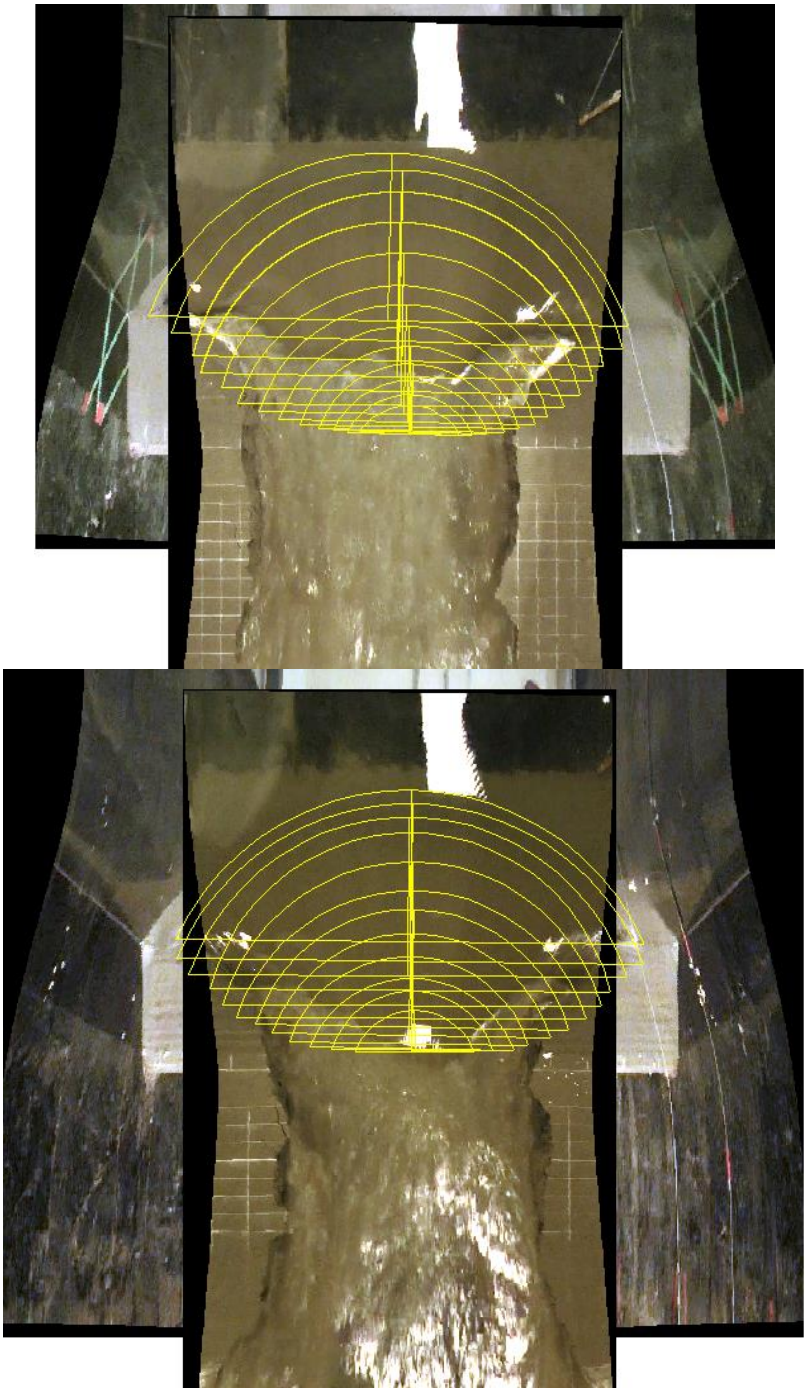

Figure 6.19: Two examples of asymmetry showing georeferenced upstream and planform view images from ArcGIS superimposed by arcs representing the breach channel entrance at various times (top) Test No. 3, $t = 120s$) (bottom) Test No. 4, $t = 110s$)

The morphology of the control section at the breach channel entrance is represented in Figure 6.20 and Figure 6.21. A plot of showing the evolution of the discharge efficiency is shown in Figure 6.22.

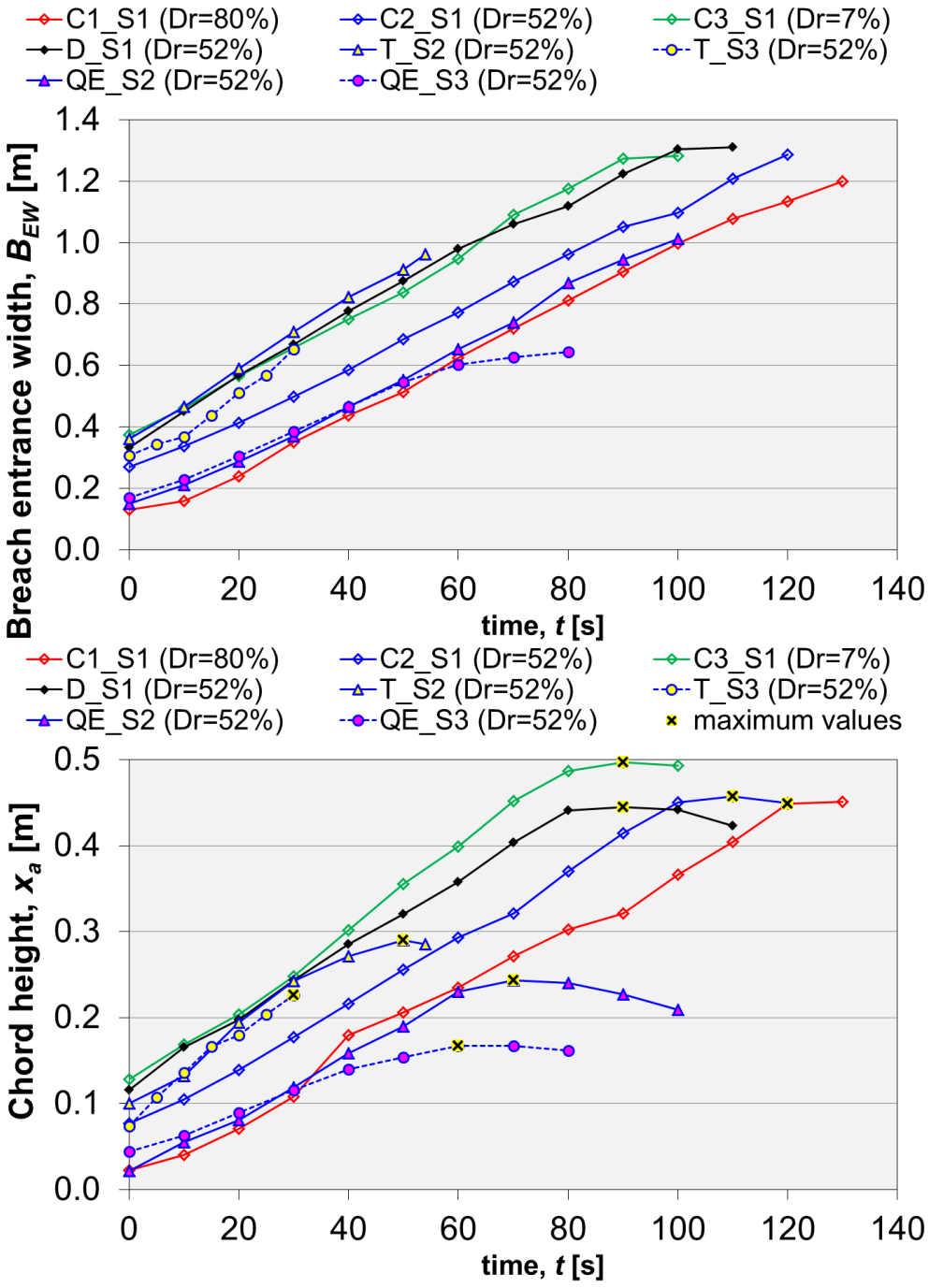

Figure 6.20: Morphology of the breach channel control section represented by entrance (top) width (bottom) chord height showing maximum values

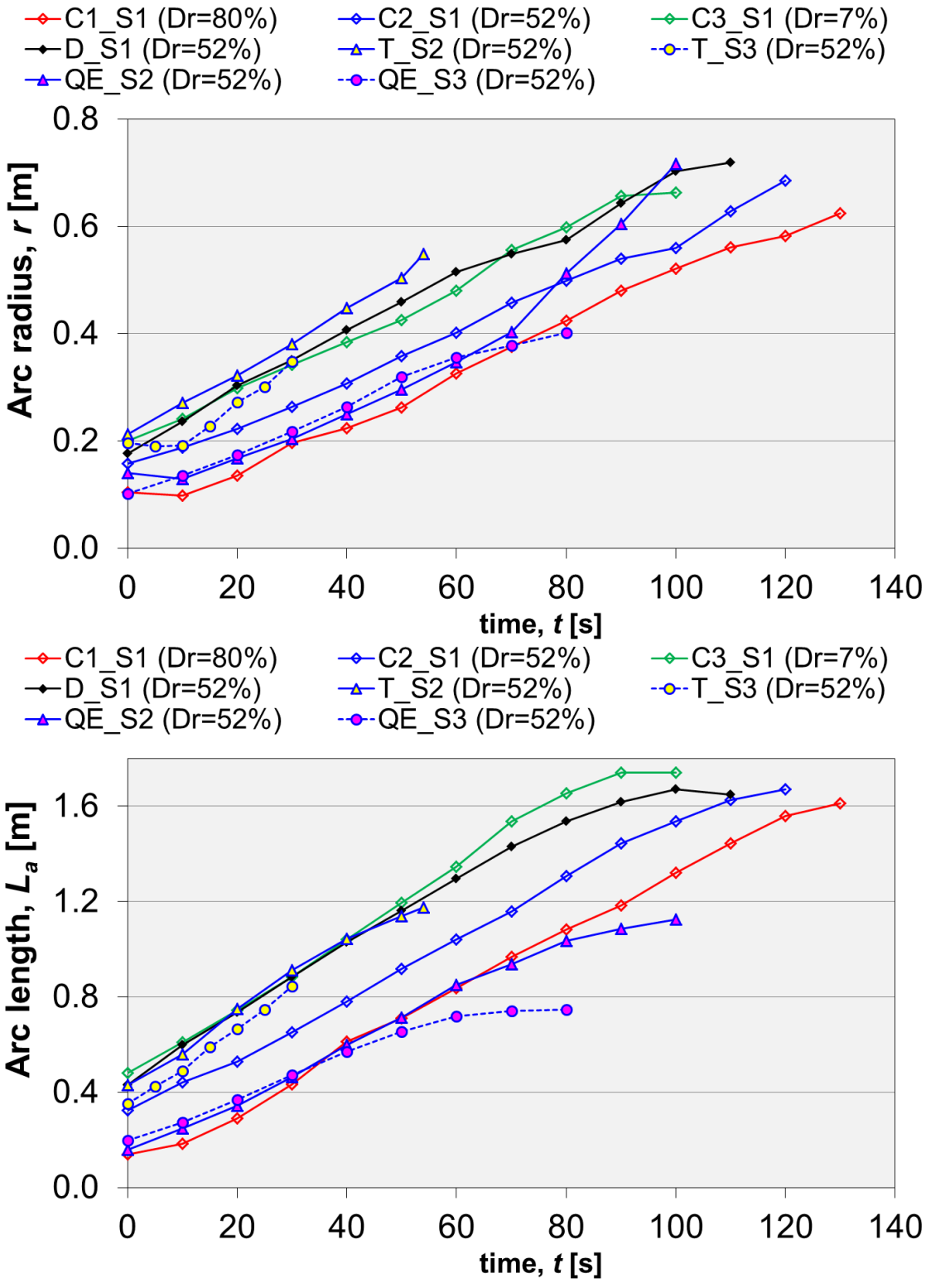

Figure 6.21: Morphology of the breach channel control section represented by the arc entrance (top) radius (bottom) arc length

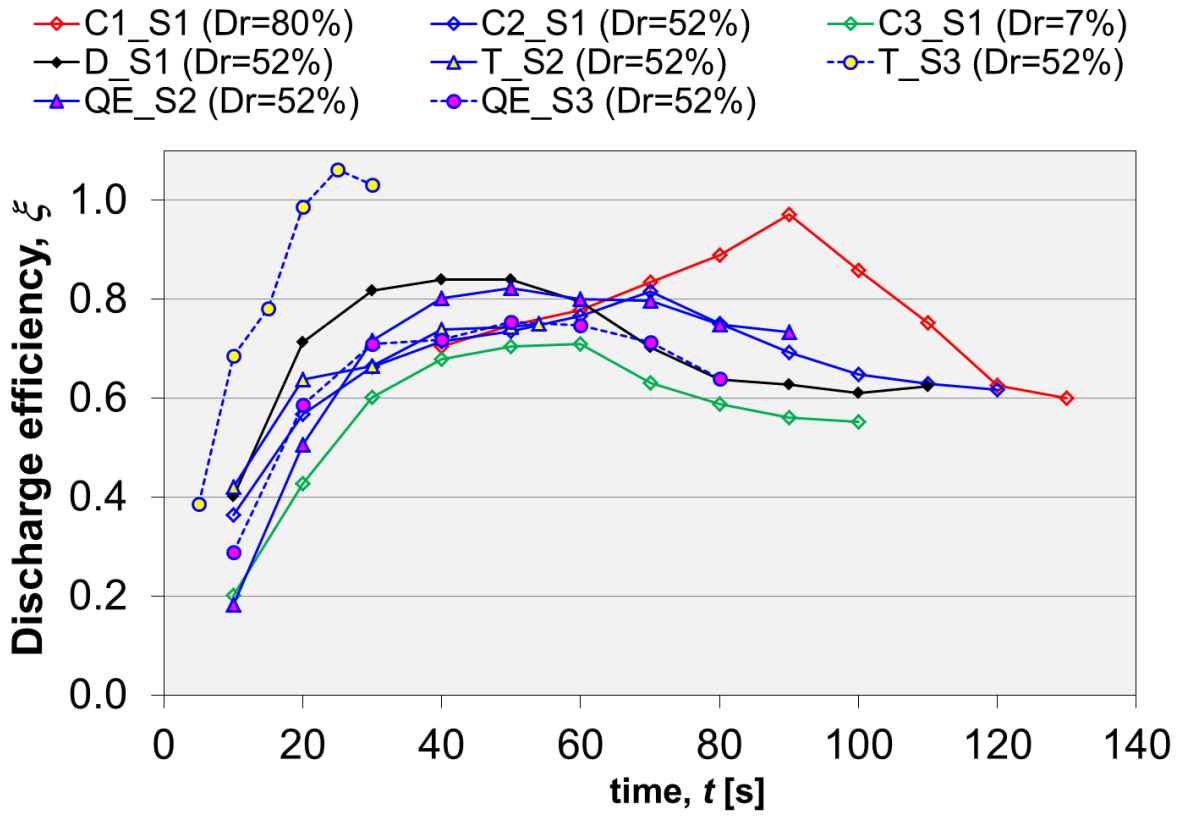

Figure 6.22: Evolution of ratio between measured and estimated breach outflow with respect to time

As shown in Figure 6.22, the estimated breach channel outflow was generally over predicted (*i.e.* $\xi < 1$). A few seconds following the onset of the breach, the discharge efficiency was very low. This implied that the breach outflow was controlled from downstream and not at the apparent control section forming on the upstream slope. In the case of an embankment breach, backwater conditions were caused by the following three mechanisms: flow resistance due to undercutting erosion at the breach channel entrance as well as erosion on the downstream slope, constriction at the breach channel entrance, and flow obstruction in the breach channel due to side-slope failures.

At the early breach stages, undercutting was significant, particularly in the looser embankments. The undercutting mechanism was less distinct in the embankment model constructed with the highest relative density. This is also reflected in Figure

6.20 and Figure 6.21, where the denser embankment models exhibited smaller breach channel dimensions for the same breach outflow. The enhanced shear strength of the denser embankment material rendered the embankment more resistant to erosion and less susceptible to side-slope failures. Consequently, the time for overhang development and side-slope failure frequency was reduced in the denser embankment models. This essentially diminished the flow submergence in the breach channel and therefore increased the breach discharge efficiency.

As the elevation of the inflection point decreased due to downward erosion, inertial forces dominated the backwater effects. As a result, the breach channel's discharge efficiency increased to a peak value, ξ_P (see Figure 6.22). Two additional embankment breach parameters related to the discharge efficiency have been addressed: breach entrance arc width-to-length ratio, L_a/r, and the arc angle, θ. The evolution of those two parameters with respect to time is illustrated in Figure 6.23. Similar to the discharge efficiency, those parameters were optimised at a particular breach time. However, upstream control was only realised in Tests No. 1 and 7, since based on Equation (6.8), the estimated discharge efficiency (as shown in Figure 6.22) reached the measured value. This was due to the narrower breach channel entrance crest forming on the (steeper) downstream slope in the tilted models, particularly for the test where $X_{rr} = 1/3$. It is important to note that it is not possible for the discharge efficiency to exceed unity (*e.g.* Test No. 7) since this would imply supercritical conditions (*i.e.* $Fr > 1$) at the breach channel's inflection (Froude-critical) point. It is therefore presumed that an error was due to optical refraction, broad demarcation or asymmetry in breach channel morphology.

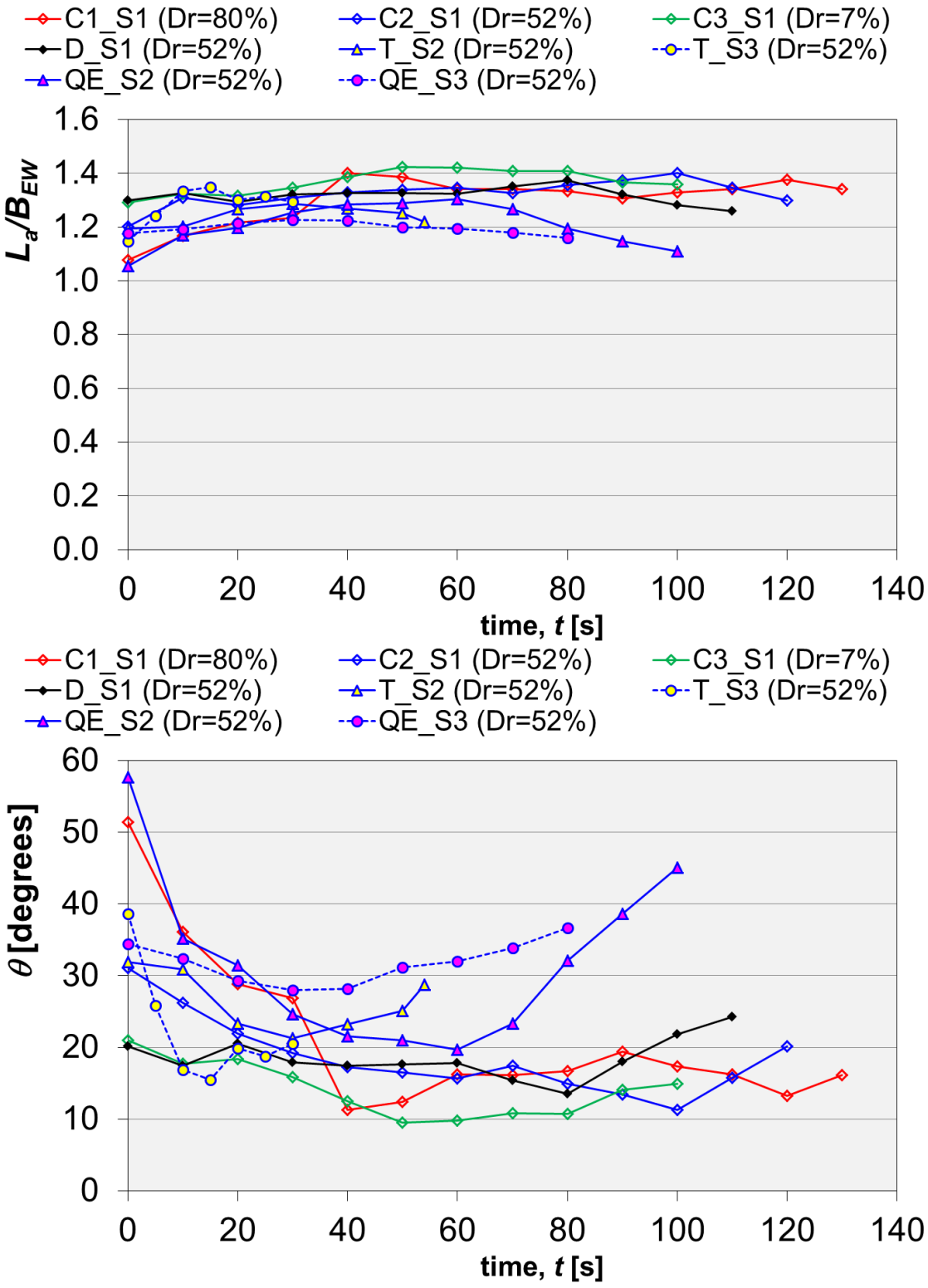

Figure 6.23: Evolution of two discharge efficiency related dimensionless parameters (top) breach channel entrance crest length-to-width ratio (bottom) arc angle

For the undrained embankment model (D_S1 or Test No. 5), the breach channel exhibited larger dimensions than the benchmark test (C2-S1 or Tests No. 2 and 3), as shown in Figure 6.20 and Figure 6.21. The discharge efficiency also increased sooner and had a slightly larger peak value. The absence of a drain reduced the flow resistance, particularly at the initial stages of the breach. This diminished the backwater effects and allowed the finer sediment to be transported with less effort. After reaching a peak value, the discharge efficiency then followed a reduction throughout the time in which the breach channel entrance remained visible. Further side-slope failures in the breach channel were a large contribution to flow obstruction. In the case of the densest embankment model, this drop was more rapid due to the relatively larger size of side-slope failures occurring in succession. For the quasi-exact scale series, the discharge efficiency trend was similar to the benchmark tests. The time-scales, however, were not the same. The peak discharge efficiency for the smallest geometric quasi-exact scales was slightly lower since they were more sensitive to backwater effects due to breach flow submergence.

From Figure 6.20 and Figure 6.21, it can be shown that the breach channel entrance dimensions progressed linearly with time with the exception of the chord height which reached a peak value in later breach stages. According to Equation (6.8), the chord height and breach channel entrance width represent the dimensions which dominate the breach channel outflow. The characteristic width, $B_{EW,a}$, has been defined as the breach channel entrance width corresponding to the maximum chord height, $x_{a,max}$ at time, t_a (*i.e.* $t = t_a$ at $\max[x_a]$). As shown in Table 6.3, this time roughly corresponded to the time-to-peak measured from the breach outflow hydrograph (i.e. $t_a \approx t_P$).

Table 6.3: Summary of breach channel control section results for Phase II

Test No.	Test series	Scale ratios			Crest height, h_{cr} [m]	Characteristics at maximum chord height			Time-to-peak, t_P [s]	Peak ξ and corresponding time	
		X_{rr}	Z_{rr}	D_r [%]		x_a [m]	B_{EW}† [m]	$t^{\ddagger}$ [s]		ξ_P	t [s]
1	D	1	1	80	0.30	0.449	1.134	120	125	0.972	90
3*	D	1	1	52	0.30	0.457	1.208	110	113	0.817	70
4	D	1	1	7	0.30	0.497	1.274	90	90	0.709	60
5	E	1	1	52	0.30	0.445	1.224	90	95	0.841	50
6	F	$1/2$	1	52	0.30	0.290	0.912	50	54	0.750	50
7	F	$1/3$	1	52	0.30	0.226	0.652	30	36	1.062	25
8	G	$1/2$	$1/2$	52	0.15	0.243	0.740	70	79	0.823	50
10	G	$1/3$	$1/3$	52	0.10	0.167	0.602	60	64	0.754	50

†corresponds to $B_{EW,a}$; ‡corresponds to t_a; *benchmark test

It was therefore necessary to nondimensionalize all the parameters using this characteristic width. The dimensionless parameters described by the breach channel entrance width, chord height, arc radius and arc length, respectively, were then defined as:

$$B_{EW}^{*} = \frac{B_{EW}}{B_{EW,a}} \tag{6.17}$$

$$x_a^{*} = \frac{x_a}{B_{EW,a}} \tag{6.18}$$

$$r^{*} = \frac{r}{B_{EW,a}} \tag{6.19}$$

$$L_a^{*} = \frac{L_a}{B_{EW,a}} \tag{6.20}$$

The difference in geometric scales in the tilted and quasi-exact scale series, also gave rise to different time scales. As a result, the time scales were nondimensionalized using the time-to-peak in order to investigate the distortion in the results. The evolution of the dimensionless parameters with respect to a time normalised by the time-to-peak, t^{*}, (*i.e.* $t^{*} = t/t_P$) is shown in Figure 6.24 and Figure 6.25. The evolution of the parameters depicting discharge efficiency (*i.e.* ξ, L_a/r and θ) with respect to the normalised time is shown in Figure 6.26 and Figure 6.27.

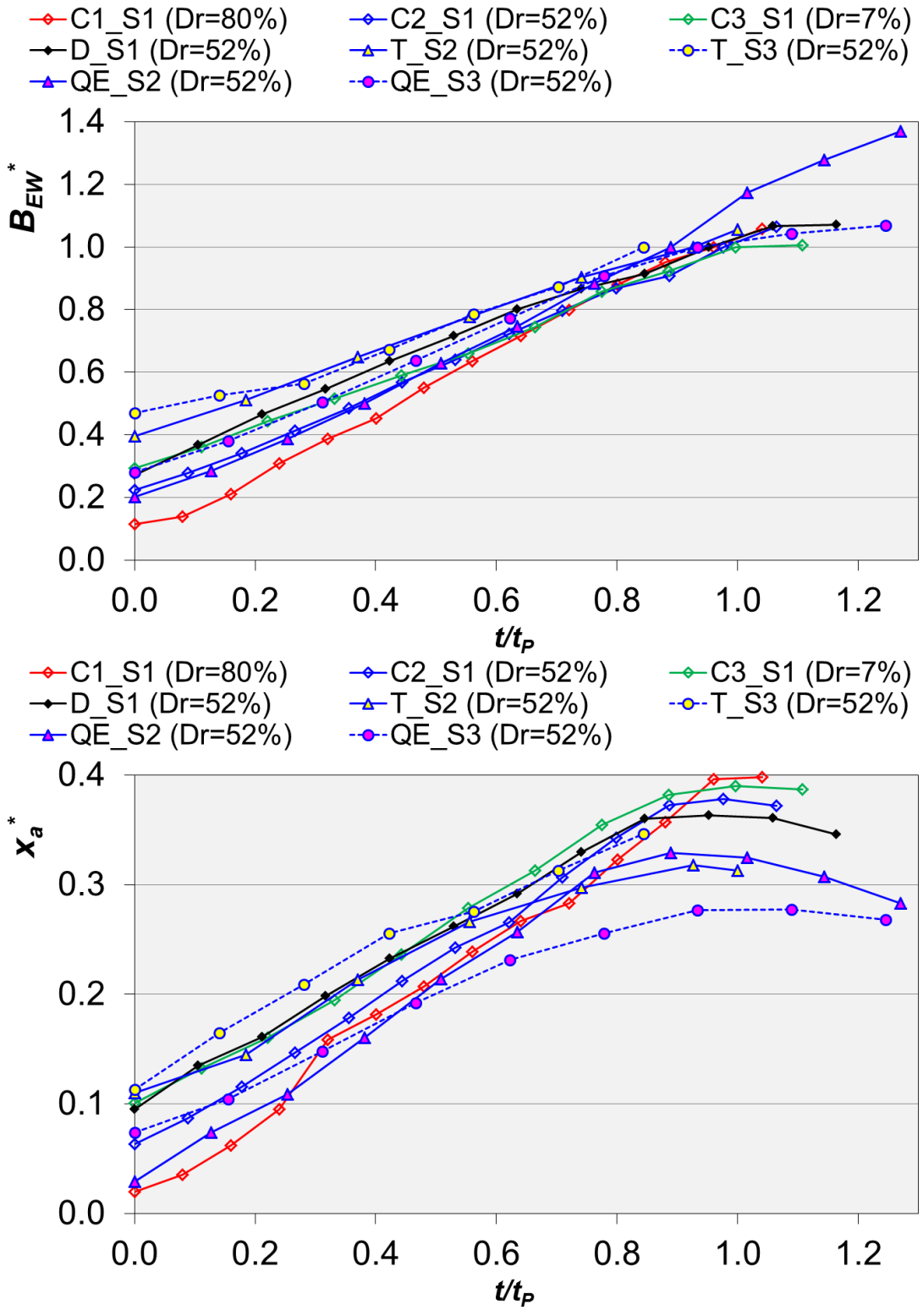

Figure 6.24: Morphology of the breach channel control section with respect to a normalised time represented by the dimensionless arc entrance (top) width (bottom) chord height

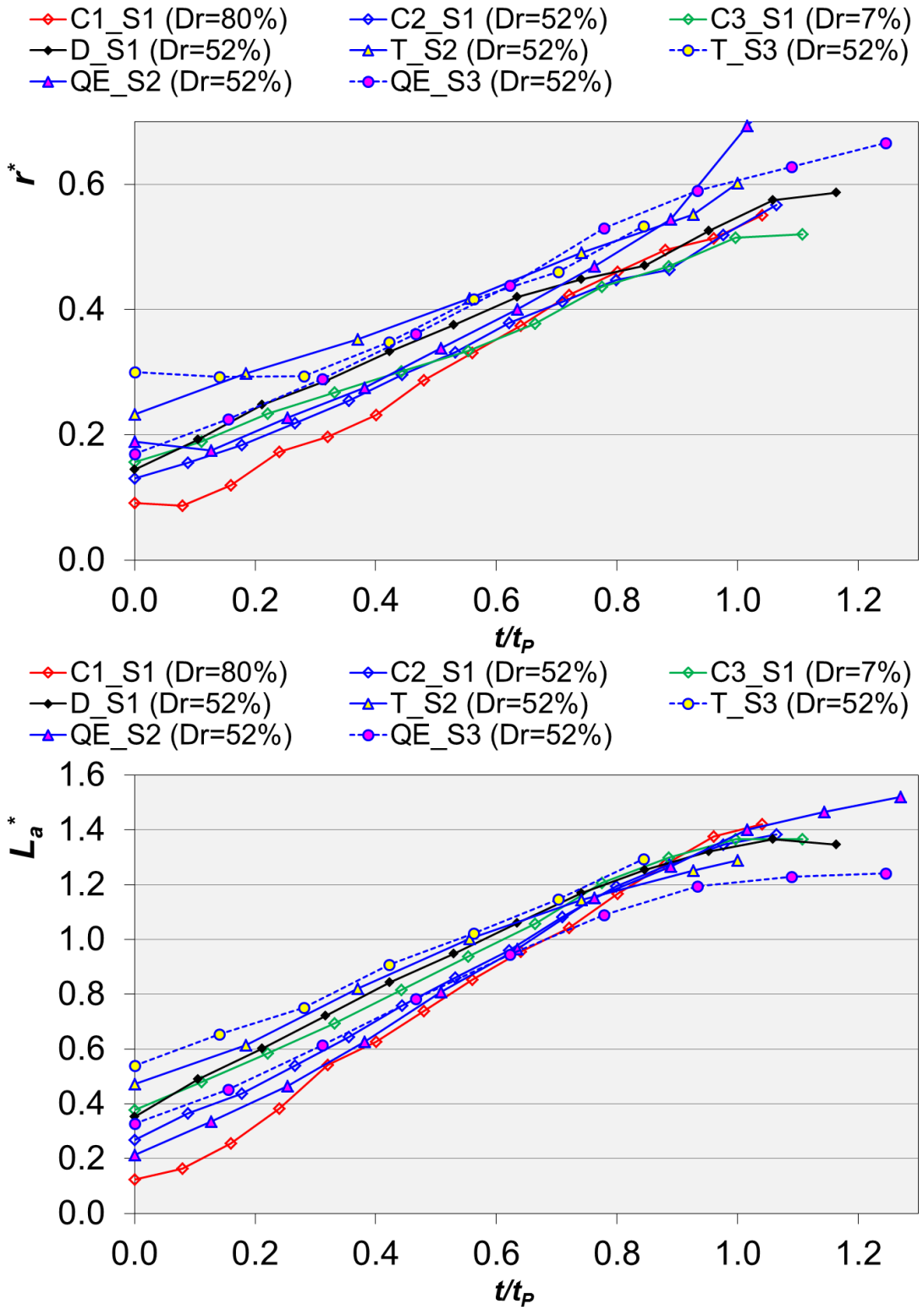

Figure 6.25: Morphology of the breach channel control section with respect to a normalised time represented by the dimensionless arc entrance (top) radius (bottom) length

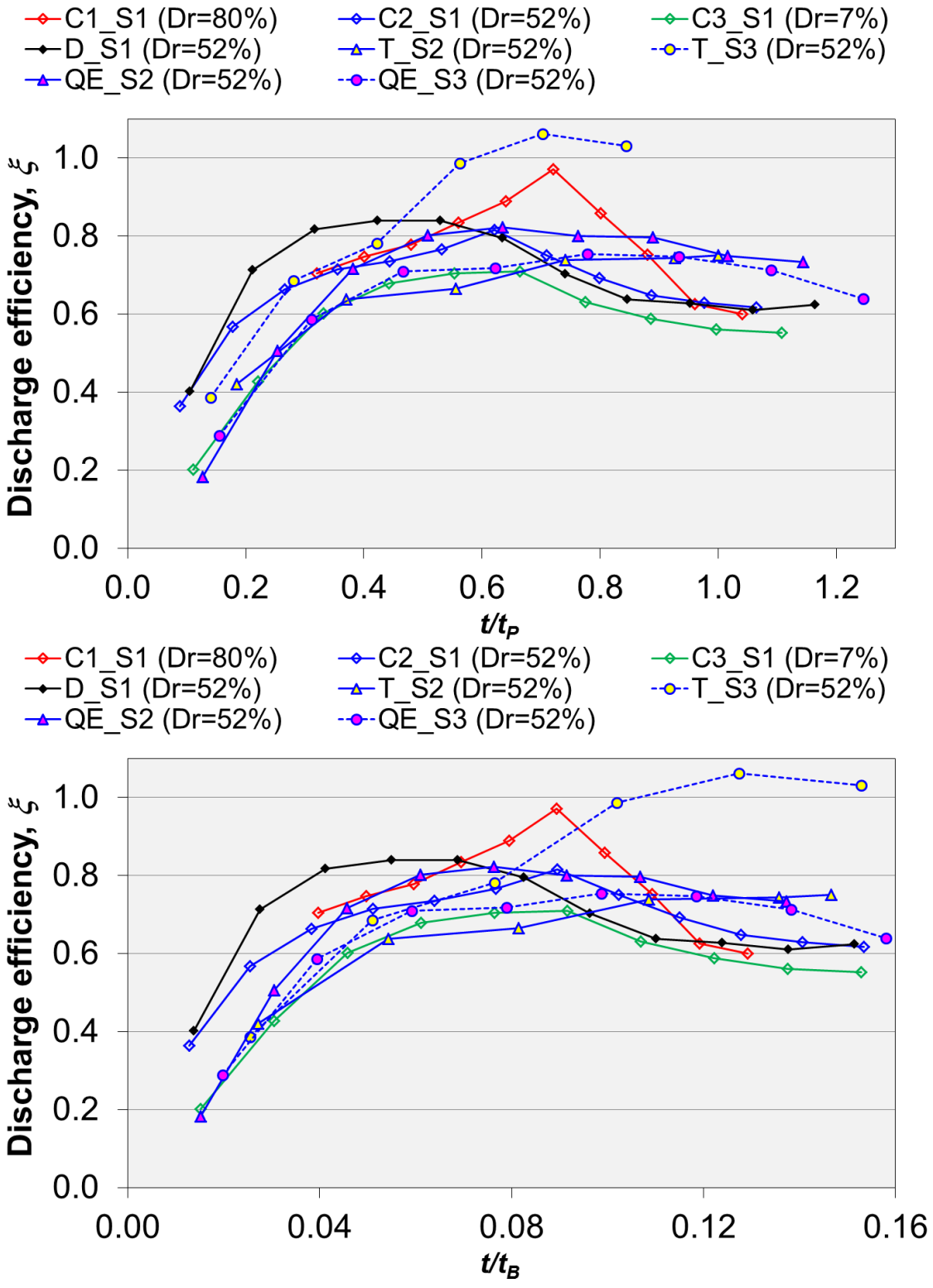

Figure 6.26: Evolution of ratio between measured and estimated breach outflow with respect to a time normalised by (top) time-to-peak (bottom) base-time

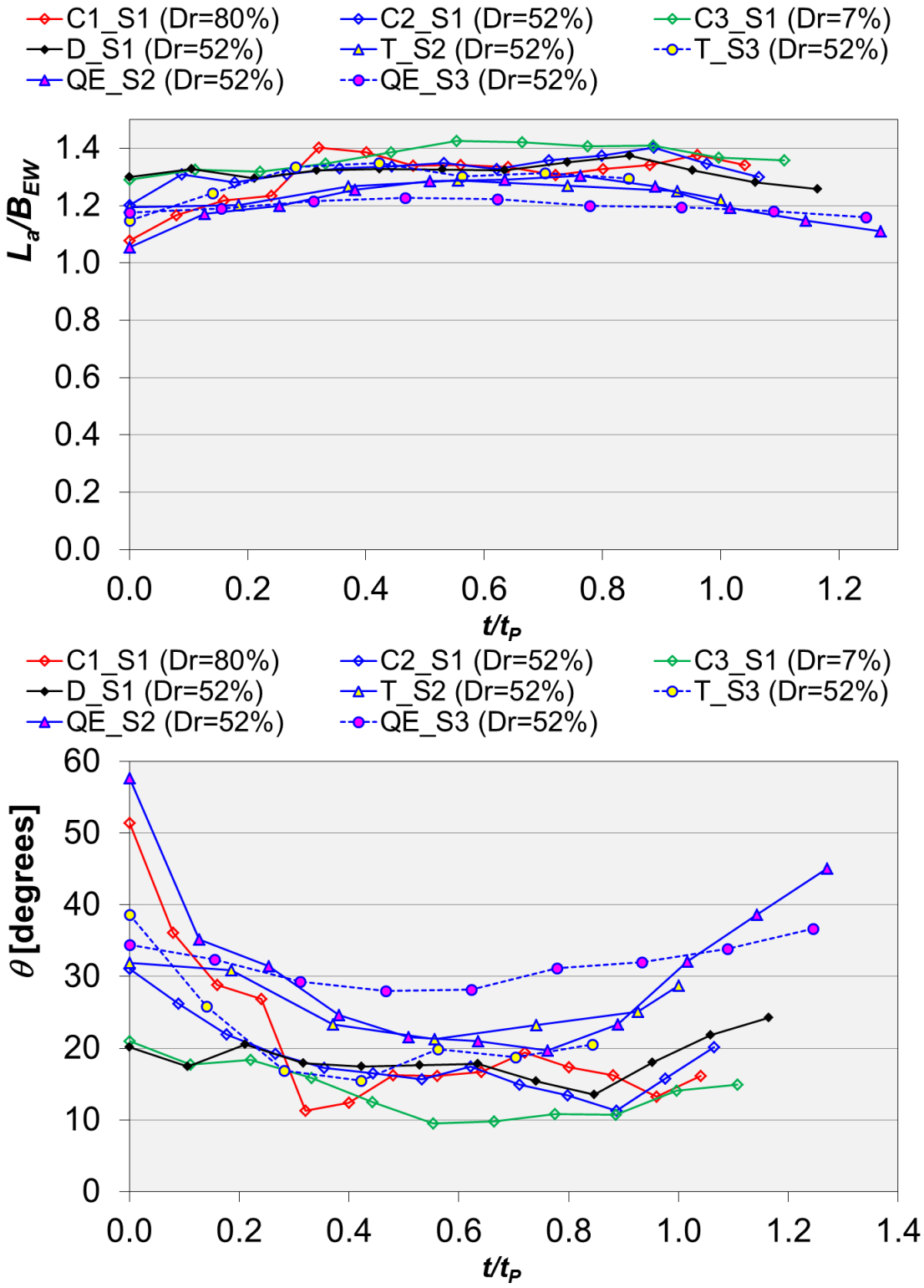

Figure 6.27: Evolution of two discharge efficiency related dimensionless parameters with respect to a time normalised by time-to-peak (top) breach channel entrance crest length-to-width ratio (bottom) arc angle

The temporally-normalised evolution plots for the dimensionless breach channel entrance parameters and discharge efficiency helped perceive certain trends. The discharge efficiency for both drainage configurations was initially the same, until when the drainage element in the drained embankment model was exposed to the breach flow and which caused larger backwater effects. After the drainage layer in the path of the breach channel was washed away, the evolution of the discharge efficiency became identical to the benchmark test. It can be seen from Figure 6.25 that at peak flow conditions, the dimensionless arc length is maximum, with a value of approximately 1.4, with the exception of the tilted geometric scale series and scale $1/3$ of the quasi-exact scale series due to distorted time scales and submergence conditions, respectively.

From Figure 6.26 and Figure 6.27, it can be shown that the peak discharge efficiency was at approximately 70% the time-to-peak. The normalised time corresponding to the peak breach channel discharge for the tilted geometric scale series models deviated from that value due to the distorted time scales. The values for ξ_P and the corresponding normalised time as well as third order best-fit polynomials and the corresponding square of the multiple correlation coefficient, R^2, for Phase II tests is summarised in Table 6.4. Best-fit expressions describing the evolution of the dimensionless parameters shown in Figure 6.24 and Figure 6.25 with respect to the normalised time are shown in Table 6.5.

.

Table 6.4: Best-fit expression and peak values for breach channel discharge efficiency

Test No.	Test series	Scale ratios			h_{cr} [m]	Breach channel discharge efficiency and normalised time			
		X_{rr}	Z_{rr}	D_r [%]		ξ_P	$t^{*\dagger}$	Best-fit expression	R^2 value
1	D	1	1	80	0.30	0.972	0.72	$\xi = -1.3282t^{*3} + 0.653t^{*2} + 0.9467t^{*} + 0.3571$	0.8457
3‡	D	1	1	52	0.30	0.817	0.62	$\xi = 1.5549t^{*3} - 3.8674t^{*2} + 2.776t^{*} + 0.1613$	0.9631
4	D	1	1	7	0.30	0.709	0.66	$\xi = 2.1069t^{*3} - 5.1713t^{*2} + 3.7898t^{*} - 0.1666$	0.9948
5	E	1	1	52	0.30	0.841	0.53	$\xi = 2.9512t^{*3} - 6.5384t^{*2} + 4.11t^{*} + 0.0657$	0.9693
6	F	$1/2$	1	52	0.30	0.750	1.00	$\xi = 1.2604t^{*3} - 2.9339t^{*2} + 2.3437t^{*} + 0.0849$	0.9766
7	F	$1/3$	1	52	0.30	1.062	0.70	$\xi = -0.7802t^{*3} - 0.4139t^{*2} + 1.979t^{*} + 0.1319$	0.9835
8	G	$1/2$	$1/2$	52	0.15	0.823	0.64	$\xi = 2.0506t^{*3} - 5.3398t^{*2} + 4.3157t^{*} - 0.2792$	0.9972
10	G	$1/3$	$1/3$	52	0.10	0.754	0.78	$\xi = 0.966t^{*3} - 2.9952t^{*2} + 2.8045t^{*} - 0.0592$	0.9726

†normalised time corresponding to peak breach channel discharge efficiency, ξ_P; ‡benchmark test

Table 6.5: Best-fit expressions describing morphology of dimensionless breach channel entrance parameters with respect to normalised time

Test No.	Test series	Scale ratios X_{rr}	Scale ratios Z_{rr}	Scale ratios D_r [%]	h_{cr} [m]	Best-fit expression	R^2 value
1	D	1	1	80	0.30	$B_{EW}^* = 0.9703t^* + 0.0811$	0.9963
						$x_a^* = -0.0489t^{*2} + 0.4364t^* + 0.0072$	0.9933
						$L_a^* = 1.3317t^* + 0.0873$	0.9963
3†	D	1	1	52	0.30	$B_{EW}^* = 0.8088t^* + 0.2089$	0.9984
						$x_a^* = -0.0784t^{*2} + 0.4077t^* + 0.051$	0.9884
						$L_a^* = 1.1121t^* + 0.263$	0.9952
4	D	1	1	7	0.30	$B_{EW}^* = 0.689t^* + 0.2906$	0.9929
						$x_a^* = -0.107t^{*2} + 0.4079t^* + 0.0865$	0.9855
						$L_a^* = 0.977t^* + 0.3852$	0.9862
5	E	1	1	52	0.30	$B_{EW}^* = 0.7433t^* + 0.3019$	0.9946
						$x_a^* = -0.1795t^{*2} + 0.4514t^* + 0.0835$	0.9821
						$L_a^* = 0.9855t^* + 0.3993$	0.9891
6	F	1/2	1	52	0.30	$B_{EW}^* = 0.6628t^* + 0.3985$	0.9984
						$x_a^* = -0.1473t^{*2} + 0.3687t^* + 0.0993$	0.9856
						$L_a^* = 0.8379t^* + 0.49$	0.9887
7	F	1/3	1	52	0.30	$B_{EW}^* = 0.6369t^* + 0.4297$	0.9759
						$x_a^* = -0.1065t^{*2} + 0.3601t^* + 0.115$	0.9962
						$L_a^* = 0.8952t^* + 0.5243$	0.9973
8	G	1/2	1/2	52	0.15	$B_{EW}^* = 0.9537t^* + 0.1611$	0.9941
						$x_a^* = -0.2668t^{*2} + 0.5739t^* + 0.0042$	0.9679
						$L_a^* = 1.2145t^* + 0.1865$	0.9971
10	G	1/3	1/3	52	0.10	$B_{EW}^* = 0.7477t^* + 0.2835$	0.9889
						$x_a^* = -0.1516t^{*2} + 0.362t^* + 0.061$	0.9874
						$L_a^* = 0.8866t^* + 0.3465$	0.9826

†benchmark test

The head above the inflection point at the centreline of the breach channel entrance was calculated using Equation (6.10) at different times. The computed heads, as shown in Figure 6.28, reached values as large as 18cm for the large-scale tests. Figure 6.28 also shows the variation in head above the centreline inflection point nondimensionalized by the crest elevation with respect to the normalised time.

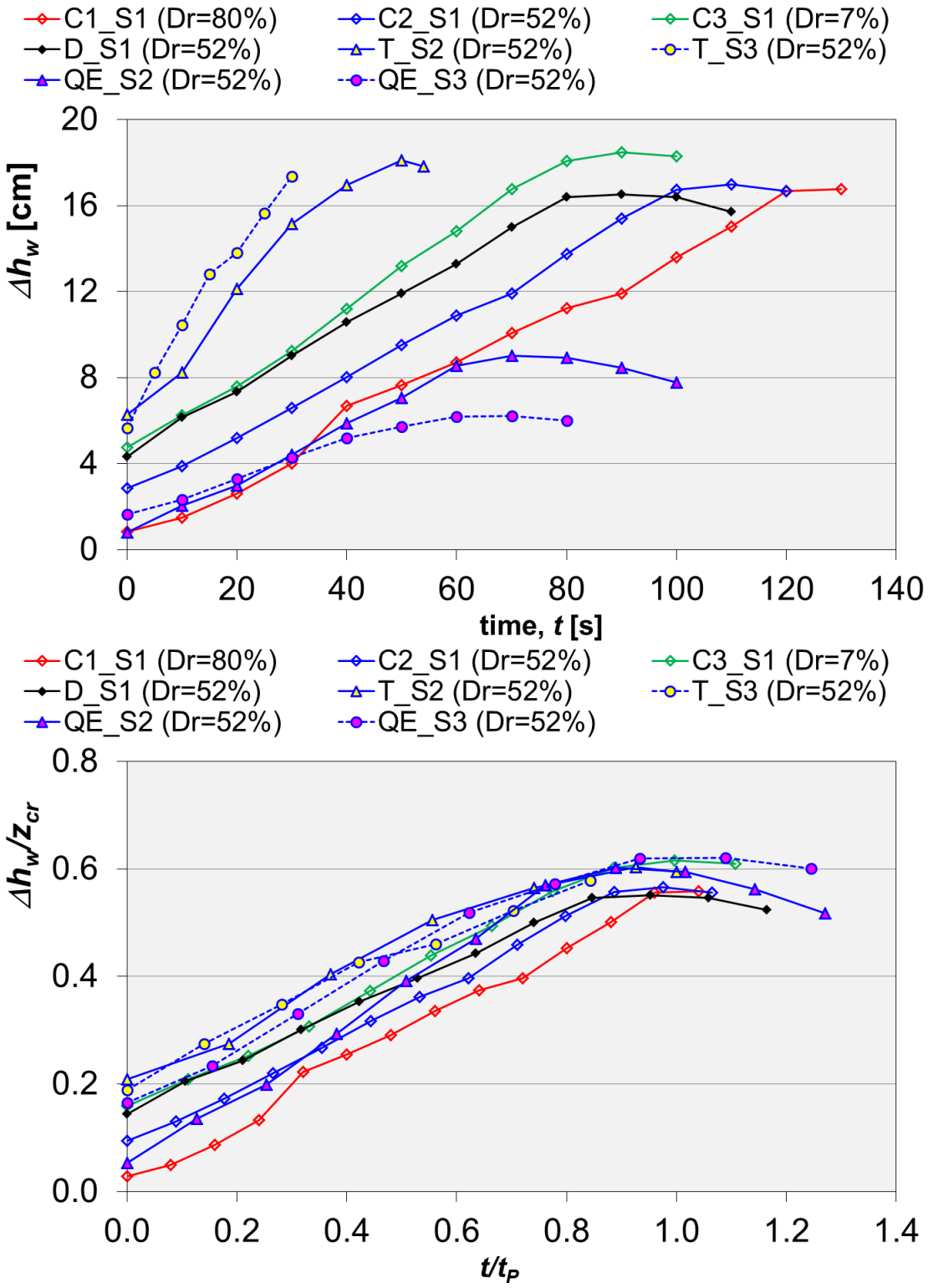

Figure 6.28: Head above inflection point at centreline of breach channel entrance (top) dimensional plot (bottom) dimensionless plot (head is normalised by crest elevation and time is normalised by time-to-peak)

6.7 Discussion

The different construction technique, drainage layer as well as embankment material used in 3-D breach overtopping tests of Phase I made it impractical to integrate any of its data with that of Phase II. Nonetheless, the preliminary experimental work (*i.e.* Phase I) was useful in identifying the requirements and scope of the 3-D breach overtopping test series. The results of the Phase II tests are discussed with respect to two aspects: evaluation of the Froude-criterion in scaling breach outflow for tilted and quasi-exact geometries (*i.e.* using hydraulic parameters), and the similarity of upstream breach channel morphology and time-dependence of the breach discharge efficiency for the all test series (*i.e.* for both hydraulic and geotechnical parameters).

It is evident from Figure 6.16 to Figure 6.18 that the Froude criterion can be effectively applied to predict the embankment breach parameters Q_P and t_P as well as the flow characteristics during the entire breach duration between a prototype and a titled model. In the case of quasi-exact geometric scale series, only t_P was in good agreement with the Froude criterion. The peak flow estimate was lower due the influence of relatively higher tailwater conditions and the consequent scale effects due to the roughness, entrainment and settling properties of the relatively coarser sediments (particularly the drain material). This was reflected throughout the entire duration of the breach and was more evident in the smallest quasi-exact geometric scales.

Although the base-time for the tilted geometric scales was in better agreement with the Froude criterion than the quasi-exact geometric scales, this embankment outflow characteristic cannot be entirely relied upon. The criterion for determining base-time was based on the time when the computed breach outflow yielded zero values. It was also found that this zero-flow criterion was very sensitive to the wave gauge data filtration parameters which resulted in base-time parameter variations as large as ±100s. For smaller geometric scales, this can be significant. There were reasons

other than the (somewhat subjective) zero-flow criterion which may have caused a discrepancy in the base-time of the outflow hydrograph. The reasons are as follows:

- Scale effects due to low Reynolds and high Weber numbers (*i.e.* viscous and surface tension forces dominated the inertial forces) at very low flows
- Lower relative flow submergence (*i.e.* η/d_{50}) decreased the grain Reynolds numbers resulting in smooth hydraulic boundaries (*i.e.* undeveloped flow regimes where $Re^* < 70$). As a result, the resistance parameter between the model series was different (Julién, 1992) and consequently so was the erosion.
- Sedimentation patterns and wave forms downstream the breach channel from subsequent earlier breach phases are highly sensitive at low flows.

Given the above reasons, the Froude criterion may not be very reliable at scaling the base-time of the outflow hydrograph in comparison to the time-to-peak and peak flow. However, the base-time (or failure time as it is referred to in some studies) remains to be an important parameter used in normalizing the temporal breach outflow hydrograph characteristics. Therefore, in this study, the time-to-peak was chosen as the most suitable normalising temporal characteristic. It is suggested to explore other normalising temporal characteristics which are volume or peak-flow dependent. An example of such temporal characteristics could be the time at which a certain fraction of the impoundment is depleted or the residual flow at the receding limb as some fraction of the peak flow (*e.g.* time at 25% of Q_P on the receding limb).

The temporally-normalised evolution plots for the dimensionless breach channel entrance parameters helped shed light on the assumptions and limitations of weir-type formulations used in many embankment breach parametric models. Broad-crested weir formulations assume critical flow conditions at the breach channel constriction, where the discharge through the breach channel is regulated using a discharge coefficient. The discharge efficiency formulation derived in this chapter, was based on the Froude-critical condition at the breach channel entrance. The latter formulation, however, indicated that some level of downstream control was

present in the breach channel. It can therefore be stated that absolute regime control due to an embankment breach is neither at the constriction nor at the upstream entrance of the breach channel. Regardless of which method is selected for the prediction of breach outflow, it is necessary to take into consideration the temporal variation of the discharge-adjustment parameter due to downstream control.

Contrary to their poor prediction in Froude-scaling the outflow hydrograph characteristics, the quasi-exact geometric scale models demonstrated similarity in the discharge efficiency's time-dependence. With respect to breach channel entrance morphology, only Scale $1/2$ of the quasi-exact geometric scale series demonstrated a reasonable similarity with respect to breach channel entrance morphology. Similar to the outflow characteristics, Scale $1/3$ exhibited a deviation from the benchmark's trend due to scale effects. Due to distorted lateral time scales, the tilted geometric scale series displayed poor trend similarity for both the breach discharge efficiency as well as the breach channel entrance morphology. While the breach discharge efficiency trend was not similar in the case of the compaction series, the breach channel morphology aspect did show strong similarity at $t^* > 0.6$.

The Froude-criterion can be used with tilted embankment geometric models to predict prototype hydrograph data. If this is not a feasible solution, quasi-exact embankment models can be used to predict the evolution of the breach channel entrance and the consequent breach outflow can be predicted based on the proposed best-fit expression of the discharge efficiency. Selecting a geometric scale using quasi-exact scale series should consider scaling of resistance and sediment entrainment and settling.

The influence of compaction on the outflow hydrograph characteristics and breach channel entrance morphology was noticeable and distinct. Therefore, the compaction of noncohesive embankment models in a laboratory environment should not be arbitrary. Rather, it is suggested to scale the compaction based on erodibility. It was initially intended to investigate the influence of compaction on erodibility using

2-D overtopping tests as part of the next experimental phase. However, after all the attempts had failed at reproducing the (large-flume) *in situ* compaction curve in the smaller flume (where the 2-D overtopping tests can be performed), the scope of the erodibility tests was shifted towards the initial-soil water state. The breach flow and breach channel morphological analyses which were conducted for the drained and undrained models indicated that the initial soil-water state influenced breach erosion to a large extent. This was a compelling reason to conduct a more in-depth investigation on the influence of the seepage on overtopping as part of Phase III of the experimental program.

6.8 Conclusions and Recommendations

6.8.1 Conclusions

In Phase II of the experimental program, the chosen parameters addressed both geotechnical and hydraulic (various geometric scales) aspects. The instrumentation included wave gauges, piezometers, and video cameras. All 3-D breaching overtopping tests were conducted in the large flume (1.5m-wide), in the Hydraulics Laboratory. Construction of the embankment models was carried out by compacting the embankment material (fine sand) using an improved technique developed to mimic an actual prototype construction comprised of a vibratory and static load to apply and control compaction. A compaction and drainage test series was used, respectively, to investigate the influence of compaction and initial soil-water state on the breaching process. Similar to Phase I, breach outflow was computed from the recorded water surface elevations using a hydrologic routing method.

- A unique aspect of the 3-D breach overtopping tests was that inflow was sufficiently controlled to cause overtopping without influencing the breach failure mechanism itself.
- The novel construction method employed the optimum soil conditions based on an *in situ* assessment rather than using laboratory methods such as the

Standard Proctor Test. It was demonstrated (in Subsection C.2.3 of Appendix C) that, using either compaction method (*i.e.* dynamic or vibration), the optimum dry unit weight varied significantly when the embankment material was confined *in situ* (i.e. within a hydraulic flume) than within a laboratory mold.

- Similar to construction technique used in Phase I, a correlation between the breach outflow hydrograph's lag-time, t_L, and the initial soil-water state was observed. The difference in the lag-time between the two drainage configurations, however, was shorter for the improved construction technique. Similar to Phase I, the hydrograph characteristics, time-to-peak, t_P, base-time, t_B, and peak flow, Q_P, were almost identical between both drainage configurations.
- For the improved construction technique the mode of side-slope failures for both drainage configurations was always in the form of collapses. This was due to the higher efficiency of the novel construction technique in densifying the embankment material.
- The compaction series, using three relative densities (D_r = 7%, 52% and 80%), was useful in demonstrating the use of compaction effort as an alternative scaling criterion in mobile bed hydraulic models. A 16% attenuation in peak breach outflow was observed between the lowest and highest compaction effort, as expected, while the corresponding decrease in time-to-peak was 28%. Undercutting and the frequency of side-slope failures in the breach channel were also reduced for embankments constructed with higher compaction efforts.

Two additional (geometric) test series were designed: quasi-exact scale ($Y_{rr} = 1$; and $X_{rr} = Z_{rr} = 1/3,\ 1/2$ and 1) and tilted scale series ($Y_{rr} = Z_{rr} = 1$; and $X_{rr} = 1/3,\ 1/2$ and 1). Both geometric scale series were used to investigate the influence of different geometric scales on the breaching process, and in particular, to test the validity of the Froude number as a scaling criterion in 3-D breach overtopping hydraulic models. A photogrammetric analysis was also developed to capture the

spatial and temporal evolution of the breach channel dimensions at the curved upstream control section (*i.e.* breach channel entrance) as described in previous literature (Coleman *et al.* 2002; IMPACT, 2004a; Stretch and Parkinson, 2006; Morris *et al.* 2007). Subsequently, an expression to predict the breach outflow based on the Froude-critical condition at the curved breach channel entrance was derived. The breach discharge efficiency was then defined as the ratio between the measured and predicted breach outflow.

- With respect to the geometric scale series, the Froude criterion performed remarkably well in scaling the entire breach outflow hydrograph for tilted geometries, whereas for quasi-exact geometries, scale effects were noted, particularly for the smallest geometry.
- The Froude criterion scaled the time-to-peak reasonably well for quasi-exact geometries, whereas peak breach outflow prediction was poor. It is expected that the Froude criterion would perform better in the case of tilted geometries since the embankment breach is essentially governed by the gravity source term and the conveyance of the stored energy.
- The scaling of base-time for both geometric scales was not accurate due to subjective criteria on which zero-flow was based, as well as the influence of tailwater conditions on the receding limb of the hydrograph. A peak-flow or volume dependent temporal parameter is therefore suggested to represent the termination of the breach outflow hydrograph.
- While there was correlation between the outflow hydrograph's lag-time and embankment density and geometry, the scaling of this embankment breach characteristic was not addressed.
- For the repeated 3-D breach overtopping tests, there was good agreement with respect to the entire shape of the breach outflow hydrograph.
- The breach discharge efficiency, as defined by the dimensions of the apparent upstream control section, correlated well with the dominant breach mechanisms.

- The low discharge efficiency during the initial breach stages indicated that the breach outflow was controlled from downstream mainly due to the undercutting mechanism. Looser soil conditions and the presence of a drain also contributed to this low efficiency. Following this stage was a maximum efficiency stage, in which the inertial effects were dominant. The discharge efficiency peak was lowest in the looser embankment models as well as the smallest quasi-exact geometric scale. This phase was then followed by a reduction in discharge efficiency due to backwater effects from the submerged flow in the breach channel.
- In the case of the tilted geometries, there was no reduction in discharge efficiency, particularly for the smallest (*i.e.* steepest) geometric scale in which the breach channel entrance tended to an ogee-crested weir.
- The magnitude of the overtopping head during peak flow conditions was very large, and exceeded 50% of the embankment height in all the experiments. The breach channel dimensions (entrance width and length) exhibited a linear growth rate for all embankment models.
- There was very good similarity with respect to the breach channel morphology within the quasi-exact geometric scales, particularly when $t^* > 0.6$. In the case of the tilted geometric scales, there was poor similarity due to the distorted lateral time scales. *It is therefore suggested to resort to tilted geometric scale series when scaling is required using the breach outflow hydrograph. Whenever scaling of the breach channel morphology is required, quasi-exact geometric scale should be used*.
- Use of quasi-exact geometric scale series, however, should take into account the potential scale effects which may result in small model geometries. Smaller models are susceptible to low relative submergence due to the relative roughness (*i.e.* resistance), entrainment and deposition properties of the sediment.

6.8.2 Recommendations for Future Work

- As part of future experimental studies, geometric scale series tests could be expanded to include larger scale ratios or even field-scale embankments. Investigating the 3-D breach overtopping mechanism using larger geometric scales would offer a more comprehensive assessment of the Froude criterion, including its limitations.
- It is recommended to also introduce different grain sizes into the geometric scale series experiments. Satisfying mobile-bed modeling criteria related to resistance, entrainment and settling processes concurrently with the Froude criterion should also be investigated.
- Capture of the breach channel entrance could also be conducted using an upstream view video (or digital) camera installed below the water surface rather than using a top-view camera, which is not susceptible to errors due to light refraction.

Chapter 7
2-D Overtopping Tests (Phase III)

The third phase of the embankment breach experimental program at the University of Ottawa began in September 2011. This experimental phase, comprised of a series of 2-D overtopping tests on embankment models with the same dimensions of those tested in Phase I and II, was carried out in the small flume in the Hydraulics Laboratory. The key purpose of this experimental phase was to achieve a dense PWP measurement within a noncohesive embankment subjected to overtopping flow. As a result, an investigation of the boundary seepage mechanism across an eroding steep slope due to supercritical flow was directed. The WSL over the retreating slope and the erosion process of the embankment model was captured using photographic and video images. The real-time PWP within the embankment model body were recorded using a novel experimental 2-D configuration comprised of tensiometer-transducer devices, designed, fabricated and assembled at the Geotechnical Engineering Laboratory. The embankment models were subjected to large overtopping heads similar to those attained during Phase II of the experimental program (see Figure 6.28). A falling head test was simulated using a finite reservoir impoundment where no additional inflow was added.

Initially, compaction of the embankment material was investigated in the small flume using the same compaction technique applied for the large flume (see Subsection D.1.2 in Appendix D). A vibration compactor, specially designed for the small flume (see Subsection D.1.3 in Appendix D) failed to replicate the *in situ* compaction curves obtained in the large flume (see Section C.3 in Appendix C for the results of the *in situ* compaction). Instead, this phase addressed the initial soil-water state as a test parameter in 2-D overtopping tests. In this study, the embankment models were constructed using sand Type III under loose and dry conditions ($D_r = 7\%$). The test

description and partial results of Phase III were published in Al-Riffai and Nistor (2013a, 2013b). A journal publication for this experimental phase is in preparation at the date of submission of this thesis (Al-Riffai and Nistor, 2014b).

7.1 Development of a Novel Experimental 2-D Overtopping Configuration

The initial soil-water state of the embankment model was controlled using three drainage configurations:

- under-toe drain under steady-state seepage
- no drain under steady-state seepage
- under-toe drain under nearly dry initial conditions

The embankment models were constructed near the flume outlet in order to minimize the effects of the tailwater levels on the overtopping flow (see Figure 7.1). 2-D overtopping was simulated by impounding the reservoir to a water surface elevation higher than the embankment model crest and suddenly releasing the vertical gate as shown in Figure 7.2.

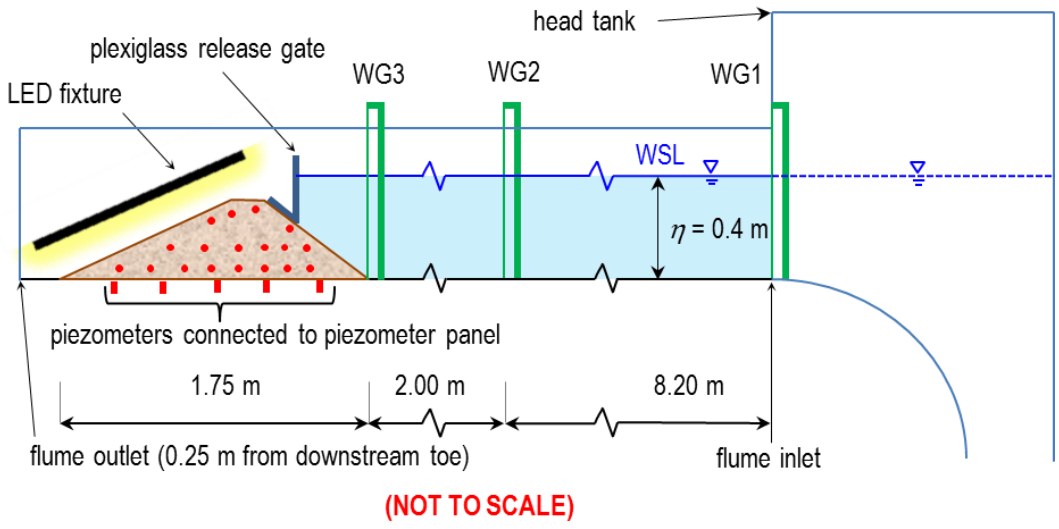

Figure 7.1: Experimental setup for Phase III showing gate design “D” and LED light fixture (PWP transducer assemblies shown as red dots)

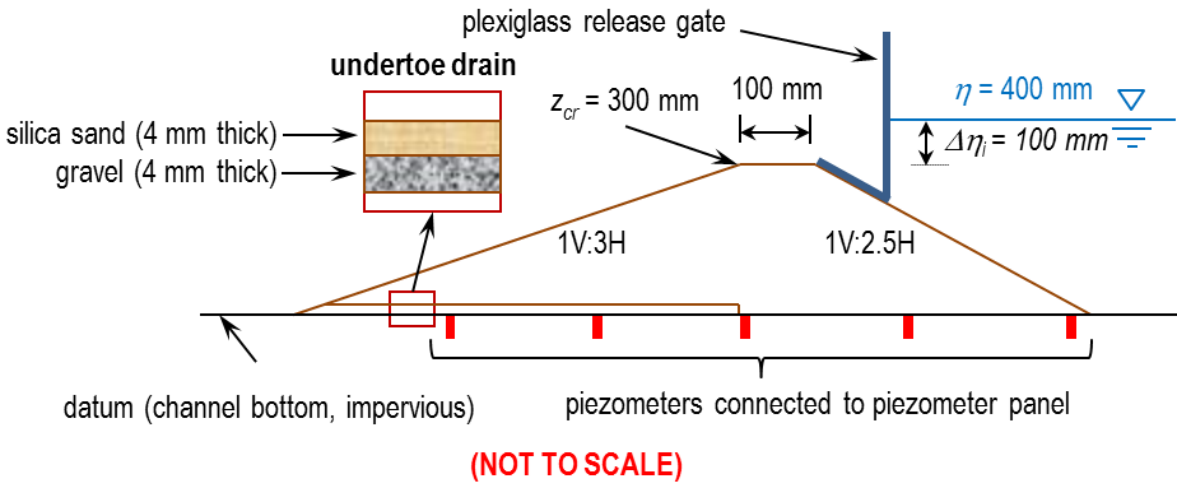

Figure 7.2: Longitudinal section of embankment model in overtopping tests showing undertoe-drain and gate design "D"

The purpose of the three drainage tests (Series "H") was to simulate overtopping and investigate the consequent erosion under various initial soil-water states and subsequent PWP. PWP measurements in the embankment material were conducted by installing tensiometer-transducer-probe assembly (TTPA) devices, designed, assembled, tested and calibrated in the Geotechnical Engineering Laboratory, through the flume walls and through the embankment's soil. Several modeling parameters were investigated prior to finalizing the experimental setup for Phase III of the experimental program. Four pilot tests, as shown in Table 7.1, were therefore conducted to investigate various lighting and photographic installations (described in detail in Subsection D.3.3 in Appendix D) to optimise the visibility of the bed and water surface profiles during overtopping and the subsequent erosion. The pilot tests were also used to develop the design for the release gate (see Section D.7 in Appendix D for details) as well as determine an initial overtopping head, $\Delta\eta_0$, suitable for the tests (see Subsection 7.1.1 for details). Test repeatability was also investigated in this experimental phase.

Table 7.1: Test matrix for Phase III (Series “H”)

Test No.	Test series	Date	$\Delta\eta_0$ [cm]	Release gate design	Data collection†	Notes
1	Pilot	3 Nov. 2011	2	A	VF	Leakage on left side of gate led to failure.
2	Pilot	9 Nov. 2011	2	A	VF	Successfully overtopped.
3	Pilot	20 Dec. 2011	5	B	VF	Successfully overtopped.
4	Pilot	6 Jan. 2012	5	B	DI/PZ	Leakage between gate membrane and upstream slope after 2cm of impoundment led to piping failure and breaching. Failed test.
5	Drain	19 Jan. 2012	5	C	VF/DI/WG/PWP/PZ	Successfully overtopped.
6	Drain	26 Jan. 2012	10	D	VF/DI/WG/PWP/PZ	Successfully overtopped.
7	No drain	20 Jun. 2012	10	D	VF/DI/WG/PWP/PZ	Delay in gate release led to some partial sliding of downstream slope prior to overtopping. Failed test.
8	Drain	30 Jun. 2012	10	D	VF/DI/WG/PWP/PZ	Test No. 6 repeated. Successfully overtopped.
9	No drain	7 Jul. 2012	10	D	PZ	Test No. 7 repeated. Leakage between gate and upstream slope due to high PWP after impoundment, leading to piping failure and breaching. Failed test.
10	No drain	11 Jul. 2012	10	D	VF/DI/WG/PWP/PZ	Test No. 7 repeated. Successfully overtopped.
11	Drain/ Dry	1 Aug. 2012	10	D	PZ	Leakage between gate and upstream slope after successful impoundment led to partial piping failure. Failed test.
12	Drain/ Dry	10 Aug. 2012	10	E	VF/DI/WG/PWP	Successfully overtopped.
13	Drain/ Dry	8 Sep. 2012	10	E	VF/DI/WG/PWP/PZ	Test No. 11 repeated. Successfully overtopped

†VF: video footage; DI: digital images; WG: wave gauge data; PWP: pore-water-pressure data; PZ: piezometric head data

7.1.1 Overtopping Head

The initial overtopping head, $\Delta\eta_0$, was investigated during the pilot tests. The overtopping head in the first two pilot tests was 2cm and was then increased to 5cm in the following two pilot tests. The overtopping flow due to small overtopping heads resulted in non-uniform erosion indicated by the formation of antidunes on the downstream slope (see Figure 7.3). The overtopping head was therefore increased to 10cm to achieve a smoother bed profile and higher Froude numbers. It was also advantageous to simulate 2-D erosion under similar hydraulic heads computed over the breach channel crest centreline in Phase II tests (see Figure 6.28). It was not possible to increase the overtopping head any further since the experiments were conducted after steady-state seepage conditions had been established and where PWP were already high. Increasing the overtopping head any further would have undermined the downstream slope of the embankment model. The embankment model constructed without a drain represented the threshold for a downstream slope slide failure. In fact, Test No. 9 failed and was repeated for that very same reason.

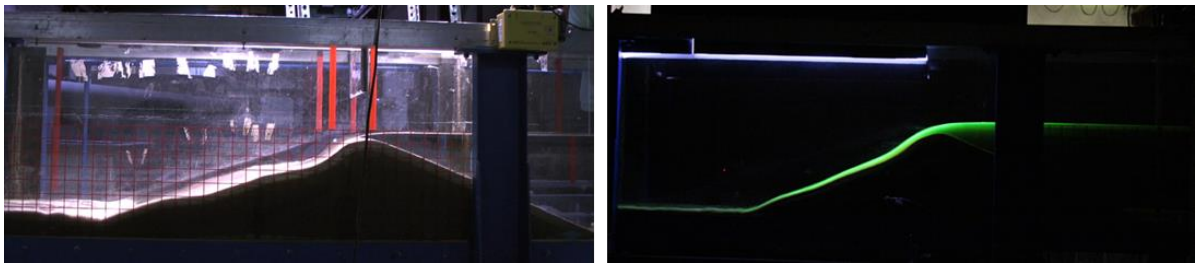

Figure 7.3: Antidune formation during overtopping (left) $\Delta\eta_0$ = 2cm (Test No. 2) (right) $\Delta\eta_0$ = 5cm (Test No. 5)

7.1.2 Instrumentation

The time-history of the WSL in the upstream impoundment was recorded using three wave-gauges. Five piezometers, installed at the embankment foundation, were employed to measure the piezometric head and define the steady-state seepage criterion (see Figure 7.2). PWP measurement inside the embankment models was conducted using tensiometer-transducer-probe assemblies (TTPAs). The TTPAs

were based on the design of tensiometer-transducer devices used in a column apparatus to investigate the 1-D unsaturated-saturated response of sand-geotextile systems (Bathurst *et al.* 2007). Up to sixteen TTPAs were installed through both side-walls of the flume and through the embankment's soil.

The micro-TTPA (M-TTPA) were assembled using a porous ceramic 2mm in diameter and 2cm long (SDEC 220; SDEC, 2010) while the standard-TTPA (S-TTPA) used a porous ceramic cup 6mm in diameter and 2.5cm long (SDEC 230; SDEC, 2010). Both assemblies are shown in Figure 7.4. Although the pressure transducer used in the assembly was designed for operation in dry mediums (*e.g.* air), calibration as well as response time tests were conducted to confirm their applicability in wet media such as water. Section D.6 and Subsection D.2.2 of Appendix D include the installation instructions and the results of the calibration and response time tests conducted in the Geotechnical Engineering Laboratory.

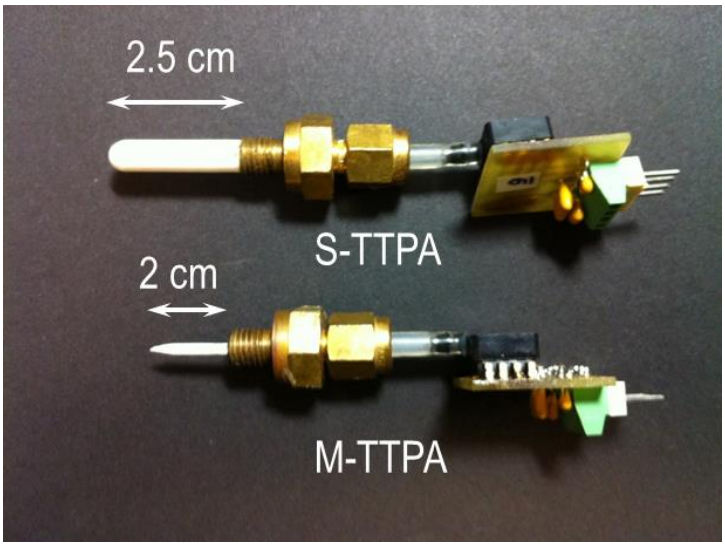

Figure 7.4: M-TTPA and S-TTPA

The M-TTPAs were advantageous over the S-TTPAs in terms of their smaller size and were therefore less intrusive within the soil and water mediums. However, they posed a great difficulty in terms of installation and usage due to their extremely fragile nature. Testing and calibration of both assemblies, however, revealed that

both TTPAs were almost identical with respect to response time and linearity for PWP measurement (see Subsection D.2.2 of Appendix D for results on performance). The TTPAs were installed through the side-walls by means of a threaded brass connector fitted with an O-seal. The side-walls at the downstream end of the flume were replaced with Lexan sheet panels in order to accommodate the installation of the TTPAs.

A total of nineteen holes (seventeen on the right-side and two on the left-side) were drilled and tapped (size 5/16” and 24 threads per inch) as shown in Figure 7.5. The locations of the holes were based on the slope retreat patterns observed in the pilot tests such that at least three probes would be in the vicinity of the soil bed throughout the erosion process.

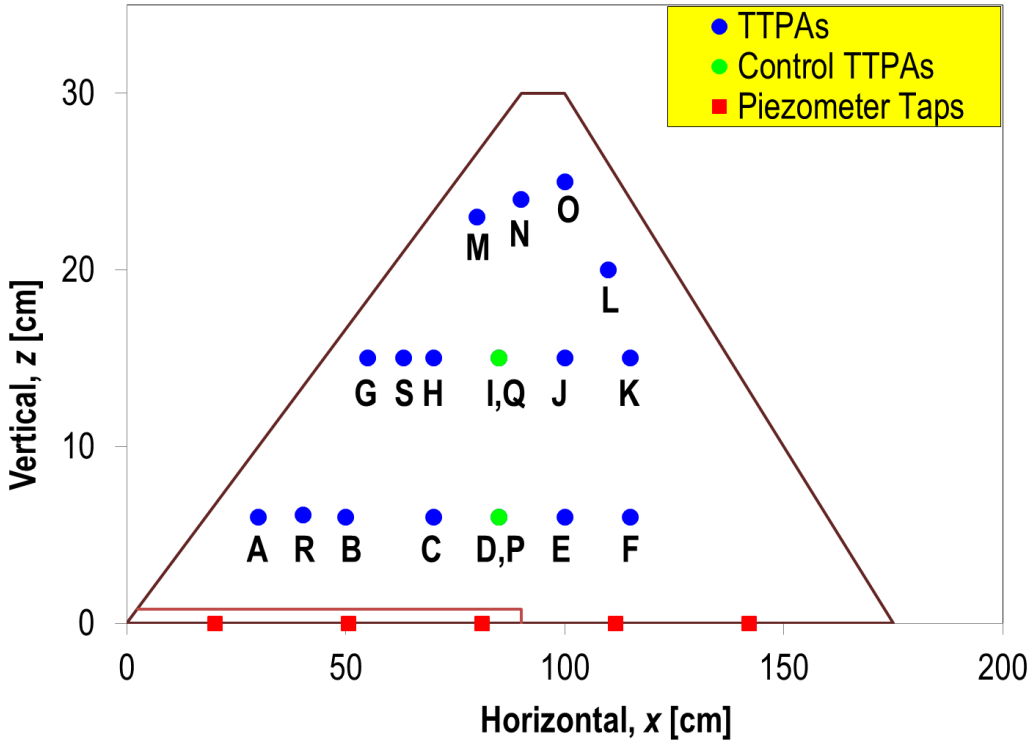

Figure 7.5: Locations of TTPAs (control TTPAs "P" and "Q" on left-side wall; locations “F” and “K” remained unused) and piezometers installed on flume side-walls and bottom, respectively

Configuration A was first adopted in earlier tests using a total of fourteen TTPAs. Two additional TTPAs ("R" and "S") were later installed to achieve a denser distribution (Configuration B). A matrix showing both configurations and the corresponding location of the TTPAs is shown in Table 7.2 and Figure 7.5, respectively.

Table 7.2: TTPA configurations used in overtopping tests

Configuration			
A (14 TTPAs)		B (16 TTPAs)	
TTPA No.	TTPA location	TTPA No.	TTPA location
1	A	1	A
2	B	2	R
3	C	3	B
4A†	D	4	C
5	E	5A†	D
6	G	6	E
7	H	7	G
8	I	8	S
9	J	9	H
10	L	10	I
11	M	11	J
12	N	12	L
13	O	13	M
4B†	P	14	N
-	-	15	O
-	-	5B†	P

†TTPAs installed on both sides of the flume as a control check (TTPA 5A was installed on the right-side wall of the flume; TTPA 5B was installed on the left-side wall of the flume)

As shown in Figure 7.5, all TTPAs were installed on the right-side flume wall except for one (*i.e.* Location "P") which was installed on the opposite side-wall (corresponding to Location "D"). The TTPA which was installed in this location was

used as a control check measurement. Table 7.3 shows the type of TTPA configuration corresponding to each 2-D overtopping test, including test parameters and the categories of data collected.

Table 7.3: Overtopping tests and corresponding TTPA configuration

Test No.	Test series	Date	$\Delta\eta_0$ [cm]	Data collection	Configuration	Notes
1	Pilot	3 Nov. 2011	2	VF	-	Unsuccessful test (piping failure)
2	Pilot	9 Nov. 2011	2	VF	-	Successful test
3	Pilot	20 Dec. 2011	5	VF	-	Successful test
4	Pilot	6 Jan. 2012	5	DI/PZ	-	Unsuccessful test (piping failure)
5	Drain	19 Jan. 2012	5	VF/DI/WG/PWP/PZ	A	Successful test
6	Drain	26 Jan. 2012	10	VF/DI/WG/PWP/PZ	A	Successful test
7	No drain	20 Jun. 2012	10	VF/DI/WG/PWP/PZ	B	Partial sliding
8	Drain	30 Jun. 2012	10	VF/DI/WG/PWP/PZ	B	Successful test (Test No. 6 repeated)
9	No drain	7 Jul. 2012	10	PZ	-	Unsuccessful test (piping failure)
10	No drain	11 Jul. 2012	10	VF/DI/WG/PWP/PZ	B	Successful test (Test No. 7 repeated)
11	Drain/Dry	1 Aug. 2012	10	PZ	-	Unsuccessful test (piping failure)
12	Drain/Dry	10 Aug. 2012	10	VF/DI/WG/PWP	B	Successful test
13	Drain/Dry	8 Sep. 2012	10	VF/DI/WG/PWP/PZ	B	Successful test (Test No. 12 repeated)

VF: video footage; DI: digital images; WG: wave gauge data; PWP: pore-water-pressure data; PZ: piezometric head data

The TTPAs were installed in the flume side-walls and through the soil after the reservoir had been drained to avoid saturated soil from leaking out of the tapped holes. It was then necessary to remove the soil in which the TTPA occupied by

using augers, slightly smaller in size than the porous ceramic cups. This process was carried out to avoid compaction of the surrounding soil and prevent the potential fracture of the fragile porous ceramic cups. Figure 7.6 shows the TTPAs installed on the left-side and right-side of the small flume.

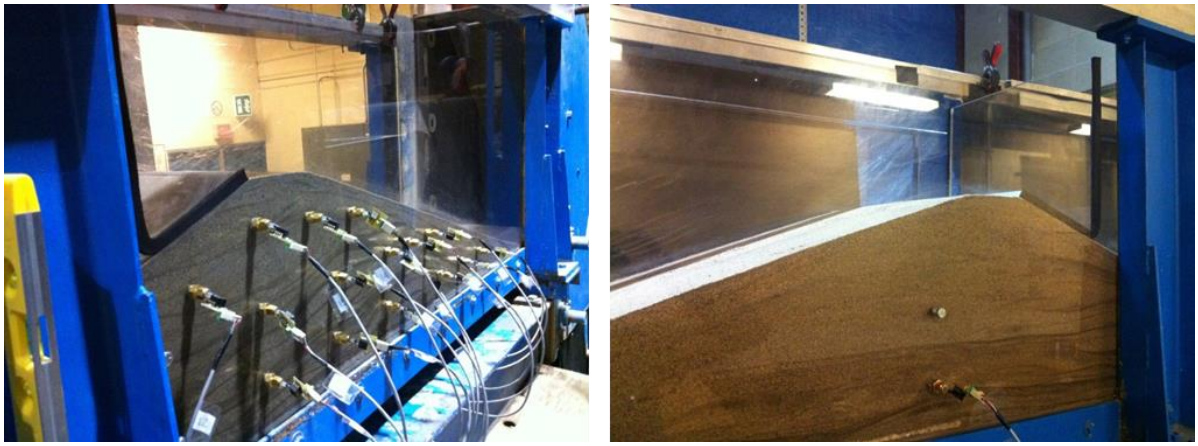

Figure 7.6: TTPAs installed through flume side-walls prior to impoundment and overtopping (left) right-side (right) left-side

7.1.3 Construction Process and Experimental Setup

Construction of the embankment models was similar to construction of the low compaction embankment model of Phase II of the experimental program (*i.e.* large flume). The construction and experimental setup can be described in the following steps:

1. After the installation of the drainage element (as per Figure 7.7), the embankment material (sand Type III) was backfilled carefully into the flume in dry and loose form.
2. After construction, all the embankment models were saturated by slowly filling the reservoir (3-4 mm/min) up to a water level, $\eta = 28cm$, after which steady-state seepage was then confirmed.
3. The reservoir was then drained and the embankment models' shoulder slopes and crest were trimmed using wooden planks. The dry unit weight of

the embankment models, γ_d = 15.5 kN/m^3 ($D_r = 7\%$), was determined from previous *in situ* measurements (see Subsection C.2.3 in Appendix C).

4. The reservoir was again impounded at three water surface levels (10cm, 20cm and 28cm) and the piezometric head and PWP from the TTPAs were recorded at the embankment models' foundation (see Figure 7.1 and Figure 7.2).
5. In addition to the three steady-state seepage tests, a falling head test was also performed by draining the reservoir impoundment and recording the WSL and PWP using the wave gauges and TTPAs, respectively. The valves installed on the piezometer lines were closed before draining the reservoir to prevent water initially present in the piezometer column from entering into the embankment model and affecting the test results.
6. Prior to overtopping, the photography and lighting installations were setup and the release gate installed on the upstream slope as shown in Figure 7.1 and Figure 7.2.
7. The impoundment level was increased to 40cm and the piezometric head was recorded after steady-state seepage had been established. The piezometer valves were then closed.
8. The release gate was raised and the embankment models were overtopped.

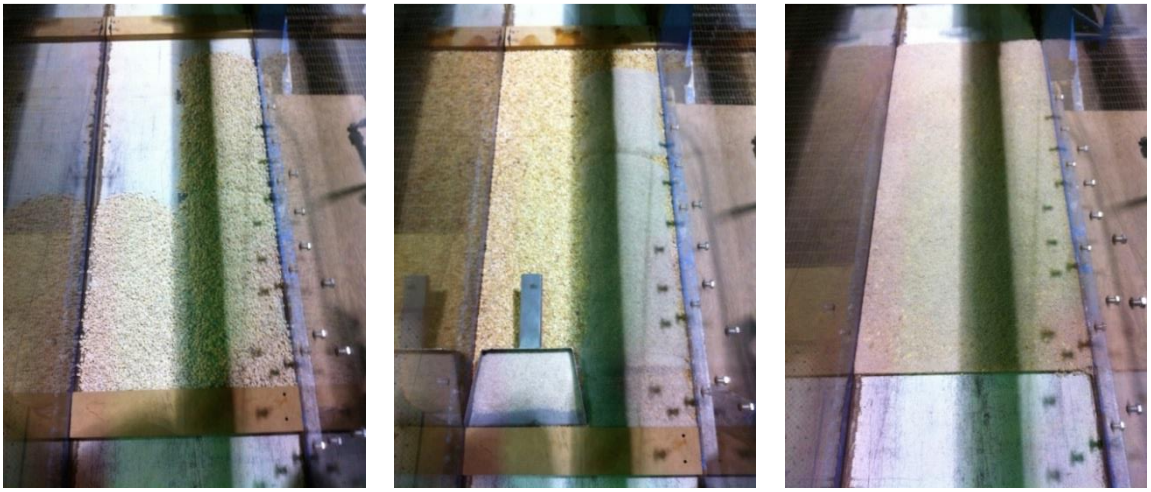

Figure 7.7: View from upstream showing (left) installation of gravel medium (middle) installation of filter medium (right) completed undertoe drain

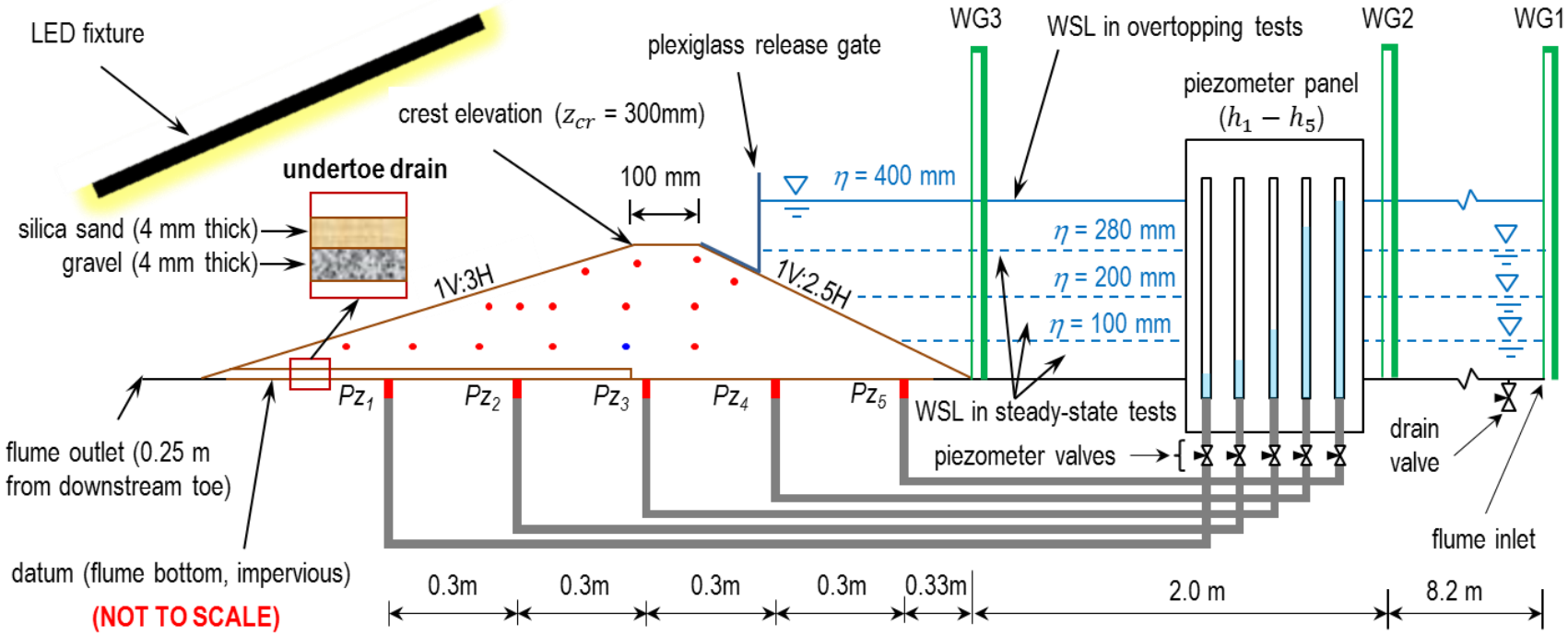

Figure 7.8: Setup in small hydraulic flume showing: TTPAs (blue dot corresponds to control check measurement), wave-gauges, light emitting diode (LED) fixture, release gate, piezometric head measurements (piezometers and connection to piezometer panel), three water surface levels using in steady-state tests and water surface level prior to overtopping (not shown is the head tank at the upstream section of the small flume)

For the “drain/dry” configuration, the near-dry conditions were simulated by allowing the model to dry for a period of 7-8 days after reservoir drainage following Step No. 5. Prior to impoundment, the upstream slope of the embankment model was impermeated using a plastic lining (see Section D.7 in Appendix D for impermeabilization procedure). Once the water surface level reached 40cm, the impermeable lining was removed rapidly and Step No. 6 resumed. A complete setup of the 2-D overtopping experiments is shown in Figure 7.8.

7.2 Data Acquisition Procedure

Phase III of the experimental program was divided into the following five tasks:

- Calibration (see Section D.2 in Appendix D)
- Steady-state seepage tests
- Falling head tests
- 2-D Overtopping (erosion) tests

The PWP measurements along with the piezometric head measurements conducted in the last three tests were useful in verifying the homogeneity of the construction for the three drainage configurations. Data acquisition for the wave gauges and TTPAs was conducted using data loggers, NI USB-6009 and NI USB-6210, respectively. For the 2-D overtopping tests, it was necessary to synchronize the wave gauge and PWP measurements, as well as the time-lapse device (also connected to the NI USB-6210 data logger) which was used to trigger the digital cameras. This was carried out by integrating the data collection for each instrument using virtual instrument subroutines (VIS) compiled on LabView for each of the above tests. Video footage was synchronized with the wave-gauges, TTPAs and digital camera images using visual indicators such as switching lights on/off or raising the release gate.

7.3 Data Extraction, Analysis and Results

7.3.1 Breach Outflow Hydrographs

The time-history of the overtopping discharge was computed using the hydrologic routing method in the form of a FORTRAN code as performed in Phase I and Phase II of the experimental program (see Section E.6 of Appendix E). The hydrographs computed for the three embankment configurations in Phase III, shown in Figure 7.9, clearly indicated that erosion is influenced by the initial soil-water state of the downstream slope. The presence of an undertoe horizontal drain, described by having lower initial PWPs, gave rise to a slower erosion process. Meanwhile, the erosion process in the embankment models with nearly dry initial conditions was even slower due to a higher erosion resistance. The overtopping discharge exhibited two peaks, where the first peak was always higher. Test repeatability as represented by the outflow hydrograph for the 2-D overtopping tests was reflected well, with the exception of Test No. 7 which exhibited a higher initial peak than the same embankment configuration defined by Test No. 10. This can be explained by the delay in releasing the gate prior to overtopping in Test No. 7 which led to a partial slide of the downstream slope. Initial conditions were therefore not identical between Tests No. 7 and 10.

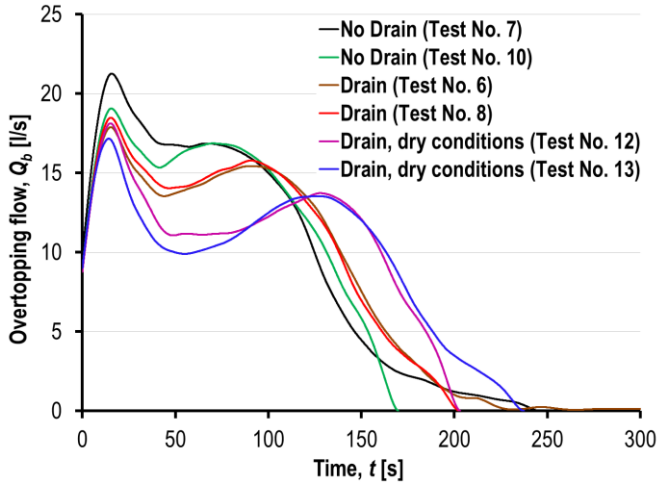

Figure 7.9: Outflow hydrographs computed for overtopping tests (Phase III), lagged to time of vertical gate release

7.3.2 Piezometric and PWP Measurements

The piezometric measurements at the embankment foundation for the three drainage configurations are shown in Subsection F.1 of Appendix F. Test repeatability as represented by these measurements was well represented with the exception of Test No. 7 (see Figure F-2 in Appendix F). It was later revealed that during steady-state seepage, longer waiting periods were necessary for the complete removal of the entrapped air within the piezometer lines. Improper maintenance of the piezometers may have caused such a discrepancy. Also shown in Figure F-1 to Figure F-3 in Appendix F are comparisons between the measured and numerical piezometric heads at the embankment foundations for the steady-state seepage tests.

The steady-state numerical simulations were carried out using SEEP/W (GEO-SLOPE, 2007). Similar to Phase I of the experimental program, calibration was carried out using the embankment model without an undertoe-drain. Properties of the embankment material such as saturated hydraulic conductivity (see Figure C-11 in Appendix C), saturation and residual water contents (see Subsection C.2.2 of Appendix C), SWCC and hydraulic conductivity function (see Figure C-20 in Appendix C) were used as input parameters in SEEP/W. The steady-state seepage tests were simulated with SEEP/W using the initial desorption SWCC. Although hysteresis in the capillary-moisture relationship of the embankment material was predicted (see Figure C-18 and Figure C-19 in Appendix C), it was assumed that such effects on the hydraulic conductivity function were negligible. The numerical model was calibrated by adjusting the anisotropy ratio, k_{saty}/k_{satx}, such that the steady-state output of the piezometric heads at the embankment model foundation matched the recorded values. Trial and error adjustments resulted in an anisotropy ratio equal to 0.6 for the four water surface elevations used in the upstream impoundment as represented by the steady-state seepage tests. Four hydraulic conductivity functions (Brooks and Corey, 1964; Green and Corey, 1971; van Genuchten, 1980; Fredlund and Xing, 1994) were tested in the numerical

simulations. All models yielded similar results since $\psi < \mathrm{RSV}$ during all steady-state simulations.

The steady-state seepage simulations were then conducted once the undertoe-drain material properties were defined within SEEP/W. From Figure F-1 to Figure F-3 in Appendix F, it can be shown that the piezometric heads were over predicted for both drainage configurations where $\eta_r >$ 280mm and under predicted where $\eta_r < 200\mathrm{mm}$. This can also be shown in Table F-1 to Table F-4 of Appendix F. For the four WSLs where steady-state conditions were simulated, the average difference in PWP between the experimental and numerical values ranged between an equivalent of +7mm-H_20 and −9mm-H_20. The maximum and minimum difference between the experimental and numerical PWP in all steady-state simulations were equivalent to +19 mm-H_20 and –32 mm-H_20, respectively. Generally, control TTPAs No. 5A and 5B were somehow consistent in terms of PWP measurement. The average difference in PWP between the two TTPAs for all the steady-state simulations was < 11mm-H_20.

A particular design feature in the release gate was adopted as a preventative measure to piping failures. The inclined surface of the release gate which rested on the upstream slope was particularly useful in dissipating the high exit hydraulic gradients near the crest. Despite this design feature, high hydraulic gradients still existed. Figure F-4 through Figure F-7 in Appendix F show steady-state PWP distributions and discharge velocity field vectors through the embankment body, generated by SEEP/W. These plots helped clarify the cause by which the earlier embankment models had failed prematurely by piping (*e.g.* Test No. 4, 9 and 11). Figure F-7 in Appendix F which describes the discharge velocity field for the undrained embankment model, revealed that the large discharge velocities concentrated at the upstream slope developed as a result of high exit hydraulic gradients on the downstream side of the embankment crest. Nevertheless, gate release design “D” helped alleviate such consequences (see Section D.7 in Appendix D for details on the other designs used).

The falling head tests were then simulated using SEEP/W. Figure F-8, Figure F-9 and Figure F-10 in Appendix F, show a comparison between experimental and numerical simulation for the undrained, drained and drained-dry embankment models, respectively, using a duration of 800s. The numerical simulations for all three embankment configurations were quite similar to the experimental runs. The steady-state PWP numerical predictions were slower and tended to values lower than the measured ones at the end of the transient numerical simulation. Similar to the steady-state seepage simulations, the results of the transient numerical simulations, as represented by the falling head tests, were insensitive to the different hydraulic conductivity functions used (*i.e.* Brooks and Corey, 1964; Green and Corey, 1971; van Genuchten, 1980; Fredlund and Xing, 1994).

It is important to note that the embankment model with an undertoe-drain and which was overtopped under dry conditions (*i.e.* Test No. 13) was essentially the same as the drained embankment model (*i.e.* Test No. 8). Therefore, it is expected that the PWP measurements from the steady-state and falling head tests for that particular embankment model (*i.e.* before the drying process had taken place) would be the same as any embankment model with an undertoe-drain. It can be shown from Figure F-9 and Figure F-10 in Appendix F that falling reservoir head tests for the two embankment configurations featuring an undertoe-drain were in fact very similar. The measured lag between the PWP time-history indicated by the two control TTPAs was also very short.

The measured drainage rate during the falling reservoir head was always lower than the drawdown rate. In the case of the undrained embankment model, this drainage rate was lower than the drained embankment model. This is expected since the presence of an undertoe-drain facilitated the drainage of pore-waters. The PWP time-history due to the falling reservoir head for two embankment configurations (drain versus no drain) is also shown in Figure 7.10 using a shorter time-span for the sake of clarity.

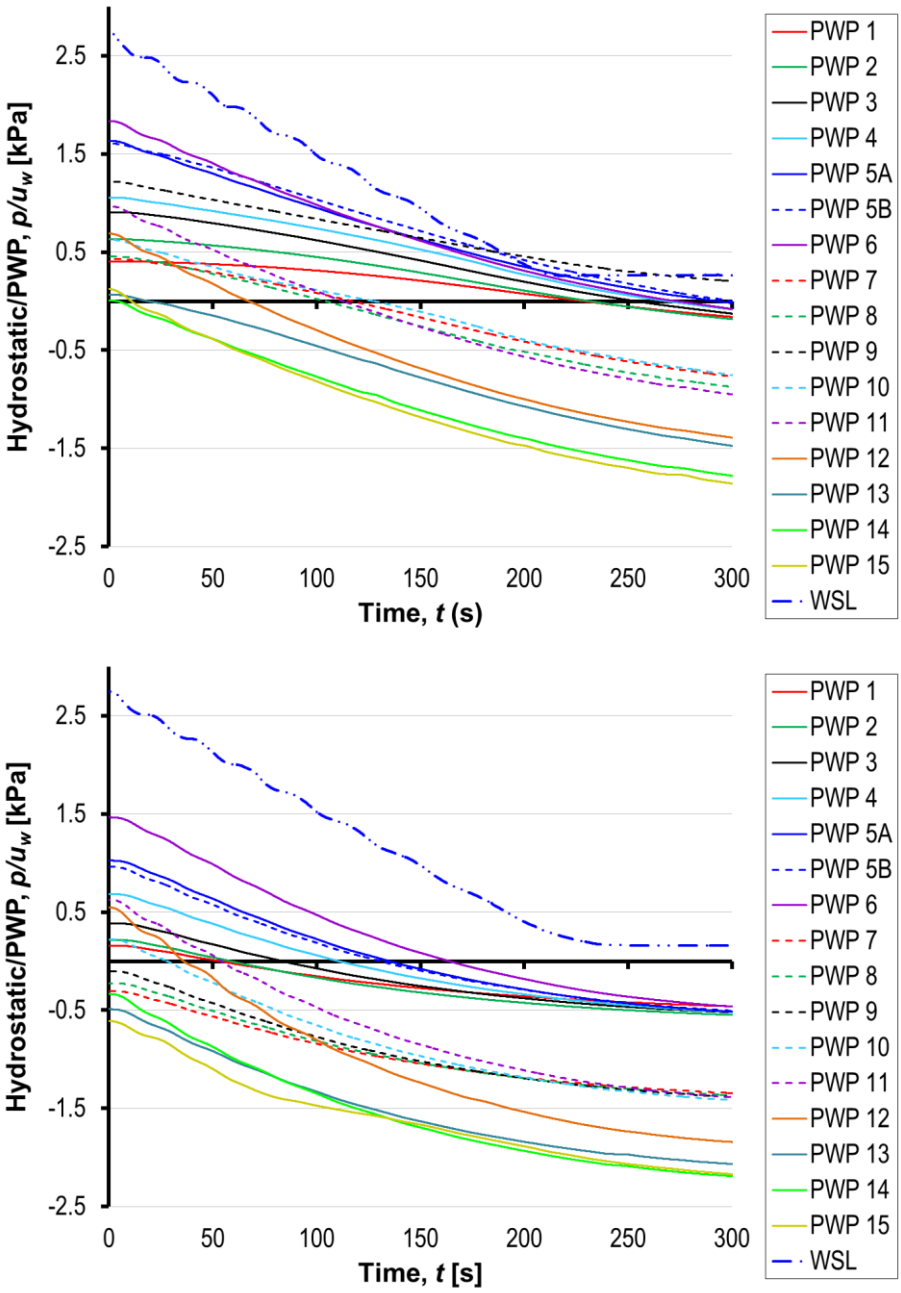

Figure 7.10: PWP time-history due to falling reservoir head (top) undrained embankment model (Test No. 10) (bottom) drained embankment model (Test No. 8)

The PWP time-history due to overtopping flow, as shown in Figure F-11 of Appendix F, indicated an overall drainage in the embankment body, with the exception of the model with an undertoe-drain which was overtopped under nearly dry conditions. For the two embankments with initially positive PWPs, the sudden gate release was

clearly marked by the sharp drop followed by a sudden regain in PWP for the TTPAs near the upstream slope (*e.g.* TTPA No. 12 and 15). Soon after overtopping was initiated, the PWP within the embankment body was seen to rise slightly due to water infiltrating through the embankment crest. However, the time periods which followed the initial overtopping resulted in considerable drainage. As the TTPAs came into contact with the overtopping flow, this drainage rate was even higher. The PWP time-history due to overtopping, as shown in Figure F-11 of Appendix F, clearly shows that erosion accelerated the drainage, in which the rate was even higher than that of reservoir drawdown. Contrary to the falling reservoir head tests, the drainage rate in the overtopping tests for the undrained embankment model was higher than that of the drained embankment model with saturated initial conditions.

In the case of the embankment model with a drain and overtopped under dry conditions, the removal of the upstream impermeabilization was marked by a gradual PWP increase in the TTPAs near the upstream slope (i.e. TTPA 12 and 15). This was due to the water infiltrating from the upstream reservoir and into the upstream shoulder slope. The sudden gate release for this particular embankment configuration was then marked by a sudden rise in PWP, as indicated by most of the TTPAs, due to the impact of the overtopping flow. The PWPs for the TTPAs in the much drier zones, however, remained negative and steady until erosion progressed to the point where the overtopping flow came into contact with them. The contact between the overtopping flow and the remaining TTPAs was marked by a sharp increase in PWP over a time period which lasted between 2 to 4 seconds.

A larger illustration of the PWP time-history due to overtopping flow for the two embankment models with the initially positive PWPs is provided in Figure 7.11. It can be shown that the PWPs approached 0kPa before the TTPAs came into contact with the overtopping flow. The moment of contact between the TTPAs and the overtopping flow, was defined by a sudden decrease followed by a regain in PWP. This phenomenon in which the TTPAs recorded negative values followed by an

increase in PWP to atmospheric conditions, lasted 2 to 3 seconds (see Figure F-11 of Appendix F).

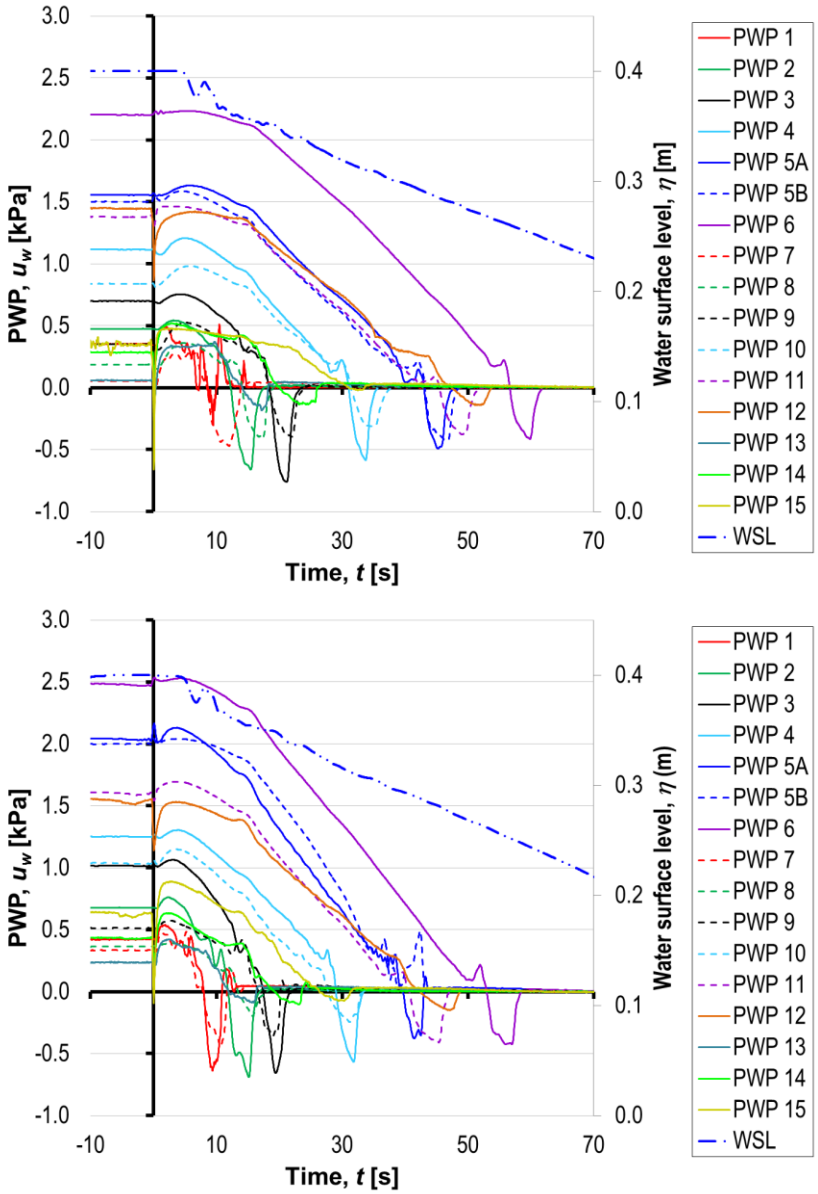

Figure 7.11: PWP time-history due to overtopping for embankment models with (top) undertoe-drain (Test No. 8) (bottom) no drain (Test No. 10)

It was initially presumed that the negative PWPs recorded by the TTPAs were reflected by conditions in the soil. Therefore, this phenomenon was investigated by placing one TTPA downstream of a sluice gate under fully submerged conditions.

The same PWP transient response was observed after the TTPA was exposed to similar Froude numbers (approximately 3.0). It was then revealed that the negative PWPs were due to flow accelerating around the cylindrical probes of the TTPAs. Despite the difference in initial soil-water state of the downstream slope between the drained and undrained configurations, the PWP at the eroding soil boundary maintained a value close to 0kPa. This observation prompted an investigation into the boundary seepage mechanism rather than on the soil-water state alone.

7.3.3 Water Surface and Bed Profile Measurements

Images captured with the digital photo cameras were used to define the water surface and bed profiles, while the video footage was useful in documenting and observing the erosion process in motion. A fluorescent dye mixed with the water in the upstream reservoir enhanced the visibility of the water surface and bed profiles. The images captured from the digital camera using the ISO-6400 setting and 1/80s shutter speed were imported into ArcGIS for analysis. After georeferencing the images, they were transformed in accordance with a 4 cm x 4 cm reference grid placed over the flume walls to adjust for distortions due to the camera's perspective view (see Subsection D.3.3 in Appendix D), using the same transformation steps described in Subsection 6.4. The water surface and bed profiles were digitized, extracted and transformed into nodes with x and y coordinates to be used in the transient flownet analysis described in the following subsection. Section F.4 of Appendix F contains the water surface and bed profiles at various times throughout the overtopping event for the three embankment configurations.

7.3.4 Transient Flownet Analysis

The PWP recorded using the TTPAs, as shown in Figure 7.11 and Figure F-11 of Appendix F, were also imported into the GIS software at 2-second time intervals. A PWP distribution through the longitudinal section of the embankment model was produced at those time intervals using Kriging or spline interpolations (see Figure 7.12). The interpolations were carried out at instances where the probes were

closest to the eroding bed in order to capture, to a certain extent, the nonlinearity of the near-boundary hydraulic gradients. The PWP was then converted into piezometric head as $h = u_w/\gamma_f + z$, and a raster file comprised of the piezometric head distribution was generated.

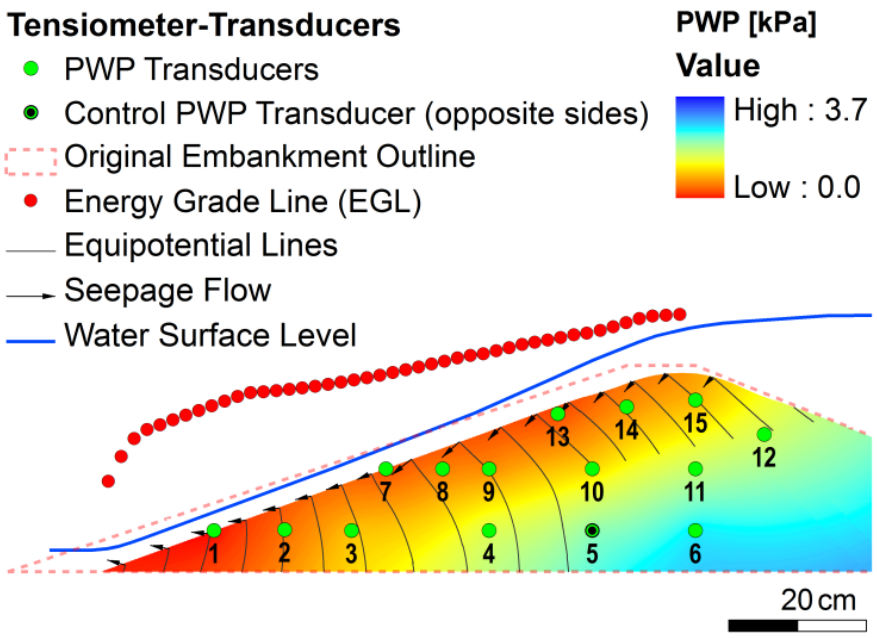

Figure 7.12: PWP interpolation and transient flownet analysis (Test No. 6, t = 6 seconds)

Two important tools within ArcGIS facilitated the means by which a flownet could be generated on the downstream slope of the embankment model: “slope” and “aspect”. The “slope” tool determines the maximum rate of spatial change of any raster value, and since the raster value was defined by the piezometric head, then the resulting slope is the maximum hydraulic gradient. The “aspect” tool determines the downslope direction of the maximum slope in degrees measured clockwise from the north bearing. Essentially, the slope and aspect tools can be used to describe the exit hydraulic gradient and the seepage angle, respectively, at the soil-water boundary (see Figure 7.13).

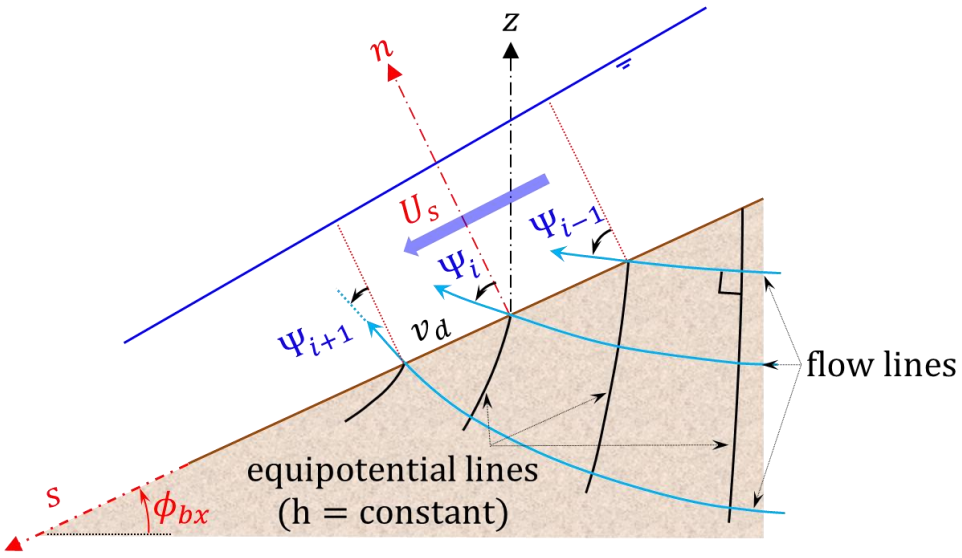

Figure 7.13: Flownet on an overtopped steep slope showing upward seepage (Ψ_{i-1}, Ψ_i and Ψ_{i+1} are seepage angles for three adjacent flow lines)

7.3.5 Hydrodynamics in the Boundary Seepage Zone

A fluid accelerating over a steep slope is subjected to forces due to hydrostatic pressure, gravity and boundary shear, F_τ, as well as an upward boundary flux as shown in Figure 7.14. Downstream the embankment's crest and the subhydrostatic (*i.e.* recirculation) zone, the vertical velocities and accelerations can be neglected. In this gradually-varied flow (and hydrostatic) region, the 1-D continuity and momentum equations for unsteady flow influenced by seepage can be expressed using a local coordinate system (s, n) as follows:

$$\frac{\partial \eta_n}{\partial t} + \frac{\partial (U_s \eta_n)}{\partial s} = v_d \tag{7.1}$$

$$\frac{\partial (U_s \eta_n)}{\partial t} + \frac{\partial (U_s^2 \eta_n)}{\partial s} = -g(\cos^2 \phi_{bx}) \eta_n \frac{\partial \eta_n}{\partial s} + g \eta_n \sin \phi_{bx} - \frac{\tau_b}{\rho} \tag{7.2}$$

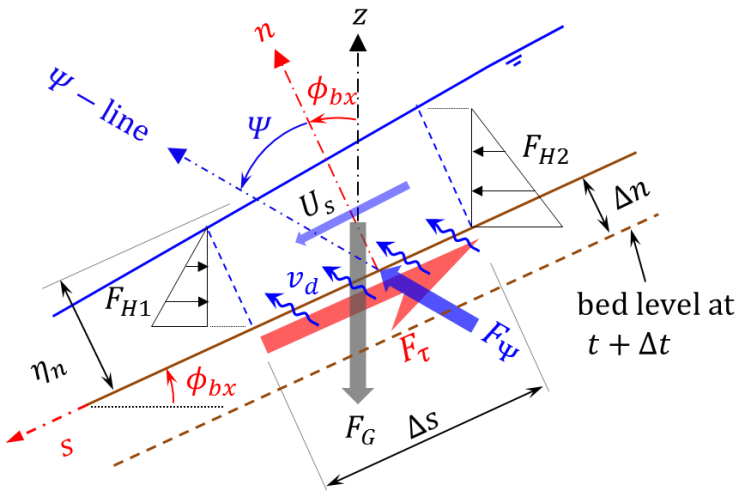

Figure 7.14: Forces acting on accelerating fluid influenced by seepage (F_{H1} and F_{H2}: LHS and RHS hydrostatic pressure forces, respectively)

From Equations (7.1) and (7.2), the boundary shear stress due to seepage can be expressed as follows:

$$\tau_b = \rho\eta_n \left[g \sin\phi_{bx} - g\cos^2\phi_{bx} \frac{\partial \eta_n}{\partial s} - U_s \frac{\partial U_s}{\partial s} - \frac{U_s v_d}{\eta_n} - \frac{\partial U_s}{\partial t} \right] \tag{7.3}$$

The derivation of Equation (7.3) is based on hydrostatic pressure and gradually varied flow assumptions. Other equations for τ_b have been derived by Cheng and Chiew (1998) and Francalanci *et al.* (2008) as shown in Equations (4.222) and (4.223), respectively. However, these expressions are based on steady flow conditions and pressure distributions pertaining to mild slopes. The effects of steep slopes and unsteady flow conditions in Equation (7.3) are reflected in the second and fifth term, respectively. As stated by Francalanci *et al.* (2008), the first term in Equation (7.3) can be described as the bed shear stress under uniform and steady flow conditions, the third term represents the influence of local accelerations and the fourth term represents the direct contribution due to seepage. The expression by Cheng and Chiew (1998) also differs from Equation (7.3) since it includes a momentum correction factor for the velocity profile.

A 1-D hydrodynamic FORTRAN code (see Section E.7 in Appendix E) was then developed to extrapolate and solve, respectively, the flow and erosion parameters using graphical methods and formulations shown in Table 7.4 (Note: changes to the presented FORTRAN code are currently ongoing).

Table 7.4: Flow and erosion parameters extracted by 1-D hydrodynamic code

Extracted parameter	Method/Equation
Specific discharge, q [m^2/s]	Hydrologic routing
Vertical flow depth, η_z [m]	Graphically interpolated
Orthogonal flow depth, η_n [m]	Graphically interpolated and Equation (4.48)
Pressure-head equivalent flow depth, η_h [m]	$\eta_n \cos\phi_b$, Equations (4.49) and (4.50)
Bed slope angle, ϕ_{bx} [radians]	$\tan^{-1}(\Delta z_b/\Delta x)$
Water surface angle at vertical projection, ϕ_{wz} [radians]	$\Delta\eta/\Delta x)_z$
Water surface angle at orthogonal projection, ϕ_{wn} [radians]	$\Delta\eta/\Delta x)_n$
Depth-averaged velocity, U_s [m/s]	q/η_n
Froude number, Fr	$U_s/\sqrt{g\eta_n}$
Hydraulic radius, R_h [m]	Equation (4.55)
Total energy, E [m]	Equation (4.52)
Friction slope along streamline, S_{fs}	Equation (7.5)
Bed shear stress, τ_b [Pa]	Equations (7.4), (4.222), and (7.3)
Shear velocity, u^* [m/s]	$\sqrt{\tau_b/\rho}$
Dimensionless shear stress, τ^*	Equation (4.65)
Dimensionless shear stress due to boundary seepage, τ^*_Ψ	Equation (7.8)
Seepage angle, Ψ [radians]	Using "aspect" tool in ArcGIS
Exit hydraulic gradient, i_e	Using "slope" tool in ArcGIS
Critical hydraulic gradient, i_c	Equation (4.201)
Discharge velocity†, v_d [m/s]	$k_{sat} i_e$
Orthogonal volumetric erosion rate, $\dot{E}_n$ [m/s]	$\Delta n/\Delta t$
Total sediment transport rate, q_{ts} [m^2/s]	Equation (7.7)
Dimensionless transport rate, q^*	Equation (4.69)

†Under unsaturated conditions, the hydraulic conductivity function, $k_w(\psi)$, should be used (*i.e.* Equations (4.175), (4.176), (4.178) and GEO-SLOPE, 2007)

Flownet data such as the exit hydraulic gradient and seepage angle were mapped onto the digitized bed nodes as part of a bed input file, while the x and y coordinates of the water surface comprised the WSL input file. The two input files along with the measured outflow hydrograph were input into the FORTRAN code and extraction of the flow parameters was based on a 1-D spatial discretization of the physical domain ($\Delta s = 2\text{cm}$). Temporal discretization ($\Delta t = 2s$) was also considered in order to account for the effects of unsteady flow conditions due to overtopping. Since Equation (7.3) is based on a local coordinate system (s, n), Equations (4.53), (4.55), (4.127) and (4.218) were modified as:

$$\tau_b = \gamma_f R_h S_{fs} \tag{7.4}$$

where, S_{fs} is the friction slope with respect to the local coordinate system, and can be expressed as:

$$S_{fs} = \frac{\Delta E}{\Delta s} \tag{7.5}$$

$$R_h = \frac{\eta_n(b-\eta_n)}{b} \tag{7.6}$$

$$\frac{\Delta q_{ts}}{\Delta s} = -(1-\lambda)\frac{\Delta n}{\Delta t} \tag{7.7}$$

$$\frac{\tau_{\Psi}^*}{\tau^*} = \frac{1}{\left(1-\frac{i_e \cos(\phi_{bx}+\Psi)}{i_c}\right)} \tag{7.8}$$

The transient flownet analysis was conducted with three time-steps for Test No. 6. As shown in Figure 7.15, the computed bed shear stress based on the modified 1-D SWEs were generally overestimated in the recirculation zone and further upstream. This is due to gradually varied flow conditions and hydrostatic pressure distribution assumed by the 1-D SWEs. The effects of curvature above the upstream slope and embankment crest were very pronounced; hence the computations using the friction slope, defined by Equation (7.4), were more realistic. Both formulations, however, overestimated the shear stress, particularly at the recirculation zone. This can be noted from the erosion rate and mobility relationships shown in Figure 7.16.

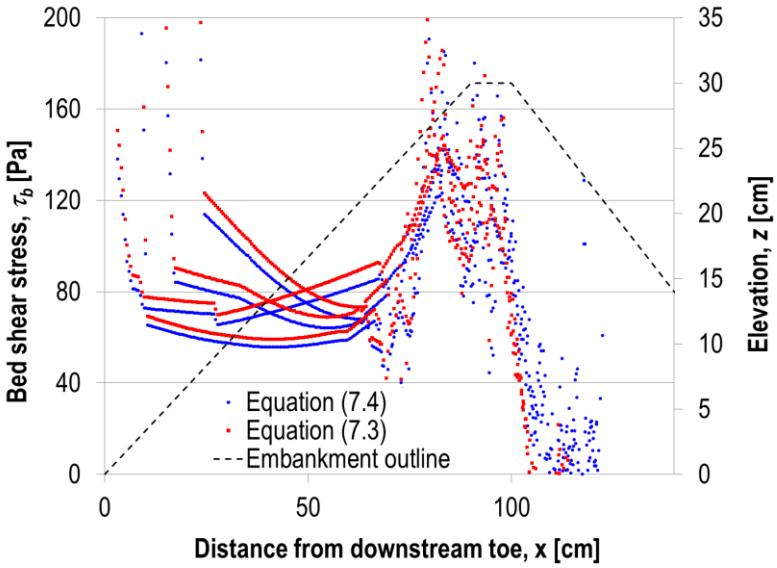

Figure 7.15: Shear stress distribution for three time-steps showing initial outline of embankment model (Test No. 6)

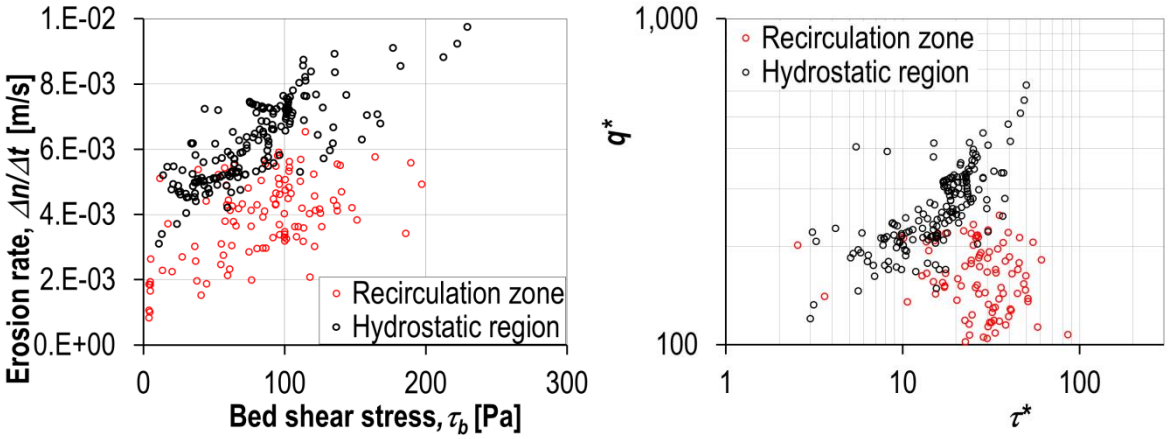

Figure 7.16: Erosion (Test No. 6) as indicated in supercritical hydrostatic region and recirculation zones by (left) an erosion rate (right) a mobility relationship

The computed bed shear stresses were very high ($3 < \tau^* < 50$). From the corresponding grain Reynolds numbers ($50 < Re^* < 80$) and the modified Shields curve (see Figure 4.14), the critical dimensionless bed shear stress was extrapolated to a value equal to 0.04. This implies that the bed shear stress was two to three orders of magnitude higher than that of the threshold for motion (*i.e.* $\tau^* \gg \tau_c^*$). As a result, incipient motion was not considered in this analysis.

As shown in Figure 7.17, Froude numbers computed at the embankment crest were always less than 1, where values ranged between 0.75 and 0.85 which indicated flow submergence at the crest. At the downstream toe, Froude numbers reached approximately 2.5. The Froude numbers reported by the numerical model BRES ranged between 1 and 4, depending on the breaching stage, with higher values during early stages (Visser, 2000). Similar Froude numbers were also reported in 2-D overtopping tests by Schmocker and Hager (2009). The overtopping velocities, also shown in Figure 7.17, exhibited a similar trend to the Froude numbers.

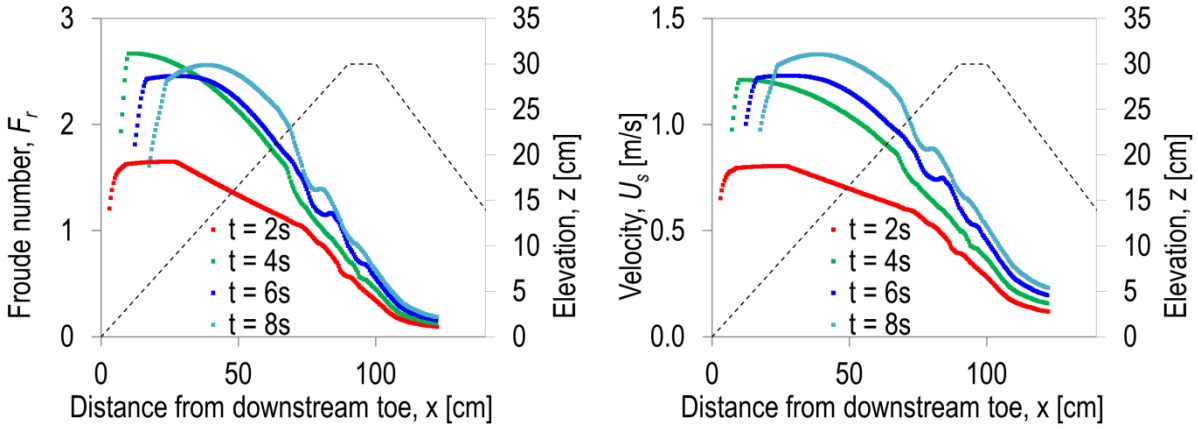

Figure 7.17: Initial embankment outline in test No. 6 showing (left) Froude numbers (right) overtopping velocity

The boundary seepage direction did not influence the bed shear stress. The fourth term in Equation (7.3) was always less than 1Pa and the contribution from the unsteady term ranged between 2 to 3Pa. This can be explained by the high Froude numbers which indicate that inertial effects were the most dominant. However, the effect of boundary seepage on the dimensionless shear stress defined by Equation (7.8) was quite significant. Figure 7.12 shows the instantaneous flownet after 6 seconds of overtopping in Test No. 6. It can be noted that upstream locations with lower Froude numbers are characterized by downward seepage, whereas downstream locations with high Froude numbers are characterized by upward seepage. Also indicated in Figure 7.18, large increases in sediment mobility were shown for downstream locations, characterized by higher bed shear stresses.

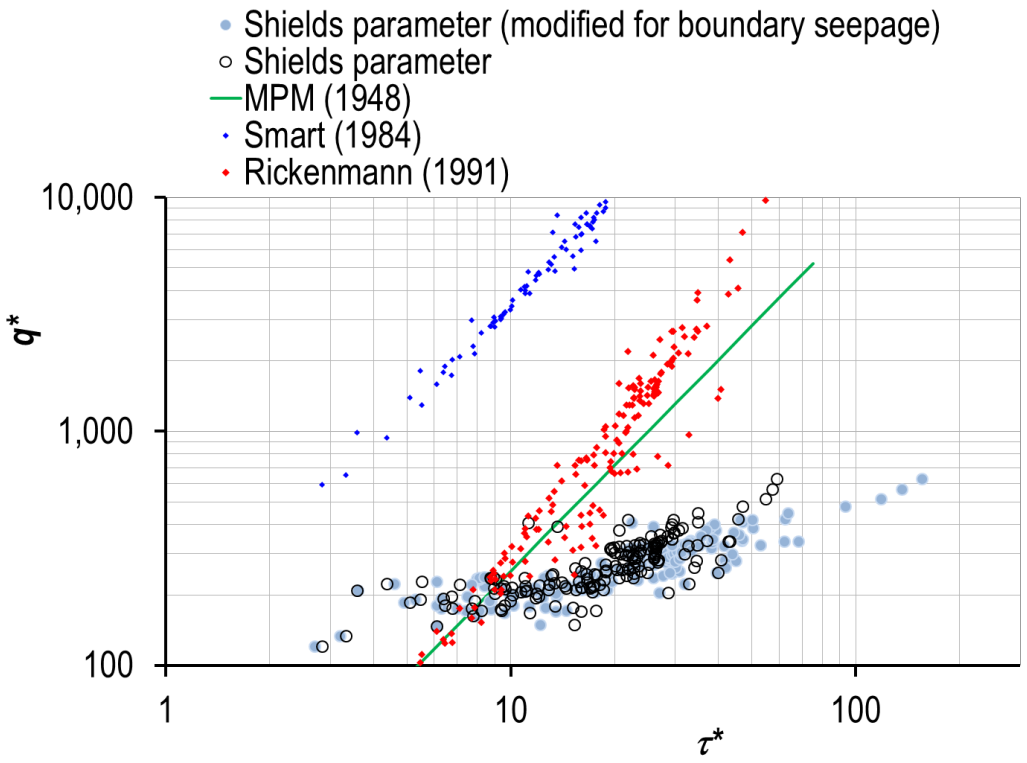

Figure 7.18: Dimensionless transport rate and Shields parameter relationship for three time-steps (Test No. 6)

7.4 Discussion

Several lessons have been learned from the experimental technique employed for the 2-D overtopping tests. Unlike the previous experimental phase which did not present any difficulty or malfunction, there were a fair number of embankment failures in Phase III. The main cause behind the piping failures was the large overtopping head used in the 2-D overtopping tests. However, a particular gate design was developed to dissipate the high exit hydraulic gradients at the embankment crest and avert such premature failures. Another major drawback which caused significant delays was the fragility of the M-TTPAs used. Using probes with a 2 mm diameter certainly minimised intrusion within the soil and water mediums, however, their assembly, calibration and installation was very tedious. Predrilling the embankment model prior to installation of the M-TTPAs proved very useful. Also, the images captured using the digital cameras, revealed that there was

some slight movement in the objects. This was due to the digital cameras' shutter by which vibrations resonated. Fortunately, a version of a code capable of registering images, developed at the Department of Image Processing at the University of Ottawa, was made available and solved this problem. This issue could have been averted by weighing down the cameras using weights or by activating the mirror lock-up feature. Given the requirements and instrumentation used in the 2-D overtopping tests, a much higher level of detail was required than the 3-D breach overtopping tests. The experimental setup was, however, refined and documented with a high level of detail, similar to the 3-D breach overtopping tests.

The similarity in PWP time-history due to overtopping flow between the two control TTPAs indicated a uniform erosion and homogeneity of the embankment material across the width of the flume. There was also a similarity in the measured piezometric head and PWP time-history due to a falling reservoir head and steady-state seepage between the two drained embankment configurations (before any drying process took place). Also, after observing the PWP time-history for the two control TTPAs under steady-state and falling head conditions (see Appendix F), it can be stated that the homogeneity of the construction of the small flume embankment models was to a large extent consistent.

The computed dimensionless shear stress for the three time-steps analysed were very high. Visser (1998) also reported values for the dimensionless shear stress less than 1 at the downstream vertex of the crest, and values ranging between 10 and above 100 near the downstream toe. Although the mobility relationship included a large scatter in data (see Figure 7.18), it can still be argued that both the MPM (1948) and the Rickenmann formulations over predicted the transport rate for the same bed shear stress. Sediment transport predictions using the Smart (1984) formulation were at least one order of magnitude higher than the measured values. This may be due to the non-equilibrium nature of the erosion mechanism due to overtopping flows.

Although using a large initial overtopping head was a challenge, it prevented the formation of anti-dunes on the downstream slope and consequently additional curvature effects. Due to the shallowness of the flow and high flow velocities, the process of digitizing pronounced curvatures introduced large errors. The presence of curvatures, as illustrated by Figure 7.3, did not result in realistic estimates for the bed shear stress since the hydrostatic assumption was invalid. It was therefore necessary to establish a flat bed surface as well as maximise the length of the reach in which a hydrostatic pressure distribution was present. Based on the images captured, the development of a knickpoint downstream the crest was observed, similar to the studies by Powledge *et al.* (1989) and Kirsten *et al.* (2000). Downstream of the recirculation zone the curvatures in the water surface and bed profiles were minimised, and therefore the computations using Equation (7.3) were not affected since the hydrostatic assumption was valid in this particular case.

The PWP transient response due to overtopping flow in the case of the drained embankment model with nearly dry initial conditions was characterised by steady values until the moment when the overtopping flow came into contact with the TTPAs. Following that moment, the PWP transient response was characterised by a sharp increase, with very short periods (approximately 2-4seconds) (see Figure F-11 of Appendix F). This particular configuration, unlike the two other configurations, therefore exhibited a constant flownet while erosion of the soil boundary took place. The seepage mechanism in the drier and consequently unsaturated zone was dominated by the high rate of erosion. As a result, the transient flownet technique described in Subsection 7.3.4 would not apply since much shorter time-steps would be required. This temporal discretization simply could not be supported since the digital cameras captured images at 1 second intervals (the undrained embankment configuration used 0.5 second intervals). In addition, it is expected that large errors would arise given the rapid change in PWP and lower erosion depths. Nevertheless, the PWP measurements for this particular embankment configuration were useful in clarifying some aspects related to the boundary seepage mechanism.

In the case of flow overtopping a noncohesive embankment, there will be a second phreatic surface developing at the sloping bed due to infiltration (*i.e.* boundary influx). The wetting front and erosion mechanisms are highly coupled and their development will depend on many parameters and conditions. Listed below is a hypothesis with respect to the parameters and conditions that are important for determining the wetting front. This is based on an understanding of the theory behind erosion, breach flow hydraulics and seepage in the saturated and unsaturated zones.

- Hydraulic (overtopping) boundary conditions: These are characterised by the effective bed shear-stress and the net entrainment rate of the soil. As a result, the wetting front advance rate will be largely influenced by the hydraulic forces and how they vary with space and time. The wetting front mechanism will also depend on the magnitude (*i.e.* hydraulic gradient) as well as direction (*i.e.* angle) of the seepage forces due to the overtopping flow.
- Soil-water interphase condition: This is characterised by the thickness of the wetting front and the rate by which it advances. As a result, this condition will be largely influenced by the saturated hydraulic conductivity as well as the net entrainment rate of the soil.
- Soil matrix boundary conditions: These are characterised by the saturated hydraulic conductivity of the soil, matric suction, AEV and slope of the wetting SWCC.
- Soil matrix initial conditions: The initial soil-state will play an influential role on how the erosion/deposition mechanism takes place, as well as the wetting front rate of advance. For a higher soil tension, the soil particles will be in a state of apparent cohesion and will enhance the stability of the bed. On the other hand, the boundary layer in the overtopping flow will decrease giving rise to a higher bed shear stress. Higher soil tensions will also result in a lower hydraulic conductivity and a slower rate of advance for the wetting front.

Perhaps the two most important factors in this mechanism are the hydraulic conductivity and the erodibility of the soil. While the former will depend on pore-size (in other words, k_{sat}) and the soil-state (*i.e.* $u_a - u_w$) of the underlying soil, the latter will depend on the transport rate under boundary seepage. Therefore, the wetting front advance will be more pronounced in an embankment material, coarser than the one which has been used. Simulation of the wetting front rate of advance using numerical methods will require an appropriate spatial discretization at the soil boundary. The erosion of the downstream face of an embankment and the consequent drawdown in the reservoir, will give rise to a lowered saturated zone. Similar to the wetting front advance, a suitable discretization approach would also be required in order to capture the retreat of the lower phreatic surface.

7.5 Conclusions and Recommendations

7.5.1 Conclusions

For the first time in 2-D overtopping tests, the time-history of PWPs through an embankment model was measured using a large number of PWP transducer devices (*i.e.* TTPAs). In this novel experimental setup of Phase III, a total of fifteen TTPAs were installed through the side-walls of the flume, and one TTPA was installed on the opposite side as a control measurement. Initially, two designs of the PWP transducer devices were fabricated and tested in the Geotechnical Engineering Laboratory: a micro and standard tensiometer-transducer probe assembly (*i.e.* M-TTPA and S-TTPA). Both TTPAs were mainly comprised of a porous ceramic cup (2mm and 6mm in diameter for the M-TTPA and S-TTPA, respectively) and a pressure transducer, capable of measuring positive and negative PWPs (ranging between +7kPa and -7kPa).

Other instrumentation used in this experimental phase included wave gauges, piezometers, and video and digital cameras. In a narrow hydraulic flume (0.38m wide), a drainage test series was used to investigate the influence of initial soil-water state on the erodibility of noncohesive embankment models. Three embankment

model configurations were overtopped using an initial overtopping head equal to one-third of the embankment crest height: “with drain”, “without drain” and “with drain under nearly dry conditions”. Three test measurement series were conducted for each drainage configuration: steady-state seepage (mainly using three WSLs), a falling reservoir head, and overtopping erosion. Test repeatability was also investigated for the three measurement series as part of this experimental phase. Similar to the Phase I and II, breach outflow was computed from the recorded water surface elevations using a hydrologic routing method.

- The calibration results indicated that the sensitivity of the pressure transducer used was not influenced by the water medium (see Subsection D.2.2 of Appendix D for results of the calibration and response time tests). Falling and rising heads at rates one order of magnitude higher than the saturated hydraulic conductivity of the embankment material used revealed that the response time was instantaneous with deviations of 0.6 to 1.6 mm-H_20, where a time period of 1 to 1.6s was required for the PWP to stabilise completely.
- Good agreement was observed in all three measurement series with respect to repeatability. The PWP deviation in the control TTPA was also minor. This confirmed the level of control and consistency applied in the construction process as well as the homogeneity in erosion.
- The high exit hydraulic gradients on the upstream slope in the undrained embankment configuration resulted in multiple premature failures by piping. This problem was solved using a gate design which dissipated the PWPs near the embankment crest.
- The outflow hydrographs for the three configurations indicated that the erodibility of noncohesive embankments was largely influenced by the initial soil-water state.
- It was also found that erosion accelerated the drainage rate within the pores of the embankment material, particularly for the undrained embankment model.

- The PWP at the soil boundary remained near atmospheric values during the entire overtopping event for both “drain” and “without drain” model configurations.
- A transient flownet analysis was developed to extract the exit hydraulic gradient and seepage angle at the soil-water interface for three time-steps using one of the embankment configurations (Test No. 6).
- It was revealed that boundary seepage was oriented downward in upstream locations and upward in the downstream locations.
- An expression for bed shear stress using the unsteady 1-D SWE modified to account for boundary seepage and steep slopes was derived.
- The bed shear stress on the downstream shoulder slope was determined using the derived equation and the flow parameters which were extracted from the water surface and bed profiles at 2-second time-intervals and 2 cm space-steps. The calculated bed shear stress was two to three orders of magnitude higher than the critical values ($3 < \tau^* < 50$) while Froude numbers reached approximately 2.7 at the downstream toe.
- The dimensionless shear stress was then modified to account for upward and downward seepage using the method by Baldock and Holmes (1998) and Cheng and Chiew (1999b). This method, however, cannot be applied for the drained embankment configuration which was overtopped under nearly dry conditions, since the advance rate of the wetting front at the soil boundary was much slower than the erosion rate.
- A method for representing the mobility of noncohesive sediment due to overtopping flow was demonstrated using the same dataset extracted from the drained embankment configuration (*i.e.* Test No. 6) using three time-steps only.

The 2-D overtopping tests conducted in the laboratory were not scaled representations of any particular prototype. While the maximum range of PWPs through the embankment model was only +4kPa to -7kPa (*i.e.* using the drained configuration under nearly dry conditions), smaller variations in the PWP range did

in fact influence the peak breach outflow and rate of erosion. This does not necessarily imply that prototypes that are equipped with drainage systems, and which possibly exhibit PWPs far beyond the range achieved in the laboratory flume, will experience similar peak outflow reductions or resistance to erosion. Rather than that, the present work focuses on the significance of developing experimental techniques as well as scaling criteria based on both the PWP distribution and erodibility.

7.5.2 Recommendations for Future Work

- In the case of the 2-D overtopping tests, future test parameters could include coarser soils which would then give rise to a more distinct wetting front. This would be a benefit in terms of extending the instrumentation technique to wetting fronts with more rapid advance rates. The advance of the wetting front could be measured by using small dual-wire conductivity probes similar to those used in the study by Ho (2000), and which are very simple to design and install.
- The intent of using an undrained embankment configuration was to generate higher drainage rates. Although this was realised in the 2-D overtopping tests, a further accelerated drainage rate could be achieved by using a setup with a constant reservoir head. This would also extend the erosion rate and, consequently, the mobility relationship in 2-D overtopping experiments.
- Further investigations are necessary to quantify the contribution of both erosion and the fluctuating pressure field near the bed in accelerating flow on the seepage forces across an eroding bed.
- The influence of boundary seepage on overtopping flow and erosion should also be investigated numerically. This can be achieved by coupling fundamental formulations which govern flow hydrodynamics and flow through porous media (*e.g.* by means of the Navier-Stokes and Richards' equations, respectively). Hydrodynamic equations which consider non-hydrostatic pressure distributions such as the 1-D Boussinesq or non-hydrostatic SVE

(Audusse *et al.* 2011) would be more suitable for the solving the flow parameters where there is pronounced slope curvature. Also, an expression for the bed shear stress, similar to the one derived in this study, could be incorporated in such numerical models. This would result in better estimates of the bed shear stress at the upstream slope and crest, as well as in the recirculation zone. Consequently, if integrated with the transient flownet analysis described herein, such a model could incorporate the seepage mechanism in upstream reaches and extend the range of the mobility relationship in 2-D overtopping flow.

- The lighting and photographic installations used in the 2-D overtopping tests were by far the most important factors which determined the quality of the captured images. It is therefore suggested to develop and optimise new lighting techniques and make use of higher definition digital cameras. Using cameras capable of capturing higher frame rates would be beneficial for the developed transient flownet analysis, especially if smaller time-steps are required.

It would be useful to conduct experimental programs were erosion is investigated using unsteady, rapidly-varying and supercritical flow conditions, including various grain sizes. This would result in erodibility expressions which would be useful in scenarios where erosion is governed by non-equilibrium conditions.

Chapter 8

Summary

This research study was geared towards understanding in detail the breach mechanisms of noncohesive earth fill embankments due to overtopping. The proposed comprehensive analytical and experimental program has provided significant insight into the influence of geotechnical and hydraulic modeling parameters on the spatial and temporal characteristics of breach morphology. The instrumentation used in the experimental program, conducted in the Hydraulics Laboratory, included wave gauges, piezometers, PWP transducer devices and video and/or digital cameras. In all this experimental work, breach outflow was computed from the recorded water surface elevations using a hydrologic routing method. The aspect of duplicability was also investigated in the physical tests.

Preliminary work in this research comprised of a sensitivity analysis using two embankment breach numerical models: NWS-BREACH and HR-BREACH. The numerical simulations were useful since they have shed light on the modeling requirements, processes and logic behind two very common physically-based mathematical modeling, especially with regards to erosion and side-slope failure within the breach channel. Preliminary work also included physical tests (Phase I), in which three-dimensional breach overtopping tests were conducted in both narrow and wide hydraulic flumes. Other than revealing that compaction effort construction and initial soil-water state should not be treated arbitrarily, the preliminary experiments were very useful in helping the author become familiarised with the experimental setup as well as develop methods to improve the control of test parameters in three-dimensional breach overtopping laboratory tests. The preliminary tests were also useful in facilitating the selection of potential parameters which were investigated in the upcoming phases of the experimental program.

In Phase II, a novel construction technique for compacting noncohesive embankment models in a laboratory flume to mimic an actual prototype was developed where compaction was applied using vibration and controlled using a static load. The optimum soil conditions were targeted based on *in situ* assessments rather than on the Standard Proctor test. Inflow into the upstream reservoir was sufficiently controlled to cause overtopping without influencing the breach failure mechanism itself. In addition to the two geotechnical parameters used in Phase I, two additional hydraulic parameters comprised of geometric scale series: tilted and quasi-exact scales. The two geometric scale series were used to evaluate the Froude criterion in three-dimensional breach overtopping tests using noncohesive embankment material. A nonintrusive photogrammetric mapping technique was also applied to extract the dimensions of an ogee-like crest forming on the upstream slope of the embankment models. Using the Froude-critical criterion at this control section, an expression for estimating the breach outflow was derived. Best-fit expressions describing morphology of dimensionless breach channel entrance parameters and the discharge efficiency with respect to a normalised time were also presented.

In Phase III of the experimental program, a novel experimental two-dimensional configuration used to measure the PWP time-history through a noncohesive embankment model due to overtopping flow was developed. Two designs of the PWP measurement devices were fabricated and tested in the Geotechnical Engineering Laboratory, a standard and a micro tensiometer-transducer probe assembly. A drainage series, where three initial soil-water states were simulated, was used to investigate the pore-water-pressure time-history and erodibility of the noncohesive embankment material due to an unsteady overtopping surge. The overtopping head was deliberately maximized (*i.e.* one-third the embankment crest height) based on values obtained from Phase II (three-dimensional breach overtopping) tests. An experimental-numerical hybrid approach was then applied to estimate the bed shear stress in the presence of boundary seepage on steep slopes. This experimental element of this approach involved the extraction of

seepage parameters using a transient flownet analysis. The numerical element of this approach involved the extraction of hydraulic parameters by discretizing the physical domain and computing the bed shear stress based on the derived one-dimensional unsteady St. Venant equations in the presence of boundary seepage and steep slopes. This approach was also used to demonstrate a method for representing the mobility relationship of noncohesive sediment due to overtopping flow based on modification of the Shields parameter to boundary seepage.

Following an exhaustive research program and the outcomes presented in this thesis, one important point needs to be emphasized. The results and contributions of this experimental study are not expected to immediately improve the design standards of noncohesive earth embankments subjected to overtopping flow; instead they focus on improving modeling approaches in laboratory experiments. The parameters investigated and the corresponding results, however, have been shown to be very important with respect to the processes governing breach failures in noncohesive earth embankments and their effect on breach channel development and the breach outflow hydrograph due to overtopping flow.

References

Abrahams, A.D. (2003). Bed-load transport equation for sheet flow, *Journal of Hydraulic Engineering,* 129(2): 159-163.

Ackers, P. and White, W.R. (1973). Sediment transport: new approach and analysis, *Journal of the Hydraulics Division*, HY11: 2041-2060.

AlQaser, G.N. (1991). Progressive failure of an overtopped embankment, PhD Thesis, Colorado State University, Fort Collins, U.S.A.

Al-Riffai, M. (2006). Sensitivity analysis on dam breach parameters using two numerical models: NWS-BREACH and HR-BREACH, Comparative study on dam breaching numerical models (25 August, 2006), Department of Civil Engineering, University of Ottawa, Ottawa, Canada.

Al-Riffai, M., Nistor, I., Vanapalli, S. and Orendorff, B. (2007). Overtopping of earth embankments: Sensitivity analysis of dam breaching using two numerical models, Proceedings of the 60th Canadian Geotechnical Conference, Ottawa, Canada, 21-24 October, 2007 (pp. 1213-1220).

Al-Riffai, M. and Orendorff, B. (2009). Breaching of earth dams: Experimental modeling due to blasts, Faculty of Engineering Graduate Studies Research Day, University of Ottawa, Ottawa, Canada, 5 February, 2009.

Al-Riffai, M., Nistor, I., Orendorff, B., Rennie, C.D. and St-Germain, P. (2009). Influence of compaction and toe-drains on the formation of breach channels of overtopped earth embankments: An experimental study, *Proceedings of the 33rd IAHR World Congress*, Vancouver, Canada, 9–14 August, 2009.

Al-Riffai, M. and Nistor, I. (2010a). Impact and analysis of geotechnical processes on earthfill dam breaching, *Natural hazards*, 55(1): 15-27.

Al-Riffai, M. and Nistor, I. (2010b). Breach channel morphology in the unsaturated zone and under various compaction densities, *Canadian Dam Association 2010 Annual Conference*, Niagara Falls, Canada, 2–7 October, 2010.

Al-Riffai, M. and Nistor, I. (2011). Effects of compaction and slope steepness on the retreat of a sand bed under supercritical flow, *Proceedings of the 34th IAHR World Congress*, Brisbane, Australia, 26 June – 1 July, 2011.

Al-Riffai, M. Nistor, I. and Bartens, T. (2011). Dam breaching experiments using scale series, *2011 Canadian Society of Civil Engineers (CSCE) Annual Conference*, Ottawa, Canada, 14–17 June, 2011.

Al-Riffai, M. and Nistor, I. (2013a). Influence of seepage on the erodibility of overtopped noncohesive embankments, *21st CSCE Hydrotechnical Speciality Conference*, Banff, Canada, 14-17 May, 2013.

Al-Riffai, M. and Nistor, I (2013b). Influence of boundary seepage on the erodibility of overtopped embankments: A novel measurement and experimental technique, *Proceedings of the 35th IAHR World Congress*, Chengdu, China, 8–13 September, 2013.

Al-Riffai, M. and Nistor, I. (2014a). Breach channel morphology and outflow prediction using scale series, *manuscript in preparation*.

Al-Riffai, M. and Nistor, I. (2014b). Development of a novel experimental technique for measurement of boundary seepage in overtopped noncohesive earthfill embankment physical models, *manuscript in preparation*.

Annandale, G.W. (1995). Erodibility, *Journal of Hydraulic Research*, 33(4): 471-494.

Arenillas, M., and Castillo, J.C. (2003). Dams from the Roman era in Spain. Analysis of design forms, *Proceedings of the First International Congress on Construction History*, Madrid, Spain, 20–24 January, 2003.

Armanini, A. (1995). Non-uniform sediment transport: dynamics of the active layer, *Journal of Hydraulic Research*, 33(5): 611-622.

Armanini, A. and Di Silvio, G. (1988). A one-dimensional model for the transport of a sediment mixture in non-equilibrium conditions, *Journal of Hydraulic Research*, 26(3): 275-292.

Arya, L.M. and Paris, J.F. (1981). A physicoempirical model to predict the soil moisture characteristic from particle-size distribution and bulk density data, *Soil Science Society of America Journal*, 45(6): 1023-1030.

ASTM (2000a). American Society for Testing and Materials, Standard test method for capillary-moisture relationships for coarse-and medium-textured soils by porous-plate apparatus, ASTM D2325-68.

ASTM (2000b). American Society for Testing and Materials, Standard test methods for maximum index density and unit Weight of soils using a vibratory table ASTM D4253–00 (reapproved 2006).

ASTM (2000c). American Society for Testing and Materials, Standard test methods for minimum index density and unit weight of soils and calculation of relative density, ASTM D4254–00 (reapproved 2006).

ASTM (2004). American Society for Testing and Materials, Standard test method for direct shear test of soils under consolidated drained conditions, ASTM D3080-04.

ASTM (2005). American Society for Testing and Materials, Standard test methods for laboratory determination of water (moisture) content of soil and rock by mass, ASTM D2216-05.

ASTM (2006a). American Society for Testing and Materials, Standard test method for permeability of granular soils (constant head), D2434–68.

ASTM (2006b). American Society for Testing and Materials, Standard test methods for specific gravity of soil solids by water pycnometer, D854-06e1.

ASTM (2007a). American Society for Testing and Materials, Standard test method for density and unit weight of soil in place by sand-cone method, ASTM D1556-07.

ASTM (2007b). American Society for Testing and Materials, Standard test methods for laboratory compaction characteristics of soil using standard effort (12400 ft-lbf/ft^3 (600 kN-m/m^3)), ASTM D698-07e1.

ASTM (2007c). American Society for Testing and Materials, Standard test method for particle-size analysis of soils, ASTM D422-63.

ASTM (2010). American Society for Testing and Materials, Standard practice for classification of soils for engineering purposes (Unified Soil Classification System), ASTM D2487-10.

Audusse, E., Bristeau, M.O., Perthame, B. and Sainte-Marie, J. (2011). A multilayer Saint-Venant system with mass exchanges for Shallow Water flows. Derivation and numerical validation, *ESAIM: Mathematical Modelling and Numerical Analysis*, 45(01): 169-200.

Bagnold, R.A. (1966). An approach to the sediment transport problem from general physics, US Geological Survey Professional Paper 422-I, 37p.

Baldock, T.E. and Holmes, P. (1998). Seepage effects on sediment transport by waves and currents, *Coastal Engineering 1998*, ASCE, Copenhagen, Denmark, 3: 3601-3614.

Baldock, T.E. and Nielsen, P. (2010). Discussion of "Effect of seepage-induced nonhydrostatic pressure distribution on bed-load transport and bed morphodynamics" by Simona Francalanci, Gary Parker, and Luca Solari, *Journal of Hydraulic Engineering*, 136(1): 77-79.

Barbour, S.L. (1998). Nineteenth Canadian Geotechnical Colloquium: The soil-water characteristic curve: a historical perspective, *Canadian Geotechnical Journal*, 35(5): 873-894.

Basco, D.R. (1989). Limitations of de Saint Venant in dam-break analysis, *Journal of Hydraulic Engineering*, 115(7): 950-965.

Bathurst, J.C., Graf, W.H. and Cao, H.H. (1987). Bed load discharge equations for steep mountain rivers, In *Sediment Transport in Gravel-Bed Rivers*, C.R. Thorne, J.C. Bathurst and R.D. Hey (eds.), John Wiley and Sons Ltd., New York, p453-491.

Bathurst, R.J., Ho, A.F. and Siemens, G. (2007). A column apparatus for investigation of 1-D unsaturated–saturated response of sand–geotextile systems, *ASTM Geotechnical Testing Journal*, 30(6): 433–441.

Bechteler, W. and Broich, K. (1991) (cited in Morris *et al.* 2009b). Effects in dambreak modelling, *Proceedings of the 24th IAHR World Congress*, Madrid, Spain, 9–13 September (pp. 189-200).

Bechteler, W. and Kulisch, H. (1998). Description of Test Case No. 1 on dam erosion, *Proceedings of the 2nd CADAM Workshop, Concerted Action on Dam-Break Modelling (CADAM) Programme*, Munich, Germany, 8–9 October, 1998.

Bhattacharyya, K. (2011). Purpose and Perspectives. The Lower Damodar River, *India*, 1-22.

Biscarini, C., Di Francesco, S. and Manciola, P. (2010). CFD modelling approach for dam break flow studies, *Hydrology and Earth System Sciences*, 14: 705-718.

Bisschop, F., Visser, P., van Rhee, C. and Verhagen, H.J. (2010). Erosion due to high flow velocities: a description of relevant processes, *32nd International Conference of Coastal Engineering*, Shanghai, China, 30 June – 5 July, 2010.

Bor, A. (2008). Numerical modeling of unsteady and non-equilibrium sediment transport in rivers, Master's Thesis, İzmir Institute of Technology, İzmir, Turkey.

Botros, F.E., Onsoy, Y.S., Ginn, T.R. and Harter, T. (2012). Richards equation–based modeling to estimate flow and nitrate transport in a deep alluvial vadose zone, *Vadose Zone Journal*, 11(4).

Bretas, E. M., Lemos, J. V., and Lourenço, P. B. (2012). Masonry Dams: Analysis of the Historical Profiles of Sazilly, Delocre, and Rankine, *International Journal of Architectural Heritage*, 6(1), 19-45.

Broich, K. (1998a). Conclusions from the test case modelling, *Proceedings of the 2nd CADAM Workshop, Concerted Action on Dam-Break Modelling (CADAM) Programme*, Munich, Germany, 8–9 October, 1998.

Broich, K. (1998b). Mathematical modelling of dam-break erosion caused by overtopping, *Proceedings of the 2nd CADAM Workshop, Concerted Action on Dam-Break Modelling (CADAM) Programme*, Munich, Germany, 8–9 October, 1998.

Broich, K. (2003). Sediment transport in breach formation process, *Proceedings of the 3rd IMPACT Project Workshop*, Louvain-la-Neuve, Belgium, 5–7 November, 2003 (CD-ROM).

Brooks, R.H. and Corey, A.T. (1964) (cited in van Genuchten, 1980). Hydraulic properties of porous media, Hydrology Papers, Colorado State University, Fort Collins, Colorado.

Brown, R.J. and Rogers, D.C. (1977) (cited in Fread, 1984a). A simulation of the hydraulic events during and following the Teton Dam failure, *Proceedings of the Dam-Break Flood Routing Workshop*. Water Resources Council, 131-163.

Brunner, U. (2000). The great dam and the Sabean oasis of Ma'rib, *Irrigation and Drainage* Systems, 14: 167-182.

Brunner, U. and Haefner, H. (1986). The successful floodwater farming system of the Sabeans, Yemen Arab Republic, *Applied Geography*, 6: 77-86.

Buffington, J.M. and Montgomery, D.R. (1997). A systematic analysis of eight decades of incipient motion studies, with special reference to gravel-bedded rivers, *Water Resources Research*, 33(8): 1993-2029.

Burdine, N.T. (1953). Relative permeability calculations from pore size distribution data, *Journal of Petroleum Technology*, 5(3): 71-78.

Cedergren, H.R. (1997). Seepage, drainage, and flow nets (3rd ed.), John Wiley & Sons Inc., New York.

Chang, D.S. and Zhang, L.M. (2010). Simulation of the erosion process of landslide dams due to overtopping considering variations in soil erodibility along depth, *Natural Hazards and Earth System Sciences*, 10(4): 933-946.

Chanson, H. (1999). The Hydraulics of Open Channel Flow: An Introduction, Arnold, London.

Chant, C. (2008). Allied Bombers:1939-45. Zenith Press.

Chapuis, R.P. (2004). Predicting the saturated hydraulic conductivity of sand and gravel using effective diameter and void ratio, *Canadian Geotechnical Journal*, 41(5): 787-795.

Chaudhry, M.H. (2008). Open-channel flow (2nd ed.), Springer, New York.

Chee, S. P. (1978). Mobile controls for water resources projects, *Journal of the American Water Resources Association*, 14(1): 99-108.

Chen, Y.H. and Anderson, B.A. (1987) (cited in Wang and Bowles, 2006a). Development of a methodology for estimating embankment damage due to flow overtopping. Final Report, Simons, Li and Associates Inc. for Federal Highway Admin and Forest Service, Contract No DTFH61-82-00104, SLA Project No DC-FHA-01

Chen, X. and Chiew, Y.-M. (2004). Velocity distribution of turbulent open-channel flow with bed suction, *Journal of Hydraulic Engineering*, 130(2): 140-148.

Chen, X., Ma, J. and Dey, S. (2010). Sediment transport on arbitrary slopes: Simplified model, *Journal of Hydraulic Engineering*, 136(5): 311-317.

Cheng, N.S. and Chiew, Y.-M. (1998). Turbulent open-channel flow with upward seepage, *Journal of Hydraulic Research*, 36(3): 415-431.

Cheng, N.S. and Chiew, Y.-M. (1999a). Analysis of initiation of sediment suspension from bed load, *Journal of Hydraulic Engineering*, 125(8): 855-861.

Cheng, N.S. and Chiew, Y.-M. (1999b). Incipient sediment motion with upward seepage, *Journal of Hydraulic Research*, 37(5): 665-681.

Chiew, Y.-M. and Parker, G. (1994). Incipient sediment motion on non-horizontal slopes, *Journal of Hydraulic Research*, 32(5): 649-660.

Chinnarasri, C., Jirakitlerd, S. and Wongwises, S. (2004). Embankment dam breach and its outflow characteristics, *Civil Engineering and Environmental Systems*, 21(4): 247-264.

Chinnarasri, C., Tingsanchali, T., Weesakul, S., and Wongwises, S. (2003). Flow patterns and damage of dike overtopping, *International Journal of Sediment Research*, 18(4), 301-309.

Chu-Agor, M.L., Fox, G.A. and Wilson, G.V. (2009). Empirical sediment transport function predicting seepage erosion undercutting for cohesive bank failure prediction, *Journal of Hydrology*, 377(1): 155-164.

Clague, J.J. and Evans, S.G. (2000). A Review of catastrophic drainage of moraine-dammed lakes in British Columbia, *Quaternary Science Reviews*, 19:1763-1783.
Coleman, S.E., Andrews, D.P. and Webby, M.G. (2002). Overtopping breaching of noncohesive homogeneous embankments, *Journal of Hydraulic Engineering*, 128(9): 829-838.
Coleman, S.E., Webby, M.G. and Andrews, D.P. (2004). Closure to "Overtopping breaching of noncohesive homogeneous embankments" by Coleman, S.E., Andrews, D.P. and Webby. M.G. (2002). *Journal of Hydraulic Engineering*, 130(4): 374-376.
Costa, J.E. (1985). Floods from dam failures, *U.S. Geological Survey*, Open-File Report 85-560, 54p.
Craig, R.F. (2004). Craig's soil mechanics (7th ed.), Spon Press, New York.
Cristofano, E.A. (1965) (cited in Fread, 1984a). Method of computing erosion rate for failure of earthfill dams, United States Bureau of Reclamation, Denver, Colorado.
Crowe, C.T., Elger, D. F., Williams, B.C. and Roberson, J.A. (2009). Engineering fluid mechanics (9th ed.), John Wiley & Sons, Inc., New Jersey.
Daluz Vieira, J.H. (1983). Conditions governing the use of approximations for the Saint-Vénant equations for shallow surface water flow, *Journal of Hydrology*, 60: 43-58.
Dam (2012). *Encyclopædia Britannica Online Academic Edition*. Web. 14 Nov. 2012. http://www.britannica.com/EBchecked/topic/150337/dam
Das, B.M. (2002). Principles of geotechnical engineering (5th ed.), Brooks/Cole/Thomas Learning, Pacific Grove.
Davies, T.R., Manville, V.R., Kunz, M. and Donaldini, L. (2007). Modeling landslide dambreak flood magnitudes: Case study, *Journal of Hydraulic Engineering*, 133(7): 713–720.
D'Eliso, C. (2007). Breaching of sea dikes initiated by wave overtopping: A tiered and modular modeling approach, PhD Thesis, University of Braunschweig, Braunschweig, Germany, and University of Florence, Florence, Italy.
Den Adel, H. (1987) (cited in van Rhee, 2010). Re-analysis of permeability measurements using Forchheimer's equation, Report CO-272550/56 (in Dutch), GeoDelft, Deltares, Delft, The Netherlands.
Dey, S. and Zanke, U.C. (2004). Sediment threshold with upward seepage, *Journal of Engineering Mechanics*, 130(9): 1118-1123.
Danish Hydraulic Institute (2009). Mike 11 - A Modelling system for rivers and channels (reference manual), Horsholm, Denmark.
Dodge, R.A. (1988). Overtopping flow on low embankment dams - Summary report of model tests, Report No. REC-ERC-88-3, U.S. Bureau of Reclamation, Denver, Colorado.
Dunne, T. (1990). Hydrology, mechanics, and geomorphic implications of erosion by subsurface flow, Geological Society or America, Special Paper 252: 1-28.
Dupont, E., Dewals, B.J., Archambeau, P., Erpicum, S. and Pirotton, M. (2007). Experimental and numerical study of the breaching of an embankment dam, *Proceedings of the 32nd IAHR World Congress*, Venice, Italy, 1–6 July, 2007.
El-Yussif, F. (1983). Condensed history of water resources developments in Mesopotamia. *Water International*, 8(1), 19-22.
Evans, S. G. (1986). The maximum discharge of outburst floods caused by the breaching of man-made and natural dams, *Canadian Geotechnical Journal*, 23(3): 385–387.
EWRI TC (2011). Earthen embankment breaching, ASCE/EWRI Task Committee on Dam/Levee Breaching forum article, *Journal of Hydraulic Engineering*, 137(12); 1549-1564.
Faëh, R. (2007). Numerical modeling of breach erosion of river embankments, *Journal of Hydraulic Engineering*, 133(9): 1000-1009.

Fahlbusch, H. (2009). Early dams, *Proceedings of the Institution of Civil Engineers - Engineering History and Heritage*, 162(1): 13-18.

Federal Emergency Management Agency (FEMA) (2004). Federal guidelines for dam safety: Hazard potential classification system or dams, FEMA-333, U.S. Department of Homeland Security, October 1998 (reprinted January 2004).

Federal Emergency Management Agency (FEMA) (2005). The National dam safety program research needs workshop: Embankment dam failure analysis, FEMA-541, U.S. Department of Homeland Security, September 2005.

Federal Emergency Management Agency (FEMA) (2009). Dam safety in the United States - A progress report on the National dam safety program - Fiscal Years 2007 and 2007, P-759, U.S. Department of Homeland Security, February 2009.

Feliciano-Cestero, J.A. (2010). Levee breach by overtopping: The effects of soil properties, Master's Thesis, University of South Carolina, Columbia, U.S.A.

Feng, M. and Fredlund, D.G. (1999) (cited in Pham *et al.* 2003). Hysteretic influence associated with thermal conductivity sensor measurements, 52nd Canadian Geotechnical Conference, Regina, Saskatchewan, 25–30 October, 1999 (pp. 651–657).

Fernandez Luque, R. and van Beek, R. (1976). Erosion and transport of bed-load sediment, *Journal of Hydraulic Research*, 14(2): 127-144.

Flores-Berrones, R. and Lopez-Acosta, N.P. (2011). Internal erosion due to water flow through earth dams and earth structures. In *Soil Erosion Studies*, D.F. Godone and S. Stanchi (eds.), InTech, p283-306.

Foster, M., Fell, R. and Spannagle, M. (2000). The statistics of embankment dam failures and accidents, *Canadian Geotechnical Journal*, 37:1000-1024.

Fox, G.A., Heeren, D.M., Wilson, G.V., Langendoen, E.J., Fox, A.K. and Chu-Agor, M.L. (2010). Numerically predicting seepage gradient forces and erosion: Sensitivity to soil hydraulic properties, *Journal of Hydrology*, 389(3): 354-362.

Franca, M. and Almeida, A.B. (2002). Experimental tests on rockfill dam breaching process, *International Symposium on Hydraulic and Hydrological Aspects of Reliability and Safety Assessment of Hydraulic Structures*, St. Petersburg, Russia, 29 May – 2 June, 2002.

Franca, M.J. and Almeida, A.B. (2004). A computational model of rockfill dam breaching caused by overtopping (RoDaB), *Journal of Hydraulic Research*, 42(2): 197-206.

Francalanci, S., Parker, G. and Solari, L. (2008). Effect of seepage-induced nonhydrostatic pressure distribution on bed-load transport and bed morphodynamics, *Journal of Hydraulic Engineering*, 134(4): 378-389.

Francalanci, S., Parker, G. and Solari, L. (2010). Closure to "Effect of seepage-induced nonhydrostatic pressure distribution on bedload transport and bed morphodynamics" by S. Francalanci, G. Parker and L. Solari, *Journal of Hydraulic Engineering*, 136(1): 77-79.

Francaviglia, V.M. (2000). Dating the ancient dam of Mā'rib (Yemen), *Journal of Archaeological Science*, 27: 645–653.

Freescale (2011). Integrated silicon pressure sensor on-chip signal conditioned, temperature compensated and calibrated, Freescale Semiconductors Inc., (Revision 2), November 2011.

Fread, D.L. (1977). The development and testing of a dam-break flood forecasting model, Proceedings of Dam-Break Flood Modeling Workshop, US Water Resources Council, Washington DC, 164-197.

Fread, D.L. (1984a). A breach erosion model for earthen dams, *Proceedings of Specialty Conference on Delineation of Landslide, Flash Flood, and Debris Flow Hazards in Utah*, Utah State University, Logan, Utah, 14–15 June, 1984.

Fread, D.L. (1984b). DAMBRK: the NWS dam-break flood forecasting model. Hydrologic Research Laboratory, Office of Hydrology, National Weather Service, National Oceanic and Atmospheric Administration, Silver Spring, Maryland.

Fread, D.L. (1991). BREACH: An erosion model for earthen dam failures, Hydrologic Research Laboratory, Office of Hydrology, National Weather Service, National Oceanic and Atmospheric Administration, Silver Spring, Maryland, Revision 1 - August 1991 (Original Revision, July 1988).

Fread, D.L. and Lewis, J.M. (1998). NWS FLDWAV model, Hydrologic Research Laboratory, Office of Hydrology, National Weather Service, National Oceanic and Atmospheric Administration, Silver Spring, Maryland.

Fredlund D.G. (1987). Slope stability analysis incorporating the effect of soil suction. In *Slope Stability: Geotechnical Engineering and Geomorphology*, M.G. Anderson and K.S. Richards (eds.), John Wiley & Sons, Chichester, p113–144.

Fredlund, D.G. (1996). The Emergence of unsaturated soil mechanics, The Fourth Spencer Buchanan Lecture, Texas A&M University, College Station, Texas, 8 November, 1996, 39p.

Fredlund, D.G. (2000). The 1999 RM Hardy Lecture: The implementation of unsaturated soil mechanics into geotechnical engineering, *Canadian Geotechnical Journal*, 37(5): 963-986.

Fredlund, D.G. (2006). Unsaturated soil mechanics in engineering practice, *Journal of Geotechnical and Geoenvironmental Engineering*, 132(3): 286-321.

Fredlund, D.G. and Morgenstern, N.R. (1977). Stress state variables for unsaturated soils, *Journal of the Geotechnical Engineering Division*, 103(5): 447-466.

Fredlund, D.G., Morgenstern, N.R. and Widger, R.A. (1978). The shear strength of unsaturated soils, *Canadian Geotechnical Journal*, 15(3): 313-321.

Fredlund, D.G. and Rahardjo, H. (1993) (cited in Ng and Menzies, 2007). Soil mechanics for unsaturated soils, John Wiley & Sons Inc., New York.

Fredlund, D.G. and Xing, A. (1994). Equations for the soil-water characteristic curve, *Canadian Geotechnical Journal*, 31(4): 521-532.

Fredlund, D.G., Xing, A. and Huang, S. (1994). Predicting the permeability function for unsaturated soils using the soil-water characteristic curve, Canadian Geotechnical Journal, 31(4): 533-546.

Fredlund, M.D., Fredlund, D.G. and Wilson, G.W. (2000). An equation to represent grain-size distribution, *Canadian Geotechnical Journal*, 37(4): 817-827.

French, R. (1985). Open-channel hydraulics, McGraw-Hill, New York.

Froehlich, D.C. (1995a) (cited in Wahl, 2004). Embankment Dam Breach Parameters Revisited, *Proceedings of Water Resources Engineering Conference*, ASCE, New York, 887-891.

Froehlich, D.C. (1995b). Peak Outflow from Breached Embankment Dam, *Journal Water Resources Planning and Management Division*, ASCE 121(1): 90-97.

Froehlich, D.C. (2008). Embankment dam breach parameters and their uncertainties, *Journal of Hydraulic Engineering*, 134(12): 1708-1721.

Fujisawa, K., Kobayashi, A. and Yamamoto, K. (2008). Erosion rates of compacted soils for embankments, *Doboku Gakkai Ronbunshuu C*, 64(2): 403-410.

Gao, P. and Abrahams, A.D. (2004). Bedload transport resistance in rough open-channel flows, *Earth Surface Processes and Landforms*, 29(4): 423-435.

Garbrecht, G. (1996). Historical water storage for irrigation in the Fayum depression (Egypt), *Irrigation and Drainage*, 10: 47-76.
Gaucher, J., Marche, C. and Mahdi, T.F. (2010). Experimental investigation of the hydraulic erosion of noncohesive compacted soils, *Journal of Hydraulic Engineering*, 136(11): 901-913.
Gee, D.M. (2008). Comparison of dam breach parameter estimators, *Proceedings of World Environmental and Water Resources Congress*, Kansas City, Missouri, May 17–21, 2009.
Geisenhainer, P. and Kortenhaus, A. (2006). Hydraulic model tests on breaching with and without waves: Description of experiment performed at LWI, FLOODsite Report T06-06-02 (Revision 2_6_03), HR Wallingford, UK. Web. 15 Nov. 2012. http://www.floodsite.net
Geisenhainer, P. and Oumeraci, H. (2008). Seadike breach initiation and development: Large scale experiments in GWK, FLOODsite Report T06-08-12 (Revision 1_0_Pn), HR Wallingford, UK. Web. 15 Nov. 2012. http://www.floodsite.net
George, D.L. (2011). Adaptive finite volume methods with well-balanced Riemann solvers for modeling floods in rugged terrain: Application to the Malpasset dam-break flood (France, 1959), *International Journal for Numerical Methods in Fluids*, 66(8): 1000-1018.
GEO-SLOPE (2004). Seepage modeling with SEEP/W: An engineering methodology, GEO-SLOPE International Ltd., Calgary, Canada.
GEO-SLOPE (2007). Seepage modeling with SEEP/W: An engineering methodology, GEO-SLOPE International Ltd., Calgary, Canada.
Giuseppetti, G. and Molinaro, P. (1989) (cited in Morris *et al.* 2009b). A mathematical model of the erosion of an embankment dam by overtopping, *International Symposium on Analytical Evaluation of Dam Related Safety Problems*, Copenhagen, Denmark, 5 July, 1989 (pp. 329-341).
Goldin, A.L. and Rasskazov, L.N. (1992). Geotechnika 2: Design of earth dams, A.A. Balkema, Rotterdam.
Govers, G. (1987). Initiation of motion in overland flow, *Sedimentology*, 34(6): 1157-1164.
Graham, W.J. (1999). A procedure for estimating loss of life caused by dam failure. US Department of the Interior, Bureau of Reclamation, Dam Safety Office.
Graham, W.J. (2009). Major U.S. dam failures: their cause, resultant losses, and impact on dam safety programs and engineering practice, *Proceedings of the History Symposium of the World Environmental and Water Resources Congress*, Kansas City, MO, 17–19, May 2009.
Grahl-Madsen, M.A. (2009). Century of Turbine Research without Innovation? *Small Hydro Action for Promotion of Efficient Solutions R&D Actors Network Meeting*, Gdansk, Poland, September 2009.
Green, R.E. and Corey, J.C. (1971). Calculation of hydraulic conductivity: A further evaluation of some predictive methods, *Soil Science Society of America Journal*, 35(1): 3-8.
Guo, J. (2002). Hunter Rouse and Shields diagram, *Proceedings of the 13th IAHR-APD Congress*, 6-8 August, 2002, Singapore (pp. 1096-1098).
Hagen, V.K. (1982) (cited in Pierce *et al.* 2010). Re-evaluation of design floods and dam safety, *Proceedings of the 14th Congress of International Commission on Large Dams*, ICOLD, Paris, France.
Hager, W.H. and Hutter, D.D.K. (1984). Approximate treatment of plane channel flow, *Acta Mechanica*, 51(1-2): 31-48.

Hager, W.H. and Hager, K. (1985). Application limits for the kinematic wave approximation, *Nordic Hydrology*, 16: 203-212.

Hahn, W., Hanson, G.J. and Cook, K.R. (2000). Breach Morphology Observations of Embankment Overtopping Tests, *Proceedings of the Joint Conference on Water Resources Engineering and Water Resources Planning and Management*, Minneapolis, Minnesota, 30 July – 2 August, 2000.

Haines, W.B. (1930). Studies in the physical properties of soil. V. The hysteresis effect in capillary properties, and the modes of moisture distribution associated therewith, *The Journal of Agricultural Science*, 20(1): 97-116.

Hanson, G.J. and Temple, D.M. (2001). Evaluating mechanics of embankment erosion during overtopping, Proceedings of the Seventh Federal Interagency Sedimentation Conference, Reno, Nevada, 25–29 March, 2001.

Hanson, G.J., Cook, K.R., Hahn IV, W. and Britton, S.L. (2003). Evaluating erosion widening and headcut migration rates for embankment overtopping tests, *Proceedings of the 2003 ASAE Annual International Meeting*. Las Vegas, Nevada, 27–30 July, 2003.

Hanson, G.J., Cook, K.R. and Hunt, S.L. (2005). Physical modeling of overtopping erosion and breach formation of cohesive embankments, *Transactions of the ASAE*, 48(5): 1783-1794.

Hanson, G. J. and S. L. Hunt. (2007). Lessons learned using laboratory JET method to measure soil erodibility of compacted soils, *Applied Engineering in Agriculture*, 23(3): 305-312.

Hanson, G.J., Tejral, R.D., Hunt, S.L. and Temple, D.M. (2010). Internal erosion and impact of erosion resistance, *Proceedings of the 30th Annual US Society on Dams Meeting and Conference*, Sacramento, California, 12–16 April, 2010, pp. 773-784.

Harris, G.W. and Wagner, D.A. (1967) (cited in Fread, 1984a). Outflow from breached earth dams. University of Utah, Salt Lake City, Utah.

Hassan, M.A.A.M. and Morris, M. (2008). IMPACT Project field tests data analysis, FLOODsite Report T04-08-04 (Revision 3_3_P01), HR Wallingford, UK. Web. 15 Nov. 2012. http://www.floodsite.net

Harr, M.E. (1991). Groundwater and seepage, Dover Publications Inc., New York.

Havnø, K., Van Kalken, T. and Olesen, K. (1989) (cited in Morris *et al.* 2009b). A Modelling package for dam break simulation, *International Symposium on Analytical Evaluation of Dam Related Safety Problems*, Copenhagen, Denmark, 5 July, 1989 (pp. 387-397).

Hilf, J.W. (1956) (cited in Ng and Menzies, 2007). An investigation of pore-water pressure in compacted cohesive soils, PhD Thesis, Technical Memorandum No. 654, U.S. Department of the Interior, Bureau of Reclamation, Design and Construction Division, Denver, CO.

Ho, A.F. (2000). Experimental and numerical investigation of infiltration ponding in one-dimensional sand-geotextile columns, MSc Thesis, Queen's University, Kingston, Canada.

Howard, A.D. and McLane, C.F. (1988). Erosion of cohesionless sediment by groundwater seepage, *Water Resources Research*, 24(10): 1659-1674.

Hoyt, W.G. and Langbein, W.B. (1955). *Floods*, Princeton University Press, New Jersey, U.S.A.

Hu, C. and Hui, Y. (1996). Bed-load transport. I: Mechanical characteristics, *Journal of Hydraulic Engineering*, 122(5): 245-254.

Hunt, S.L., Hanson, G.J., Cook, K.R. and Kadavy, K.C. (2005). Breach widening observations from earthen embankment tests, *Transactions of the ASAE*, 48(3): 1115-1120.

Hughes, S.A. (1993). Physical models and laboratory techniques in coastal engineering, Vol. 7, World Scientific, Singapore.
ICOLD (1973) (cited in Costa, 1985). *Lessons from dam incidents*, Boston, Massachusetts, U.S. Commission on Large Dams (abridged edition).
IMPACT (2004a). Breach formation (WP2) - Technical Report, HR-Wallingford, UK. Web. 15 Nov. 2012. http://www.impact-project.net
IMPACT (2004b). Risk and uncertainty (WP5) - Technical Report, HR-Wallingford, UK. Web. 15 Nov. 2012. http://www.impact-project.net
Istanbulluoglu, E., Tarboton, D. G., Pack, R.T. and Luce, C. H. (2003). A sediment transport model for incision of gullies on steep topography, *Water Resources Research*, 39(4): 1103.
Jamsedjee, K.B.A. (1891). The Sudarśana or Lake Beautiful of the Girnâr Inscriptions, B.C. 300 – A.D. 450 (Introduction by O. Codrington), *Journal of the Asiatic Society of Bombay*, 18(49): 47-55.
Julién, P.Y. (2002). River Mechanics, Cambridge University Press, Cambridge.
Julién, P.Y. and Simons, D.B. (1985). Sediment transport capacity of overland flow, *Transactions of the American Society of Agricultural Engineers*, 28(3): 755-762.
Julién, P.Y. and Lan, Y. (1991). Rheology of hyperconcentrations, Journal of hydraulic engineering, 117(3): 346-353.
Kahawita, R. (2007). Dam breach modelling – A literature review of numerical models, Report for CEA Technologies Inc. (CEATI), Dam Safety Interest Group (DSIG), CEATI Report No. T032700-0207C.
Keulegan, G.H. (1938) (cited in French, 1985). Laws of turbulent flow in open channels, Research Paper RP 1151, *Journal of Research*, U.S. Bureau of Standards, 21: 707-741.
Kirkpatrick, G.W. (1977) (cited in Wahl, 2004). Evaluation guidelines for spillway adequacy, *Proceedings of the Engineering Foundation Conference*, ASCE, New York, 395–414.
Kirsten, H.A.D., Moore, J.S., Kirsten, L.H. and Temple, D.M. (2000). Erodibility criterion for auxiliary spillways of dams, *International Journal of Sediment Research*, 15(1): 93-107.
Kooi, H. and Beaumont, C. (1994). Escarpment evolution on high-elevation rifted margins: Insights derived from a surface processes model that combines diffusion, advection, and reaction, *Journal of Geophysical Research*, 99(B6): 12191-12209.
Korup, O. (2002). Recent research on landslide dams - A literature review with special attention to New Zealand, *Progress in Physical Geography*, 26(2), 206-235.
Krahn, J. (2004). Stability modeling with SLOPE/W: An engineering methodology, GEO-SLOPE/W international Ltd., Calgary, Canada.
Kulisch, H. (1994) (cited in Bechteler and Kulisch, 1998). Physical 3D-simulations of erosion-caused dam-breaks, *International Workshop on Floods and Inundations related to Large Earth Movements*, Trento, Italy, 4–7 October, 1994
Kutzner, C. (1997). Earth and rockfill dams: Principles of design and construction, A.A. Balkema, Rotterdam.
Lamborn, M.J. (1986) (cited in Vanapalli and Fredlund, 1999). A micromechanical approach to modeling partly saturated soil, PhD Thesis, Texas A & M University, College Station, U.S.A.
Lane, E.W. (1953) (cited in Raudkivi, 1998). Design of stable channels, *Proceedings of the American Society of Civil Engineers*, ASCE, 79: 1-31.
Lane, N, (2007). Aging infrastructure: dam safety, *CRS Report for Congress, RL33108, Congressional Research Service*, January 2007.

Larocque, L.A., Imran, J. and Chaudhry, M.H. (2013). 3D numerical simulation of partial breach dam-break flow using the LES and k–ϵ turbulence models, *Journal of Hydraulic Research*, 51(2): 145-157.

Lary, D. (2001). Drowned earth: The strategic breaching of the Yellow River Dyke, 1938. *War in History*, 8(2): 191-207.

Lecointe, G. (1998). Breaching mechanisms of embankments: An overview of previous studies and the models produced, *Proceedings of the 2nd CADAM Workshop, Concerted Action on Dam-Break Modelling (CADAM) Programme*, Munich, Germany, 8–9 October, 1998.

Li, L., Pan, Y., Amini, F. and Kuang, C. (2012). Full scale study of combined wave and surge overtopping of a levee with RCC strengthening system, *Ocean Engineering*, 54: 70-86.

Li, R. 2005. Flood control in the Yellow River Basin in China. *Water Encyclopedia*. 45–50.

Liu, D., Pang, L. and Xie, B. (2009). Typhoon disaster in China: prediction, prevention, and mitigation, *Natural Hazards*, 49(3): 421-436.

Litrico, X. and Fromion, V. (2009). Modeling and control of hydrosystems, Springer, London.

Little, G. (1959). Seven Wonders. *Engineering and Science*, 22(6), 23-28.

Loeser, C. J. (1973). Water Management in China, top priority for 2500 years, *Journal of the American Water Resources Association*, 9(1): 145-154.

Lou, W.C. (1981) (cited in Fread, 1984a; Singh, 1996). Mathematical modeling of earth dam breaches, Unpublished Ph.D. Thesis, Colorado State University, Fort Collins, CO.

Loukola, E. and Huokuna, M. (1998). A Numerical erosion model for embankment dam and its use for risk assessment, *Proceedings of the 2nd CADAM Workshop, Concerted Action on Dam-Break Modelling (CADAM) Programme*, Munich, Germany, 8–9 October, 1998.

Lu, Y., Chiew, Y.-M. and Cheng, N.S. (2008). Review of seepage effects on turbulent open-channel flow and sediment entrainment, *Journal of Hydraulic Research*, 46(4): 476-488.

MacDonald, T.C. and Langridge-Monopolis, J. (1984). Breaching characteristics of dam failures, *Journal of Hydraulic Engineering*, 110(5): 567-586.

Macchione, F. (2008). Model for predicting floods due to earthen dam breaching. I: Formulation and evaluation, *Journal of Hydraulic Engineering*, 134(12): 1688-1696.

Macchione, F. and Sirangelo, B. (1988). Study of earth dam erosion due to overtopping, *Proceedings of the Technical Conference on Hydrology of Disasters*, Geneva, Switzerland, 2–3 November, 1988 (pp. 212-219).

Macchione, F. and Rino, A. (1999). Prediction capabilities of a simplified dam-breach model, *Proceedings of the 3rd CADAM Workshop, Concerted Action on Dam-Break Modelling (CADAM) Programme*, Milan, Italy, 6–7 May, 1999.

Manville, V. (2001) (cited in Wishart, 2007). Techniques for evaluating the size of potential dam-break floods from natural dams, Wellington, Institute of Geological & Nuclear Sciences Science Report 2001/28, 70 p.

Martin, C.S. (1970). Effect of a porous sand bed on incipient sediment motion, *Water Resources Research*, 6(4): 1162-1174.

Martin, C.S. and Aral, M.M. (1971). Seepage force on interfacial bed particles, *Journal of the Hydraulics Division*, 97(7): 1081-1100.

Martins, R. (1981). Hydraulics of overflow rockfill dams, Laboratório Nacional Engenharia Civil, Ministério da Habitação e Obras Públicas, Report 559, Lisbon, Portugal.

Mays, L. W. (2010). Water Technology in Ancient Egypt. *Ancient Water Technologies*, 53-65.

McCann, M.W. (2009). National performance of dams program, Stanford University. Web. 15 Aug. 2009. http://npdp.stanford.edu

Meyer-Peter, E. and Müller, R. (1948). Formulas for bed-load transport, *Proceedings of the 2nd Meeting of the International Association for Hydraulic Structures Research*, Stockholm, Sweden, 7–9 June, 1948 (pp. 39-64).

Miller, J. (1984). Basic concepts of kinematic-wave models, U.S. Geological Survey Professional Paper 1302, U.S. Department of the Interior, Washington, DC.

Miller, M.C., McCave, I.N. and Komar, P. (1977). Threshold of sediment motion under unidirectional currents, *Sedimentology*, 24(4): 507-527.

Mohamed, M.A.A. (2002). Embankment breach formation and modelling methods, PhD Thesis, Open University, Buckinghamshire, United Kingdom.

Mohamed, M.A.A., Samuels, P.G., Ghataora, G.S. and Morris, M.W. (1999). A new methodology to model the breaching of non-cohesive homogeneous embankments, *Proceedings of the 4th CADAM Workshop, Concerted Action on Dam-Break Modelling (CADAM) Programme*, Zaragoza, Spain, 17–18 November, 1999.

Mohamed, M.A.A., Samuels, P.G., Morris, M.W. and Ghataora, G.S. (2002). Improving the accuracy of prediction of breach formation through embankment dams and flood embankments, *River Flow 2002: 1st International Conference on Fluvial Hydraulics*, Louvain-la-Neuve, Belgium, 3–6 September, 2002 (pp. 663-673).

Mohapatra, P.K. and Chaudhry, M.H. (2004). Numerical solution of Boussinesq equations to simulate dam-break flows, *Journal of Hydraulic Engineering*, 130(2): 156-159.

Morris, M.W. (1998). Issues and conclusions from the Munich meeting, *Proceedings of the 2nd CADAM Workshop, Concerted Action on Dam-Break Modelling (CADAM) Programme*, Munich, Germany, 8–9 October, 1998.

Morris, M.W. (2002a). Review of modelling work undertaken so far (Workshop Presentation), *Proceedings of the 2nd IMPACT Project Workshop*, Mo i Rana, Norway, 12–13 September, 2002. Web. 15 Nov. 2012. http://www.impact-project.net

Morris, M.W. (2002b). Breach physical modelling – Test 2 (Workshop Presentation), *Proceedings of the 2nd IMPACT Project Workshop*, Mo i Rana, Norway, 12–13 September, 2002. Web. 15 Nov. 2012. http://www.impact-project.net

Morris, M.W. (2002c). Breach physical modelling – Test 3 (Workshop Presentation), *Proceedings of the 2nd IMPACT Project Workshop*, Mo i Rana, Norway, 12–13 September, 2002. Web. 15 Nov. 2012. http://www.impact-project.net

Morris, M.W. (2005). IMPACT Project: Final Technical Report – January 2005, IMPACT Project, HR Wallingford, Web. 15 Nov. 2012. http://www.impact-project.net

Morris, M.W., Galland, J.-C. and Balabanis, P. (1998). CADAM aims and objectives, *Proceedings of the 1st CADAM Workshop, Concerted Action on Dam-Break Modelling (CADAM) Programme*, Wallingford, UK, 2–3 March, 1998.

Morris, M.W. and Hassan, M.A.A.M. (2004). Breach Formation: Laboratory and numerical modelling (Workshop Presentation), *Proceedings of the 4th IMPACT Project Workshop*, Zaragoza, Spain, 3–5 November, 2002 (CD-ROM).

Morris, M.W., Hassan, M.A.A.M., Zech, Y., Soares-Frazao, S., Alcrudo, F. and Boukalova, Z. (2004). CADAM / IMPACT / FLOODSITE, *Proceedings of the Association of State Dam Safety Officials (ASDSO) Annual Conference*, Phoenix, Arizona, September 26–30, 2004.

Morris, M.W., Hassan, M.A.A.M. and Vaskinn, K.A. (2007). Breach formation: Field test and laboratory experiments, *Journal of Hydraulic Research*, 45(sup1): 9–17.

Morris, M.W., Hassan, M., Kortenhaus, A. and Visser, P. (2009a). Breaching processes: A state of the art review, FLOODsite Report T06-06-03 (Revision 5_2_P01), HR Wallingford, UK. Web. 15 Nov. 2012. http://www.floodsite.net

Morris, M.W, Kortenhaus, A. and Visser, P. (2009b). Modelling breach initiation and growth, FLOODsite Report T06-08-02 (Revision 1_9_P01), HR Wallingford, UK. Web. 15 Nov. 2012. http://www.floodsite.net

Mualem, Y. (1974). A conceptual model of hysteresis, *Water Resources Research*, 10(3): 514-520.

Mualem, Y. (1976). A new model for predicting the hydraulic conductivity of unsaturated porous media, *Water Resources research*, 12(3): 513-522.

Mualem, Y. (1978). Hydraulic conductivity of unsaturated porous media: generalized macroscopic approach. *Water Resources Research*, 14(2): 325-334.

Mujumdar, P.P. (2001). Flood wave propagation - The Saint Venant equations, *Resonance*, May 2001, 66-73.

Newhouse, S., Burns, S.E., Bhatia, S.K., Avila, C.M.C. and Hunt, B.E. (2010). Earth dam failure by erosion, a case history, *Proceedings of the Fifth International Conference on Scour and Erosion*, San Francisco, U.S.A., 7–10 November, 2010.

Nielsen, P. (1998). Coastal groundwater dynamics, *Proceedings of the Third Coastal Dynamics Conference*, Plymouth, United Kingdom, June 1997 (pp. 546–555).

Nielsen, P., Robert, S., Møller-Christiansen, B. and Oliva, P. (2001). Infiltration effects on sediment mobility under waves, *Coastal Engineering*, 42(2): 105-114.

Nistor, I. and Rennie, C.D. (2005). Modelling and risk evaluation of dam structural safety, *Proceedings of the Annual Conference of the Canadian Society for Civil Engineering*, CSCE, Toronto, Canada (CD-ROM).

Ng, C.W.W. and Pang, Y.W. (2000). Experimental investigations of the soil-water characteristics of a volcanic soil, *Canadian Geotechnical Journal*, 37(6): 1252-1264.

Ng, C.W. and Menzies, B. (2007). Advanced unsaturated soil mechanics and engineering, Taylor and Francis, London.

Ng, C.W.W. and Shi, Q. (1998). A numerical investigation of the stability of unsaturated soil slopes subjected to transient seepage, *Computers and Geotechnics*, 22(1): 1-28.

Nogueira, V.D.Q. (1984) (cited in EWRI TC, 2011). A mathematical model of progressive earth dam failure, PhD Thesis, Colorado State University, Fort Collins, CO.

NRCS (1997). Chapter 51 - Earth spillway erosion model, National Engineering Handbook, Part 628 Dams (pp. 1-10).

Öberg, A.L. and Sällfors, G. (1997). Determination of shear strength parameters of unsaturated silts and sands based on the water retention curve, *ASTM Geotechnical Testing Journal*, 20(1): 40-48.

Oh, W.T. and Vanapalli, S.K. (2010). The relationship between the elastic and shear modulus of unsaturated soils, *5th International Conference on Unsaturated Soils*, Barcelona, Spain, 6-8 September 2010 (pp. 341-346).

Ohio Department of Natural Resources (1994). Fact Sheet 94-31. Dam safety: seepage through earthen dams, Division of Soil and Water Resources, Dam Safety Engineering Program. Web. 13 Dec. 2005. http://www.dnr.state.oh.us/water/pubs/fs_div/fctsht31/tabid/4117/Default.aspx

Olsen, N.R.D. (2012). Numerical modelling and hydraulics (3rd ed.) [Lecture notes], Department of Hydraulic and Environmental Engineering, Norwegian University of Science and Technology, Norway. Web. 05 Nov. 2013. http://folk.ntnu.no/nilsol/tvm4155/flures6.pdf

Onda, Y. and Itakura, N. (1997). An experimental study on the burrowing activity of river crabs on subsurface water movement and piping erosion, *Geomorphology*, 20: 279-288.

Öziş, Ü (1996). Historical water schemes in Turkey, *Water Resources Development*, 12(3): 347-383.

Orendorff, B.D. (2009). An experimental study of embankment dam breaching, Master's Thesis, University of Ottawa, Ottawa, Canada.

Orendorff, B.D., Al-Riffai, M., Rennie, C.D., Nistor, I. and St-Germain, P. (2009). The effects of initial breach geometry on dam breach morphology, *Proceedings of the 33rd IAHR World Congress*, Vancouver, Canada, 9–14 August, 2009.

Orendorff, B., Nistor, I. and Al-Riffai, M. and Rennie, C.D. (2013). Breach outflow characteristics of non-cohesive embankment dams subject to blast, *Canadian Journal of Civil Engineering*, 40(3): 243-253.

Paquier, A., Nogues, P. and Herledan, R. (1998). Model of piping in order to compute dambreak wave, *Proceedings of the 2nd CADAM Workshop, Concerted Action on Dam-Break Modelling (CADAM) Programme*, Munich, Germany, 8–9 October, 1998.

Parker, G. (2013). Lecture notes on the interaction of flow and sediment in rivers and the ocean [Lecture notes], University of Minnesota. Web. 05 Nov. 2013. http://hydrolab.illinois.edu/people/parkerg/_private/CourseNotes/CISMnot1.pdf

Parkinson, M. and Stretch, D. (2007). Breaching timescales and peak outflows for perched, temporary open estuaries, *Coastal Engineering Journal*, 49(3): 267-290.

Parlange, J.-Y. (1976). Capillary hysteresis and the relationship between drying and wetting curves, *Water Resources Research*, 12(2): 224-228.

Pereira, C. (1973) (cited in Bhattacharyya, 2011). *Land use and water resources*, Cambridge University Press.

Petitjean, A. (1998). Some words of history…, *Proceedings of the 1st CADAM Workshop, Concerted Action on Dam-Break Modelling (CADAM) Programme*, Wallingford, UK, 2–3 March, 1998.

Peviani, M.A. (1999). Simulation of earth-dams breaking processes by means of a morphological numerical model, *Proceedings of the 4th CADAM Workshop, Concerted Action on Dam-Break Modelling (CADAM) Programme*, Zaragoza, Spain, 17–18 November, 1999.

Pierce, M.W., Thornton, C.I. and Abt, S.R. (2010). Predicting peak outflow from breached embankment dams, *Journal of Hydrologic Engineering*, 15(5): 338-349.

Pickert, G., Jirka, G.H., Bieberstein, A., and Brauns, J. (2004). Soil/water interaction during the breaching process of overtopped embankments, *Proceedings of the 2nd International Conference on River Flow*, Naples, Italy, 23–25 June, 2004 (pp. 903-910).

Pickert, G., Weitbrecht, V. and Bieberstein, A. (2011). Breaching of overtopped river embankments controlled by apparent cohesion, *Journal of Hydraulic Research*, 49(2): 143-156.

Pham, H.Q., Fredlund, D.G. and Barbour, S.L. (2003). A practical hysteresis model for the soil-water characteristic curve for soils with negligible volume change, *Géotechnique*, 53(2): 293-298.

Pham, H.Q., Fredlund, D.G. and Barbour, S.L. (2005). A study of hysteresis models for soil-water characteristic curves, *Canadian Geotechnical Journal*, 42(6): 1548-1568.

Plew, D., Debnath, K., Aberle, J., Nikora, V. and Cooper, G. (2007). In situ flume for studying cohesive and non-cohesive sediment erosion. *Proceedings of the 32nd IAHR World Congress*, Venice, Italy, 1–6 July, 2007.

Pope, S.B. (2000). Turbulent flows, Cambridge University Press, New York.

Ponce, V.M. and Tsivoglou, A.J. (1981). Modeling gradual dam breaches, *Journal of the Hydraulics Division*, 107(7): 829-838.

Powledge, G.R., Ralston, D.C., Miller, P., Chen, Y.H., Clopper, P.E. and Temple, D.M. (1989). Mechanics of overflow erosion on embankments. I: Research activities, *Journal of Hydraulic Engineering*, 115(8): 1040-1055.

Prasuhn, A.L. (1992). Fundamentals of hydraulic engineering, Oxford University Press, New York.
Prosser, I.P. and Rustomji, P. (2000). Sediment transport capacity relations for overland flow, *Progress in Physical Geography*, 24(2): 179-193.
Pugh, C.A. (1985). Hydraulic model studies of fuse plug embankments, REC-ERC-85-7, U.S. Bureau of Reclamation, Denver, CO (December 1985).
Raudkivi, A.J. (1998). Loose boundary hydraulics, Balkema, Rotterdam.
Rennie, C.D. (2009). MATLAB code: Butterworth filter, University of Ottawa, Ottawa, Canada.
Richards, L.A. (1931). Capillary conduction of liquids through porous mediums, *Journal of Applied Physics*, 1(5): 318-333.
Richardson, J.F. and Zaki, W.N. (1954) (cited in van Rijn, 1984c). Sedimentation and fluidization: I, *Transactions of the institution of Chemical Engineers*, 32: 35–53.
Rickenmann, D. (1991). Hyperconcentrated flow and sediment transport at steep slopes, *Journal of Hydraulic Engineering*, 117(11): 1419-1439.
Rickenmann, D. (1997). Sediment transport in Swiss torrents, *Earth surface processes and landforms*, 22(10): 937-951.
Rico, M., Benito, G. and Diez-Herrero, A. (2008). Floods from tailings dam failures, *Journal of Hazardous Materials*, 154(1): 79-87.
Rowe, P.N. (1987) (cited in van Rhee, 2010). A convenient empirical equation for estimation of the Richardson-Zaki exponent, *Chemical Engineering Science*, 42(11): 2795-2796.
Rozov, A.L. (2003). Modeling of washout of dams, *Journal of Hydraulic Research*, 41(6): 565-577.
Sainte-Marie, J. and Bristeau M.-O. (2008). Derivation of a non-hydrostatic shallow water model; Comparison with Saint-Venant and Boussinesq systems, *Discrete and Continuous Dynamical Systems - Series B*, 10: 733–759.
Schlichting, H. (1968) (cited in French, 1985). Boundary-layer theory (6th ed.), McGraw-Hill Book Company, New York.
Schmocker, L. and Hager, W.H. (2009). Modelling dike breaching due to overtopping, *Journal of Hydraulic Research*, 47(5): 585–597.
Schmocker, L. (2011). Hydraulics of dike breaching, PhD Thesis, ETH Zürich, Zurich, Switzerland.
Schmocker, L. and Hager, W.H. (2012). Plane dike-breach due to overtopping: effects of sediment, dike height and discharge, *Journal of Hydraulic Research*, 50(6): 576-586.
Schnitter, N.J. (1994) (cited in Bhattacharyya, 2011). *A history of dams*, A.A. Balkema Publishers, Rotterdam.
Schoklitsch, A. (1962) (cited in Bathurst *et al.* 1987). Handbuch des wasserbaus (3rd ed.), Springer-Verlag, Vienna.
SDEC (2010). SDEC France, Web. 21 May 2010. http://www.sdec-france.com/
Smart, G.M. (1984). Sediment transport formula for steep channels, *Journal of Hydraulic Engineering*, 110(3): 267-276.
Spinewine, B., Delobbe, A., Elslander, L. and Zech, Y. (2004). Experimental investigation of the breach growth process in sand dikes. *River Flow 2002: 2nd International Conference on Fluvial Hydraulics*, Naples, Italy, 23–25 June, 2004 (pp. 23-25).
Shields, A. (1936). Anwendung der aenlichkeitsmechanik und der turbulenzforschung auf die geschiebebewegung. Mitteilungen der Preussischen Versuchsanstalt fur Wasserbau und Schiffbau, Berlin, Germany, translated to English by W.P. Ott and J.C. van Uchelen, CalTech, Pasadena, CA.
Shuibo, P., Mingsen, Q., Liangxian, W., Guoyi, X., Yongqiang, S., Longda, X., Cuiyu, M., Loukola, E., Pyyny, J., Reiter, P., Rytkönen, T. and Alanko., M. (1993). Part I:

Investigation report on dam safety research in China, Chinese-Finnish Cooperative Research Work on Dam Break Hydrodynamics, Series A 167, National Board of Waters and the Environment, Helsinki, Finland, 92 p.

Simmler, H. and Samet, L. (1982). Dam failure from overtopping studied on a hydraulic model, *Proceedings of the 14th Congress of the International Commission on Large Dams*, ICOLD, Rio de Janeiro, Brazil, 3–7 May, 1982.

Simon, A. and Collison, A.J. (2001). Pore-water pressure effects on the detachment of cohesive streambeds: seepage forces and matric suction, *Earth Surface Processes and Landforms*, 26(13): 1421-1442.

Singh, B. and Varshney, R.S. (1995). Engineering for embankment dams, A.A. Balkema, Rotterdam.

Singh, K.P. and Snorrason, A. (1984). Sensitivity of outflow peaks and flood stages to the selection of dam breach parameters and simulation models, *Journal of Hydrology*, 68(1): 295-310.

Singh, U. (2008). *A History of Ancient and Early medieval India: from the Stone Age to the 12th century*, Prentice Hall.

Singh, V.P. (1996). *Dam breach modeling technology*, Water Science and Technology Library, vol. 17, Kluwer Academic Publisher, The Netherlands.

Singh, V.P. and Quiroga, C.A. (1988). Dimensionless analytical solutions for dam-breach erosion. *Journal of Hydraulic Research*, 26(2): 179-197.

Singh, V.P. and Scarlatos, P.D. (1988). Analysis of gradual earth-dam failure, *Journal of Hydraulic Engineering*, 114(1): 21-42.

Singh, V.P., Scarlatos, P.D., Collins, J.G. and Jourdan, M.R. (1988). Breach erosion of earthfill dams (BEED) model, *Natural Hazards*, 1(2): 161-180.

Smalley, I. (1992). The Teton dam: Rhyolite foundation + loess core = disaster, *Geology Today*, 8(1): 19–22.

Smart, G.M. (1984). Sediment transport formula for steep channels, *Journal of Hydraulic Engineering*, 110(3): 267-276.

Smith, N.A.M. (1970). The Roman dams of Subiaco, *Technology and Culture*, 11(1): 58-68.

Soil Conservation Service (SCS) (1981). Simplified dam-breach routing procedure. Technical Release No. 66 (Rev. 1), USDA, Washington, DC.

Song, T., Chiew, Y.-M. and Chin, C.O. (1998). Effect of bed-load movement on flow friction factor, *Journal of Hydraulic Engineering*, 124(2): 165-175.

Steetzel, H.J. and Visser, P.J. (1992). Profile development of dunes due to overflow, *Proceedings of the International Conference of Coastal Engineering*, Venice, Italy, 4–9 October, 1992, pp. 2669-2679.

Stretch, D. and Parkinson, M. (2006). The breaching of sand barriers at perched, temporary, open/closed estuaries – A model study, Coastal Engineering Journal, 48(1); 13-30.

Tayfur, G. and Singh, V.P. (2012). Transport capacity models for unsteady and non-equilibrium sediment transport in alluvial channels, *Computers and Electronics in Agriculture*, 86: 26-33.

Thomas, H.H. (1976). The engineering of large dams: Volume 1, John Wiley & Sons Ltd., London.

Tingsanchali, T. and Chinnarasri, C. (2001). Numerical modelling of dam failure due to overtopping, *Hydrological Sciences Journal*, 46(1): 113-130.

Tinney, E.R. and Hsu, H.Y. (1961). Mechanics of washout of an erodible fuse plug, *Journal of the Hydraulics Division*, 87(3): 1-29.

Topping, A.R. (1998). Foreword. *The river dragon has come! The Three Gorges Dam and the fate of China's Yangtze River and its people*, By Dai Qing, M.E. Sharpe Inc., New York.

Tsakiris, G., Bellos, V. and Ziogas, C. (2010). Embankment dam failure: a downstream flood hazard assessment, *European Water*, 32: 35-45.

Ulrich, T. (1987). Stability of rock protection on slopes, *Journal of Hydraulic Engineering*, 113(7): 879-891.

UMS (2012). T5 Tensiometer, *UMS*. Web. 15 Nov. 2012. http://www.ums-muc.de/en/products/tensiometer/t5.html

U.S. Army Corps of Engineers (USACE) (1979). Appendix D. Recommended guidelines for safety inspection of dams, ER 1110-2-106, U.S. Army Corps of Engineers, Washington, DC, September 1979.

U.S. Bureau of Reclamation (USBR) (1987). Design of small dams, United States Department of the Interior, Denver, Colorado.

U.S. Bureau of Reclamation (USBR) (1988). Downstream hazard classification guidelines. ACER Technical Memorandum No. 11, U.S. Department of the Interior, Denver, Colorado.

U.S. Bureau of Reclamation (USBR) (2002). Federal Investigative Board: Report of failure of Kelly Barnes Dam flood and findings, *United States Bureau of Reclamation*. Web. 26 Jun. 2010. http://ga.water.usgs.gov/publications/ToccoaFIBReport

Vanapalli, S.K. (1994). Simple test procedures and their interpretation in evaluating the shear strength of an unsaturated soil, PhD Thesis, University of Saskatchewan, Saskatoon, Canada.

Vanapalli, S.K., Fredlund, D.G., Pufahl, D.E. and Clifton, A.W. (1996). Model for the prediction of shear strength with respect to soil suction, *Canadian Geotechnical Journal*, 33(3): 379-392.

Vanapalli, S.K., Sillers, W.S. and Fredlund, M.D. (1998). The meaning and relevance of residual water content to unsaturated soils, *Proceedings of the 51st Canadian Geotechnical Conference*, Edmonton, Canada, 4–7 October, 1998 (pp. 101-108).

Vanapalli, S.K. and Fredlund, D.G. (1999). Empirical procedures to predict the shear strength of unsaturated soils, *11th Asian Regional Conference on Soil Mechanics and Geotechnical Engineering*, Seoul, Korea, 16-20 August, 1999 (pp. 93-96).

Van Genuchten, M.T. (1980). A closed-form equation for predicting the hydraulic conductivity of unsaturated soils, *Soil Science Society of America Journal*, 44(5): 892-898.

Vanoni, V.A. (1975) (cited in Prasuhn, 1992). Sedimentation engineering, *ASCE Manuals and Reports on Engineering Practice*, No. 54, New York.

Vanoni, V.A. and Brooks, N.H. (1957) (cited in Francalanci *et al.* 2008). Laboratory studies of the roughness and suspended load of streams, Rep. No. E68, Sedimentation Laboratory, California Institute of Technology, Pasadena, California.

Van Rhee, C. (2010). Sediment entrainment at high flow velocity, *Journal of Hydraulic Engineering*, 136(9): 572-582.

Van Rhee, C. and Bezuijen, A. (1992). Influence of seepage on stability of sandy slope, *Journal of Geotechnical Engineering*, 118(8): 1236-1240.

Van Rijn, L. (1984a). Sediment Pick-Up Functions, *Journal of Hydraulic Engineering*, 110(10): 1494–1502.

Van Rijn, L. C. (1984b). Sediment transport, part I: bed load transport. *Journal of hydraulic Engineering*, 110(10): 1431-1456.

Van Rijn, L.C. (1984c). Sediment transport, Part II: Suspended load transport, *Journal of Hydraulic Engineering*, 110(11): 1613-1641.

Van Rijn, L.C. (1993) (cited in Visser, 1995). Principles of sediment transport in rivers, estuaries and coastal seas, Aqua Publications, Amsterdam, The Netherlands.

Van Rijn, L. C. (2007). Unified view of sediment transport by currents and waves. I: Initiation of motion, bed roughness, and bed-load transport, *Journal of Hydraulic Engineering*, 133(6): 649-667.

Vaskinn, K.A. (2004). Physical modeling of breach formation: Large scale field tests (Workshop Presentation), *Proceedings of the 4th IMPACT Project Workshop*, Zaragoza, Spain, 3–5 November, 2002 (CD-ROM).

Vaskinn, K.A., Løvoll, A. and Höeg, K. (2004). WP2.1 Breach formation: Large scale embankment failure, IMPACT Project, Web. 15 Nov. 2012. http://www.impact-project.net

Visser, P.J. (1988). A model for breach growth in a dike-burst, *Proceedings of the International Conference on Coastal Engineering*, Malaga, Spain, June 20–26, 1988, pp. 1897-1910.

Visser, P.J. (1995). Application of sediment transport formulae to sand-dike breach erosion, Communications on Hydraulic and Geotechnical Engineering, Report 94-7, Faculty of Civil Engineering, Delft University of Technology (TU Delft), Delft, The Netherlands.

Visser, P.J. (1998). Breach growth in sand-dikes, PhD Thesis, Delft University of Technology, Delft, The Netherlands.

Visser, P. J. (2000). A Model for breach erosion in sand-dikes. *Proceedings of the International Conference on Coastal Engineering*, ASCE, Vol. 4, Sidney, Australia, 16–21 July, 2000, pp. 3829-3842.

Visser, P.J., Vrijling, J.K. and Verhagen, H.J. (1990). A field experiment on breach growth in sand-dikes, *Proceedings of the 22nd International Conference on Coastal Engineering*, Chapter 158, Delft, The Netherlands, pp. 2087-2100.

Von Thun, J.L. and Gillette, D.R. (1990) (cited in Wahl, 2004). Guidance on breach parameters, Internal Memorandum, U.S. Bureau of Reclamation, U.S. Dept. of the Interior, Denver, CO.

Wahl, T.L. (1998). Prediction of embankment dam breach parameters - A literature review and needs assessment. Dam Safety Report No. DSO-98-004, *Dam Safety Office*, US Department of the Interior, US Bureau of Reclamation, Denver, CO, 1998.

Wahl, T.L. (2004). Uncertainty of predictions of embankment dam breach parameters, *Journal of Hydraulic Engineering*, 130(5): 389-397

Wahl, T.L. (2007). Laboratory investigations of embankment dam erosion and breach processes, Report for CEA Technologies Inc. (CEATI), Dam Safety Interest Group (DSIG), CEATI Report No. T032700-0207A.

Wahl, T.L., Lentz, D.J. and Feinberg, B.D. (2011). Physical hydraulic modeling of canal breaches, *2011 Dam Safety Conference*, *Association of State Dam Safety Officials,* ASDSO, Washington, D.C., 26–29 September, 2011.

Walder, J.S. and O'Connor, J.E. (1997). Methods for predicting peak discharge of floods caused by failure of natural and constructed earth dams, *Water Resources Research*, 33(10): 2337-2348.

Wan, C.F. and Fell, R. (2004). Investigation of rate of erosion of soils in embankment dams, *Journal of Geotechnical and Geoenvironmental Engineering*, 130(4): 373-380.

Wang, H.F. and Anderson, M. P. (1982). Introduction to groundwater modeling: finite difference and finite element methods, W.H. Freeman and Company, San Francisco.

Wang, Z. and Bowles, D.S. (2006a). Three-dimensional non-cohesive earthen dam breach model. Part 1: Theory and methodology, *Advances in Water Resources*, 29(10): 1528-1545.

Wang, Z. and Bowles, D.S. (2006b). Three-dimensional non-cohesive earthen dam breach model. Part 2: Validation and applications, *Advances in Water Resources*, 29(10): 1490-1503.

Wang, Z. and Bowles, D.S. (2006c). Dam breach simulations with multiple breach locations under wind and wave actions, *Advances in Water Resources*, 29(8): 1222-1237.
Webby, M.G. (1996). Discussion of "Peak outflow from breached embankment dam" (Froehlich, 1995b), *Journal of Water Resources Planning and Management*, 122(4): 316–317.
Welty, J.R., Wicks, C.E., Rorrer, G. and Wilson, R.E. (2009). Fundamentals of momentum, heat, and mass transfer (4th ed.), John Wiley & Sons, New York.
Wetmore, J.N. and Fread, D.L. (1984). The NWS Simplified dam break flood forecasting model for desk-top and hand-held microcomputers, Federal Emergency Management Agency (FEMA).
Wilson, K.C. (1966). Bed-load transport at high shear stress, *Journal of the Hydraulics Division*, 92(11): 49-59.
Wilson, K.C. (1987). Analysis of bed-load motion at high shear stress, *Journal of Hydraulic Engineering*, 113(1): 97-103.
Winterwerp, J.C., Bakker, W.T., Mastbergen, D.R. and van Rossum, H. (1992). Hyperconcentrated sand-water mixture flows over erodible bed, *Journal of Hydraulic Engineering*, 118(11): 1508-1525.
Wishart, J.S. (2007). Overtopping breaching of rock-avalanche dams, Master's Thesis, University of Canterbury, Canterbury, Australia.
Wohl, E.E. (2000). *Inland flood hazards: human, riparian, and aquatic communities*, Cambridge University Press.
Wu, W. (2004). Depth-averaged two-dimensional numerical modeling of unsteady flow and nonuniform sediment transport in open channels, *Journal of Hydraulic Engineering*, 130(10): 1013-1024.
Wu, W., Rodi, W. and Wenka, T. (2000). 3D numerical modeling of flow and sediment transport in open channels, *Journal of Hydraulic Engineering*, 126(1): 4-15.
Wurbs, R. A. (1992). Military Hydrology: Report 21, Regulation of streamflow by dams and associated modeling capabilities (No. WES/MP/EL-79-6-21), Army Engineer Waterways Experiment Station Vicksburg MS Environmental Lab.
Xu, Y. and Zhang, L.M. (2009). Breaching parameters for earth and rockfill dams, *Journal of Geotechnical and Geoenvironmental Engineering*, 135(12): 1957-1970.
Yang, C.T. (1973). Incipient motion and sediment transport, *Journal of the Hydraulics Division*, HY10: 1679-1704.
Yang, C.T. (1979). Unit stream power equations for total load, *Journal of Hydrology*, 40(1): 123-138.
Yang, C.T. (1996). Sediment transport: theory and practice, McGraw-Hill, New York.
Yang, C.T. (2006). Erosion and sedimentation manual. Technical Service Center, US Bureau of Reclamation, Denver, Colorado.
Yang, C.T. and Simões, F.J. (1999). Sediment transport and river morphologic changes, *Proceedings of the 4th CADAM Workshop, Concerted Action on Dam-Break Modelling (CADAM) Programme*, Zaragoza, Spain, 17–18 November, 1999.
Yang, H., Rahardjo, H., Leong, E.C. and Fredlund, D.G. (2004). Factors affecting drying and wetting soil-water characteristic curves of sandy soils, *Canadian Geotechnical Journal*, 41(5): 908-920.
Yang C.T. and Ahn J. (2011). User's manual for GSTARS4 (Generalized Sediment Transport model for Alluvial River Simulation version 4.0), Hydroscience and Training Center, Colorado State University, Fort Collins, Colorado, U.S.A..
Yen, B.C. (1993). *Reliability and Uncertainty Analyses in Hydraulic Design: A Report*. American Society of Civil Engineers, ASCE.

Yen, B.C. (2002). Open channel flow resistance, *Journal of Hydraulic Engineering*, 128(1): 20-39.

Young, S., Balluz, L. and Malilay, J. (2004). Natural and technologic hazardous material releases during and after natural disasters: A review, *Science of the Total Environment*, 322(1): 3-20.

Yue, W., Lin, C.-L. and Patel, V. (2003). Numerical simulation of unsteady multidimensional free surface motions by level set method, *International Journal for Numerical Methods in Fluids*, 42: 853-884.

Zhang, L.M., Xu, Y. and Jia, J.S. (2009). Analysis of earth dam failures: A database approach. *Georisk*, 3(3), 184-189.

Zhang, J., Li, Y., Xuan, G., Wang, X. and Li, J. (2009). Overtopping breaching of cohesive homogeneous earth dam with different cohesive strength, *Science in China Series E: Technological Sciences*, 52(10): 3024-3029.

Zhu, Y.H. (2006). Breach growth in clay-dikes, PhD Thesis, Delft University of Technology, Delft, The Netherlands.

Zhu, Y.H., Visser, P.J. and Vrijling, J.K. (2004). Review on embankment dam breach modeling, *New Developments in Dam Engineering*, Taylor & Francis Group, London, UK, 1189-1196.

Zhu, Y.H, Visser, P.J. and Vrijling, J.K. (2006). Laboratory observations of embankment breaching, *Proceedings of the 7th International Conference on Hydroscience and Engineering*, Philadelphia, Pennsylvania, 10–13 September, 2006.

Appendix A
Physically-Based Embankment Breach Mathematical Models

Table A-1: Physically-based embankment breach mathematical models (updated from Morris *et al.* 2009b; EWRI TC, 2011)

Model	Category	Failure Modes	Hydrodynamics	Erosion	Breach Geometry	Notes
Cristofano (1965)	Simplified	Overtopping	BCW flow	Cristofano empirical formula	Trapezoidal	Constant breach width
Harris and Wagner (1967)	Simplified	Overtopping	BCW flow	Schoklitsch (1934) bedload (modified)	Parabolic	Constant top width/depth ratio (3.75)
BRDAM (Brown and Rogers, 1977)	Simplified	Overtopping Piping	BCW flow Orifice flow	Schoklitsch (1934) bedload	Parabolic Circular (piping failure)	
DAMBRK (Fread, 1977)	Simplified	Overtopping	BCW flow	Linear erosion	Rectangular, triangular and trapezoidal	1-D downstream flood routing
Lou (1981)	Simplified	Overtopping	1-D SVE	Du Buoy Einstein 1-D Exner (sediment continuity)	Cosine curve shape	
Ponce and Tsivoglou (1981)	Simplified	Overtopping	1-D SVE	Meyer-Peter and Müller (1948) 1-D Exner (sediment continuity)	Top width a function of discharge	No lateral erosion after time-to-peak
Nogueira (1984)	Simplified	Overtopping	SVE	Meyer-Peter and Müller (1948) Exner equation (sediment continuity)	Determined by effective shear stress No side-slope instability	
NWS-BREACH (Fread, 1984)	Simplified	Overtopping Piping	BCW flow Orifice flow Quasi-steady uniform flow	Smart (1984)	Rectangular and Trapezoidal Circular (piping failure)	Homogeneous, composite & grass-lined embankments Slope stability and sudden collapse mechanisms Tailwater submergence
NWS-SMPDBK (Wetmore and Fread, 1984)	Simplified	Overtopping	Weir flow	None	Rectangular	
BEED (Singh and Scarlatos, 1985)	Simplified	Overtopping	Weir flow Quasi steady uniform flow	Einstein-Brown bedload formula 1-D Exner (sediment continuity)	Trapezoidal Side-slope instability	Tailwater submergence Flood routing algorithm
Giuseppetti and Molinaro (1989)	Simplified	Overtopping	BCW flow	Engelund and Smart	Triangular	
Havnø et al. (1989)	N/A	Overtopping	N/A	Engelund and Smart Meyer-Peter and Müller (1948) Linear predetermined	Trapezoidal	

Model	Category	Failure Modes	Hydrodynamics	Erosion	Breach Geometry	Notes
DEICH_P (Bechteler and Broich, 1991; Broich, 1998a, b)	Parametric	Overtopping	Weir flow	Meyer-Peter and Müller (1948) Smart (1984) Exner equation (sediment continuity)	Trapezoidal	Core collapse control
BREACH (Steetzel and De Vroeg, 1998)	Simplified	Overtopping	Weir flow	Bagnold and Visser (1989)	Rectangular	Sand dikes
BRES (Visser, 1998)	Simplified	Overtopping	BCW flow	Bedload: Engelund-Hansen (1967); Van Rijn (1984); Wilson (1987); Bagnold and Visser (1998) Suspended Sediment Load: Galappatti and Vreugdenhill (1985)	Trapezoidal	Sand dikes (BRES 1.0)
DEICH_N1 and DEICH_N2 (Broich, 1998a, b)	Non-simplified	Overtopping	1-D/2-D SWE	Meyer-Peter and Müller (1948) 1-D/2-D Exner (sediment continuity)	Erosion dependent	DEICH_N2: First 2-D breach numerical model
EDBEACH (Loukola and Huokuna, 1998)	Simplified	Overtopping Piping	BCW flow Orifice flow Quasi-steady uniform flow	Meyer-Peter and Müller (1948)	Trapezoidal Circular (piping failure) Based on maximum sediment load capacity	Homogeneous and composite embankments Allows linking to 1-D and2-D flood routing models
Renard and Rupro (Paquier *et al.* 1998)	Simplified	Piping	Orifice flow	Meyer-Peter and Müller (1948)	Circular (piping failure)	Roof of pipe fails after pipe diameter >= 2/3 embankment height Peak flow is based on statistical data
Peviani (1999)	Non-simplified	Overtopping	1-D SWE	Di Silvio and Peviani (1989) 1-D Exner (sediment continuity)	Trapezoidal Slope stability analysis	
Tingsanchali and Chinnarasri (2001)	Non-simplified	Overtopping	1-D SWE	Meyer-Peter and Müller (1948) Smart (1984) Bagnold-Visser (1988) Rickenmann (1991) Takahashi (1991) 1-D Exner (sediment continuity)	No lateral erosion	Stability of downstream slope using ordinary method of slices Plane overtopping

Model	Category	Failure Modes	Hydrodynamics	Erosion	Breach Geometry	Notes
HR-BREACH (Mohamed et al. 2002)	Simplified	Overtopping Piping	Weir flow	Smart (1984) (cohesive and noncohesive) Yang Bagnold-Visser (1988) Chen (sand) Chen (clay 1) Chen (clay 2) Hanson	Based on shear stress distribution in trapezoidal channels and slope failures due to bending and shear	
NCP-BREACH (Coleman et al. 2002)	Simplified	Overtopping	Weir flow	Empirical erosion rate, based on small-scale experiments	Parabolic	No slope stability assessment
Rozov (2003)	Non-simplified	Overtopping	Weir flow Energy equation	Voinich-Syanojenski (1972) Exner equation (sediment continuity)	Rectangular	
RoDaB (Franca and Almeida, 2004)	Simplified	Overtopping	Weir flow	Empirical relationship 1-D Exner (sediment continuity)	Average lateral to bottom erosion rate ratio (0.8)	Rockfill dams
Wang and Bowles (2006a, b, c)	Non-simplified	Overtopping	2-D SWE	Chang (1992) empirical formula for erosion Smart (1984) for transport capacity	Breach flow and erosion dependent 3-D slope stability analysis	Multiple breach locations Wind and wave action
2dMB (Fäeh, 2007)	Non-simplified	Overtopping	2-D Navier-Stokes	Empirical relationships for bedload and suspended sediment load Meyer-Peter and Müller (1948), Smart and Jaeggi and Schoklitsch (1934) Non-equilibrium transport	Determined by vertical and lateral erosion- Side-slope instability	Hiding function
Macchione (2008) Macchione and Rino (2008)	Simplified	Overtopping Piping	Weir flow	Macchione (1986)	Triangular/Trapezoidal	Input: stage curve and dam geometry
MIKE-11 (Danish Hydraulic Institute, 2009)	Simplified	Overtopping Piping	BCW flow Orifice flow	Engelund-Hansen Exner equation (sediment continuity)	Trapezoidal (overtopping) Circular (piping)	

BCW: Broad-crested weir flow

A.1 NWS-BREACH Model

The NWS-BREACH model's physical relationships use the theoretical principles of dam hydraulics, fluvial erosion and sedimentation, hydrologic mass balances (reservoir storage and inflow hydrograph) and soil mechanics (dam geometry and soil properties). Its computational structure allows for a continuous interplay between such principles and the mechanisms that govern the breach.

A.1.1 Breach Initiation

During the initial stages of the breach, the supercritical flow above the dam crest and downstream slope is governed by the following weir-flow equation:

$$Q_b = 3B_0(\eta_r - z_{BB})^{1.5} \quad \text{(A-1)}$$

where, B_0 is the instantaneous breach width, η_{bc} is the elevation of the breach channel bottom and η_r is the elevation of the free surface in the reservoir. Lengths and discharge are input with units [ft] and [cfs], respectively.

A.1.2 Breach Formation and Propagation

Once overtopping is initiated, erosion in the breach channel takes place at the apex of the downstream slope. The breach channel pivots at the toe of the embankment as the most upstream point of the breach channel moves upstream towards the reservoir as shown in Figure A-1. Once the channel has reached position line A-A, erosion takes place in the vertical direction where the slope of the breach remains constant and in-line with position line B-B.

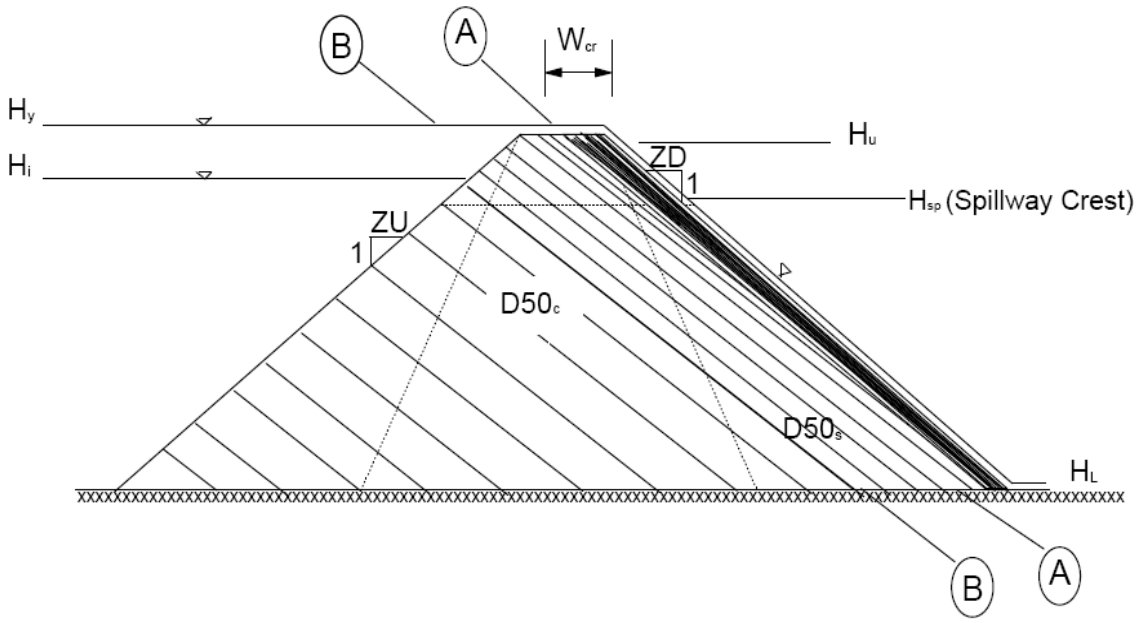

Figure A-1: Side view of dam showing conceptualized overtopping sequence (Fread, 1991)

A.1.2.1 Breach Width

The algorithm calculates the instantaneous breach channel width based on an input parameter, initial breach channel flow depth, y_0, as follows:

$$B_0 = B_r y_0 \tag{A-2}$$

where, B_r is the breach channel width-to-depth ratio defined by the user.

The Froude-critical flow depth in the breach channel is then approximated using the following relationship:

$$\eta_c = \frac{2}{3}(\eta_r - z_{BB}) \tag{A-3}$$

The program then calculates the breach width based on the side-slope stability of the channel, which is a function of the cohesion, c, and angle of internal friction, ϕ, for the embankment material. The erosion of channel is based on equal transport rates for the channel bed and sides, where a stability assessment of the side slopes is carried out simultaneously. The resulting breach cross-section is that of a

trapezoid as shown in Figure A-2. In the occurrence of a side failure, the channel bed erosion is temporarily discontinued until the slumped material is transported by the breach outflow. The breach channel ceases to erode downward once the breach channel bottom elevation reaches the valley floor, however, breach morphology proceeds as a (lateral) widening phase. The model assumes a non-erodible valley floor; however, this may not be the case for certain embankments.

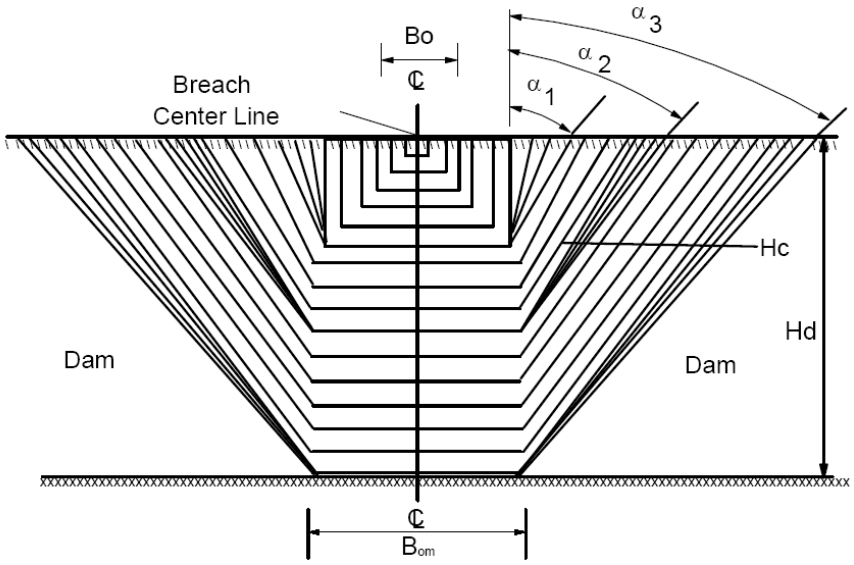

Figure A-2: Front view of dam with breach formation sequence (Fread, 1991)

A.1.2.2 Breach Channel Hydraulics

The model assumes normal flow depth throughout the breach channel and can be justified for long channel reaches as observed by Visser (1998). The normal flow depth, y_n, is based on the imperial Manning formulation:

$$y_n = \left(\frac{Q_b n_M}{1.49 B_0 S_b^{0.5}}\right)^{0.6} \quad \text{(A-4)}$$

where, *t*he Manning coefficient can be computed using Strickler's formulation (see Equation (4.24)).

It is important to note that the Strickler formulation neither considers form roughness, nor roughness due to flow convection at the breach channel inlet. The model, however, does correct the breach outflow as a result of tailwater submergence.

A.1.2.3 Sediment Transport

The model utilizes the equation derived by Smart (1984) which modifies the MPM formulation to steep slopes, such that:

$$Q_s = 3.64\left(\frac{d_{90}}{d_{30}}\right)^{0.2}\rho\frac{R_h^{2/3}}{n_M}S_b^{1.1}(R_hS_b - \Omega_c) \quad \text{(A-5)}$$

where Q_s is the sediment transport rate in units [cfs], and Ω_c is the critical shear stress parameter defined as:

Noncohesive $$\Omega_c = 0.0054\tau_{c,s}^* d_{50} \quad \text{(A-6)}$$

Cohesive $$\Omega_c = \frac{b_c}{62.4}PI^{c_c} \quad \text{(A-7)}$$

where, b_c and c_c are empirical coefficients ($0.003 \leq b_c \leq 0.019$ and $0.58 \leq c_c \leq 0.84$), and $\tau_{c,s}^*$ is the dimensionless critical shear stress modified for steep slopes as follows:

$$\tau_{c,s}^* = \tau_c^* a_s \quad \text{(A-8)}$$

where, τ_c^* is the dimensionless critical shear stress parameter obtained from the Shields curve and a_s is a parameter which accounts the effects of steep slopes and can be defined as:

$$a_s = \cos\phi_b(1 - 1.54\tan\phi_b) \quad \text{(A-9)}$$

where, ϕ_b is in units [degrees].

The formulations, variables and parameters presented in the Fread (1991) differ slightly than those defined in the paper by Smart (1984) due to the use of imperial units.

A.1.2.4 Breach Enlargement by Sudden Collapse

During the migration of the breach channel towards the upstream slope, a force balance is carried out on a wedge-shaped upper portion of the dam as shown in Figure A-3 below. At each time-step, the algorithm conducts a force balance between the hydrostatic forces in the reservoir and the resisting shear forces induced in the embankment zones, acting along both sides and bottom of the wedge (see Figure 4.22). In the event where the shear forces are destabilized, the wedge fails as a mass collapse.

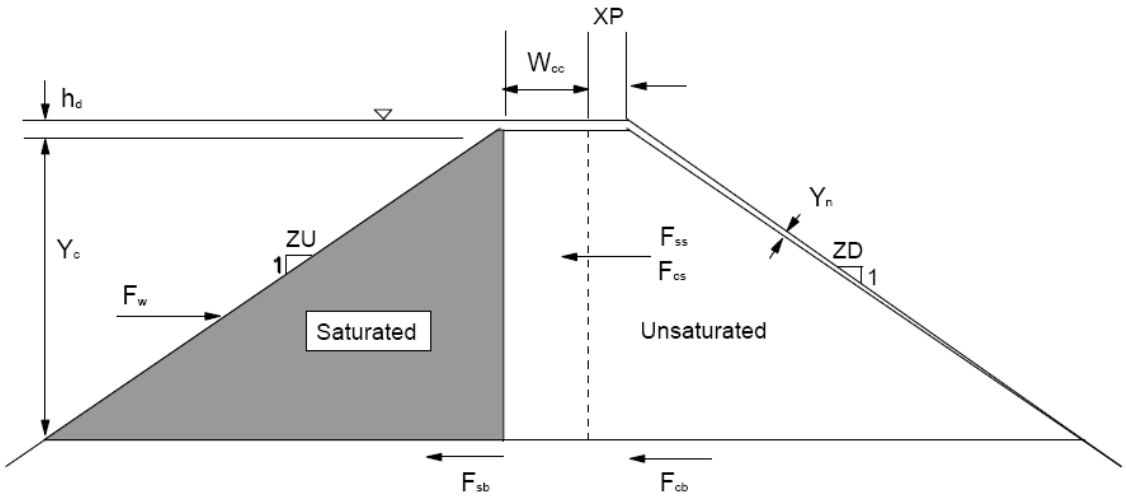

Figure A-3: Side view showing forces used in assessment of sudden collapses (Fread, 1991)

A.1.2.5 Other Features in NWS-BREACH

NWS-BREACH is unique to earlier physically-based models since it considers both man-made and landslide embankments and accounts for non-homogenous (*i.e.* zoned) embankments. Furthermore, NWS-BREACH predicts the outflow hydrograph with respect to second most common failure mechanism; piping. The model is also capable of performing a breach analysis on vegetated and lined downstream surfaces while the outflow from spillways can be considered during reservoir routing. The model also takes into account the choking effect on the breach outflow due to tailwater submergence.

A.2 HR-BREACH Model: New Methodologies

HR-BREACH is very similar to the NWS-BREACH model; however, it has incorporated a few changes to its physical-mathematical relationships that govern the breach process. The provided program was written in C++ code, unlike NWS which is written in FORTRAN. The model utilizes a Graphical User Interface which renders the program more user friendly (see Figure A-4).

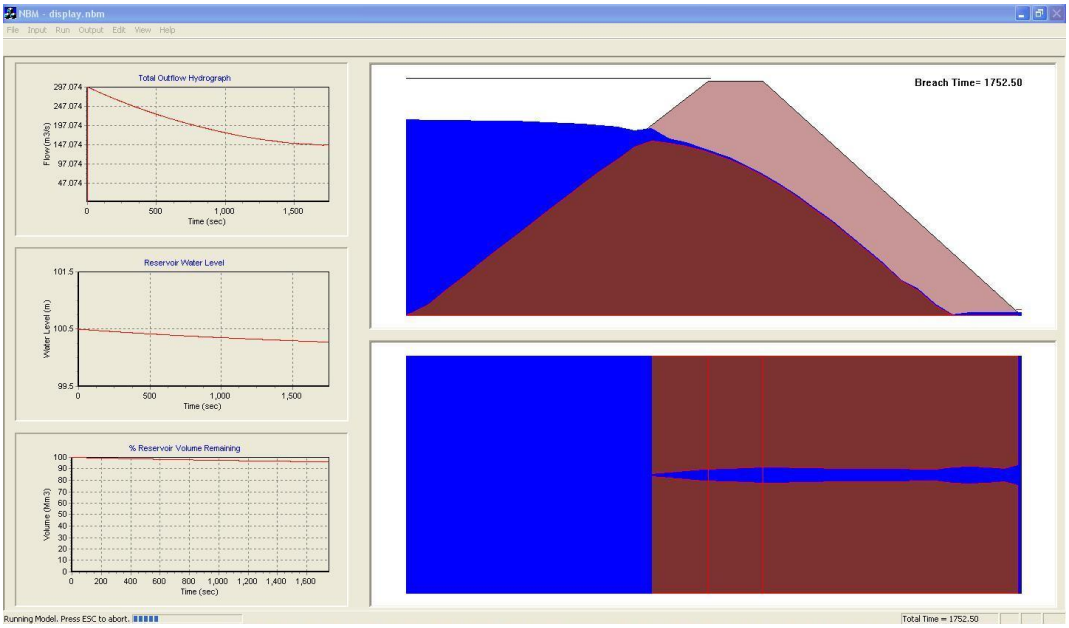

Figure A-4: HR-BREACH user interface during simulation

A.2.1 Data Input

Data input is carried out using an input wizard menu. Almost the same input parameters used in HR-BREACH are present in NWS-BREACH except for two main parameters: space-step, Δx, and the embankment material's tensile strength, σ_f (see Subsection A.2.5).

The downstream boundary conditions can be input in terms of valley cross-section, bed slope and Manning roughness as well as a rating curve or elevation-time relationship. The inflow conditions can also be input using a reservoir head-time

relationship. More than eight data input points can be entered for inflow conditions as well as for the reservoir area and stage. Separate values for d_{90} and d_{30} can also be entered instead of the compulsory d_{90}/d_{30} ratio in NWS-BREACH. The parameters, PI, b_c and c_c, for cohesive soils can be input independently for the shell material as well as for the embankment core, unlike NWS-BREACH where an average value is used. The initial breach depth and width can be input independently unlike NWS where a breach depth-to-width ratio is compulsory. However, the model reports the value of the maximum breach width only, unlike NWS-BREACH which reports the maximum top and bottom widths independently.

A.2.2 Data Output

The output options include the default minimum report which reports the breach characteristics at the defined time-step, a quick report which includes the hydraulic and sediment calculations at each time step, and a detailed report which includes the hydraulic and sediment calculations for each iteration in every time-step. All input and output data are in SI (Metric) units.

The model is capable of using 8 different sediment transport formulations:

- Smart (1984) formulation for both cohesive and noncohesive sediments (*i.e.* similar to NWS)
- Yang
- Bagnold-Visser
- Chen (Sand)
- Chen (Clay 1)
- Chen (Clay 2)
- Hanson

A.2.3 Probabilistic Approach

The model performs Monte Carlo simulations which are based on a probabilistic approach, which takes into account uncertainties of the material and quality of

construction (Mohamed *et al.* 2002). Three categories are defined for material quality: very good, good and poor where a sigmoid function is used to represent the probability distribution for the factor of safety, FOS, as shown in Figure A-5.

$$p(\mathrm{FOS}) = \frac{1}{1+\mathbf{e}^{a_u(\mathrm{FOS}-1)}} \tag{A-10}$$

where, a_u is an uncertainty coefficient.

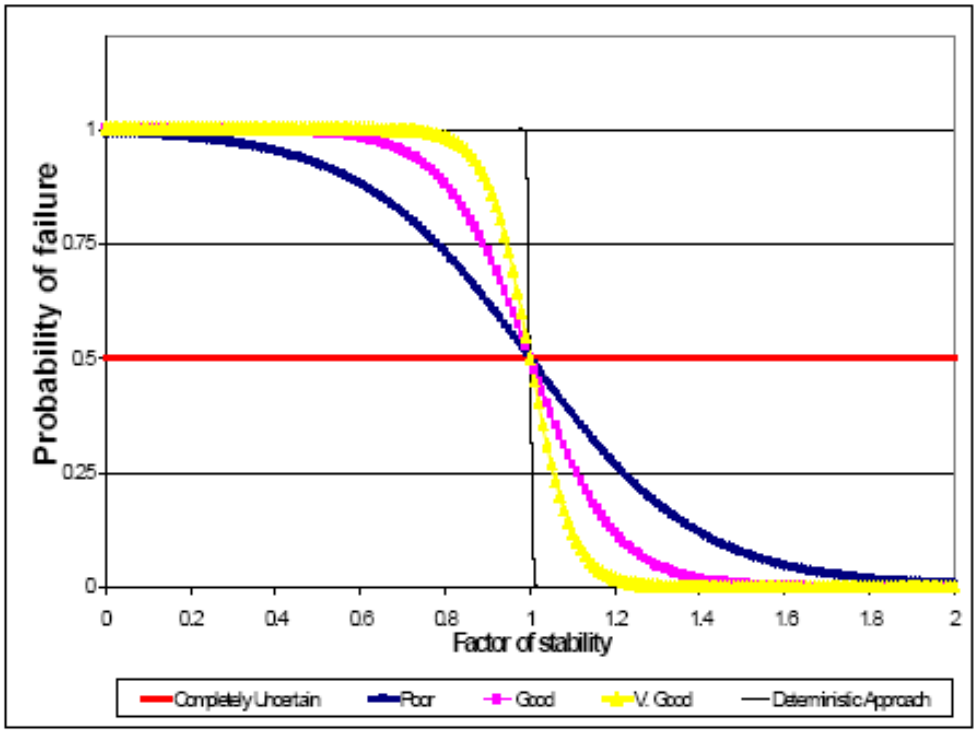

Figure A-5: Probability distribution functions for the slope stability factor of safety (Mohamed *et al.* 1999)

A.2.4 Slope Retreat

The study by Visser (1998) stated that the breach channel slope angle on the downstream face (shown as β_0 in Figure A-6) is adequate to establish normal flow conditions. This angle will not exceed a limit, β_1, for quasi-steady non-uniform flow conditions where a "break" in the breach channel will develop as shown in Figure A-6.

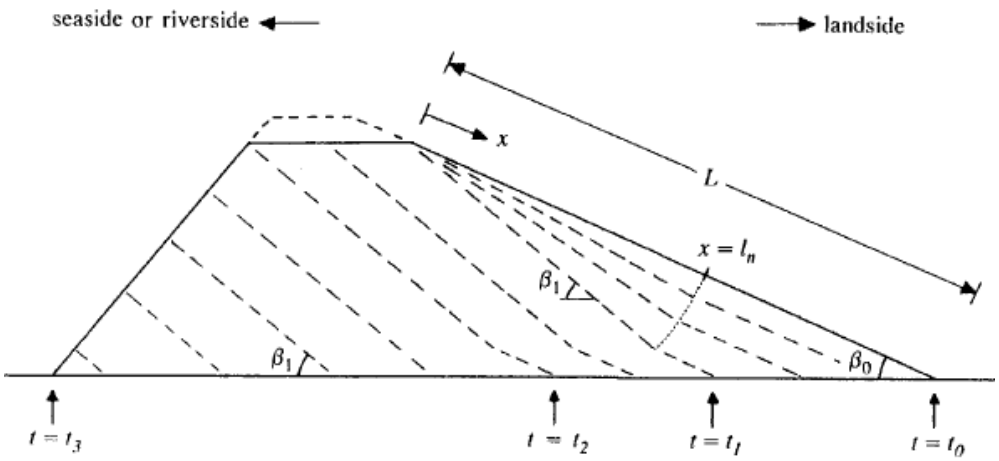

Figure A-6: Erosion of downstream slope during first three stages by Visser (1998)

However, for relatively shorter reaches, the breach slope will be constant with a value equal to the maximum slope angle as shown in Figure A-7. This break possibly corresponds to the transition in energy dissipation rate within the breach channel. Mohamed *et al.* (1999) computes the slope retreat based on a weighted average of the sediment transport rate calculated at finite sections along the slope as follows:

$$\overline{Q_s} = \frac{\sum_i^{imax}\left[\left(\frac{Q_{s,i}+Q_{s,i+1}}{2}\right)(x_{i+1}-x_i)\right]}{L_{DS}} \tag{A-11}$$

where $\overline{Q_s}$ is average sediment transport rate in units [m^3/s], and L_{DS} is length of the downstream slope.

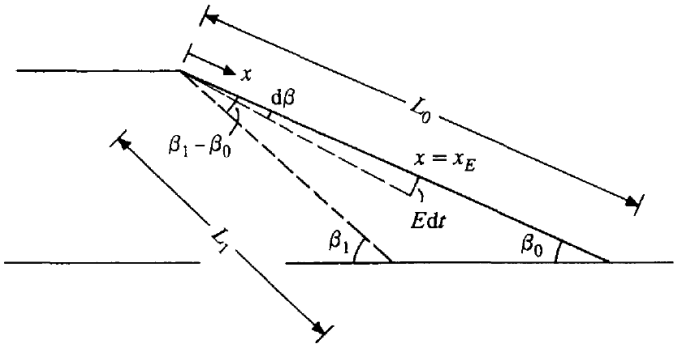

Figure A-7: Longitudinal section of breach channel in unsteady flow (Visser, 1998)

A.2.5 Top Width Adjustment

Mohamed *et al.* (1999) proposed a new methodology for adjusting the top width of the breach channel due to bed erosion. Similar to Fread (1991), they assumed that the breach channel initiates with a rectangular cross-section. However, they stated that the erosion in the breach-channel bottom and sides of the initial rectangular channel will be due to the shear stress distribution proposed by Lane (1953). Accordingly, the bottom width and depth of the breach channel will increase as shown in Figure A-8 and Figure A-9. The top width will remain constant since it is not exposed to the flow. The top width is then adjusted due to side-slope instabilities.

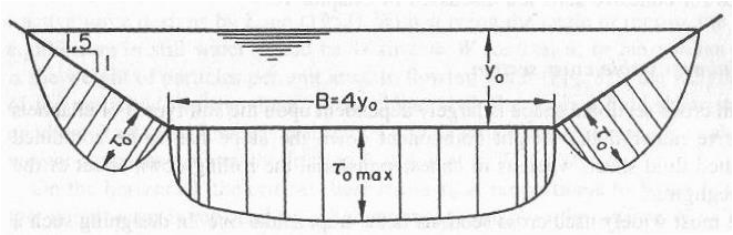

Figure A-8: Distribution of shear stress in a trapezoidal section (Lane, 1952, from Raudkivi, 1998)

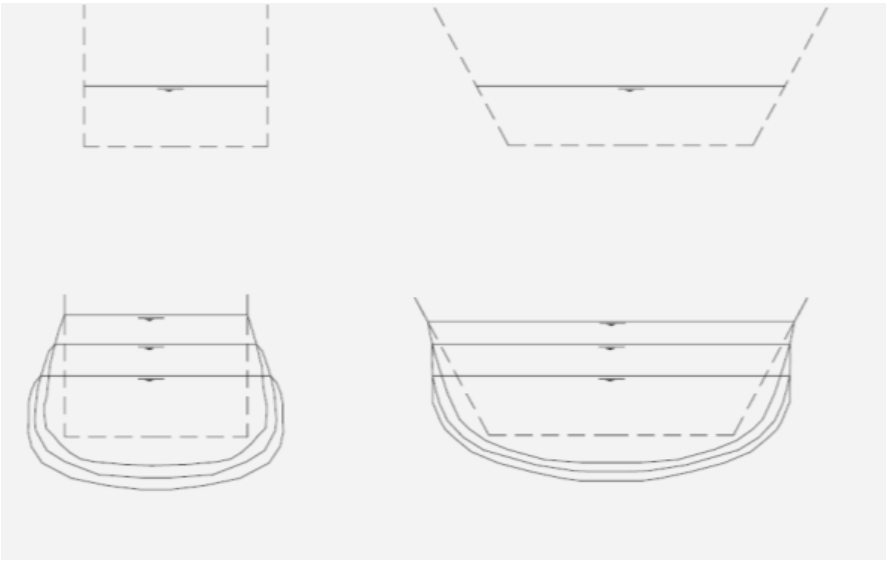

Figure A-9: Rectangular and trapezoidal breach channels (top) prior to erosion (bottom) after three successive erosion time-steps (Mohamed *et al.* 1999)

Side-slope instabilities can take place either in bending or in shear. In bending, a tension crack develops as the tensile force exerted on the channel walls exceeds that of the tensile strength of the soil. Once the side-walls collapse, the breach channel becomes rectangular in cross-section and the erosion process continues while successive assessments of side-slope stability are carried out. The bending moment , M_0, acting on the overhanging material is computed as the summation of the moments due to the saturated, unsaturated and dry regions in the breach channel as well as the hydrostatic forces exerted on the breach channel side-walls (see Figure A-10 below). It is unclear, however, if negative PWP in the unsaturated zone above the phreatic surface are considered in the shear stress analysis.

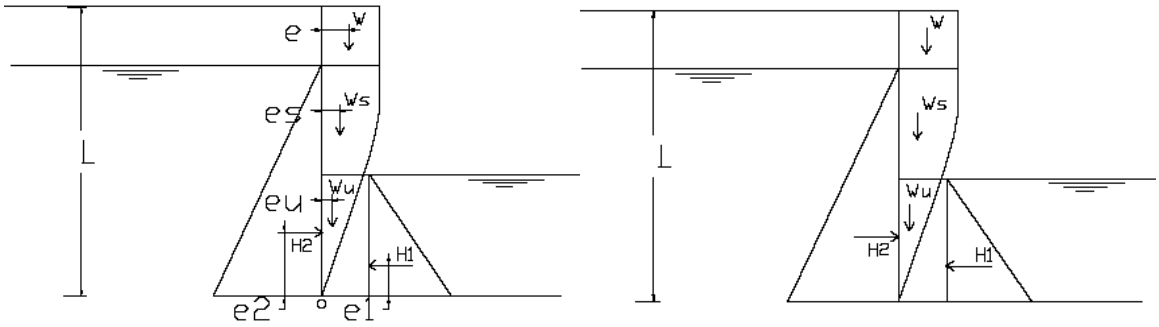

Figure A-10: (Left) Forces and eccentricities considered in bending failure analysis (right) Forces in shear failure analysis (Mohamed *et al.* 2002)

The tensile stress acting on the failure planes, σ_a, can be determined from the following relationship, where failure occurs if $\sigma_a > \sigma_f$:

$$\sigma_a = \frac{(H_2 - H_1)}{L} + \frac{6M_0}{L^2} \qquad \text{(A-12)}$$

The second mode of slope instability is due to shear failure, and is more likely to occur in non-cohesive embankments once the destabilizing forces exceed the stabilizing forces as illustrated in Figure A-10. The stability criterion used in this analysis is based on the FOS using equilibrium of forces.

A.2.6 Monte Carlo Simulations

An alternative method for determining uncertainty can be conducted by means of a Monte Carlo analysis. In this type of analysis, several runs are carried out for the entire range of input parameters (IMPACT, 2004b). Based on the probability distribution, the output of the runs are then ranked, while confidence limits defined by the user (usually 5% and 95%) determine the range (or uncertainty) of the embankment breach characteristic of interest (see Figure A-11). Figure A-12 shows the output, which is a peak flow distribution from a Monte Carlo run performed using HR-BREACH. The variation of 9 input parameters required a total of 1,000 simulations. Based on a 5% and 95% confidence limit, the range of uncertainty is 55 – 180m^3/s, with a likely peak outflow of 120m^3/s. Such simulations, however, are very time consuming.

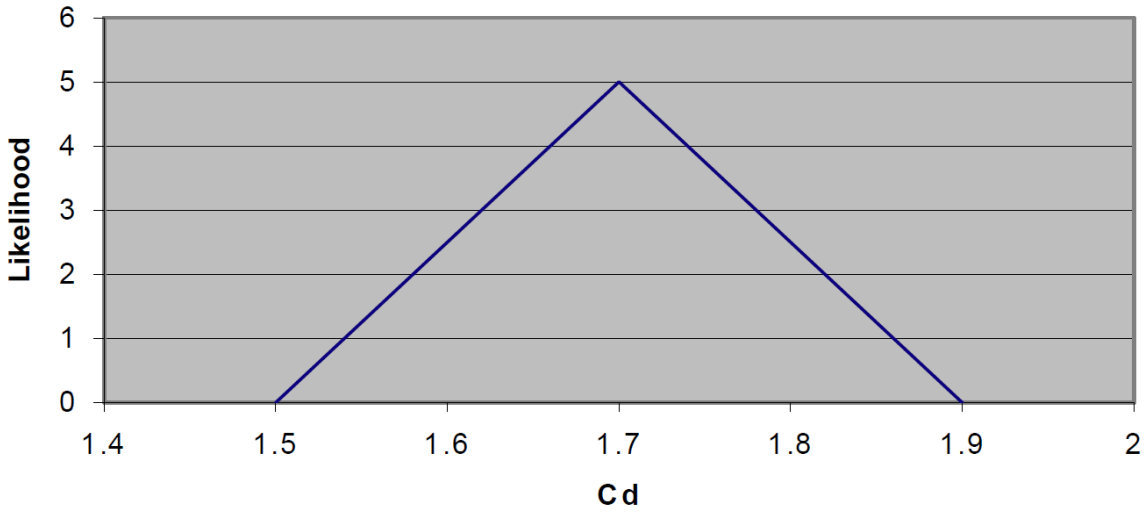

Figure A-11: Triangular probability distribution for coefficient of discharge, C_d (IMPACT, 2004b)

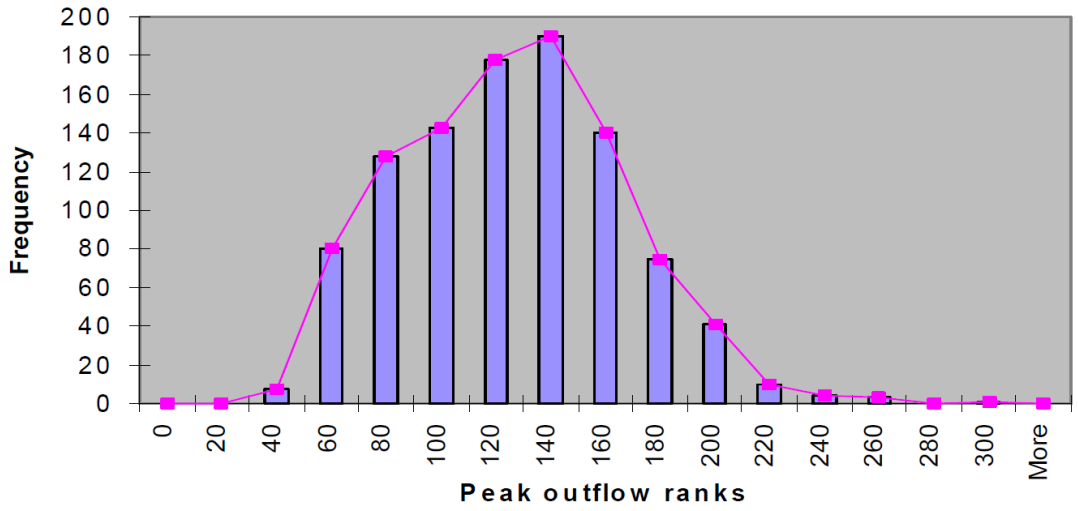

Figure A-12: Peak outflow distribution from Monte Carlo analysis using HR-BEACH based on 9 input parameters (IMPACT, 2004b)

A.3 BRES Model (Visser, 1998)

Visser (1998) developed the BRES model, which predicts the breach shape and the outflow hydrograph following the breach of sand dikes. It was calibrated using data from the Zwin Channel field tests in 1989 (Visser *et al.* 1990) and 1994 (Visser, 2000) and the Delft University of Technology (TU Delft) laboratory experiments in 1988 (Visser, 1988) and 1996 (Visser, 2000) which are described in greater detail in Subsections B.1.1 and B.2.1 in Appendix B. The model was validated using eye witness data of the breach development following the breach of the Noord Dike in Papendrecht, Netherlands, which occurred on February 1, 1953 (Visser, 2000). The five-stage breach process of the BRES model is illustrated in Figure A-6, Figure A-7 and Figure A-13, and can be summarised as follows:

1. Steepening of the slope angle, β_0, of the downstream face to a critical value, β_1, ($t_0 < t \leq t_1$)
2. Erosion of the downstream slope upstream at an angle, β_0 and consequential decrease of crest width ($t_1 < t \leq t_2$)
3. Lowering of the dike's crest with a constant side-slope angles and consequential increase of breach top width ($t_2 < t \leq t_3$)

4. Lateral growth of the breach channel whereas the flow regime through the breach channel is critical ($t_3 < t \leq t_4$)
5. Lateral growth of the breach channel whereas the flow regime through the breach channel is subcritical ($t_4 < t \leq t_5$)

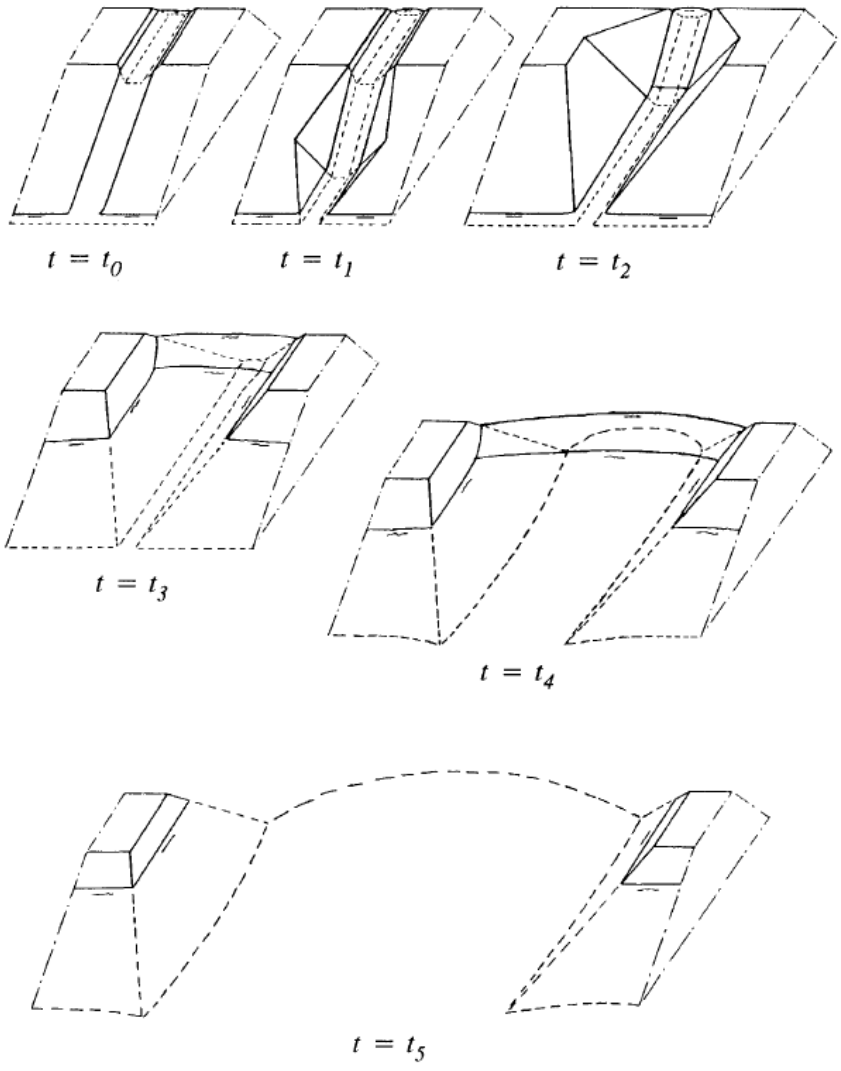

Figure A-13: Schematic showing five breach stages by Visser (1998)

The steepening of the breach channel in Stage 1 is attributed to accelerating flow, whereas the break in the slope in the downstream reaches occurs after normal flow conditions have been established.

Appendix B

Embankment Breach Experimental Programs

Table B-1: Embankment breach laboratory and field experimental programs (updated after Wahl, 2007; EWRI TC, 2011)

Organization	Dates	Test Description	Literature Cited	No. of Tests	Research Focus
Washington State University (Pullman, WA)	1959	Fuse plug embankment laboratory and field tests	Tinney and Hsu (1961)	13	Washout mechanics and rate Similitude relationships
University of Windsor (Windsor, ON)	1978	Laboratory tests on fuse-plug embankments	Chee (1978)	unknown (>33 estimated)	Fuse-plug breaching
Graz University of Technology (Graz, Austria)	< 1982	Laboratory tests of homogeneous and composite embankments	Simmler and Samet (1982)	22	Fill material (grain size, uniformity, grain shape, angle of repose) Embankment zoning (impervious element location) Reservoir storage volume Shoulder slopes Compaction
USBR (Denver, CO)	1985	Laboratory tests on overtopping flow of low embankment dams	Pugh (1985)	8	Washout mechanics and rates Similitude relationships Embankment size Pilot channel size and position Structural configuration
USBR (Denver, CO)	mid-1980s	Laboratory tests on overtopping flow of low embankment dams	Dodge (1988)	9	Downstream protection Downstream slope gradation Unit discharge Degree of compaction
Delft University of Technology (TUD) (Delft, Netherlands)	1988	Laboratory tests of sand dikes	Visser (1988)	3	Development and verification of a mathematical model
Chinese Ministry of Water Resources	1978-1982	Fuse plug embankment field tests	Shuibo *et al.* (1993); Loukola and Huokona (1998)	55	Initial water surface level Scale series Clay core configurations
Chinese-Finnish Cooperative Research Work on Dam Break Hydrodynamics	1992-1993				
Engineering Research Center, Colorado State University (Fort Collins, CO)	1988	Outdoor flume overtopping tests	AlQaser (1991)	2	Overfall progression

Organization	Dates	Test Description	Literature Cited	No. of Tests	Research Focus
University of the Federal Armed Forces (Munich, Germany)	< 1994	Laboratory tests of overtopped noncohesive embankments	Kulisch (1994); Bechteler and Kulisch (1998); Broich (1998a)	7	Grain size
Technical Advisory Committee on Water Defences (TAW) (Netherlands)	1989, 1994	Field tests of sea (sand) dikes	Visser *et al.* (1990); Visser (1998); Visser (2000)	2	Development and verification of a mathematical model
Delft University of Technology (TUD) (Delft, Netherlands)	1992	Laboratory tests of sand dikes	Steetzel and Visser (1992); Visser (1995, 1998)	9	Validations of sediment transport formulations
Delft University of Technology (TUD) (Delft, Netherlands)	1996	Laboratory tests of sand dikes	Visser (1998)	1	Development and verification of a mathematical model
HR-Wallingford, Wallingford (Wallingford, UK)	1998	Laboratory tests of overtopped noncohesive embankments	Mohamed *et al.* (1999)	3	New methodology for side-slope failures Crest widths
University of Birmingham (Birmingham, UK)	1998	Laboratory tests of overtopped sand embankments	Lecointe (1998)	2	Cross-channel dam and river bank failures
USDA ARS-HERU (Stillwater, OK)	1998-2001	Full-scale overtopping tests	Hahn *et al.* (2000); Hanson *et al.* (2003); Hanson *et al.* (2005)	7	Breach erosion process and headcut migration for various soils and compaction water contents
USDA ARS-HERU (Stillwater, OK)	1999	Outdoor flume tests	Hanson and Temple (2001)	4	Vegetated and non-vegetated channels Unit discharge
Asian Institute of Technology, Khlong Nueng (Pathum Thani, Thailand)	2000, 2003	Laboratory tests of overtopped noncohesive embankments	Tingsanchali and Chinnarasri (2001); Chinnarasri *et al.* (2003)	20	Calibration of numerical model Erosion and sliding failure modes in overtopping Grain size (and gradation) Downstream slope Overtopping height Inflow
Asian Institute of Technology, Khlong Nueng (Pathum Thani, Thailand)	< 2004	Laboratory tests of overtopped cohesive embankments	Chinnarasri *et al.* (2004)	9	Downstream slope Grain size Inflow Scaling embankment breaching characteristics

Organization	Dates	Test Description	Literature Cited	No. of Tests	Research Focus
CEHIDRO, Instituto Superior Technico (Lisbon, Portugal)	2001	Laboratory tests of overtopped rockfill dams	Franca and Almeida (2002, 2004)	22	Rockfill dams
University of Auckland (Auckland, New Zealand)	1996-1998	Laboratory tests on overtopped noncohesive embankments	Coleman *et al.* (2002)	4	Dimensionless breach characteristics Various grain sizes
IMPACT Project - HR Wallingford (Wallingford, UK)	2002	Laboratory tests on overtopped embankments (test series 1)	IMPACT (2004a); Morris *et al.* (2007)	9	Homogeneous non-cohesive embankments
IMPACT Project - HR Wallingford (Wallingford, UK)	2003	Laboratory tests on overtopped embankments (test series 2)		8	Homogeneous cohesive embankments
IMPACT Project - HR Wallingford (Wallingford, UK)	2003	Laboratory tests on piping failure of embankments (test series 3)		5	Piping failures
IMPACT Project - Mo i Rana (Nordland County, Norway)	2002-2003	Field tests on embankment overtopping and piping	Vaskinn *et al.* (2004); Morris *et al.* (2007)	5	Rockfill, composite, homogeneous, cohesive and non-cohesive embankments
Norwegian National Research Programme, SWECO Gröner (Norway)	2002	Field tests on embankment overtopping and piping	Vaskinn *et al.* (2004)	2	Rockfill embankments
USDA ARS-HERU (Stillwater, OK)	2003	Large-scale embankment tests	Hunt *et al.* (2005)	3	Influence of soil material and compaction water content on breach widening phase
Institute of Hydromechanics, University of Karlsruhe (Karlsruhe, Germany)	< 2004	Laboratory tests of overtopped noncohesive embankments	Pickert *et al.* (2004)	3	Unsaturated soil and side slope collapses Grain size
Université Catholique de Louvain (Louvain-la-Neuve, Belgium)	< 2004	Laboratory tests of overtopped sand dikes	Spinewine *et al.* (2004)	11	Nonintrusive breach evolution measuring system Erodible bed
Department of Civil Engineering, University of KwaZulu-Natal (Durban, South Africa)	2005	Laboratory tests of estuary sand berms	Stretch and Parkinson (2006); Parkinson and Stretch (2007)	24	Scaling of geometric relationships

Organization	Dates	Test Description	Literature Cited	No. of Tests	Research Focus
Leichtweiß-Institute for Hydraulic Engineering and Water Resources, (Braunschweig, Germany)	2005	Laboratory tests of overtopped dikes with and without waves	Geisenhainer and Kortenhaus (2006)	16	Overflow and wave overtopping Clay lining Landward and seaward breach initiation
Delft University of Technology (TUD) (Delft, Netherlands)	2005	Laboratory tests of overtopped dikes	Zhu *et al.* (2006)	5	Cohesive vs. noncohesive Compaction water content in cohesive embankments
Wairakei Research Centre (Taupo, New Zealand)	< 2007	Laboratory tests of overtopped landslide dams	Davies *et al.* (2007)	16	Landslide dams Valley bed slope Upstream and downstream slope factors
University of Canterbury (Christchurch, New Zealand	< 2007	Laboratory tests of overtopped noncohesive embankments	Wishart (2007)	44	Rock-avalanche dams Scaling Saturation Armouring
Nanjing Hydraulic Research Institute (Anhui, China)	< 2009	Field tests on cohesive embankments	J. Zhang *et al.*(2009)	4	Soil cohesion
Swiss Federal Institute of Technology (ETH Zurich) (Zurich, Switzerland)	2009	Laboratory tests on overtopped river dikes	Schmocker and Hager (2009, 2012)	39	Plane dike tests Test repeatability Side-wall effects Scale effects by means of scale families
USDA ARS-HERU (Stillwater, OK)	< 2010	Large-scale embankment piping tests	Hanson *et al.* (2010)	4	Influence of soil material on internal erosion and piping failure mechanism
USBR (Denver, CO)	2010	Laboratory tests of canal overtopping and piping	Wahl *et al.*(2011)	3	Physical modeling of canal breaches Scaling
Institute of Hydromechanics, University of Karlsruhe (Karlsruhe, Germany)	< 2011	Laboratory tests of overtopped noncohesive river embankments	Pickert *et al.* (2011)	7	Unsaturated soil and side slope collapses Grain size
O.H. Hinsdale Wave Research Laboratory, Oregon State University (Corvalis, OR)	2011	Full-scale levee overtopping tests	Li *et al.* (2012)	17	Influence of wave and surge attacks on turf mats

Table B-2: Test matrix showing embankment breach experimental programs (laboratory)

Parameter	Date	1988	1992	< 1994	June 3, 1996	1996-1998	1998	< 2000	< 2000
	Literature Cited	Visser (1988)	Steetzel and Visser (1992) Visser (1995, 1998)	Bechteler and Kulisch (1998) Broich (1998a)	Visser (2000)	Coleman *et al.* (2002)	Mohamed *et al.* (1999)	Tingsanchali and Chinnarasri (2001)	Chinnarasri *et al.* (2003)
Soil Type		Sand	Sand	Sand	Sand	Sand	Sand	Sand	Sand
Embankment Configuration		Homogeneous	Homogeneous	Homogeneous	Homogeneous	Homogeneous with downstream toe-drain	Homogeneous	Homogeneous	Homogeneous with bentonite upstream face lining
Failure Mechanism		Overtopping	Overtopping	Overtopping	Overtopping	Overtopping	Overtopping	Overtopping	Overtopping
Head Conditions		Constant	Constant	Falling	Constant	Constant	Falling	Falling + Constant Inflow	Falling + Constant Inflow
Flume Dimensions, [m]	**Depth**	N/A	1.2	N/A	0.8	N/A	N/A	1.0	1.0
	Length		50.0	25.0 (approx.)	34.0	12.0	N/A	35.0	35.0
	Width	T1: 6 T2/3: 0.5	1.0	1.296	16.6	2.4	N/A	1.0	1.0
Crest Dimensions, [m]	**Height**	0.6	0.7	0.24	0.15	0.3	0.3	0.8	0.8
	Length	T1: 6 T2/3: 0.5	0.4	1.296	9	2.21	N/A	1.0	1.0
	Width	0.2	1.3	0.24	0.2	T1-3: 0.065 T4: 0.0	T1: 0.2 T2: 0.3 T3: 0.5	0.3	0.3

Parameter		Date	1988	1992	< 1994	June 3, 1996	1996-1998	1998	< 2000	< 2000
		Literature Cited	Visser (1988)	Steetzel and Visser (1992) Visser (1995, 1998)	Bechteler and Kulisch (1998) Broich (1998a)	Visser (2000)	Coleman *et al.* (2002)	Mohamed *et al.* (1999)	Tingsanchali and Chinnarasri (2001)	Chinnarasri *et al.* (2003)
Embankment Width, [m]			5.0	T1/5/5A/7: 5.5 T2: 12.1 T3/4/6: 1:21.1	1.44	1.1	T1-3: 1.685 T4: 1.5	T1: 0.8 T2: 0.9 T3: 1.1	A1-A4, C1/4: 5.1 B1-B3: 6.7 C2/3: 4.7	T1/6: 4.3 T2/7: 4.7 T3/8: 5.1 T4/5/9: 6.7
Pilot Channel Dimensions, [m]	Depth		N/A	N/A	R1: 0.10 R2: 0.06	0.03	0.02	N/A	Plane Overtopping (ΔH = 0.03 except B2/3, ΔH = 0.05)	Plane Overtopping (ΔH = 0.03 except T5/9, ΔH = 0.05)
	Top Width				R1: 0.135 R2: 0.09	0.10	N/A	N/A		
	Side-Slope [V:H]				1:1.732	N/A	N/A	N/A		
Upstream Slope [V:H]			1:4	T0/1/5/5A/7: 1:4 T2: 1:15 T3/4/6: 1:30/40	1:3	1:2	T1-3: 1:2.7 T4: 1:2.5	1:1	1:3	1:3
Downstream Slope [V:H]				1:3	1:2	1:4	T1/2/3: 1:2.7 T4: 1:2.5		A1-A4, C1/4: 1:3 B1-B4: 1:5 C2/3: 1:2.5	T1/6: 1:2 T2/7: 1:2.5 T3/8: 1:3 T4/5/9: 1:5
Hydrodynamic/Soil Measurements			N/A	Velocity + WSL	Velocity + WSL	WSL, Velocity + Discharge	WSL + Discharge	N/A	WSL, Velocity, Discharge	WSL, Velocity, Discharge
Breach Evolution Measurements			Video camera	Video camera	2 Profile followers Downstream Video and cameras Sand trap + strain transducer	4 video cameras 1 top-view photo camera	Video camera	Video camera	Video cameras, photo camera	Video cameras, photo camera

Parameter	Date	1988	1992	< 1994	June 3, 1996	1996-1998	1998	< 2000	< 2000
	Literature Cited	Visser (1988)	Steetzel and Visser (1992) Visser (1995, 1998)	Bechteler and Kulisch (1998) Broich (1998a)	Visser (2000)	Coleman *et al.* (2002)	Mohamed *et al.* (1999)	Tingsanchali and Chinnarasri (2001)	Chinnarasri *et al.* (2003)
Grain Size, [mm]	d_{10}	N/A	0.069 T5/5A/6: 0.150	N/A	0.070	N/A	N/A	N/A	N/A
	d_{30}	N/A	N/A	R1: 2.0 (d_{35}) R2: 2.0 (d_{35})	N/A	N/A	N/A	A1/2, B1/2, C1/2: 0.52 A3/4, B3, C3/4: 0.26	T1-5: 0.52 T6-9 0.26
	d_{50}	T1/3: 0.100 T2: 0.200	0.105 T5/5A/6: 0.218	R1: 2.0 R2: 0.9	0.088	T1: 0.5 T2: 0.9 T3: 1.6 T4: 2.4	0.3 - 0.5	A1/2, B1/2, C1/2: 0.86 A3/4, B3, C3/4: 0.36	T1-5: 0.86 T6-9 0.36
	d_{60}	N/A	N/A	R1: 2.2 R2: 2.3	N/A	N/A	N/A	N/A	N/A
	d_{90}	N/A	0.150 T5/5A/6: 0.290	R1: 2.7 R2: 4.5	0.120	N/A	N/A	A1/2, B1/2, C1/2: 3.80 A3/4, B3, C3/4: 0.58	T1-5: 3.80 T6-9 0.58
Dry Unit Weight, [kN/m^3]		N/A	16.04 T7: 14.30	R1: 15.98 R2: 18.41	N/A	N/A	N/A	N/A	N/A
Parameters Varied		grain size	downstream slope, wave attack, grain size, void ratio	grain size, gradation, unit weight	none	grain size, crest width, upstream and downstream slopes	crest width	grain size, gradation downstream slope, initial overtopping head, reservoir inflow	grain size, gradation downstream slope, initial overtopping head, reservoir inflow

Parameter	Date	1988	1992	< 1994	June 3, 1996	1996-1998	1998	< 2000	< 2000
	Literature Cited	**Visser (1988)**	**Steetzel and Visser (1992) Visser (1995, 1998)**	**Bechteler and Kulisch (1998) Broich (1998a)**	**Visser (2000)**	**Coleman *et al.* (2002)**	**Mohamed *et al.* (1999)**	**Tingsanchali and Chinnarasri (2001)**	**Chinnarasri *et al.* (2003)**
Uniqueness of Simulation		large scale	large scale	sediment trap with strain-transducer	erodible foundation	breach profile measurement below WSL	very steep shoulder slopes	large scale high downstream slope range	large scale, large downstream slope range

Parameter	Date	< 2004	2002 (Series 1)	2003 (series 2)	2003 (Series 3)	< 2004	2005	< 2009	< 2011
	Literature Cited	**Chinnarasri *et al.* (2004)**	**IMPACT (2004a) Morris and Hassan (2004) Morris *et al.* (2007)**			**Pickert *et al.* (2004)**	**Stretch and Parkinson (2006); Parkinson and Stretch (2007)**	**Schmocker and Hager (2009, 2012)**	**Pickert *et al.* (2011)**
Soil Type		70% Sand / 30% Clay mixture	Sand	Clay or Moraine	N/A	Silt and Sand	Sand	Sand and gravel	Sand
Embankment Configuration		Homogeneous with clay upstream lining Case C: 3cm clay lining	Homogeneous	Homogeneous	Homogeneous	Homogeneous with downstream toe-drain	Homogeneous	Homogeneous with upstream toe-drain	Homogeneous with downstream toe-drain
Failure Mechanism		Overtopping	Overtopping	Overtopping	Piping	Overtopping	Overtopping	Overtopping	Overtopping
Head Conditions		Falling + Constant Inflow	Falling + Constant Inflow	Falling + Constant Inflow	N/A	Constant	Falling	Falling + Constant Inflow	Constant
Flume Dimensions, [m]	**Depth**	1.4	0.8	0.8	T18,19: N/A T20-22: 0.8	0.7	0.2	N/A	0.7
	Length	13.6	50.0	50.0	T18,19: N/A T20-22: 1.0	15.0	4.0	8.0	15.0
	Width	4.0 - 8.5	10.0	10.0	T18,19: N/A T20-22: 1.0	1.0	2.0	0.4	1.0
Crest Dimensions, [m]	**Height**	0.6	0.5	0.6	N/A	0.3	B1/2/4: 0.08, 0.15 B3: 0.08, 0.18	0.1, 0.2, 0.4	0.3
	Length	4.0	4.1	4.1	N/A	1.9	2	0.1, 0.2, 0.4	1.9
	Width	0.3	T1-6,8,9: 0.2 T7: 0.3	0.2	N/A	0.1	B1/4: 0.0 B2: 0.1 B3: 0.3	0.05, 0.10, 0.20	0.1

Parameter	Date	< 2004	2002 (Series 1)	2003 (series 2)	2003 (Series 3)	< 2004	2005	< 2009	< 2011
	Literature Cited	**Chinnarasri *et al.* (2004)**	**IMPACT (2004a) Morris and Hassan (2004) Morris *et al.* (2007)**			**Pickert *et al.* (2004)**	**Stretch and Parkinson (2006); Parkinson and Stretch (2007)**	**Schmocker and Hager (2009, 2012)**	**Pickert *et al.* (2011)**
Embankment Width, [m]		A1/2, B2/3, C3: 3.3 A3, B1, C1/2: 3.9	T1-5,8,9: 1.9 T6: 2.05 T7: 2.0	T10-14,17: 2.6 T15: 2.0 T16: 3.2	N/A	1.0	B1: 0.4, 0.75 B2: 0.5, 0.85 B3: 0.7, 1.05 B4: 0.56, 1.05	0.45, 0.90, 1.80	1.0
Pilot Channel Dimensions, [m]	**Depth**	0.05	0.01	0.05	0.02 (pipe diameter)	0.02	0.01	-	0.005
	Top Width	0.2	0.2	0.3	N/A	0.02	N/A		0.02
	Side-Slope [V:H]	-	N/A	N/A	N/A	-			-
Upstream Slope [V:H]		1:3	1:1.7	1:2	N/A	1:3	1:2	1:2	1:3
Downstream Slope [V:H]		A1/2, B2/3, C3: 1:2 A3, B1, C1/2: 1:3	T1-5,7-9: 1:1.7 T6: 1:2.0	T10-14,17: 1:2 T15: 1:1 T16: 1:3	N/A		B1/2/4: 1:3 B3: 1:5		
Hydrodynamic/Soil Measurements		WSL, Velocity	WSL, Velocity profile, PWP	WSL, Velocity profile, PWP	N/A	WSL, PWP, Discharge, sediment weight	WSL	WSL	WSL, PWP, discharge + sediment weight
Breach Evolution Measurements		Video camera, 2 high-speed digital cameras + series of staff gauges	Video cameras, photo camera	Video cameras, photo camera	Video cameras, photo camera	Fringe projection + video camera	Video camera	Video camera	Fringe projection, video camera + photo camera

Parameter	Date	< 2004	2002 (Series 1)	2003 (series 2)	2003 (Series 3)	< 2004	2005	< 2009	< 2011
	Literature Cited	Chinnarasri *et al.* (2004)	IMPACT (2004a) Morris and Hassan (2004) Morris *et al.* (2007)			Pickert *et al.* (2004)	Stretch and Parkinson (2006); Parkinson and Stretch (2007)	Schmocker and Hager (2009, 2012)	Pickert *et al.* (2011)
Grain Size, [mm]	d_{10}	N/A	T1,8: 0.51 (uniform) T2-4: 0.15 (uniform) T5-7,9: 0.08 (non-uniform)	T10-16: 0.001 T17: 0.015	T18,19: 0.015 T20-22: N/A	N/A	$\frac{1}{3}d_{60}$	N/A	*f*S: 0.100 *m*S: 0.180 *c*S: 0.495
	d_{30}	N/A	T1,8: 0.6 (uniform) T2-4: 0.2 (uniform) T5-7,9: 0.13 (non-uniform)	T10-16:0.0025 T17: 0.11	T18,19: 0.11 T20-22: N/A	N/A	N/A	N/A	*f*S: 0.14 *m*S: 0.28 *c*S: 0.5
	d_{50}	A1-3: 0.060 B1-3: 0.034 C1-3: 0.044	T1,8: 0.7 (uniform) T2-4: 0.25 (uniform) T5-7,9: 0.25 (non-uniform)	T10-16: 0.0045 T17: 0.7	T18,19: 0.7 T20-22: 0.003	T1: 2.000 T2: 0.220 T3: 0.035	0.6	1, 2, 4, 8	*f*S: 0.185 *m*S: 0.365 *c*S: 0.640
	d_{65}	N/A	T1,8: 0.8 (uniform) T2-4: 0.27 (uniform) T5-7,9: 0.4 (non-uniform)	T10-16: 0.007 T17: 1.5	T18,19: 1.5 T20-22: 0.007	N/A	N/A	N/A	*f*S: 0.2 (d_{60}) *m*S: 0.39 (d_{60}) *c*S: 0.68 (d_{60})
	d_{90}	N/A	T1,8: 0.95 (uniform) T2-4: 0.45 (uniform) T5-7,9: 1.4 (non-uniform)	T10-16: 0.018 T17: 4	T18,19: 4 T20-22: 0.04	N/A	N/A	N/A	*f*S: 0.32 *m*S: 0.49 *c*S: 0.91
Dry Unit Weight, [kN/m^3]		N/A	N/A	N/A	N/A	N/A	N/A	N/A	*f*S: 14.29 *m*S: 15.04 *c*S: 14.71

Parameter	Date	< 2004	2002 (Series 1)	2003 (series 2)	2003 (Series 3)	< 2004	2005	< 2009	< 2011
	Literature Cited	**Chinnarasri *et al.* (2004)**	**IMPACT (2004a) Morris and Hassan (2004) Morris *et al.* (2007)**			**Pickert *et al.* (2004)**	**Stretch and Parkinson (2006); Parkinson and Stretch (2007)**	**Schmocker and Hager (2009, 2012)**	**Pickert *et al.* (2011)**
Parameters Varied		grains size, downstream slope, inflow	Grain size, gradation Breach location Crest width and downstream slope	grain size, compaction, construction water content, downstream slope	embankment material	grain size	storage, crest height and width, downstream slope	grain size, complete geometric scale, inflow	grain size (*mS* test repeated 5 times)
Uniqueness of Simulation		Large-scale	Geometry and properties scaled from field tests, repeatability	Geometry and properties scaled from field tests, repeatability	Piping failure mechanism Geometry and properties scaled from field tests, repeatability	Measurement of breach profile below WSL using fringe projection Matric suction potential Sediment weighing probe	Various geometric scales and berm shapes	Extensive repeatability Scale series Side-wall effects	Measurement of breach profile below WSL using fringe projection Matric suction potential Sediment weighing probe

The first embankment breach physical tests were conducted using fuse plug embankment models in Washington State University in 1959 (Tinney and Hsu, 1961). Ten laboratory tests and three large-scale field tests were conducted as part of a feasibility investigation of a fuse plug known as the Oxbow project Idaho spillway. The results from their physical models were used in conjunction with the theory of breach erosion mechanics to express similitude laws of washout rates for erodible embankments. In 1978, an experimental program comprising several breach tests was conducted in laboratory flumes and scour basins at the University of Windsor (Chee, 1978). The purpose of the experimental program was to investigate the breach development and washout rate of fuse plug embankment physical models. The test included a wide range of embankment sizes (0.3 m to 1.5 m in height and 0.2 m to 2.3 m in crest length) as well as grain sizes, specific gravity and geometric and structural configurations. Similar to the study by Tinney and Hsu (1961), a similitude relationship for the washout time was expressed. In the mid-1980s, several laboratory tests were conducted by the U.S. Bureau of Reclamation (USBR) on fuse plug embankments and low embankments (Pugh, 1985; Dodge, 1988). Several parameters were investigated including embankment geometry, soil gradation, pilot channel size and location, degree of compaction and breach overtopping unit discharge. In this appendix, several other laboratory and field tests are described.

B.1 Laboratory Tests

B.1.1 Delft University of Technology (TU Delft, Delft, Netherlands)

The first breach experiment on homogeneous sand dikes was performed in the late 1980s, at the Delft University of Technology (TUD) to develop and validate a mathematical model (Visser, 1988). Three large-scale experiments (h_D = 0.6m) were conducted using two grain sizes (d_{50} = 0.100 and 0.200mm) and under constant head conditions. A second series of breach experiments by TUD were conducted on large-scale dikes (h_D = 0.7m) in the early 1990s using different upstream slope

configurations (1:4, 1:15 and 1:30 to 1:40), grain sizes (d_{50} = 0.100 and 0.220mm) and porosities (λ = 0.38 and 0.45) (Steetzel and Visser, 1992). The head above the dike's crest was kept constant, except in one of the test where the dike was subjected to a wave attack. A summary of the findings state that increasing the inclination of the upstream slope, wave attacks, and larger grain sizes generally increases the erosion rate of sand dikes. The effects of lower degrees of compaction increased erosion rate only by 5%. The method of construction or compaction of the sand dike was not mentioned in the literature. Erosion rate data from the experiments was used to compare the applicability and performance of several classical sediment transport formulations (Visser, 1995; Visser, 1998).

On June 3, 1996, a third test was conducted at TUD to investigate the erosion of dikes with an erodible foundation. The test was comprised of a smaller-scale sand dike, with a crest height, width and length of 0.15m, 1.1m and 9m, respectively. The model was constructed in a wave basin 34 m long x 16.6m wide x 0.7m deep with a sand bed 50cm thick (see Figure B-1 and Table B-1). The water surface level and velocities were measured using wave height probes and electromagnetic flow velocity metres, respectively. A pilot channel, 3cm deep and 10cm wide was cut into the dike's crest, where a damming structure was placed in the pilot channel to temporarily block the flow through it. The pilot channel was located against the glass wall therefore restricting the lateral breach evolution in one direction only (Visser 1998).

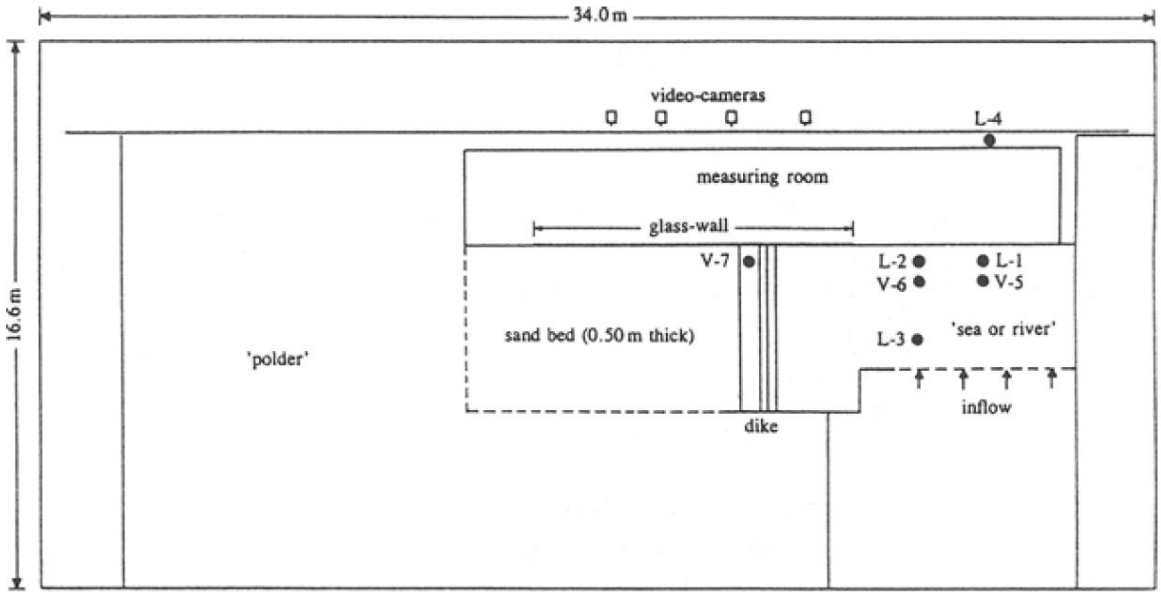

Figure B-1: Top view of sand-dike in laboratory test showing locations of the water surface level (L1–L4) and (V5–V7) probes (Visser, 2000)

The study by Visser (2000) describes the filling procedure for the upstream reservoir using two pipes (pump capacity 0.66m^3/s) and the consequence breach of the sand dike. It is stated that water level in the upstream reservoir was “kept constant as good and as long as possible”, however, it can be shown from Figure B-2 below that the water surface levels fluctuated significantly, bearing in mind that the laboratory model was only 15cm high.

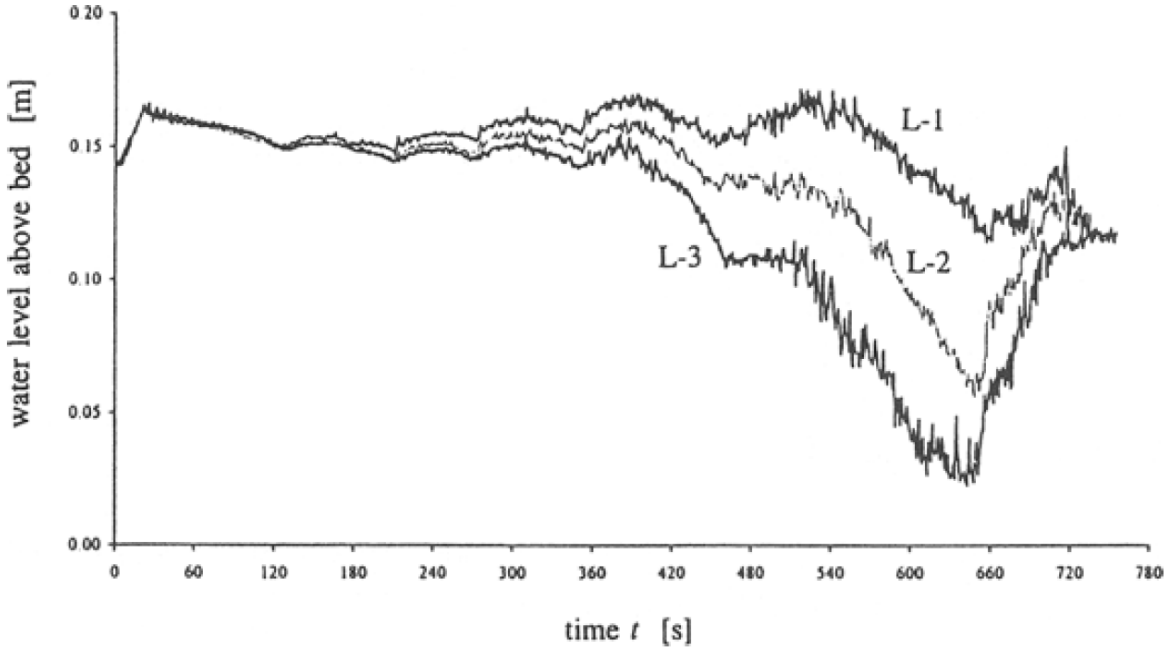

Figure B-2: Water surface level measured at upstream locations (Visser, 2000)

B.1.2 University of the Federal Armed Forces - Institute of Hydraulics (Munich, Germany)

During the CADAM meeting in Munich in 1998, Bechteler and Kulisch (1998) and Broich (1998a) presented two test cases from a series of embankment overtopping experiments performed by Kulisch (1994) at the institute of Hydraulics at the Federal Armed Forces University in Munich. The two test cases were used as a means to validate using “blind tests”, a number of numerical models, developed by research groups who have participated at the meeting. The two experiments were performed in 1.3m wide reservoir approximately 25m long, shown in Figure B-3 and in Table B-1.

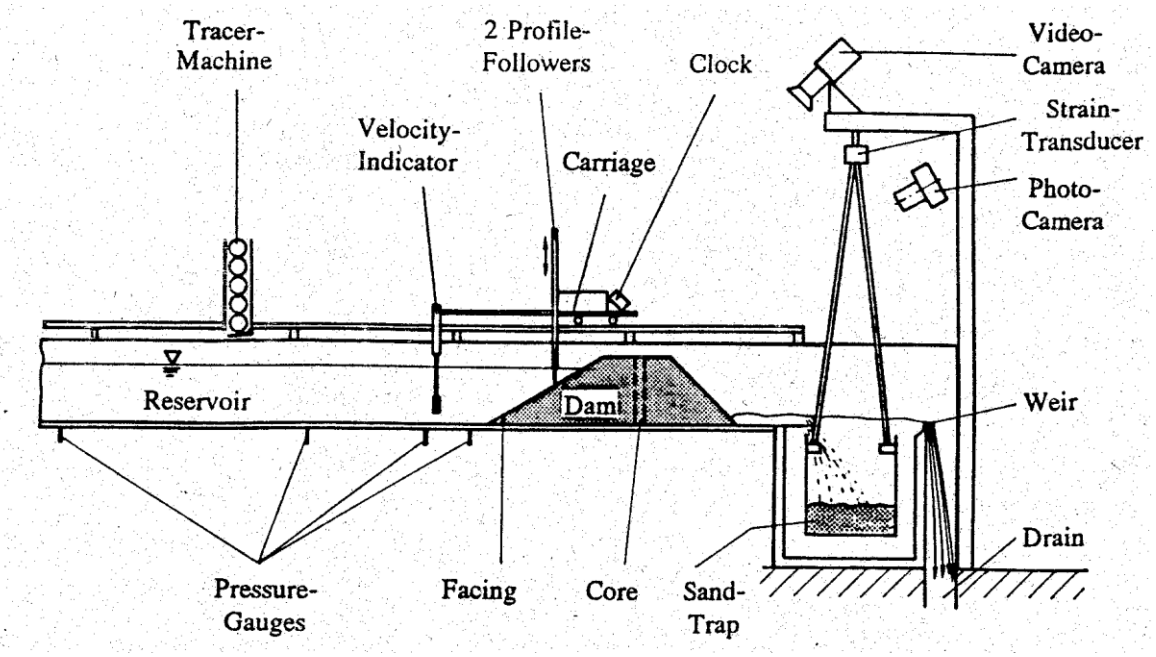

Figure B-3: Experimental setup (Bechteler and Kulisch, 1998)

Downstream the embankment dam is a sediment trap connected to strain-transducer to measure the weight of the fallen sand. The upstream slope of the noncohesive embankments was lined with a thin cohesive layer as a means for maintaining the embankment dry. A video camera and a photo camera were mounted downstream to monitor the evolution of the breach channel. Two profile followers mounted on a carriage were used to record the evolution of the breach channel. A velocity indicator was mounted upstream of the embankment to measure flow velocity. Pressure sensors in the upstream reservoir were used to transmit and record water surface levels. Data from pressure sensors and strain-transducer was later converted to hydrographs comprised of breach outflow and reservoir surface level and erosion curves of the breached embankment. A trapezoidal pilot channel was cut into the centreline of the embankments' crest to initiate the breach. The first run comprised of a uniform sand (d_{50} = 2.0mm) while the second run was comprised of non-uniform sand (d_{50} = 1.5mm).

B.1.3 University of Auckland (Auckland, New Zealand)

The study by Coleman *et al.* (2002) presents the results of two series of breach experiments presented in 1996 and 1998 by Master's students at the University of Auckland, New Zealand. The two studies were small-scale investigations of noncohesive embankments. The first experimental setup was comprised of triangular embankments (*i.e.* no crest) using volcanic gravel and 1:2.5 upstream and downstream slopes, while the second series of experiments utilized finer noncohesive materials, ranging from medium sand to fine gravel, and a 0.065m crest width with 1:2.7 upstream and downstream slopes (see Table B-1). All sediments had a friction angle of 32°. The embankments were constructed at the downstream end of the flume, thus eliminating tailwater effects as shown in Figure B-4. Downstream the flume was a stilling basin where the water spills over a sharp crested weir before flowing into a second basin consisting of a 52° V-notch weir. The water surface level in the upstream reservoir was controlled using a side-spill weir thus simulating a very large reservoir. The computed approach velocity head was 0.004m (1.3% of the approach piezometric head) and was thus neglected from the total head controlled upstream by the side-spill weir. A flap gate was installed upstream the embankment and was activated to halt the experiment after a required duration of time.

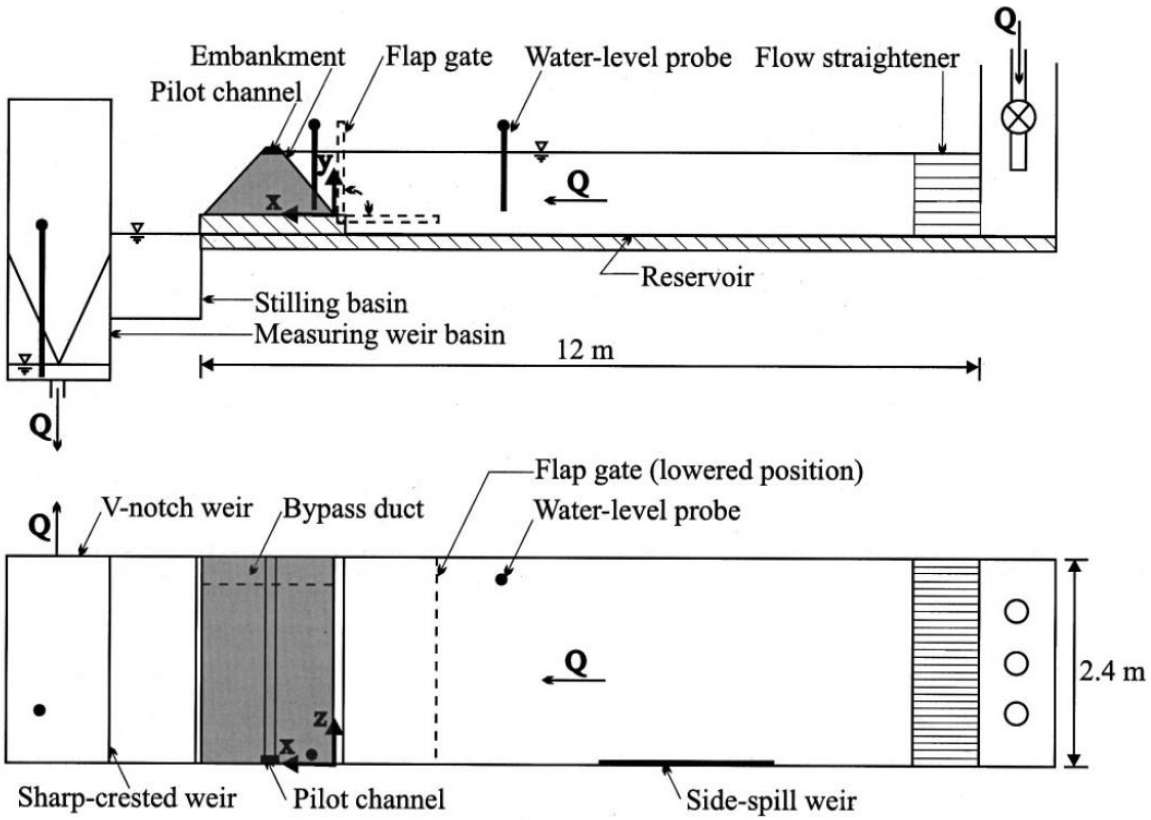

Figure B-4: Experimental setup (Coleman *et al.* 2002)

The water surface level was measured using three capacitance probes in the following locations: upstream reservoir, V-notch basin and between the flap gate and embankment crest. Little information is giving on the construction technique, however, it is mentioned that the second study included a toe-drain in the three models were as all three materials were compacted using the same compaction effort. A triangular pilot channel, 2cm deep, was cut into the embankment crest at the flume wall to initiate a half breach channel. This technique maximized breach widening for the available flume, where the glass walls acted as the breach centreline, whereas influence of the sidewalls on the breach outflow was neglected.

The experiment was ceased by activating the flap gate and draining the water using a bypass duct to investigate the breach evolution at the desired intervals. Figure B-5 shows the measured breach outflow for one particular test (medium sand) using the water surface levels in the V-notch weir basin (solid line) and the capacitance

probes in the upstream reservoir (plotted lines), confirming the repeatability success of the experiments.

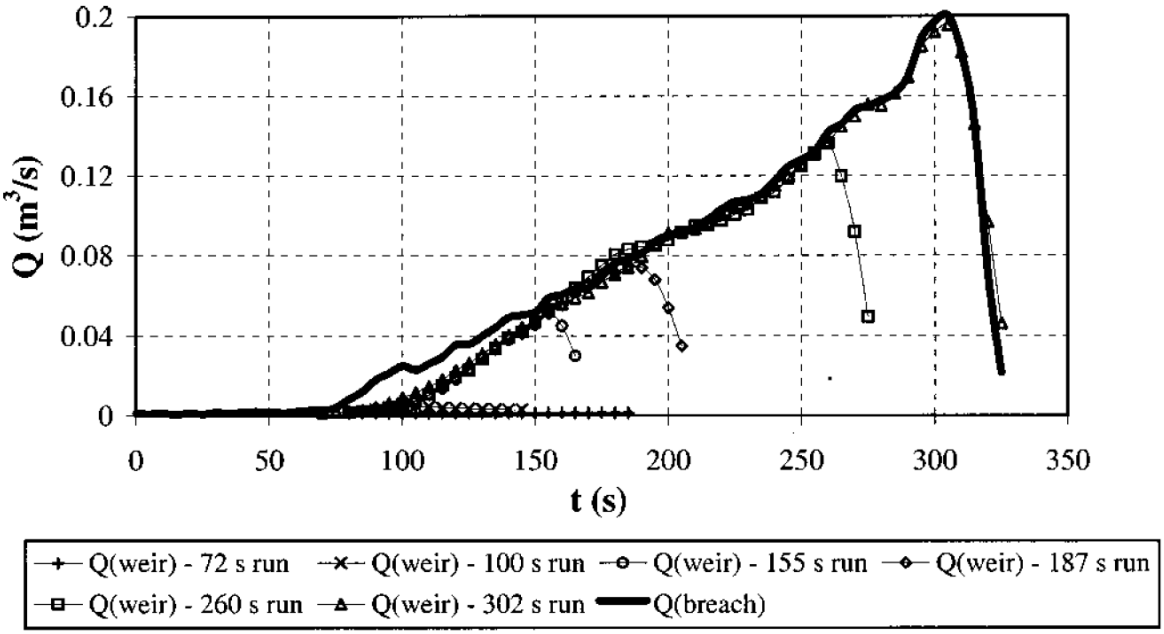

Figure B-5: Discharge measured for medium sand experiment for consecutive runs (Coleman *et al.* 2002)

The breach channel dimensions below the water surface level was mapped, whereas the embankment was reconstructed and the breach process repeated successively. Prior to the vertical erosion to the embankment foundation, the planform view of the breach channel was described to have a distinctive hourglass or Venturi shape (Pickert *et al.* 2004, 2011; Geisenhainer and Kortenhaus, 2006; Stretch and Parkinson, 2006; Wishart, 2007), typical of minimum energy loss channels (see Figure B-6). Another observation by the authors is the parabolic breach channel cross-section, also shown in Figure B-6. The authors postulate that the presumption of breach channel cross-section having trapezoidal cross-sectional shapes is based on the final dimensions, which may be influenced by the falling head in the reservoir. Coleman *et al.* (2002) also state that after the erosion of the downstream toe, the slope retreat of the breach channel was described to pivot

about a point downstream along the base of the embankment (see Figure B-7), similar to observation made by Visser (1998).

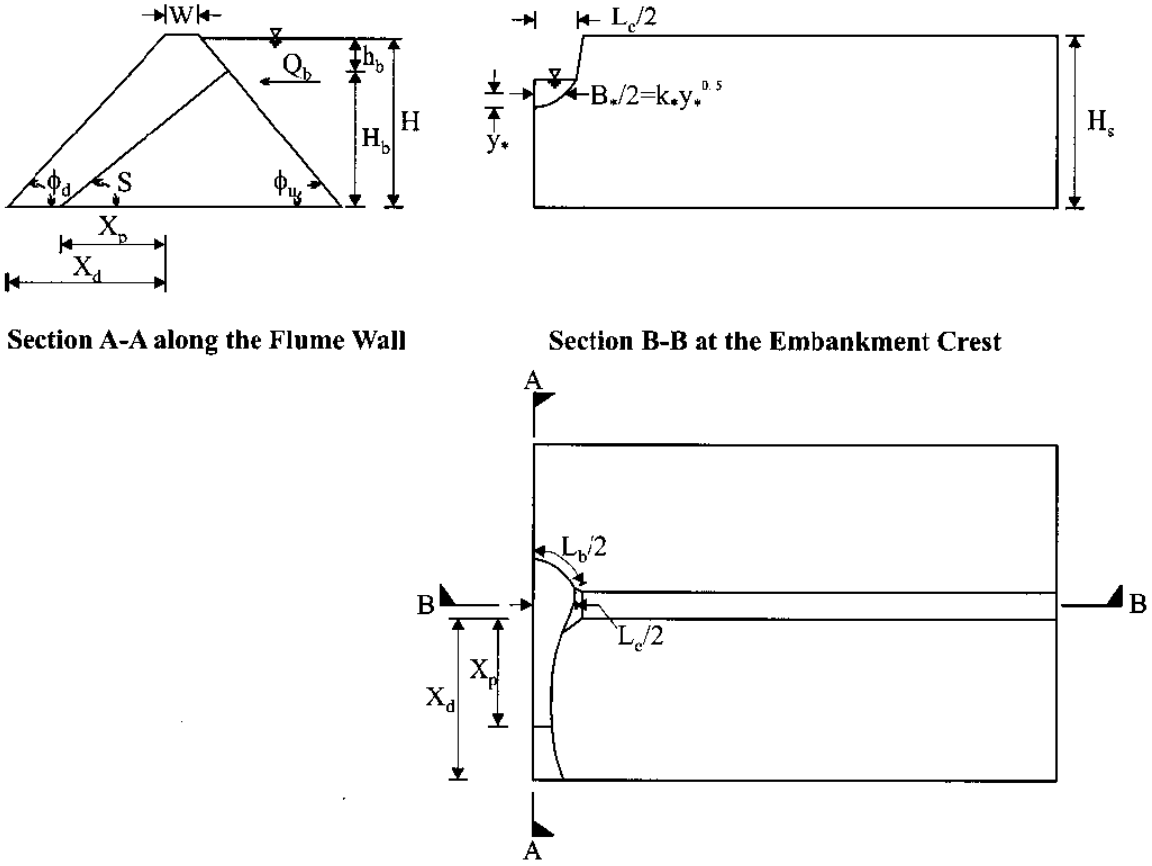

Figure B-6: Plan view of embankment showing breach channel below water surface level (Coleman *et al.* 2002)

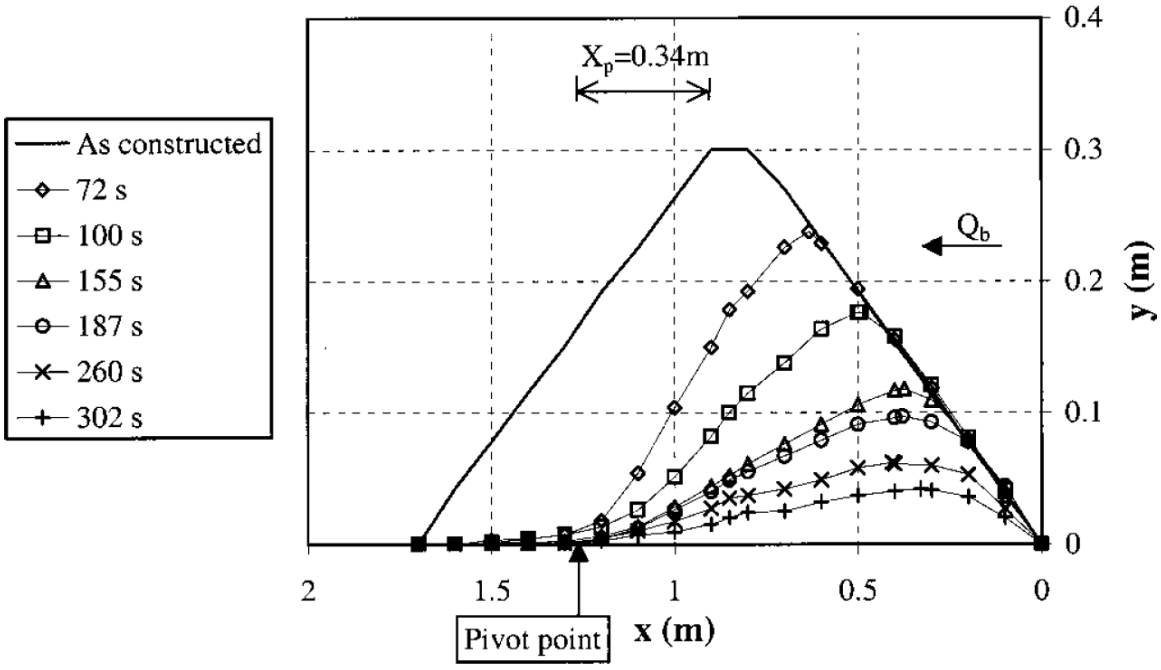

Figure B-7: Slope retreat for medium sand embankment (Coleman *et al.* 2002)

Using the surveyed breach channel dimensions, an expression for the breach width was developed in terms of the vertical distance measured from the breach channel invert and the water surface level, as shown in Figure B-6. The evolution of the breach channel invert elevation at the crest centreline, H_b (z_c in this study), and horizontal width of the crest, L_e, was expressed in dimensionless form (normalised using the embankment crest height) as shown in Figure B-8.

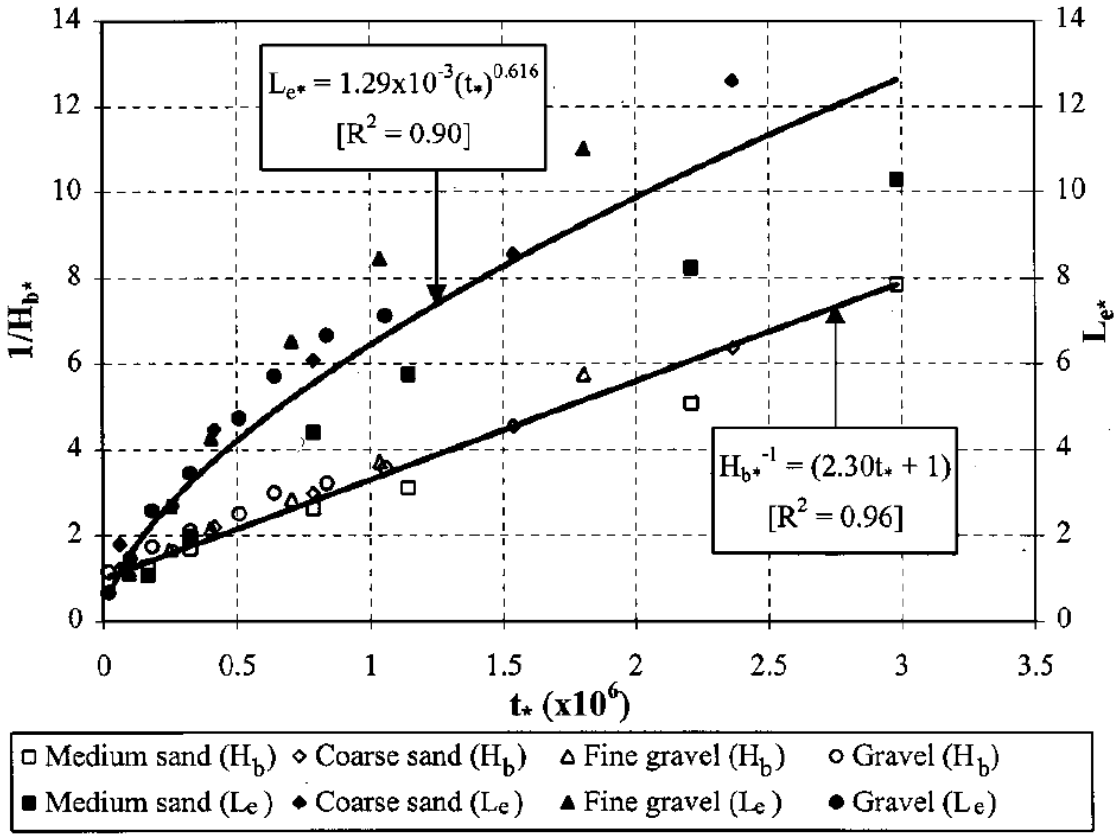

Figure B-8: Evolution of breach channel crest width and invert elevation at the centreline in dimensionless form (Coleman et al. 2002)

An expression between the flow cross-sectional area through the breach channel invert, A_b, and breach channel crest length, L_b (L_a in this study), (normalised by the reservoir elevation) was also expressed in terms of the dimensionless hydraulic head at the centreline of the breach channel invert, h_b, (also normalised by the reservoir elevation) as shown in Figure B-9. The authors then express the breach outflow in terms of the breach channel crest length and hydraulic head at the invert centreline in dimensionless form as shown in Figure B-10.

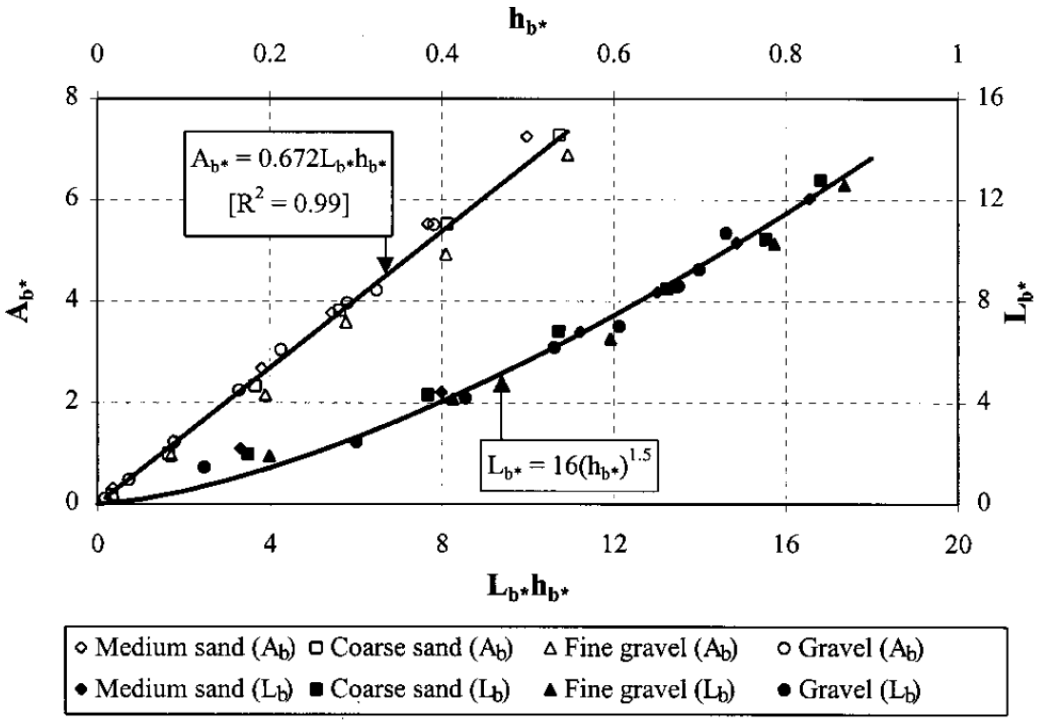

Figure B-9: Dimensionless relationships in Coleman *et al.* 2002

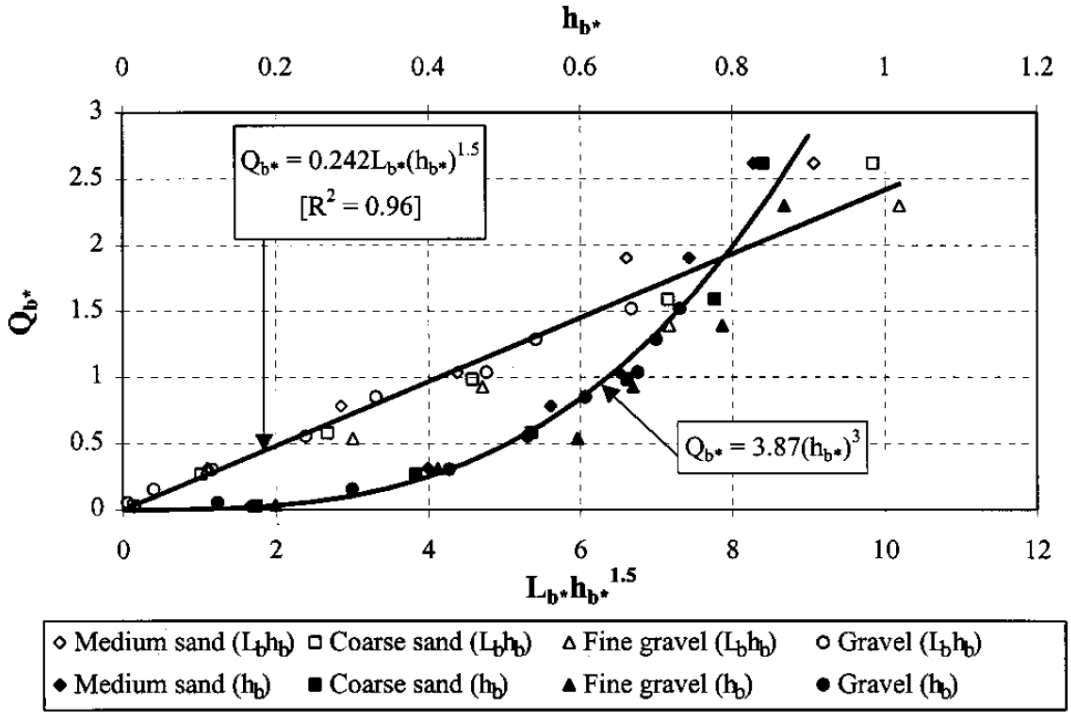

Figure B-10: Breach outflow expressed in terms of crest length and hydraulic head in Coleman *et al.* 2002

The authors state that for constant head conditions the lateral evolution rates will continue to decrease, as shown in Figure B-9, until one of the two phenomena are satisfied: erosion reaches of the valley walls, or the sediment removal from the embankment is balanced by the supply rate from upstream reaches. The authors, however, suggest that a similar breach evolution analysis be conducted under falling head conditions in order to identify trends associated with constant head experimental models.

B.1.4 HR-Wallingford (Wallingford, UK)

During the Zaragoza CADAM meeting, Mohamed *et al.* (1999) presented a new methodology for assessing side-slope failures, based on three experiments conducted at HR-Wallingford. Little detail is given on the tests, except for the basic embankment properties and geometry. The embankments were homogeneous, constructed from a noncohesive material (d_{50} ranged between 0.3mm and 0.5mm), with a crest height and shoulder slopes of 0.3m and 1:1, respectively (see Table B-1). Three crest widths were tested: 0.2m, 0.3m and 0.5m. The test cases were qualitative and established the foundation upon which the new methodology is based on.

Observations from the experiments state that lateral erosion was higher near the bed than at the water line. Large overhangs were seen to collapse in successions, and consequently increased the top width of the breach channel. The final cross-section of the breach channel had an almost parabolic shape, as observed by Coleman *et al.* (2002), with near vertical side-slopes at the top of the breach channel. The side-slope angles near the breach bottom were equal to the angle of repose of the embankment material. Mohamed *et al.* (1999) stated that deficiencies in predicting the breach growth by numerical models, particularly in the lateral direction, stems from the following two assumptions: erosion is uniform between the breach channel bottom and side-slopes, and that erosion takes place above the water line (implied by the constant breach shape premise). Furthermore, the side-slope stability analysis will yield inaccurate results based on the above mentioned

assumptions. The methodology proposed by their study is based on the influence of the boundary shear stress distribution on erosion as shown in Figure A-9 of Appendix A, and Figure B-11 below. The work presented by Mohamed *et al.* (1999) has been incorporated into the HR-BREACH numerical model, which is described in more detail in Subsection A.2 of Appendix A.

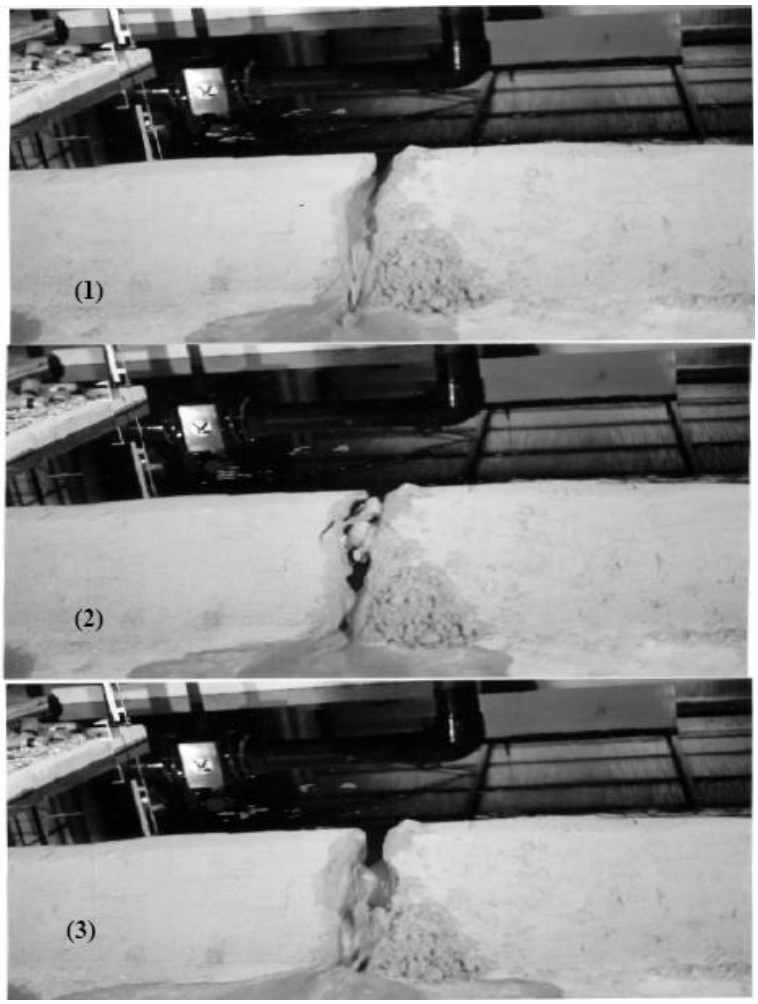

Figure B-11: Observed parabolic shape in breach channel with near vertical side-walls (Mohamed *et al.* 1999)

Three series of laboratory tests have been conducted at HR Wallingford in the UK, under the IMPACT Project during 2002 and 2003. The 1:10 scaling of the laboratory models was based on the Norwegian *Mo i Rana* large scale field tests, described in Subsection B.2.4. The first series, based on Field Test No. 3 (see Table B-13 and

Table B-14), were comprised of nine overtopping tests of noncohesive embankment models where parameters such as embankment geometry, breach location, and material gradation were varied in their experimental setup. The second series of tests were comprised of eight overtopping tests on cohesive embankment models (clay and moraine) with various embankment geometries, degrees of compaction and construction water content, using two soil gradations. The third series of tests were comprised of five piping tests on cohesive embankments. The IMPACT Project laboratory tests were conducted in a 10m wide (embankment test section 4.1m in width), 0.8 deep and 52.1m long flume and are described in more detail in several IMPACT Project literature (Morris, 2002a, b ,c; IMPACT, 2004a; Morris and Hassan, 2004; Morris *et al.* 2007) and documented in Table B-1.

The digital Appendix (*i.e.* CD-ROM) of Morris *et al.* (2007), included sample data for one of the clay embankment tests (second series, Test No. 10). Amongst the data were files containing the time history of water surface levels, pressure sensors, velocity data, breach top width, inflow as well as soil properties and the final breach channel longitudinal profile. Instrument photos, construction instructions and literature on the investigation of scaling techniques for cohesive and noncohesive sediments were also provided. Inflow was supplied at the upstream end of the reservoir and measured using orifice plates and manometers, while the water surface levels were measured at the headwater, upstream the embankment and at the tail water at the sediment trap using ultrasonic sensors. The approach velocity profile at the breach channel centreline was recorded using an assembly of 3 ADVs.

Compaction for the clay embankments was carried out in layers, 6 – 8cm thick. The embankment material was compacted manually using a plunger after its mixture with water. The density was monitored and controlled using a nuclear densometer probe (see Figure B-12 for the instrumentation used in the laboratory tests). Footage from video cameras and photographic digital cameras mounted upstream, downstream and above the embankment crest were used to monitor breach development and determine breach width growth rate.

Figure B-12: Instrumentation used in IMPACT Project laboratory tests (clockwise from top left figure): ultrasonic sensors, orifice plates and manometer assembly, ADV assembly, nuclear densometer probe, pressure sensor (Morris *et al.* 2007)

For the first test series, the three gradations used were: d_{50} = 0.70 – 0.9mm with uniform gradation, d_{50} = 0.25mm with uniform gradation and d_{50} = 0.25mm with wide gradation as shown in Figure B-13 below. The presentation by Vaskinn (2004) reports that the d_{50} for Field Test No. 3 was between 4mm and 10mm and the maximum grain size < 60mm, while the study by Hassan and Morris (2008) stated that d_{50} was 4.65mm. The gravel material was compacted using a 4-ton roller compactor. After considering a range of approaches in scaling the field test sediment including; mobile bed modeling, sediment entrainment and fall velocities and Reynolds or Froude criteria, a direct geometric scaling was used (Morris, 2002a; Morris *et al.* 2007). Although the method of construction for the cohesive embankments was mentioned in Morris *et al.* (2007), there was no mention of the construction method for the noncohesive laboratory test (*i.e.* second series). Results shown in the IMPACT Project detailed technical reports indicate that inflow conditions were fixed throughout the experiment (approximately 0.08m^3/s) where the inflow was ceased after the breach channel had developed.

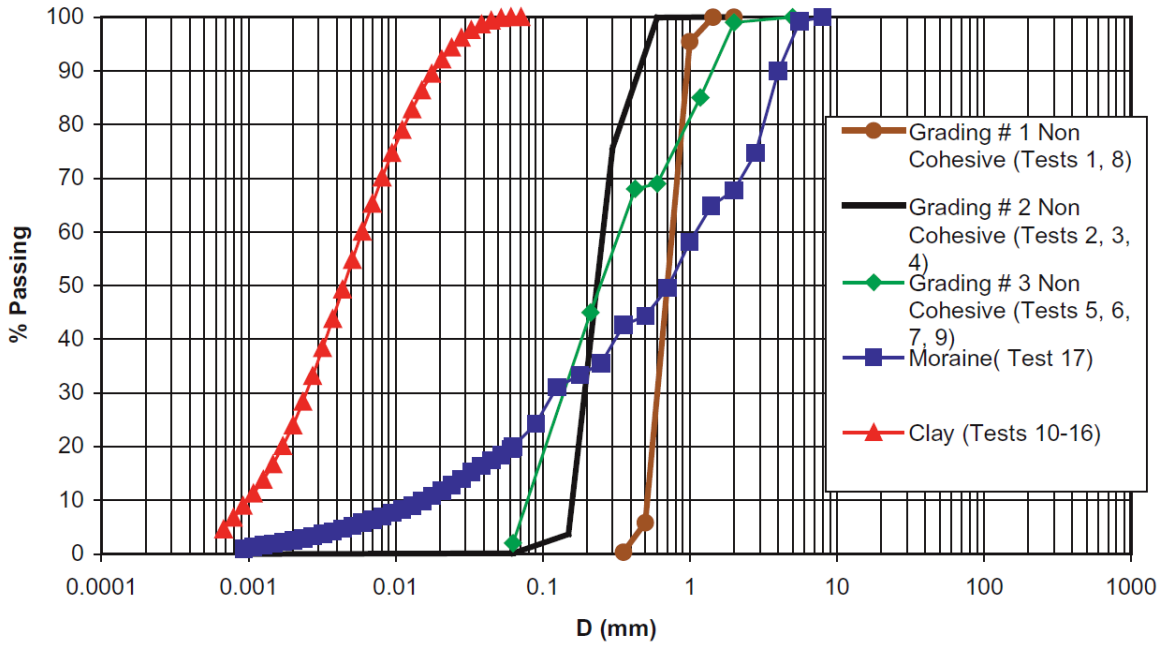

Figure B-13: Embankment model soil gradations for IMPACT laboratory tests (Morris *et al.* 2007)

Results for the repeatability tests were not presented; however, they were reported as successful. The detailed technical report stated that variations in breach were negligible for the different soil materials, crest widths and downstream slopes. The breach location tests, however, indicated significant variations in peak outflow when breached at the centreline (Test No. 2) and at the flume side-walls (Test No. 4), 0.91m^3/s and 0.67m^3/s, respectively. Time-to-peak was measured at 1.20 hours and 0.84 hours, respectively. While peak outflow may have varied slightly, the time-to-peak variations were somehow larger, as shown in Table B-3. The IMPACT Project detailed technical report (IMPACT, 2004a) stated that the peak outflow and time-to-peak for the third field test (*i.e.* gravel embankment dam) were 117m^3/s and 2.45 hours, respectively. Such values when compared to the Froude scaled embankment characteristic as shown in Table B-3 are quite different. Inflow for the field tests was not mentioned in any of the IMPACT Project literature.

Table B-3: Experimental results from first series of IMPACT Project laboratory tests (IMPACT, 2004a)

Test No.	Test Description	Test Objective	Benchmark Parameter	$Q_P)_{mm}$ [m^3/s]	$t_P)_{mm}$ [hours]	η_{max} [†] [m]	Variation [‡] [%] ΔQ_P	Variation [‡] [%] Δt_P	$Q_P)_{pp}$ [§] [m^3/s]	$t_P)_{pp}$ [§] [hours]
1	Pilot test	Setup / Trial	-	N/A	N/A	N/A	N/A	N/A	N/A	N/A
2	d_{50} = 0.25mm, uniform	Effect of sediment uniformity	-	0.91	1.20	0.49	-	-	288	3.8
3	d_{50} = 0.25mm, uniform	Assessment of repeatability	Identical to Test No. 2	N/A	N/A	N/A	N/A	N/A	N/A	N/A
4	Initial breach against abutment	Assessment of breach location	Centreline breach	0.67	0.84	0.48	-26	-30	212	2.7
5	d_{50} = 0.25mm, wide gradation	Direct replication of Field Test No. 3	d_{50} = 0.25mm, uniform	0.87	0.80	0.48	-4	-33	275	2.5
6	Steeper downstream (D/S) slope (1V:2H)	Assessment of D/S slope	D/S slope = 1V:1.7H	0.92	0.80	0.49	1	-33	291	2.5
7	Different crest width (0.3m)	Assessment of crest width	w_{cr} = 0.2m	0.88	0.81	0.49	-3	-33	278	2.6
8	d_{50} = 0.7mm, uniform	Assessment of sediment size	d_{50} = 0.25mm, uniform	N/A	N/A	N/A	N/A	N/A	N/A	N/A
9	Allowing seepage before failure	Assessment of seepage	No seepage before failure	0.82	1.20	0.48	-10	0	259	3.8

[†]Maximum water surface level in upstream reservoir; [‡]percentage variation with respect to Test No. 2 (benchmark test); [§]scaled embankment breach characteristics for prototype based on Froude criterion

The second series test results are described in IMPACT (2004a) and Morris *et al.* (2007). A constant head was established after a breach had been initiated, where inflow did not exceed 0.25m^3/s (see Figure 3.7). An exception was Test No. 13 (see Table B-4), where inflow was increased to a maximum value of approximately 0.08m^3/s, since breach outflow did not change significantly even after 3.43 hours of testing. The embankment material which was compacted at optimum conditions resisted erosion and was reported as a partial breach failure. The remains of this test were left overnight and later overtopped in (Test No. 14 in Table B-4) to assess the effect of seepage. In general, the initial failure mechanism for the cohesive embankments tests were several headcuts on the downstream slope, which later combined into one single headcut and migrated upstream. Consequently, a deep headcut was formed where the erosion on the upstream face was downward. The vertical erosion endured until the foundation of the embankment model. After the full development of a breach channel lateral erosion then became the dominant mechanism. Erosion below the water surface level was observed, and which led to side-slope collapses similar to the noncohesive tests but less frequent. Lateral widening rates were also much smaller than the noncohesive tests.

The results of the embankment breach characteristics for the second series tests are shown in Table B-4. The effect of compaction, water content and embankment material were significant, whereas changes to the downstream slope were considered less significant (despite the high variation in time-to-peak). Laboratory jet-tests performed on embankment material samples which have been compacted at water contents corresponding to Test No. 10 and 13 indicated 93% variation in erodibility. The IMPACT Project detailed technical report (IMPACT, 2004a) stated that the peak outflow and time-to-peak for the second field test (*i.e.* clay embankment dam) were 340 – 390m^3/s and 4.9 – 5.1 hours, respectively. Such values when compared to the Froude scaled embankment characteristic as shown in Table B-4 are quite different. Also, the reported inflow for that particular field test was increased linearly to a peak value of approximately 375m^3/s before being lowered again to a plateau of 190m^3/s.

Table B-4: Experimental results from second series of IMPACT Project laboratory tests (IMPACT, 2004a)

Test No.	Test Description	Test Objective	Benchmark Test Parameter	$Q_P)_{mm}$ [m^3/s]	$t_P)_{mm}$ [hours]	η_{max} [†] [m]	Variation [‡] [%]		$Q_P)_{pp}$ [§] [m^3/s]	$t_P)_{pp}$ [§] [hours]
							ΔQ_P	Δt_P		
10	Replicate of Field Test No. 2	Direct replication of field event	-	0.31	0.67	0.46	-	-	98	2.1
11	Replicate of Field Test No. 2	Assessment of repeatability	Identical to Lab Test No. 10	0.34	0.70	0.40	10	4	108	2.2
12	Different compaction effort	Assessment of compaction effort	Double the compaction effort	0.53	0.26	0.47	71	-61	168	0.8
13	Construction water content near optimum (ω = 30%)	Assessment of construction water content	Natural water content, ω = 24%	0.09	3.43	0.60	-71	412	28	10.8
14	Remains of Test No. 13 (partial failure)	Assessment of seepage	No seepage before failure	0.28	1.84	0.51	-10	175	89	5.8
15	Steep downstream slope (1V:2H)	Assessment of steeper slope	Slope = 1V:2H	0.35	0.35	0.35	13	-48	111	1.1
16	Mild downstream slope (1V:3H)	Assessment of milder slope	Slope = 1V:2H	0.43	0.32	0.40	39	-52	136	1.0
17	Moraine dam (d_{50} = 0.715mm), < 10% fines	Assessment of soil gradation	d_{50} = 0.005mm, 24 - 43% clay	0.61	0.14	0.46	97	-79	193	0.4

[†]Maximum water surface level in upstream reservoir; [‡]percentage variation with respect to Test No. 10 (benchmark test); [§]scaled embankment breach characteristics for prototype based on Froude criterion

Such values correspond to values of 1.19m^3/s and 0.6m^3/s, respectively, using the Froude scaling criterion, which is different than the constant inflow that was supplied in the second series laboratory tests (0.25m^3/s) as shown in Figure 3.7.

B.1.5 Asian Institute of Technology (Khlong Nueng, Pathum Thani, Thailand)

The study by Tingsanchali and Chinnarasri (2001) reports a series of laboratory tests performed on noncohesive homogeneous embankments at the Asian Institute of Technology in Khlong Nueng, Thailand. The experiments were carried out in a 35m long flume, 1m wide and 1m deep as shown in Figure B-14. The upstream slope, crest width and crest height of the model were fixed at 1:3, 0.3m and 0.8m, whereas the downstream slope was varied throughout the eleven tests (see Table B-1). Two embankment materials were used, a coarse sand with d_{50} = 0.86mm and a finer sand with d_{50} = 0.36mm. The eleven experiments were comprised of three test cases: Test Case "*A*", a fixed bed (using a plywood embankment model with sand glued over the solid boundaries), Test Case "*B*", mobile bed, and Test Case, "*C*", a mobile bed but with steeper slopes used for calibrating a slope slide mode in their numerical model.

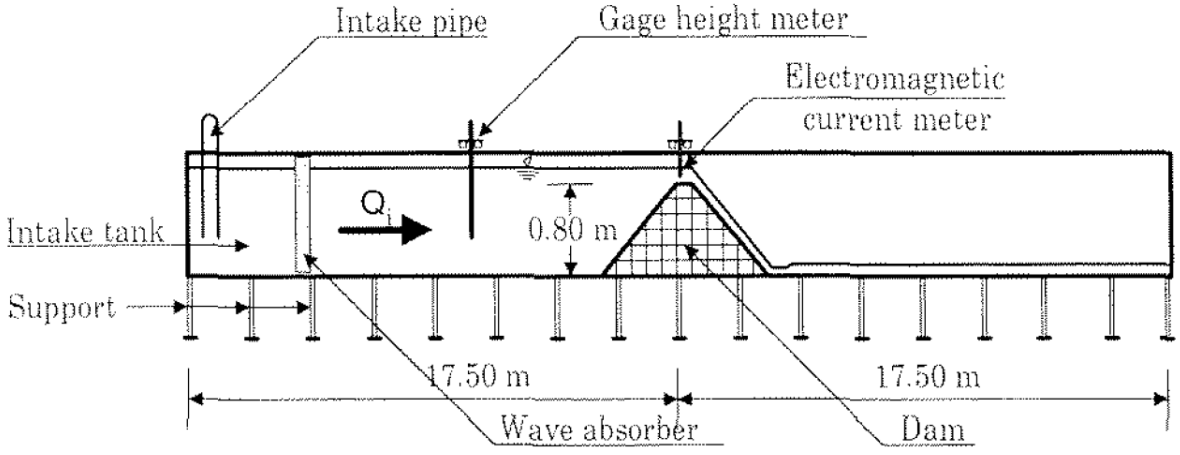

Figure B-14: Test setup for Tingsanchali and Chinnarasri (2001)

A constant inflow (varied throughout the tests) was supplied to the upstream reservoir where the hydraulic head above the embankment crest was 3cm and 5cm,

depending on the test case. The breach was initiated by lifting a vertical gate located upstream the embankment model crest, thus simulating 2-D or planar overtopping. A total of 6 wave gauges were used to record water surface elevation. In addition to the wave gauges, 2-D electromagnetic current meters were installed over the centreline of the model's crest to measure the velocity of the overtopping flow. A 90° V-notch weir measuring basin was used downstream the model to measure the breach outflow. For the mobile bed conditions, the model was constructed in a series of 5cm lifts, where the embankment material was sprayed with water before compaction. The side-view of the erosion process was recorded using a video camera and a high-speed photo camera. The purpose of the eleven experiments was to calibrate a numerical model developed for breach erosion and slope sliding due to planar overtopping.

Chinnarasri *et al.* (2003) report two series of mobile bed overtopping experiments using the same embankment and soil parameters to Tingsanchali and Chinnarasri (2001), except for two additional tests, where the downstream slope was 1:2 for Test Case B and C of the 2001 study (see Table B-1). Test Case A which was under fixed bed conditions, was not included in their study. The same construction technique and hydraulic flume performed in 2001 is reported in the 2003 study, except that the models were lined with a thin layer of bentonite to control seepage through the embankment. The purpose of this study was to investigate the failure mechanisms and rate of homogeneous noncohesive dikes under to overtopping flow. The study identified the damage caused by overtopping erosion in four stages, as shown in Figure B-15. Their study also computed erosion rates (referred to as degradation rate in their study), mm/s, from the side-view images captured, where results from four out of nine tests were shown as shown in Figure B-16.

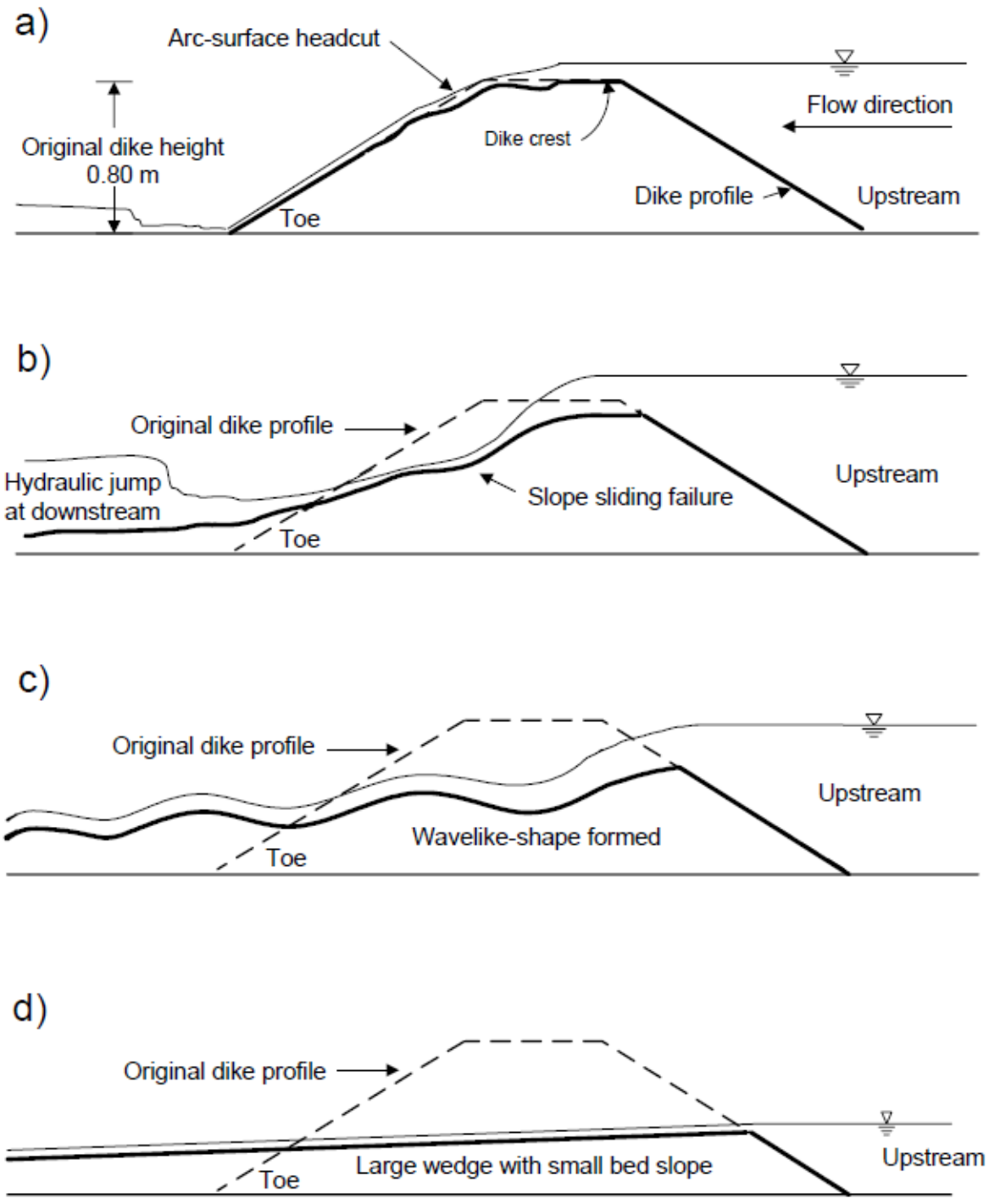

Figure B-15: Four stages of dike damage under overtopping flow (Chinnarasri *et al.* 2003)

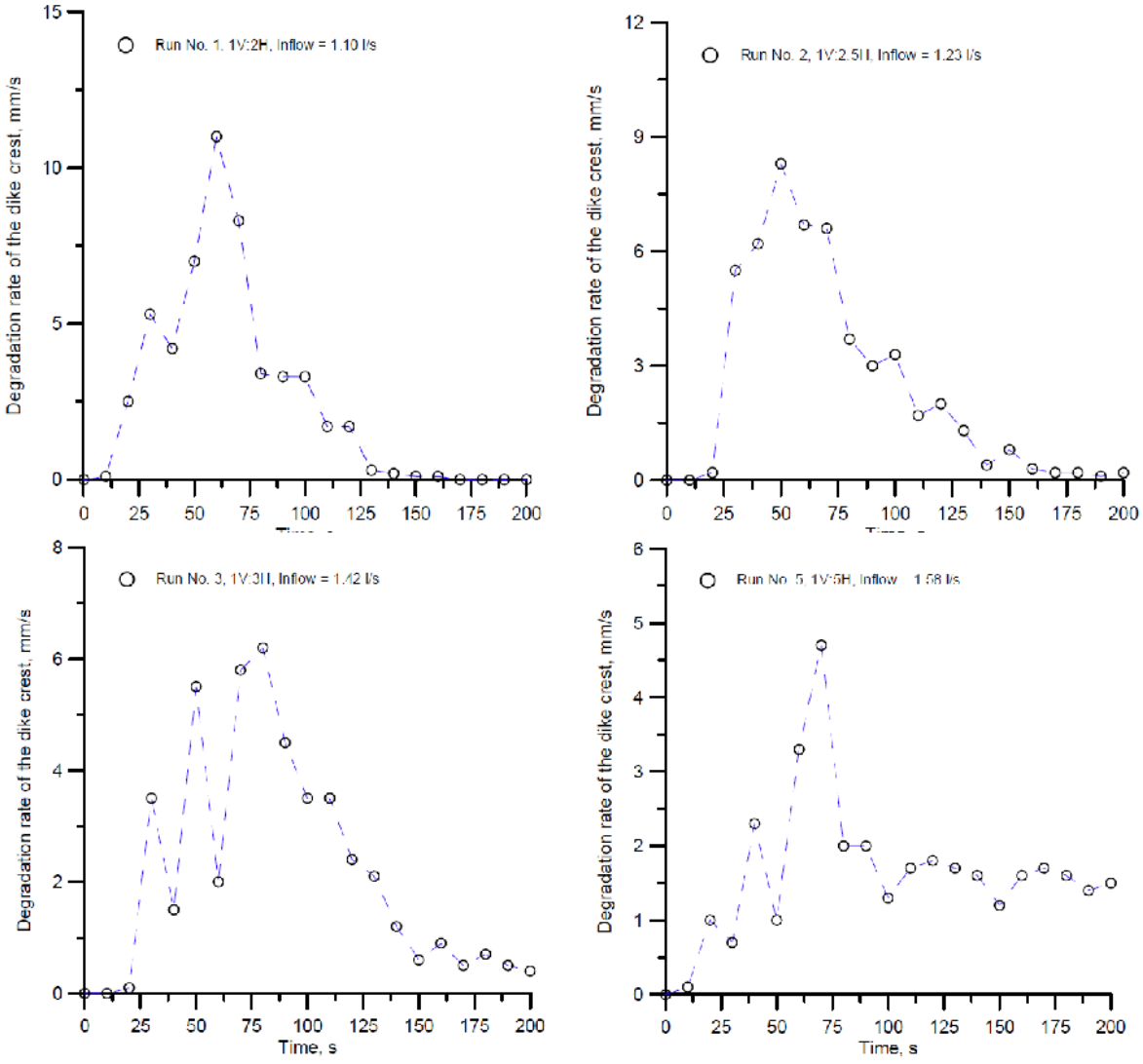

Figure B-16: Degradation rates for Tests No. 1, 2, 3 and 5 (Chinnarasri *et al.* 2003)

The investigation by Chinnarasri *et al.* (2004) reports 9 additional embankment overtopping tests performed at the Asian Institute of Technology. The tests performed were comprised of 0.6m high embankment models, with a crest width and upstream slope were fixed at 0.3m and 1:3, respectively. The authors state that the embankments were constructed using noncohesive material, however, the sand (70%) and clay (30%) mixture would exhibit cohesive properties. Two embankment materials were used for the first two test cases, were the noncohesive materials in the mixture was coarse sand and fine sand, yielding median grain sizes equal to

0.06mm and 0.034mm, respectively. A third test case comprised of a material with a median grain size of 0.044mm, where embankment model was lined with a 3cm thick clay layer. Other than grain size and upstream protection, the downstream slope was varied throughout the tests. All the embankment models, however, were lined with a thin layer of clay on the upstream slope. With respect to compaction, similar construction techniques in previous studies were applied. A rectangular breach pilot channel, 0.05m deep x 0.20m wide, was cut into the embankment crest centreline to initiate the breach. The experiments were carried out in a large basin with a sediment trap located downstream the embankment model prevented variations in tailwater conditions from influencing the experiments (see Figure B-17).

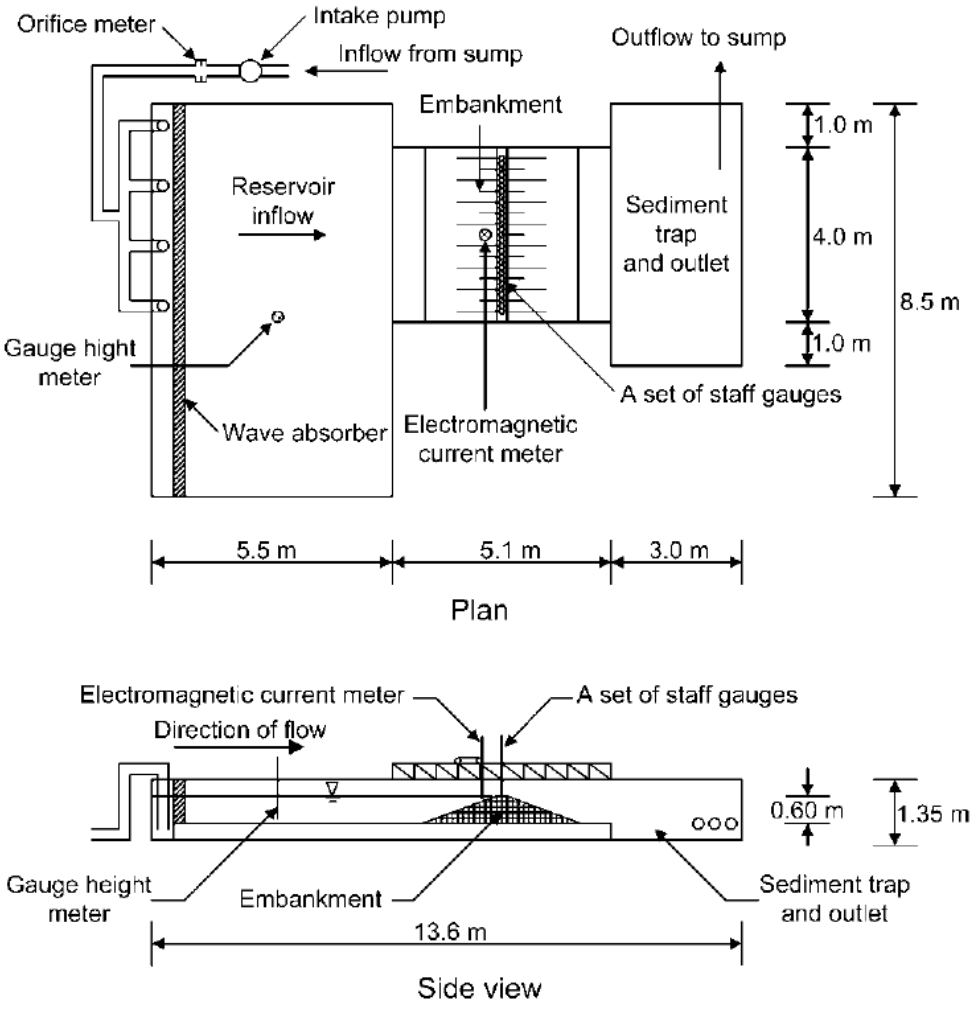

Figure B-17: Test setup (Chinnarasri *et al.* 2004)

The inflow to the upstream reservoir, measured using an orifice flow meter, was increased until outflow through the pilot channel was observed. The reservoir water surface elevation was recorded using a calibrated depth gauge, while a 2-D electromagnetic current meter, mounted on a carriage, was used to measure velocities through the breach channel at locations which could be varied transversely, longitudinally and vertically. Breach outflow was computed using two methods: by variations in storage volume with respect to time and by using the 2-D velocities measured at the breach cross-section. The maximum variation in peak discharge between the two methods was within 10%. The authors accept this range of error and therefore have utilized the second method. Breach channel dimensions were measured using a series of thin staff gauges mounted directly above. The authors state that the breach evolution was confirmed using video cameras and 2 high-speed digital cameras.

The authors state that during the initial breach phases, the breach process was mainly comprised of vertical erosion, where the longitudinal profile of the breach channel was parallel to the downstream slope. In later stages, lateral erosion was dominant. Despite the sediment trap, a hydraulic jump was observed on the downstream slope. Chinnarasri *et al.* (2004) state that the widening phase of the breach was due to a combination of tractive shear forces and side-slope collapses, as observed by Coleman *et al.* (2002) and mentioned by Pickert *et al.* (2004). The breach channel cross-section evolved from the initial rectangular shape, to an oval-triangular one and finally to a trapezoidal geometry as shown in Figure B-18. Their study also describes a dimensionless analysis, comprised of performed. Based on a dimensionless analysis, comprised of results and test parameters such as peak discharge, time-to-peak, grain size, embankment height, downstream slope and reservoir volume the authors propose an embankment breach parametric study.

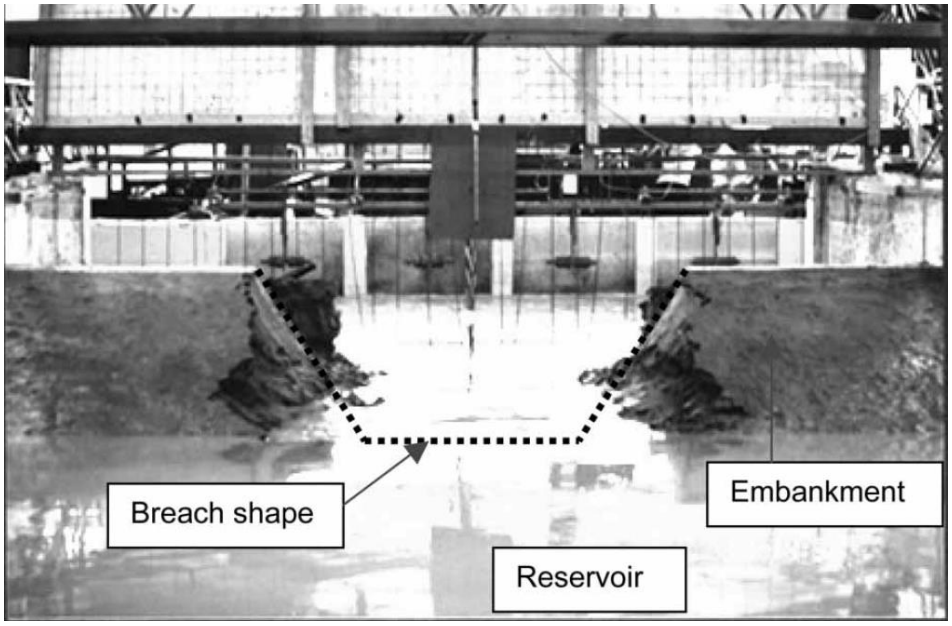

Figure B-18: Final breach shape from the second test case (Chinnarasri *et al.* 2004)

B.1.6 University of Karlsruhe - Institute of Hydromechanics (Karlsruhe, Germany)

The studies by Pickert *et al.* (2004, 2011) investigated the influence of important geotechnical parameters such as grain size and matric suction on breach processes that have been neglected in previous mathematical as well as physical models. Their first investigation was comprised of three noncohesive homogeneous embankment models, 0.3m high, 1m wide, and 1.9m long, with a crest width of 0.1m and shoulder slopes of 1:3 (see Figure B-19 and Table B-1). The embankments models were constructed in a 15m long x 1m wide x 0.7m deep flume at the Institute for Hydromechanics of the University of Karlsruhe, using coarse silt, medium sand and coarse silt, with d_{50} values of 0.035mm, 0.22mm, and 2.00mm, respectively (Pickert *et al.* 2004). The 2011 study used fine sand (*fS*), medium sand (*mS*) and a coarse sand (*cS*) with d_{50} values of 0.18mm, 0.22mm, and 0.035mm, respectively, as shown in Figure B-20. The experiment comprised of medium sand was repeated 5 times to ensure repeatability. The measured angle of internal friction for *fS*, *mS* and *cS* were 31.7°, 33.2° and 37°, respectively. The models were compacted in six layers, each 0.05m high, with a water content equal to 5% and a material

compaction factor (referred to as ‘degree of densification’ in the 2011 study) equal to 50%. Although their studies do not explicitly mention whether this relative factor pertains to density or compaction, such low values can only imply that the degree of densification recorded was the relative density, D_r.

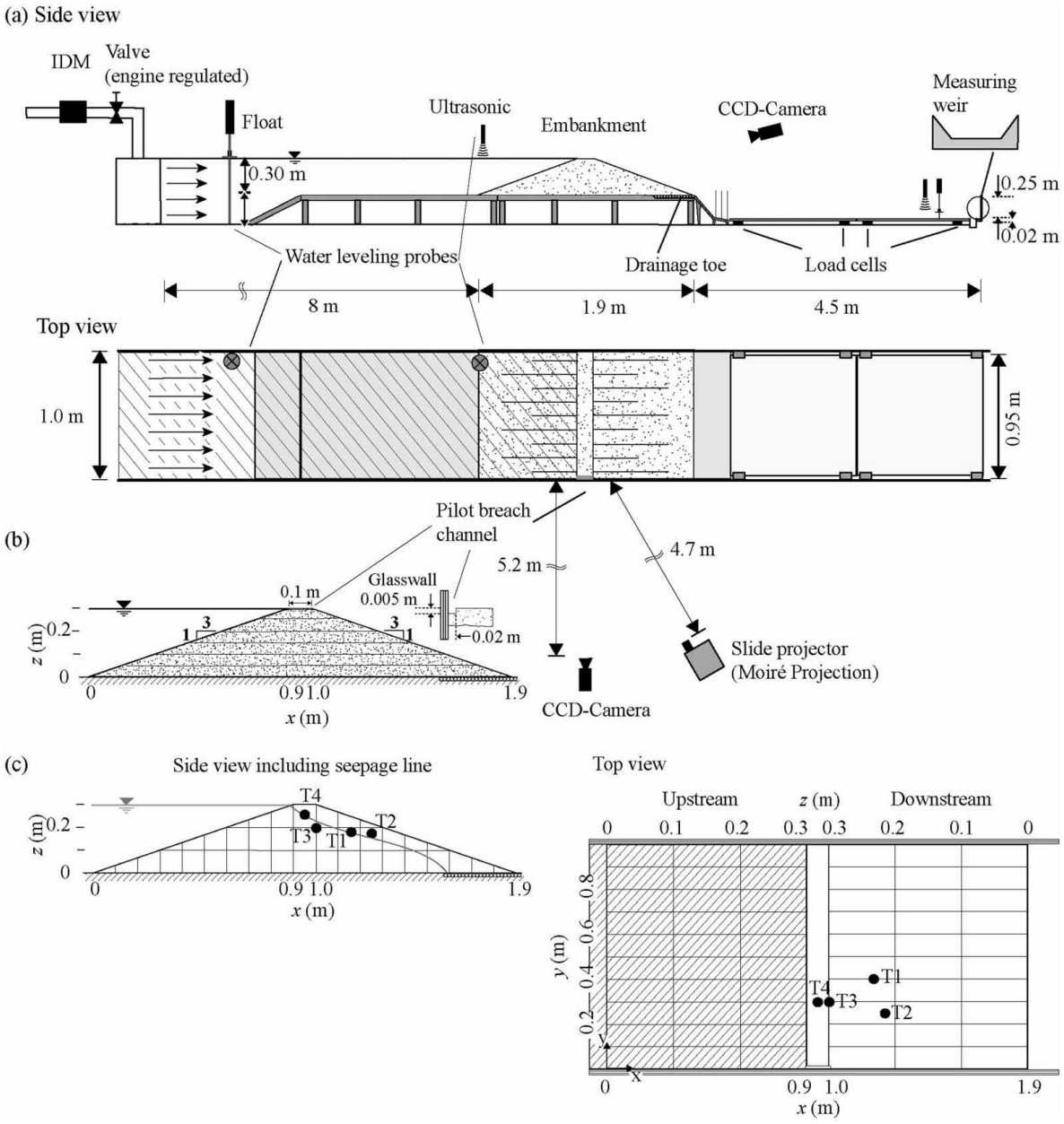

Figure B-19: Experimental setup (a) side and planform views (b) side-view of embankment model and frontal view of pilot channel (c) location of tensiometer probes for medium sand test (Pickert *et al.* 2011)

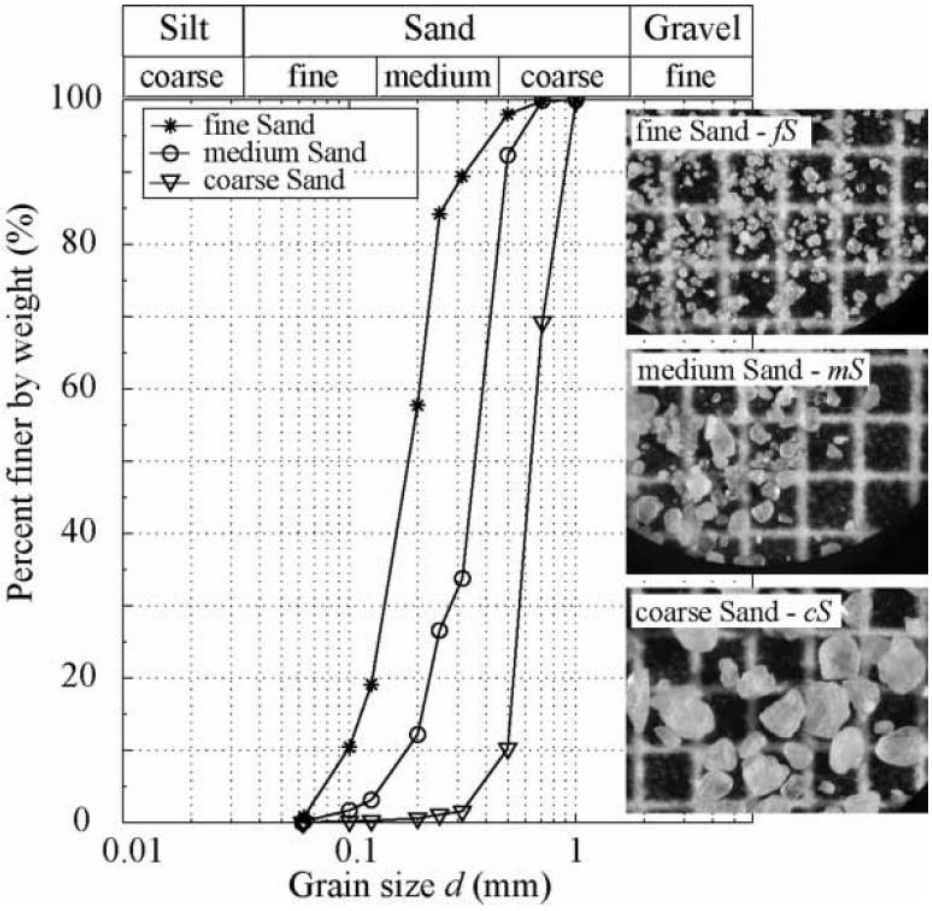

Figure B-20: GSD cited by Pickert *et al.* (2011)

The models were geometrically scaled 1:10, although their grain size was not scaled to the prototype since no measurements of PWP are available in prototype tests (Pickert *et al.* 2011). Seepage through the embankment models was controlled using a toe-drain, and a rectangular pilot channel, 0.02m wide and 0.02m (0.005m as reported in the 2011 study) deep cut along the entire width of the crest on the glass wall of the flume, similar to the technique used by Coleman *et al.* (2002). The reservoir was filled up slowly to ensure steady-state seepage while a plug dammed the pilot channel was removed when the water surface level reached 0.29m and 0.295m (*i.e.* 0.01m and 0.005m below the embankment crest), as stated in the 2004 and 2011 study, respectively. Three grids were installed downstream the embankment model to reduce the flow velocity and capture the eroded sediment, while a weighing scale located downstream the grids measured the instantaneous

weight of the eroded sediment and water flowing through the breach. The deposition rate was 95% with ± 1% accuracy as determined during calibration. The breach outflow was measured through a trapezoidal weir downstream the weighing scale. The weight of the sediment was calculated by subtracting the weight of the water from the total weight measured by the scale. Water level probes located in the upstream reservoir and weir measuring basin were used to record water surface elevation, while an inductive flow metre was used to measure inflow. A constant head was provided by the inflow pump. Two ultrasonic devices were used in the 2011 to supplement water surface level measurements. The test was stopped once an elevation difference between the upstream reservoir and embankment crest exceeded 0.03m, or, once the widening of the breach channel entrance reached the opposite wall of the flume. Up to six tensiometer probes (see Figure 3.12), 8cm long and 0.5cm in diameter, were installed during construction at different locations along the length, width and depth of the embankment models (only four are indicated in the setup and results of the 2011 study, *i.e.* Figure B-19 and Figure 3.13). The temporal response of the tensiometers was 1.7kPa/s and their measurement range was +0.8kPa and -1.0kPa. After observing Figure B-19, it seems that the tensiometers were positioned such that they coincide with the initial phreatic surface. The air entry values for *fS*, *mS* and *cS* were 2.7kPa, 1.4kPa and 0.8kPa, respectively.

The breach process was recorded from the side as well as from the top. A nonintrusive mapping technique known as ‘Fringe Projection’ was used to capture the half breach evolution using the side-view camera and slide projector as shown in Figure B-21 to Figure B-24. Using the information from the angle of the projector, its distance from the object, the optics of the projector-camera system and angle relative to the projector and surface, reconstruction of the breach contour can be determined successfully, as shown in Figure B-25. Observations from the experiments indicate the hourglass or Venturi shape, as observed by other researchers (Coleman *et al.* 2002; Pickert *et al.* 2004; Geisenhainer and Kortenhaus, 2006; Stretch and Parkinson, 2006; Wishart, 2007). Collapsing material

overhangs were also observed during the experiment (Coleman *et al.* 2002; Geisenhainer and Kortenhaus, 2006). The researchers attribute this phenomenon to apparent cohesion, or soil suction. From the observed erosion patterns in Figure B-22 to Figure B-24 and erosion curves in Figure B-26 for the embankments, the authors classify the breach process into two distinct stages:

- Breach initiation: The slope retreat of the breach channel is parallel to the downstream slope and flow rates are low;
- Breaching: A rapid increase in the eroded sediment and breach outflow, as the regressive erosion in the breach channel reaches the upstream slope.

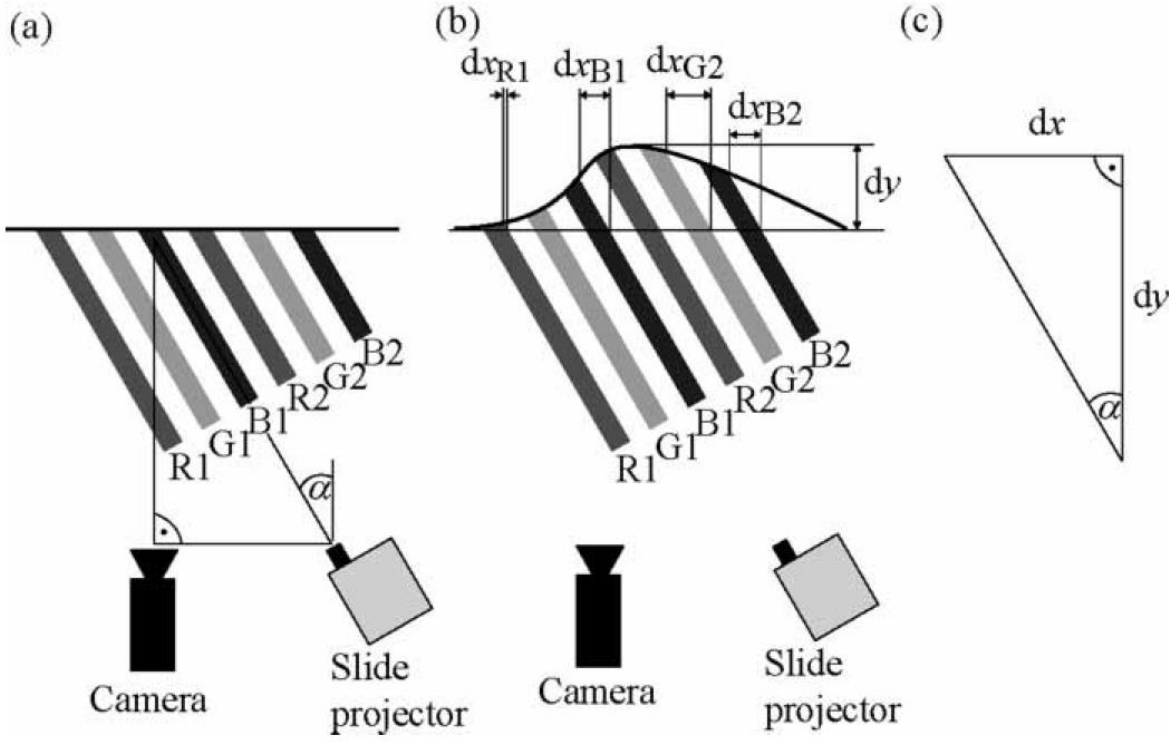

Figure B-21: Fringe projection technique (a) initial setup (b) altered setup (c) geometrical correlation (Pickert *et al.* 2011)

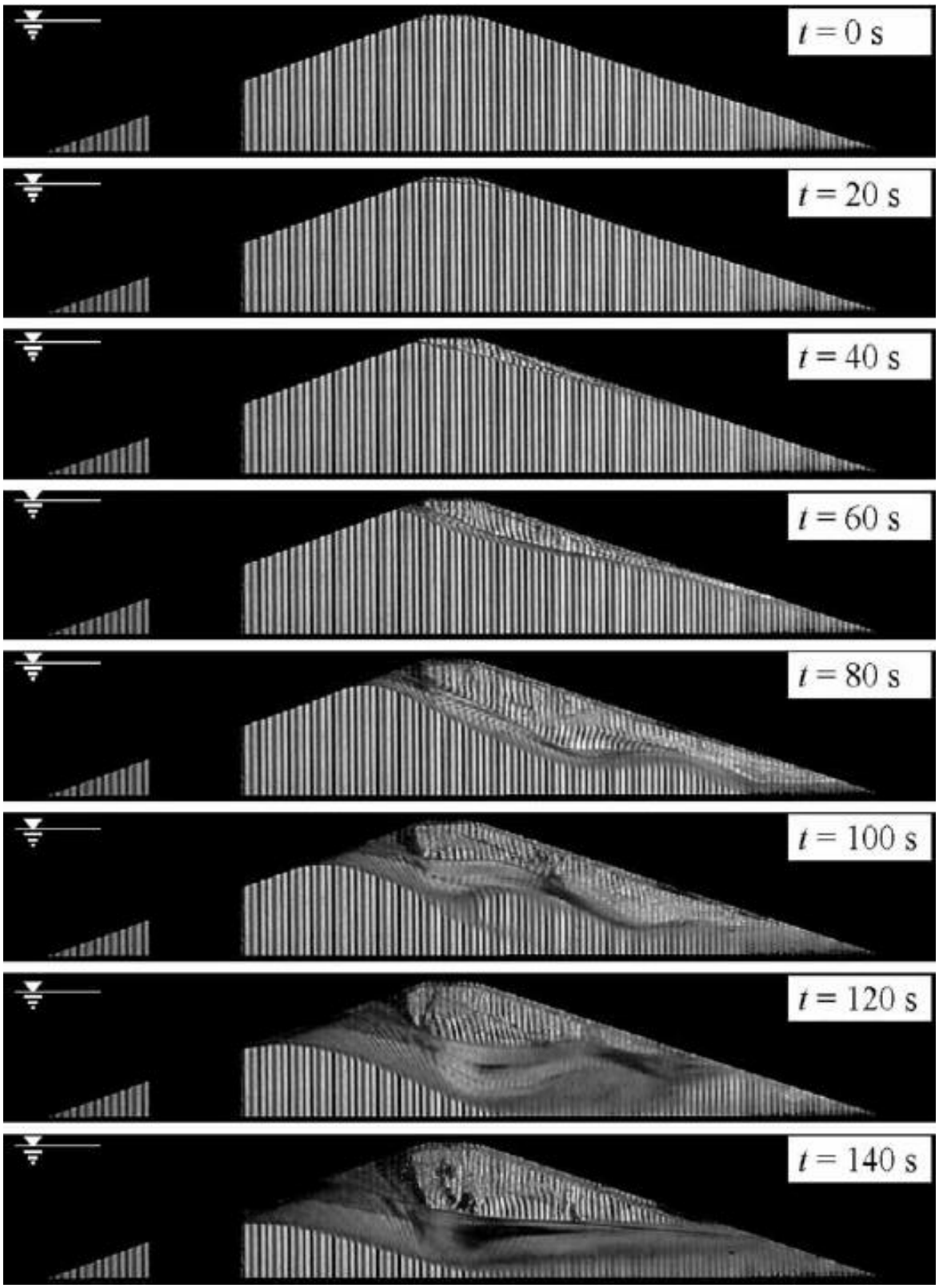

Figure B-22: Breach evolution for medium sand, *mS* (Pickert *et al.* 2011)

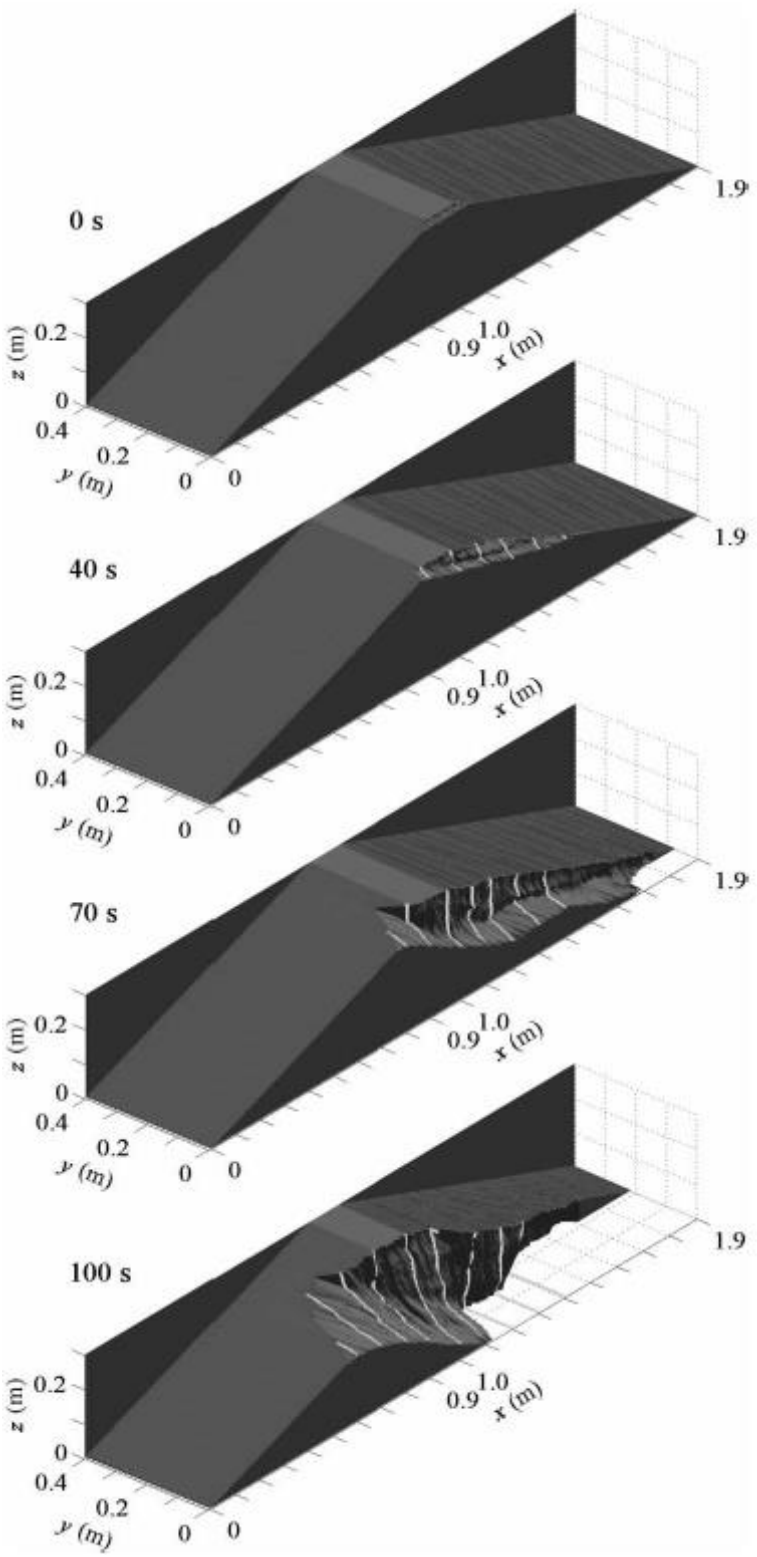

Figure B-23: Breach channel cross-sections at longitudinal sections (shown in white lines) developing with time for medium sand (Pickert *et al.* 2011)

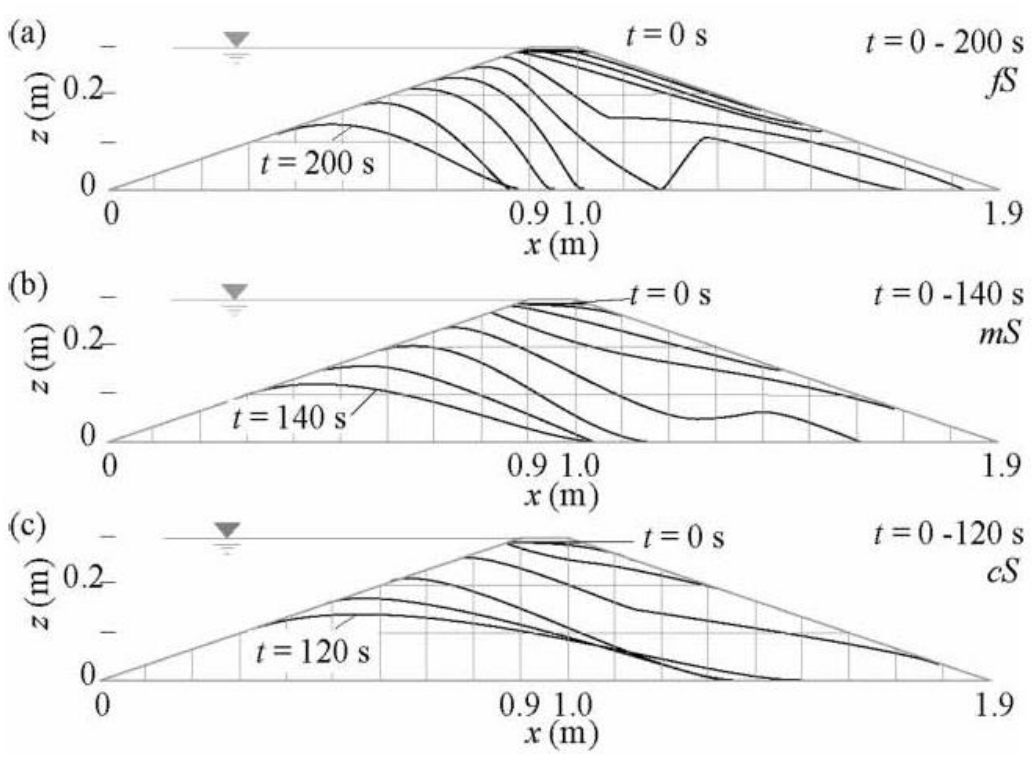

Figure B-24: Longitudinal breach profile adjacent to flume walls at 20s intervals for (a) *fS* (b) *mS* (c) *cS* (Pickert *et al.* 2011)

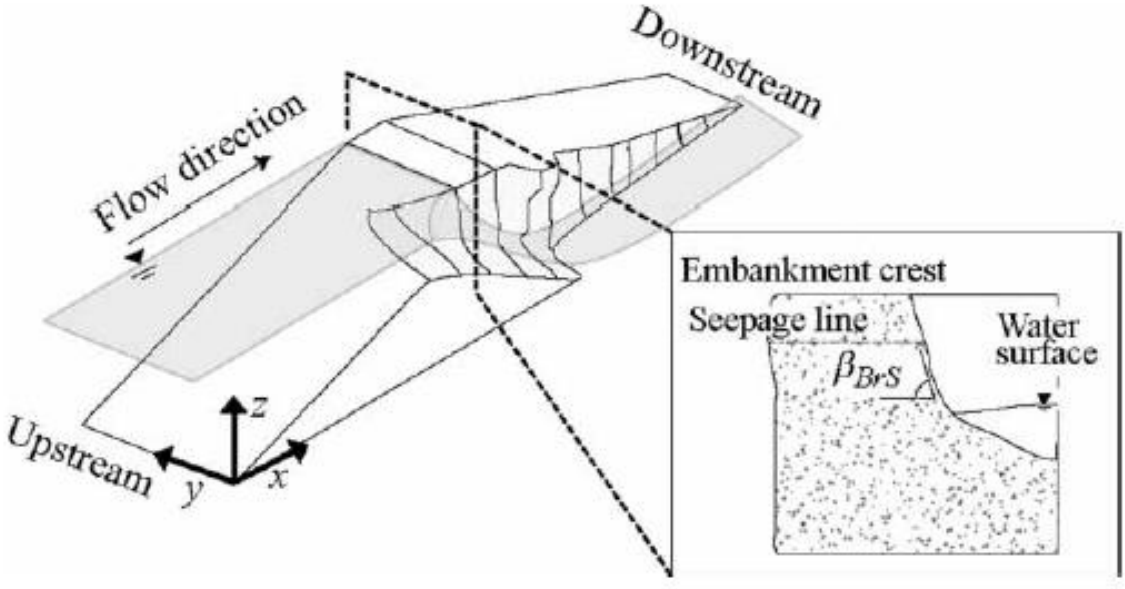

Figure B-25: Breach channel as shown in isometric view and cross-section as seen from upstream indicating side-slope angle (Pickert *et al.* 2011)

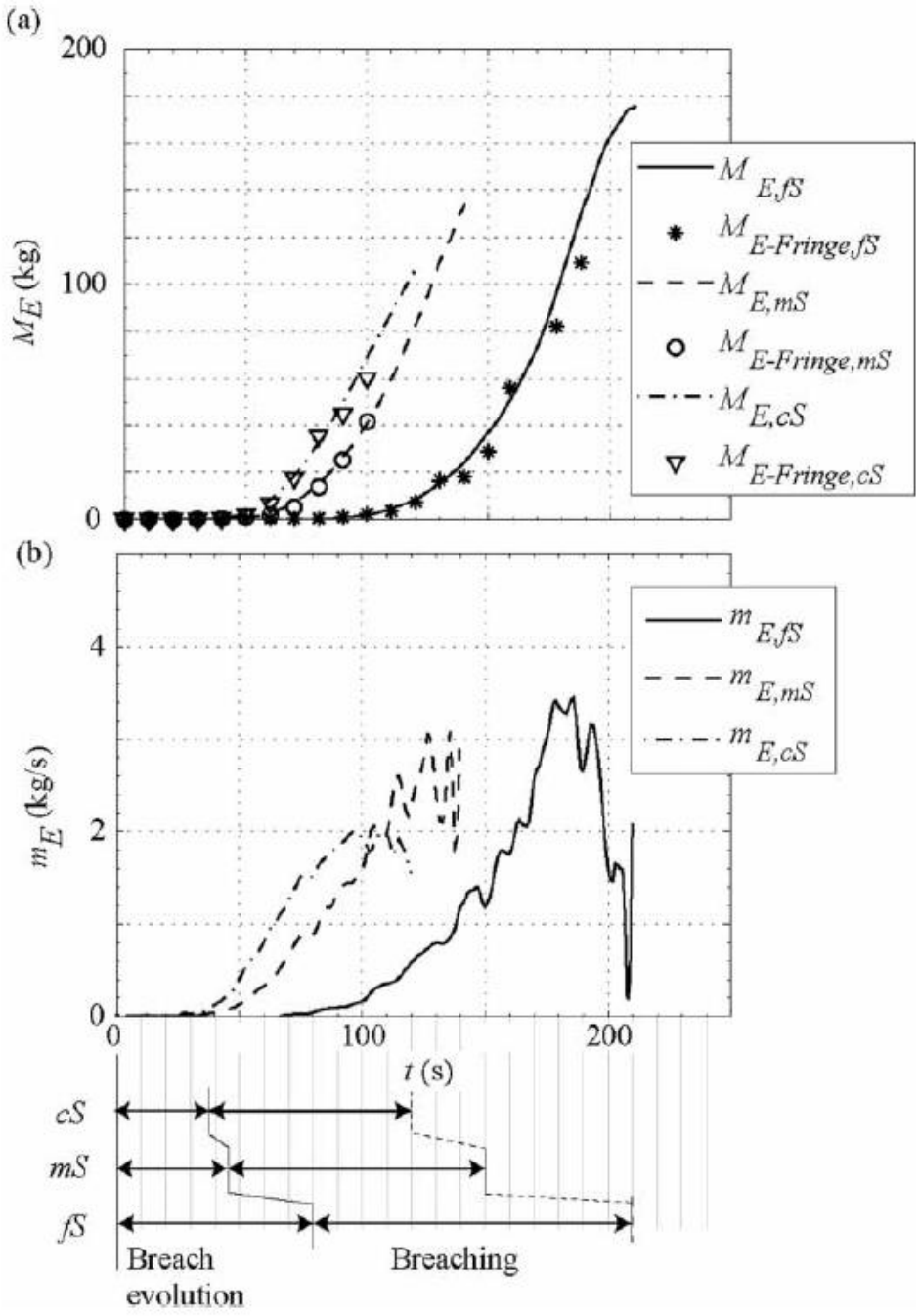

Figure B-26: Erosion curve for *cS*, *mS* and *fS* (a) mass (b) erosion rate (Pickert *et al.* 2011)

From the breach channel cross-sections and hydrographs obtained, breach flow velocities ranged between 0.2 and 2.4m/s, depending on the longitudinal section.

Overflow depth ranged from 0.005m during the start of the experiment, and 0.20m towards the end. In Figure B-24, a scour hole can be seen to develop during the breach process for the fine and medium sands, indicating a headcut type of erosion. For the coarse sand, the erosion was more constant since the side-slope failures were more frequent (*i.e.* lower suction values). This is indicated by the multiple peaks in the mass curves in Figure B-26 for *fS* and *mS*. Figure B-27 below shows the extent of erosion (and its dominance) with respect to the vertical and lateral directions, as well as the side-slope angle of the breach channel for the different materials used.

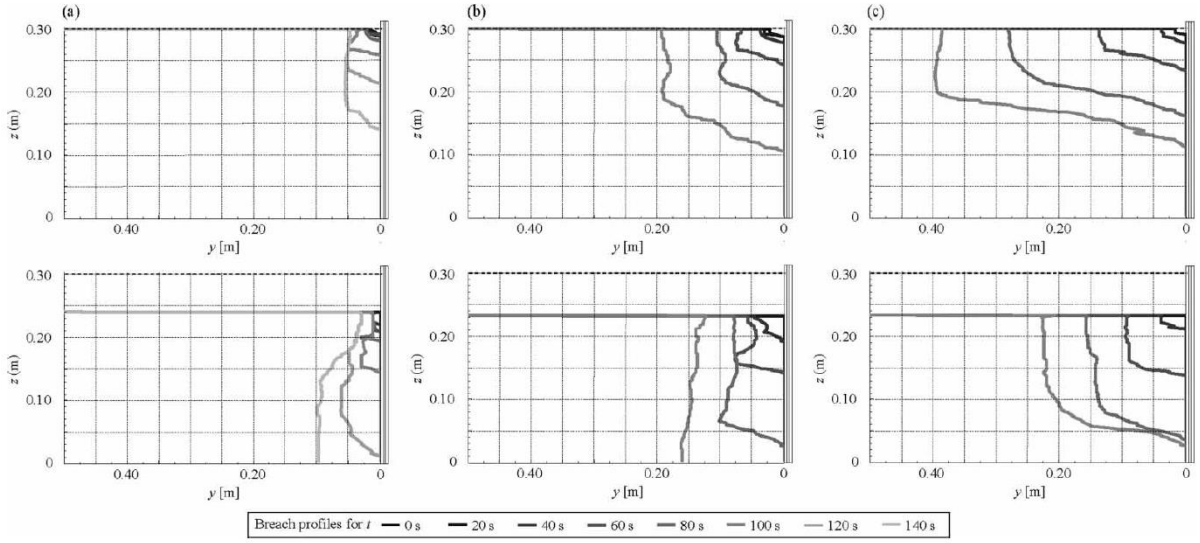

Figure B-27: Breach channel cross-sections (looking downstream) at 20s intervals at x = 0.9m (above) and x = 1.2m (below) for (a) *fS* (b) *mS* (c) *cS* (Pickert *et al.* 2011)

It is clear that the suction forces the finer material maintains steeper (and even adverse) side-slope angles. The 2011 study also defines two types of side-slope failure, one occurring under shear in coarse sediments, and another occurring under tension in fine sediments. Figure B-28 shows the overhang material in fine sand, where side-slope angles are lower than 90° (acute) whereas for the coarse sand, angles are larger than 90° (obtuse). In Figure 3.13, PWP measurements were truncated once the tensiometer becomes in contact with water or air and according to the 2011 study, those final measurements represent the failure points. The

authors then determine the mean values of the final readings from the 4 (or more) tensiometers for *fS*, *mS* and *cS* to be -2.4kPa, -1.1kPa and -0.5kPa, respectively. Those values according to the authors correlate well with the air entry values of the three materials used. The authors then related the capillary height, h_c, to the PWP, and express it in terms of a characteristic pore-diameter, d_w, using the following equation:

$$h_c = \frac{4\sigma}{\rho g d_w} \tag{B-1}$$

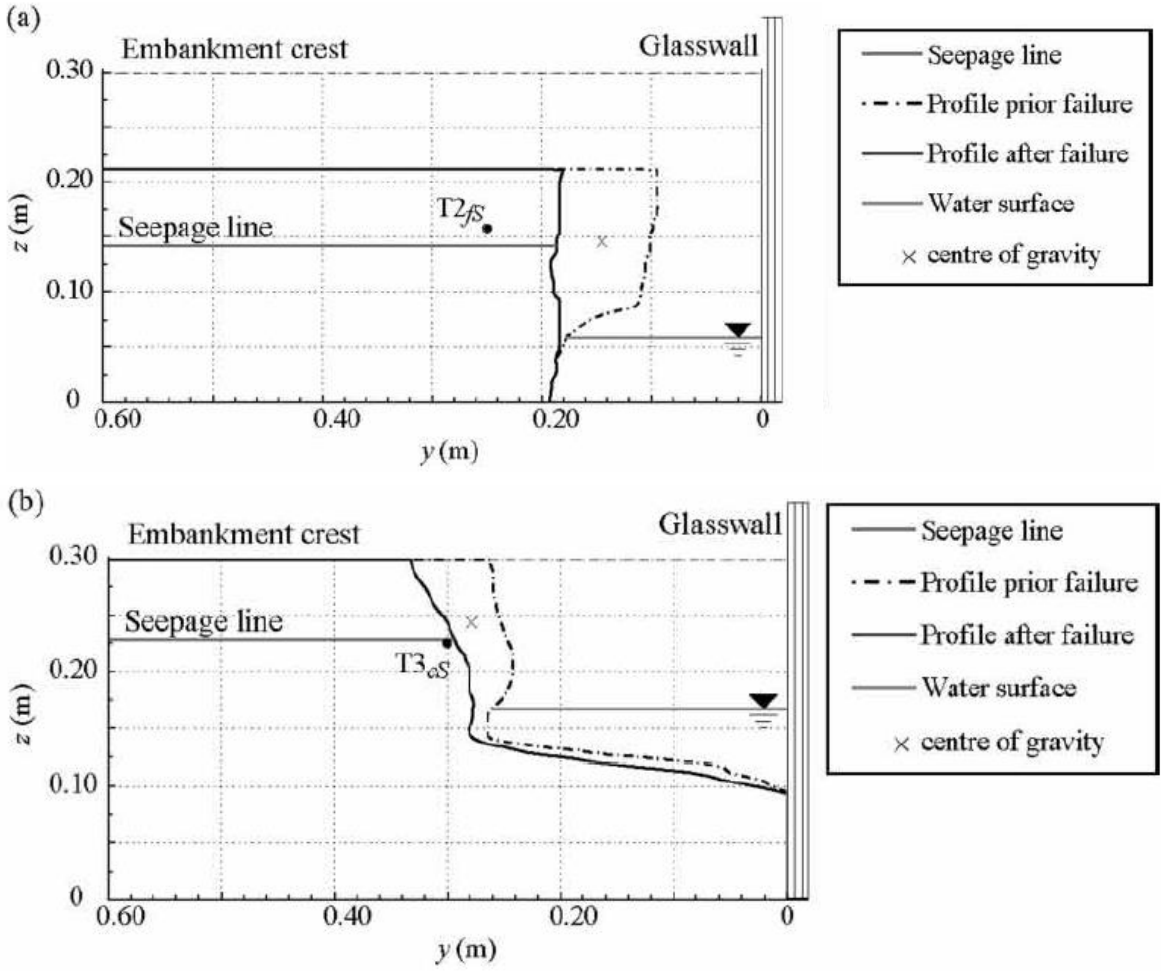

Figure B-28: Downstream view showing breach channel cross-sections before and after failure for (a) *fS* at x = 1.27 and t = 151s (b) *cS* at x = 1.0m and t = 94.8s (Pickert *et al.* 2011)

Using dimensionless analysis, the authors define two dimensionless groups using the breach outflow and time, whereas the dimensionless hydrograph is plotted for their own data in Figure B-29 and with two other data sets in Figure B-30. The authors propose a relationship between the two dimensionless groups for all three data sets, and distinguish between two types of breach processes; one that is controlled by 'apparent cohesion' (where d_0 < 1mm) and another which is controlled by the shear stresses generated by the breach outflow.

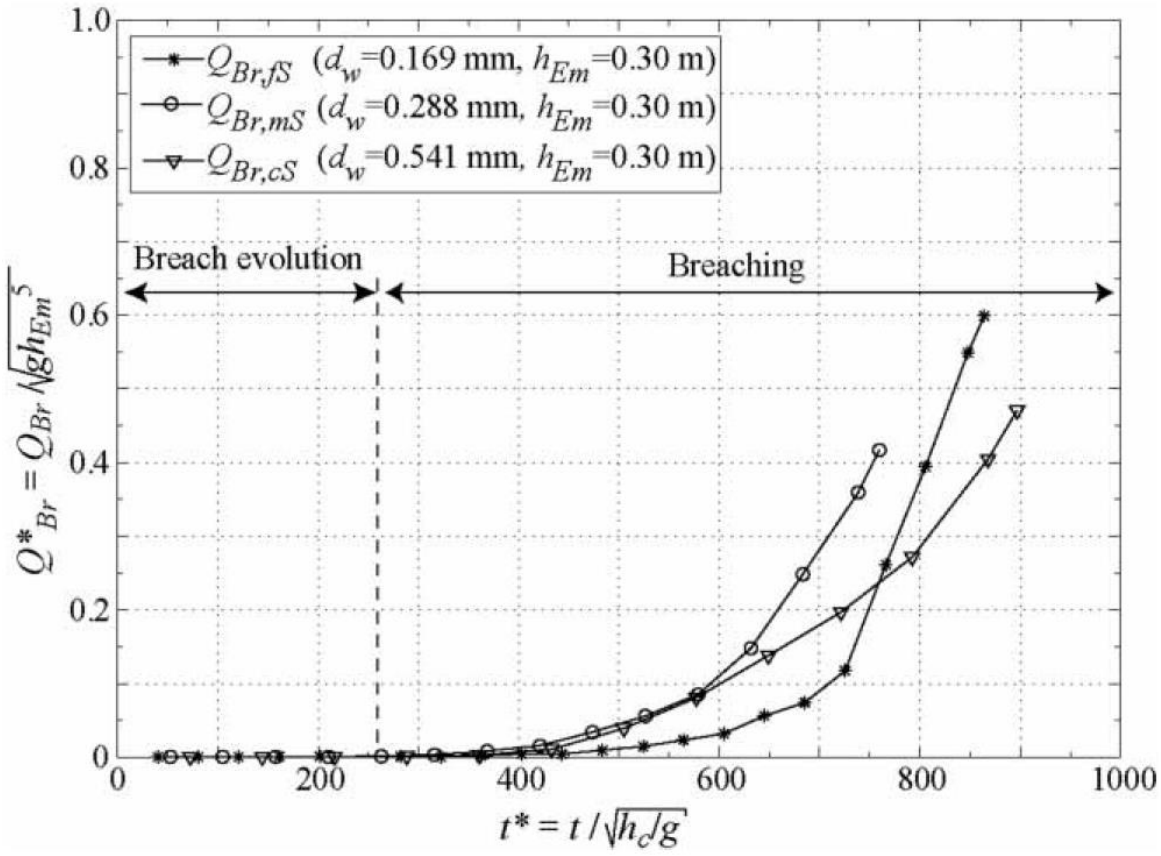

Figure B-29: Dimensionless outflow hydrograph for *fS*, *mS* and *cS* (Pickert *et al.* 2011)

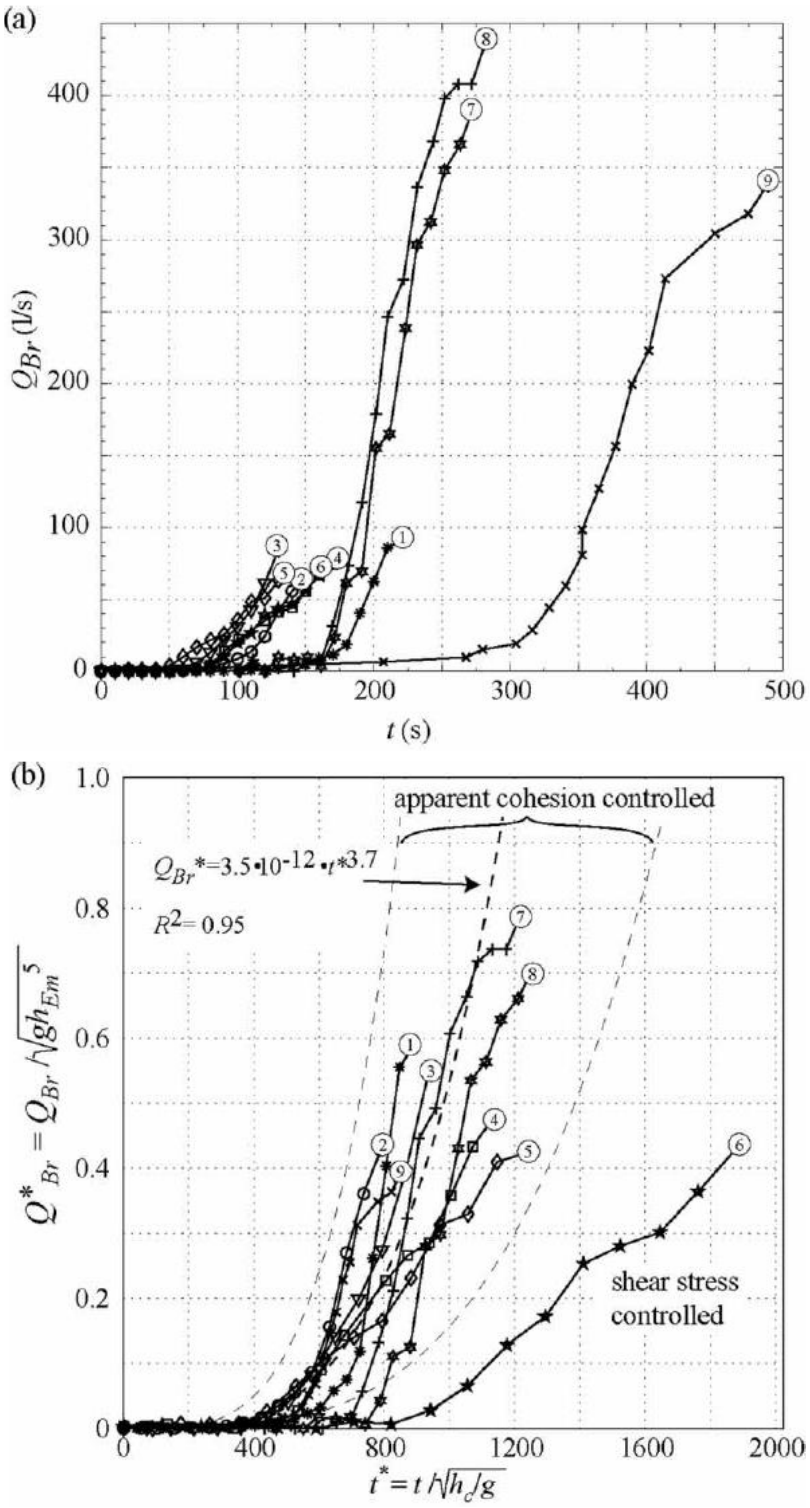

Figure B-30: Dimensionless outflow hydrograph cited in Pickert *et al.* (2011) study for (a) three different studies (b) Pickert *et al.* (2011)

B.1.7 University of KwaZulu-Natal (Durban, South Africa)

In 2005, tests were conducted at the Department of Civil Engineering, University of KwaZulu-Natal in Durban, South Africa to investigate the breach process in sand barriers in temporarily open/closed estuaries. A total of twenty four models, constructed and tested using sand (d_{50} = 0.6mm) in a model estuary basin 2m wide x 4 long and 0.2m deep is described in the study by Stretch and Parkinson (2006) and Parkinson and Stretch (2007). Very little detail is given on the construction method of the models; however, the authors state that a V-notch, 1cm deep, was carved into the crest's centreline to initiate breach at the centre. A test matrix of the experimental investigation is summarised in Table B-1. A video camera, mounted upstream of the embankment was used to record breach evolution as well as water surface levels. Various embankment geometries were incorporated into the tests to investigate the breach process.

The investigation described the breach process using two phases; initiation and formation. During the initiation phase, scouring of the downstream face created a channel which conveyed the flow downstream, whereas the embankment's upstream crest remained intact and the water surface level nearly steady. During the formation phase, erosion of the upstream crest of the breach channel resulted in a significant downward erosion followed by lateral erosion and widening. In general, the breach process was similar to those observed by Coleman *et al.* (2002) and Visser (1998), except that in the latter the reservoir elevation was kept constant. The final breach channel shape was described as having a Venturi or hourglass plan view with near vertical side-slopes and overhangs (see Figure B-31), as observed by Coleman *et al.* (2002), Pickert *et al.* (2004, 2011), Geisenhainer and Kortenhaus (2006), Stretch and Parkinson (2006) and Wishart (2007). The distinctive curved or crescent-shaped upstream breach channel entrance was also reported as per observations by Coleman *et al.* (2002), IMPACT (2004a) and Morris *et al.* (2007).

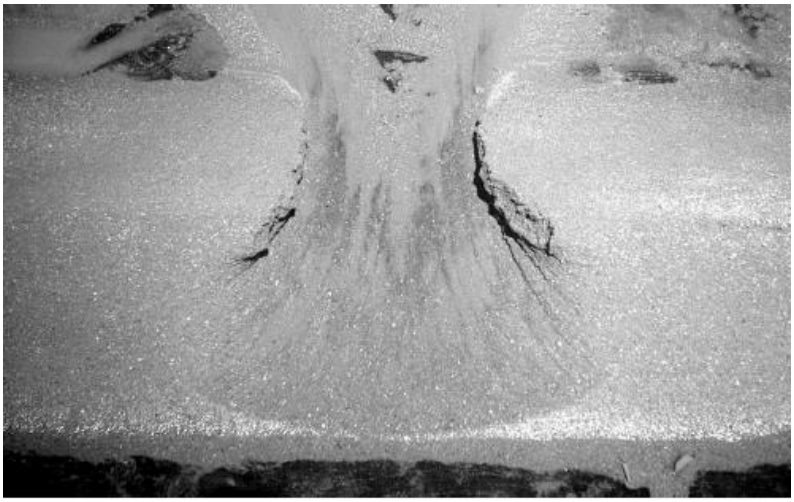

Figure B-31: View from upstream after a breach showing a Venturi shaped breach channel with a crescent-shaped upstream crest (Stretch and Parkinson, 2006)

Breach width was computed from images captured by the video camera, while breach volumes were estimated as being the product of the breach width and embankment cross-section. Breach outflow volumes were computed from reservoir volume-stage relationships at certain time intervals. Using data from twenty four embankment configurations, the authors were able to investigate dimensionless relationships between variables pertaining to final dimensions of breach width, reservoir hydraulic head, embankment width, and eroded or breach volumes. Stretch and Parkinson (2006) stated that the breach width is proportional to the cube-root of the outflow volume a relationship referred to as the "$1/3$ rule" in their literature.

As can be shown from Figure B-32 and Figure B-33, the dimensionless breach width is constant for all model parameters. Further analysis of the data was carried out during the intermediate breach times by Parkinson and Stretch (2007). Their study indicates that while the $1/3$ rule applies to the final breach width, it under predicts the breach width at early stages of the breach mechanism due to the exponential increase in breach width which depends on the applied hydraulic head in the reservoir (see Figure B-34).

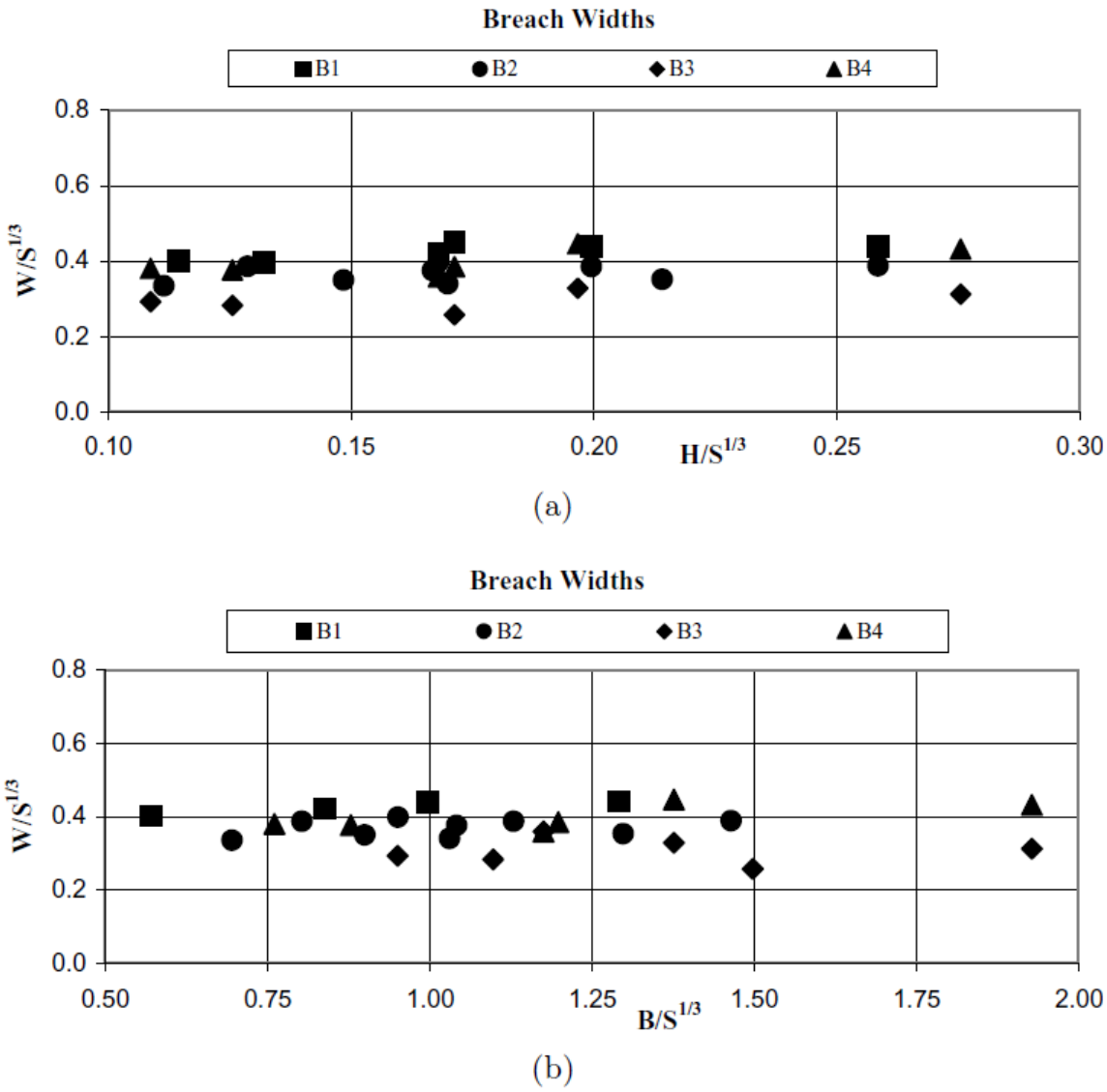

Figure B-32: Dimensionless final breach width for different sand barrier shapes plotted against (a) reservoir hydraulic head (b) barrier length (Stretch and Parkinson, 2006)

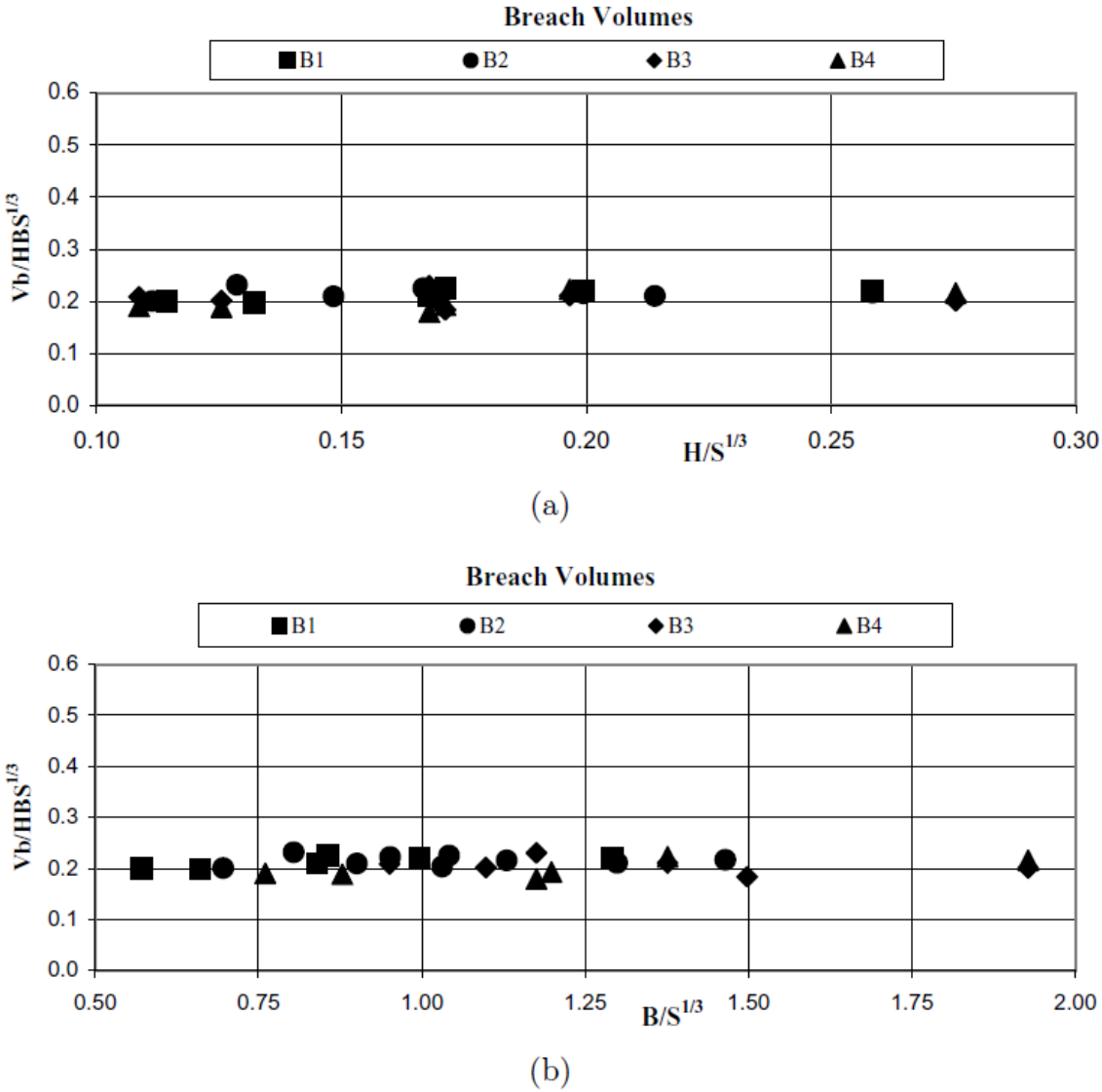

Figure B-33: Dimensionless final breach volume for different sand barrier shapes plotted against (a) reservoir hydraulic head (b) barrier length (Stretch and Parkinson, 2006)

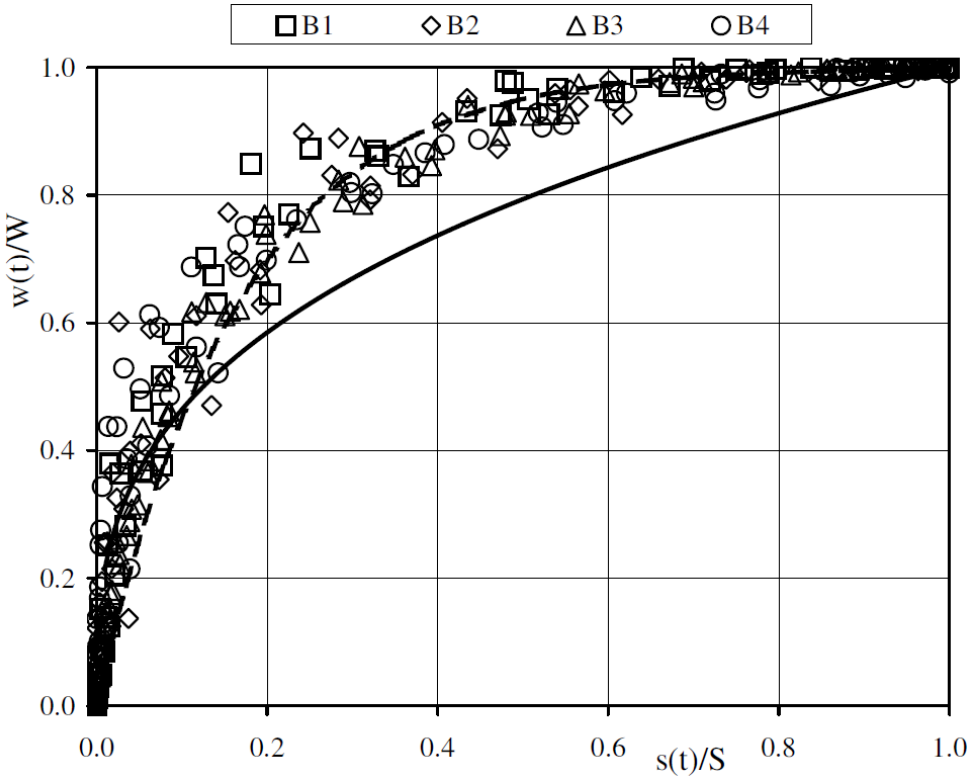

Figure B-34: Normalised plot between breach width and outflow volume. Dashed line is a curve fit of data; the solid represents the ⅓ rule (Parkinson and Stretch, 2007)

B.1.8 Swiss Federal Institute of Technology (Zurich, Switzerland)

An extensive experimental program was conducted at the Laboratory of Hydraulics, Hydrology and Glaciology of the Swiss Federal Institute of Technology in Zurich, Switzerland, on noncohesive homogeneous river dikes. The study by Schmocker and Hager (2009) revisits plane overtopping and the consequential vertical erosion by investigating the influence of scale effects and limitations due to grain size and embankment geometry on breach formation. The authors present a simple trapezoidal shape laboratory model with mild shoulder slopes and without any surface protection or fine sediments in order to control the breach parameters and isolate the breach process from complex mechanisms such as sliding failure or internal erosion. Figure B-35 below shows the experimental setup of the investigation. A total of thirty nine experiments were performed. The test program

was comprised of nine exact scale series, fifteen repeatability and fifteen side-wall effects tests.

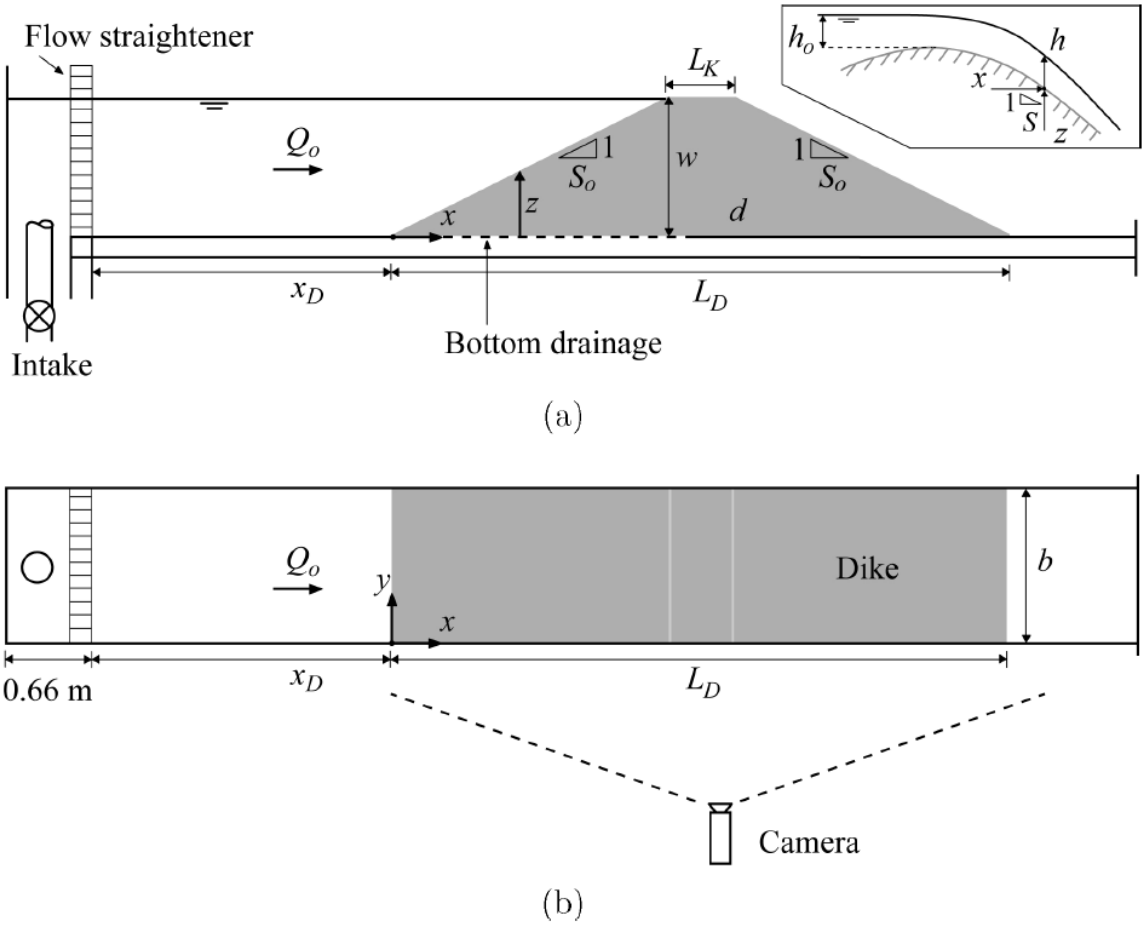

Figure B-35: Experimental setup (Schmocker and Hager, 2009)

Scale series tests (see Figure B-36) were comprised of three exact geometric scales, L_{rr} = 1, 0.5 and 0.25, investigated using different three scale families of inflow and grain size ranges for each of the constructed scale. The model/prototype relationships of the breach characteristics (*e.g.* outflow, storage volume, velocity and time) were investigated using the Froude criterion, since gravity forces dominate in free surface flow. The sediment scaling was satisfied geometrically and based on the Shields number (*i.e.* dimensionless threshold criterion) although this does not imply that the tractive shear stress would also be scaled. The repeatability tests were carried out three times using five overall configurations comprised of various

geometries, grain size and inflow. The side-wall effect tests were carried out with five identical configurations using three flume widths, 0.1m, 0.2m and the full 0.4m width for various dike scales while inflow and grain size was varied according to the Froude criterion.

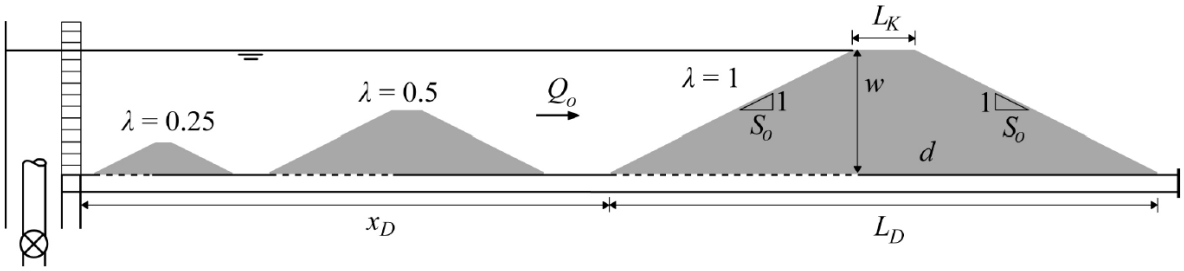

Figure B-36: Scale series tests (Schmocker and Hager, 2009)

The authors state that the dike material was installed in a dry state, without compaction. The setup of the drainage element used differs from that of which has been used in the tests of Coleman *et al.* (2002). In this study, the drainage element was installed on the upstream side of the dike, between the upstream toe and upstream apex of the crest as shown in Figure B-35 and Figure B-36. This was achieved by constructing the dike over a false floor made of PVC material. The drainage area was drilled with 2cm holes in a 5cm x 3.5cm template across the width and length of the flume. A finer mesh with a pore size of 0.5mm was installed over the drainage area to prevent washout of the sediment. Filling the reservoir with the constant inflow to the dike's crest level took about 30 seconds; meanwhile, the discharge through the drain was measured at 3-6% of the approach flow. The authors state that seepage was not scaled since the Froude criterion cannot be used to scale processes which are attributed to other effects (*i.e.* surface tension). They state that seepage was controlled for satisfying the stability of the slopes. From previous tests, it was observed that seepage did in fact contribute to the failure of the dike by slope slides. This was more obvious for grain sizes as large as 8mm. Hence the large grain sizes was excluded from the repeatability and side-wall effects tests, and were only included in the scale series tests.

Generally, duplicability of the tests were simulated well, with limitations found for larger grain sizes (*e.g.* d_0 = 4mm), although the variations in the transient dike profile decreased for larger inflows. These tests also demonstrated that profile variations were largest at the initial overtopping stage, where maximum deviations < 10mm and occurred at the dike's initial crest section or downstream toe. For the side-wall effects tests, limitations were observed for small widths (0.10m). With respect to the scale series tests, there were limitations in erosion, especially during intermediate times, for dikes with L_{rr} = 0.25 due to the shallower overtopping depths. The authors attribute this behaviour to the dominance of viscous forces over gravity forces in models constructed using smaller scales. Larger dikes tended to erode faster due to higher turbulence intensities. It was also found that the scale family for the largest grain size range (*i.e.* 2, 4, 8mm versus the two other scale families using 1, 2, 4mm) yielded the largest variability in breach profiles, due to the governance of sliding failures observed in the downstream slope for larger sediments due to the immediate saturation (see Figure B-37 and Figure B-38). Apart from the influence of the large grain size on slope sliding, scale effects are negligible.

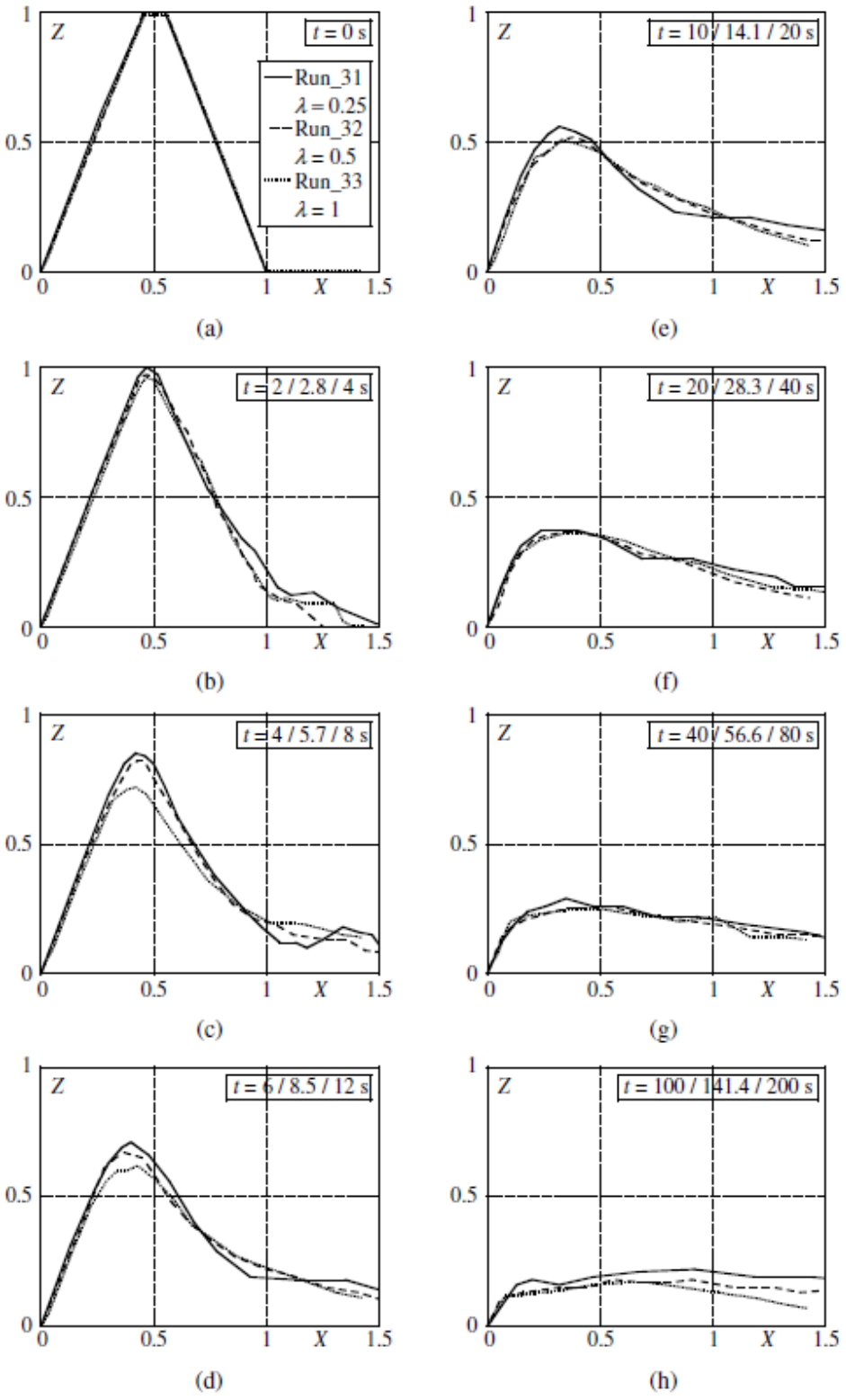

Figure B-37: Scale family I (d_0 = 1, 2 and 4mm for L_{rr} = 0.25, 0.5 and 1.0, respectively) showing normalized dike profile at various times (Schmocker and Hager, 2009)

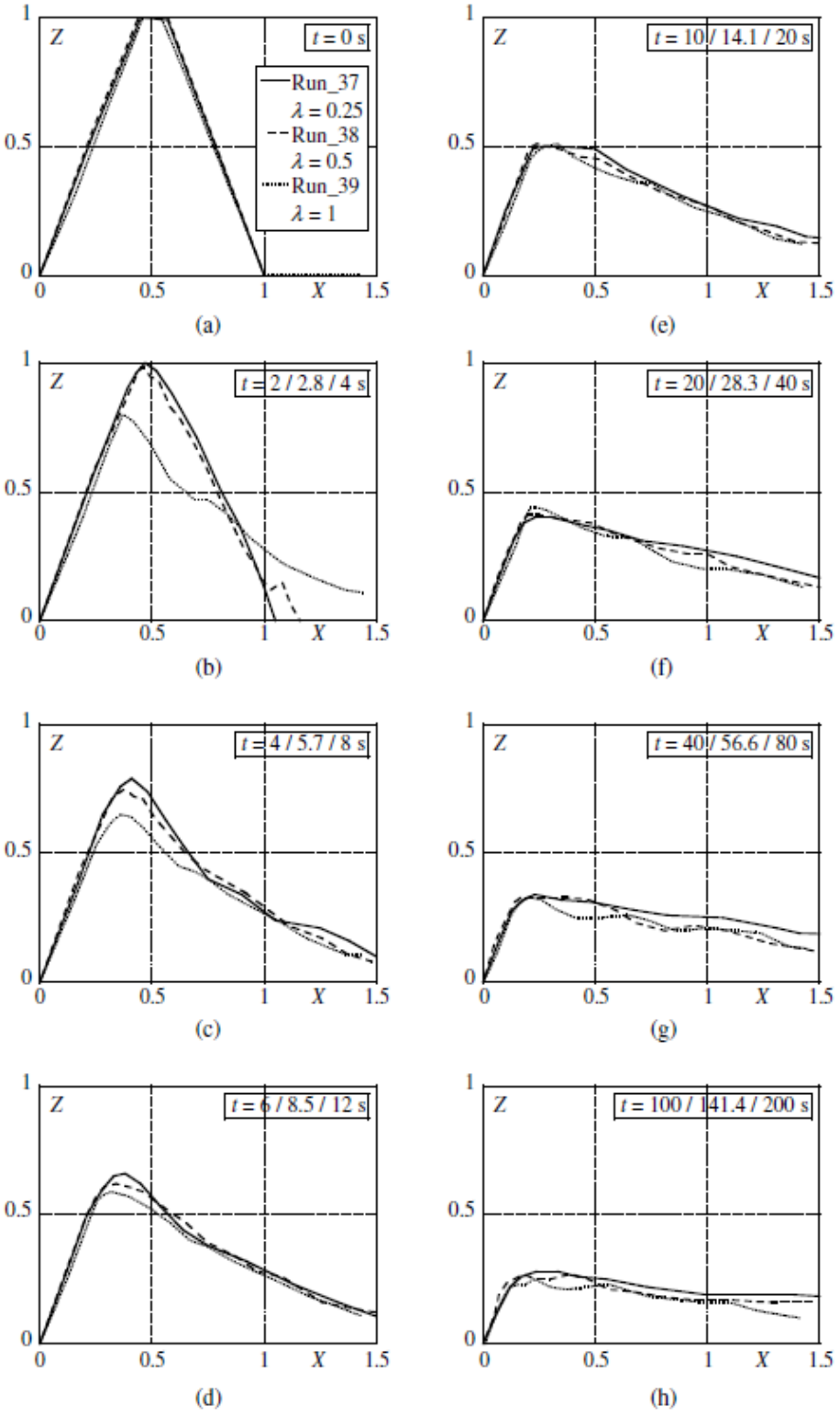

Figure B-38: Scale family III (d_0 = 2, 4 and 8mm for L_{rr} = 0.25, 0.5 and 1.0, respectively) showing normalized dike profile at various times (Schmocker and Hager, 2009)

In the study, the velocities was along the breach profile were computed and the Froude number plotted at various times for the three scale families used. During breach initiation, Froude numbers were high and were later observed to drop. From Figure B-39, it can be seen that there are variations in the Froude number computed for the three scales. The study recommends minimum dike dimensions, grain size and specific discharge for mobile-bed laboratory models simulating overtopping flow ($1mm < d_0 < 4mm$, $z_{cr} > 0.2m$, $b > 0.2m$, and $q > 20\ l/s/m$).

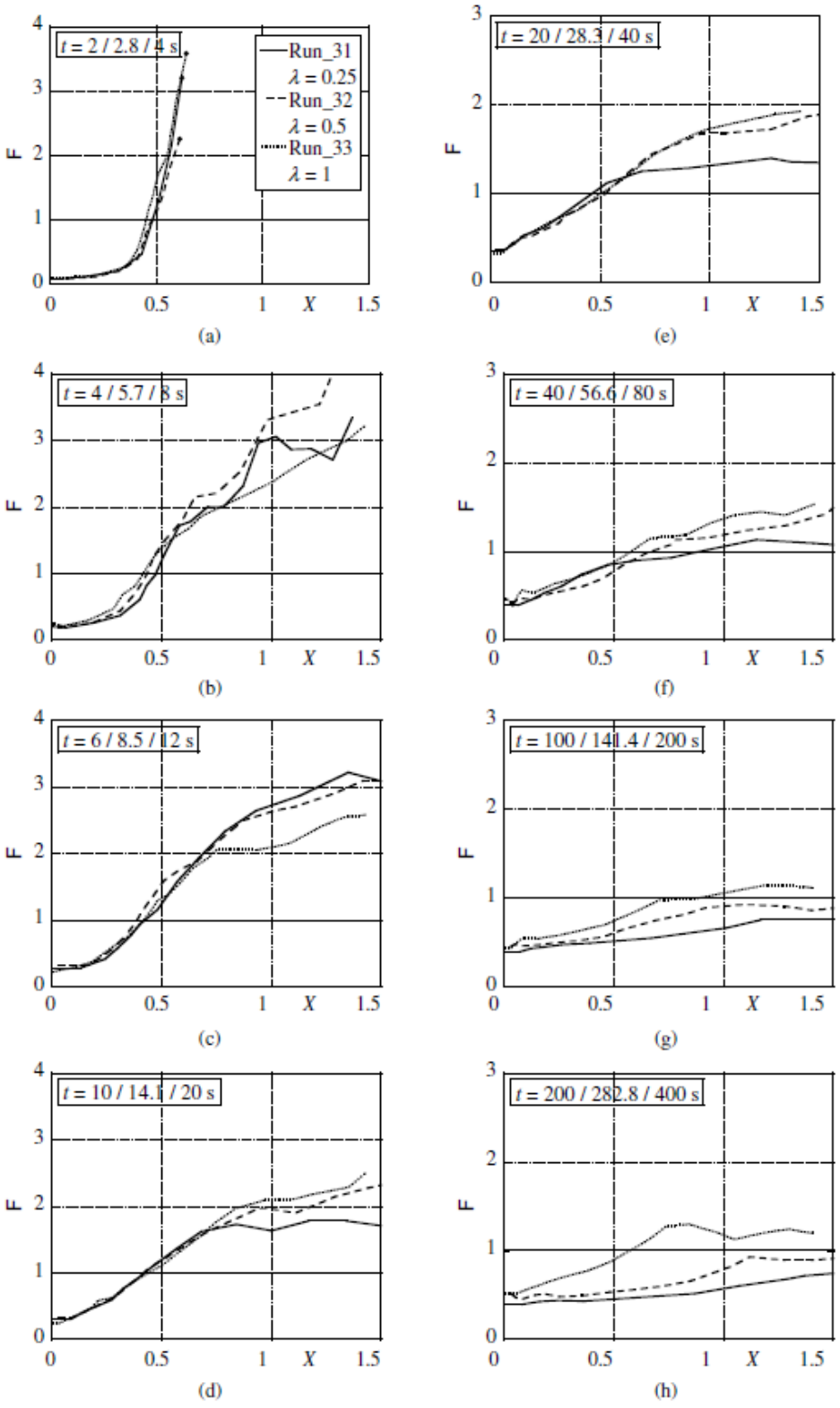

Figure B-39: Froude number variation along breach profile for scale family I (d = 1, 2 and 4mm for λ = 0.25, 0.5 and 1.0, respectively) at various times (Schmocker and Hager, 2009)

B.2 Field Tests

B.2.1 Zwin Channel Sand Dikes (Netherlands)

The study by Visser (1990) describes the first field test conducted in the Zwin Channel, a tidal inlet, 50 to 100 m wide, at the Belgian-Dutch border on December 13, 1989. The test initiated and directed by the Netherlands Technical Advisory Committee on Water Defences (TAW), comprised of a sand dike constructed at the inlet at low tide. The 2.2m high x 50m long x 17.35m wide dike was constructed with local sand (d_{50} = 0.2mm). A pilot channel, 0.2m deep and 0.5m wide was cut on top of the dike's crest centreline to initiate the breach. Although, the main purpose of the test was to observe the breach development process, measurements of velocities as well as water surface elevations upstream and downstream the formed breach channel were recorded using propeller current metres and tide-gauges, respectively. The observations of this field test, along with other laboratory tests conducted at Delft University, helped distinguish the 40 minute breach process into 4 stages, and later developed into 5 stages by Visser (1998).

The second Zwin Channel field test was conducted on October 7, 1994 in the same location as the first field test mentioned above. The study by Visser (2000) describes the field test comprising of a sand dike, 2.6 m high, 20 m wide and 200 m long. A trapezoidal pilot channel was cute into the dike's crest centreline. A 0.8 m deep trapezoidal pilot channel with a top and bottom width of 3.6 m and 1m, respectively, was cut through the centreline of the dike crest to initiate the breach channel. Flow velocities and water surface elevation was measured at three locations upstream and downstream using current velocity metres and pressure probes. In addition to the velocity and water surface elevation measurements, 40 vibration probes were installed under the sandy Zwin Channel to record the evolution of the breach channel. The entire breach process lasted for ~ 60 minutes. Data from the field test was used to calibrate and validate the sediment transport module for BRES, a physically-based numerical model by Visser (1998). Computations of the breach top width using the Bagnold-Visser (1988) sediment transport formulation in the early

stages of the breach, and van Rijn and Engelund-Hansen formulation for the later stages was compared with the measurements from the field test. It can be seen that the computations are in good agreement with the measurements in Figure B-40. The parameters for both field tests are summarised in Table B-5.

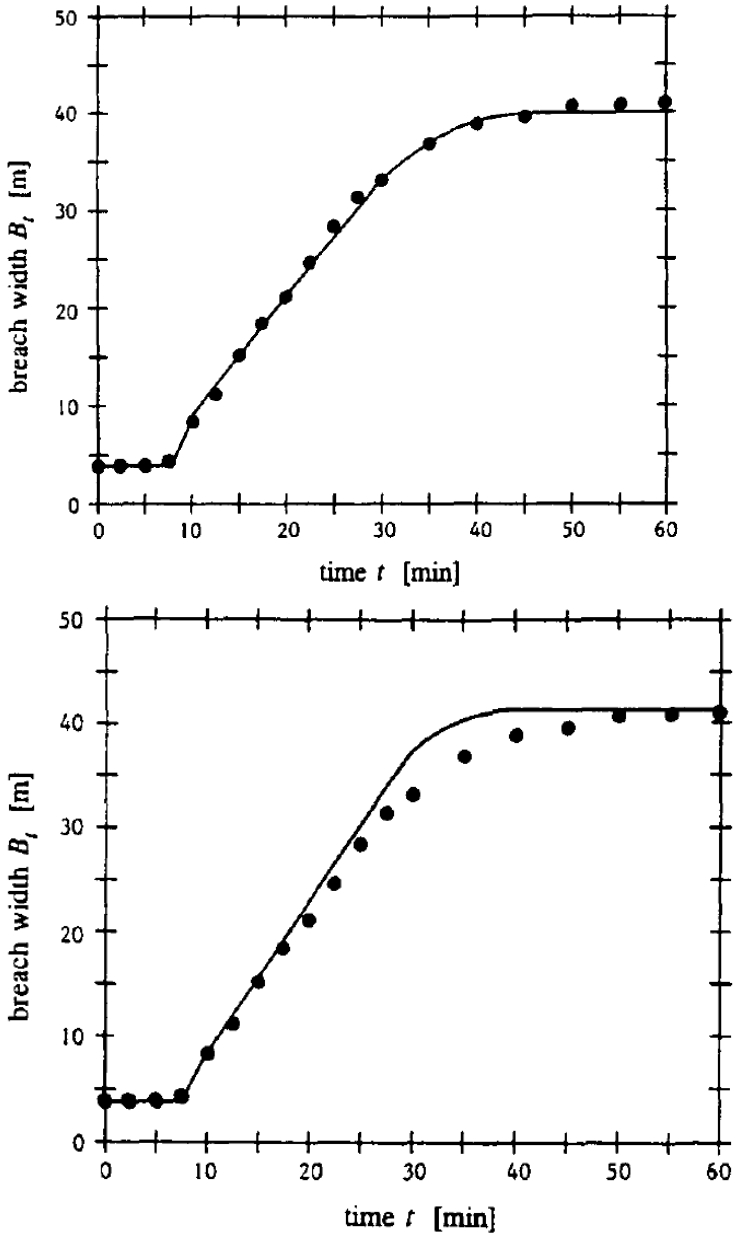

Figure B-40: Comparison of breach top width evolution between numerical (solid line) and measurements (dots) the early breach stages using Bagnold-Visser (1988) sediment formulation and later stages using (top) van Rijn formulation and (bottom) Engelund-Hansen formulation

Table B-5: Test matrix for Zwin field tests (Visser, 1990, 2000)

Date	Dike material	d_{50} [mm]	Crest dimensions, [m]			Slopes, [V:H]		Dike width, [m]	Pilot channel dimensions, [m]		
			z_{cr}	L_{cr}	w_{cr}	Upstream	Downstream		Depth	Top Width	Side-Slope
13-Dec-89	Sand	0.2	2.2	50	8	1:1.25	1:3	17.35	0.20	0.50	N/A
07-Oct-94	Sand	0.2	2.6	200	8	1:1.60	1:3	20.00	0.80	3.60	1.625

B.2.2 Chinese-Finnish Cooperative Research Work on Dambreak Hydrodynamics

The report by Shuibo *et al.* (1993) stated that between 1954 and 1980, approximately 3.4% of earth embankments (of which about 63% where homogeneous embankments) in China had failed. Approximately 64% of the failures were caused from technical problems in spillways, insufficient spillway capacity and extreme storms. With over 65,000 houses destroyed and 1,963 killed, the Chinese government addressed their dam safety problem by upgrading their existing embankment infrastructure with secondary emergency spillways and fuse-plug embankments. Since the end of the 1970s, there has been an interest by the Chinese government to conduct large-scale *in situ* tests on fuse-plug embankment models. In 1991, collaboration was made between the Ministry of Water Resources of the People's Republic of China (CMWR) and the National Board of Waters and the Environment of the Republic of Finland (FNBWE) to investigate and improve dam safety research in China. Table B-6 and Table B-7, include a summary of a series of investigations performed by the Chinese-Finnish cooperation on three fuse-plug embankments. Other investigations by the cooperation also included physical model tests using rigid bed models of fuse-plug embankments and dambreak numerical modeling.

Table B-6: Field test prototype data (Shuibo *et al.* 1993)

Reservoir Name	Tests	Prototype Data				
		Fuse Plug Type	Height, [m]	Width, [m]	Length, [m]	Slopes
Dahuofang	2	Inclined clay core gravel fill	9	N/A	110	N/A
Nanshan	1	Inclined clay core gravel fill	4.5-5.5	19.5	134	Upstream: 1V:1H Downstream: 1V:1.5H
Yahekou: Phase I	31	Central clay core sand fill	11.2	Crest: 5	N/A	Upstream: 1V:3H Downstream: 1V:2.5H
Yahekou: Phase II	21	Inclined clay core sand fill				
Yahekou: Phase I (Detail)	-	Inclined clay core sand fill				

The first field test described in the report was to investigate the failure rate of an inclined clay core gravel fill fuse-plug embankment in the Dahuofang reservoir. The 3m-high model was constructed using the same materials and construction technique as the prototype. The embankment shell material, gravel (d_{50} = 10 mm), was compacted in layers, using a tractor, while the core material, loam ($0.005mm < d_{50} < 0.05mm$), was compacted using a pneumatic-tired roller. Geometric similarity was considered only in the cross-section. The two large-scale models were tested under different initial water surface elevations in the impoundment while maintaining a constant head. A pilot channel 0.63m deep was dug onto the embankment crest to initiate the breach. The results from this test conclude that the final breach shapes were similar, but the down cutting rate was three times higher for the test for the higher WSL. There was no mention of prototype failure for this test.

Table B-7: Field test model data (Shuibo *et al.* 1993)

Reservoir Name	Tests	Model Data									Parameters varied
		L_{rr}	Height, [m]	Fixed crest height, [m]	Width, [m]	Length, [m]	Pilot channel dimensions, [m]	η, [m]	V_{R_3} [m^3]	γ_d [kN/m^3]	
Dahuofang	2	$1/3$	3	-	N/A	15.4	Depth: 0.63	Test Run 1: 0.43 Test Run 2: 0.28	7,000	Core: 16.0 Shell: 20.0	Initial WSL
Nanshan	1	$1/2$	2.5	1.5	6.7	13.5	Width: 2.0 Depth: 0.50	0.31	1,900	Core: 16.2 Shell: 16.9	N/A
Yahekou: Phase I	31	Various		-	N/A	N/A	N/A	N/A	N/A	N/A	L_{rr}: $1/2$, $1/4$, $1/8$
Yahekou: Phase II	21										L_{rr}: $1/2$, $1/5$, $1/7.5$, $1/10$, $1/15$, $1/120$
Yahekou: Phase I (Detail)	-	$1/2$	5.6		Dam: 34.8 Crest: 4	30.5	Width: 1.5 Depth: 1.3	0.8	46,000	Core: 16.4 Shell: N/A	-

The second field test described in the report was conducted by the CMWR on March 25, 1978 with the purpose of investigating the failure mechanism of an inclined clay core gravel fill fuse plug embankment in the Nanshan reservoir. The test was performed to compare the failure rate with an expected value. The construction of the embankment was carried out in 15-20cm lifts, where the material was compacted using tampers. It is important to note that a filter medium ($0.5mm < d_{50} < 2mm$) was used between the inclined clay core (d_{50}~$0.05mm$) and shell material ($d_{50} > 20mm$). The optimum water content of the fill materials, ω, was 18%, where compaction took place at dry of optimum conditions. The crest height of the model embankment was 2.5m high, with a fixed crest, 1.5m high. The main conclusions of this test were the following:

1. The erosion process in fuse-plug embankments can be divided into three mechanisms; downstream slope erosion of the shell material, erosion of the inclined core and the consequent collapse of the inclined core. The relation between the average erosion rate, $\dot{\bar{E}}$, of the prototype and model can be described as follows:

$$\dot{\bar{E}}_{pp} = \dot{\bar{E}}_{mm} L_{rr}^{0.55} \tag{B-2}$$

where, L_{rr} is the geometric or length scale of the model (prototype to model geometric ratio).

2. The hydraulic head in the pilot channel, the type and thickness of the inclined clay core affected the erosion rate, however, the filter and shell materials did not significantly affect erosion rate. Note: the fact erosion rate was quantified for different types and thicknesses of filter and shell materials, suggests that more than one test was performed. There was no mention of other model tests or prototype tests in the report.
3. The hydraulic head in the pilot channel was sufficient to breach and eventually cause failure in the fuse plug embankment model.

The third field test included rigorous scale series modeling using an overall 52 test runs. The first phase of this field test was designed to establish erosion rate prototype-model relationships for inclined clay core sand-filled fuse plug embankment models using three scale series tests (1:2, 1:4 and 1:8), while the second phase was conducted for models with a central clay core sand-fill configuration using six scale series tests (1:2, 1:5, 1:7.5, 1:10, 1:15 and 1:20). Only one of the tests, conducted in March 18, 1982, in the spillway chute of the main embankment was described in detail (see Yahekou Phase I (Detail) - 5.6m high model in Table B-6 and Table B-7). The 5.6m high central clay core embankment model, with a crest width of 4m, was constructed with a pilot channel 1.5 m wide and 1.3 m deep lined with bricks and some grout work using cement mortar. The core material, a heavy silty loam ($0.005mm < d_{50} < 0.05mm$), was compacted using a tamper, while the shell material, coarse sand ($0.25mm < d_{50} < 2mm$), with a degree of compaction 67% of maximum. The upstream and downstream slopes were protected with block stones and heavy loam, respectively, each 0.3m thick. Water gauges and suspension cables installed along the pilot channel centreline were used to measure water surface elevation. Velocity measurements were recorded at three locations, one 12.1 m downstream from the embankment's axis and two 49.7 m further downstream. A total of 577 conductivity probes were embedded within the embankment's cross-section along the embankment's axis to monitor the erosion process and breach evolution. At 22'40", erosion in the pilot channel section reached the foundation, and a breach discharge measured at 210 m^3/s yielded velocities at 5.35 m/s downstream. The next 10'20", erosion resumed in the lateral direction until the entire embankment was washed away. The test was useful to investigate factors, such as the core thickness and the type of pilot channel lining, as means to ensure the functionality of fuse-plug embankments as fail-safe systems in the event of extreme storms. A relation between the average erosion rate, $\dot{\bar{E}}$, of the prototype and model can be described as follows:

$$\dot{\bar{E}}_P = \dot{\bar{E}}_m L_{rr}^{0.489} \tag{B-3}$$

Data from this test was used to validate the Loukola and Huokona (1998) numerical model.

B.2.3 U.S. Department of Agriculture (USDA) Agricultural Research Service (ARS) Outdoor Flume and Full-Scale Models (Stillwater, Oklahoma, USA)

In the late 1990s, the U.S. Department of Agriculture (USDA) Agricultural Research Service Hydraulic Engineering Research Unit (ARS-HERU) performed a series of outdoor flume studies and full-scale breach field tests using earthen embankments. The outdoor laboratory tests comprised of four overtopping experiments to investigate erosion in two soils at different overtopping flows. The test procedure was described by Hahn *et al.* (2000) and Hanson and Temple (2001). A 37m long embankment, 3m high, with a crest width of 2.4m and 1V:3H upstream and downstream slopes, was constructed over a relatively non-erodible clay foundation with a 9% slope (see Figure B-41).

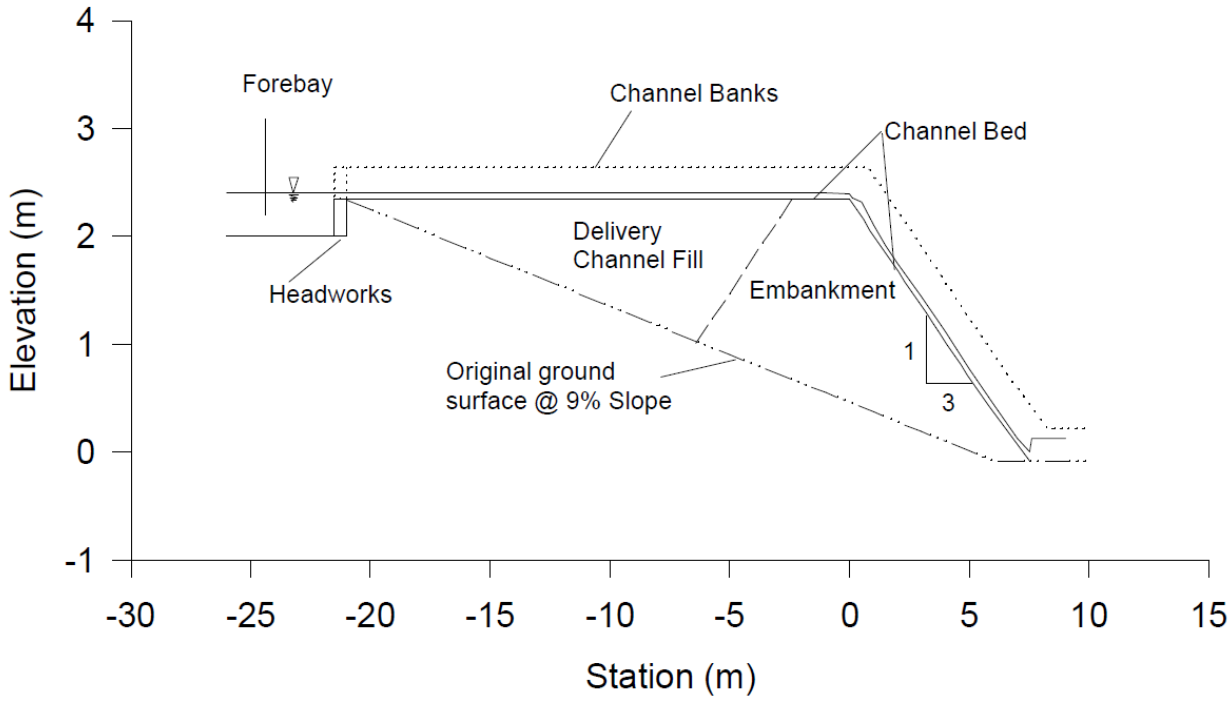

Figure B-41: Cross-section of embankment in outdoor flume (Hanson and Temple, 2001)

The embankment material was a silty sand (USCS Type CL-ML), with a plasticity index, PI, ranging between 0 and 7 for the samples collected and tested. Construction of the embankment was carried out in 15cm lifts and compacted at a dry unit weight, γ_d = 17.66 kN/m^3 and at a water content, ω = 12%. Standard proctor tests indicated that optimum water content for the embankment soil was 12% and the maximum dry unit weight was 18.64kN/m^3. Six test sections were prepared by cutting trapezoidal pilot channels, 1m wide and 1m deep with side-slopes 1V:1H, into the embankment crest centrelines and down the downstream slope to initiate the breach at the centre. Two fescue-grass vegetated channels were tested at two overtopping discharges, 0.2m^3/s and 0.6m^3/s, for 75 hours and 51 hours, respectively, while the two non-vegetated channels were tested for 72 hours and 51 hours, respectively at two overtopping discharges, 0.2m^3/s and 0.6m^3/s. A summary of the test results can be found in Table B-8. Measured centreline profiles of the test sections over the testing duration reveal that erosion rate for the non-vegetated channels was significantly higher than the vegetated test sections (see Figure B-42 and Figure B-43).

Table B-8: Test summary (Hanson and Temple, 2001)

Test #	1	2	3	4
Vegetation	Fescue	-	Fescue	-
Discharge, [m^3/s]	0.2	0.2	0.6	0.6
Average flow depth, [m]	0.17	0.07	0.24	0.13
Mean velocity, [m/s]	2.6	3.0	4.5	5.4
Peak velocity, [m/s]	4.6	4.3	6.0	6.1
Test duration, [hrs]	75	72	75	51
Critical specific head, [m]	0.3	0.3	0.7	0.7

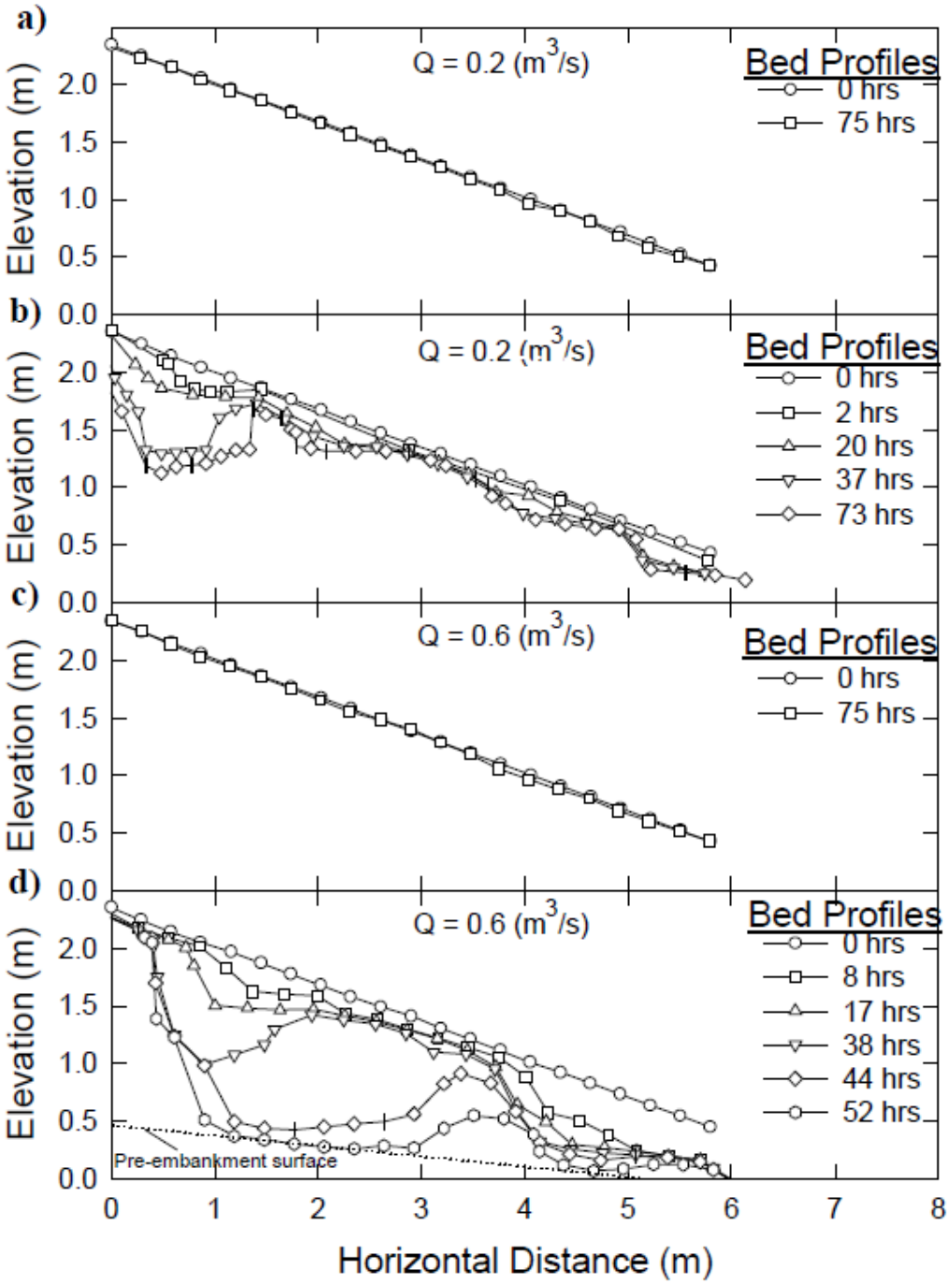

Figure B-42: Centreline bed profiles (a) vegetated channel, Q = 0.2m^3/s (b) non-vegetated channel, Q = 0.2m^3/s (c) vegetated channel, Q = 0.6m^3/s (d) non-vegetated channel, Q = 0.6m^3/s (Hanson and Temple, 2001)

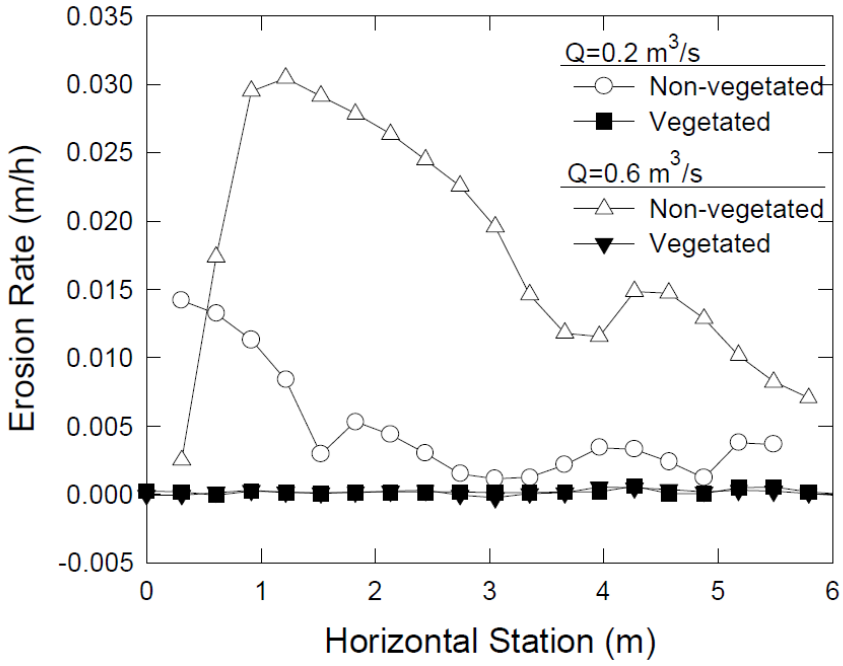

Figure B-43: Average erosion rate for vegetated and non-vegetated channels (Hanson and Temple, 2001)

The test procedure for seven full-scale overtopping was described in detail by Hahn *et al.* (2000) and Hanson *et al.* (2005). Three embankments were constructed in the USDA-HERU facilities of Stillwater, Oklahoma (see Figure B-44) using three different materials; two non-plastic silty-sands (USCS Type – SM) and lean clay (USCS Type CL) as shown in Table B-9. The construction of the overtopping tests began in spring 1998 and was completed in April 1999. The embankments were constructed in 14cm lifts using self-propelled vibratory pad-foot rollers using two passes at 94% degree of compaction according to Standard Proctor Tests performed on soil samples. Samples obtained from the compacted material were collected such that grains size distributions, Atterberg Limits, water content, dry unit weight, unconfined compressive strength, τ_u, and critical shear stress, were later determined in the Natural Resources Conservation Service (NRCS) National Soil Testing Laboratory (NSTL) as shown in Table B-10. The study by Hahn *et al.* (2000) reports the angle of internal friction and soil cohesion for *in situ* samples collected from the first three overtopping tests as follows: 26.5°, 13.3°, and 20.0°, for angles of

internal friction, and 0.8 kPa, 10.3kPa and 8.2 kPa for soil cohesion. It is clear that soil 2 (silty-sand) exhibits cohesive properties for a silty-sand.

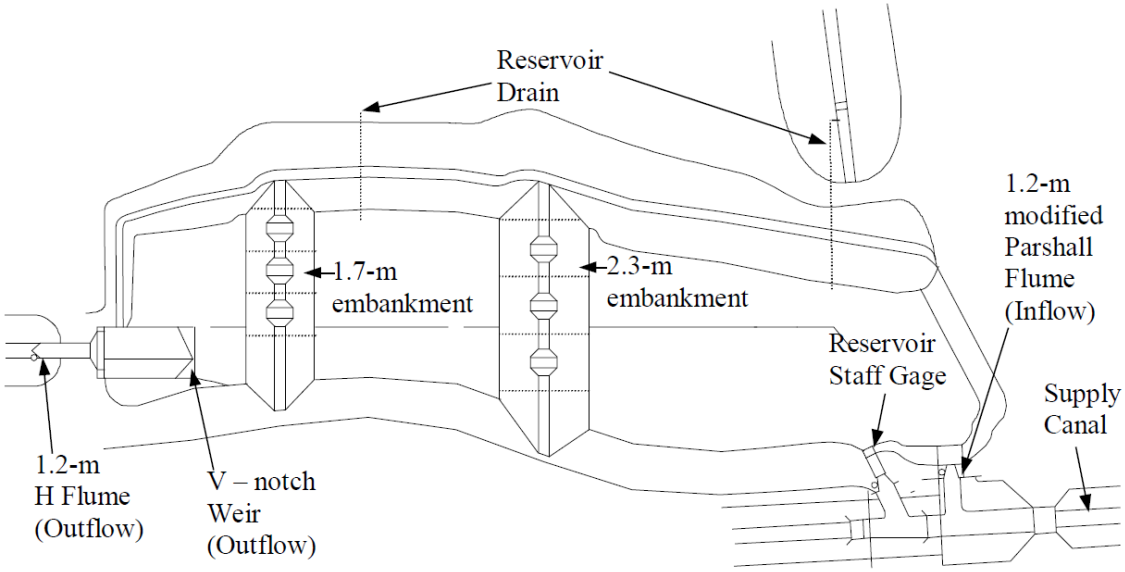

Figure B-44: Plan view of USDA ARS-HERU facilities for full-scale overtopping tests (Hahn *et al.* 2000)

Table B-9: Soil properties used in full-scale overtopping tests (Hanson *et al.* 2005)

Soil #	1	2	3
Unified Soil Classification System	SM - Silty Sand	SM - Silty Sand	CL - Lean Clay
Grain size analysis			
% Sand > 0.075mm	70	63	25
% Silt > 0.002mm	25	31	49
% Clay > 0.002mm	5	6	26
Atterberg Limits			
Liquid Limit	-	-	34
Plastic Limit			17
Plasticity Index			17
Standard Proctor tests			
Optimum water content, OWC [%]	9	10.5	14
Maximum dry unit weight, γ_d [kN/m^3]	17.95	18.14	17.46

Table B-10: Test matrix for full-scale overtopping tests (Hanson *et al.* 2005)

Test #	Soil #	Emb. #	Crest test section dimensions, [m]			Embankment properties					Pilot channel dimensions†, [m]			Upstream boundary conditions
			Height	Width	Length	ω [%]	γ_d [kN/m^3]	τ_u [kPa]	k_d [cm^3/Ns]	τ_c [Pa]	Depth	Bottom width	Inflow, [m^3/s]	Max. Head, [m]
1	1					8.7	16.87	20	10.3	0.14				
2	2	1	2.3	7.3	1.84	12.1	16.97	32	2.0	0.14	0.46	1.83	0.46	1
3	3					16.4	16.19	63	0.039	15				
4	1					11.5	16.97	22	14.2	0.14				
5	2	2	1.5	4.9	1.90	14.5	17.07	31	8.0	0.14	0.3	1.22	0.3	0.3
6	3					17.8	16.38	82	0.038	10				
7	2	3	2.3	12	1.74	11.5	17.36	39	2.4	0.14	0.46	8.2	0.3	2

†Embankment and side-slopes for the pilot channel are 1V:3H

Embankments 1 and 2 were comprised of three test sections, each were 2.3m high x 7.3m wide and 1.5m high x 12m wide, respectively. Embankment 3 which was 2.3m high, had one 12m wide test section (see Table B-10). The surfaces of embankments 1 and 2 were seeded with fescue grass as a means of protecting the slopes from rainfall erosion prior to testing, while the surfaces of embankment 3 were covered with Bermudagrass pieces. However, a 0.3m wide strip was removed to localise the flow and erosion at the centreline of the embankment's downstream slope (Hanson *et al.* 2005). Trapezoidal channels were cut into the embankment crest centrelines to initiate the breach at the centre. Upstream, downstream and side-slope slopes were 1V:3H.

The upstream reservoir was filled to 1.2m and 1.0m for the 2.3m and 1.5m high embankments, respectively. Prior to overtopping, the upstream reservoir was filled to water surface levels 0.46m, 0.30m and 0.30m above the pilot channel bottoms for embankments 1, 2 and 3, respectively, using a supply canal where inflow was measured using a Parshall flume. The three studies state that inflow stabilized quickly during the tests, and was maintained at relatively constant values of 1.0, 0.3 and 2.0 m^3/s, for embankments 1, 2 and 3, respectively (see Figure B-45). The breach outflow was determined using three methods: a downstream V-notch weir and H-flume, and change in storage measurements with time recorded. An overhead rolling carriage fixed with a point gauge was utilized to take measurements of the longitudinal and transverse water surface and bed profiles in the breach channel as shown in Figure B-46. Three digital cameras, set to capture images at 1 to 3 minute intervals, and a video camera mounted downstream of the breach channel were used to record the breach process and were later analysed using photogrammetric techniques. After the overtopping tests were completed, JET tests were performed on soil samples in each test section to determine the erodibility coefficient.

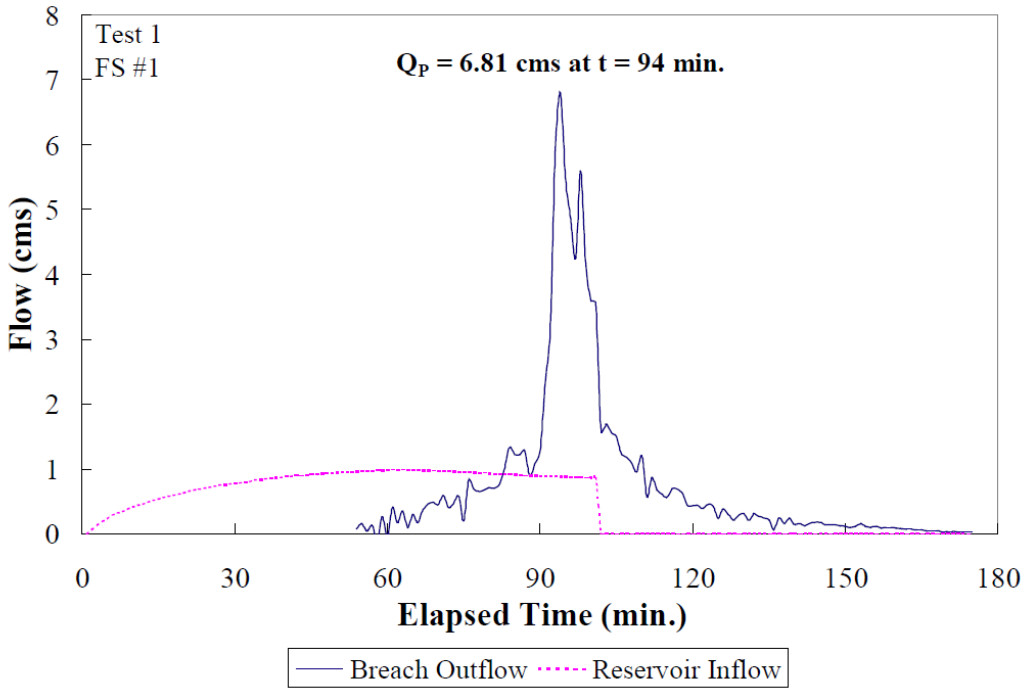

Figure B-45: Inflow and breach outflow hydrographs for full-scale overtopping test # 1 (Hahn *et al.* 2000)

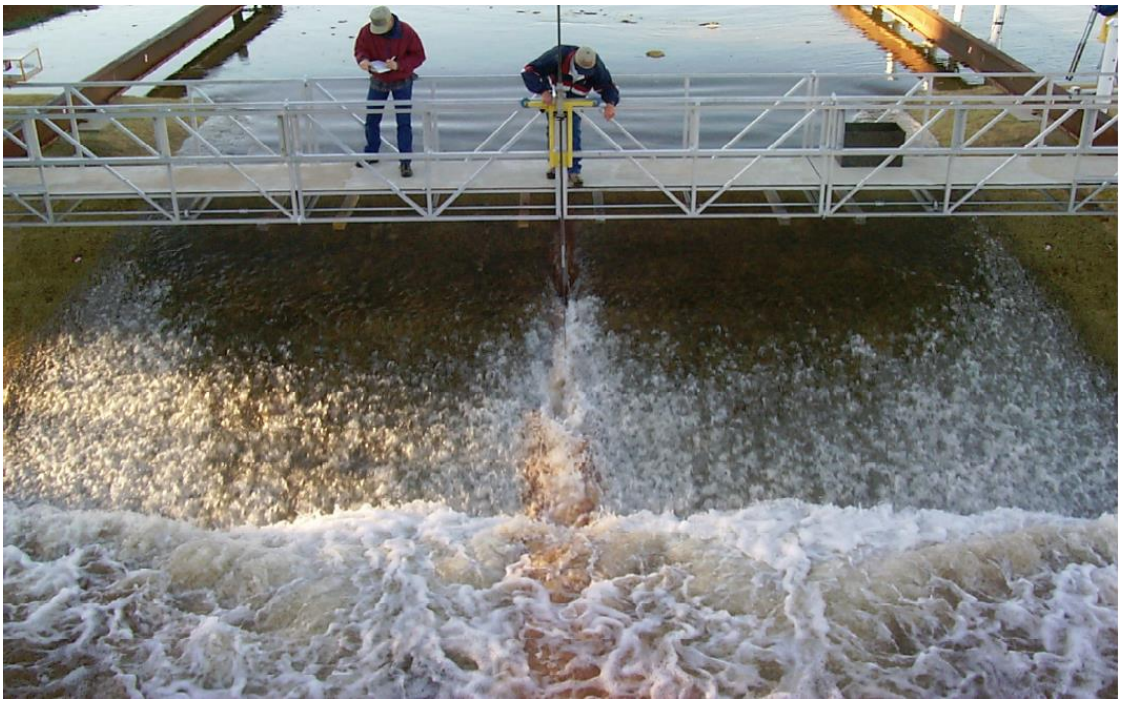

Figure B-46: Overhead rolling carriage at USDA ARS-HERU (Hanson *et al.* 2003)

Hahn *et al.* (2000) described the breach process for the overtopping tests in the four following stages as shown in Figure B-47:

- Stage I, t_0-t_1: Initiation of rill erosion with some minor headcut development on upstream reaches of the downstream slope;
- Stage II, t_1-t_2: Headcut advance from the downstream crest to the upstream crest and erosion widening of the eroded surface;
- Stage III, t_2-t_3: Breach formation begins, where the embankment crest is lowered due to further headcut migration;
- Stage IV, t_3-t_4: Breach channel advances towards upstream toe of embankment, followed by breach widening as the reservoir is depleted.

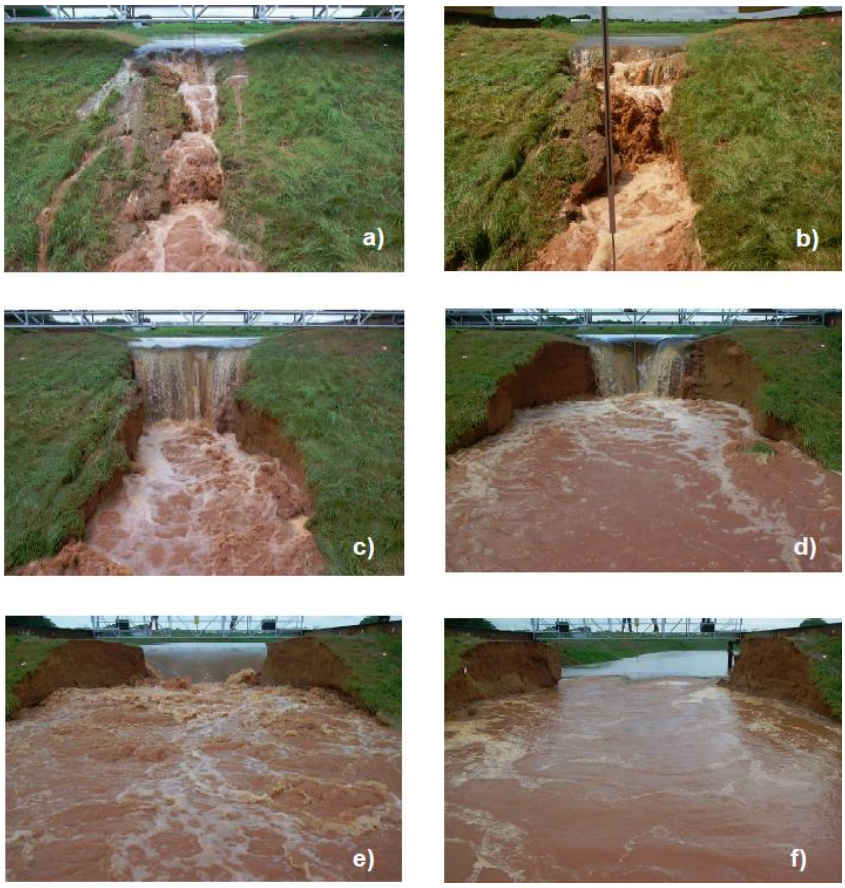

Figure B-47: Erosion and breach widening processes in full-scale overtopping test # 1 by Hanson *et al.* (2005): (a) stage I (t = 7min); (b) stage I (t = 13min); (c) transition from stage I to stage II (t = 16min); (d) transition from stage II to stage III (t = 31min); (e) transition from stage III to stage IV (t = 40min); (f) stage IV (t = 51min)

A summary of the breach stages I, II and III for the overtopping tests are shown in Table B-11.

Table B-11: Timing for breach stages I, II and II for overtopping tests (Hanson *et al.* 2005)

Test #	Emb. #	Soil #	Breach initiation		Breach formation	Peak outflow [m^3/s]	Erosion width [m]
			Stage I: t_1-t_0 [min]	Stage II: t_1-t_2 [min]	Stage III: t_3-t_2 [min]		
1		1	16	15	20	6.5	6.9
2	1	2	54	266	112	1.8	6.2
3		3	164	> 1,036	-	1.0	4.2
4		1	18	22	68	2.3	3.3
5	2	2	80	1,092	361	1.3	3.3
6		3	166	> 4,200	-	0.3	2.4
7	3	2	51	256	52	4.2	4.5

*The side-slopes of the breach channel were 1V:1H

Hahn *et al.* (2000) expresses the rate of headcut migration as follows:

$$\frac{dx}{dt} = \frac{X_T k_d (\tau_b - \tau_c)}{E_V} \tag{B-4}$$

where X_T is the average distance of movement at each mass failure, k_d is the erodibility coefficient, and E_V is the amount of erosion required in the bank face to induce failure.

Hanson *et al.* (2005) also express the headcut migration rate in terms of the specific discharge and overfall height, H_0, whose product describes a quantity of energy dissipation, and a material dependent coefficient, C_X, as follows:

$$\frac{dx}{dt} = C_X (q H_O)^{1/3} \tag{B-5}$$

Hanson *et al.* (2003) expresses the headcut migration and breach widening coefficient using the following expressions below:

$$C_X = \frac{dx/dt}{(qH_O)^{1/3}} \quad \text{(B-6)}$$

$$C_W = \frac{dy/dt}{(qH_O)^{1/3}} \quad \text{(B-7)}$$

Figure B-48 and Figure B-49 show the headcut migration rate and breach widening rates is influenced by compaction water content.

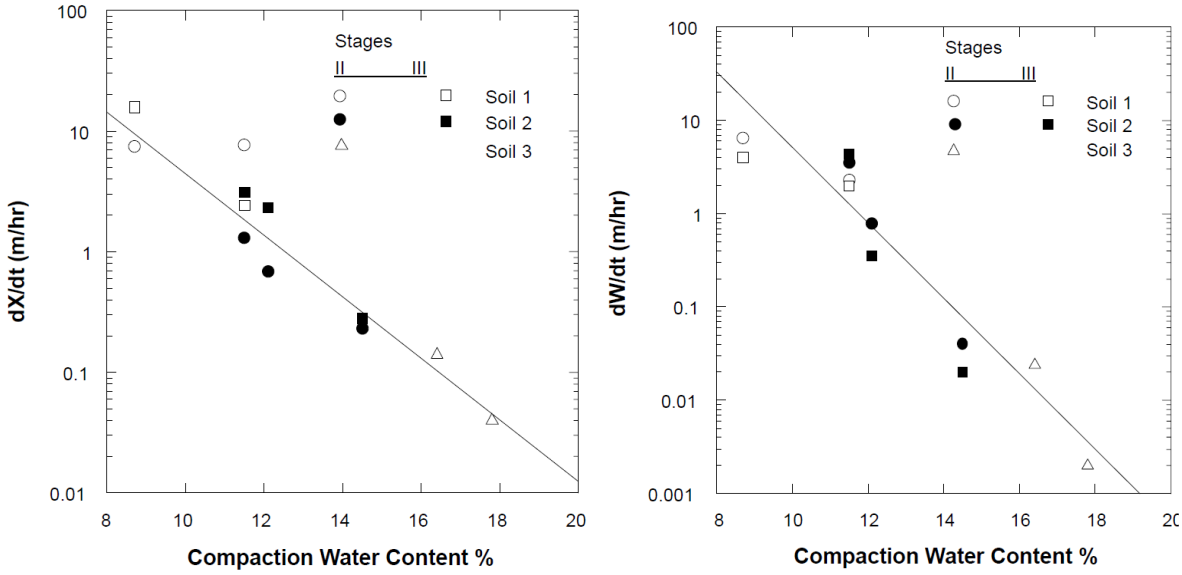

Figure B-48: Influence of compaction water content on (a) headcut migration rate (b) breach widening (Hanson *et al.* 2005)

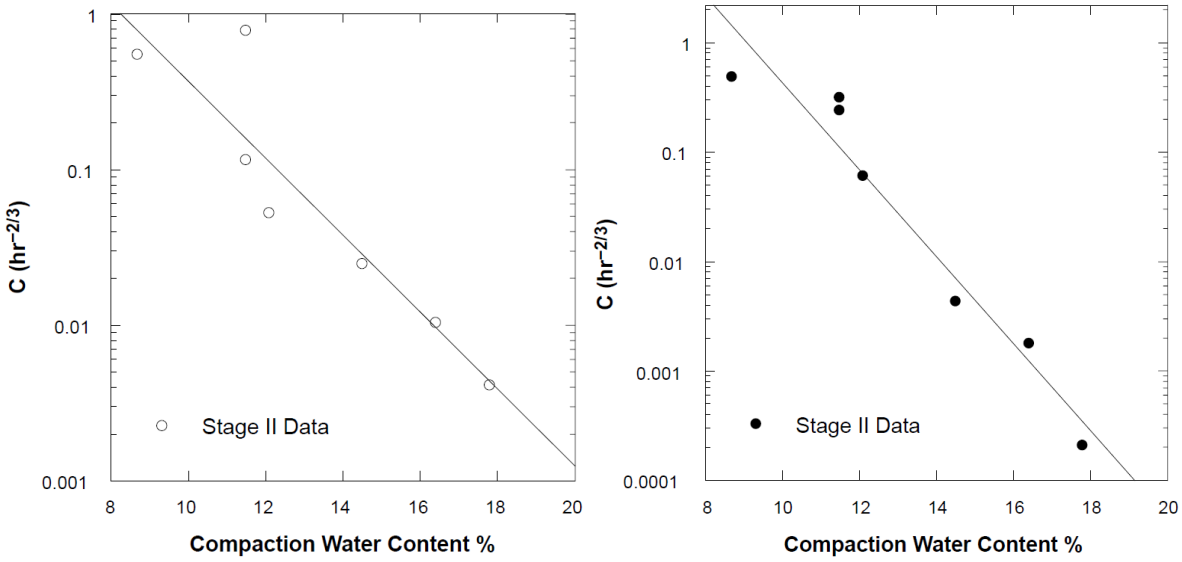

Figure B-49: Influence of compaction water content on coefficient for (a) headcut migration (b) breach widening (Hanson *et al.* 2005)

In 2003, three large-scale overtopping tests were performed by the USDA ARS-HERU to investigate breach widening in Phase II and III of earth embankments (Hunt *et al.* 2005). The embankment heights were 1.3m with 1.8m crest widths and 1V:3H upstream and downstream slopes with test sections 5.5m wide, and a 0.3m wide notch cut into the crest's centreline to initiate the breach. The embankments were constructed using 9cm lifts using a self-propelled vibratory pad-foot roller with two passes. Two embankments were constructed using the same soil and dry unit weight, but with different water contents as shown in Table B-12 (*i.e.* soil # 1 is compacted wet of optimum).

Table B-12: Embankment soil properties for large-scale tests (Hunt *et al.* 2005)

Emb. #	Soil #	Sand > 0.075mm [%]	Fines > 0.002mm [%]	Fines < 0.002mm [%]	PI	USCS Type	ω [%]	γ_d [kN/m^3]
1	2	63	31	6	-	SM – Silty Sand	12.2	17.6
2	2						10.7	17.6
3	3	25	49	26	17	CL – Lean Clay	16.2	16.7

The embankments overtopping took place under constant head conditions, while measurements of the breach channel were recorded in a similar fashion to the full-scale tests. Observations from the overtopping tests were similar to Mohamed *et al.* (1999) and Coleman *et al.* (2002), which state that undercutting of the breach channel side-slopes resulted in large overhang material (Geisenhainer and Kortenhaus, 2006; Pickert *et al.* 2011) to fail into the breach channel, as shown in Figure B-50. Breach widening rates for embankments 1, 2 and 3, were measured at 0.075mm/s, 0.244mm/s and 0.006mm/s, respectively. It is clear that compaction water content of the silty sand played a large role in breach erosion (widening rate was 3.3 times faster for wet of optimum conditions). The experimental study by Hanson *et al.* (2005) demonstrates that a small change in compaction water content could increase the breach widening rate by almost two orders of magnitudes (see Figure B-49). However, it is important to note that the results include more than one type of soil, whereas the hydraulic loading between the seven tests is varied due to the different embankment configurations. As expected, for the test case where lean clay was used in the study by Hunt *et al.* (2005), the erosion was hindered due to the high cohesive forces present.

Figure B-50: Crack formation leading to overhang failure (Hunt *et al.* 2005)

Further large-scale conducted in the USDA ARS-HERU facilities investigated the influence of soil material on internal erosion. The study by Hanson *et al.* (2010)

described two out of four piping tests conducted. Four 1.3m high embankments with a crest width of 1.8m and upstream and downstream slopes of 1V:3H were constructed using 9cm lifts using the same equipment described in previous ARS-HERU outdoor tests. The embankments materials ranged from plastic sandy-silt with 6% fines (USCS Type SM) to lean clay (USCS Type CL) with 26% fines and were constructed with a 40mm steel pipe to simulate the piping failure. After filling the reservoir, the pipe was removed leaving a 40mm conduit through the embankment body. The tests were performed under constant head conditions, and the pipe dimensions were recorded over 60 minutes for the SM soil and over 4,000 minutes for the CL soil. After 13 minutes, the piping roof collapsed for the SM soil, whereas the pipe remained intact for the entire duration of the test using the CL soil. The erodibility coefficient of soil samples, compacted at Standard Proctor compaction efforts, was measured using small-scale equipment such as JET test equipment. This coefficient was then used to justify the breach enlargement of piping failures in large-scale embankments conducted in this study.

B.2.4 *Mo i Rana* Large-Scale Field Tests (Nordland County, Norway)

In 2002 and 2003, a total of seven large scale field tests (4.5 – 6m high) were conducted in Nordland County, near the town of *Mo i Rana*, Norway, in a test site 600m downstream of the Røssvassdammen dam (see Table B-13). Five of the field tests were conducted under the IMPACT project and two were conducted under a separate working group. Vaskinn (2004), Vaskinn *et al.* (2004), Morris *et al.* (2007) and Hassan and Morris (2008) describe the five IMPACT project field tests in some detail (see Table B-14).

Table B-13: *Mo i Rana* field test desciption (Vaskinn *et al.* 2004; Hassan and Morris, 2008)

Field Test	Project	Breach mechanism	Embankment configuration	Objective
1	EC	Overtopping	Homogeneous rockfill	Investigation of beach of rockfill dams under high seepage flow
2	IMPACT	Overtopping	Homogeneous clayfill (CL: 15% Sand, 25% Clay)	Effect of maximum cohesion on breach mechanisms
3	EC-IMPACT	Overtopping	Homogeneous gravelfill (<5% fines) with rockfill downstream slope protection	Effect of minimum cohesion on breach mechanisms
4	EC	Overtopping	Homogeneous rockfill	Almost identical to Field Test 1
5	IMPACT	Overtopping	Rockfill with central moraine core	Breach failure in composite dam due to overtopping
6	IMPACT	Piping	Rockfill with central moraine core	Breach failure in composite dam due to piping
7	IMPACT	Piping	Homogeneous moraine	To compare with Field Test 6

Five of the field tests were conducted under the IMPACT project and two were conducted under a separate working group. Vaskinn (2004), Vaskinn *et al.* (2004), Morris *et al.* (2007) and Hassan and Morris (2008) describe the five IMPACT project field tests in some detail (see Table B-14). A total of four gauges were used in the field tests, two of which were water level gauges installed in the upstream reservoir for measuring the water surface level. The remaining two gauges were installed downstream the embankments and were comprised of a V-notch weir for measuring discharge less than $0.1m^3/s$, and a tailwater level gauges capable of measuring discharge greater than $10m^3/s$. Up to eight piezometers were installed in the embankment during construction to measure PWP. The presentation by Vaskinn (2004) reports the use of pressure sensors. Approximately one hundred breach sensors, comprised of tilt sensors and microprocessors, were also embedded in the embankments to monitor the rate of breach development.

Table B-14: Embankment dimensions and soil properties (Vaskinn *et al.* 2004; Hassan and Morris, 2008)

Field Test	Crest [m]		Shoulder Slopes (V:H)	Pilot channel [m]		Lift height [m]	Soil properties					
	Height	Width		Depth	Width		ω [%]	d_{50} [mm]	λ	ϕ [°]	c [kN/m^2]	γ_d [kN/m^3]
2	6	2	1:2.0	0.5	3	0.15/0.4	30	0.009	0.47	23	4.9	14.7
3	5	2	1:1.7	0.1	2	0.5	7	4.65	0.22	42	0.9	21.15
5	6	3	1:1.5	0.2	8	0.5/1	6[†] 2.6[‡]	7[†] 85[‡]	0.21[†] 0.16[‡]	42	20[†] 0[‡]	20.5[†] 20.8[‡]
6	6	3	1:1.5	*	0.215[§]	0.5	6[†] 2.6[‡]	7[†] 85[‡]	0.21[†] 0.16[‡]	42	20[†] 0[‡]	20.5[†] 20.9[‡]
7	4.5	3	1:1.3	*	0.2[§]	0.5	6	7	0.21	42	20	20.5

[†]Moraine; [‡]Rockfill; *Pipe above dam foundation; [§]Pipe diameter

Markings were also installed on the embankment surface for conducting a breach evolution analysis using three digital video cameras and several photo cameras. The breach was initiated using a pilot channel (or conduit for the piping tests) installed at the embankment's centreline to ensure that the breach occurs away from valley walls.

Generally, erosion of the downstream face of the embankments was slow, until the moment the erosion in the breach channel reached the upstream face, breaching was much more rapid (Morris *et al.* 2007). Another observation by Morris *et al.* (2007), was that breaching first progressed vertically to the valley floor before developing laterally. The study by Vaskinn *et al.* (2004) stated that breach evolution for the homogeneous clay embankment (*i.e.* Field Test 2) was faster than the homogeneous gravel embankment (*i.e.* Field Test 3), an outcome which was not expected. It is important to note that during the construction of the clay embankment, prolonged rain which resulted in high water contents (~28-33%) rendered the compaction of the 15cm lift heights difficult, and therefore the lift height was increased to 40cm at elevations 1.5-2m above the embankment's foundation, as well as using lower static loads. The study by Hassan and Morris (2008) and Vaskinn *et al.* (2004) state that the rate of breach growth was likely affected by the wet conditions and the two distinct layers with different soil properties (and

erodibility). With respect to the rockfill dam with a moraine core breached under piping flow (*i.e.* Field Test 6), breach evolution was very slow, whereas overtopping failure was initiated once the piping conduit reached the embankment's crest. Vaskinn *et al.* (2004) that the breach width was smaller than the overtopping test for the same embankment configuration (*i.e.* Field Test 5). The piping failure was observed to occur much faster in the homogeneous embankment (Field Test 7) than the composite one (Field Test 6), however, peak flows were almost identical for both tests. Although the rate of lateral erosion could not be determined for this study, Morris *et al.* (2007) stated that the presence of a cohesive core could very well alter the breach growth rate significantly. The authors, however, define the potential failure modes in a cohesive core wall as follows: sliding, overturning or bending.

B.2.5 Dawa Reservoir Large-Scale Field Tests (Anhui, China)

The largest embankment field tests to date took place in the Dawa Reservoir, Chuzhou, Anhui province, China. Overtopping and piping tests were carried out on 9.7m high and 120m long cohesive embankments, with a crest width of 3m, and a reservoir capacity of 100,000m^3. The purpose of this study, as stated by J. Zhang *et al.* (2009), was to better understand the breaching mechanisms in cohesive embankments with large clay contents similar to those in Chinese dams (10% to 30%). Table B-15 summarises the four field tests described in their study. The embankments were constructed at water contents near optimum. Although the water content in Field Test 1 was higher than in Field Test 2, both field tests were considered identical, and were used to verify repeatability. The measurements in the study included: velocities in the breach channel using ADVs, reservoir levels using eight pressure sensors, tailwater conditions using video cameras, breach headcut erosion using embedded deformation sensors, breach lateral widening and morphology using image analysis from video cameras.

Table B-15: Embankment test parameters (J. Zhang *et al.* 2009)

Embankment property	Field Test 1	Field Test 2	Field Test 3	Field Test 4
Clay content [%]	11.50	11.50	17.80	33.0
Relative compaction, R_c [%]	97	96	98	92
Water content, ω [%]	19.42	15.74	17.60	28.55
Soil cohesion, c [kPa]	9.3	7.5	13.0	39.5
Angle of internal friction, ϕ [degrees]	28.3	27.8	16	14.4
Critical grain velocity, u_c^* [m/s]	0.06	0.06	0.17	0.35

The qualitative study describes the breaching mechanisms in cohesive embankments as follows: headcut erosion processes in stratified material, 'helix flow' in upstream and downstream reaches of the breach channel and side-slope failure mechanisms within the breach channel as shown in Figure B-51 to Figure B-53. The same undercutting process due to an elongated 'vortex' action occurring near the breach channel sides has been described by Morris *et al.* (2009b), Paul Samuels (personal communication, October 7, 2010) and reported in the field tests of *Mo i Rana*, Norway (IMPACT, 2004a). The embankment with low soil cohesion exhibited sliding failures while the embankments with a higher cohesive strength exhibited side-slope slumping as shown in Figure B-53.

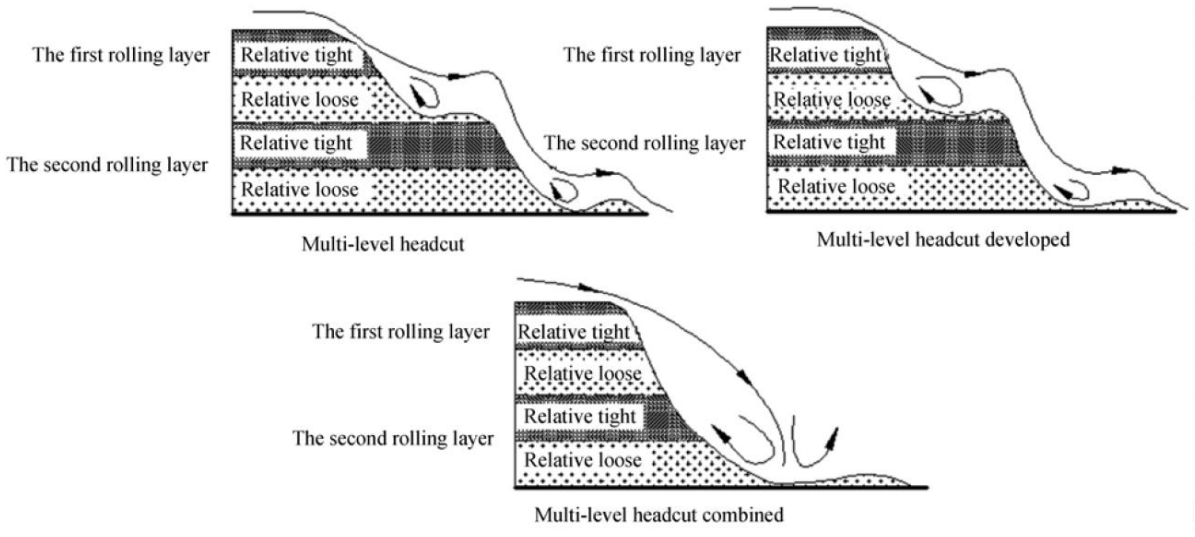

Figure B-51: Multilevel headcut erosion (J. Zhang *et al.* 2009)

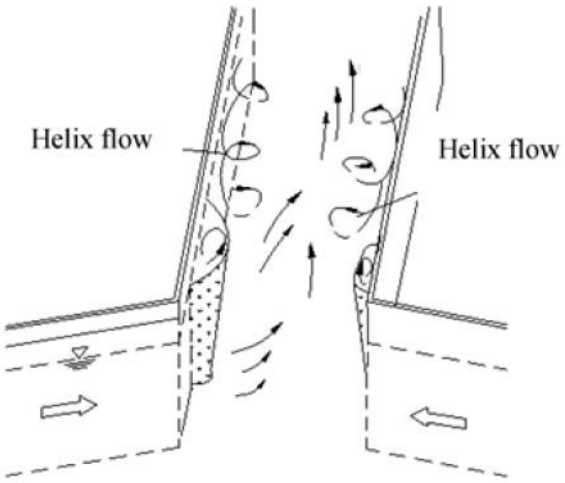

Figure B-52: Helix flow patterns in breach channel (J. Zhang *et al.* 2009)

Figure B-53: Failure mechanism (left) slumping due to bending failure (right) sliding due to shear failure (J. Zhang *et al.* 2009)

The authors also relate the breach dimensions and peak flow to soil cohesion. Table B-16 indicates that both vertical and lateral widening is highly dependent on soil cohesion. For Field Test 3, it is obvious that the side-slopes in the breach channel were adverse with large overhangs. The authors also stated that the breach width is much larger than the breach depth, which indicates that lateral erosion and widening was the dominant mechanism in cohesive embankments. The study stated that the helical flow observed in the breach channel was a critical breaching mechanism since it undermined the side-slopes by undercutting due to its high sediment

transport capacity. This observation is in agreement with field tests described in the study by Morris *et al.* (2007) (see Figure B-54).

Table B-16: Embankment breach characteristics (J. Zhang *et al.* 2009)

Test	c [kPa]	Depth [m]	Top width [m]	Bottom width [m]	Q_P [m^3/s]	Vertical erosion rate [cm/s]	Lateral widening rate [cm/s]	Breach shape
2	7.5	4.1	17.0	3.7	42.3	0.440	1.490	Trapezoidal (inverted)
3	13.0	1.7	2.1	7.1	3.7	0.022	0.065	Trapezoidal
4	39.5	1.1	1.3	0.9	1.07	0.011	0.024	Large hole

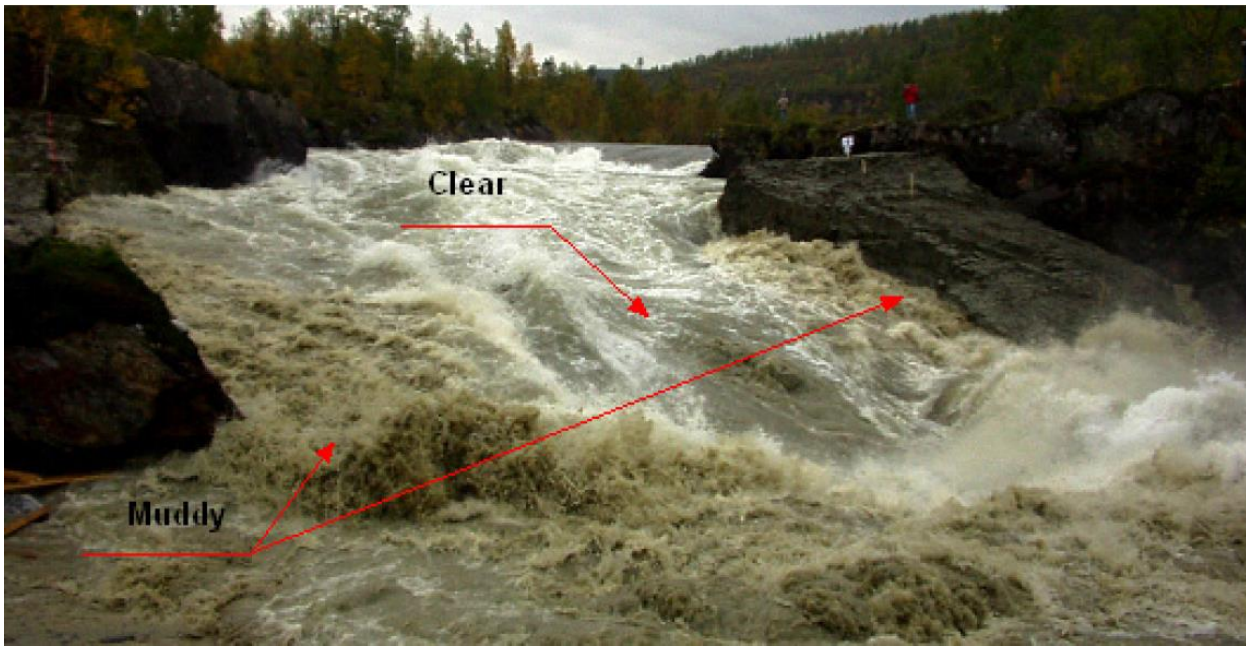

Figure B-54: Observations of sediment transport in overtopping field test (Morris *et al.* 2007)

Appendix C

Geotechnical Engineering Investigations

C.1 Experimental Phase I Embankment Materials: Sand Type I and Type II

C.1.1 Grain-size distribution analysis (ASTM D422-63)

The embankment material was selected based on the scaling of a typical noncohesive soil used in the construction of a prototype embankment. A typical median particle size diameter, d_{50}, equal to 5mm for a prototype material based on a 1:100 geometric scale would result in a median particle size diameter of 0.05mm for the model. However, a soil with such a small grain size would exhibit cohesive properties. Therefore, the finest noncohesive sands were considered for the embankment material. Embankment material samples obtained from various local sources such as quarries and/or suppliers of construction materials were analysed in the Geotechnical Engineering Laboratory using GSD tests (ASTM 2007c) as shown in Figure C-1. Based on availability, cost and least percentage of fines, the embankment material was procured from Burnside, a local Ottawa Valley quarry, in bulk quantities.

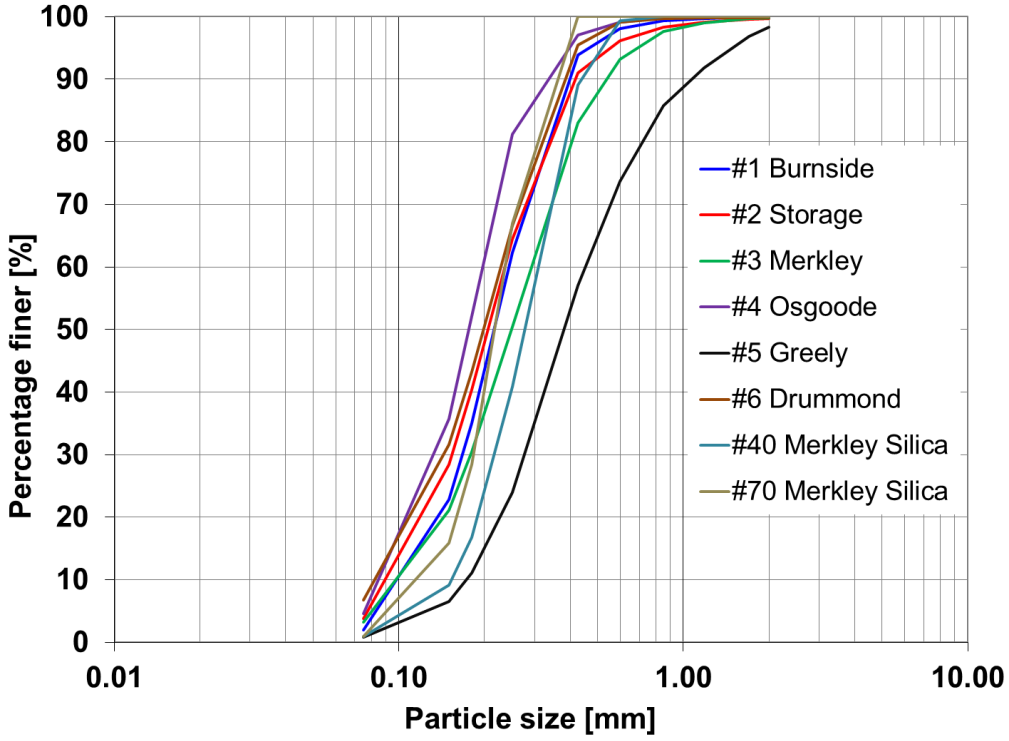

Figure C-1: Grain size distribution of suggested embankment materials

Based on the USCS classification (ASTM, 2010) this embankment material was determined to be poorly graded fine sand (*i.e.* USCS Type – SP). Further GSD tests conducted on five random samples from the first shipment of sand (*i.e.* sand Type I) revealed that variations were negligible, and that the sand was in fact finer than the previously obtained sample from the quarry (see Figure C-2).

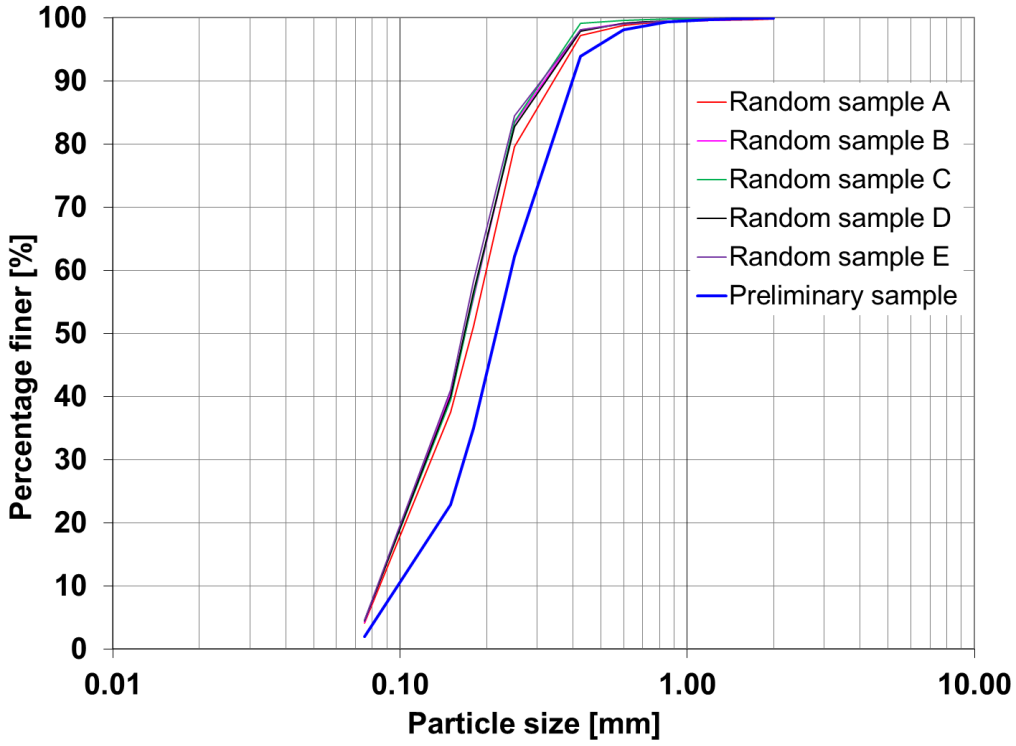

Figure C-2: Grain size distribution of five random samples obtained from bulk shipment (sand Type I)

The embankment material supply was depleted after completing the small flume tests; therefore a second shipment of noncohesive embankment material (sand Type II) was procured from the same stock pile of the same quarry (Burnside). From the GSD analyses shown in Figure C-3, sand Type II was slightly larger than sand Type I. There also appears to be a gap in gradation which may be due to the fact that the second bulk shipment was collected at a later date. However, both sands were considered to have similar gradations. For the drainage series, an inverted horizontal undertoe drainage blanket comprised of a coarse medium (driveway

gravel, herein described as gravel Type I) and filter medium (Silica sand, 6mm thickness) was used. A GSD for the coarse and filter mediums are shown in Figure C-3. Table C-1 summarises the gradations and coefficients of curvature, C_C, uniformity, C_U, and standard deviation obtained from GSD analyses (ASTM, 2007c), respectively.

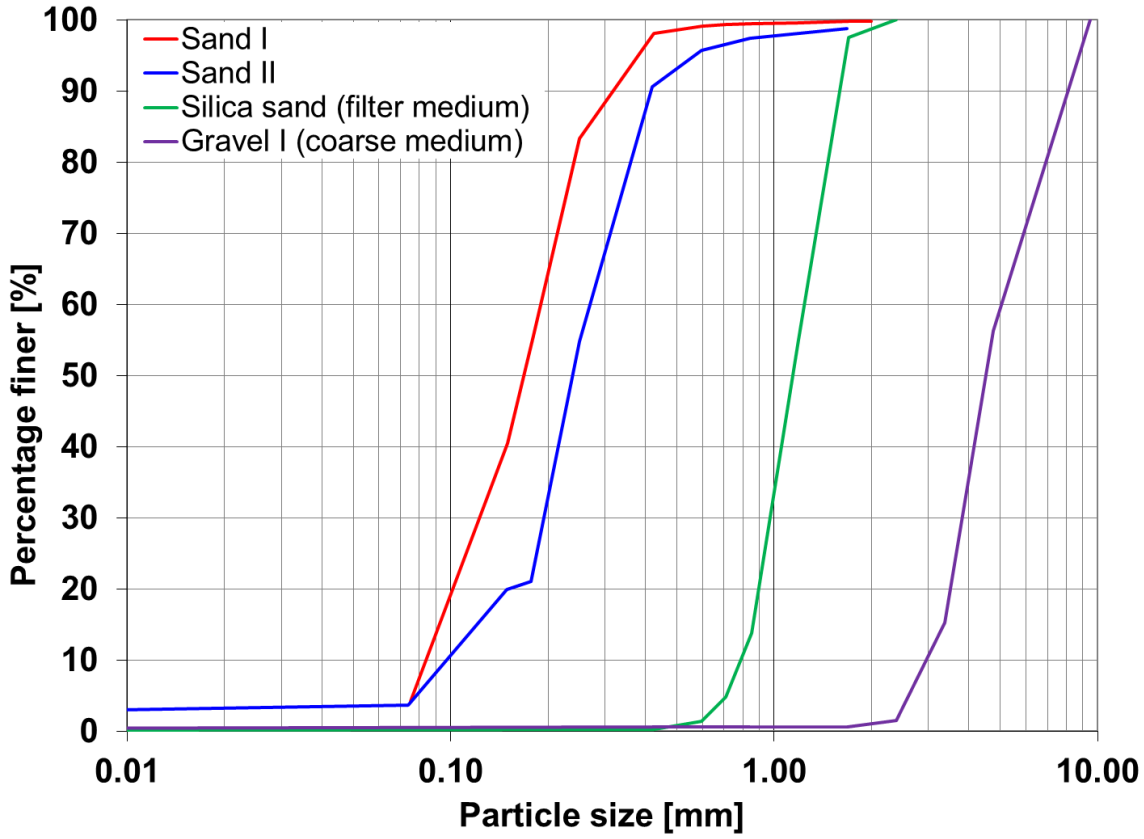

Figure C-3: Grain size distribution of embankment materials used in Phase I

Table C-1: Gradation summary for embankment materials determined from GSD analyses (ASTM, 2007c): Phase I

Embankment material	Dimensions in [mm]					C_C	C_U	σ_s	% gravel	% fines†
	d_{10}	d_{30}	d_{50}	d_{60}	d_{90}					
Sand Type I	0.084	0.125	0.170	0.191	0.324	0.97	2.26	1.65	0.0	4.4
Sand Type II	0.098	0.194	0.238	0.270	0.416	1.42	2.76	1.74	0.0	3.6
Silica sand	0.790	0.970	1.140	1.245	1.595	0.96	1.58	1.32	0.0	0.0
Gravel Type I	2.950	3.800	4.500	5.050	8.100	0.97	1.71	1.48	100.0	0.0

†$d_0 < 0.075mm$

C.1.2 Specific gravity tests (ASTM D854-06e1)

Specific gravity tests (ASTM, 2006b) were performed on three random samples for sand Type I in the Geotechnical Engineering Laboratory. The average specific gravity, G_s, for the three samples was determined to be 2.75. This value appears to be higher than the typical value for naturally occurring granular materials such as sand. This can be explained by the high iron mineral content which was clear once the sample was exposed to magnetic fields.

C.1.3 Direct shear test (ASTM D3080-04)

Direct shear tests (ASTM, 2004) were performed on a random sample of sand Type I in the Geotechnical Engineering Laboratory. The drained shear strength parameters for the dry sand were determined from the shear failure envelope as shown in Figure C-4. Since sand Type I was noncohesive, with less than 5% fines (smaller than No. 200 sieve), the line of best fit for the shear failure envelope data must have a zero intercept since the soil cohesion under drained conditions, c' is 0kPa. From the slope of the line of best fit, the equivalent angle of internal friction under drained conditions, ϕ', was determined as 36.2°.

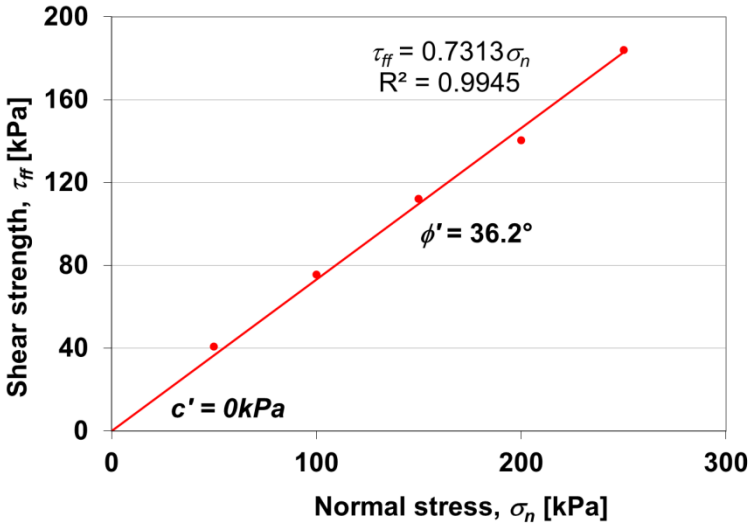

Figure C-4: Shear failure envelope determined from direct shear test for sand Type I (ASTM, 2004)

C.1.4 Constant head permeability tests (ASTM D2434–68)

The saturated permeability of sand Type I was measured in the Geotechnical Engineering Laboratory under constant head conditions (ASTM, 2006a). Figure C-5 below shows the measured saturated hydraulic conductivity, k_{sat}, for four different void ratios of sand Type I.

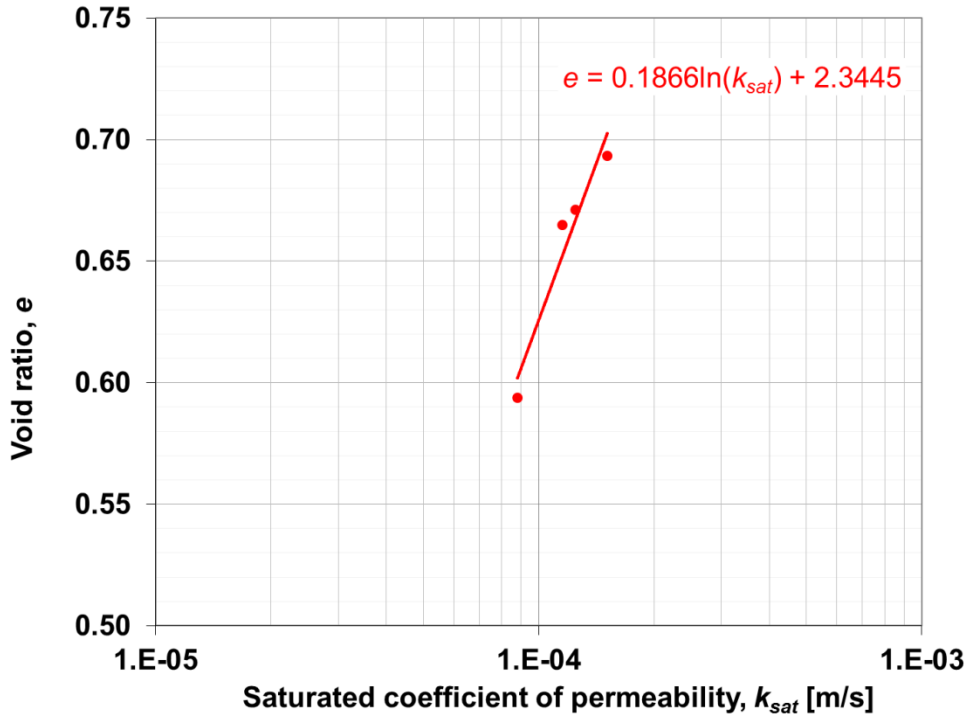

Figure C-5: Variation of saturated hydraulic conductivity with void ratio (ASTM, 2006a)

C.1.5 Proctor tests (ASTM D698-07e1)

Compaction tests were carried out in the Geotechnical Engineering Laboratory using the Standard Proctor (ASTM, 2007b) at various compaction efforts and water contents. Figure C-6 shows the results of the Standard Proctor test (25 blows) compared with higher and lower number of blows. In conventional Proctor tests, 20 blows per soil layer tends to be the minimum number, however, since the focus of the investigation was compaction, it was necessary to determine the optimum water content for even very low compactions. The minimum number of blows which can be

applied without altering the uniformity of the soil was 2. The results obtained from applying 1 blow were not reliable. Similar to the Proctor tests, the embankment models in this experimental phase were constructed using dynamic compaction. However, since the difference in confinement between the Proctor mold and the hydraulic flume was different, it was not practical to correlate densities of the embankment models based on the energy applied during compaction. While the fraction of energy transferred to the soil is absorbed in compaction, the remaining fraction was used in breaking away the compaction (Jules-Angel Infante-Sedano, personal communication, 2010). It was therefore necessary to investigate the dry unit weight relationship with water content *in situ*.

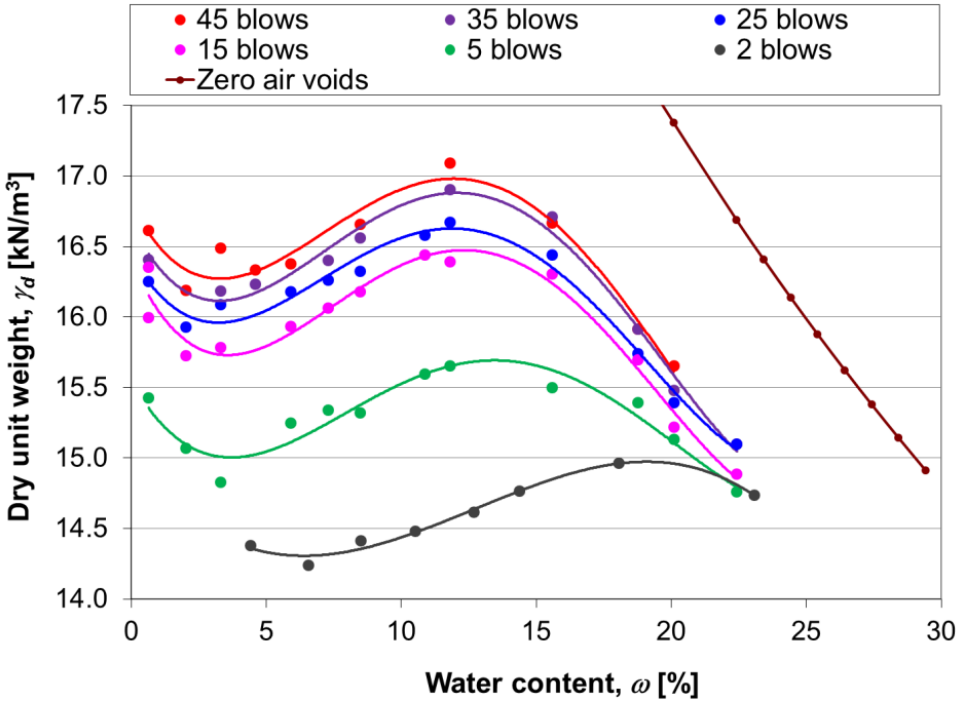

Figure C-6: Proctor compaction tests for sand Type I (ASTM, 2007b)

C.1.6 *In situ* Density Determination Tests (ASTM D1556-07)

The density of the compacted embankment models was investigated in the small flume of the Hydraulic Laboratory where the spatial breach overtopping tests took place. The embankment material was prepared by mixing sand Type I with water at

5% and 11%, which represented the natural water content of the bulk sand and optimum water contents as determined by the Standard Proctor test, respectively. After the preparation of the embankment material, 25cm high embankment models were constructed in the small flume by dropping an 8.7kg hand tamper from a known elevation over 5cm lifts. After construction, the *in situ* dry unit weight was determined at two locations (each within the upper and lower regions) of the embankment model using the sand-cone method (ASTM, 2007a). Variations in dry unit weight between the two locations were less than 5%. It was found that *in situ* compaction for lower water contents (*i.e.* 5%) yields lower dry unit weights than loose dry conditions, which was somewhat counterintuitive.

After confirming the dry unit weight under loose conditions and *in situ* several times, it was deduced that this phenomenon was due to the inefficient method of compaction at low water contents, especially with the absence of formwork which was necessary to confine the embankment material in the flume during compaction. Formwork was therefore incorporated into the construction technique for embankment models which underwent breaching (see Subsection D.1.1.1 in Appendix D). Figure C-7 shows the relationship between *in situ* dry unit weight and the number of blows applied by the hand tamper using the two water contents. It was assumed that formwork had negligible impact on *in situ* density at high water contents. Another assumption was that compaction in the large flume (1.5m wide) would yield the same relationship obtained for the small flume (0.38m wide) shown in Figure C-7.

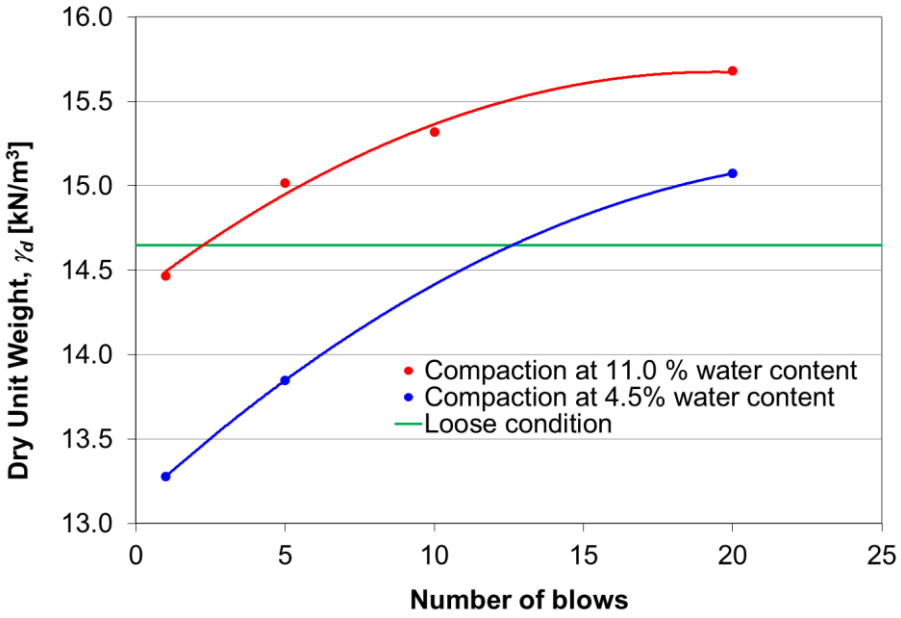

Figure C-7: *In situ* dry unit weight determined by dynamic compaction for sand Type I

C.2 Experimental Phase II and III Embankment Materials

C.2.1 Standard Geotechnical Laboratory Investigations

The new embankment material, sand Type III, was procured from Merkely Supply Ltd, an Ottawa construction materials vendor which acquires its sand from Burnside, the same quarry where sand Type I and sand Type II was obtained from. A total of 6 tons of the poorly graded fine sand (*i.e.* USCS classification – SP; ASTM, 2010) was procured in 1-ton bulk bags. The physical appearance of sand Type III was almost identical to sand Type I and sand Type II, however, some geotechnical tests revealed minor differences between the three batches. A very similar type of gravel used in constructing the drainage element in Phase I was procured from Merkely Supply Ltd (*i.e.* gravel Type II) for constructing the drainage elements in Phase II and Phase III of the experimental program. The same filter medium (Silica sand) used in Phase I was used in Phase II and Phase III of the experimental program. The horizontal multilayer drain constructed in Phase II and Phase III satisfies the gradation design for horizontal blankets as proposed by USBR (1987). Table C-2 summarises the standard geotechnical tests conducted on sand Type III and

provides an index of their results. Table C-3 summarises the GSD results of the embankment materials used in all phases of the experimental program.

Table C-2: Summary of standard geotechnical tests performed on sand Type III

ASTM Description	ASTM No.	Sampling	Result
Grain size distribution analysis	D422-63 (ASTM, 2007c)	1 sample/bag (6 samples)	(see Figure C-8, Figure C-9 and Table C-3)
Specific gravity tests	D854-06e1 (ASTM, 2006b)	1 sample/bag (3 samples)	$G_s = 2.75$
Constant head hydraulic conductivity tests	D2434–68 (ASTM, 2006a)	1 sample/bag (3 samples)	(see Figure C-10 and Figure C-11)
Proctor tests	D698-07e1 (ASTM, 2007b)	1 sample/bag (4 samples)	(see Figure C-12)
Maximum index density	D4253–00 (ASTM, 2000b)	1 sample/bag (5 samples)	γ_d = 18.5kN/m^3; $e = 0.459$
Minimum index density	D4254–00 (ASTM, 2000c)	1 sample/bag (5 samples)	γ_d = 15.3kN/m^3; $e = 0.762$

Table C-3: Gradation summary for embankment materials determined from GSD analyses (ASTM, 2007c): Experimental phases I, II and III

Soil	Phase	Particle size [mm]					C_C	C_U	σ_s	% gravel	% fines†
		d_{10}	d_{30}	d_{50}	d_{60}	d_{90}					
Sand Type I	I	0.084	0.125	0.170	0.191	0.324	0.97	2.26	1.65	0.0	4.4
Sand Type II	I	0.098	0.194	0.238	0.270	0.416	1.42	2.76	1.74	0.0	3.6
Sand Type III	II, III	0.097	0.175	0.245	0.290	0.560	1.10	3.00	1.90	0.0	3.0
Silica sand	I, II, III	0.790	0.970	1.140	1.245	1.595	0.96	1.58	1.32	0.0	0.0
Gravel Type I	I	2.950	3.800	4.500	5.050	8.100	0.97	1.71	1.48	100.0	0.0
Gravel Type II	II, III	2.660	3.490	4.090	4.424	5.750	1.04	1.66	1.36	100.0	0.0

†$d_0 < 0.075mm$

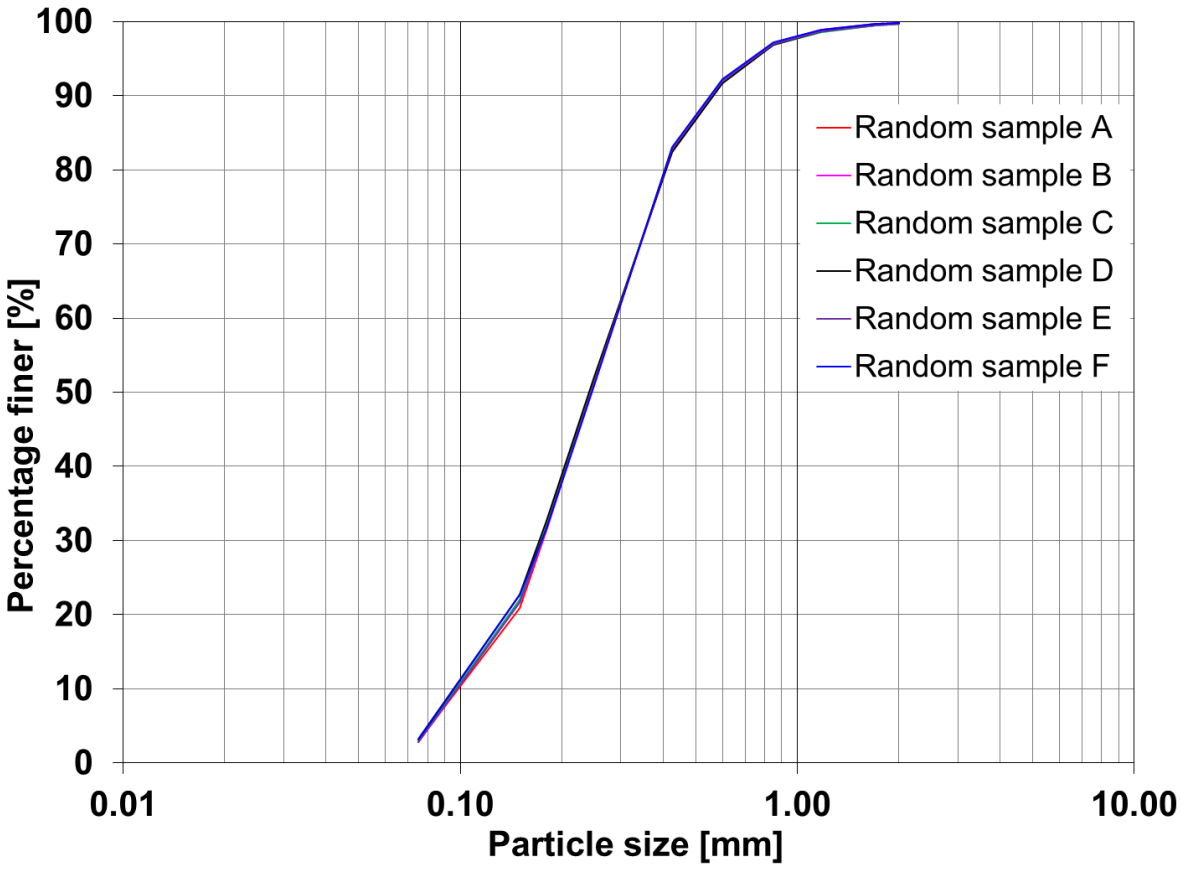

Figure C-8: Grain size distribution of six random samples for sand Type III

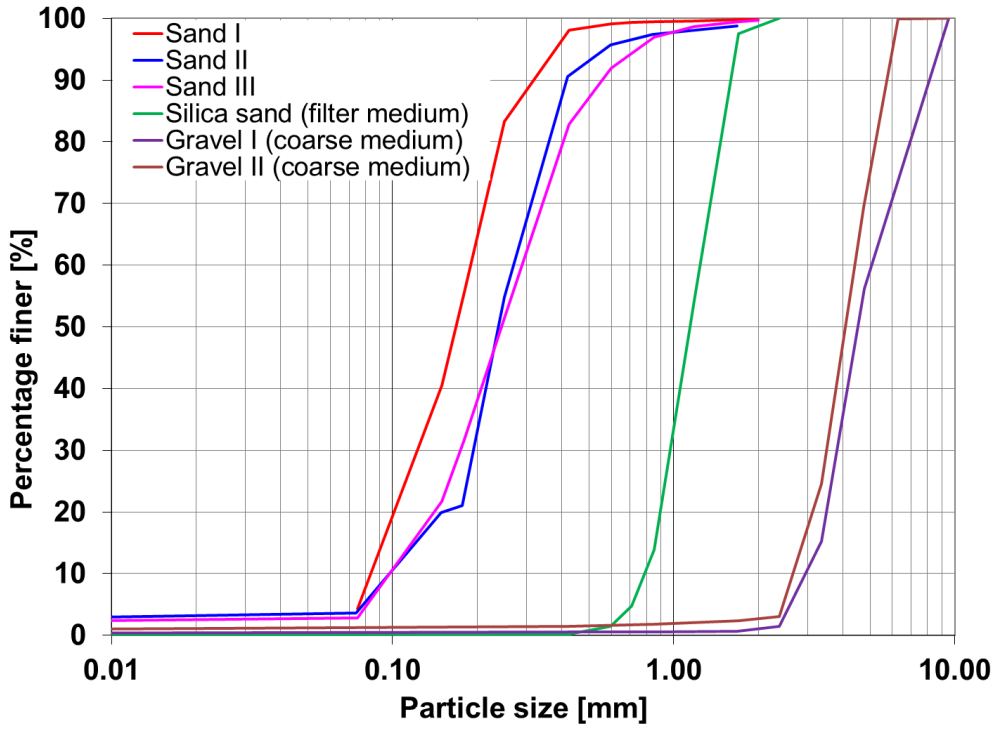

Figure C-9: Grain size distribution of embankment materials used in Phase I, II and III

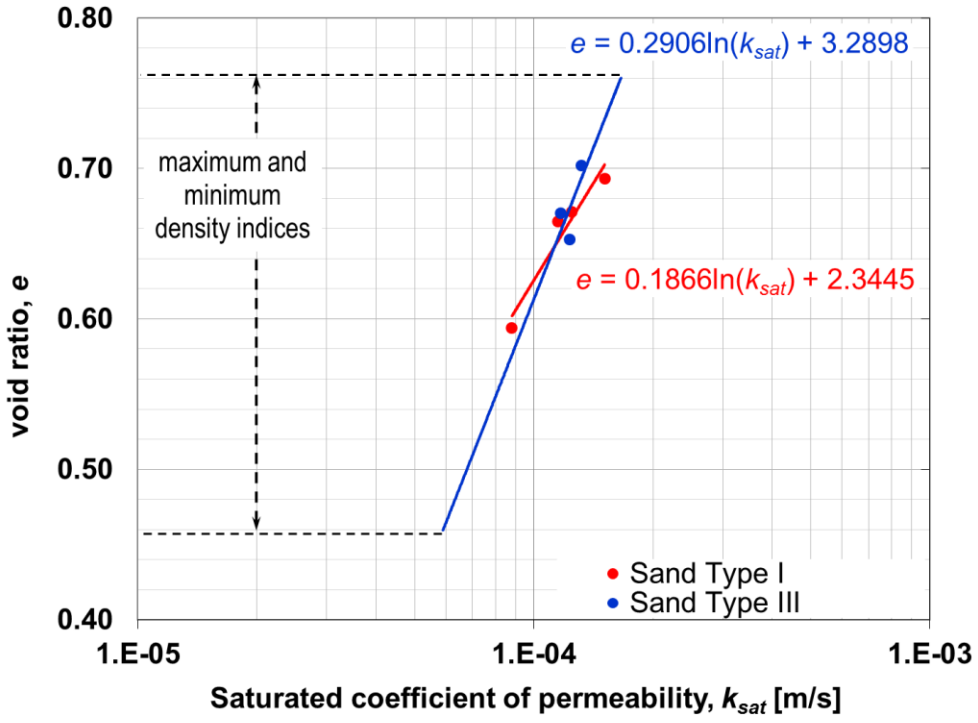

Figure C-10: Variation of saturated hydraulic conductivity with void ratio (ASTM, 2006a) for sand Type I and sand Type III

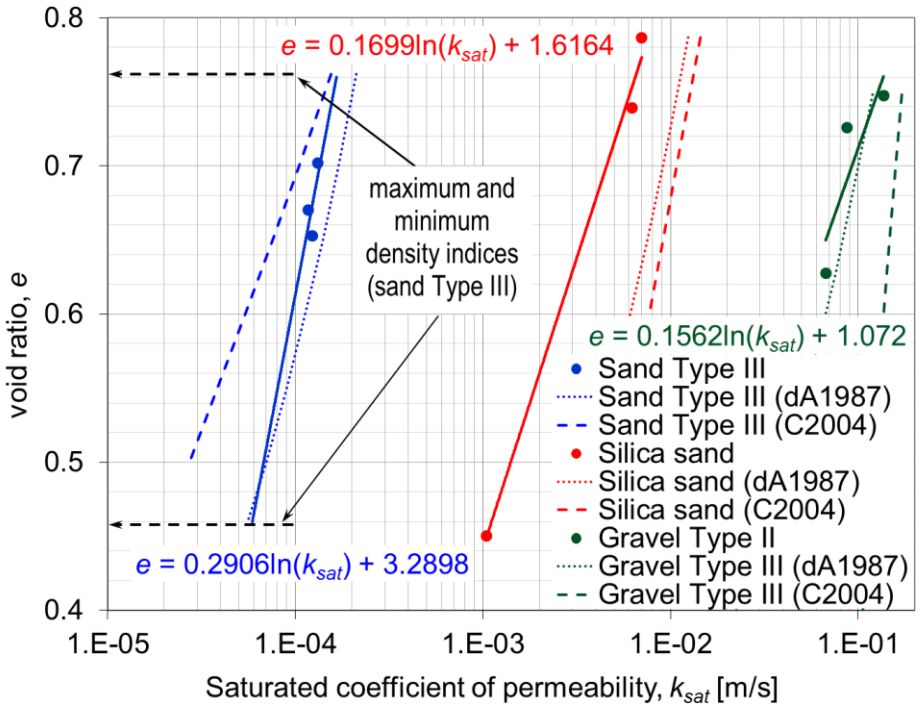

Figure C-11: Measured (ASTM, 2006a) and predicted (dA1987: den Adel, 1987; C2004: Chapuis, 2004) saturated hydraulic conductivity versus void ratio

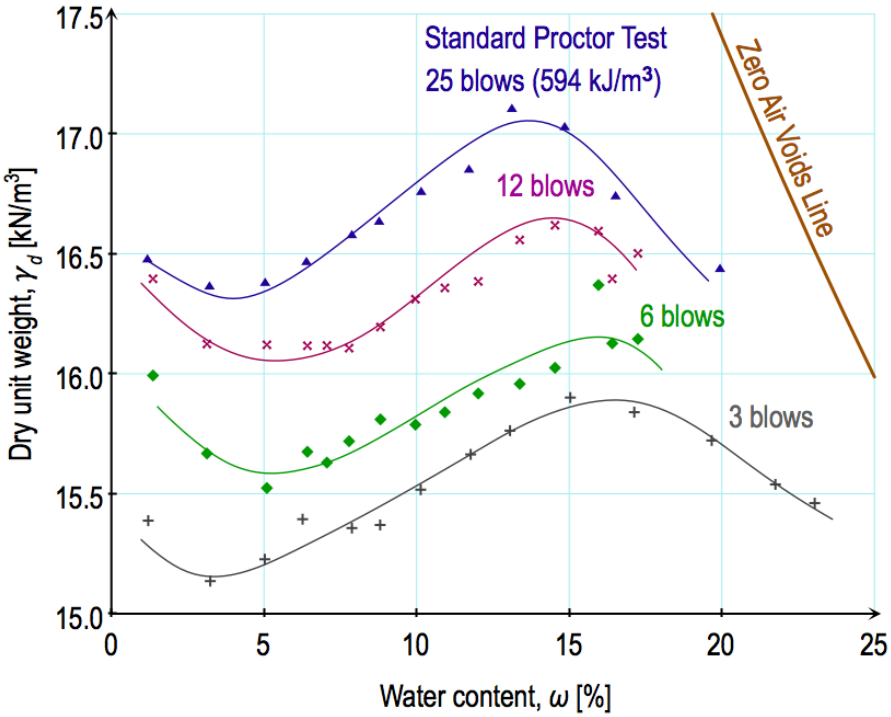

Figure C-12: Proctor compaction tests for sand Type III (ASTM, 2007b)

As shown in Figure C-8, the variations between the six samples of sand Type III were negligible, whereas sand Type II is very similar to sand Type III as shown in Figure C-9. The saturated hydraulic conductivity for sand Type III was measured using the constant head conductivity test (ASTM, 2006a). As shown in Figure C-10, the hydraulic conductivities for sand Type I and III were similar. The saturated hydraulic conductivity was also measured for the filter medium and gravel medium, silica sand and gravel Type II, respectively. A comparison between the measured (ASTM, 2006a) and predicted hydraulic conductivities, using the methods by den Adel (1987) and Chapuis (2004), for all Phase II and III embankment materials is shown in Figure C-11. Proctor tests (ASTM, 2007b) for sand Type III revealed higher compaction unit weights than sand Type I, whereas the compaction curves appear somehow flatter. Based on the similarity between sand Type III and sand Type I, the angle of internal friction, ϕ', for sand Type III was assumed to be the same as that of sand Type I (*i.e.* ϕ' = 36.2°). A direct shear test (ASTM, 2004) for sand Type III was therefore not performed.

C.2.2 Soil Water Characteristics Curve (ASTM D2325-68)

In addition to the standard geotechnical tests, a capillary-moisture relationship test (*i.e.* SWCC) for sand Type III was conducted in the Geotechnical Engineering Laboratory using the Tempe cell pressure apparatus shown in Figure C-13 below (ASTM, 2000a). A dry loose soil specimen (γ_d= 15.5 kN/m^3; $D_r = 7\%$) of known mass and dimensions was placed in the Tempe cell pressure apparatus. The soil specimen was then slowly saturated after coming into contact with the saturated high air-entry disc (HAED). Following the saturation process, the Tempe cell pressure apparatus was weighed and soil specimen was then dried by controlling the air pressure. The air pressure was incremented after ensuring that there was no change in mass.

Equilibrium time was approximately 48 hours. It was not possible to take measurements beyond an air pressure of 100kPa due to the limitation of the pressure gauge. Two pressure gauges were used for the standard test, with

maximum readings of 10kPa and 100kPa, to ensure that the AEV and RSV, were captured accurately. After the test was completed, the gravimetric water content was measured by oven-drying the soil specimen, and the water contents at the corresponding air pressures was back-calculated by adding the mass of the water drained during desorption. It was assumed that varying the densification will have little impact on the capillary-moisture retention relationship for the noncohesive embankment material.

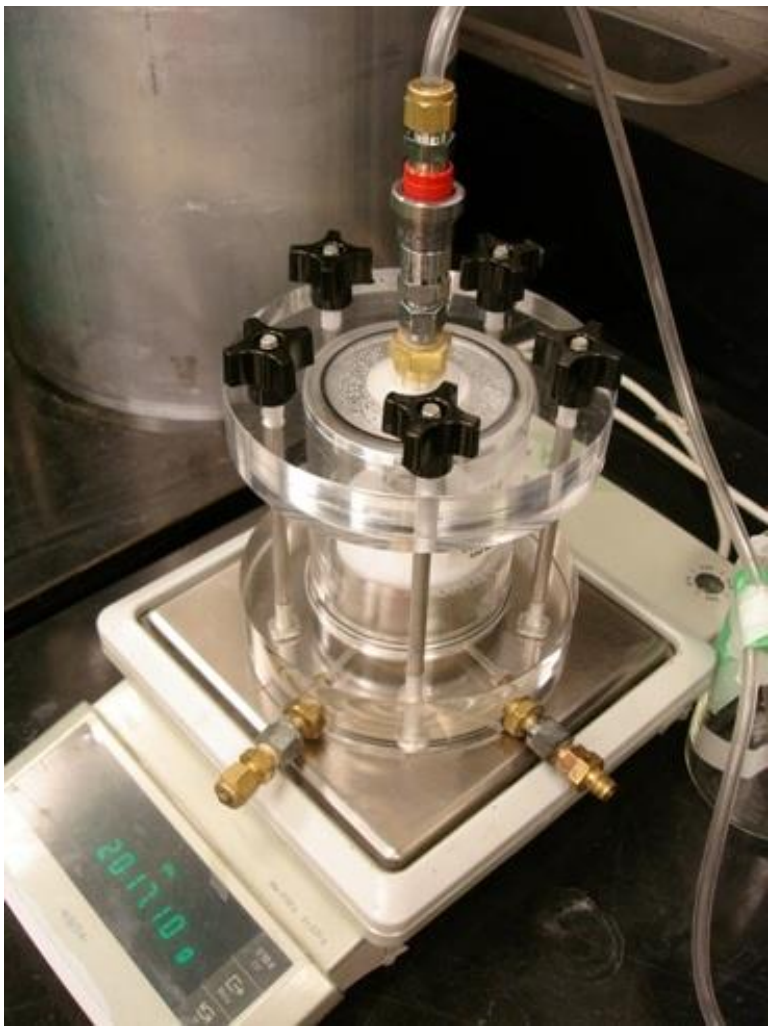

Figure C-13: Tempe cell pressure apparatus used in Geotechnical Engineering Laboratory

The SWCC shown in Figure C-14 was determined at a suction ranging between 0kPa to 100kPa, under desorption conditions. The estimated portion of the initial

desorption SWCC at high suctions was determined using the graphical construction procedure described in Vanapalli *et al.* (1998). Figure C-15 shows the predicted SWCC using the methods by Arya and Paris (1981) and Fredlund and Xing (1994) which were available in SEEP/W (GEO-SLOPE, 2004). A plot of the effective degree of saturation versus matric suction can be found in Figure C-16. The extracted SWCC parameters were as follows:

- Air Entry Value (AEV): 2.1kPa
- Residual Suction Value (RSV): 7kPa
- Residual Degree of Saturation, $\mathbb{S}_r$: 0.1 ($\theta_r = 0.037$)
- Saturated volumetric water content, θ_s: 0.366
- Arithmetic maximum slope for initial desorption SWCC, $[(1-\mathbb{S}_r)/(\psi_r - \psi_b)]$: 0.184 [1/kPa]
- Arithmetic maximum slope of effective degree of saturation versus matric suction plot (see Figure C-16),$[(1-\mathbb{S}_e)/(\psi_r - \psi_b)]$: 0.205 [1/kPa]
- Pore-size distribution index, λ_ψ: 1.93

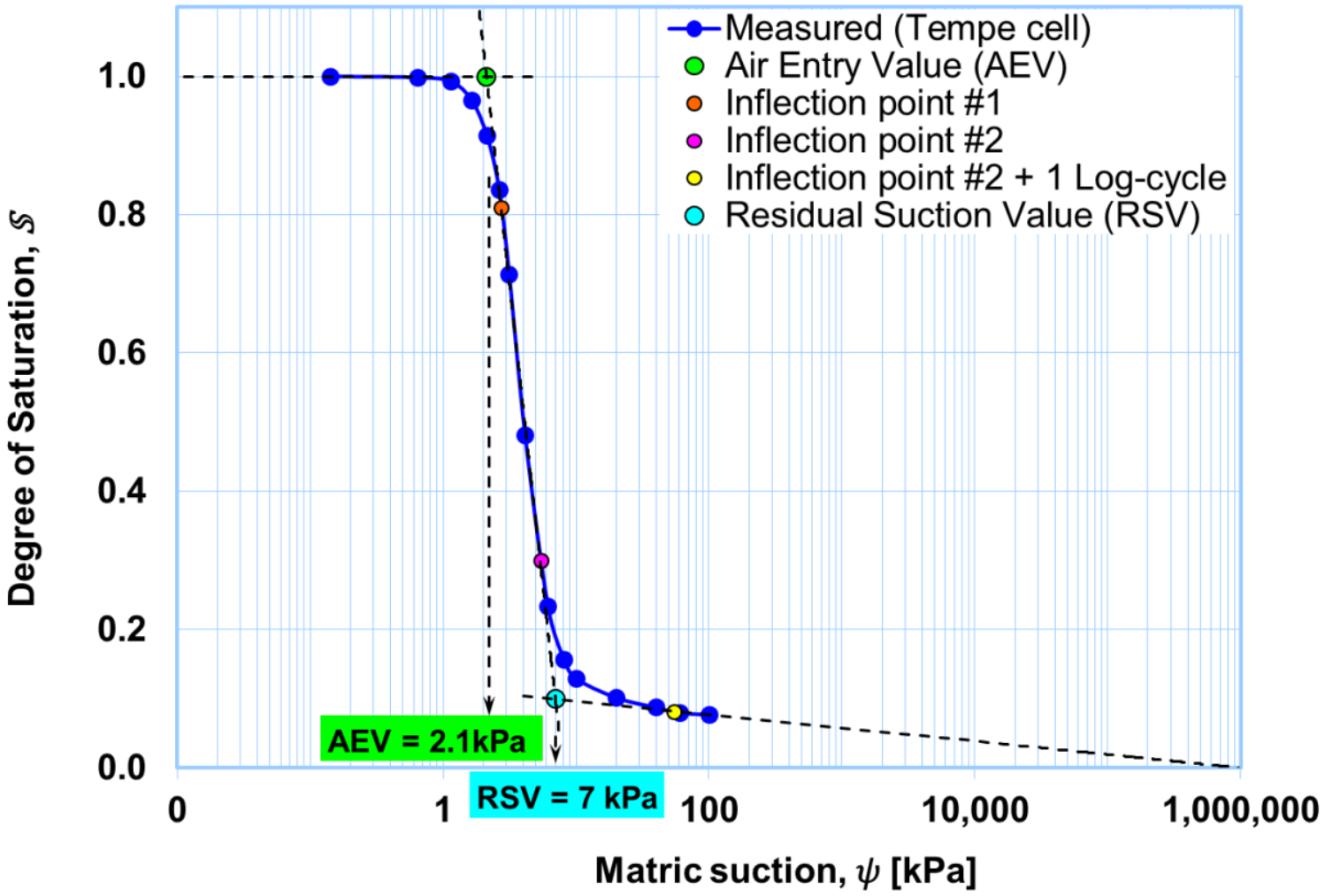

Figure C-14: Measured (ASTM, 2000a) initial desorption SWCC for sand Type III

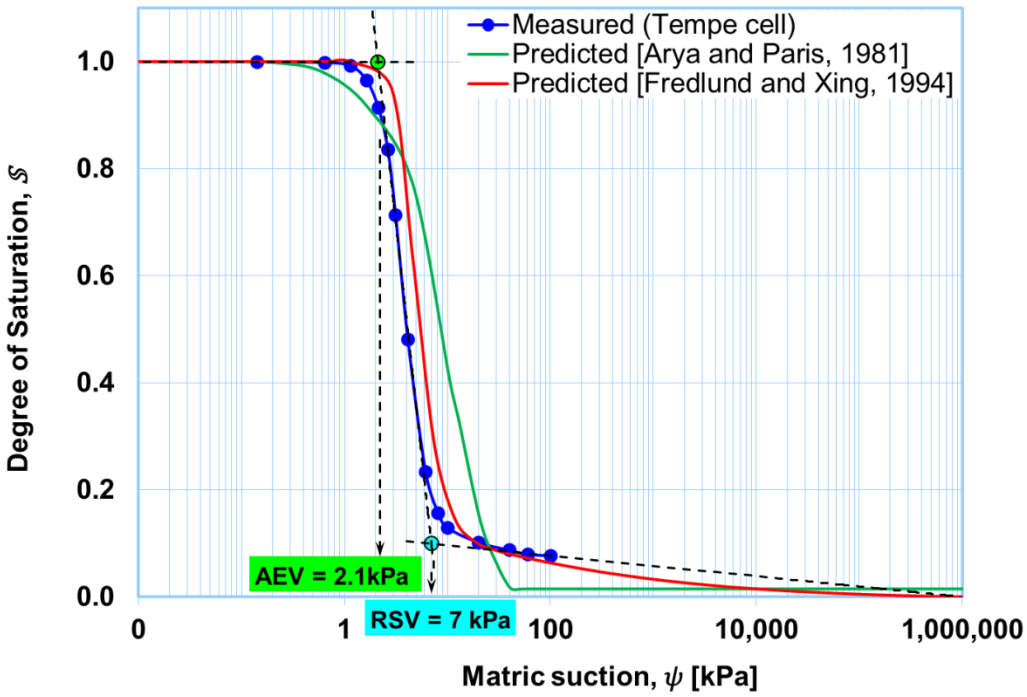

Figure C-15: Comparison between measured SWCC (ASTM, 2000a) and predicted SWCCs using GSD for sand Type III (Arya and Paris, 1981 with GEO-SLOPE, 2004; Fredlund and Xing, 1994 with GEO-SLOPE, 2007)

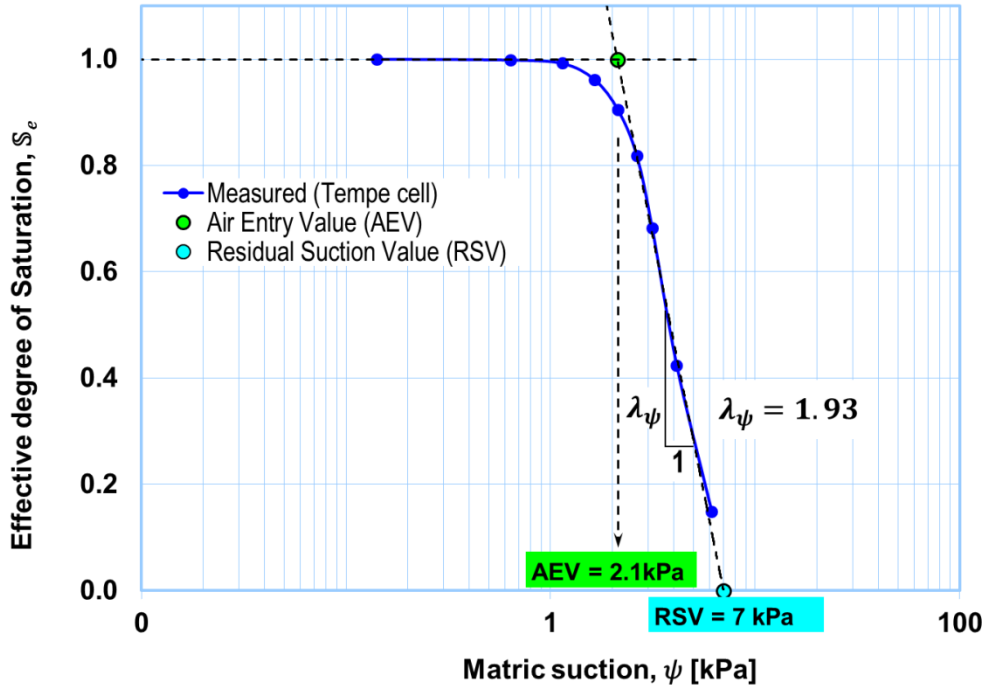

Figure C-16: Effective degree of saturation versus matric suction for fine sand Type III

Best-fit curves were plotted for the four mathematical models described in Subsection 4.5.2 (Brooks and Corey, 1964; Mualem, 1976; van Genuchten, 1980; Fredlund and Xing, 1994) using the measured initial desorption SWCC data as shown in Figure C-17. The corresponding curve-fitting parameters for each of the mathematical models are summarised in Table C-4. From Figure C-17 it can be shown that the Brooks and Corey (1964) model is unable to estimate the SWCC at soil suctions below the AEV, however, it does provide a good estimate above this value. The curve-fits by the models of Mualem (1976) and van Genuchten (1980) are almost identical, and gave a very accurate curve-fit up to a soil suction of 100kPa. However, they both overestimate the degree of saturation above this value for soil suction. The correction-factor in the Fredlund and Xing (1994) model gave rise to a more realistic SWCC at higher suctions, however, it underestimated the degree of saturation beyond a suction equal to 20kPa.

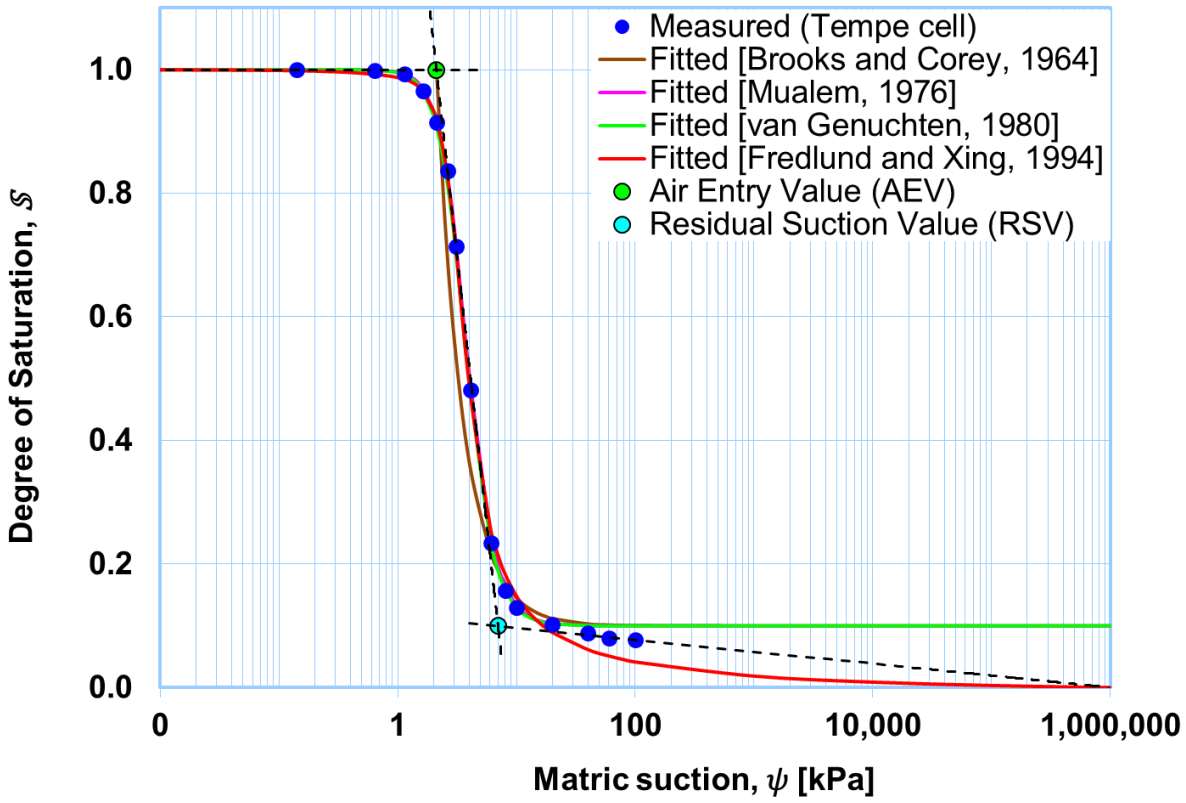

Figure C-17: Fitted SWCCs for sand Type III using mathematical models (Brooks and Corey, 1964; Mualem, 1976; van Genuchten, 1980; Fredlund and Xing, 1994)

Table C-4: Summary of curve-fitting parameters for measured SWCC data

Curve-fitting model	Curve-fitting parameter				
	λ_ψ	α_ψ	a_ψ	m_ψ	n_ψ
Brooks and Corey (1964)	4.88	-	-	-	-
Mualem (1976)	-	0.29	-	0.76	4.1
van Genuchten (1980)	-	0.29	-	0.80	4.0
Fredlund and Xing (1994)	-	-	3.0	1.02	5.0

Since only the initial desorption SWCC was measured, it was necessary to obtain information regarding the hysteresis effects for the embankment material. Therefore, the simple scaling method by Pham *et al.* (2005) was employed to predict the two bounding SWCCs (see Figure C-18 and Figure C-19). The method by Pham *et al.* (2005) requires that the initial desorption curve be fitted using the expression by Feng and Fredlund (1999). The correction factor by Fredlund and Xing (1994) was applied to the Feng and Fredlund expression. From Figure C-19 it can be shown that the Feng and Fredlund expression provides a very good estimate at high soil-suction values for the initial desorption SWCC. A summary of the SWCC parameters for the initial desorption and the two bounding SWCCs are shown in Table C-5. The initial desorption SWCC parameters (*i.e.* AEV, maximum slope and RSV) obtained using the Feng and Fredlund (1999) expression were very similar to the measured values. The two bounding curves were predicted using a maximum saturation value of 0.9 and a distance and slope ratio of 0.2 log-cycles and 1.0, respectively. Figure C-20 shows a comparison between four predicted hydraulic conductivity functions.

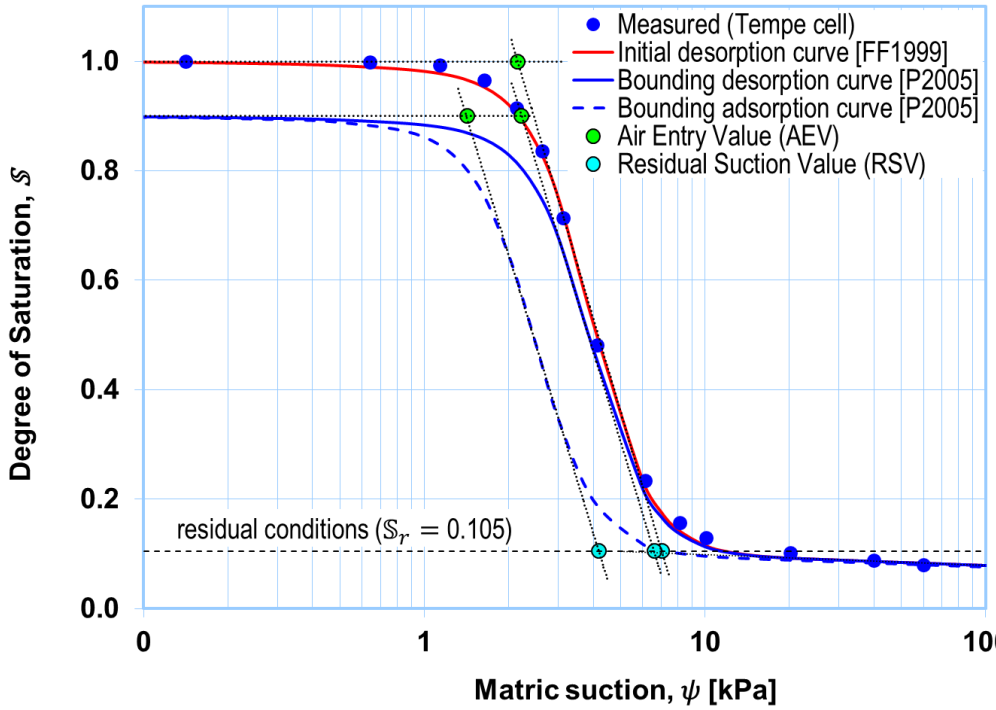

Figure C-18: Predicted hysteresis curves for sand Type III showing low soil-suction range (FF1999: Feng and Fredlund, 1999; P2005: Pham et al. 2005)

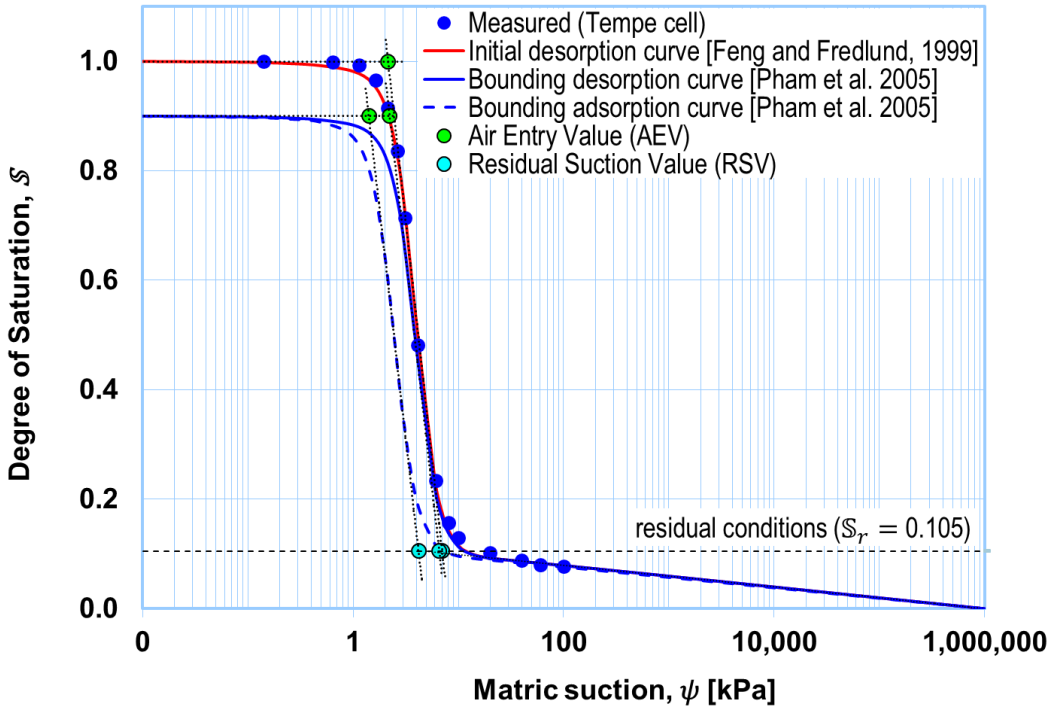

Figure C-19: Predicted hysteresis curves for sand Type III showing full soil-suction range

Table C-5: Summary of parameters obtained from predicted hysteresis SWCCs using the method by Pham et al. (2005)

SWCC	SWCC Parameters						
	b_ψ	d_ψ	$\mathbb{S}_r$	$\mathbb{S}_u$	AEV [kPa]	RSV [kPa]	Maximum slope [1/kPa]
Initial desorption	250	4.0	0.105	1.0	2.15	7.05	0.195
Bounding desorption	250	4.0	0.105	0.9	2.22	6.60	0.200
Bounding adsorption	40	4.0	0.105	0.9	1.42	4.20	0.327

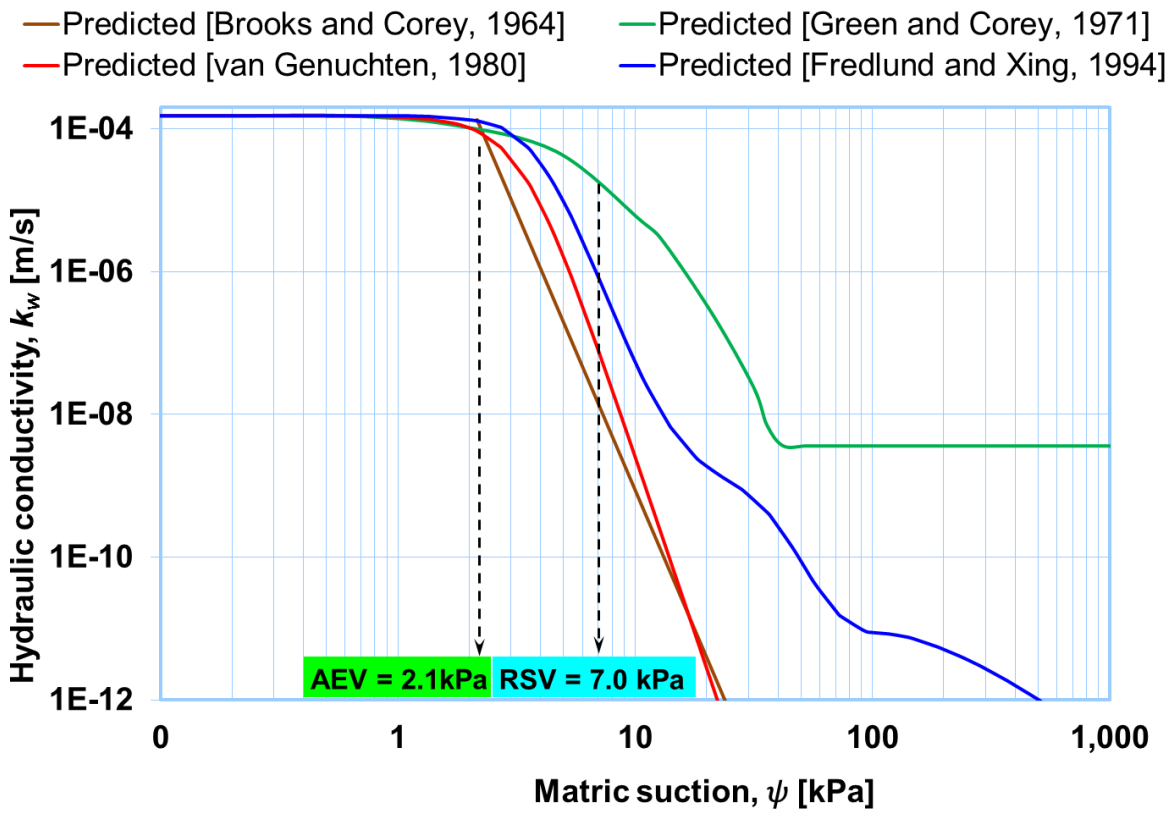

Figure C-20: Comparison between thee predicted hydraulic conductivity functions (Brooks and Corey, 1964 using Equation (4.175); Green and Corey, 1971 with GEO-SLOPE, 2004; van Genuchten (1980) and Fredlund and Xing (1994) with GEO-SLOPE, 2007)

While the methods by Brooks and Corey (1964) and van Genuchten (1980) predicted similar hydraulic conductivity functions, the methods by Fredlund and Xing (1994) and Green and Corey (1971) yielded values by one order and two orders of magnitude higher, respectively, at the RSV. It is important to note that although the hysteretic SWCC for the embankment material were predicted, modeling of the

steady-state and falling head conditions described in Subsection 7.3.2 was carried out using the initial desorption SWCC. It is assumed that the hysteresis in the capillary-moisture relationship of the embankment material, as shown in Figure C-18 and Figure C-19, has negligible effects on seepage in the partially-saturated zone.

C.2.3 *In situ* Density Determination Tests (ASTM D1556-07)

In situ density determination tests were conducted on partial embankments comprised of two lifts using the footprint of the compactor (*i.e.* 71cm long x 150cm wide x 10cm high) shown in Figure C-21 and Figure C-22. Plastic lining was used to isolate the formwork and compactor from the embankment material in order to prevent damage of the soil lifts upon their removal. Three sand cone tests were performed for each compacted footprint.

Figure C-21: *In situ* density determination of compacted partial embankment comprising of 2 lifts (*i.e.* 10cm high)

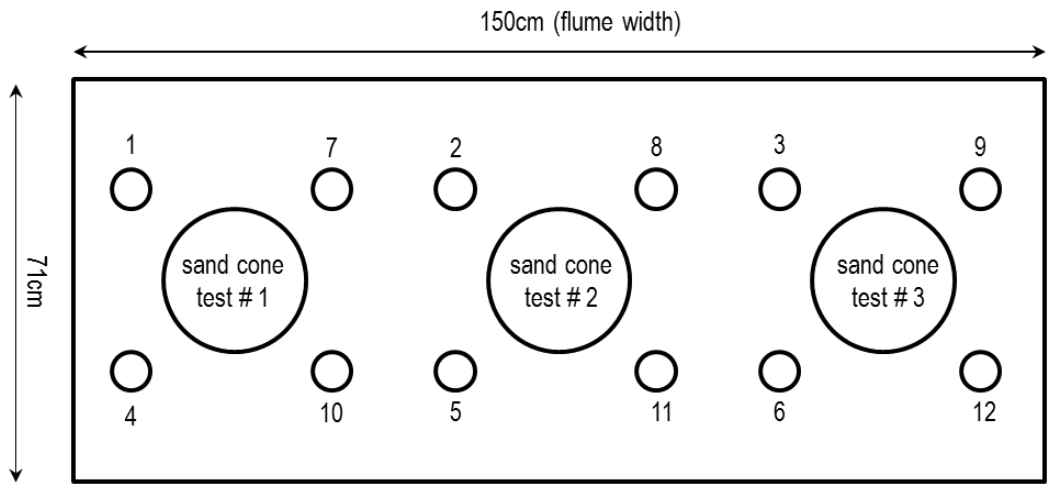

Figure C-22: Compacted footprint showing locations of sand cone tests and water content samples (upper lift: 1 – 6; lower lift: 7 – 12)

A total of 12 compacted soil specimens were also extracted from the compacted footprint using a hollow cylinder (see Figure D-7 in Appendix D) for determining the water content of the embankment material after compaction as shown in Figure C-22. The cylindrical specimens were then divided into two halves in order to determine the water content in the upper and lower lifts (six samples per lift). The water content from the six compacted samples in the upper and lower lifts was compared to the six samples collected prior to compaction from similar locations. During compaction, water from the embankment material exfiltrated through the formwork, resulting in a 1 – 1.5% drop in water content. The variation in water content between the three sand cone samples and the six compacted cylindrical samples was 0.5% and 1.0%, respectively. In this study, the construction water content was determined as the average water content of the three sand cone tests. Variations in water content between the three sand cone samples and 6 compacted cylindrical samples was less than 1.5%. The variation in water content between the six embankment material samples prior to compaction was 1.5 – 2.0%. These variations were seen as sufficient to consider the mixing and compaction as an efficient technique.

The highest compaction effort (γ_d = 17.8kN/m^3; $e = 0.516$; $D_r = 80\%$) was produced using both vibration and a 4kPa static load applied using the hydraulic jack (see Subsection D.1.2 in Appendix D). It was not possible to increase the static load any further since the weight of the frame and the concrete bricks were insufficient to sustain themselves as a larger counterweight. A lower compaction effort (γ_d = 16.8kN/m^3; $e = 0.606$; $D_r = 52\%$;) was produced using the vibration from the compactor without the static load. The vibration for the lower compaction effort was applied using a duration equal to 20 seconds. For the two applied compaction efforts, the *in situ* density of the compacted embankment material was determined for various water contents as shown in Figure C-23. Several attempts were made to decrease the compaction effort by reducing the vibration frequency (using a variable supply voltage source to the A/C motor) as well as decreasing the static load to 2kPa. The resulting compaction curve was no different than the lower compaction effort, and therefore it was not possible to achieve an intermediate compaction effort due to the proximity of the optimum dry unit weight between the high and low compaction efforts. Other attempts at achieving an intermediate compaction curve using smaller vibratory time durations (*i.e.* < 20 seconds) failed. Therefore, the lower compaction effort attained using the vibratory compactor without a static load herein is described as the intermediate compaction effort.

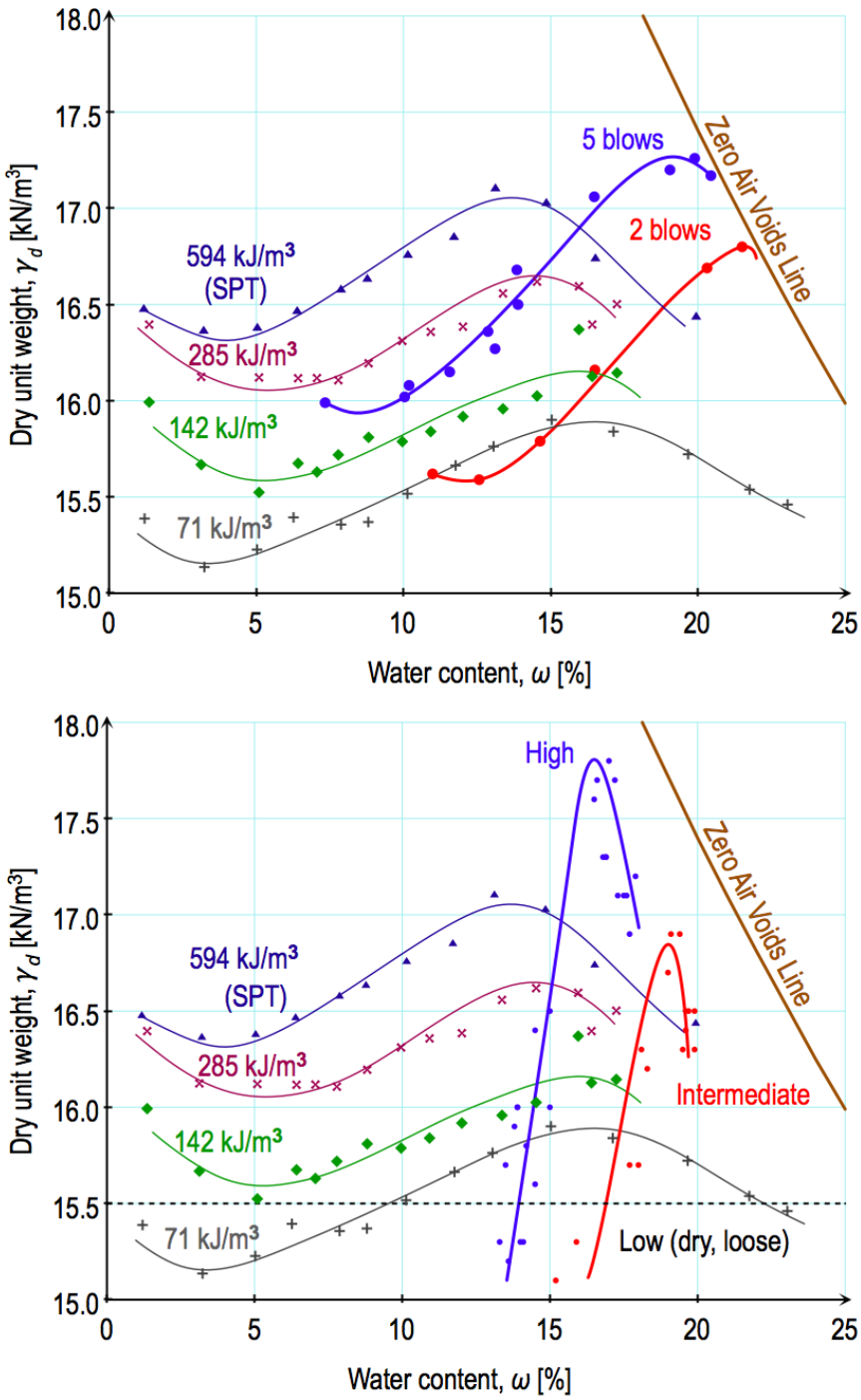

Figure C-23: Compaction curves for *in situ* and laboratory (*i.e.* Proctor test) methods (top) dynamic compaction technique (bottom) vibration compaction technique

A third and even lower compaction effort was then simulated by constructing embankment models using the embankment material under dry loose conditions.

The embankment model was compacted under its own weight during impoundment, and yielded a dry unit weight, γ_d = 15.5kN/m^3 ($e = 0.74$; $D_r = 7\%$), after being allowed to saturate.

The compaction curve using the dynamic compaction technique adopted in Phase I of the experimental program was also determined as a separate compaction test as shown in Figure C-23 for 2 and 5 blows using the 8.7kg tamper. It is clear from Figure C-23, that the variation of the dry unit weight with water content for the four compaction energies applied using Proctor test equipment (ASTM, 2007b) and the two compactions applied using the *in situ* technique follow different maximum dry unit weight and optimum water content (OWC) values. This is due to the difference in confinement of each technique (*i.e.* Proctor mold which is much smaller and more water-tight than the large flume of the Hydraulics Laboratory). The larger *in situ* confinement also allows the soil to move more freely, and as water content in the soil increases, the percentage of mechanical energy absorbed into the soil increases. While the OWC for the *in situ* compaction technique was near saturation, the water content after *in situ* compaction decreased due to water seeping through the formwork used.

C.3 Experimental Phase III – *In Situ* Density Determination Tests for Sand Type III in Small Hydraulic Flume (ASTM D1556-07) (*Failed Attempt*)

The water content was varied in several *in situ* compaction tests using a 4kPa static load applied to the compaction lift whereas the *in situ* density of the compacted embankment material was determined using the sand cone method (ASTM, 2007a). As shown in Figure C-24, the optimum conditions for the target compaction curve obtained in the large flume using the applied static load could not be achieved. Attempts using water contents higher than the optimum value for the target compaction curve always yielded low dry unit weights and water contents after compaction. This was due to the vibration which the soil-water mixture was subjected to, which resulted in fluidization of the embankment material and seepage through the formwork and loss in water content after the vibration had ceased. This

phenomenon is characterized by the high vibration-confinement ratio attributed to the narrower flume.

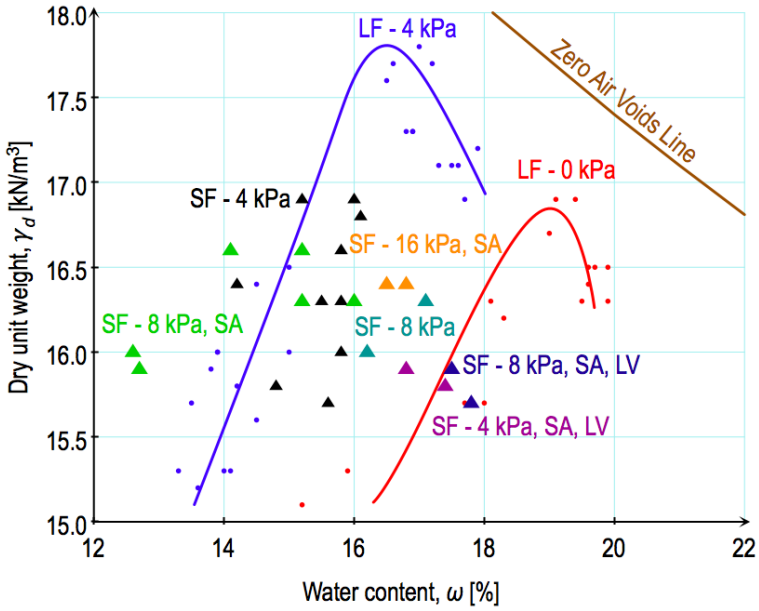

Figure C-24: Compaction curves in large flume compared against data collected from small flume *in situ* tests (LF: large flume tests; SF: small flume tests)

An attempt at using a higher applied static load (16 kPa) was made; however, this only resulted in achieving lower dry unit weights for higher water contents. An attempt at decreasing the vibration frequency as well as using a shock absorber between the motor and compactor plate was also made (see Figure D-26 in Appendix D). Using a shock absorber resulted in achieving higher water contents, however, the target optimum conditions could to be achieved. A last attempt at using a high static load (8kPa) coupled with the shock absorber failed to achieve the target optimum conditions. A recommendation for resolving this confinement matter is to use a smaller lift height (*i.e.* < 5cm). However, sufficient time had already been exhausted in investigating the compaction, therefore it was decided to abandon the small flume compaction project and focus on investigating erosion using another soil parameter, such as initial degree of saturation.

Appendix D

Embankment Construction Techniques, Equipment Design and Instrument Installation Instructions and Calibration

D.1 Embankment Model Construction Techniques

D.1.1 Phase I of Experimental Program – Dynamic Compaction Technique

D.1.1.1 Small Flume Tests

Construction of the embankment models was carried out in the following steps:

- For the drainage series, an inverted horizontal toe-drain comprised of a coarse medium (gravel Type I, 9mm thickness) and filter medium (Silica sand, 6mm thickness) spanned from the downstream toe to a point in the embankment foundation located at the base of the vertical of the downstream apex of the crest (see Figure 5.11). The horizontal multilayer drain satisfies the gradation design for horizontal blankets as proposed by USBR (1987).
- Water was added to the soil to achieve near optimum conditions (~11%). Optimum water content values were based on Standard Proctor tests conducted in the Geotechnical Engineering Laboratory (see Subsections C.1.5 and C.1.6 in Appendix C).
- Two soil samples were taken from the soil-water mixture from each lift to confirm the construction water content (ASTM D2216-05).
- The embankment models were constructed in 5-6cm lifts using formwork specifically designed for the small flume (see Figure D-1).
- The embankment lifts were dynamically compacted using a 8.7kg hand tamper (19cm long x 25cm wide) installed on a movable carriage (see Figure D-1 and Figure D-2), similar to the method in experimental work by Shuibo *et al.* (1993), Spinewine *et al.* (2004), Geisenhainer and Kortenhaus (2006) and Morris *et al.* (2007). The tamper was dropped over the soil's levelled surface from 5cm or 10cm heights, depending on the required compaction efforts.
- The excess material from the step-shaped embankment model was removed and the shoulder slopes and crest was shaped and trimmed using a thin plywood plank and trowel, respectively.

- The upstream reservoir was impounded slowly (~3-4mm/min) using water drawn from an underground reservoir by means of a pump. The impoundment ceased once the WSL was 2cm below the embankment model crest. The slow filling ensured that saturation was uniform to avoid any differential settlement in the embankment model.
- Saturation of the embankment model was clearly observed through the glass side-walls during the first impoundment due to the low initial water contents (see Figure D-3 and Figure D-4). Once saturation was established, the reservoir was drained completely for further preparations. The time for reaching steady-state seepage conditions was recorded. Generally, steady-state seepage was achieved within 45 to 55 minutes depending on the compaction and presence of a drainage element.
- The bed elevation of the embankment's surface was confirmed using point gauges. The accuracy of the embankment profile was within ±1.5mm.
- Gridlines were installed on the embankment surface using a chalk line, in order to extrapolate the dimensions of the breach channel from captured footage. Gridlines were also installed on the glass side-walls of the flume as shown in Figure D-4.
- A triangular pilot channel 2cm deep, with 1V:1H side-slopes, was carved onto the embankment model crest's centreline to initiate the breach away from the glass side-walls (see Figure 5.10 and Figure 5.11). The pilot channel invert elevation, z_{pb}, was 2cm below the crest elevation.

Figure D-1: Formwork used in construction of small flume embankment models

Figure D-2: Movable carriage with compactor in small flume

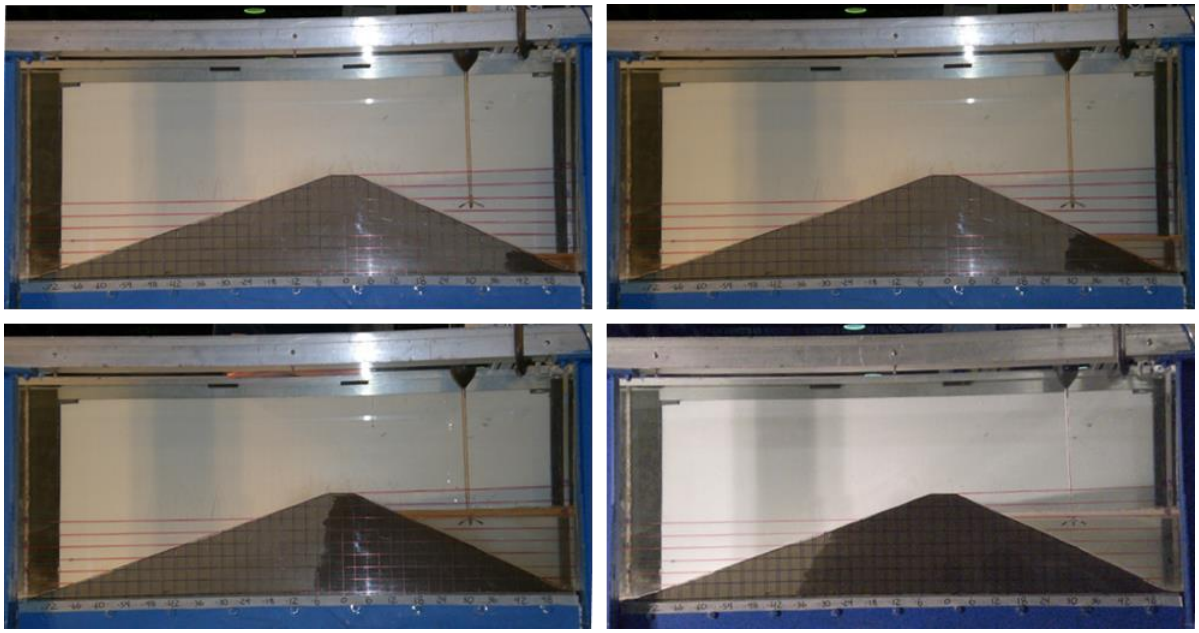

Figure D-3: Process of impoundment and saturation of embankment models in small flume

Figure D-4: Small flume embankment (left) during reservoir impoundment (right) after impoundment showing gridlines on downstream slopes and glass side-walls

D.1.1.2 Large Flume Tests

Construction of the embankment models was carried out similar to the small flume embankment models. The embankment models' shell material was sand Type II while the same drain and filter medium, gravel Type I and silica sand, respectively; of the small flume tests were used. Although sand Type II had a slightly different particle size than sand Type I, both sands were assumed to be similar in properties,

which did not necessitate a repetition of the geotechnical tests. All the large flume embankment models were constructed using the same compaction effort (5 blows, dropped from a 10cm height) using the same hand tamper. A second movable carriage was especially designed and fabricated to accommodate the hand tamper in the wide flume as shown in Figure D-5. Based on the small flume *in situ* density tests, the embankment model dry unit weight was 15.02kN/m^3.

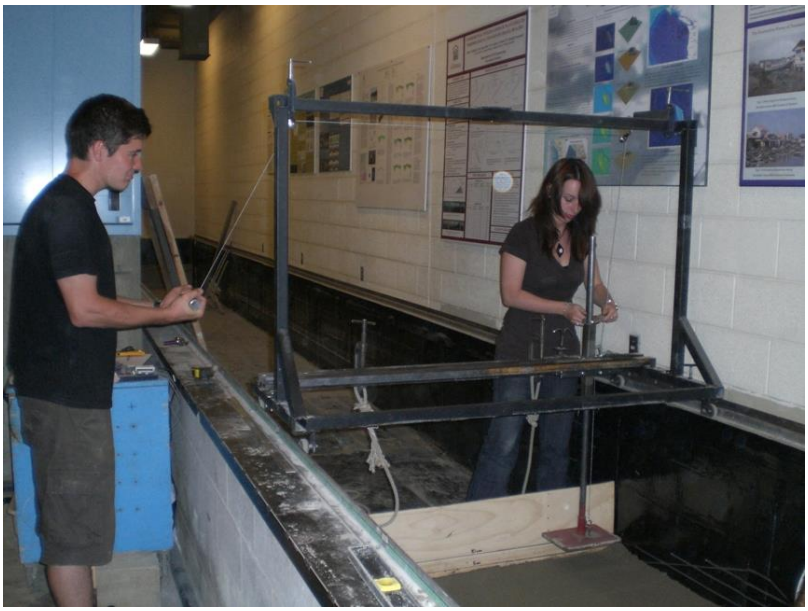

Figure D-5: Compaction in large flume using tamper connected to movable rig

The compaction method in the large flume was identical to that of the small flume with the exception of formwork. Formwork was comprised of concrete blocks placed between both ends of the 5cm lift as shown in Figure D-6. Upon completion of a lift, the concrete blocks were placed above the compacted lift to confine the next lift. Since there the large flume was not equipped with piezometer taps at the flume bed nor glass side-walls, the criterion for steady-state seepage was based on the drainage series conducted in the small flume. Figure D-6 shows the construction process of the embankment models in the large flume. After the completion of the embankment models, 5cm x 5cm gridlines were installed on the embankment surface.

Figure D-6: Embankment model construction in large flume for Phase I (top) installation of under toe-drain (middle) form work (bottom) shaping of embankment surface

D.1.2 Phase II of Experimental Program – Novel Compaction Technique

Embankment model construction was adapted to mimic a prototype construction, using both a vibratory and static load for applying compaction to the noncohesive

soil. Several attempts were made before refining the compaction process to produce a 30cm high embankment models using uniform soil lifts, 5cm high, using different compaction efforts. The methods used vibration as the primary means of applying compaction where the compaction effort was controlled using various static loads. Specially designed instruments as well as additional readily available tools used in the construction process are shown in Figure D-7.

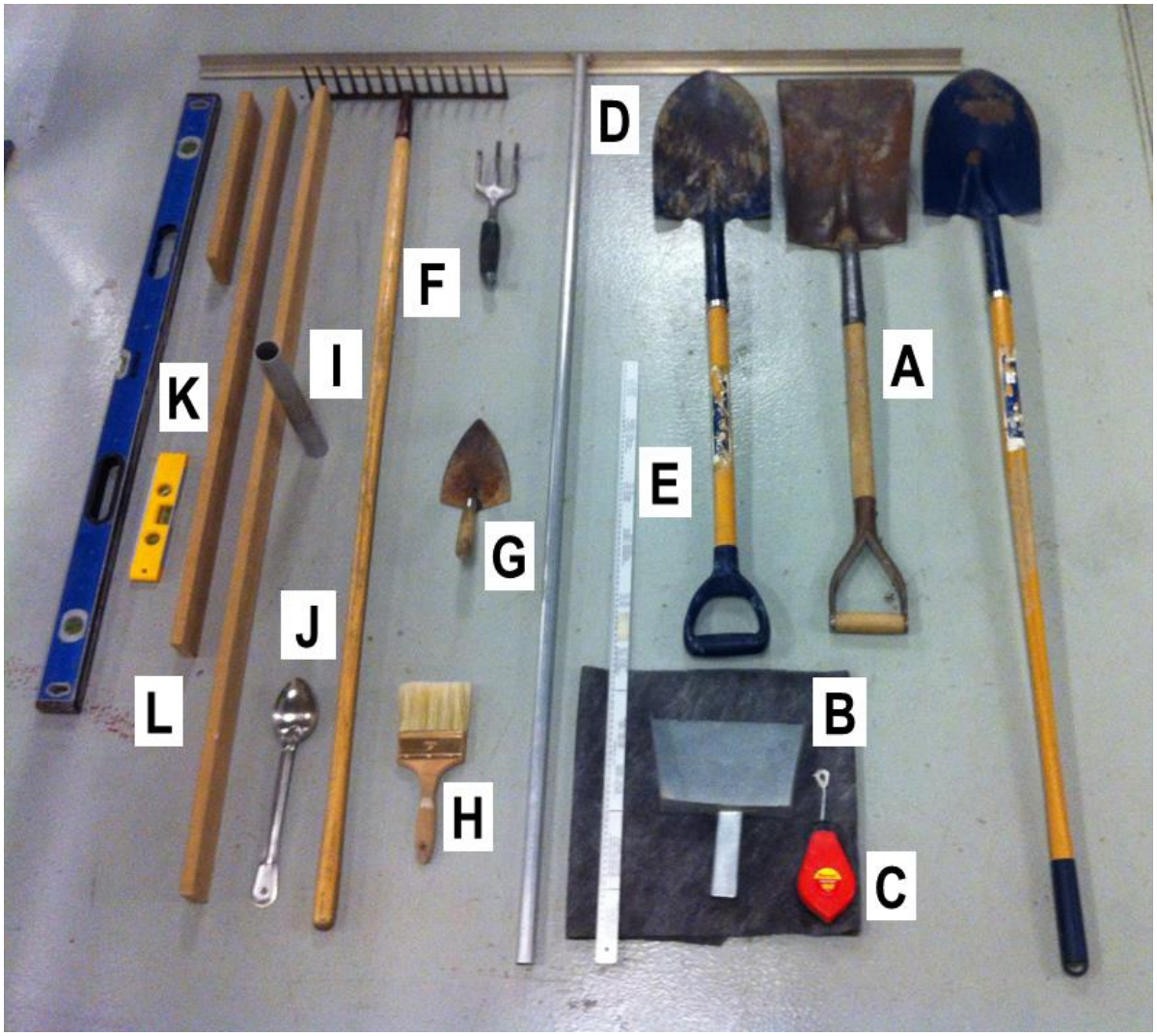

Figure D-7: Tools and instruments used in Phase II of embankment model construction (A – large shovels; B – small shovel; C - chalk line; D – leveller; E – metre rule or tape measure; F – large and small rakes; G – trowel; H – brush for fine levelling; I – hollow tube for post-compaction sampling; J – spoon for soil sampling; K – large and small spirit levels; L – ½" thick wooden planks for carving embankment surfaces)

D.1.2.1 Initial Compaction Trials

The first attempt incorporated the use of six 5/8” thick Medium Density Foam (MDF) boards, sized in accordance with each of the six soil lift footprints, and reinforced with 1.5” x 1.5” structural spruce studs spanning the length of the footprint, as shown in Figure D-8 and Figure D-9. Both sides of the MDF boards were coated with enamel to prevent expansion from moisture. Water was added to the fine sand and thoroughly mixed using a large rake and the soil-water mixture was then backfilled between plywood formwork using shovels and levelled using a rake as shown in Figure D-10. The formwork, comprised of 5/16” thick plywood planks and assembled into L-shapes, was installed on the upstream and downstream ends of the embankment lift footprint, and weighed down using concrete bricks (see Figure D-11). This formwork ensured the confinement of the embankment material during the compaction process.

Figure D-8: Six MDF boards sized in accordance with embankment lift footprints showing side with smooth surface

Figure D-9: Second largest MDF board showing opposite surface reinforced with 1.5" x 1.5" spruce studs spaced 15" apart

Figure D-10: Embankment material (left) mixing (middle) levelling (right) sampling

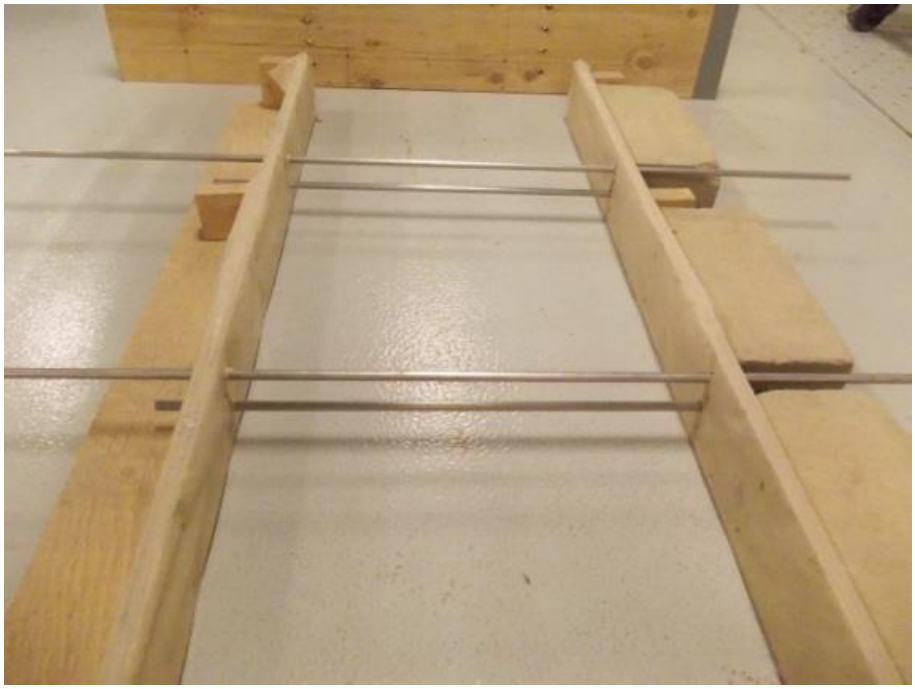

Figure D-11: Formwork comprised of L-shaped 5/16" plywood angles used to construct up to 2 lifts per footprint

The construction water content was confirmed from three to nine soil samples depending on the footprint size (see Figure D-10). The MDF board side with the smooth surface was then placed over the soil-water mixture whereas vibration was applied using a concrete vibrator needle over the opposite side of the MDF board (see Figure D-12). The vibration was applied uniformly over the surface of the board while the static load was simulated by placing concrete bricks over the longitudinal reinforcement of the board assembly. The compaction process was tested for two lifts (*i.e.* using a 10cm high partial embankment model) using 1, 2 and 5-minute durations, whereas the soil density was measured *in situ* using the sand cone method (ASTM, 2007a). The first attempt was deemed a failure since it was found that large areas in the soil lifts remained uncompacted, even though several compaction durations and water contents were tested. Two potential reasons behind this nonuniformity were as follows: insufficient static load applied onto the board and nonuniform initial soil lift height.

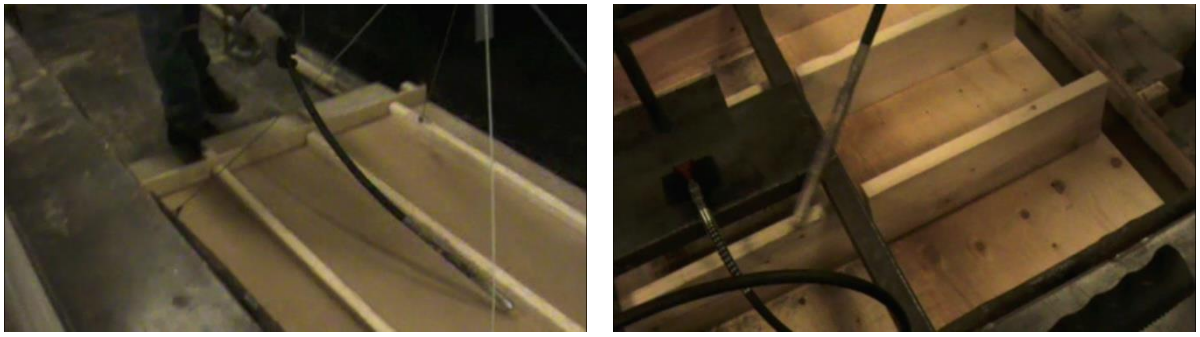

Figure D-12: Transferring vibration to soil using concrete needle vibrator by means of (left) MDF board (right) steel frame and wooden planks

The challenge of lift height uniformity mentioned above was dealt with as part of a second attempt in compaction of the embankment material. Two holes were drilled into the plywood formwork to accommodate steel rods, used to serve as guides while levelling the embankment material to ensure a consistent lift height prior to compaction as shown in Figure D-11. The location of the steel rods with respect to the formwork bottom was determined by trial and error such that the final lift height after compaction was 5 cm. The embankment models were constructed using thee footprints (*i.e.* two lifts per footprint), instead of six footprints as per the MDF boards mentioned previously (*i.e.* one lift per footprint). After levelling the soil-water mixture, the excess material was removed using ½" thick wooden planks as shown in Figure D-13. However, controlling the uniformity of the lift heights still resulted in uncompacted regions within the lifts. The inefficiency of this compaction method was attributed to the low static load applied.

Figure D-13: Levelling soil lifts prior to compaction

The third attempt investigated the use of a larger static load by means of a hydraulic jack and steel rod assembly comprised of two pieces: a hollow steel pipe and a solid threaded rod, each with a rectangular flange welded to one end as shown in Figure D-14.

Figure D-14: Hydraulic jack and two steel rods used for applying large static loads

The height of the concentric steel rod assembly was adjusted by means of a nut and washer screwed onto the threaded piece. A bracket comprised of a collar and a flat plate welded onto one end, shown in Figure D-14, was fabricated to secure the hydraulic jack over the MDF board. The force produced by the hydraulic jack was transmitted onto the MDF board reinforcements via two 4” x 2” wooden planks; whereas the rod assembly was positioned between the hydraulic jack and the I-beam on the gantry frame as shown in Figure D-15 and Figure D-16 (see Section D.4 in Appendix D for details of the gantry frame design).

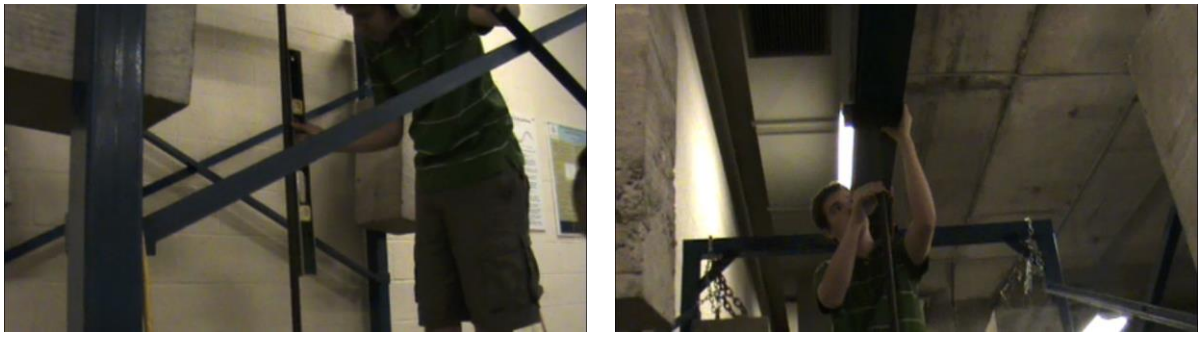

Figure D-15: Steel rod assembly (left) undergoing alignment (right) fixed to I-beam on HSS steel frame

Figure D-16: Gantry frame with 4 concrete bricks acting as additional counterweight

Based on a previous load cell calibration between the hydraulic jack force and the corresponding dial gauge pressure, the force transmitted by the hydraulic jack was adjusted to yield a 4kPa static pressure over the soil lift footprint. For the largest MDF board (*i.e.* the bottom two soil lifts), an additional counterweight comprised of four 110kg concrete blocks attached to the four corners of the gantry frame, were used to match the very high static load (see Figure D-16). The soil lifts were compacted by activating the hydraulic jack to the required static load, followed by vibrating the MDF board using the concrete vibrator needle. Once the vibration started, the soil lift was consolidated whereas the required hydraulic jack pressure

was matched (manually) until no further drop in dial pressure was observed. The criterion for no further decrease in dial pressure signified maximum compaction under the static load applied. Similar to the first technique, certain zones within the soil lifts remained uncompacted. It was later revealed that the MDF board acted as a dampener to the applied vibration. A larger concrete vibrator needle was tested, but to no avail, the attempt once more failed.

D.1.2.2 Finalised Compaction Method

The fourth attempt investigated the use of a newly designed compactor comprised of a steel vibrating plate as shown in Figure D-17. The compactor constructed in the Hydraulic Laboratory consisted of a 3/16” steel plate (28” long x 59” wide) and a 2” x 2” HSS steel frame (22” long x 47” wide) centered and welded on top. A 9,650 rpm A/C motor yielding a power output of 0.106kW, was mounted onto a steel base plate welded onto the centre of the HSS steel frame. A U-shaped 2” x 2” HSS steel frame welded on the main HSS steel frame facilitated the means for clamping the hydraulic jack bracket onto the vibrating compactor and transmitting the static load onto the soil. Similar to the previous method, the hydraulic jack was activated to the required static load followed by starting the motor which transmitted the vibration to the wet soil through the HSS steel frame and plate as shown in Figure D-18. The steel compactor plate proved to be effective since the compaction in the soil lifts, determined using the sand cone method (ASTM, 2007a) was uniform. The construction technique was therefore adopted as the *in situ* compaction method for the large flume embankment models.

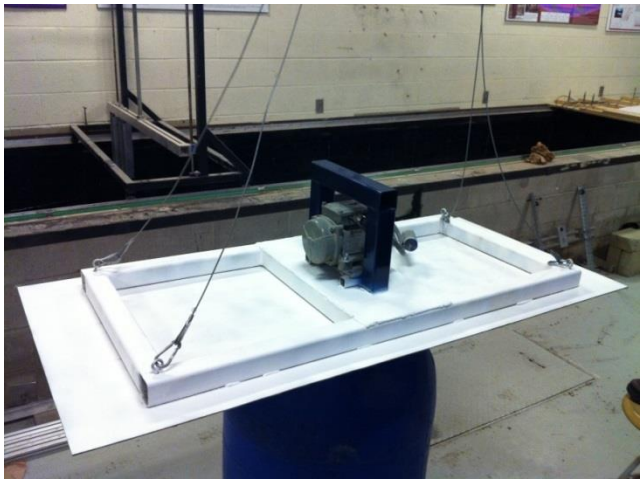

Figure D-17: Large flume compactor

Figure D-18: Hydraulic jack used to apply static load onto large flume compactor

D.1.2.3 Embankment Construction

The preparation of the embankment material and installation of the undertoe-drain was very similar to the large flume technique discussed previously in Phase I of the experimental program (see Figure D-19). Figure D-20 and Figure D-21 show the construction process of the embankment shell material, trimming of the shoulder slopes and crest, installation of V-notch on the embankment crest centreline and gridlines on the should slopes, and impoundment of the reservoir. Larger formwork was used in constructing the tilted and quasi-exact scale embankment models (see Subsections 6.2.3 and 6.2.4) with longitudinal scale ratios, $X_{rr} = 1/2$ and $1/3$, since the length of the footprint of the lifts was generally smaller (see Figure D-22 and Figure D-23).

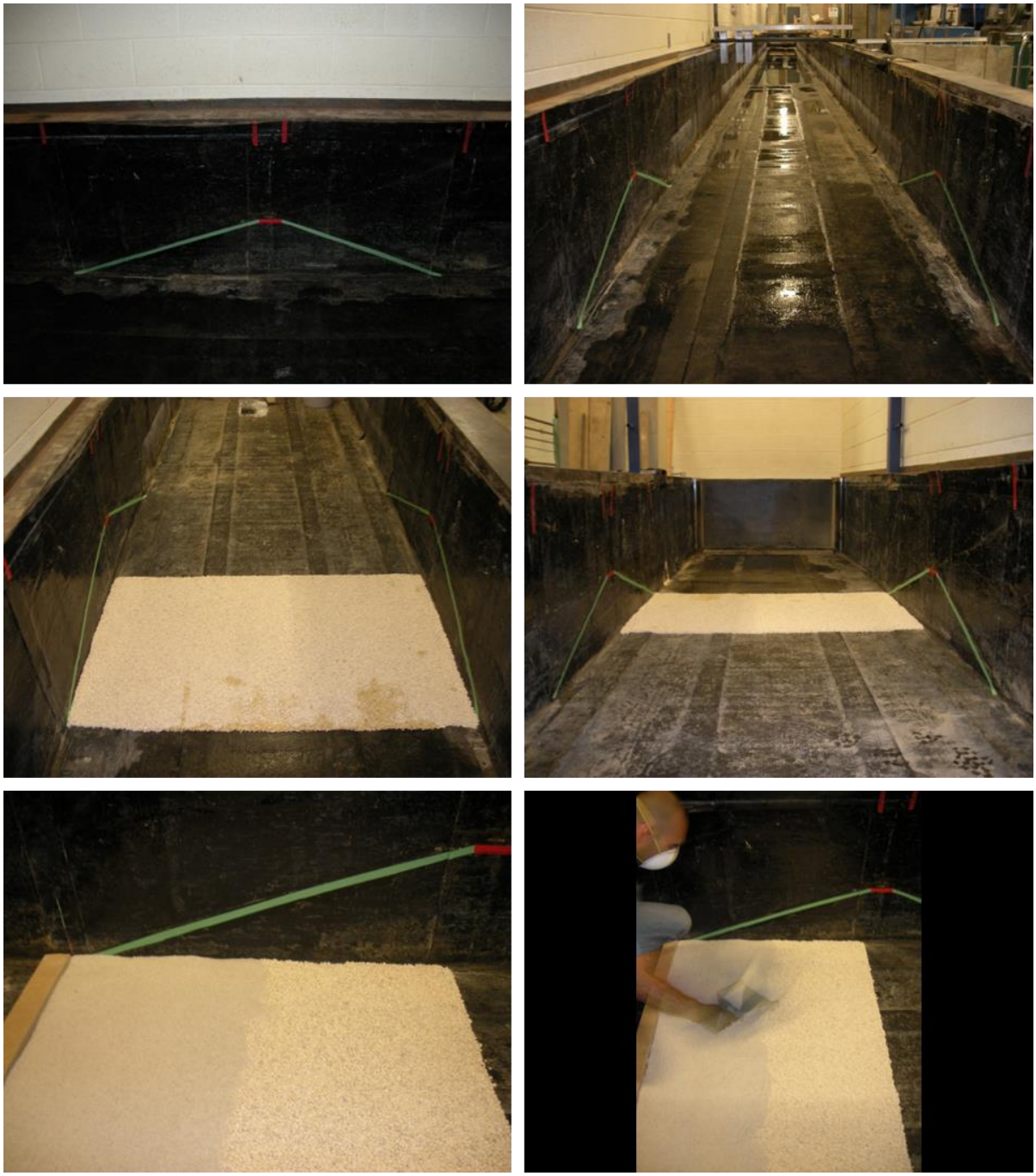

Figure D-19: Installation of undertoe-drain (top) embankment outline on side-walls of large flume (middle) installation of gravel medium (bottom) installation of filter sand medium

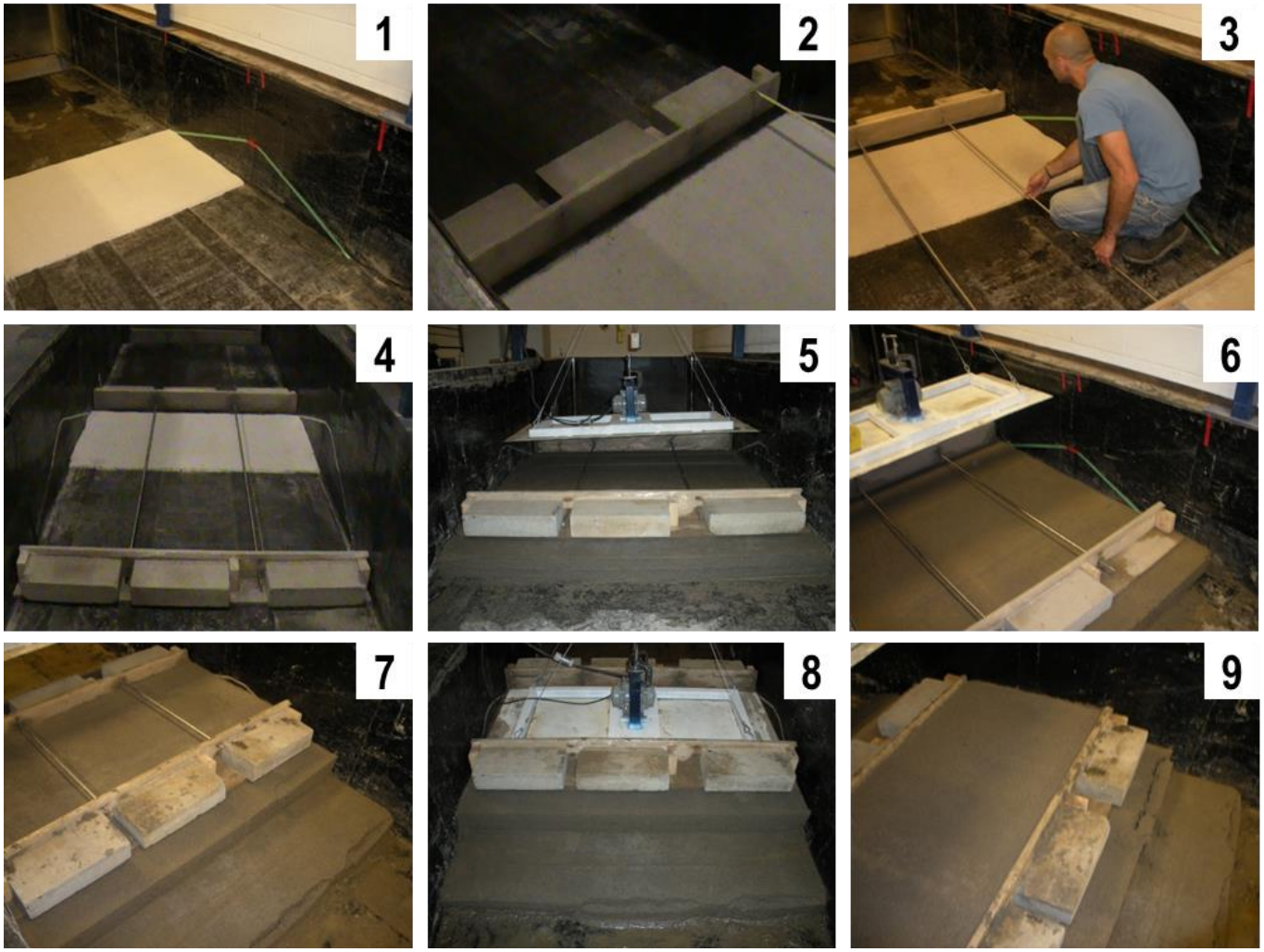

Figure D-20: Construction process showing (1) installed undertoe drain, (2-4) formwork installation and (5-9) embankment material compaction for six lifts (two lifts per footprint)

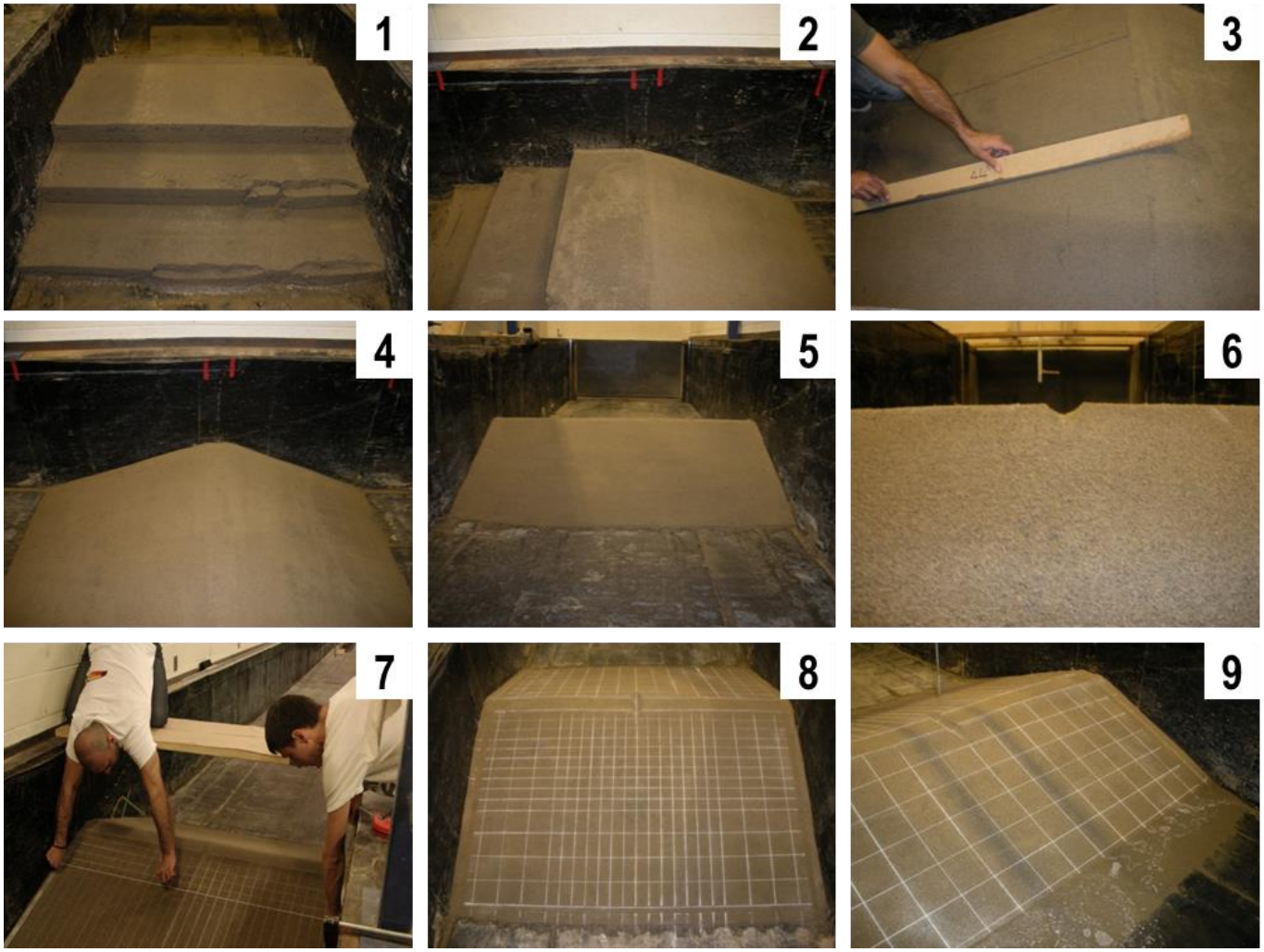

Figure D-21: Construction process showing (1) initial embankment shape (3 footprints, 6 lifts), (2-5) trimming of embankment shoulder slopes, (6) installation of V-notch on embankment crest centreline, (7-8) installation of gridlines and (9) impoundment

Figure D-22: Formwork comprised of L-shaped 5/16" plywood angles used to construct up to six lifts per footprint

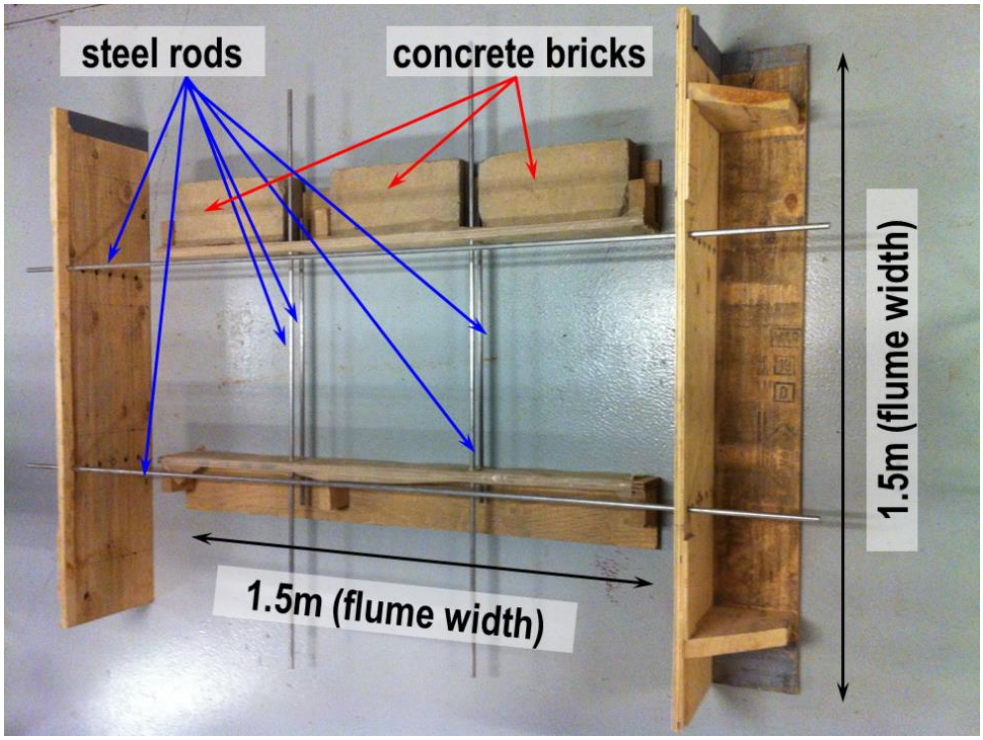

Figure D-23: Small and large formwork showing stainless steel rods and concrete bricks

D.1.3 Phase III of Experimental Program – Novel Compaction Technique (*Failed Attempt*)

The same technique applied to compact the 30cm high embankment models in the large flume tests (see Subsection D.1.2), to mimic a prototype construction using a vibratory and static load for noncohesive soils, was adapted to the small flume. The embankment material, similar in the large flume, was compacted in 5cm high soil lifts. A steel vibrating compactor, shown in Figure D-24, was specially designed for the small flume. The compactor constructed in the Hydraulic Laboratory consisted of a 3/16” steel plate (27” long x 15” wide) and a 1” x 1” HSS steel frame (25” long x 13” wide) centered and welded on top. The same A/C motor used in the large flume tests was mounted onto a steel base plate welded onto the centre of the HSS steel frame. Two U-shaped 1” x 1” HSS steel frame welded on the main HSS steel frame facilitated the means for clamping the hydraulic jack bracket onto the vibrating compactor and transmitting the static load onto the soil. Similar to the large flume compaction method, the hydraulic jack was activated to the required static load followed by starting the motor, which transmitted the vibration to the wet soil through the HSS steel frame and plate as shown in Figure D-18.

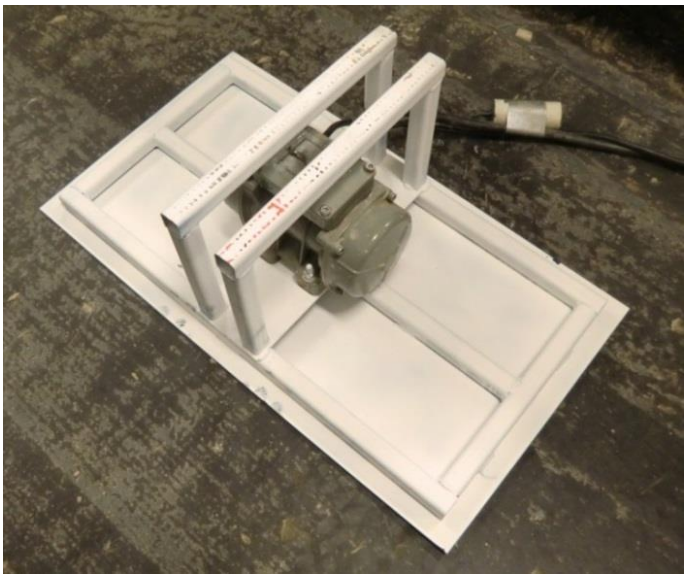

Figure D-24: Small flume vibratory compactor

A similar steel rod assembly with a shorter adjustable height and a 1” x 1” HSS steel support frame (27” long x 24” wide x 6” high), clamped to the small flume, were used to transfer the static load onto the soil lift footprint (see Figure D-25). The same hydraulic jack used for the large flume *in situ* compaction tests was used for the small flume.

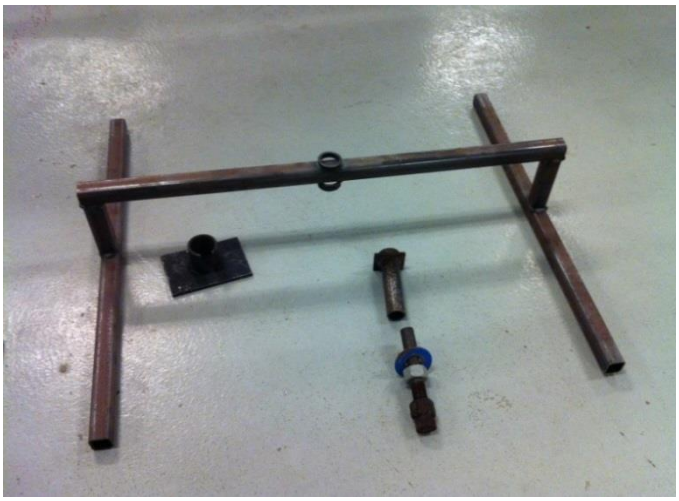

Figure D-25: Steel rod assembly with shorter adjustable heights and HSS steel support frame used in small flume compaction tests

The compaction technique was tested for two lifts (*i.e.* using a 10cm high partial embankment model) whereas the soil density was measured *in situ* using the sand cone method (ASTM, 2007a). Formwork, comprised of 5/16” thick plywood planks and assembled into L-shapes, was installed on the upstream and downstream ends of the embankment lift footprint as shown in Figure D-26, and was weighed down using concrete bricks. The formwork was drilled with two sets of holes to accommodate the steel rods used for levelling the embankment material following the procedure in the large flume (see Figure D-13). The compaction process was discarded after failing to replicate the compaction curves obtained for the large flume tests (see Section C.3 in Appendix C for the results of the *in situ* compaction tests).

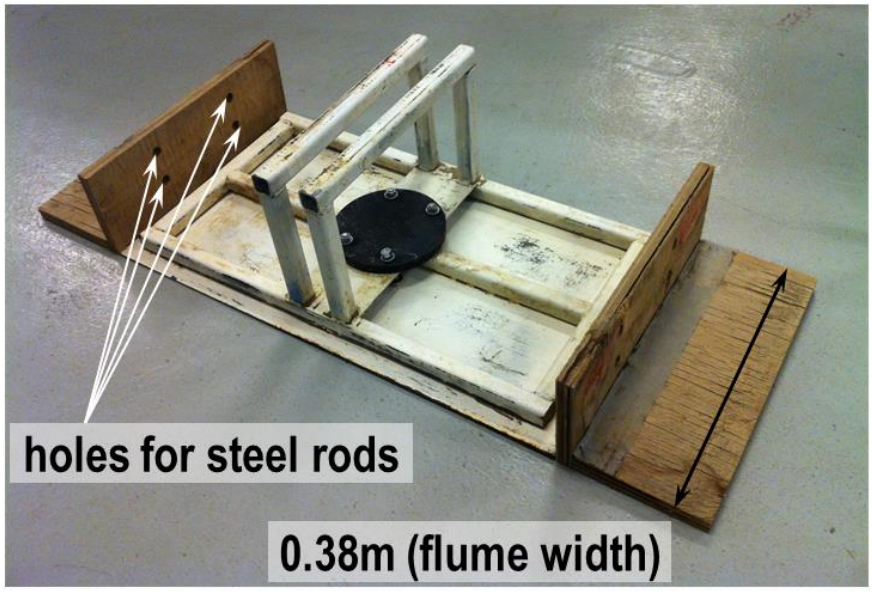

Figure D-26: Formwork and compactor for small flume in situ compaction tests showing shock absorber used in damping vibration

D.2 Instrument Calibration

D.2.1 WG-50 Capacitance Wave Gauges

Calibration of the wave gauges was carried out in a container (see Figure D-27) using three water surface elevations (0, 20cm and 45cm). The input signal to the wave gauges was a 12VDC analog power source whereas the output signals were recorded using a data logger (NI USB-6009). For the three water surface levels, the output voltage was time-averaged (over 60 second calibration runs) and plotted as shown in Figure D-28. The resulting intercept along with the wave gauge's voltage-water surface level sensitivity, defined by the slope of the plot, was input into the data acquisition system in the form of a linear equation. Once the wave gauges were installed into the flume (in their appropriate location), the intercept of the plot was then adjusted such that the output from the wave gauges corresponded with the impoundment WSL (usually η = 25cm or 28cm). The WSL was recorded by means of a point gauge, within an accuracy of ±0.05mm.

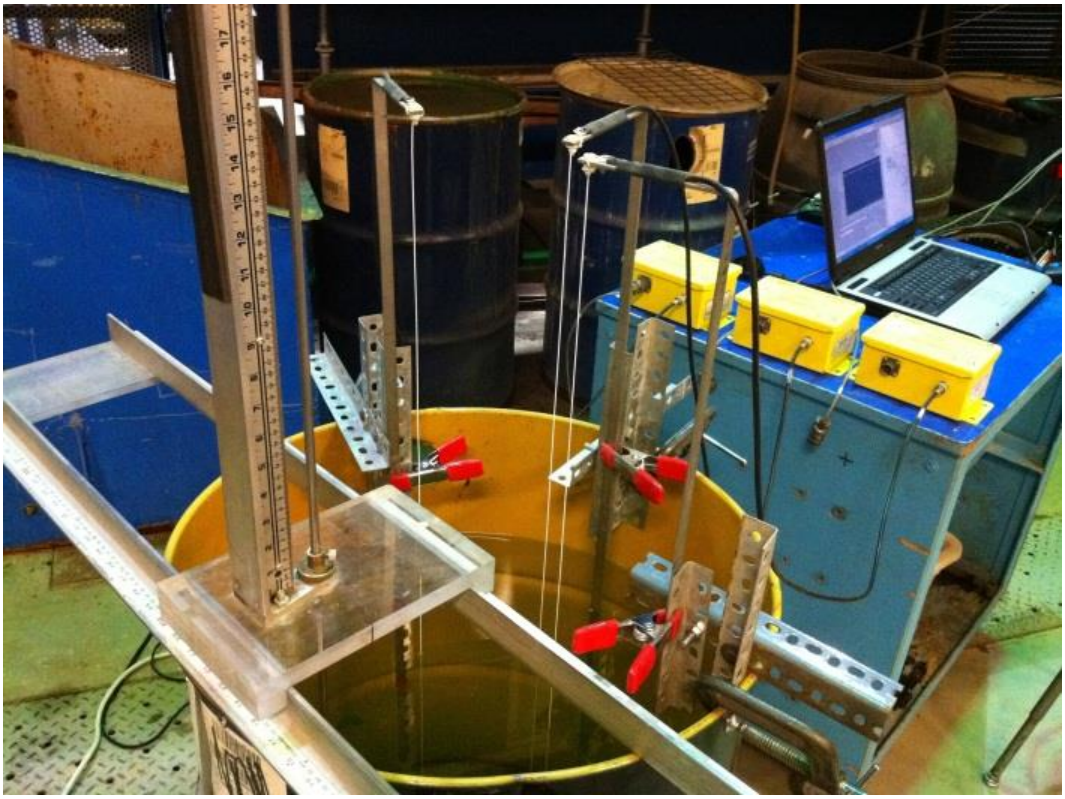

Figure D-27: Calibration of three wave gauges in container showing point gauge

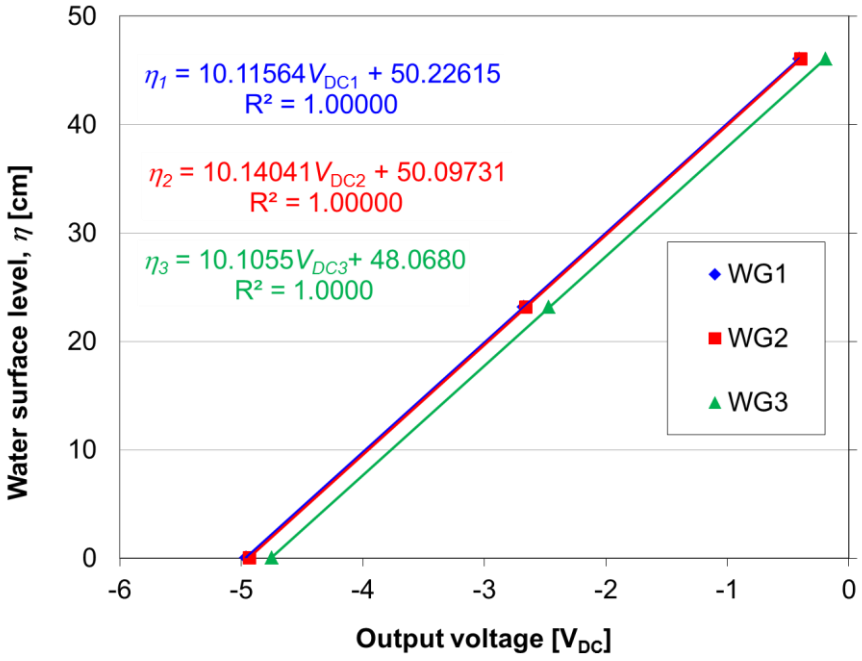

Figure D-28: Calibration curve for three wave gauges

D.2.2 Tensiometer-Transducer-Probe Assemblies (TTPAs)

The calibration and response time for the TTPAs was determined using a procedure similar to the work by Ho (2000) (see Section D.6 for the installation instructions of the TTPAs). The storage and calibration container was connected to a rail-mounted mobile reservoir and manometer using PVC tubes to vary and record the head above the TTPAs (see Figure D-29). The input signal to the TTPAs was supplied using a 5VDC analog power source while the output signals were recorded by means of a data logger (NI USB-6210). Calibration of the PPTAs was conducted in the storage container under various heads to simulate the typical PWP range in the soil during overtopping, and under rising and falling head conditions to simulate wetting and drying of the soil, respectively (see Figure D-29). The calibration results revealed a nearly identical calibration curve to that of the manufacturer with no difference between rising and falling head conditions (see Figure D-30).

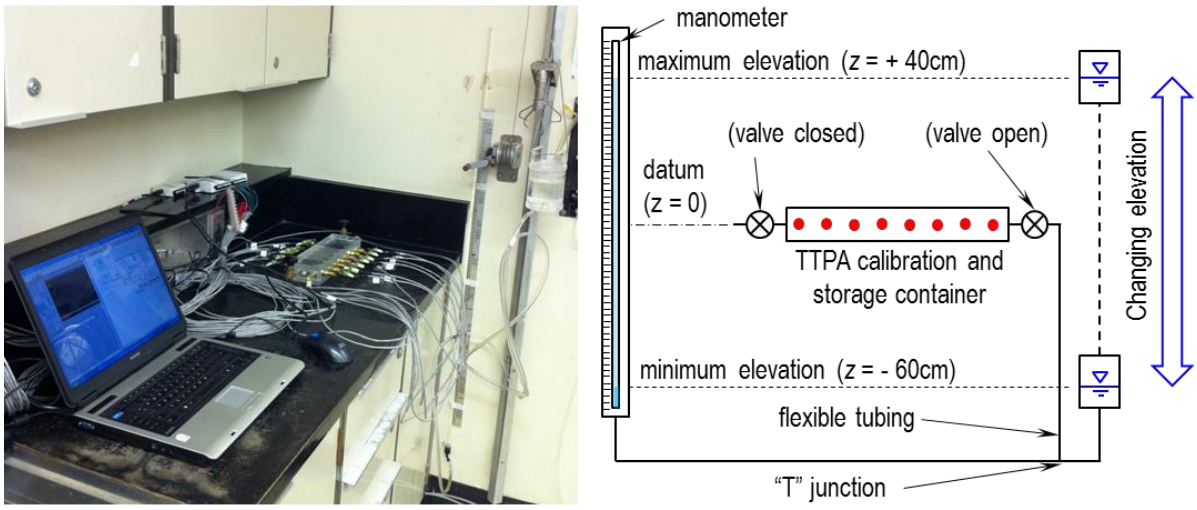

Figure D-29: TTPA calibration setup in Geotechnical Engineering Laboratory

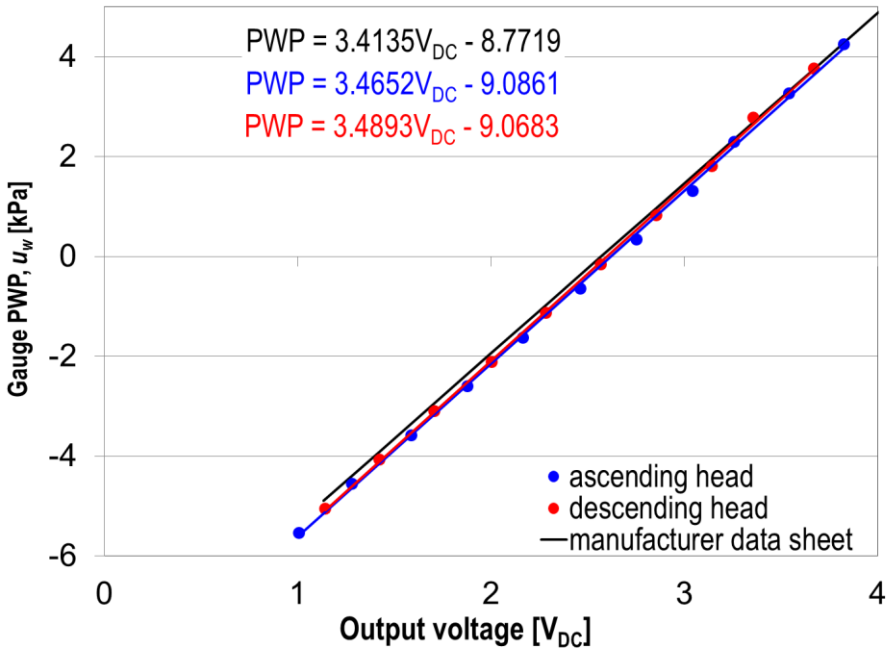

Figure D-30: Example of calibration curve for TTPA No. 9 (used in overtopping Test No. 6)

The response time for the S-TTPAs and M-TTPAs was investigated by varying the head above the storage and calibration container at a rate (approximately 1 cm/s), which was much higher than the saturated hydraulic conductivity of the soil (k_{sat} = 1.53 x 10^{-2} cm/s, ASTM D2434–68), followed by instantaneously fixing the head at 20cm (*i.e.* 2 kPa) increments. This process was conducted for rising as well as falling head conditions to investigate the response time due to drying and wetting, respectively. Test results indicated that the response time was nearly instantaneous during head variation. However, fixing the head resulted in a water hammer effect which caused the PWP to deviate by 0.016 kPa and 0.02 kPa within 1.4s and 1.0s, respectively, under failing and rising head conditions, respectively. Figure D-31 shows the response for both M-TTPA and S-TTPA under both falling and rising head conditions. The response of the M-TTPA and S-TTPA was very similar, except that the larger porous ceramic cup in the S-TTPA was slightly more effective at damping the oscillations. The tests were conducted also within the negative PWP range for both TTPAs under falling and rising head conditions, whereas a similar behaviour was noted. Calibration of the TTPAs was performed prior to each experiment,

whereas the response time was conducted for three experiments only (Tests No. 4, 6 and 7).

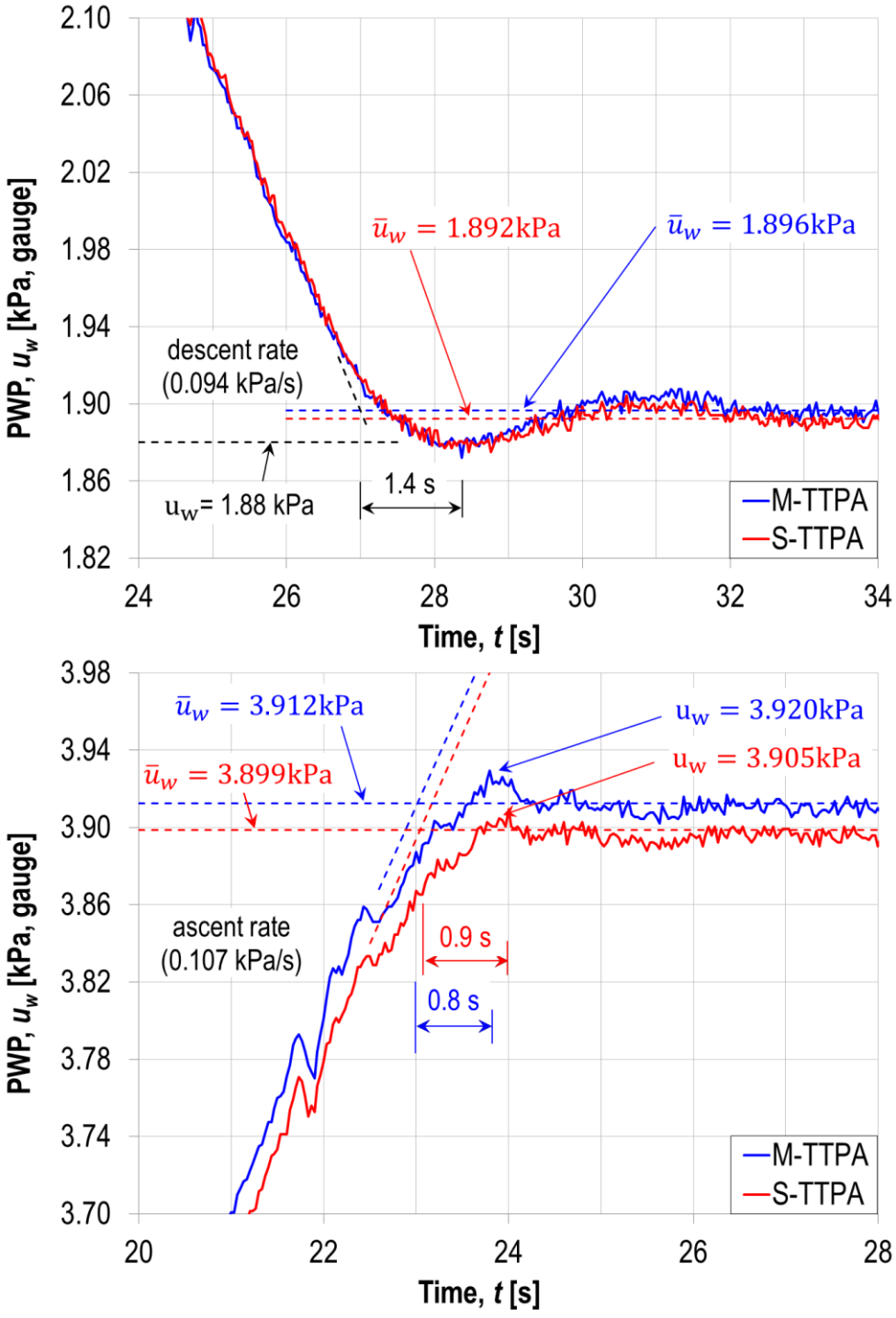

Figure D-31: TTPA response under (top) falling head conditions (bottom) rising head conditions ($\bar{u}_w$: average PWP)

D.3 Lighting, Video and Photography Installations

D.3.1 Phase I of Experimental Program - Small Flume Tests

Floodlight halogen lamps mounted on the camera fixtures were used to provide the appropriate illumination for the tests. A photo showing the experimental setup can also be seen in Figure D-32 below, however, not shown is the camera and lighting fixture which was mounted directly above the embankment model's crest (see Figure 5.12). The fourth video camera and lighting setup used to capture the side-view footage of tailwater depths as well as planar overtopping flow is shown in Figure D-33.

Figure D-32: Experimental setup in small flume showing video cameras and light fixtures installed upstream and downstream of the embankment model

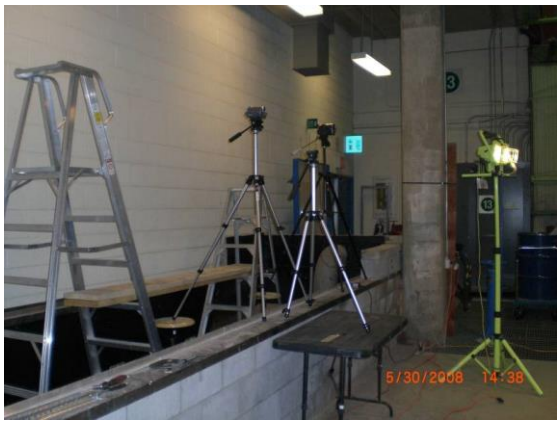

Figure D-33: Video camera and lighting setup used to capture side-view footage

D.3.2 Phase I and Phase II of Experimental Program - Large Flume Tests

Similar to the small flume tests, the video footage was captured using three high definition video cameras mounted on fixtures as shown in Figure D-34. Unlike the small flume tests, the floodlight halogen lamps were mounted on the upstream and downstream fixtures only. Not shown in Figure D-34, is the top view video camera, mounted on a tall stand installed on the side of the large flume. While the lighting was useful in defining the contours of the embankment models during overtopping, they produced a glare on the water surface and which impeded the visibility of the breach entrance forming on the upstream slope. The lighting installations therefore not used in the 3-D breach overtopping tests in Phase II of the experimental program.

Figure D-34: lighting and video camera fixtures used in large flume (left) downstream (right) above embankment crest and downstream

D.3.3 Phase III of Experimental Program - Planar Overtopping Tests

The lighting for the experiment was a key parameter for optimizing the photogrammetric operation since it is crucial to produce images showing distinct water surface and bed profiles. Initially, the same light fixture used in the small flume during Phase I was used (see Figure D-34). However, since both video and digital

cameras were used to capture side-view images, a direct light source from the top resulted in glare, especially with respect to the water surface profile. Therefore, a light filter was fabricated using parchment paper and Balsa wood sticks and placed below the light source in order to diffuse the light on the model as shown in Figure D-35 and Figure D-36.

Figure D-35: Light filter constructed using parchment paper and Balsa wood sticks

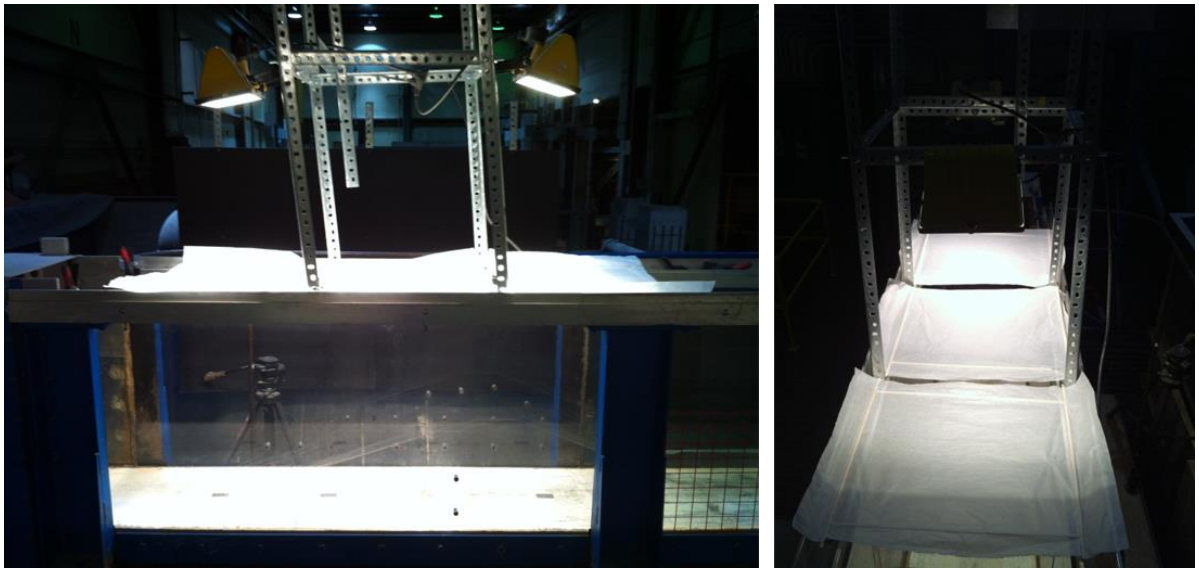

Figure D-36: Light filters shown placed below light source (left) side-view (right) upstream view

However, during Test No. 3, some light reflection on the downstream slope was observed through the camera lens, as shown in Figure D-37. Two other light installations were constructed and tested. The first light installation was comprised of a solid housing constructed from board (multi-ply sheets) formed into a “C” shape (one upper side and one frontal and posterior rim) as shown in Figure D-38. Two 12VDC LED light strips were bonded inside the housing and covered with parchment paper to diffuse the light.

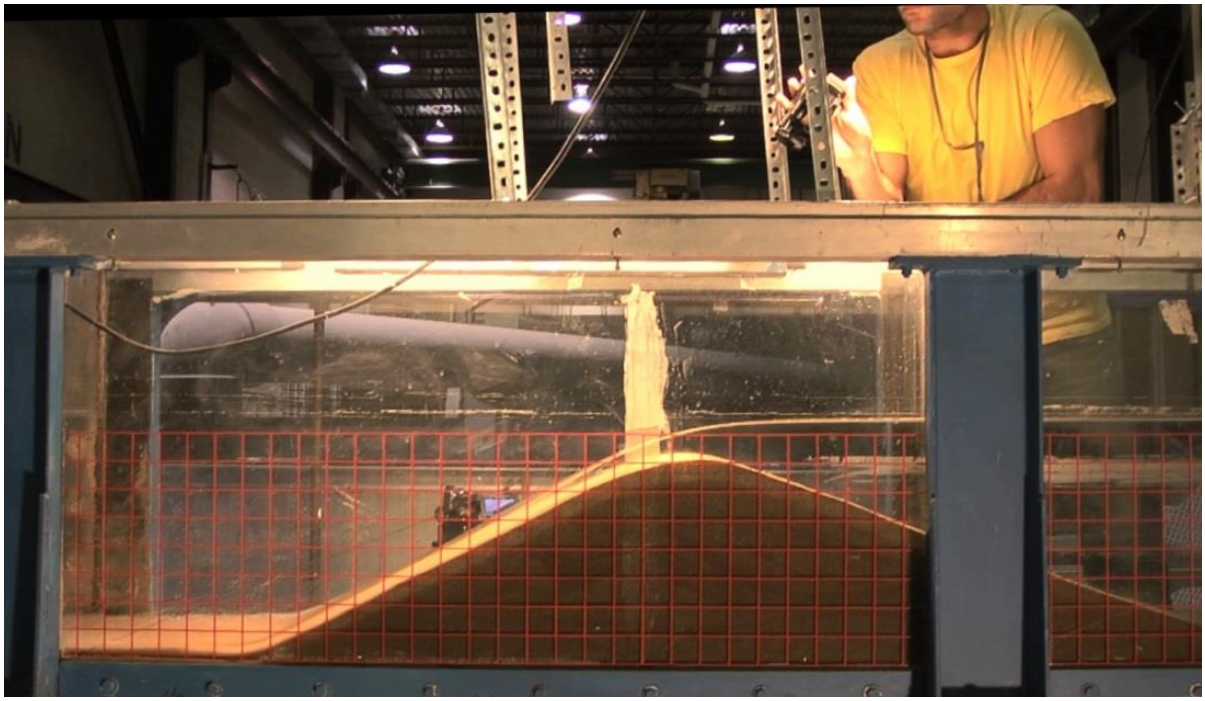

Figure D-37: Test No. 3 using light filter installation showing a large degree of light reflected from downstream slope

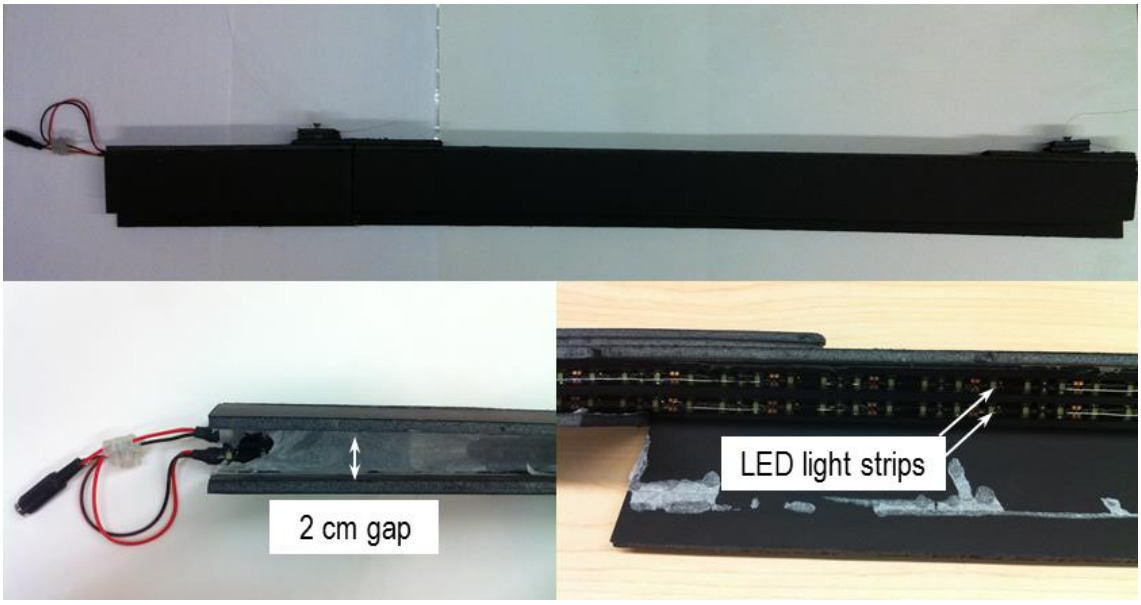

Figure D-38: LED fixture used for planar overtopping tests Phase III (top) 1m long x 8cm wide fixture assembly (bottom left) view into “C” section showing 2 cm gap (bottom right) parchment paper removed showing 2 LED light strips

The LED fixture was placed against the inside of the flume side-walls and the gap in the housing adjusted such that the light was focused in such a way that it illuminates a thin area of the water surface adjacent to the side-walls. The second light installation was comprised of black light bulbs mounted onto a fixture and clamped onto the inside of the flume side-walls to illuminate the overtopping flow (see Figure D-39).

Figure D-39: Black light fixtures

The two light fixtures were tested under subcritical flow conditions with and without soil as bed material. Fluorescent dye was added to the water and the ambient light was turned off to enhance visualization of the flow. Figure D-40 below shows a test of the LED fixture under subcritical flow conditions without a dye and no bed material. Figure D-41 below shows a test conducted on both light installations using soil as the bed material. The two light fixtures were also tested in overtopping Test No. 4 in which the embankment model was breached prematurely after a piping failure initiated beneath the gate. Although the overtopping test was a failure itself, the performance of the light fixtures was investigated during planar overtopping in later stages of the breach as shown in Figure D-42. It was determined that the LED fixture was most suitable for the planar overtopping tests since it defined the water surface profile clearly. The black light fixtures illuminated the overtopping flow very well until after the erosion progressed downwards which then resulted in a somehow poorer illumination. Furthermore, in downstream regions with higher erosive capacities, light from the low-powered black light bulbs did not penetrate the sediment laden flow adequately and therefore did not depict a clear and well-defined soil boundary. The LED fixtures shown in Figure D-41 and Figure D-42 were then modified with a longer frontal rim, in order to minimize the glare on the video and digital camera lens and to focus the light onto a smaller area adjacent to the flume side-walls (see Figure D-43).

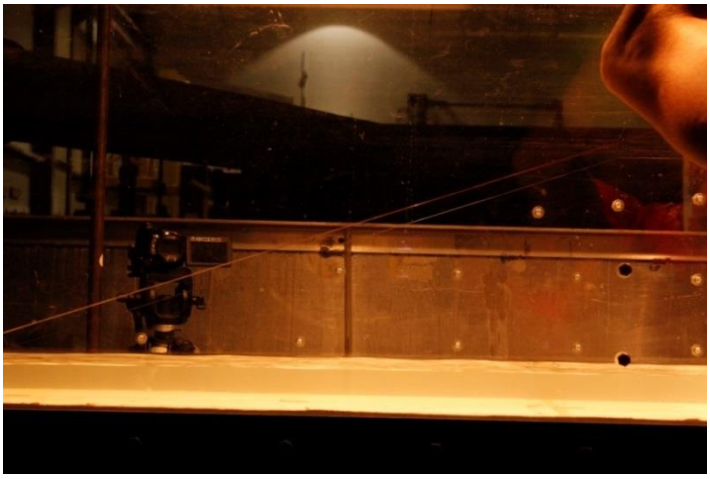

Figure D-40: Testing LED fixture under subcritical flow conditions

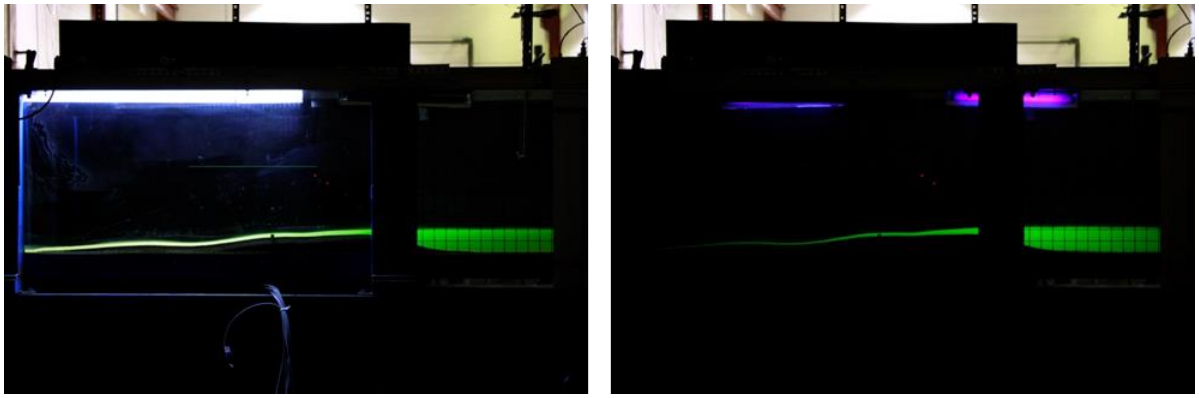

Figure D-41: Testing light installations under subcritical conditions using sand Type III as bed material (left) LED fixture (right) black light fixtures

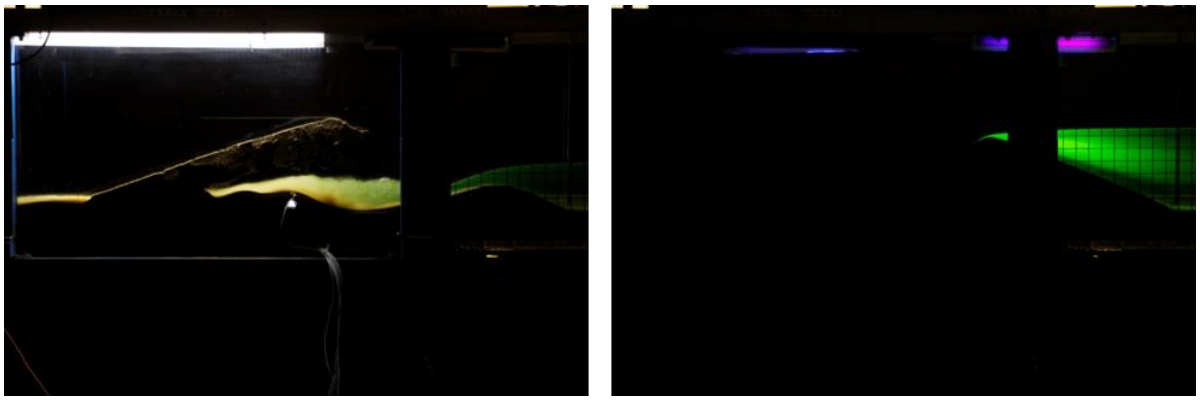

Figure D-42: Testing light installations in Test No. 4 (left) LED fixture (right) black light fixtures

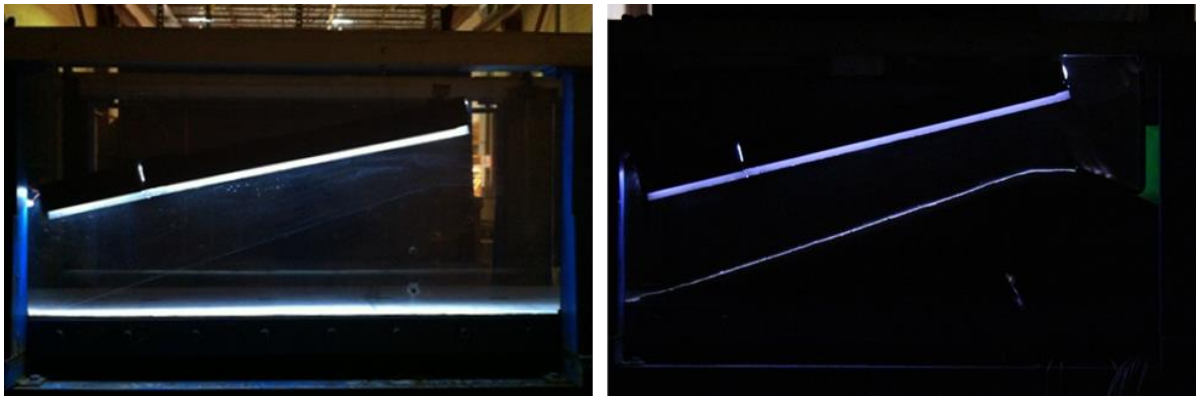

Figure D-43: LED light fixture (left) without embankment model (right) with embankment model

A black backdrop was installed on the right side of the embankment model to isolate the object and reduce noise from shadows and imperfections as well as highlight the details of the illuminated flow (see Figure D-44). Two digital cameras (Canon EOS Rebel 2Ti, 18 Megapixels) mounted on tripods, were used to capture digital photographs of the overtopping flow from the left-side at different film sensitivities and shutter speeds (ISO-6400, 1/80s and ISO-3200, 1/40s). Although the two digital cameras captured the same images, the two settings provided two different outcomes due to the movements in the water surface level. Images from the ISO-6400 sensitivity and 1/80s shutter speed digital camera were selected in the photogrammetric analysis on the basis of image sharpness. The focus of the two digital cameras' focus was manually adjusted whereas the exposure program was set to "TV" (shutter-priority autoexposure). This setting resulted in a focal length and exposure (f-stop) of 55mm and f/5.6, respectively. The two digital cameras were connected to a time-lapse device set to capture pictures at 1 frame/second except for the "no drain" tests (*i.e.* Tests No. 7, 9 and 10) where the erosion was more rapid and therefore the frame rate was set to 2 frames/second. The white balance for both digital cameras was manually adjusted according to a "fluorescent" colour temperature.

Figure D-44: Black backdrop installation on right-side of flume

Two high definition video cameras mounted on tripods were used to capture side-view video footage (left and right) of the embankment model to confirm the homogeneity of the overtopping and erosion process with respect to both sides of the flume (see Figure D-40 and Figure D-45). Since the two digital cameras captured images from the left side of the embankment model, illumination was provided using the LED fixture. Meanwhile, the illumination for the right-side video camera was provided by means of the black light fixture. A third high definition video camera was used to capture roaming footage of the experiment. After the experiment was complete, a 4cm x 4cm grid was installed on the flume side-walls and images from both video and digital cameras were captured in order to constitute a frame of reference to account for the cameras' skewed perspective (see Figure D-46 and Figure D-47). Unfortunately, the Mirror Lock-up (MLU) feature was not setup for the digital cameras which gave rise to some slight movement in the cameras due to the shutter's motion. As a result, there was some slight misalignment in the images captured. An image registration code was used to rectify this misalignment.

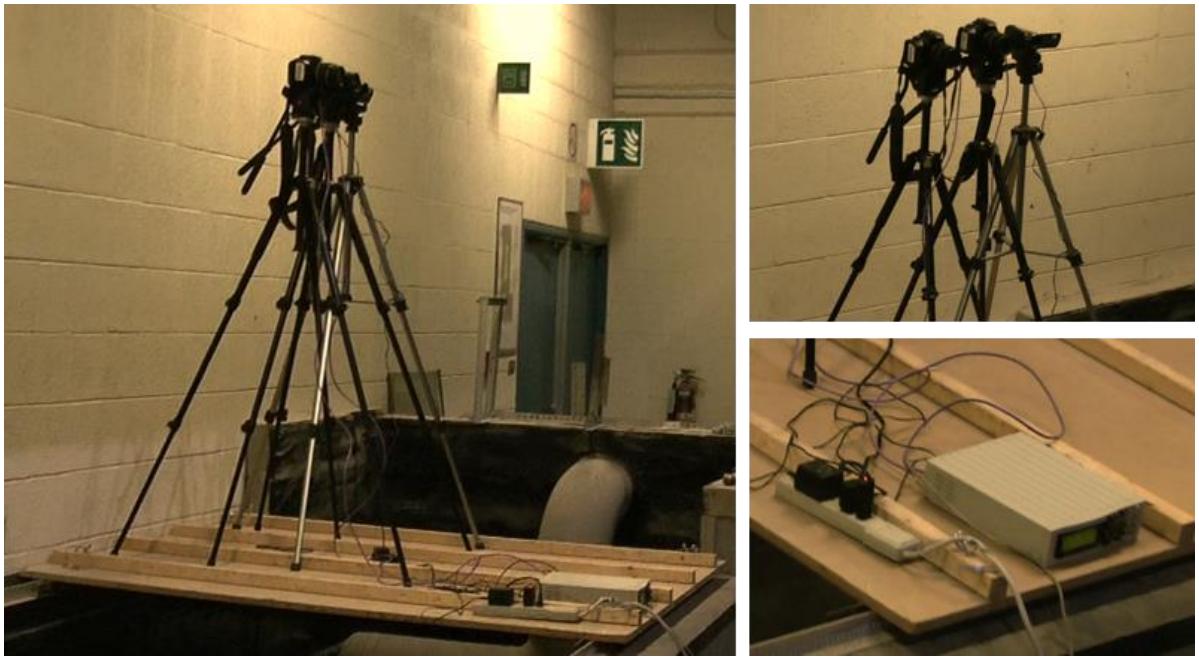

Figure D-45: Photography setup on left-side of embankment model showing two digital cameras, high definition video camera and time-lapse device

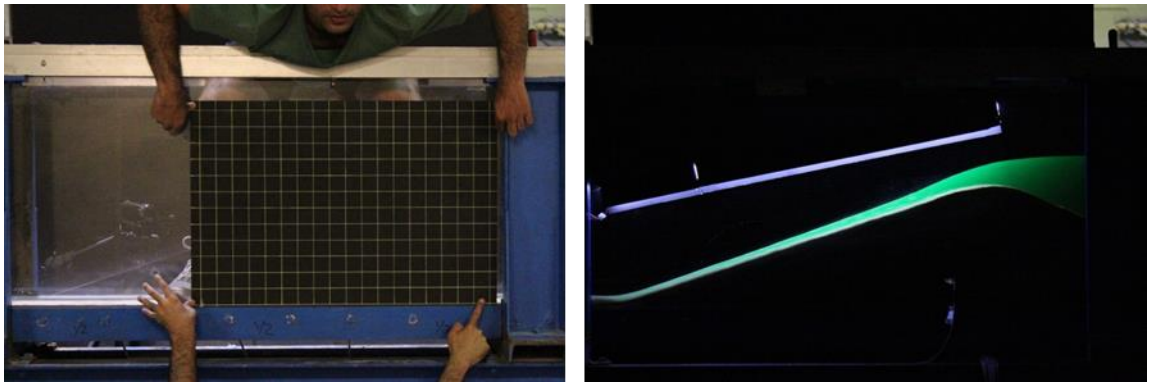

Figure D-46: Images captured from left-side digital camera for Test No. 13 showing (left) reference grid (right) overtopping flow

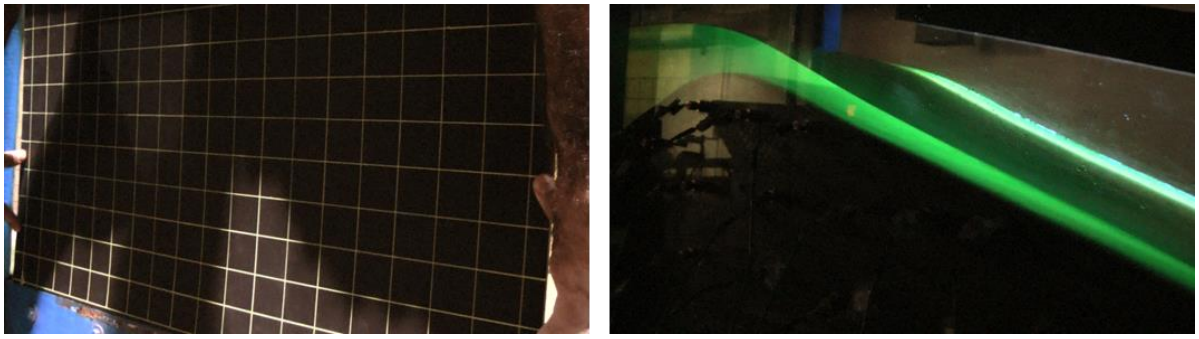

Figure D-47: Images captured from right-side video camera from Test No. 13 showing (left) reference grid (right) overtopping flow

D.4 Gantry Frame Design

A gantry frame comprised of four supports (3” x 3” hollow structural section (HSS) steel), an overhead I-beam and two cross braces, designed and constructed in the Hydraulics Laboratory, was installed above the large flume walls as shown in Figure D-48 and Figure D-49. The gantry frame weighed approximately 350kg, and functioned as a point of application and counterweight for the applied static load during the compaction process as well as hoisting the sediment trap in and out of the Hydraulics Laboratory reservoir (see Section D.5).

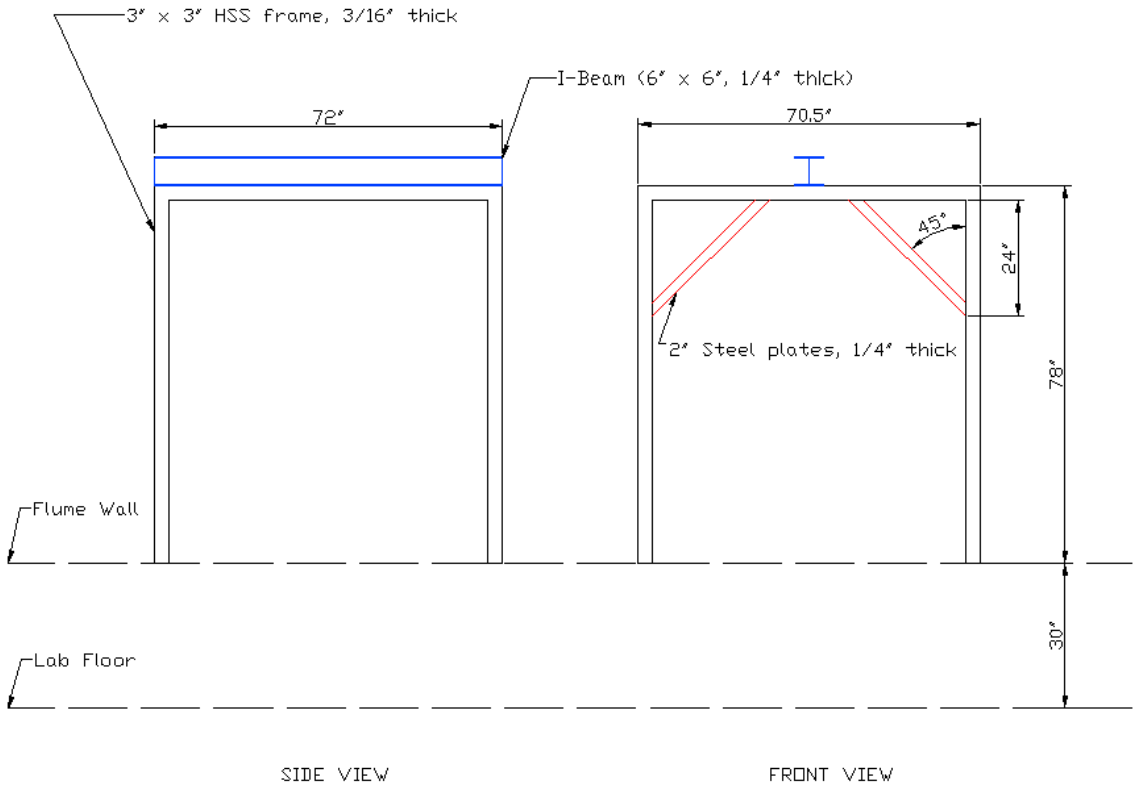

Figure D-48: HSS steel gantry frame dimensions

Figure D-49: Gantry frame (in preparation)

D.5 Sediment Trap Design

The sediment trap (1.32m wide x 0.76m long x 1.43m high) was constructed using a 2” x 2” HSS steel frame in the Hydraulics Laboratory. A 2” x 2” mesh, comprised of steel wire (gauge 11) was welded onto the frame of the sediment trap on the five faces of the cage as shown in Figure D-50 and Figure D-51. The sediment cage was lined with a non-woven high flow geotextile (200R, Terrafix ®) with an apparent opening size = 0.212mm (d_{50} for sand Type III was 0.245mm) as shown in Figure D-51.

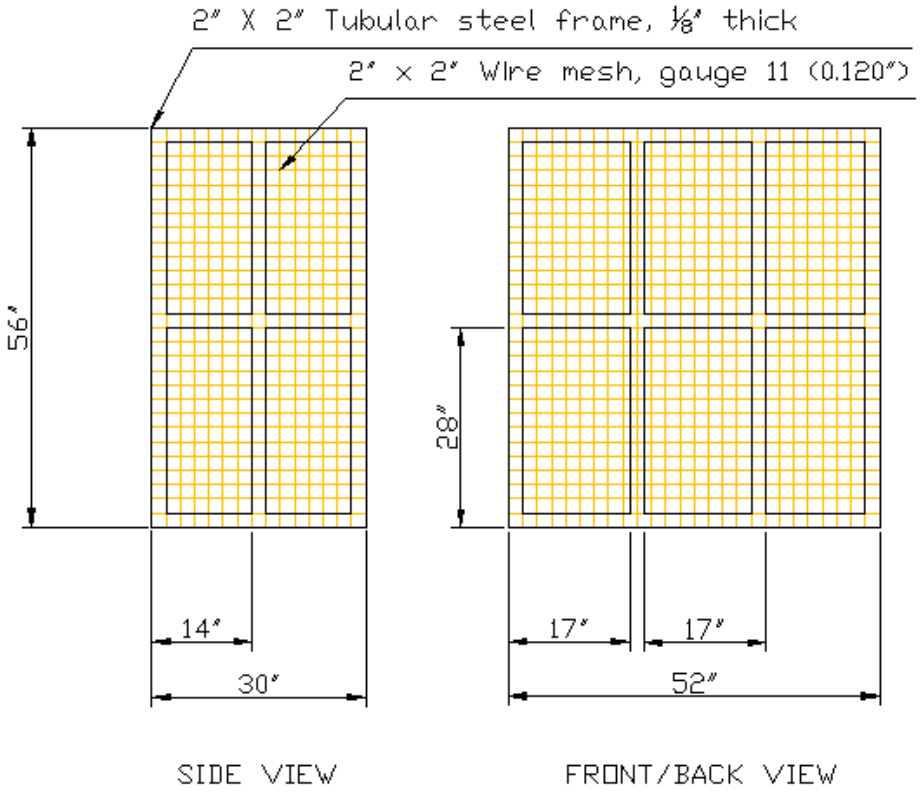

Figure D-50: Sediment trap dimensions

Figure D-51: Sediment trap (left) cage in preparation (right) with geotextile installed

D.6 Installation of Tensiometer-Transducer Probe Assemblies (M-TTPA and S-TTPA)

The TTPAs were comprised of a temperature compensated and calibrated pressure transducer (MPXV7007GP and MPXV7007DP, see Figure D-52) capable of measuring both positive and negative pressures (±7 kPa) and a porous ceramic cup fixed onto a nylon capillary tube and brass connector housing (B-200-1-OR) as shown in Figure D-53. The MPXV7007GP and MPXV7007DP pressure transducers read gauge and differential pressure, respectively; however both pressure-transducer models used were identical in specifications with the exception of the location of the second port. For the MPXV7007DP model, the second port was left unconnected and therefore was also used to record gauge pressure.

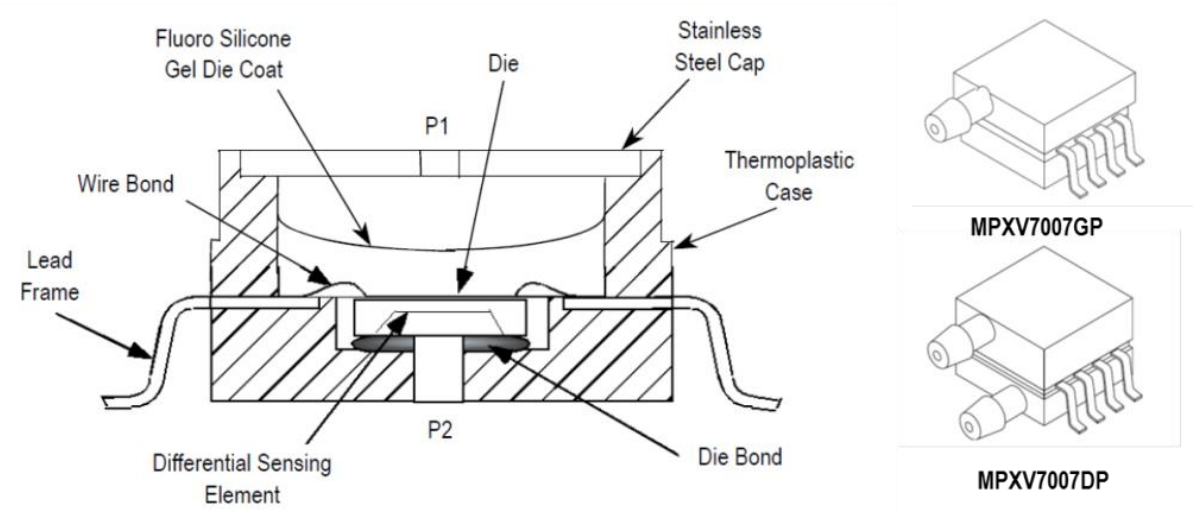

Figure D-52: MPXV7007 pressure sensor (left) cross-section (right) MPXV7007GP and MPXV7007DP models (Freescale, 2011)

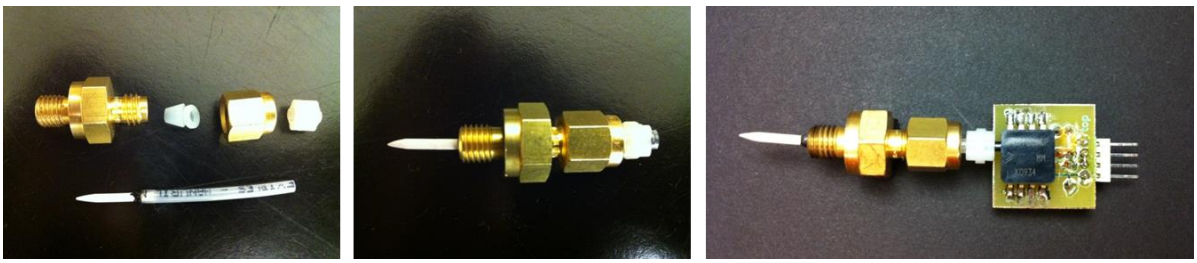

Figure D-53: Pictures showing (left) tensiometer components: brass connector, plastic front and back ferrules, micro porous ceramic cup, 1/8" nylon capillary tube and plastic collar (middle) tensiometer-probe assembly (right) micro tensiometer-transducer probe assembly

The pressure transducer was designed for operation in dry mediums (*e.g.* air), however, a similar device have been tested using an aquatic medium in other experimental investigations (Bathurst *et al.* 2007). The response time for the pressure transducer is 1ms and has a sensitivity of 286mV/kPa for a medium consisting of air. Therefore, specific tests were designed to validate their functionality and accuracy using water as an operating medium (see Subsection D.2.2 for the results of calibration and response time tests conducted in the Geotechnical Laboratory). The global and incremental accuracy of the pressure transducers reported by the manufacturer was ±0.7 kPa (7 cm-H_20) and ±0.07 kPa

(7 mm-H_20), respectively. The accuracy and sensitivity of the measurement was 0.005kPa (0.5 mm-H_20) and 0.00016 kPa (0.0016 mm-H_20), respectively.

The pressure transducers were soldered onto printed circuit boards in accordance with the recommended power supply decoupling and output filtering (Freescale, 2011) as shown in Figure D-54. Both the pressure transducer and the tensiometer-probe assembly were saturated with deionized and de-aired water (see Figure D-55) whereas the entire assembly was then connected under submerged conditions to prevent air from entering into the water medium. For the MPXV7007GP pressure transducer, it was concealed prior to its saturation to prevent water from entering the second port. For the MPXV7007DP model, this was circumvented by capping the second port using a long flexible tube. Immediately after their assembly, the TTPAs were placed in a container, specially designed for storage and calibration, and filled with deionized and deaired water (see Figure D-56).

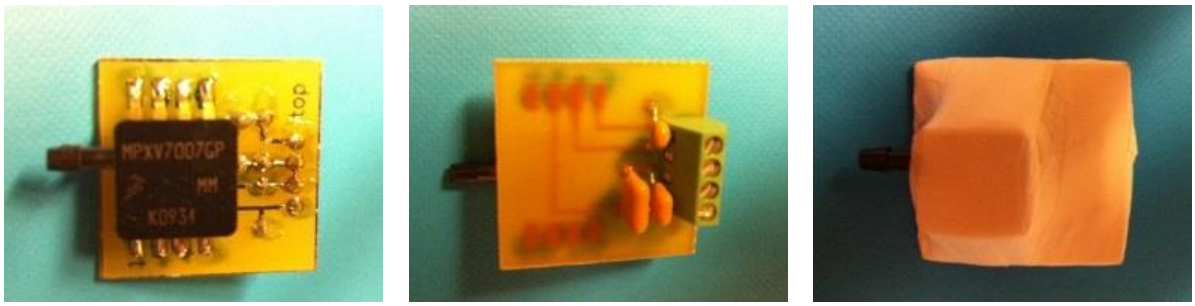

Figure D-54: MPXV7007GP pressure transducer connected to printed circuit board and protected prior to saturation

Figure D-55: Saturation process for (left) tensiometer-probe assembly (right) pressure transducer assembly using MPXV7007DP model

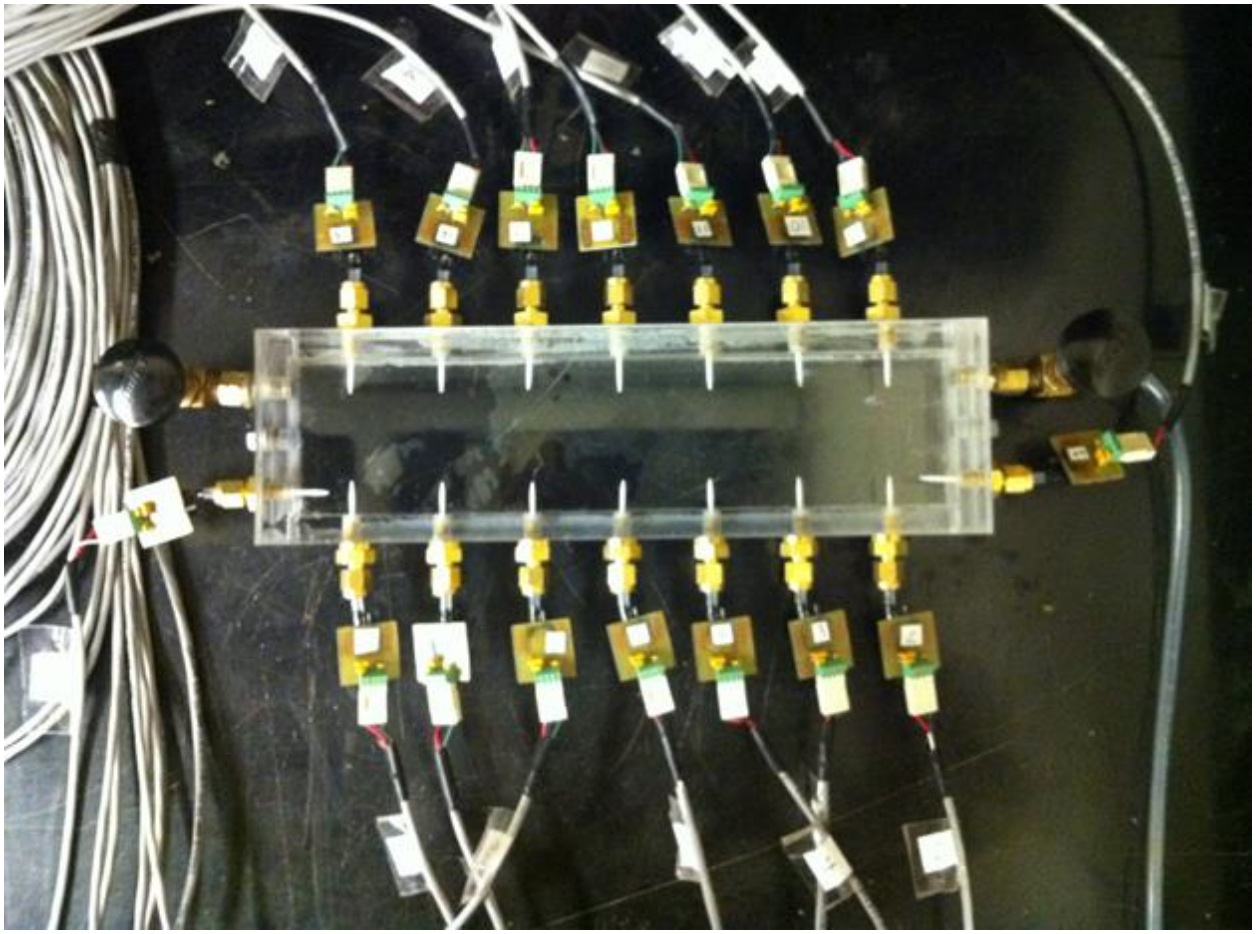

Figure D-56: Container used for storage and calibration of M-TTPAs

D.7 Release Gate Design for Planar Overtopping Tests

Overtopping was simulated by lifting a vertical release gate spanning the width of the flume (38.1cm) after the water surface level of the impoundment reached the target value and steady-state seepage was attained (see Figure D-57 and Figure D-58). The first design ("A") was comprised of a 1/8" thick Plexiglas plate with neoprene sponge rubber adhered onto both sides (see Figure D-59). The width of the gate was adjusted such that the gate could be gently forced in between the flume side-walls and rested on the upstream apex of the embankment model's crest. There were difficulties in maintaining a water tight seal between the gate and the side-walls (*e.g.* Test No. 1) as well as between the gate and the embankment crest, particularly for larger overtopping heads (*e.g.* Test No. 4) and high degrees of saturation (*e.g.* Test No. 9). In Test No. 2, a faint stream of water was observed from the embankment model's crest due to high exit gradients downstream the gate.

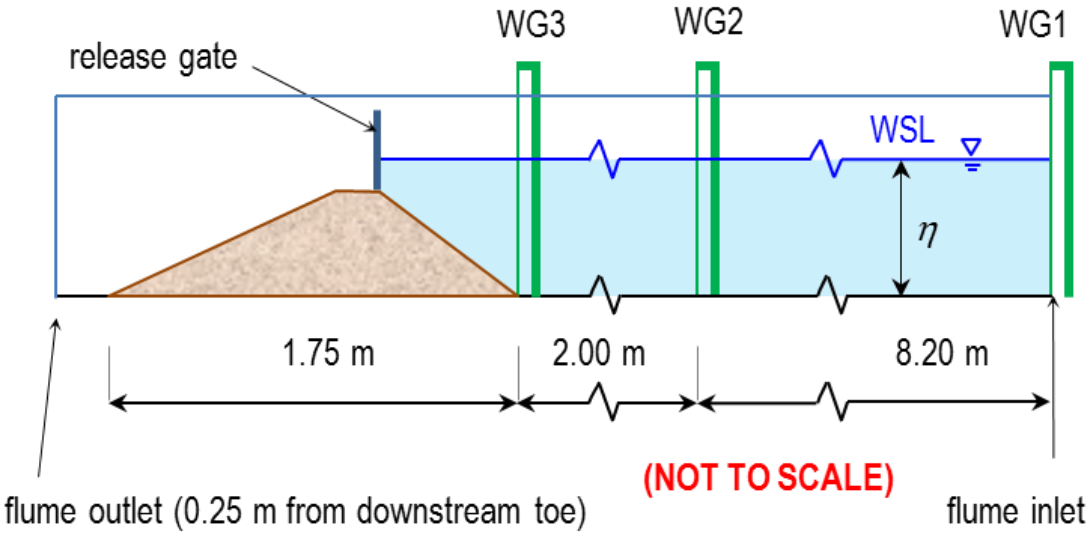

Figure D-57: Experimental setup for overtopping pilot tests in Phase III

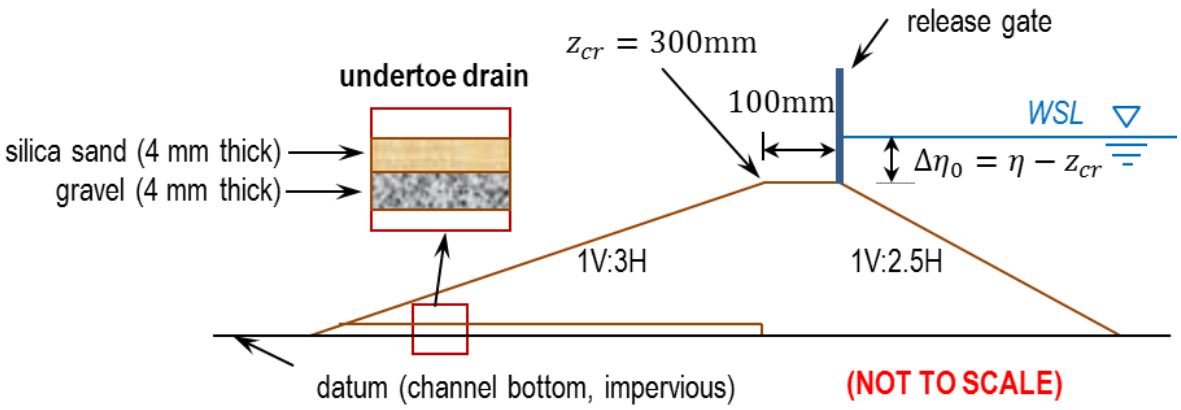

Figure D-58: Longitudinal section of embankment model in overtopping pilot tests showing undertoe-drain

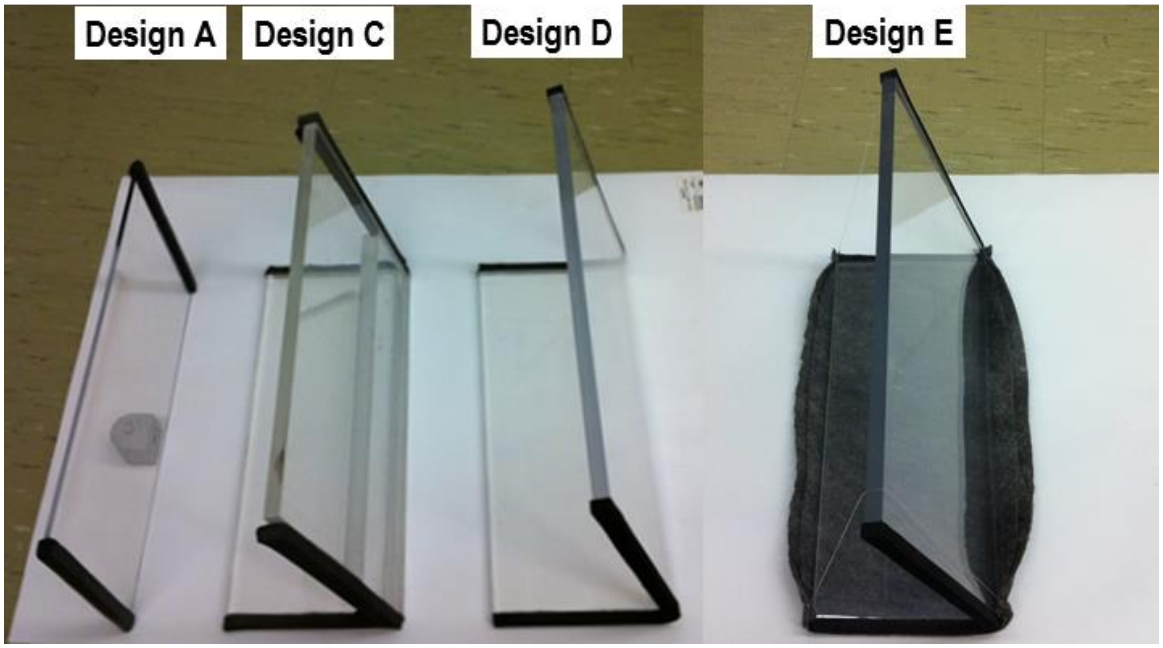

Figure D-59: Release gate designs in overtopping tests

After realizing the potential for the formation of a breach channel, the design was modified to include a thin plastic membrane on the upstream slope and upstream side of the vertical release gate to dissipate the PWP gradient (see Figure D-60). Imperfections on the upstream slope's surface eventually caused water to enter between the plastic membrane and the upstream slope, leading to a piping failure,

as occurred in Test No. 4. The gate was therefore redesigned to incorporate a rigid face in order to seal the top section of the upstream slope from water entry. Design “C” (see Figure D-59) was comprised of two ½” thick Plexiglas plates glued together to form a vertical side used for release, and an oblique side to rest on the upstream slope. The gate was redesigned once more (design “D”) by bending a single ½” Plexiglas plate to form two rigid sides instead, as shown in Figure D-59 and Figure D-61. The length of the impermeabilized upstream slope section was 13.5 cm.

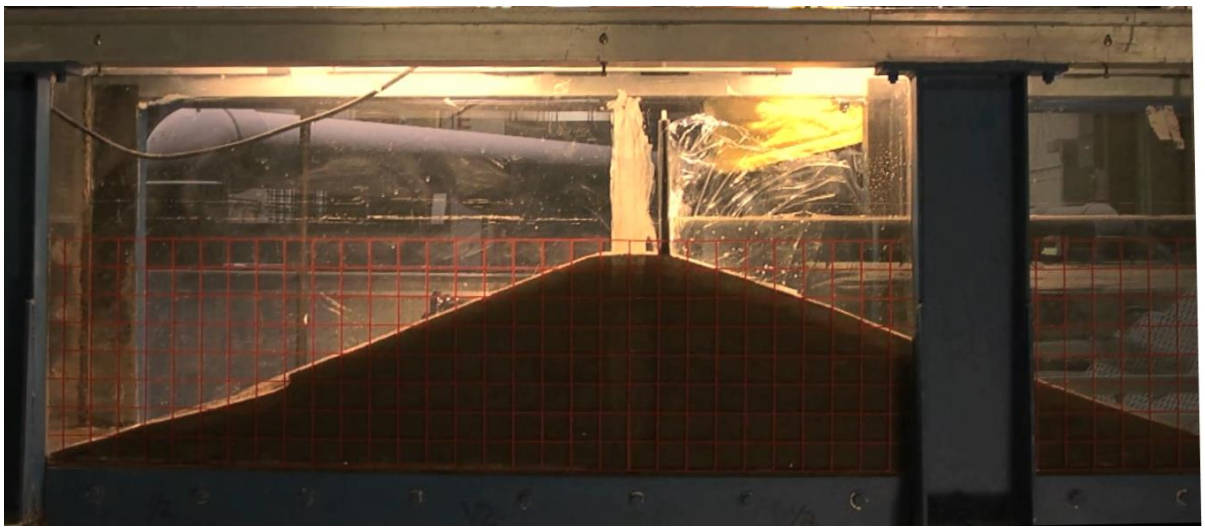

Figure D-60: Gate design "B" showing plastic membrane installed on upstream slope prior to overtopping

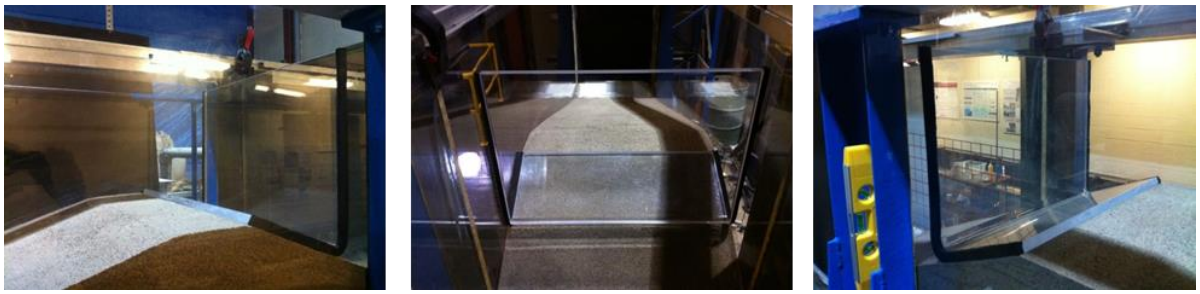

Figure D-61: Gate design "D" as viewed from (left) left side (middle) upstream (right) right side

For the dry embankment tests, it was necessary to maintain a low degree of saturation prior to overtopping. Therefore, the upstream slope was completely

impermeabilized by installing a plastic lining on its face, and sealed at the flume bottom and sides using acrylic caulking and tape (see Figure D-62). After impoundment in Test No. 11, the plastic lining was cut at the upstream toe and at the flume side-walls, however, surficial imperfections on the nearly dry upstream slope caused a stream of water to rapidly develop between the upstream slope and the release gate. This required the experiment to be aborted and the embankment model rebuilt once more. It became clear that surficial imperfections are more prone to initiate piping in drier soils; therefore for the dry embankment tests the release gate was augmented with two layers of non-woven geotextile between the release gate and the upstream slope to seal off any imperfections (see Figure D-59 and Figure D-62).

Figure D-62: Gate design "E" showing upstream slope impermeabilization as viewed from (left) upstream (middle) right side (right) downstream

Appendix E

Computer Codes

E.1 Hydrologic Routing: Small Flume, Phase I (FORTRAN 95)

```
!! This is program version 4: all units are in cm
!! NOTE: WG1 is furthest upstream (i.e. tank) and WG4 is furthest downstream (downstream apex of
crest)

PROGRAM hydrograph

IMPLICIT NONE

!! X: streamwise distance (zero reference: upstream sluice gate) (cm)
!! Y: flow depth corresponding to streamwise distance (cm)
!! L1, L2, L3, L4: shape function for WG1, WG2, WG3, WG4
!! QVnotch: steady flow over V-notch Weir (3066.4 cm3/s)
!! VTank: volume in diffuser tank (cm3)
!! X1, X2, X3, X4: streamwise distance for WG1, WG2, WG3, WG4 (cm)
!! Y1, Y2, Y3, Y4: flow depth distance for WG1, WG2, WG3, WG4 (cm)
!! t: time (s)
!! VTank: volume in diffuser tank (cm3)
!! QTank: discharge contribution from diffuser tank (cm3/s)
!! AFlume: area (side-view) in tilting flume straight section (cm2)
!! QFlume: discharge contribution from tilting flume straight section (cm3/s)
!! Freq: sampling frequency (Hz)
!! dX: space-step (cm)
!! dT: time-step (s)
!! I: space-step counter
!! n: time-step counter
!! MULT: multiplication factor for water surface slope near crest
!! SLOPE23: water surface slope between wave gauge 2 and 3
!! CRESTSLOPE: water surface slope near dam crest

REAL*8 ADummy,dT,dX,MULT,CRESTSLOPE,SLOPE23,X1,X2,X3,X4
REAL*8, DIMENSION (:,:), ALLOCATABLE :: Y
REAL*8, DIMENSION (:), ALLOCATABLE :: AFlume,L1,L2,L3,L4,QFlume,QTank,t,VTank,X,Y1,Y2,Y3,Y4
INTEGER*4 Freq,I,IMax,n,nRecords
CHARACTER*24 FileIn,FileOut,FileVol

PRINT*, 'Outflow Hydrograph Computation'
PRINT*, '******************************'
PRINT*
PRINT*, 'Enter input file name:'
READ*, FileIn

FileOut=FileIn(1:LEN(TRIM(FileIn))-4)//".dis"
FileVol=FileIn(1:LEN(TRIM(FileIn))-4)//".vol"
PRINT*, 'Enter space-step (in cm):'
READ*, dX
PRINT*, 'Enter multiplication factor for water surface slope near crest:'
READ*, MULT

!! read wave gauge header
OPEN (UNIT=5,FILE=FileIn,STATUS="OLD",ACTION="READ")
READ (5,*) nRecords
n=nRecords
READ (5,*) Freq
READ (5,*) X1,X2,X3,X4

IMax=(X4-X1)/dX
dT=1.0/Freq

!! allocate size of array for coordinates (at t = 0)
ALLOCATE(Y(0:IMax,0:n-1))
ALLOCATE(L1(0:IMax),L2(0:IMax),L3(0:IMax),L4(0:IMax))
ALLOCATE(QFlume(0:n-1),QTank(0:n-1),AFlume(0:n-1),VTank(0:n-1))
ALLOCATE(X(0:IMax),Y1(0:n-1),Y2(0:n-1),Y3(0:n-1),Y4(0:n-1),t(0:n-1))
Y(:,:)=0.0
```

```
L1(:)=0.0; L2(:)=0.0; L3(:)=0.0; L4(:)=0.0
QFlume(:)=0.0; QTank(:)=0.0; AFlume(:)=0.0; VTank(:)=0.0
X(:)=0.0; Y1(:)=0.0; Y2(:)=0.0; Y3(:)=0.0; Y4(:)=0.0; t(:)=0.0

!! initialization
t = 0.0
n = 0
I = 0

!! read wave gauge data
DO n=0,nRecords-1
  READ (5,*) t(n),Y1(n),Y2(n),Y3(n)
END DO
CLOSE (UNIT=5)

!! initial volume
VTank(0)=5.8707*(Y1(0)*Y1(0))+21172*Y1(0)
QTank(0)=0.0; QFlume(0)=0.0

!! initial discharge
X(0)=0; Y(0,0)=Y1(0)
DO I=1,IMax
  X(I)=X(I-1)+dX
  SLOPE23=(Y3(0)-Y2(0))/(X3-X2)
  CRESTSLOPE=MULT*SLOPE23
  Y4(0)=CRESTSLOPE*(X4-X3)+Y3(0)

  L1(I)=(X(I)-X2)*(X(I)-X3)*(X(I)-X4)/((X1-X2)*(X1-X3)*(X1-X4))
  L2(I)=(X(I)-X1)*(X(I)-X3)*(X(I)-X4)/((X2-X1)*(X2-X3)*(X2-X4))
  L3(I)=(X(I)-X1)*(X(I)-X2)*(X(I)-X4)/((X3-X1)*(X3-X2)*(X3-X4))
  L4(I)=(X(I)-X1)*(X(I)-X2)*(X(I)-X3)/((X4-X1)*(X4-X2)*(X4-X3))

  Y(I,0)=L1(I)*Y1(0)+L2(I)*Y2(0)+L3(I)*Y3(0)+L4(I)*Y4(0)

  ADummy=0.5*(y(I,0)+y(I-1,0))*dX
  AFlume(0)=AFlume(0)+ADummy
END DO

!! stage-volume function
DO n=1,nRecords-1
  VTank(n)=5.8707*(Y1(n)*Y1(n))+21172*Y1(n)
  QTank(n)=(VTank(n-1)-VTank(n))/dT
  X(0)=0; Y(0,n)=Y1(n)
  DO I=1,IMax
    X(I)=X(I-1)+dX
    SLOPE23=(Y3(n)-Y2(n))/(X3-X2)
    CRESTSLOPE=MULT*SLOPE23
    Y4(n)=CRESTSLOPE*(X4-X3)+Y3(n)
    L1(I)=(X(I)-X2)*(X(I)-X3)*(X(I)-X4)/((X1-X2)*(X1-X3)*(X1-X4))
    L2(I)=(X(I)-X1)*(X(I)-X3)*(X(I)-X4)/((X2-X1)*(X2-X3)*(X2-X4))
    L3(I)=(X(I)-X1)*(X(I)-X2)*(X(I)-X4)/((X3-X1)*(X3-X2)*(X3-X4))
    L4(I)=(X(I)-X1)*(X(I)-X2)*(X(I)-X3)/((X4-X1)*(X4-X2)*(X4-X3))
    Y(I,n)=L1(I)*Y1(n)+L2(I)*Y2(n)+L3(I)*Y3(n)+L4(I)*Y4(n)
    ADummy=0.5*(y(I,n)+y(I-1,n))*dX
    AFlume(n)=AFlume(n)+ADummy
  END DO
  QFlume(n)=(AFlume(n-1)-AFlume(n))*38.1/dT
END DO

!! plot hydrograph
OPEN (UNIT=6,FILE=FileOut,STATUS="NEW",ACTION="WRITE")
WRITE (6,10)
10 FORMAT (T6,'t(s)',T17,'QTank(cm3/s)',T34,'QFlume(cm3/s)',T51,'QTot(cm3/s)')
!! plot volume curve
OPEN (UNIT=7,FILE=FileVol,STATUS="NEW",ACTION="WRITE")
WRITE(7,11)
11 FORMAT (T6,'t(s)',T19,'VTank(cm3)',T36,'VFlume(cm3)',T51,'VTotal(cm3)')
```

```
DO n=0,nRecords-1
  WRITE (6,20) t(n),QTank(n),QFlume(n),QFlume(n)+QTank(n)
  20 FORMAT (F10.2,2(8X,F10.1),5X,F10.1)
  WRITE (7,21) t(n),VTank(n),AFlume(n)*0.381,VTank(n)+AFlume(n)*38.1
  21 FORMAT (F10.2,2(8X,F10.1),5X,F10.1)
END DO
CLOSE (UNIT=6)
CLOSE (UNIT=7)
END PROGRAM hydrograph
```

E.2 Butterworth Filter Algorithm (MATLAB)

```
[NUMERIC,TXT,RAW]=XLSREAD('WG_data_20_blow_high_29Aug.xls');
time=NUMERIC(:,2);
gauge1=NUMERIC(:,3);
gauge2=NUMERIC(:,4);
gauge3=NUMERIC(:,5);
gauge4=NUMERIC(:,6);

gauge1=gauge1/100;
gauge2=gauge2/100;
gauge3=gauge3/100;
gauge4=gauge4/100;

writematrixall=[];

%datawoNanN=interpolateNaN(data)
SampleFreq=30;%30 Hz
Nyquist=SampleFreq/2; %15 Hz
[b1,a1]=butter(6,.01);
[b2,a2]=butter(6,.01);
[b3,a3]=butter(6,.01);
[b4,a4]=butter(6,.01);

filtgauge1 = filtfilt(b1,a1,gauge1);
filtgauge2 = filtfilt(b2,a2,gauge2);
filtgauge3 = filtfilt(b3,a3,gauge3);
filtgauge4 = filtfilt(b4,a4,gauge4);

figure(1),clf
plot(time,gauge1,'r-',time,filtgauge1,'b-')
legend('unfilt1','filt1')
title('filt wave gauge')
xlabel('time,s')
ylabel('gauge height,cm')

figure(2),clf
plot(time,gauge2,'r-',time,filtgauge2,'b-')
legend('unfilt2','filt2')
title('filt wave gauge')
xlabel('time,s')
ylabel('gauge height,cm')

figure(3),clf
plot(time,gauge3,'r-',time,filtgauge3,'b-')
legend('unfilt3','filt3')
title('filt wave gauge')
xlabel('time,s')
ylabel('gauge height,cm')

figure(4),clf
plot(time,gauge4,'r-',time,filtgauge4,'b-')
legend('unfilt4','filt4')
title('filt wave gauge')
xlabel('time,s')
ylabel('gauge height,cm')

writematrix=[time filtgauge1 filtgauge2 filtgauge3 filtgauge4];
writematrixall=[writematrixall; writematrix];
output_header= {'time' 'filtgauge1' 'filtgauge2' 'filtgauge3' 'filtgauge4'};
xlswrite('filtgaugeout', [output_header; num2cell(writematrixall)], 'filteredWGdata');
```

E.3 Hydrologic Routing Check: Small Flume, Phase I (FORTRAN 95)

```
!! This program computes the following:
!! 1-   head above a triangular V-notch tank using the computed outflow hydrograph
!!      from a hydrologic routing method which uses WG data in the upstream reservoir
!! 2-   hydrograph for flow through triangular V-notch for the computed head above

!! wg1:          water surface elevation above V-notch [m]
!! Cw:           triangular V-notch weir coefficient [FF]
!! dt:           time-step [s]
!! Vtank:        volume of V-notch tank [m^3]
!! Atank:        area of V-notch tank (36 inches width x 69.5 inches length) [m^2]
!! t:            time [s]
!! Qw:           flow over V-notch [m^3]
!! Qw1:          flow over V-notch at previous time [m^3]
!! Qw2:          flow over V-notch at current time [m^3]
!! Qw:           flow over V-notch [m^3]
!! Qb:           breach discharge [m^3]
!! Qb1:          breach discharge at previous time [m^3]
!! Qb2:          breach discharge at current time [m^3]

!! n:            time counter [INT]
!! nRecords:     number of records in wave gauge input file [INT]

PROGRAM routing

IMPLICIT NONE

REAL*8 ATank,Cw,dt,Freq
REAL*8, DIMENSION (:), ALLOCATABLE :: Qb,Qw,t,Vtank,wg4
INTEGER*4 n,nRecords
CHARACTER*24 FileIn,FileOut

PRINT*, 'Outflow Hydrograph Computation'
PRINT*, '******************************'
PRINT*

PRINT*, 'Enter input file name:'
READ*, FileIn

FileOut=FileIn(1:LEN(TRIM(FileIn))-4)//".dis"

!! read wave gauge header
OPEN (UNIT=5,FILE=FileIn,STATUS="OLD",ACTION="READ")
READ (5,*) nRecords
READ (5,*) Freq

dt=1.0/Freq
Cw=1.38

!! allocate size of array for coordinates (at t = 0)
ALLOCATE(Qb(0:nRecords-1),Qw(0:nRecords-1),t(0:nRecords-1))
ALLOCATE(Vtank(0:nRecords-1),wg4(0:nRecords-1))
Qb(:)=0.0; Qw(:)=0.0; t(:)=0.0; VTank(:)=0.0; wg4(:)=0.0

!! read wave gauge data
DO n=0,nRecords-1
  READ (5,*) t(n),Qb(n)
END DO
CLOSE (UNIT=5)

!! initialization
Atank=36*69.5*0.0254*0.0254      !! convert to SI Units
DO n=1,nRecords-1
```

```
    wg4(n)=wg4(n-1)+(dt/Atank)*(Qb(n-1)-Cw*(wg4(n-1)**2.5))
    Qw(n)=Cw*(wg4(n)**2.5)
END DO

!! plot hydrograph and wave gauge data
OPEN (UNIT=6,FILE=FileOut,STATUS="NEW",ACTION="WRITE")
WRITE (6,10)
10 FORMAT (T6,'t[s]',T13,'Qw[m3/s]',T24,'Qw[l/s]',T34,'wg4[cm]')

DO n=0,nRecords-1
  WRITE (6,20) t(n),Qw(n),Qw(n)*1000,wg4(n)*100
  20 FORMAT (F9.3,3X,F8.6,3X,F7.3,3X,F7.3)
END DO
CLOSE (UNIT=6)

END PROGRAM routing
```

E.4 Hydrologic Routing: Large Flume, Phase I (FORTRAN 95)

```
!! This is program version 2
!! NOTE: WG1 is furthest upstream (i.e. tank) and WG5 (which is extrapolated) is
!! furthest downstream (i.e. at the upstream apex of the crest)

PROGRAM hydrograph

IMPLICIT NONE

!! dT: time-step [s]
!! X: streamwise distance (zero reference: most upstream point in LARGE channel) [m]
!! Y: flow depth corresponding to streamwise distance [m]
!! X1, X2, X3, X4, X5: streamwise distance for WG1, WG2, WG3, WG4, WG5 [m]
!! Y1, Y2, Y3, Y4, Y5: flow depth distance for WG1, WG2, WG3, WG4, WG5 [m]
!! t: time (s)
!! AFlume: area (side-view) in LARGE flume [m^2]
!! QFlume: discharge contribution from tilting flume straight section [m^3/s]
!! Freq: sampling frequency [Hz]
!! n: time-step counter
!! nRecords: number of records in input file
!! MULT: multiplication factor for water surface slope near crest
!! SLOPE34: water surface slope between wave gauge 3 and 4
!! SLOPE45: water surface slope near dam crest

REAL*8 dT,MULT,SLOPE34,SLOPE45,USslope,X1,X2,X3,X4,X5
REAL*8, DIMENSION (:), ALLOCATABLE :: AFlume,QFlume,t,Y1,Y2,Y3,Y4,Y5
INTEGER*4 Freq,n,nRecords
CHARACTER*24 FileIn,FileOut,FileVol

PRINT*, 'Outflow Hydrograph Computation'
PRINT*, '*****************************'
PRINT*
PRINT*, 'Enter input file name:'
READ*, FileIn

FileOut=FileIn(1:LEN(TRIM(FileIn))-4)//".dis"
FileVol=FileIn(1:LEN(TRIM(FileIn))-4)//".vol"

PRINT*, 'Enter multiplication factor for water surface slope near crest:'
READ*, MULT

!! read wave gauge header
OPEN (UNIT=5,FILE=FileIn,STATUS="OLD",ACTION="READ")
READ (5,*) nRecords
n=nRecords
READ (5,*) Freq
READ (5,*) X1,X2,X3,X4

dT=1.0/Freq
USslope=2.5

!! allocate size of array for coordinates (at t = 0)
ALLOCATE(QFlume(0:n-1),AFlume(0:n-1))
ALLOCATE(Y1(0:n-1),Y2(0:n-1),Y3(0:n-1),Y4(0:n-1),Y5(0:n-1),t(0:n-1))
QFlume(:)=0.0; AFlume(:)=0.0; Y1(:)=0.0; Y2(:)=0.0; Y3(:)=0.0; Y4(:)=0.0; Y5(:)=0.0; t(:)=0.0

!! read wave gauge data
DO n=0,nRecords-1
  READ (5,*) t(n),Y1(n),Y2(n),Y3(n),Y4(n)
END DO
CLOSE (UNIT=5)

!! initialization
SLOPE34=(Y4(0)-Y3(0))/(X4-X3)            !! initial slope between WG3 and WG4
SLOPE45=MULT*SLOPE34                             !! initial WS slope near crest
```

```
!! extrapolate X5 and assume elevation of solid U/S boundary = WG1
X5=X4+Y1(0)*USslope

Y5(0)=SLOPE45*(X5-X4)+Y4(0)
AFlume(0)=0.5*((Y1(0)+Y2(0))*(X2-X1)+(Y2(0)+Y3(0))*(X3-X2)+(Y3(0)+Y4(0))*(X4-X3)+(Y4(0)+Y5(0)-
Y1(0))*(X5-X4))

DO n=1,nRecords-1
  SLOPE34=(Y4(n)-Y3(n))/(X4-X3)
  SLOPE45=MULT*SLOPE34
  X5=X4+Y1(n)*USslope
  Y5(n)=SLOPE45*(X5-X4)+Y4(n)
  AFlume(n)=0.5*((Y1(n)+Y2(n))*(X2-X1)+(Y2(n)+Y3(n))*(X3-X2)+(Y3(n)+Y4(n))*(X4-X3)+(Y4(n)+Y5(n)-
Y1(n))*(X5-X4))
  QFlume(n)=(AFlume(n-1)-AFlume(n))*1.5/dT
END DO

!! plot hydrograph
OPEN (UNIT=6,FILE=FileOut,STATUS="NEW",ACTION="WRITE")
WRITE (6,10)
10 FORMAT (T6,'t(s)',T17,'QFlume(m3/s)')

!! plot volume curve
OPEN (UNIT=7,FILE=FileVol,STATUS="NEW",ACTION="WRITE")
WRITE(7,11)
11 FORMAT (T6,'t(s)',T19,'VFlume(m3)')

DO n=0,nRecords-1
  WRITE (6,20) t(n),QFlume(n)
  20 FORMAT (F10.2,8X,F10.5)
  WRITE (7,21) t(n),AFlume(n)*1.5
  21 FORMAT (F10.2,8X,F10.5)
END DO
CLOSE (UNIT=6)
CLOSE (UNIT=7)

END PROGRAM hydrograph
```

E.5 Hydrologic Routing: Large Flume, Phase II (FORTRAN 95)

```
!! This is program version 2: all units are in metres
!! NOTE: WG1 is furthest upstream (i.e. at flume inlet) and WG4 (NOTE: computed)
!! is furthest downstream (upstream apex of crest)

PROGRAM hydrograph

IMPLICIT NONE

!! dT: time-step [s]
!! X: streamwise distance (zero reference: most upstream point in large channel) [m]
!! Y: flow depth corresponding to streamwise distance [m]
!! X1, X2, X3, X4: streamwise distance for WG1, WG2, WG3, WG4, [m]
!! Y1, Y2, Y3, Y4: flow depth distance for WG1, WG2, WG3, WG4 [m]
!! t: time [s]
!! AFlume: area (side-view) in large flume [m^2]
!! QFlume: discharge contribution from tilting flume straight section [m^3/s]
!! Freq: sampling frequency [Hz]
!! Fwidth: Flume width [m]
!! n: time-step counter
!! nRecords: number of records in input file
!! MULT: multiplication factor for water surface slope near crest
!! SLOPE23: water surface slope between wave gauge 2 and 3
!! SLOPE34: water surface slope near embankment model's crest


REAL*8 dT,Fwidth,MULT,SLOPE23,SLOPE34,USslope,X1,X2,X3,X4
REAL*8, DIMENSION (:), ALLOCATABLE :: AFlume,QFlume,t,Y1,Y2,Y3,Y4
INTEGER*4 Freq,n,nRecords
CHARACTER*24 FileIn,FileOut,FileVol

PRINT*, 'Outflow Hydrograph Computation'
PRINT*, '******************************'
PRINT*
PRINT*, 'Enter input file name:'
READ*, FileIn

FileOut=FileIn(1:LEN(TRIM(FileIn))-4)//".dis"
FileVol=FileIn(1:LEN(TRIM(FileIn))-4)//".vol"

PRINT*, 'Enter multiplication factor for water surface slope near crest:'
READ*, MULT

!! read wave gauge header
OPEN (UNIT=5,FILE=FileIn,STATUS="OLD",ACTION="READ")
READ (5,*) nRecords
n=nRecords
READ (5,*) Freq
READ (5,*) X1,X2,X3

dT=1.0/Freq
USslope=2.5
Fwidth=1.48
!! allocate size of array for coordinates (at t = 0)
ALLOCATE(QFlume(0:n-1),AFlume(0:n-1))
ALLOCATE(Y1(0:n-1),Y2(0:n-1),Y3(0:n-1),Y4(0:n-1),t(0:n-1))
QFlume(:)=0.0; AFlume(:)=0.0; Y1(:)=0.0; Y2(:)=0.0; Y3(:)=0.0; Y4(:)=0.0; t(:)=0.0

!! read wave gauge data
DO n=0,nRecords-1
  READ (5,*) t(n),Y1(n),Y2(n),Y3(n)
END DO
CLOSE (UNIT=5)
```

```
!! initialization
SLOPE23=(Y3(0)-Y2(0))/(X3-X2)    !! initial slope between WG2 and WG3
SLOPE34=MULT*SLOPE23                    !! initial WS slope near crest
!! extrapolate X4 and assume elevation of solid U/S boundary = WG1 (i.e. Y1)
X4=X3+Y1(0)*USslope

Y4(0)=SLOPE34*(X4-X3)+Y3(0)
AFlume(0)=0.5*((Y1(0)+Y2(0))*(X2-X1)+(Y2(0)+Y3(0))*(X3-X2)+(Y3(0)*(X4-X3)))

DO n=1,nRecords-1
  SLOPE23=(Y3(n)-Y2(n))/(X3-X2)
  SLOPE34=MULT*SLOPE23
  Y4(n)=Y3(n)/(1-USslope*SLOPE34)
  X4=X3+USslope*Y4(n)
  AFlume(n)=0.5*((Y1(n)+Y2(n))*(X2-X1)+(Y2(n)+Y3(n))*(X3-X2)+(Y3(n)*(X4-X3)))
  QFlume(n)=(AFlume(n-1)-AFlume(n))*Fwidth/dT
END DO

!! plot hydrograph
OPEN (UNIT=6,FILE=FileOut,STATUS="NEW",ACTION="WRITE")
WRITE (6,10)
10 FORMAT (T6,'t(s)',T17,'QFlume(m3/s)')

!! plot volume curve
OPEN (UNIT=7,FILE=FileVol,STATUS="NEW",ACTION="WRITE")
WRITE(7,11)
11 FORMAT (T6,'t(s)',T19,'VFlume(m3)')

DO n=0,nRecords-1
  WRITE (6,20) t(n),QFlume(n)
  20 FORMAT (F10.2,8X,F10.5)
  WRITE (7,21) t(n),AFlume(n)*Fwidth
  21 FORMAT (F10.2,8X,F10.5)
END DO
CLOSE (UNIT=6)
CLOSE (UNIT=7)

END PROGRAM hydrograph
```

E.6 Hydrologic Routing: Small Flume, Phase III (FORTRAN 95)

```
!! This is program version 2: all units are in metres
!! NOTE: WG1 is furthest upstream (i.e. at flume inlet) and WG4 (NOTE: computed)
!! is furthest downstream (upstream apex of crest)

PROGRAM hydrograph

IMPLICIT NONE

!! dT: time-step [s]
!! Fwidth: flume width [m]
!! MULT: multiplication factor for water surface slope near crest
!! USslope: upstream should slope factor
!! X1, X2, X3, X4: streamwise distance for WG1, WG2, WG3, WG4, [m]
!! Y1, Y2, Y3, Y4: flow depth distance for WG1, WG2, WG3, WG4 [m]
!! AFlume: area (side-view) in large flume [m^2]
!! QFlume: discharge contribution from tilting flume straight section [m^3/s]
!! SLOPE23: water surface slope between wave gauge 2 and 3
!! SLOPE34: water surface slope near embankment model's crest
!! QTank: discharge contribution from head tank [m^3/s]
!! t: time [s]
!! VTank: volume in head tank [m^3]
!! Freq: sampling frequency [Hz]
!! n: time-step counter
!! nRecords: number of records in input file
!! FileIn: input file name
!! FileOut: name of output file for discharge
!! FileVol: name of output file for volume

REAL*8 dT,Fwidth,MULT,SLOPE23,USslope,X1,X2,X3
REAL*8, DIMENSION (:), ALLOCATABLE :: AFlume,SLOPE34,QFlume,QTank,t,VTank,X4,Y1,Y2,Y3,Y4
INTEGER*4 Freq,n,nRecords
CHARACTER*24 FileIn,FileOut,FileVol
PRINT*, 'Outflow Hydrograph Computation'
PRINT*, '******************************'
PRINT*
PRINT*, 'Enter input file name:'
READ*, FileIn

FileOut=FileIn(1:LEN(TRIM(FileIn))-4)//".dis"
FileVol=FileIn(1:LEN(TRIM(FileIn))-4)//".vol"

PRINT*, 'Enter multiplication factor for water surface slope near crest:'
READ*, MULT

!! read wave gauge header
OPEN (UNIT=5,FILE=FileIn,STATUS="OLD",ACTION="READ")
READ (5,*) nRecords
n=nRecords
READ (5,*) Freq
READ (5,*) X1,X2,X3

dT=1.0/Freq
USslope=2.5
Fwidth=0.381

!! allocate size of array for coordinates (at t = 0)
ALLOCATE(QFlume(0:n-1),QTank(0:n-1),AFlume(0:n-1),VTank(0:n-1))
ALLOCATE(Y1(0:n-1),Y2(0:n-1),Y3(0:n-1),Y4(0:n-1),t(0:n-1),X4(0:n-1),SLOPE34(0:n-1))
QFlume(:)=0.0; QTank(:)=0.0; AFlume(:)=0.0; VTank(:)=0.0
Y1(:)=0.0; Y2(:)=0.0; Y3(:)=0.0; Y4(:)=0.0; X4(:)=0.0; t(:)=0.0; SLOPE34(:)=0.0

!! read wave gauge data
```

```
DO n=0,nRecords-1
  READ (5,*) t(n),Y1(n),Y2(n),Y3(n)
END DO
CLOSE (UNIT=5)

!! initialization
VTank(0)=2.147953*Y1(0)                  !! initial volume
QTank(0)=0.0; QFlume(0)=0.0                      !! initial discharge
SLOPE23=(Y3(0)-Y2(0))/(X3-X2)            !! initial slope between WG2 and WG3
SLOPE34(0)=ABS(MULT*SLOPE23)             !! initial WS slope near crest
!! extrapolate X4 and assume elevation of solid U/S boundary = WG1       (i.e. flat water surface
level)
X4(0)=X3+Y1(0)*USslope
Y4(0)=SLOPE34(0)*(X4(0)-X3)+Y3(0)
AFlume(0)=0.5*((Y1(0)+Y2(0))*(X2-X1)+(Y2(0)+Y3(0))*(X3-X2)+(Y3(0)+Y4(0)-Y1(0))*(X4(0)-X3))

DO n=1,nRecords-1
  VTank(n)=2.147953*Y1(n)                        !! stage-volume function
  QTank(n)=(VTank(n-1)-VTank(n))/dT
  SLOPE23=(Y3(n)-Y2(n))/(X3-X2)
  SLOPE34(n)=ABS(MULT*SLOPE23)
  Y4(n)=Y3(n)/(1+USslope*SLOPE34(n))
  X4(n)=X3+USslope*Y4(n)
  AFlume(n)=0.5*((Y1(n)+Y2(n))*(X2-X1)+(Y2(n)+Y3(n))*(X3-X2)+(Y3(n)*(X4(n)-X3)))
  QFlume(n)=(AFlume(n-1)-AFlume(n))*Fwidth/dT
END DO

!! plot hydrograph
OPEN (UNIT=6,FILE=FileOut,STATUS="NEW",ACTION="WRITE")
WRITE (6,10)
10 FORMAT (T6,'t(s)',T17,'QTank(m3/s)',T34,'QFlume(m3/s)',T51,'QTot(m3/s)')
!! plot volume curve
OPEN (UNIT=7,FILE=FileVol,STATUS="NEW",ACTION="WRITE")
WRITE(7,11)
11 FORMAT (T6,'t(s)',T19,'VTank(m3)',T36,'VFlume(m3)',T51,'VTotal(m3)')
DO n=0,nRecords-1
  WRITE (6,20) t(n),QTank(n),QFlume(n),QFlume(n)+QTank(n)
  20 FORMAT (F10.2,2(8X,F10.5),5X,F10.5,1X,F10.5,1X,F10.5)
  WRITE (7,21) t(n),VTank(n),AFlume(n)*Fwidth,VTank(n)+AFlume(n)*Fwidth
  21 FORMAT (F10.2,2(8X,F10.5),5X,F10.5)
END DO
CLOSE (UNIT=6)
CLOSE (UNIT=7)

END PROGRAM hydrograph
```

E.7 2-D Erosion and Flow Parameters: Small Flume, Phase III (FORTRAN 95)

```
!! PARAMATERS

!! angle:                angle between bed slope and normal vector [rad]
!! aspect:               bearing of flow path with respect to vertical axis (imported from ArcGIS),
clock-wise [deg]
!! b:                    flume width [m]
!! BedX:                 x-coordinate of I-node (i.e. for bed) [cm]
!! BedZ:                 z-coordinate of I-node (i.e. for bed) [cm]
!! beta:                 momentum correction factor used in bed shear stress expression by Cheng and
Chiew (1998) [-]
!! d50:                  mean particle size [m]
!! deg2rad:              conversion from degree to radians [rad/deg]
!! dn:                   extrapolated erosion along normal direction (i.e. n-axis) [cm]
!! dndT:                 erosion rate [m/s]
!! dqbds:                specific bed load transport rate [m/s]
!! ds:                   space-step along s-coordinate [cm]
!! dsGIS:                space-step used in ArcGIS [mm] and [cm]
!! dT:                   time-step [s]
!! dVb:                  volume of sediment eroded during time-step per unit width [cm^2]
!! dz:                   extrapolated erosion along vertical direction (i.e. z-axis) [cm]
!! e:                    void ratio [-]
!! EGL:                  energy grade line [cm]
!! eta1:                 water surface level in reservoir corresponding to WG1 [m]
!! eta4:                 water surface level in reservoir corresponding to WG4 [m]
!! Fr:                   Froude number [-]
!! g:                    gravitational acceleration [m/s^2]
!! gamma:                specific weight of fluid (i.e. water) [N/m^3]
!! Gs:                   specific gravity of sediment [-]
!! i_n:                  exit hydraulic gradient along normal direction (i.e. n-axis) [-]
!! i_phi:                hydraulic gradient along direction of seepage [-] (as a percentage)
!! i_zc:                 critical hydraulic gradient along z-direction (i.e. vertical global
coordinate system) [-]
!! K_function:           permeability function (constant if saturated) [m/s]
!! miu:                  kinematic viscosity of water at 20 degrees Celsius [m^2/s]
!! m_Yn:                 slope of axis normal on discretized bed K-node (i.e. n-axis) [-]
!! Nh:                   characterization of deviation from hydrostatic conditions [-] (Francalanci et
al. 2008)
!! p:                    porosity [-]
!! PI:                   pi [-]
!! Q:                    overtopping discharge [m^3/s]
!! q_bstar:              bedload [-]
!! Re:                   Reynolds number [-]
!! Re_star:              grain Reynolds number [-]
!! Rh:                   hydraulic radius to account for side wall effects, Vanoni and Brooks (1957)
[cm]
!! rho:                  density of fluid (i.e. water) [kg/m^3]
!! s:                    s-coordinate [cm]
!! Sb:                   bed slope [rad]
!! Sf:                   friction slope [rad]
!! Sw_n:                 water surface slope (normal of discretized bed node) [rad]
!! Sw_z:                 water surface slope (vertical of discretized bed node) [rad]
!! t:                    time [s]
!! tau_b:                bed shear stress using derived St-Venant equation for steep slope under
boundary seepage [Pa]
!! tau_bI:               term I of bed shear stress derived using St-Venant equations [Pa]
!! tau_bII:              term II of bed shear stress derived using St-Venant equations [Pa]
!! tau_bIII:             term III of bed shear stress derived using St-Venant equations [Pa]
!! tau_bIV:              term IV of bed shear stress derived using St-Venant equations [Pa]
!! tau_bV:               term V of bed shear stress derived using St-Venant equations [Pa]
!! tau_b2:               bed shear stress using Eq. (19) in Cheng and Chiew (1998) [Pa]
!! tau_cmplx:            variable used to transfer values of shear stress to allow use of non-integer
exponents [UD]
!! tau_EGL:              bed shear stress using EGL [Pa]
!! tau_EGLstar:          dimensionless shear stress based on EGL [-]
```

```
!! tau_bstar:            dimensionless shear stress based on St-Venant derivation [-]
!! tau_bstar2:           dimensionless shear stress based on Cheng and Chiew (1998) [-]
!! U:                    depth-averaged overtopping velocity [m/s]
!! U_s0:                 depth-averaged overtopping velocity at s=0 (i.e. I=1) [m/s]
!! U_star:               grain velocity (based on tau_b) [m/s]
!! U_US:                 depth-averaged overtopping velocity immediately upstream the first
discretized node [cm]
!! v_dn:                 discharge velocity along normal direction [m/s]
!! vec_n:                vector between bed (i.e. K-node) and upper boundary (i.e. I-node at previous
time-step or J-node) used to determine normal distance (has two dimensions, x and z) [cm]
!! WSLX:                 x-coordinate of J-node (i.e. for WSL) [cm]
!! WSLZ:                 z-coordinate of J-node (i.e. for WSL) [cm]
!! X:                    x-coordinate of discretized bed K-node (i.e. for discretized bed) [cm]
!! Yc:                   critical flow depth [cm]
!! Yn:                   overtopping flow depth (normal to bed slope) [cm]
!! Yn2:                  overtopping flow depth (normal to bed slope) according to method by Hager and
Hutter (1984) using measured vertical flow depth, Yz [cm]
!! Yh:                   vertical component of normal flow depth on slope [cm]
!! Yh2:                  vertical component of normal flow depth on slope (also defined as pressure
head) according to method of Hager and Hutter (1984) (i.e. "h") [cm]
!! Yh3:                  vertical component of normal flow depth on slope using method similar to
Hager and Hutter (1984) (i.e. Equation (4.50))
!! Ynfd:                 normal flow depth based on Manning's equation [cm]
!! Yz:                   overtopping flow depth along vertical axis (i.e. z-direction)[cm]
!! Yz2:                  overtopping flow depth along vertical axis (i.e. z-direction) according to
method of Hager and Hutter (1984) using measured normal flow depth, Yn [cm]
!! Yz_s0:                overtopping flow depth along vertical axis (i.e. z-direction) at first node
(i.e. I=1) [cm]
!! Z:                    z-coordinate of discretized bed K-node (i.e. for discretized bed) [cm]
!! Z1:                   value used with Z2 to determine Icrest condition [cm]
!! Z2:                   value used with Z1 to determine Icrest condition [cm]
!! icond:                condition reached to determine "Icrest" node (highest elevation of
embankment) [INT]
!! istat:                status after reading record in bed/WSL files [INT]
!! I:                    counter for bed nodes (input coordinates) [INT]
!! Icrest:               I-node at which computation begins (i.e. usually at crest) [INT]
!! Imax:                 number of bed nodes for each time-step [INT]
!! Imaxval:              maximum value of bed nodes in entire array [INT]
!! Istart:               bed node at which discretization starts [INT]
!! J:                    counter for WSL nodes (input coordinates) [INT]
!! Jmax:                 number of WSL nodes for each time-step [INT]
!! Jmaxval:              maximum value of WSL nodes in entire array (INT]
!! K:                    counter for discretized bed nodes [INT]
!! Kdownstream:          number of downstream discretized bed nodes [INT]
!! Kmax:                 total number of discretized bed nodes [INT]
!! Kmaxval:              maximum value of discretized bed nodes in entire array [INT]
!! Kupstream:            number of downstream discretized bed nodes [INT]
!! n:                    counter for time-step [INT]
!! nds:                  number of GIS space-steps within discretized bed space-step [INT]
!! nRecords:             number of flow records (i.e. number of time-steps) [INT]
!! nT:                   integer of time-step used to define time-step character [INT]
!! Ucounter:             counter for discretized bed node in previous time-step used to interpolate
overtopping velocity corresponding to the same s-coordinate in current time-step [INT]
!! curve:                gradually varied flow curve type (i.e. A-2,A-3,H-2,H-3,M-1,M-2,M-3,S-1,S-2,S-
3)
!! FileBed:              name of bed file with extension corresponding to time [CH]
!! FileBedSeres:         name of bed file without extension [CH]
!! FileFlow:             name of flow file [CH]
!! FileGIS:              name of output file used in GIS [CH]
!! FileWSLSeries:        name of WSL file without extension [CH]
!! nCh:                  character corresponding to time-step (is also the extension of the bed and
WSL series files) [CH]
!! region:               location of discretized node on bed (i.e. upstream, downstream toe, crest or
recirculation zone) [CH]

PROGRAM erosion
```

```
IMPLICIT NONE

REAL*4 angle,b,beta,d50,deg2rad,ds,dsGIS,dT,e,g,gamma,Gs,miu,n_coeff,p,PI,rho,i_zc,K_function,Z1,Z2
REAL*4, DIMENSION (2) :: vec_n
REAL*4, DIMENSION (:), ALLOCATABLE :: eta1,eta4,Q,t,U_s0,Yc,Yz_s0
REAL*4, DIMENSION (:,:), ALLOCATABLE ::
aspect,BedX,BedZ,dqbds,dn,dndT,dVb,dz,EGL,Fr,i_n,i_z,Nh,q_bstar, &
                          &
Re,Re_star,Rh,s,Sb,Sf,Sw_n,Sw_z,i_phi,tau_b,tau_bI,tau_bII,tau_bIII,tau_bIV,tau_bV,tau_b2,tau_EGL, &
           &
tau_EGLstar,tau_bstar,tau_bstar2,U,U_star,v_dn,WSLX,WSLZ,X,Yh,Yh2,Yh3,Yn,Yn2,Ynfd,Yz,Yz2,Z
INTEGER*4 I,icond,Imaxval,istat,J,Jmaxval,K,Kmaxval,n,nds,nRecords,nT,Ucounter
INTEGER, DIMENSION (:), ALLOCATABLE :: Imax,Icrest,Istart,Jmax,Kcrest,Kmax,Kdownstream,Kupstream
CHARACTER(LEN=16) FileBed,FileBedSeries,FileFlow,FileGIS,FileWSL,FileWSLSeries,nCh
CHARACTER(LEN=6), DIMENSION (:,:), ALLOCATABLE :: region
CHARACTER(LEN=3), DIMENSION (:,:), ALLOCATABLE :: curve
COMPLEX tau_cmplx

!! I.   DATA INPUT AND FILE READING STATEMENTS

PRINT*, 'Erosion Rate Computation'
PRINT*, '*****************************'
PRINT*

!! 1. FLOW HEADER INPUT DATA (number of records, nRecords, dT, dsGIS, t, eta1, eta4 and Q)

PRINT*, 'Enter flow input file name:'
READ*, FileFlow

FileGIS=FileFlow(1:LEN(TRIM(FileFlow))-4)//".txt"

!! read flow input file header
OPEN (UNIT=5,FILE=FileFlow,STATUS="OLD",ACTION="READ")
READ (5,*) nRecords,dT
READ (5,*) dsGIS

!! allocate size of array for flow data
ALLOCATE(eta1(nRecords),eta4(nRecords),Q(nRecords),t(0:nRecords))
eta1(:)=0.0; eta4(:)=0.0; Q(:)=0.0; t(:)=0.0

READ (5,*) t(0)

!! read flow data
DO n=1,nRecords
  READ (5,*) t(n),eta1(n),eta4(n),Q(n)
END DO
CLOSE (UNIT=5)

PRINT*, 'Enter name of bed coordinates file series:'
READ*, FileBedSeries
Print*, 'Enter name of WSL file series:'
READ*, FileWSLSeries
PRINT*, 'Enter space-step, ds, in cm:'
READ*, ds
PRINT*, 'Enter void ratio, e:'
READ*, e

!! 2. WSL AND BED LEVEL HEADER DATA (Icrest, Imax and Jmax)

ALLOCATE(Imax(0:nRecords),Icrest(0:nRecords),Jmax(nRecords))
Imax(:)=1; Icrest(:)=1;  Jmax(:)=1

DO n=0,nRecords
  nT=INT(t(n))
  IF (nT.GT.99) THEN
    WRITE (nCh,'(I3)') nT
  ELSE IF (nT>9) THEN
```

```
    WRITE (nCh,'(I2)') nT
  ELSE
    WRITE (nCh,'(I1)') nT
  END IF
  FileBed=FileBedSeries(1:LEN(TRIM(FileBedSeries)))//"."//nCh
  OPEN (UNIT=6,FILE=FileBed,STATUS="OLD",ACTION="READ")
  I=0
  istat=0
  icond=0
  Z1=0.0; Z2=0.0
  DO
    I=I+1
    READ (6,*,IOSTAT=istat) Z1,Z1
      IF ((Z2.GE.Z1) .AND. (icond.NE.1)) THEN
      Icrest(n)=I-1
      icond=1
      ELSE
      END IF
      Z2=Z1
    IF (istat.NE.0) EXIT
  END DO
  Imax(n)=I-1
  CLOSE (UNIT=6)
  IF (n.NE.0) THEN
    FileWSL=FileWSLSeries(1:LEN(TRIM(FileWSLSeries)))//"."//nCh
    OPEN (UNIT=7,FILE=FileWSL,STATUS="OLD",ACTION="READ")
    J=0
    istat=0
    Z1=0.0
    DO
      J=J+1
      READ (7,*,IOSTAT=istat) Z1
      IF (istat.NE.0) EXIT
    END DO
    Jmax(n)=J-1
    CLOSE (UNIT=7)
  ELSE
  END IF
END DO

!! determine maximum I & J records for allocating bed and WSL array sizes
Imaxval=MAXVAL(Imax)
Jmaxval=MAXVAL(Jmax)

!! allocate size of array for bed coordinates and corresponding aspect and slopes of piezometric head
ALLOCATE(aspect(0:nRecords,Imaxval),BedX(0:nRecords,Imaxval),BedZ(0:nRecords,Imaxval),i_phi(0:nRecords
,Imaxval))
aspect(:,:)=0.0; BedX(:,:)=0.0; BedZ(:,:)=0.0; i_phi(:,:)=0.0

!! allocate size of array for WSLs at n=1 (allocated with a size corresponding to the first record,
n=1 and t=2s or 4s, etc)
ALLOCATE(WSLX(nRecords,Jmaxval),WSLZ(nRecords,Jmaxval))
WSLX(:,:)=0.0; WSLZ(:,:)=0.0

!! 3. BED LEVEL AND WSL INPUT DATA LOOP (Icrest, Imax, BedX, BedZ, i_phi, aspect, Jmax, WSLX and WSLZ)

!! read bed and WSL data
DO n=0,nRecords
  nT=INT(t(n))
  IF (nT.GT.99) THEN
    WRITE (nCh,'(I3)') nT
  ELSE IF (nT.GT.9) THEN
    WRITE (nCh,'(I2)') nT
  ELSE IF THEN
    WRITE (nCh,'(I1)') nT
  END IF
  FileBed=FileBedSeries(1:LEN(TRIM(FileBedSeries)))//"."//nCh
```

```
  OPEN (UNIT=6,FILE=FileBed,STATUS="OLD",ACTION="READ")
  DO I=1,Imax(n)
    READ (6,*) BedX(n,I),BedZ(n,I),i_phi(n,I),aspect(n,I)
  END DO
  CLOSE (UNIT=6)
  IF (n.NE.0) THEN
    FileWSL=FileWSLSeries(1:LEN(TRIM(FileWSLSeries)))//"."//nCh
    OPEN (UNIT=7,FILE=FileWSL,STATUS="OLD",ACTION="READ")
    DO J=1,Jmax(n)
      READ (7,*) WSLX(n,J),WSLZ(n,J)
    END DO
    CLOSE (UNIT=7)
  ELSE
  END IF
END DO

!! II.  PARAMETER INITIALIZATION

b=0.381
beta=1.0
d50=0.245/1000
n_coeff=0.01
p=e/(e+1)
miu=1E-6
rho=998
g=9.806
gamma=rho*g
PI=2*ACOS(0.0)                                                                    !!
alternative formula: PI=DACOS(-1.0d0)
deg2rad=PI/180.0
K_function=0.000153
Gs=2.75
i_zc=(-1.0)*(Gs-1)/(e+1)

!! III. DISCRETIZATION LOOP

dsGIS=dsGIS/10                                                                    !!
converts dsGIS from mm to cm

ALLOCATE(Istart(0:nRecords),Kcrest(nRecords),Kdownstream(nRecords),Kmax(nRecords),Kupstream(nRecords))
Istart(:)=2; Kcrest(:)=1; Kdownstream(:)=1; Kmax(:)=1; Kupstream(:)=1

IF (mod(ds,dsGIS).GT.0.0) THEN
  nds=ds/dsGIS+1
ELSE
  nds=ds/dsGIS
END IF
DO n=1,nRecords                                                                   !!
for each time-step

  Kdownstream(n)=(Imax(n)-Icrest(n)-1)/nds+1     !! computes number of discretized downstream nodes
(includes crest node)
  Kupstream(n)=(Icrest(n)-Istart(n))/nds         !! computes maximum number of discretized upstream
nodes
  Kmax(n)=Kupstream(n)+Kdownstream(n)            !! computes total number of discretized nodes
  Kcrest(n)=Kupstream(n)+1                       !! computes number of discretized node at crest
  Istart(n)=Icrest(n)-nds*Kupstream(n)
END DO

Kmaxval=MAXVAL(Kmax)

!! III. PARAMETER EXRACTION FOR COMPUTATIONAL NODES LOOP

!! 1. GEOMETRIC AND SEEPAGE PARAMETERS OF BED (s, X, Z, Sb, i_n, i_z)

!! allocate size of array for computational nodes (allocated with a size corresponding to the maximum
value read)
```

```
ALLOCATE(s(nRecords,Kmaxval),X(nRecords,Kmaxval),Z(nRecords,Kmaxval))
ALLOCATE(Sb(nRecords,Kmaxval),i_n(nRecords,Kmaxval),i_z(nRecords,Kmaxval))
s(:,:)=0.0; X(:,:)=0.0; Z(:,:)=0.0
Sb(:,:)=0.0
i_n(:,:)=0.0; i_z(:,:)=0.0

DO n=1,nRecords
  DO K=1,Kmax(n)
    s(n,K)=(K-1+REAL(Istart(n))/nds)*ds
    IF (K.EQ.1) THEN
      X(n,K)=BedX(n,Istart(n))
      Z(n,K)=BedZ(n,Istart(n))
      aspect(n,K)=aspect(n,Istart(n))
      Sb(n,K)=(BedZ(n,Istart(n)-1)-BedZ(n,Istart(n)+1))/(BedX(n,Istart(n)-1)-BedX(n,Istart(n)+1))
      i_z(n,K)=COS(aspect(n,Istart(n))*deg2rad)*i_phi(n,Istart(n))/100
      i_n(n,K)=COS(ATAN(Sb(n,K))+aspect(n,Istart(n))*deg2rad)*i_phi(n,Istart(n))/100
    ELSE
      X(n,K)=BedX(n,(K-1)*nds+Istart(n))
      Z(n,K)=BedZ(n,(K-1)*nds+Istart(n))
      aspect(n,K)=aspect(n,(K-1)*nds+Istart(n))
      Sb(n,K)=(BedZ(n,(K-1)*nds+Istart(n)-1)-BedZ(n,(K-1)*nds+Istart(n)+1))/ &
                & (BedX(n,(K-1)*nds+Istart(n)-1)-BedX(n,(K-1)*nds+Istart(n)+1))
      i_z(n,K)=COS(aspect(n,(K-1)*nds+Istart(n))*deg2rad)*i_phi(n,(K-1)*nds+Istart(n))/100
      i_n(n,K)=COS(ATAN(Sb(n,K))+aspect(n,(K-1)*nds+Istart(n))*deg2rad)*i_phi(n,(K-
1)*nds+Istart(n))/100
    END IF
  END DO
END DO

!! 2. INITIAL FLUVIAL PARAMETERS (Yz_s0, U_s0, Sw_z, Yz, dz)

!! allocated with the maximum record size read
ALLOCATE(Sw_z(nRecords,Kmaxval),Yz(nRecords,Kmaxval),dz(nRecords,Kmaxval))
ALLOCATE(Yz_s0(nRecords),U_s0(nRecords))
Sw_z(:,:)=0.0; Yz(:,:)=0.0; dz(:,:)=0.0
Yz_s0(:)=0.0; U_s0(:)=0.0

DO n=1,nRecords
  I=1
  J=1
  DO                                    !! WHILE loop to interpolate Yz and U at s=0 (i.e. I=1)
    IF (BedX(n,I).GT.WSLX(n,J)) EXIT
    J=J+1
  END DO
  Yz_s0(n)=(WSLZ(n,J-1)-WSLZ(n,J))/(WSLX(n,J-1)-WSLX(n,J))*(BedX(n,I)-WSLX(n,J))+WSLZ(n,J)-BedZ(n,I)
  U_s0(n)=Q(n)/(b*Yz_s0(n)*0.01)
  DO K=1,Kmax(n)
    DO
      IF (X(n,K).GT.WSLX(n,J)) EXIT
      J=J+1
    END DO
    Sw_z(n,K)=(WSLZ(n,J-1)-WSLZ(n,J))/(WSLX(n,J-1)-WSLX(n,J))
    Yz(n,K)=Sw_z(n,K)*(X(n,K)-WSLX(n,J))+WSLZ(n,J)-Z(n,K)
                                        !! interpolation
    DO
      IF (X(n,K).GT.BedX(n-1,I)) EXIT
      I=I+1
    END DO
    IF ((ABS(BedZ(n-1,I-1)-BedZ(n-1,I)).LT.0.0001).AND.(ABS(BedX(n-1,I-1)-BedX(n-1,I)).LT.0.0001))
THEN
      dz(n,K)=0.0
    ELSE
      dz(n,K)=(BedZ(n-1,I-1)-BedZ(n-1,I))*((X(n,K)-BedX(n-1,I))/(BedX(n-1,I-1)-BedX(n-1,I)))+BedZ(n-
1,I)-Z(n,K) !! interpolation
    END IF
  END DO
END DO
```

```
!! 3. MAIN FLUVIAL AND EROSION PARAMETERS

!! allocated with  maximum record size read
ALLOCATE(dn(nRecords,Kmaxval),dVb(nRecords,Kmaxval))
ALLOCATE(dndT(nRecords,Kmaxval),dqbds(nRecords,Kmaxval))
ALLOCATE(v_dn(nRecords,Kmaxval))
ALLOCATE(Sw_n(nRecords,Kmaxval))
ALLOCATE(Yn(nRecords,Kmaxval),Yn2(nRecords,Kmaxval))
ALLOCATE(Yh(nRecords,Kmaxval),Yh2(nRecords,Kmaxval),Yh3(nRecords,Kmaxval))
ALLOCATE(Yz2(nRecords,Kmaxval))
ALLOCATE(U(nRecords,Kmaxval),Fr(nRecords,Kmaxval),Rh(nRecords,Kmaxval))
ALLOCATE(Nh(nRecords,Kmaxval),Re(nRecords,Kmaxval))
ALLOCATE(EGL(nRecords,Kmaxval),Sf(nRecords,Kmaxval))
ALLOCATE(tau_bI(nRecords,Kmaxval),tau_bII(nRecords,Kmaxval),tau_bIII(nRecords,Kmaxval),tau_bIV(nRecord
s,Kmaxval))
ALLOCATE(tau_bV(nRecords,Kmaxval))
ALLOCATE(tau_b(nRecords,Kmaxval),tau_bstar(nRecords,Kmaxval))
ALLOCATE(tau_b2(nRecords,Kmaxval),tau_bstar2(nRecords,Kmaxval))
ALLOCATE(tau_EGL(nRecords,Kmaxval),tau_EGLstar(nRecords,Kmaxval),q_bstar(nRecords,Kmaxval))
ALLOCATE(U_star(nRecords,Kmaxval),Re_star(nRecords,Kmaxval))
dn(:,:)=0.0; dVb(:,:)=0.0
dndT(:,:)=0.0; dqbds(:,:)=0.0
v_dn(:,:)=0.0
Sw_n(:,:)=0.0
Yn(:,:)=0.0; Yn2(:,:)=0.0
Yh(:,:)=0.0; Yh2(:,:)=0.0; Yh3(:,:)=0.0
Yz2(:,:)=0.0
U(:,:)=0.0; Fr(:,:)=0.0; Rh(:,:)=0.0
Re(:,:)=0.0;Nh(:,:)=0.0
EGL(:,:)=0.0;  Sf(:,:)=0.0
tau_bI(:,:)=0.0; tau_bII(:,:)=0.0; tau_bIII(:,:)=0.0; tau_bIV(:,:)=0.0; tau_bV(:,:)=0.0
tau_b(:,:)=0.0; tau_bstar(:,:)=0.0
tau_b2(:,:)=0.0; tau_bstar2(:,:)=0.0
tau_EGL(:,:)=0.0; tau_EGLstar(:,:)=0.0; q_bstar(:,:)=0.0
U_star(:,:)=0.0; Re_star(:,:)=0.0


DO n=1,nRecords
  I=0
  J=0

  !! A. FLUVIAL AND EROSION PARAMETERS (dn, dVb, dndT, dqbds, v_dn, Yn, S_wn, Yn2, Yh, Yh2, Yh3, Yz2,
U, Fr, Rh, Nh, Re, EGL)
  DO K=1,Kmax(n)
    angle=0.0                                          !! for bed level WHILE loop
    vec_n(:)=0.0
    DO                                                 !! check that angle between bed slope and
normal approaches 90 degrees for bed level of previous time-step
      IF ((vec_n(1)+vec_n(2)*Sb(n,K)).LT.0.0) EXIT
      I=I+1
      vec_n(1)=BedX(n-1,I)-X(n,K)                      !! vector component in x-direction
      vec_n(2)=BedZ(n-1,I)-Z(n,K)                      !! vector component in z-direction
      dn(n,K)=SQRT(vec_n(1)*vec_n(1)+vec_n(2)*vec_n(2))
    END DO
    I=I-1                                              !! recompute vectors and normal distance
    vec_n(1)=BedX(n-1,I)-X(n,K)                        !! vector component in x-direction
    vec_n(2)=BedZ(n-1,I)-Z(n,K)                        !! vector component in z-direction
    IF ((ABS(vec_n(1)).LT.0.0001).AND.(ABS(vec_n(2)).LT.0.0001)) THEN     !! discards very small
erosions
      dn(n,K)=0.0
    ELSE
      dn(n,K)=SQRT(vec_n(1)*vec_n(1)+vec_n(2)*vec_n(2))
      angle=ACOS((vec_n(1)+vec_n(2)*Sb(n,K))/(dn(n,K)*SQRT(1+Sb(n,K)*Sb(n,K))))
      dn(n,K)=dn(n,K)*SIN(angle)         !! computes distance at a right angle with soil boundary
      IF (vec_n(2).LT.0.0) THEN
        dn(n,K)=(-1)*dn(n,K)
```

```
      ELSE
      END IF
    END IF
    dVb(n,K)=dn(n,K)*ds*(1-p)
    dndT(n,K)=dn(n,K)*0.01/((t(n)-t(n-1)))
    dqbds(n,K)=(1-p)*dndT(n,K)
    v_dn(n,K)=(K_function*i_n(n,K))*(-1.0)       !! v_dn is positive upwards
    angle=0.0                                    !! for WSL WHILE loop
    DO          !! checks that angle between bed slope and normal approaches 90 degrees for WSL
      IF ((vec_n(1)+vec_n(2)*Sb(n,K)).LT.0.0) EXIT
      J=J+1
      vec_n(1)=WSLX(n,J)-X(n,K)          !! vector component in x-direction
      vec_n(2)=WSLZ(n,J)-Z(n,K)          !! vector component in z-direction
    END DO
    J=J-1                                !! recompute vectors and normal distance
    Sw_n(n,K)=(WSLZ(n,J-1)-WSLZ(n,J))/(WSLX(n,J-1)-WSLX(n,J))
    vec_n(1)=WSLX(n,J)-X(n,K)            !! vector component in x-direction
    vec_n(2)=WSLZ(n,J)-Z(n,K)            !! vector component in z-direction
    Yn(n,K)=SQRT(vec_n(1)*vec_n(1)+vec_n(2)*vec_n(2))
    angle=ACOS((vec_n(1)+vec_n(2)*Sb(n,K))/(Yn(n,K)*SQRT(1+Sb(n,K)*Sb(n,K))))
    Yn(n,K)=Yn(n,K)*SIN(angle)           !! computes distance at a right angle with soil boundary
    Yn2(n,K)=Yz(n,K)*(ATAN(Sb(n,K))-ATAN(Sw_n(n,K)))/(COS(ATAN(Sb(n,K)))*(Sb(n,K)-Sw_n(n,K)))
    Yh(n,K)=Yn(n,K)*COS(ATAN(Sb(n,K)))
    Yh2(n,K)=Yn(n,K)*(SIN(ATAN(Sb(n,K)))-SIN(ATAN(Sw_n(n,K))))/(ATAN(Sb(n,K))-ATAN(Sw_n(n,K)))
    Yh3(n,K)=Yz(n,K)/(1+TAN(0.5*(ATAN(Sw_n(n,K))+ATAN(Sw_z(n,K))))* &
    & (COS(ATAN(Sb(n,K)))-COS(ATAN(Sw_n(n,K))))/(SIN(ATAN(Sw_n(n,K)))-SIN(ATAN(Sb(n,K)))))
    Yz2(n,K)=Yn(n,K)*COS(ATAN(Sb(n,K)))*(Sb(n,K)-Sw_n(n,K))/(ATAN(Sb(n,K))-ATAN(Sw_n(n,K)))
    IF (K.LT.Kcrest(n)) THEN
      U(n,K)=Q(n)/(b*Yz(n,K)/100)
      Fr(n,K)=U(n,K)/SQRT(g*Yz(n,K)/100)
      Rh(n,K)=(Yz(n,K)/(b*100))*(b*100-Yz(n,K))
    ELSE
      U(n,K)=Q(n)/(b*Yn(n,K)/100)
      Fr(n,K)=U(n,K)/SQRT(g*Yn(n,K)/100)
      Rh(n,K)=(Yn(n,K)/(b*100))*(b*100-Yn(n,K))
    END IF
    Nh(n,K)=1+beta*v_dn(n,K)/(K_function*(1-p))
    Re(n,K)=U(n,K)*4*Rh(n,K)*0.01/miu
    EGL(n,K)=Yh(n,K)+Z(n,K)+((U(n,K))**2/(2*g))*100      !! Yh(n,K) vs. Yn(n,K)
  END DO

  !! B. BED SHEAR STRESS PARAMETERS (tau_bI, tau_bIV, tau_bV, tau_bII, tau_bIII, tau_b2, Sf, tau_b)
  Ucounter=1
  DO K=1,Kupstream(n)                                    !! upstream discretized nodes
    tau_bI(n,K)=rho*g*Yz(n,K)*0.01*SIN(ATAN(Sb(n,K)))
    tau_bIV(n,K)=(-1)*rho*U(n,K)*v_dn(n,K)
    IF (n.EQ.1) THEN
      tau_bV(n,K)=0.5*U(n,K)*(-1)*rho*Yz(n,K)*0.01/dT !! average of velocity of current and previous
time-step
    ELSE
    END IF
    IF (K.EQ.1) THEN
      IF (n.NE.1) THEN
        DO
          IF (s(n-1,Ucounter).GT.s(n,K)) EXIT
          Ucounter=Ucounter+1
        END DO
        IF (Ucounter.EQ.1) THEN
          tau_bV(n,K)=(U(n,K)-((U(n-1,Ucounter)-U_s0(n-1))*s(n,K)/s(n-1,Ucounter)+U_s0(n-1)))*(-
1)*rho*Yz(n,K)*0.01/dT
        ELSE
          tau_bV(n,K)=(U(n,K)-(((U(n-1,Ucounter)-U(n-1,Ucounter-1))*(s(n,K)-s(n-1,Ucounter-
1))/ds)+U(n-1,Ucounter-1))) &
                      & *(-1)*rho*Yz(n,K)*0.01/dT
        END IF
      ELSE
      END IF
```

```
      tau_bII(n,K)=(-1)*rho*g*Yz(n,K)*0.01*(COS(ATAN(Sb(n,K)))**2)*(Yz(n,K+1)-Yz(n,K))/ds
      tau_bIII(n,K)=(-1)*rho*Yz(n,K)*U(n,K)*(U(n,K+1)-U(n,K))/ds
      tau_b2(n,K)=rho*(g*Yz(n,K)*0.01*SIN(ATAN(Sb(n,K)))-(g*Yz(n,K)*0.01*(Yz(n,K+1)-Yz(n,K))/ds)* &
                                & (COS(ATAN(Sb(n,K)))-beta*U(n,K)**2/(g*Yz(n,K)*0.01))-
2*beta*U(n,K)*v_dn(n,K))
      Sf(n,K)=(EGL(n,K)-EGL(n,K+1))/ds
    ELSE
      IF (n.NE.1) THEN
        DO
          IF (s(n-1,Ucounter).GT.s(n,K)) EXIT
          Ucounter=Ucounter+1
        END DO
        tau_bV(n,K)=(U(n,K)-(((U(n-1,Ucounter)-U(n-1,Ucounter-1))*(s(n,K)-s(n-1,Ucounter-1))/ds)+U(n-
1,Ucounter-1))) &
                  & *(-1)*rho*Yz(n,K)*0.01/dT
      ELSE
      END IF
      IF (K.EQ.Kupstream(n)) THEN
        tau_bII(n,K)=(-1)*rho*g*Yz(n,K)*0.01*(COS(ATAN(Sb(n,K)))**2)*(Yn(n,K+1)-Yz(n,K-1))/(2*ds)
        tau_b2(n,K)=rho*(g*Yz(n,K)*0.01*SIN(ATAN(Sb(n,K)))-(g*Yz(n,K)*0.01*(Yn(n,K+1)-Yz(n,K-
1))/(2*ds))* &
                                & (COS(ATAN(Sb(n,K)))-beta*U(n,K)**2/(g*Yz(n,K)*0.01))-
2*beta*U(n,K)*v_dn(n,K))
      ELSE               !! other discretized nodes (not at the crest)
        tau_bII(n,K)=(-1)*rho*g*Yz(n,K)*0.01*(COS(ATAN(Sb(n,K)))**2)*(Yz(n,K+1)-Yz(n,K-1))/(2*ds)
        tau_b2(n,K)=rho*(g*Yz(n,K)*0.01*SIN(ATAN(Sb(n,K)))-(g*Yz(n,K)*0.01*(Yz(n,K+1)-Yz(n,K-
1))/(2*ds))* &
                                & (COS(ATAN(Sb(n,K)))-beta*U(n,K)**2/(g*Yz(n,K)*0.01))-
2*beta*U(n,K)*v_dn(n,K))
      END IF
      tau_bIII(n,K)=(-1)*rho*Yz(n,K)*U(n,K)*(U(n,K+1)-U(n,K-1))/(2*ds)
      Sf(n,K)=(EGL(n,K-1)-EGL(n,K+1))/(2*ds)
    END IF
    tau_b(n,K)=tau_bI(n,K)+tau_bII(n,K)+tau_bIII(n,K)+tau_bIV(n,K)+tau_bV(n,K)
  END DO
  DO K=Kcrest(n),Kmax(n)                                    !! downstream nodes
    tau_bI(n,K)=rho*g*Yn(n,K)*0.01*SIN(ATAN(Sb(n,K)))
    tau_bIV(n,K)=(-1)*rho*U(n,K)*v_dn(n,K)
    IF (n.EQ.1) THEN
      tau_bV(n,K)=0.5*U(n,K)*(-1)*rho*Yn(n,K)*0.01/dT !! average of velocity of current and previous
time-step
    ELSE
      DO
        IF (s(n-1,Ucounter).GT.s(n,K)) EXIT
        Ucounter=Ucounter+1
      END DO
      tau_bV(n,K)=(U(n,K)-(((U(n-1,Ucounter)-U(n-1,Ucounter-1))*(s(n,K)-s(n-1,Ucounter-1))/ds)+U(n-
1,Ucounter-1))) &
                        & *(-1)*rho*Yn(n,K)*0.01/dT
    END IF
    IF (K.EQ.Kmax(n)) THEN
      tau_bII(n,K)=(-1)*rho*g*Yn(n,K)*0.01*(COS(ATAN(Sb(n,K)))**2)*(Yn(n,K)-Yn(n,K-1))/ds
      tau_bIII(n,K)=(-1)*rho*Yn(n,K)*U(n,K)*(U(n,K)-U(n,K-1))/ds

      tau_b2(n,K)=rho*(g*Yn(n,K)*0.01*SIN(ATAN(Sb(n,K)))-(g*Yn(n,K)*0.01*(Yn(n,K)-Yn(n,K-1))/ds)* &
                        & (COS(ATAN(Sb(n,K)))-beta*U(n,K)**2/(g*Yn(n,K)*0.01))-
2*beta*U(n,K)*v_dn(n,K))
      Sf(n,K)=(EGL(n,K-1)-EGL(n,K))/ds
    ELSE
      IF (K.EQ.Kcrest(n)) THEN                              !! uses Yz(n,K) for node upstream of crest
        tau_bII(n,K)=(-1)*rho*g*Yn(n,K)*0.01*(COS(ATAN(Sb(n,K)))**2)*(Yn(n,K+1)-Yz(n,K-1))/(2*ds)
        tau_b2(n,K)=rho*(g*Yn(n,K)*0.01*SIN(ATAN(Sb(n,K)))-(g*Yn(n,K)*0.01*(Yn(n,K+1)-Yz(n,K-
1))/(2*ds))* &
                                & (COS(ATAN(Sb(n,K)))-beta*U(n,K)**2/(g*Yn(n,K)*0.01))-
2*beta*U(n,K)*v_dn(n,K))
      ELSE
        tau_bII(n,K)=(-1)*rho*g*Yn(n,K)*0.01*(COS(ATAN(Sb(n,K)))**2)*(Yn(n,K+1)-Yn(n,K-1))/(2*ds)
```

```
        tau_b2(n,K)=rho*(g*Yn(n,K)*0.01*SIN(ATAN(Sb(n,K)))-(g*Yn(n,K)*0.01*(Yn(n,K+1)-Yn(n,K-
1))/(2*ds))* &
                                & (COS(ATAN(Sb(n,K)))-beta*U(n,K)**2/(g*Yn(n,K)*0.01))-
2*beta*U(n,K)*v_dn(n,K))
      END IF
      tau_bIII(n,K)=(-1)*rho*Yn(n,K)*U(n,K)*(U(n,K+1)-U(n,K-1))/(2*ds)
      Sf(n,K)=(EGL(n,K-1)-EGL(n,K+1))/(2*ds)
    END IF
    tau_b(n,K)=tau_bI(n,K)+tau_bII(n,K)+tau_bIII(n,K)+tau_bIV(n,K)+tau_bV(n,K)
  END DO

  !! C. DIMENSIONLESS MOBILITY AND TRANSPORT AND GRAIN PARAMETERS (tau_bstar, tau_bstar2, tau_EGL,
tau_EGLstar, U_star, Re_star)
  DO K=1,Kmax(n)
    tau_bstar(n,K)=tau_b(n,K)/(gamma*d50*(Gs-1)*(1-i_z(n,K)/i_zc))
    tau_bstar2(n,K)=tau_b2(n,K)/(gamma*d50*(Gs-1)*(1-i_z(n,K)/i_zc))
    tau_EGL(n,K)=gamma*Sf(n,K)*Rh(n,K)/100
    tau_EGLstar(n,K)=tau_EGL(n,K)/(gamma*d50*(Gs-1)*(1-i_z(n,K)/i_zc))
    q_bstar(n,K)=dqbds(n,K)/SQRT((Gs-1)*g*(d50**3))
    tau_cmplx=tau_b(n,K)
    IF (tau_b(n,K).LT.0) THEN
      U_star(n,K)=SQRT(CABS(tau_cmplx)/rho)*(-1.0)
    ELSE
      U_star(n,K)=SQRT(tau_b(n,K)/rho)
    END IF
    Re_star(n,K)=U_star(n,K)*d50/miu
  END DO
END DO

!! 4. MANNING'S EQUATION NORMAL FLOW DEPTH
ALLOCATE(Ynfd(nRecords,Kmaxval))
Ynfd(:,:)=0.0001

CALL MANNING(b,n_coeff,K,Kmax,Kmaxval,n,nRecords,Q,Sb,Ynfd)

ALLOCATE(Yc(nRecords))
ALLOCATE(curve(nRecords,Kmaxval),region(nRecords,Kmaxval))
Yc(:)=0.0
curve(:,:)=" "; region(:,:)=" "

!! loop to determine node region and gradually varied flow curve type
DO n=1,nRecords
  Yc(n)=100*(Q(n)*Q(n)/(b*b*g))**(1.0/3.0)
  DO K=1,Kupstream(n)                                          !! adverse slopes
    region(n,K)="    US"                 !! upstream region
    IF (Yz(n,K).GT.Yc(n)) THEN
      curve(n,K)="A-2"
    ELSE
      curve(n,K)="A-3"
    END IF
  END DO
  DO K=Kcrest(n),Kcrest(n)                !! horizontal slope
    region(n,K)=" Re_Cr"                  !! crest region
    IF (Yz(n,K).GT.Yc(n)) THEN
      curve(n,K)="H-2"
    ELSE
      curve(n,K)="H-3"
    END IF
  END DO
  DO K=Kcrest(n)+1,Kmax(n)                !! recirculation zone and hydrostatic pressure section
    IF (K.GE.(Kmax(n)-3)) THEN
      region(n,K)="DS_Toe"                !! last four nodes
    ELSE IF (ABS(Sb(n,K)-Sb(n,K-1)).LT.(0.002).AND.ABS(Sb(n,K+1)-Sb(n,K)).LT.(0.002)) THEN
      region(n,K)="  Hydr"                          !! hydrostatic pressure section
    ELSE
      region(n,K)="    Re"                          !! recirculation zone
    END IF
```

```
    IF (ABS(Ynfd(n,K)-Yc(n)).LT.0.01) THEN        !! slope is critical
      IF(Yn(n,K).GT.Yc(n)) THEN
        curve(n,K)="C-1"
      ELSE
        curve(n,K)="C-3"
      END IF
    ELSE IF (Ynfd(n,K).GT.Yc(n)) THEN            !! slope is mild
      IF (Yn(n,K).GT.Yc(n).AND.(Yn(n,K).LT.Ynfd(n,K))) THEN
        curve(n,K)="M-2"
      ELSE
        curve(n,K)="M-3"
      END IF
    ELSE                !! slope is steep (i.e. Yc(n) is greater than Ynfd(n))
      IF (Yn(n,K).GT.Yc(n)) THEN
        curve(n,K)="S-1"
      ELSE IF ((Yn(n,K).GT.Ynfd(n,K)).AND.(Yn(n,K).LT.Yc(n))) THEN
        curve(n,K)="S-2"
      ELSE
        curve(n,K)="S-3"
      END IF
    END IF
  END DO
END DO

!! IV.  DATA OUTPUT

!! header data
OPEN (UNIT=9,FILE=FileGIS,STATUS="NEW",ACTION="WRITE")
WRITE(9,90)
90 FORMAT (T3,'K',T6,'s[cm]',T12,'L[cm]',T18,'region[-
]',T31,'x[cm]',T40,'z[cm]',T47,'t[s]',T52,'Q[m3/s]', &
                          &
T60,'Rh[cm]',T67,'Yc[cm]',T74,'Yn[cm]',T81,'Yn2[cm]',T89,'Ynfd[cm]',T98,'Yh[cm]',T105,'Yh2[cm]', &
            & T113,'Yh3[cm]',T121,'Yz[cm]',T128,'Yz2[cm]',T136,'U[m/s]',T143,'Fr[-]',T152,'Re[-
]',T158,'curve[-]', &
            &
T168,'dn[cm]',T177,'dVb[cm2]',T187,'dz[cm]',T194,'dn/dt[m/s]',T205,'dqb/ds[m/s]',T217,'EGL[cm]',T228,
&
            & 'Sb[-]',T237,'Sf[-]',T244,'Sw_n[-]',T253,'Sw_z[-]',T262,'vdn[m/s]',T273,'Nh[-
]',T279,'iratio[-]',T289, &
            &
'tau_EGL[Pa]',T301,'tau_b[Pa]',T311,'tau_b2[Pa]',T322,'tau*_EGL[Pa]',T335,'tau*_b[Pa]',T346,'tau*_b2[P
a]', &
            & T358,'q*_b[-
]',T366,'tau_b_I[Pa]',T378,'tau_b_II[Pa]',T391,'tau_b_III[Pa]',T405,'tau_b_IV[Pa]',T418, &
            & 'tau_b_V[Pa]',T430,'U*[m/s]',T441,'Re*[-]',T448,'i_n[-]',T455,'i_z[-]',T462,'i_phi[-
]',T471,'aspect[deg]')

DO n=1,nRecords
  DO K=1,Kmax(n)
    WRITE (9,91) K,s(n,K),(K-1)*ds,region(n,K),X(n,K),Z(n,K),t(n),Q(n),Rh(n,K),Yc(n),Yn(n,K),Yn2(n,K),
&
                &
Ynfd(n,K)*100,Yh(n,K),Yh2(n,K),Yh3(n,K),Yz(n,K),Yz2(n,K),U(n,K),Fr(n,K),Re(n,K),curve(n,K), &
            &
dn(n,K),dVb(n,K),dz(n,K),dndT(n,k),dqbds(n,K),EGL(n,K),Sb(n,K),Sf(n,K),Sw_n(n,K),Sw_z(n,K), &
            &
v_dn(n,K),Nh(n,K),i_z(n,K)/i_zc,tau_EGL(n,K),tau_b(n,K),tau_b2(n,K),tau_EGLstar(n,K),tau_bstar(n,K), &
            &
tau_bstar2(n,K),q_bstar(n,K),tau_bI(n,K),tau_bII(n,K),tau_bIII(n,K),tau_bIV(n,K),tau_bV(n,K), &
            & U_star(n,K),Re_star(n,K),i_n(n,K),i_z(n,K),i_phi(n,K)/100,aspect(n,K)
    91 FORMAT
(T1,I3,T5,F6.2,T12,F5.1,T21,A6,T28,F8.3,T37,F8.3,T46,F5.1,T52,F7.5,T60,F6.3,T67,F6.3,T74,F6.3, &
                &
T82,F6.3,T90,F7.3,T98,F6.3,T106,F6.3,T114,F6.3,T121,F6.3,T129,F6.3,T137,F5.3,T143,F5.3,T149,E8.2, &
            &
T163,A3,T167,F7.3,T175,E10.2,T186,F7.3,T195,E9.2,T207,E9.2,T218,F6.3,T225,F8.4,T234,F8.4,T243,F8.4, &
```

```
            &
T252,F8.4,T261,E9.2,T271,F7.3,T281,F7.3,T294,F6.1,T304,F6.1,T315,F6.1,T327,F7.2,T338,F7.2,T350,F7.2, &
            &
T358,F7.1,T371,F6.1,T384,F6.1,T398,F6.1,T411,F6.1,T423,F6.1,T430,F7.4,T438,E9.2,T448,F6.3,T455,F6.3, &
            & T464,F6.3,T477,F5.1)
  END DO
END DO

CLOSE (UNIT=9)

END PROGRAM erosion

!! *********MANNING'S EQUATION************

SUBROUTINE MANNING(bm,n_coeffm,Km,Kmaxm,Kmaxvalm,nm,nRecordsm,Qm,Sbm,Ym)

!! calculates normal flow depth using Manning's equation

!! area:        cross-sectional area of overtopping flow [m^2]
!! bm:          flume width ("b" in main program) [m]
!! eps:         error used in iteration [m]
!! incr:        increment used in iteration [m]
!! LHS1:        computed LHS of Manning equation [m]
!! n_coeffm:    Manning's coefficient ("n_coeff" in main program) [FF]
!! Qm:          overtopping flow "Q" in main program [m^3/s]
!! Rh:          hydraulic radius to account for side wall effects, Vanoni and Brooks (1957) (used to
avoid "negative numbers raised to non-integer powers") [m]
!! S:           bed slope at discretized node (used to avoid "negative numbers raised to non-integer
powers") [RAD]
!! Sbm:         bed slope at discretized node ("Sb" in main program) [RAD]
!! Y:           normal flow depth (used to avoid "negative numbers raised to non-integer powers") [m]
!! Ym:          normal flow depth ("Ynfd" in main program) [m]
!! ITER:        counter for iteration used to computed Ym [INT]
!! Km:          counter for discretized bed nodes ("K" in main program) [INT]
!! Kmaxm:       number of discretized bed nodes ("Kmaxm" in main program) [INT]
!! Kmaxvalm:    maximum value of discretized bed nodes in entire array ("Kmaxval" in main program)
[INT]
!! nm:          counter for time-step ("n" in main program) [INT]
!! nRecordsm:   number of flow records (i.e. number of time-steps) ("nRecords" in main program) [INT]

IMPLICIT NONE

REAL*4, INTENT(IN) :: bm,n_coeffm
REAL*4, INTENT(IN), DIMENSION (nRecordsm) :: Qm
REAL*4, INTENT(IN), DIMENSION (nRecordsm,Kmaxvalm) :: Sbm
REAL*4, INTENT(INOUT), DIMENSION (nRecordsm,Kmaxvalm) :: Ym
REAL*4 area,LHS,LHS1,LHS2,slope,Ym1,Ym2
COMPLEX Rh

INTEGER, INTENT(IN) :: Km,Kmaxvalm,nm,nRecordsm
INTEGER, INTENT(IN), DIMENSION (nRecordsm) :: Kmaxm
INTEGER*4 ITER

DO nm=1,nRecordsm
  DO Km=1,Kmaxm(nm)
    ITER=0
    area=0.0; Rh=0.0; slope=0.0
        LHS=0.0; LHS1=0.0; LHS2=0.0
        Ym1=0.0; Ym2=0.0
    DO
      IF ((ABS(LHS-1.0).LT.0.0001).OR.(ABS(Ym(nm,Km)-Ym1).LT.0.00001).OR.(Sbm(nm,Km).LE.0)) EXIT
      Ym1=Ym(nm,Km)
      area=bm*Ym1
      Rh=(Ym1/bm)*(bm-Ym1)
      LHS1=sqrt(Sbm(nm,Km))*area*(Rh**(2.0/3.0))/(Qm(nm)*n_coeffm)
      Ym2=Ym1+0.00001
      area=bm*Ym2
```

```
      Rh=(Ym2/bm)*(bm-Ym2)
      LHS2=sqrt(Sbm(nm,Km))*area*(Rh**(2.0/3.0))/(Qm(nm)*n_coeffm)
      slope=(LHS2-LHS1)/(Ym2-Ym1)
      Ym(nm,Km)=0.5*(Ym2+((1-LHS2+Ym2*slope)/slope))
      area=bm*Ym(nm,Km)
      Rh=(Ym(nm,Km)/bm)*(bm-Ym(nm,Km))
      LHS=sqrt(Sbm(nm,Km))*area*(Rh**(2.0/3.0))/(Qm(nm)*n_coeffm)
      ITER=ITER+1
    END DO
    IF (Sbm(nm,Km).LE.0) THEN
      Ym(nm,Km)=99
    ELSE
    END IF
  END DO
END DO

END SUBROUTINE
```

Appendix F

2-D Overtopping Tests: Data and Results

F.1 Steady-State Tests: Piezometric and PWP Measurements

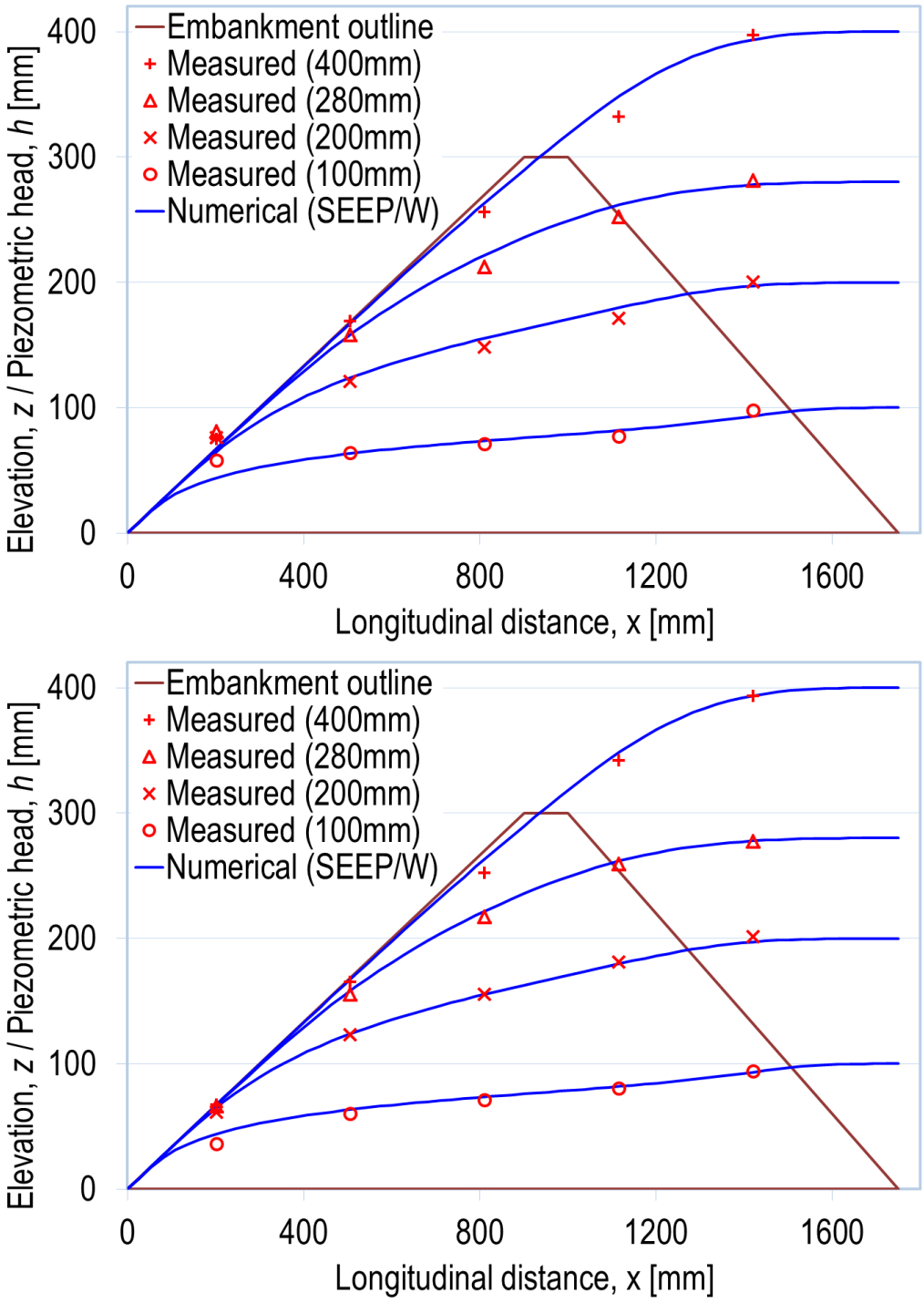

Figure F-1: Comparison between experimental and numerical piezometric head at embankment foundation for undrained configuration shown for four WSLs (in parenthesis) (above) Test No. 6 (below) Test No. 8

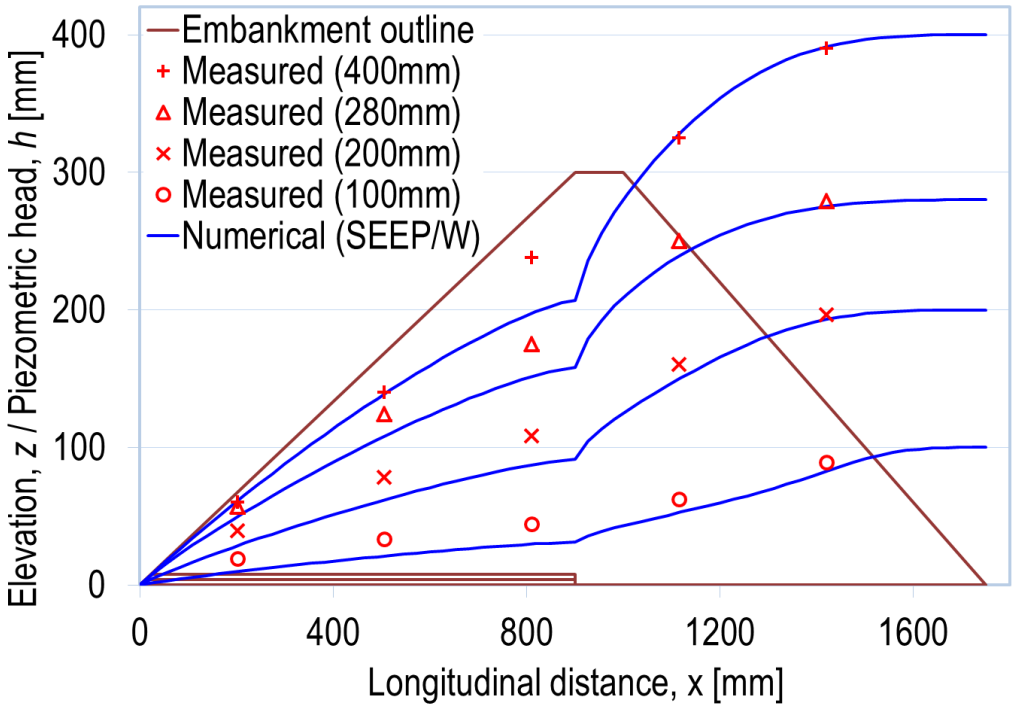

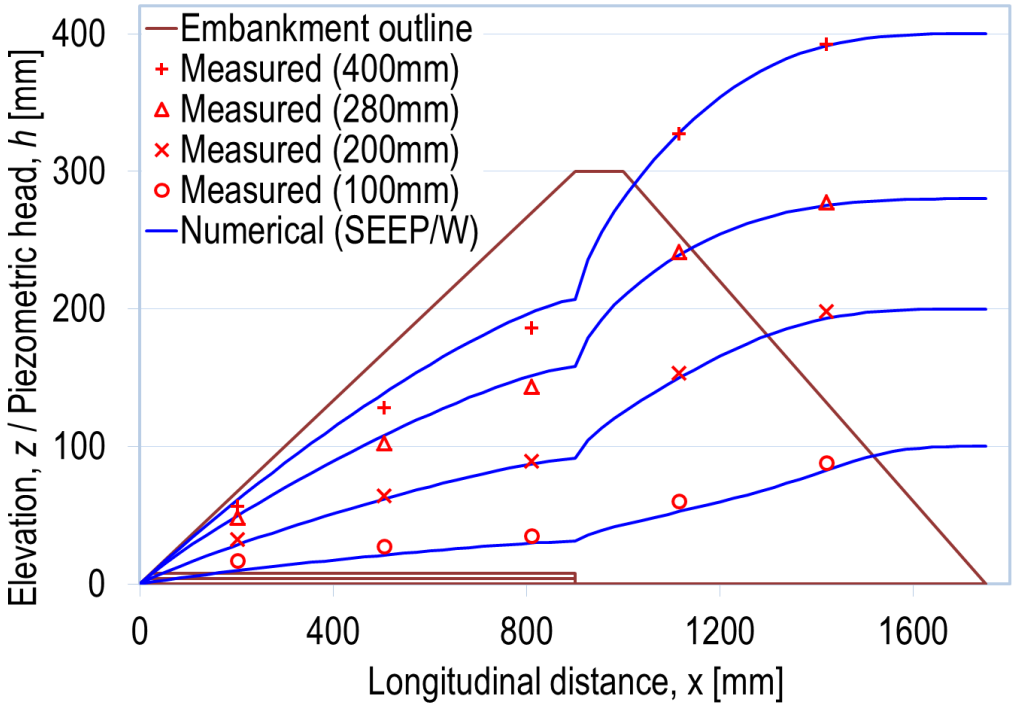

Figure F-2: Comparison between experimental and numerical piezometric head at embankment foundation for drained configuration shown for four WSLs (in parenthesis) (above) Test No. 7 (below) Test No. 10

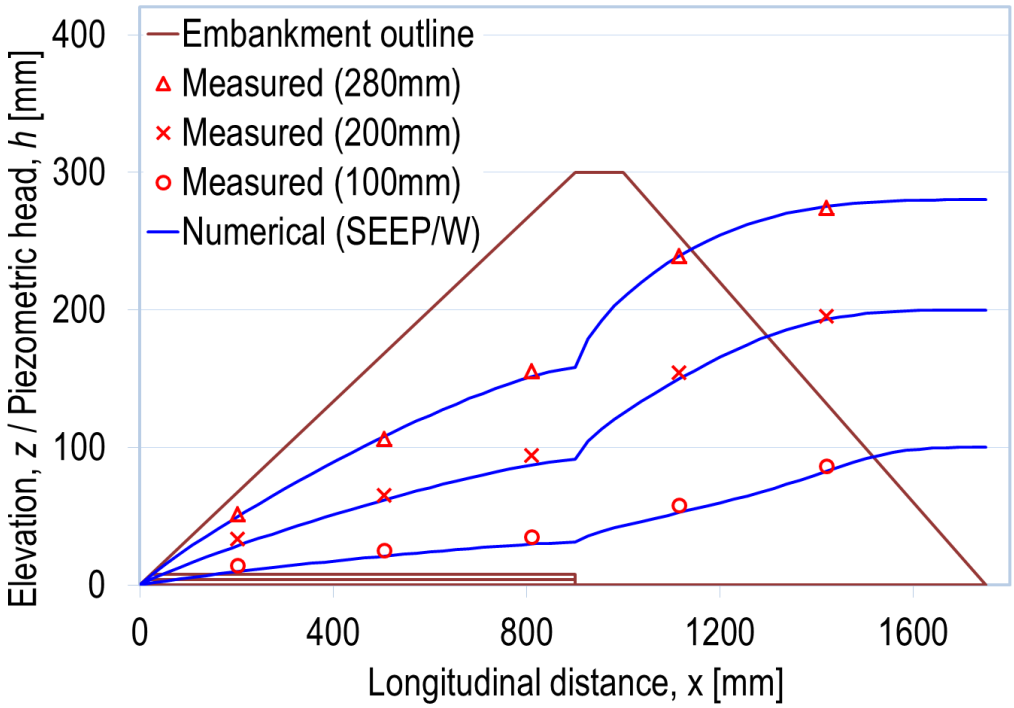

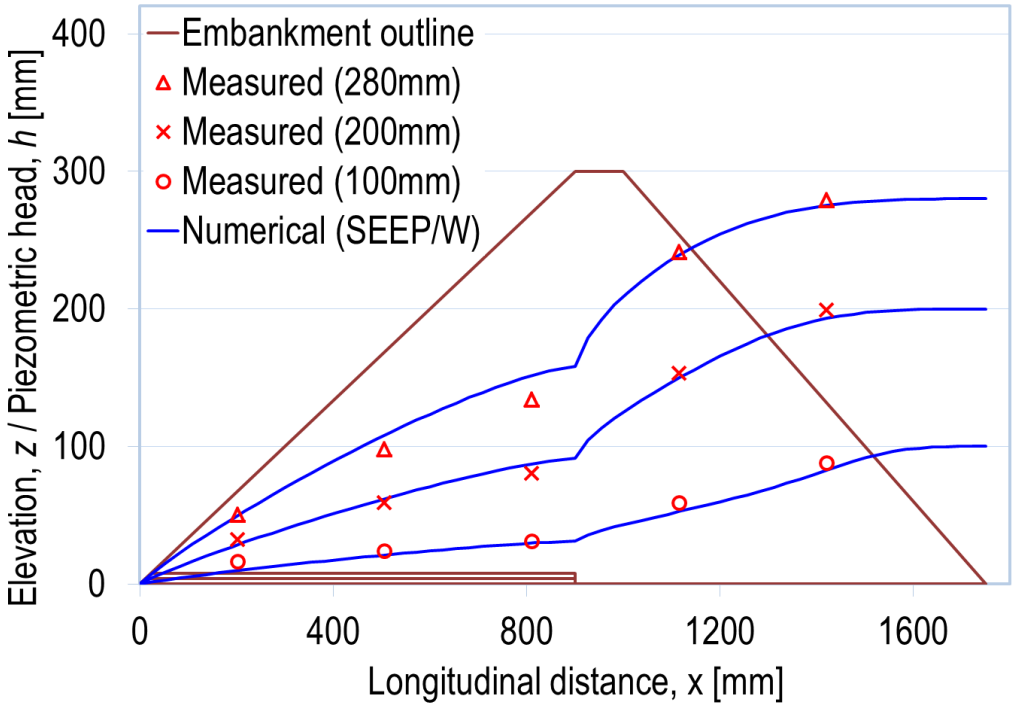

Figure F-3: Comparison between experimental and numerical piezometric head at embankment foundation for dry-drain configuration shown for four WSLs (in parenthesis) (above) Test No. 12 (below) Test No. 13

Table F-1: Comparison between experimental and numerical PWP for steady-state tests (η_r = 100mm)

TTPA No.	u_w [kPa]								
	No Drain			Drain			Drain, dry		
	Experimental†	Numerical	Δu_w	Experimental‡	Numerical	Δu_w	Experimental§	Numerical	Δu_w
1	-0.162	-0.068	-0.094	-0.320	-0.445	0.125	-0.404	-0.445	0.042
2	-0.105	-0.025	-0.080	-0.350	-0.423	0.073	-0.460	-0.423	-0.037
3	-0.008	0.033	-0.040	-0.299	-0.375	0.077	-0.292	-0.375	0.083
4	0.105	0.101	0.003	-0.268	-0.312	0.044	-0.321	-0.312	-0.010
5A	0.113	0.143	-0.030	-0.081	-0.260	0.178	-0.349	-0.260	-0.089
5B	0.001	0.143	-0.142	-0.224	-0.260	0.035	-0.276	-0.260	-0.017
6	0.093	0.182	-0.089	-0.063	-0.162	0.099	-0.182	-0.162	-0.020
7	-0.864	-0.819	-0.045	-1.093	-1.221	0.129	-1.316	-1.221	-0.094
8	*	-0.794	-	-1.155	-1.193	0.039	-1.198	-1.193	-0.005
9	*	-0.775	-	-1.087	-1.170	0.082	-1.208	-1.170	-0.038
10	-0.550	-0.737	0.187	-1.192	-1.111	-0.081	-0.964	-1.111	0.147
11	-0.729	-0.703	-0.026	-1.008	-1.036	0.028	-0.995	-1.036	0.041
12	-1.222	-1.174	-0.048	-1.358	-1.476	0.118	-1.360	-1.476	0.116
13	-1.407	-1.528	0.121	-1.794	-1.899	0.105	-1.897	-1.899	0.002
14	-1.603	-1.606	0.004	-1.965	-1.959	-0.006	-1.972	-1.959	-0.013
15	-1.676	-1.687	0.012	-1.937	-2.019	0.083	-2.051	-2.019	-0.031

†Test No. 10; ‡Test No. 8; §Test No. 13; *malfunctions in data acquisition system led to no measurements being recorded

Table F-2: Comparison between experimental and numerical PWP for steady-state tests (η_r = 200mm)

TTPA No.	u_w [kPa]								
	No Drain			Drain			Drain, dry		
	Experimental†	Numerical	Δu_w	Experimental‡	Numerical	Δu_w	Experimental§	Numerical	Δu_w
1	0.238	0.304	-0.067	-0.065	-0.169	0.103	-0.163	-0.169	0.006
2	0.442	0.471	-0.029	-0.037	-0.075	0.038	-0.159	-0.075	-0.084
3	0.619	0.621	-0.003	0.071	0.035	0.036	0.056	0.035	0.020
4	0.762	0.836	-0.074	0.218	0.221	-0.003	0.138	0.221	-0.083
5A	0.936	0.966	-0.030	0.544	0.372	0.172	0.217	0.372	-0.155
5B	0.883	0.966	-0.082	0.371	0.372	-0.001	0.289	0.372	-0.083
6	1.028	1.083	-0.055	0.725	0.646	0.079	0.598	0.646	-0.048
7	-0.201	-0.164	-0.037	-0.672	-0.738	0.067	-0.925	-0.738	-0.187
8	-0.305	-0.084	-0.220	-0.692	-0.655	-0.037	-0.758	-0.655	-0.102
9	0.025	-0.025	0.050	-0.570	-0.586	0.016	-0.712	-0.586	-0.126
10	0.116	0.092	0.024	-0.540	-0.415	-0.125	-0.336	-0.415	0.079
11	0.197	0.201	-0.005	-0.206	-0.196	-0.010	-0.161	-0.196	0.035
12	-0.252	-0.219	-0.033	-0.424	-0.516	0.092	-0.389	-0.516	0.127
13	-0.549	-0.709	0.160	-1.169	-1.204	0.035	-1.282	-1.204	-0.078
14	-0.727	-0.745	0.018	-1.244	-1.189	-0.055	-1.259	-1.189	-0.069
15	-0.755	-0.788	0.032	-1.397	-1.175	-0.222	-1.229	-1.175	-0.054

†Test No. 10; ‡Test No. 8; §Test No. 13

Table F-3: Comparison between experimental and numerical PWP for steady-state tests (η_r = 280mm)

TTPA No.	u_w [kPa]								
	No Drain			Drain			Drain, dry		
	Experimental†	Numerical	Δu_w	Experimental‡	Numerical	Δu_w	Experimental§	Numerical	Δu_w
1	0.346	0.381	-0.035	0.191	0.138	0.054	0.115	0.138	-0.023
2	0.665	0.671	-0.006	0.275	0.311	-0.035	0.191	0.311	-0.120
3	0.960	0.948	0.012	0.443	0.492	-0.049	0.459	0.492	-0.032
4	1.292	1.384	-0.092	0.733	0.813	-0.081	0.667	0.813	-0.147
5A	1.614	1.639	-0.025	1.206	1.063	0.143	0.856	1.063	-0.206
5B	1.609	1.639	-0.030	0.990	1.063	-0.072	0.930	1.063	-0.133
6	1.818	1.845	-0.027	1.549	1.465	0.084	1.409	1.465	-0.056
7	0.196	0.254	-0.058	-0.238	-0.195	-0.042	-0.475	-0.195	-0.279
8	0.182	0.425	-0.244	-0.208	-0.047	-0.161	-0.245	-0.047	-0.198
9	0.570	0.551	0.020	-0.024	0.078	-0.102	-0.135	0.078	-0.213
10	0.685	0.796	-0.111	0.139	0.380	-0.242	0.398	0.380	0.017
11	1.011	1.006	0.005	0.662	0.733	-0.072	0.767	0.733	0.034
12	0.647	0.682	-0.035	0.642	0.578	0.064	0.716	0.578	0.138
13	-0.103	-0.007	-0.096	-0.474	-0.381	-0.092	-0.553	-0.381	-0.172
14	0.031	0.045	-0.014	-0.404	-0.243	-0.161	-0.404	-0.243	-0.161
15	0.128	0.109	0.019	-0.365	-0.054	-0.311	-0.188	-0.054	-0.134

†Test No. 10; ‡Test No. 8; §Test No. 13

Table F-4: Comparison between experimental and numerical PWP for steady-state tests (η_r = 400mm)

TTPA No.	u_w [kPa]					
	No Drain			Drain		
	Experimental†	Numerical	Δu_w	Experimental‡	Numerical	Δu_w
1	0.367	0.391	-0.024	0.392	0.327	0.065
2	0.699	0.707	-0.008	0.542	0.568	-0.026
3	1.050	1.033	0.017	0.762	0.806	-0.044
4	1.437	1.654	-0.217	1.173	1.238	-0.066
5A	2.022	2.099	-0.077	1.742	1.582	0.160
5B	1.991	2.099	-0.108	1.537	1.582	-0.045
6	2.456	2.522	-0.066	2.280	2.171	0.110
7	0.290	0.320	-0.030	0.130	0.181	-0.051
8	0.340	0.579	-0.240	0.211	0.377	-0.166
9	0.581	0.787	-0.206	0.438	0.541	-0.103
10	1.096	1.232	-0.136	0.771	0.943	-0.172
11	1.625	1.672	-0.047	1.419	1.451	-0.032
12	1.503	1.564	-0.060	1.544	1.471	0.073
13	0.174	0.333	-0.159	0.079	0.163	-0.084
14	0.445	0.506	-0.061	0.216	0.348	-0.132
15	0.636	0.664	-0.028	0.424	0.558	-0.134

†Test No. 10; ‡Test No. 8; at the overtopping WSL (η_r = 400mm) for the drain/dry configuration there was seepage from the upstream impoundment, therefore steady-state tests were not conducted

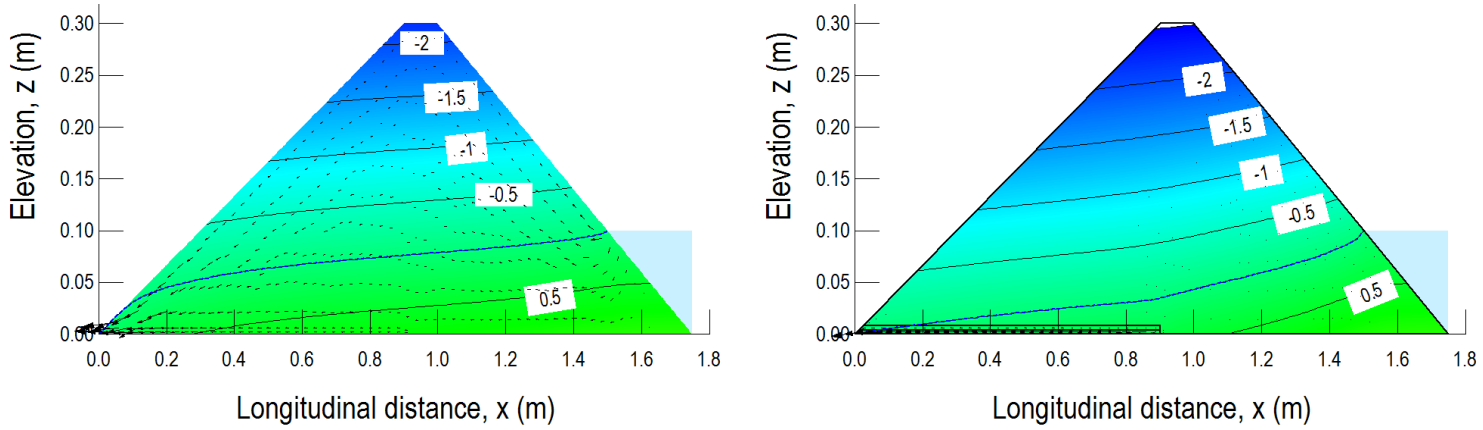

Figure F-4: Steady-state numerical simulations using SEEP/W showing phreatic surface, PWP and velocity vectors at η_r = 100mm (left) no drain (maximum discharge velocity = 5.1 x 10^{-5} m/s) (right) drain (maximum discharge velocity = 6.9 x 10^{-4} m/s)

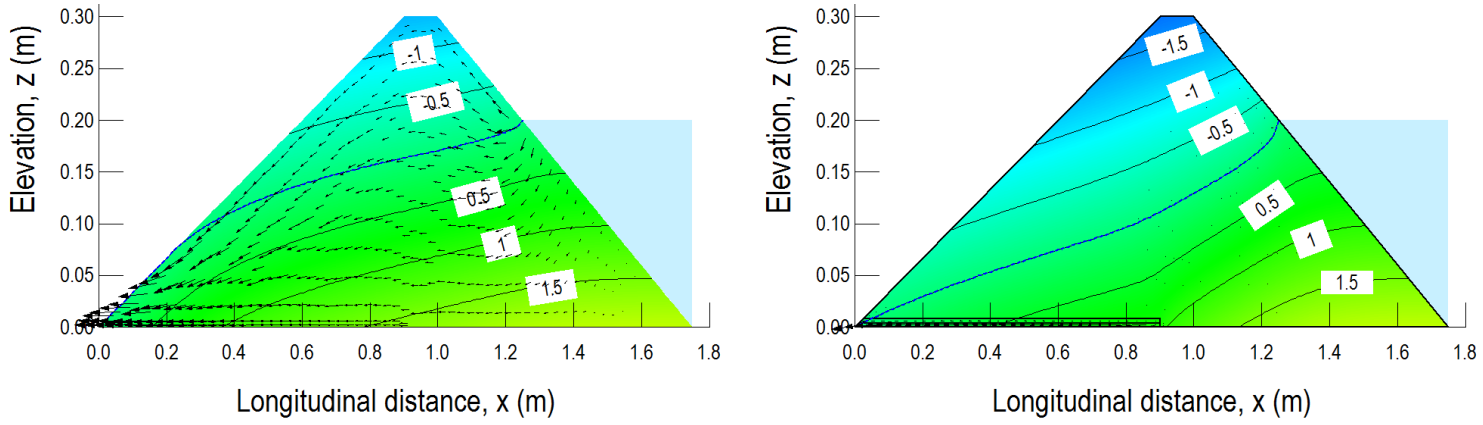

Figure F-5: Steady-state numerical simulations using SEEP/W showing phreatic surface, PWP [kPa] and velocity vectors at η_r = 200mm (left) no drain (maximum discharge velocity = 5.1 x 10^{-5} m/s) (right) drain (maximum discharge velocity = 2.0 x 10^{-3} m/s)

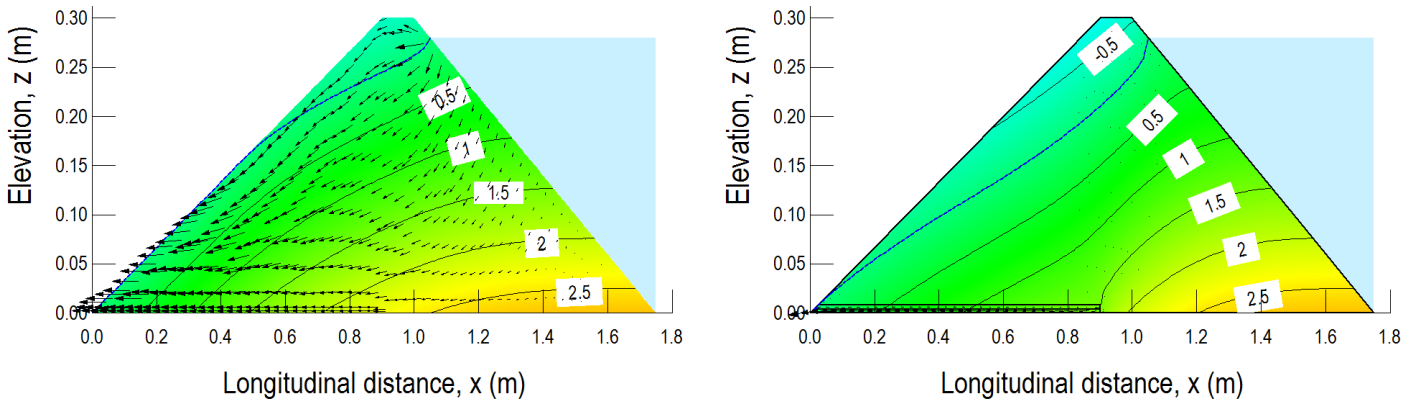

Figure F-6: Steady-state numerical simulations using SEEP/W showing phreatic surface, PWP [kPa] and velocity vectors at η_r = 280mm (left) no drain (maximum discharge velocity = 5.5 x 10^{-5} m/s) (right) drain (maximum discharge velocity = 3.6 x x10^{-3} m/s)

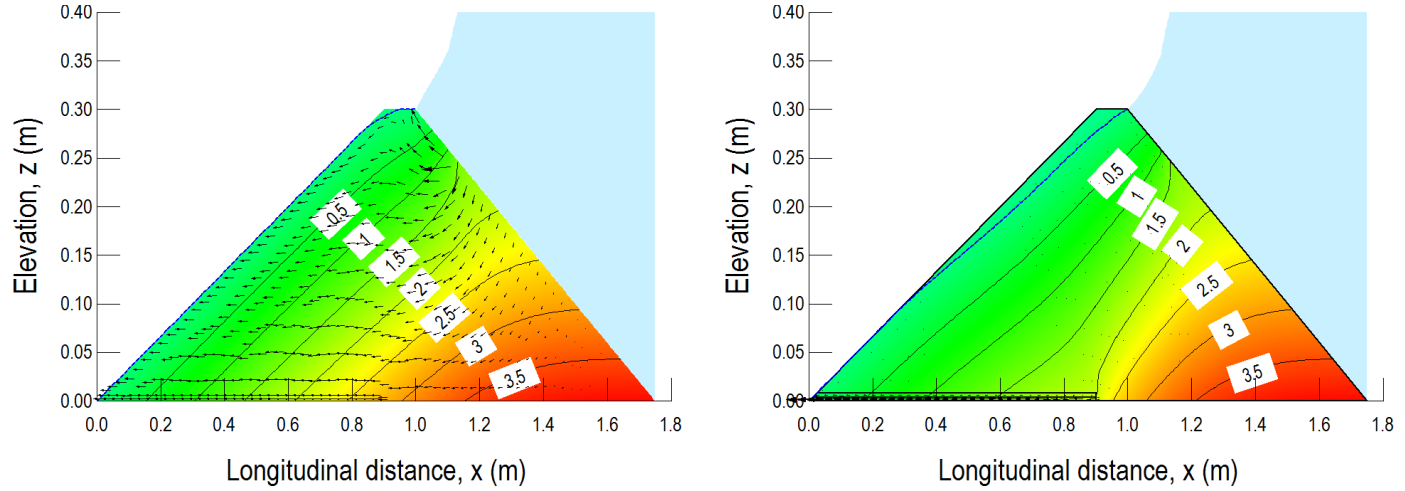

Figure F-7: Steady-state numerical simulations using SEEP/W showing phreatic surface, PWP [kPa] and velocity vectors at η_r = 400mm (left) no drain (maximum discharge velocity = 1.5 x 10^{-4} m/s) (right) drain (maximum discharge velocity = 3.9 x 10^{-3} m/s)

F.2 PWP Measurements in Falling Head Tests

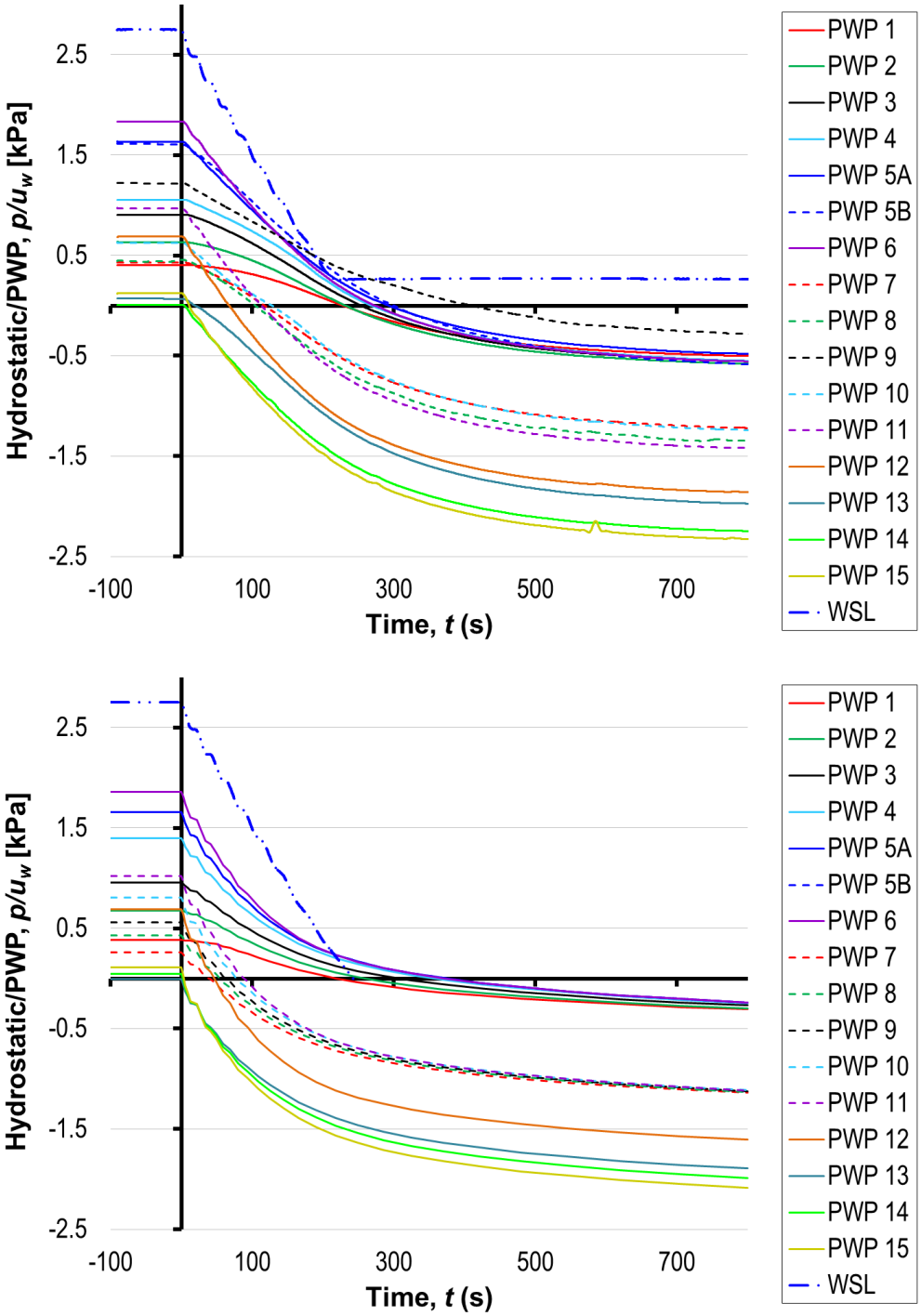

Figure F-8: Comparison of falling head simulations for embankment model without drain between (above) experimental (Test No. 10; WSL not captured below 3cm by wave gauge) (below) numerical (SEEP/W)

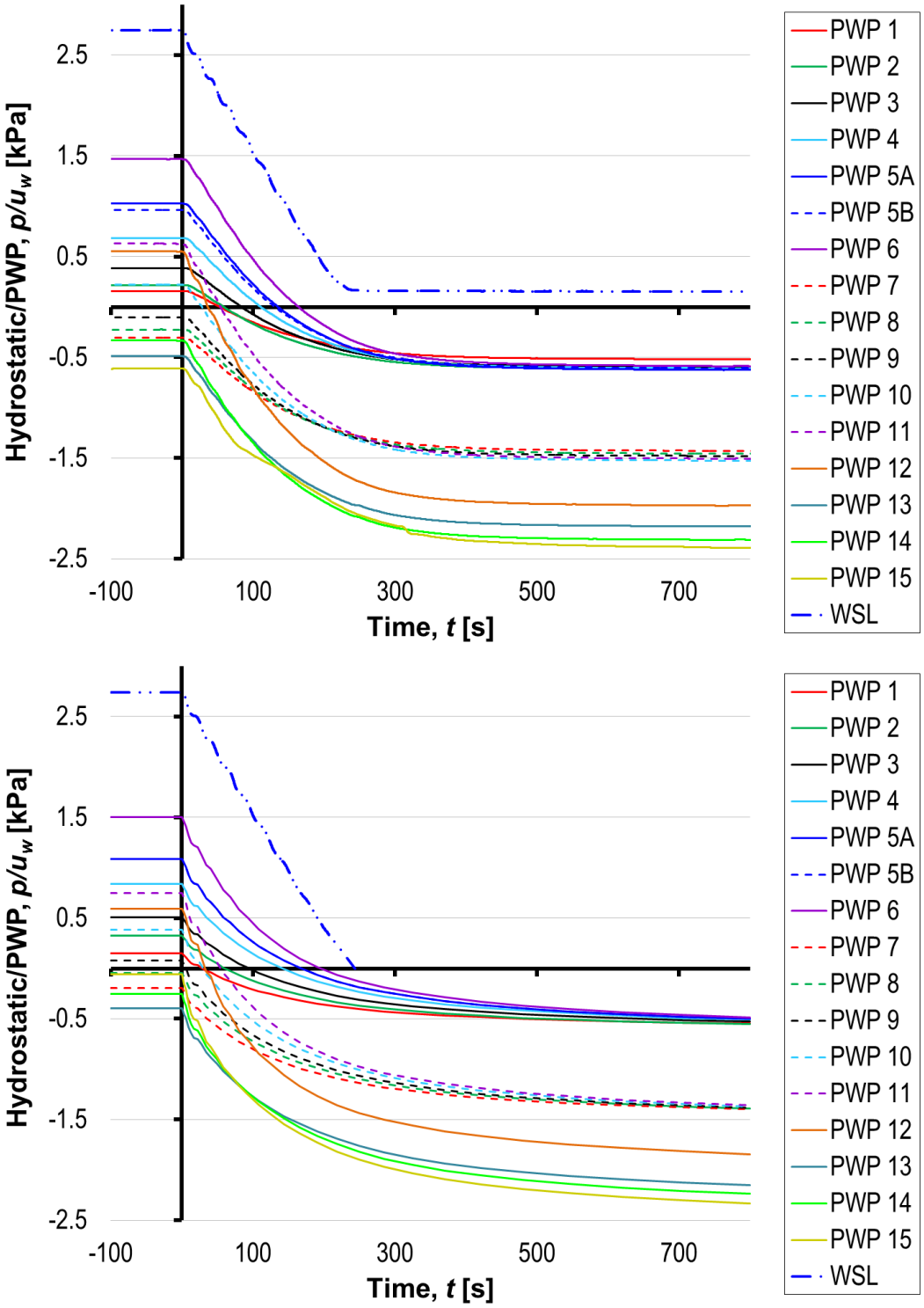

Figure F-9: Comparison of falling head simulations for embankment model with drain between (above) experimental (Test No. 8; WSL not captured below 3cm by wave gauge) (below) numerical (SEEP/W)

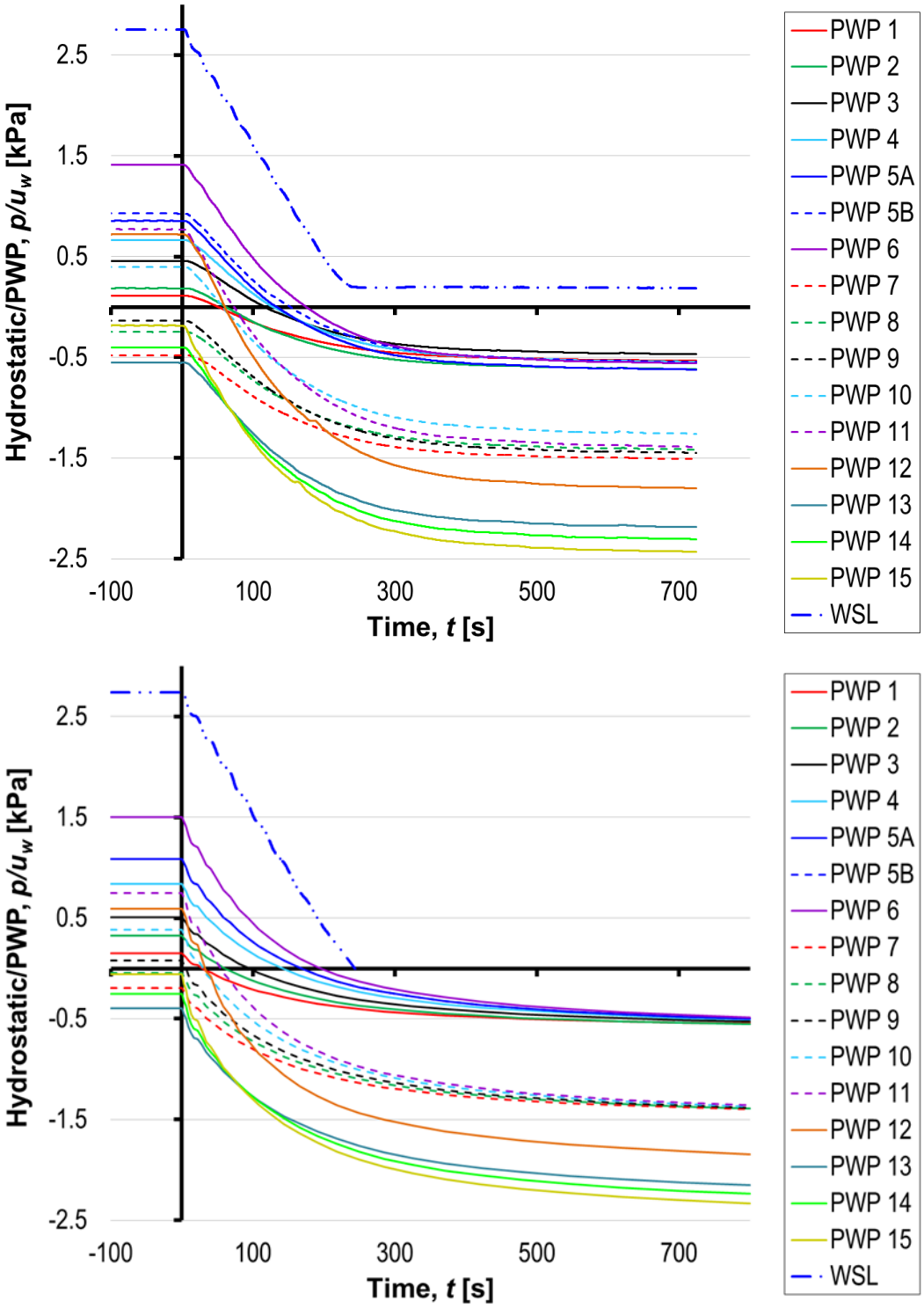

Figure F-10: Comparison of falling head simulations for embankment model with drain-dry configuration between (above) experimental (Test No. 13; WSL not captured below 3cm by wave gauge) (below) numerical (SEEP/W)

F.3 PWP Measurements in 2-D Overtopping Tests

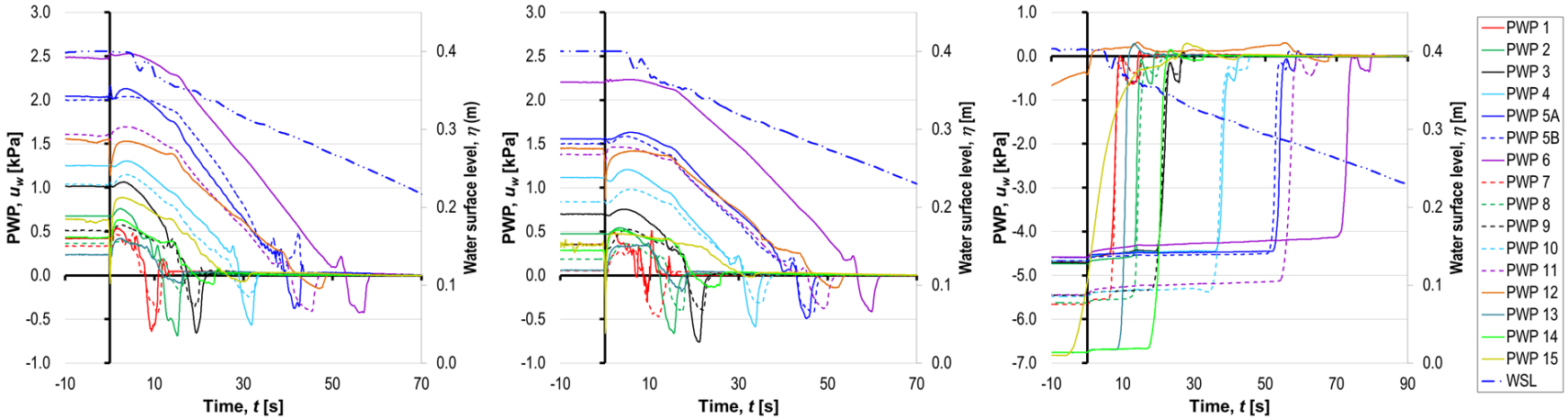

Figure F-11: Transient PWP measurements due to overtopping flow in three embankment model configurations (left) no drain (middle) with drain (right) drain-dry

F.4 Water Surface and Bed Profiles in 2-D Overtopping Tests

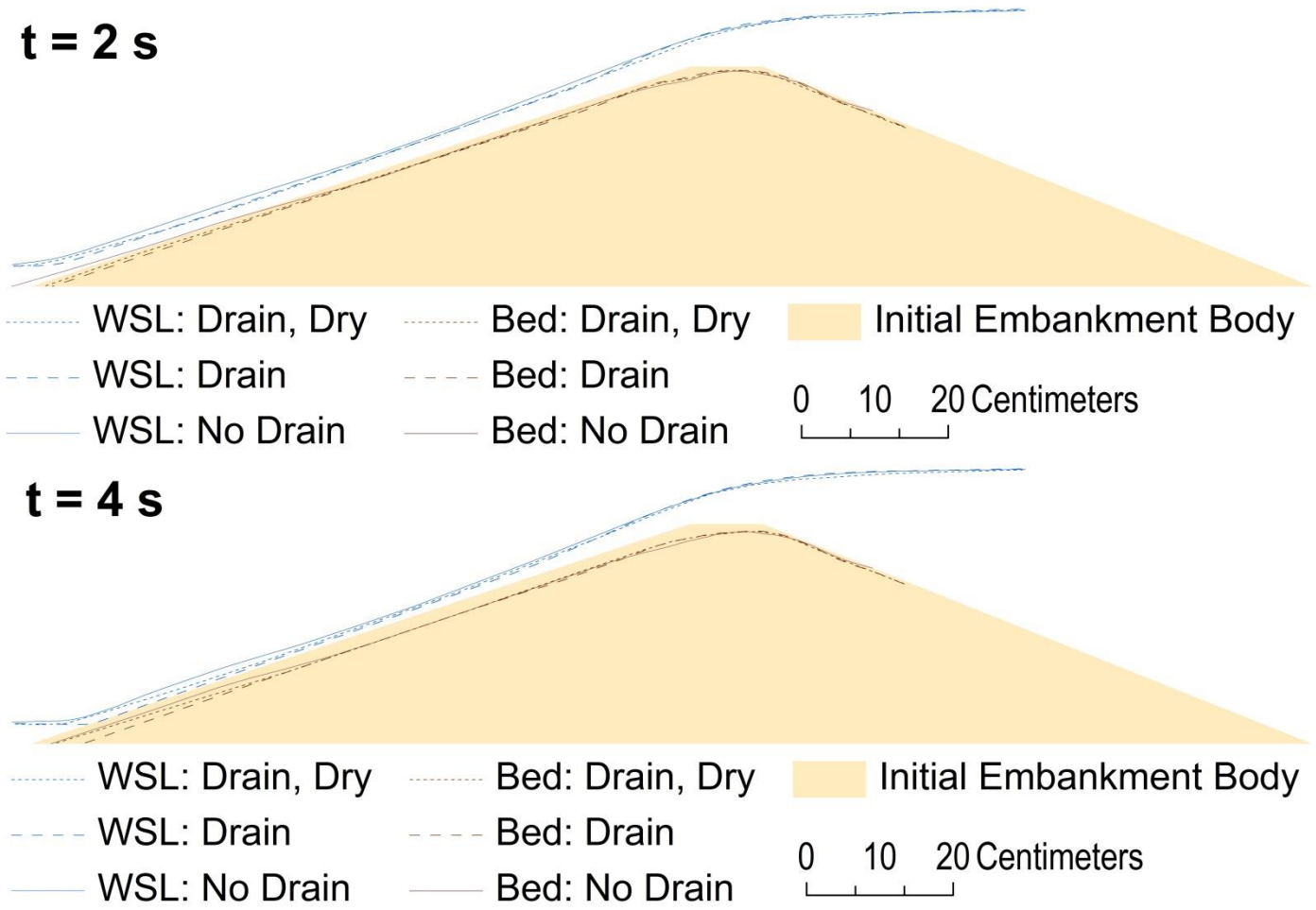

Figure F-12: Water surface and bed profiles for three embankment configurations after (above) 2s (below) 4s

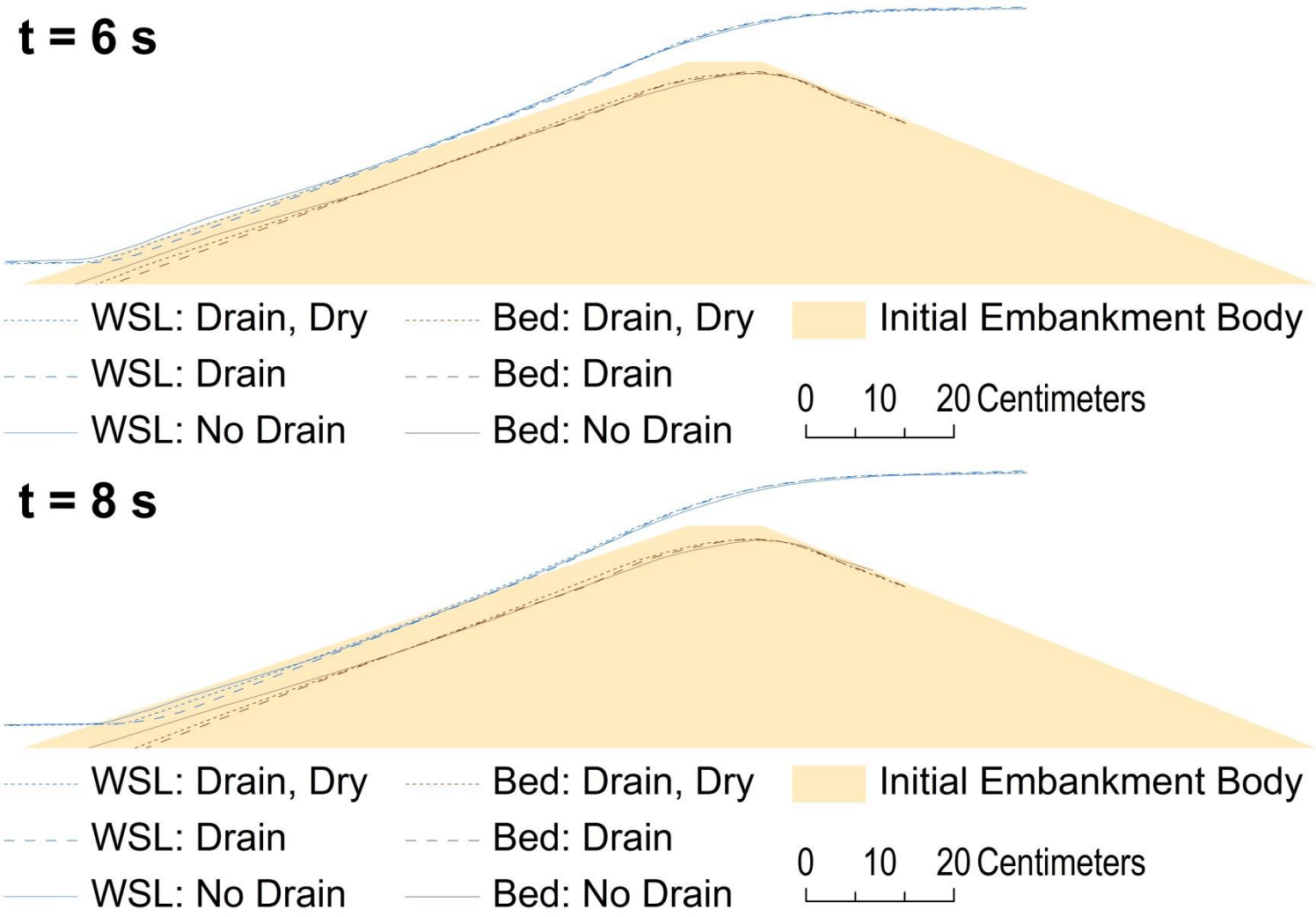

Figure F-13: Water surface and bed profiles for three embankment configurations after (above) 6s (below) 8s

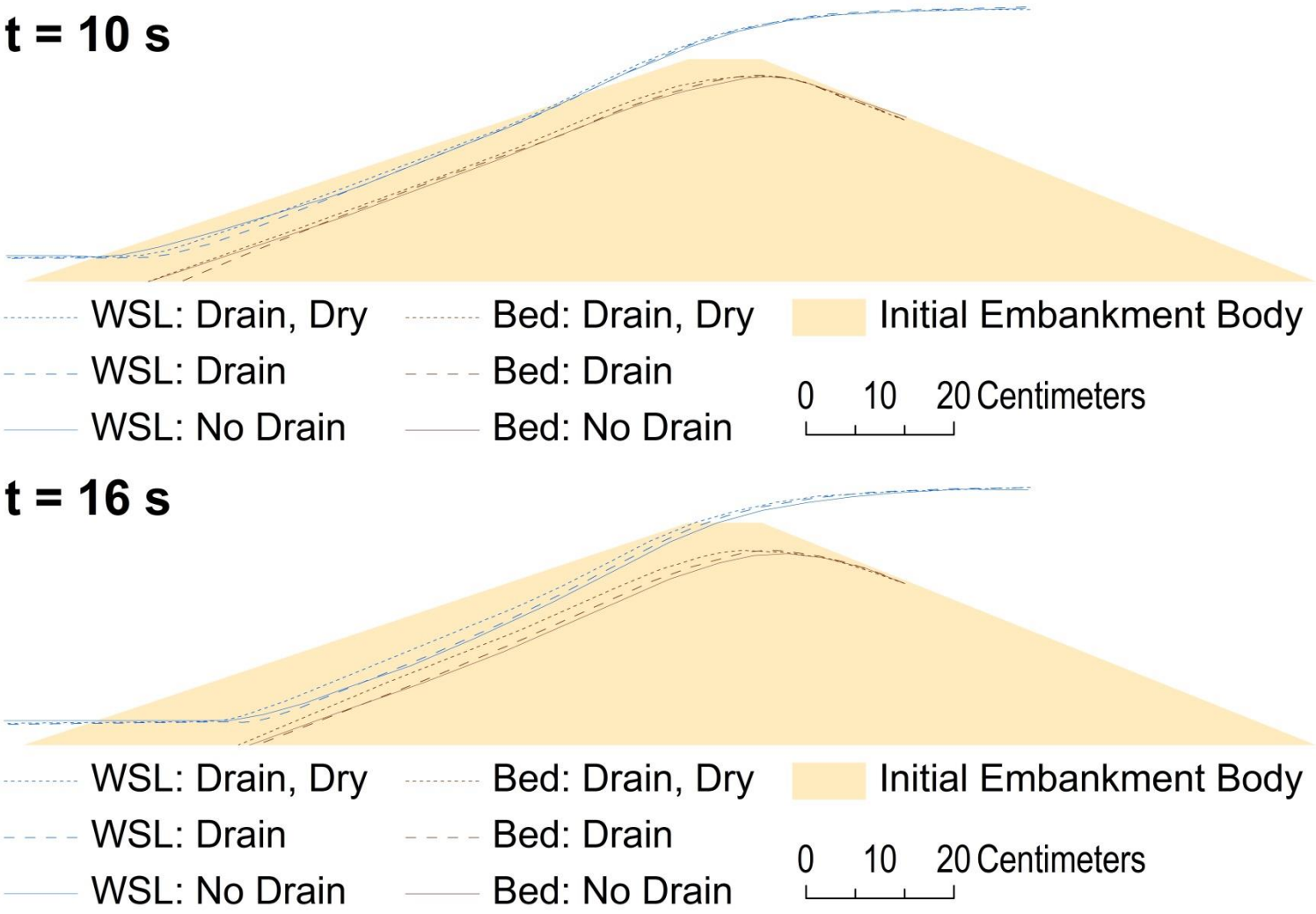

Figure F-14: Water surface and bed profiles for three embankment configurations after (above) 10s (below) 16s

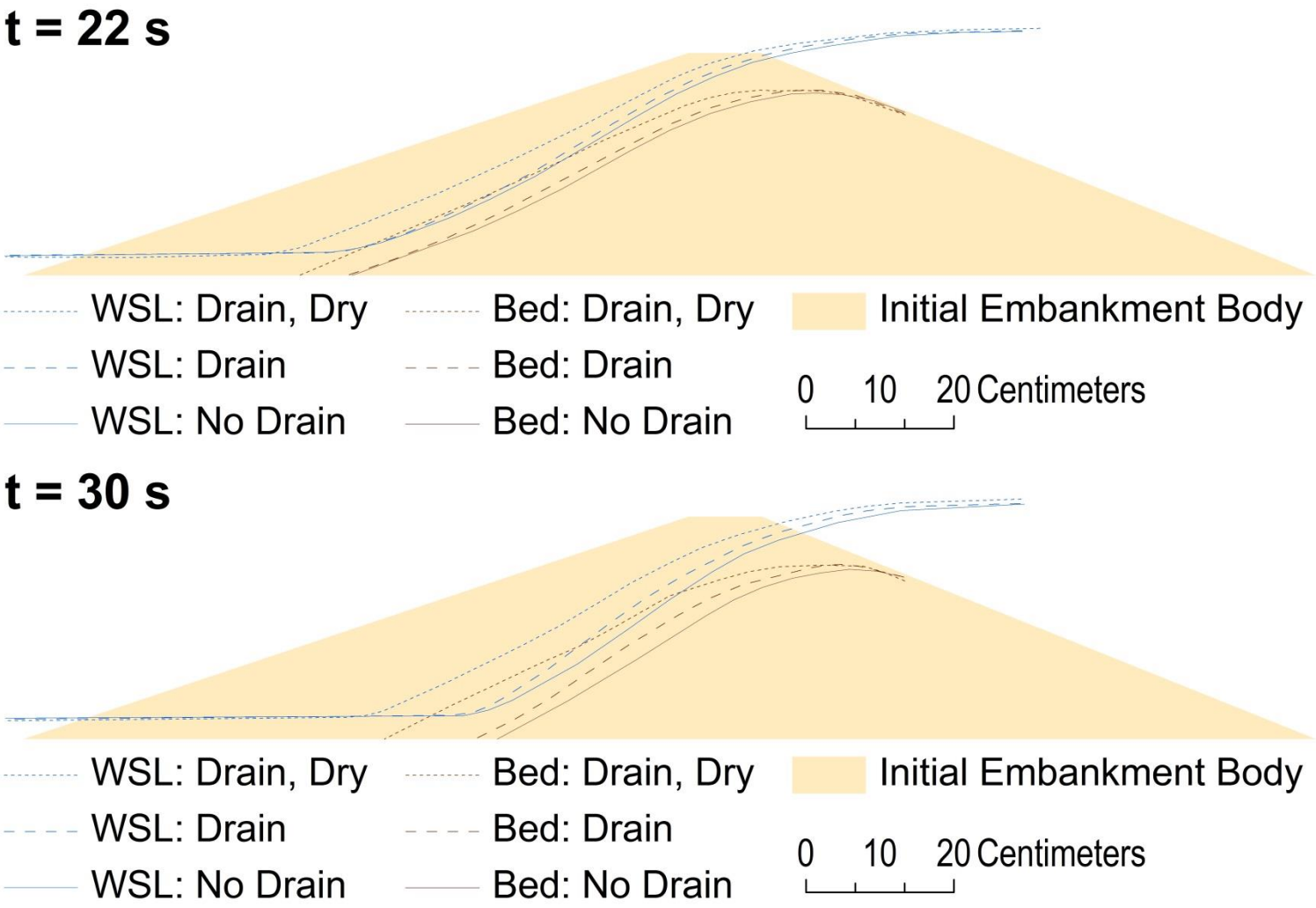

Figure F-15: Water surface and bed profiles for three embankment configurations after (above) 22s (below) 30s